Novel Fluorination Methodology Through Computational Insight – Tuning Fluoride Through Hydrogen Bonding

A thesis submitted to the Board of the Faculty of Physical Sciences, in partial fulfilment of the requirements for the degree of Doctor of Philosophy at the University of Oxford

David M. H. Ascough

Wadham College

University of Oxford

Trinity 2019

“If you cannot explain something in simple terms, you don’t understand it”

Attributed to R. Feynman, A. Einstein and several others… does it really matter who? A quote I agree with, regardless of the source, and something I bear in mind every time I teach, and every time I hear someone make something sound more complicated than necessary.

Author's Declaration

The work presented in this thesis was conducted under the supervision of Prof. Véronique Gouverneur and Prof. Robert Paton at the Department of Chemistry, University of Oxford. All of the work is my own, unless otherwise stated, and has not been submitted for any other degree at this or any other university.

David M. H. Ascough

August 2019

Table of Contents

Abstract

Even though carbon-fluorine bonds are uncommon in nature, fluorination of organic molecules is well-known to induce desirable biological properties. Methods for fluorination are therefore highly sought after; however, one of the most convenient sources of fluorine, inorganic fluoride salts, are inconvenient reagents. Inspired by the fluorinase enzyme's binding of fluoride through hydrogen bonding, this work describes the computational investigation of the effects of hydrogen bonding on fluoride reactivity and selectivity, in collaboration with experimental chemistry, to develop novel catalytic methods for asymmetric fluorination of organic molecules with simple fluoride reagents.

Chapter 1 summarizes the current state of the art for using fluoride as a reagent for fluorination of organic molecules. Computational methods and challenges in modeling such systems are also described. Chapter 2 describes the study and rationalization of experimental data on the effect of hydrogen bond donor strength on the reactivity and selectivity of urea-fluoride complexes as reagents in a model S_N2 vs E2 reaction with primary bromide substrate. This chapter also describes benchmarking of computational methods for accurate description of fluoride. Chapter 3 describes the development of hydrogen bonding phase-transfer catalysis (HB PTC) and its application to asymmetric fluorination with group 1 metal fluoride salts and chiral urea organocatalyst, including mechanistic study and computationally guided catalyst design. Chapter 4 describes the application of HB PTC to asymmetric desymmetrization of aziridinium ions. Computation yields insight into the origins of enantioselectivity and the activation of potassium fluoride as fluoride source. The final chapter discusses the computational insight into the effects of hydrogen bonding on fluoride, including consequences for enantioselectivity and catalytic kinetics.

Acknowledgements

I would like to thank my DPhil supervisors, Véronique and Rob for their support, supervision and guidance over the last three years. I first met Véronique nearly nine years ago for my undergraduate interviews at Merton. Back then, I knew very little chemistry! Throughout my undergraduate and then postgraduate degrees, Véronique has been one of the few constants, as everything else has changed. I would like to thank her for her advice and mentorship over the years – I remember distinctly that it was through a conversation with her, a few years ago, that I decided to pursue computational chemistry. I joined Rob's group at the beginning of my DPhil, when I began on this project. I am still amazed by the depth and breadth of his knowledge in chemistry; how he can be the expert in the room during every meeting with collaborators, with such diverse chemistry. It's unfortunate timing that Rob has moved to the US and I would like to thank the remainder of the Paton group, here in Oxford, for their support and friendship over the last year. Particular thanks goes to Nhu Nguyen, who has been an indispensable source of advice and guidance; someone without whom my publications would not be what they are. The Gouverneur group, of course, remains, and I would like to thank them for their input, support and friendship over the years. Particular thanks goes to those who have performed all of the synthesis interspersed in this thesis, particularly Francesco Ibba, Gabriele Pupo and Anna Vicini. This project would not have progressed so far without their efforts. A further mention goes to Alex Dürr, with whom I have had many valuable discussions over the last year or so.

On a different note, I would like to thank the SBM CDT – the format of the DPhil allowed me to try out, and eventually convert to, computational chemistry from a synthetic organic chemistry background. My life and prospects would be very different without it.

I would also like to thank my undergraduate college, Merton and my postgraduate college, Wadham for their support. Also, the benefactor who is funding my scholarship at Wadham through the SBM CDT.

I have had the privilege to teach many talented students at Merton as a Lecturer over the last four years. I would like to thank all those dedicated students who have brought much joy and amusement. It is partly to them that I dedicate the quote at the beginning of this thesis – many a time have I practiced explaining a concept to myself, only to realise that I didn't understand it as well as I thought. Sometimes this moment of enlightenment comes from expert student interrogation…

I would like to thank my family and friends. My family have been a constant source of support and encouragement over the years and I wouldn't be where I am today without them. Finally, I would like to thank my fiancée, Nhu, for too many things to write down. She is an infinite source of unconditional love and has helped guide me through the tough times over the last few years. She has opened up the world to me and is someone I have shared so many irreplaceable experiences with. Anh yêu em, Như.

Publications

Publications related to this work:

- *Asymmetric Nucleophilic Fluorination Under Hydrogen Bonding Phase-Transfer Catalysis,* G. Pupo*, F. Ibba*, **D. M. H. Ascough***, A. C. Vicini, P. Ricci, K. E. Christensen, L. Pfeifer, J. R. Morphy, J. M. Brown, R. S. Paton, V. Gouverneur *Science* **2018**, *360,* 638-642. https://science.sciencemag.org/content/360/6389/638

The reuse of material from this article is in accordance with the American Association for the Advancement of Science (AAAS) License to Publish.

- *Hydrogen Bonding Phase-Transfer Catalysis with Potassium Fluoride: Enantioselective Synthesis of β-Fluoroamines,* G. Pupo*, A. C. Vicini*, **D. M. H. Ascough**, F. Ibba, K. E. Christensen, A. L. Thompson, J. M. Brown, R. S. Paton, V. Gouverneur *J. Am. Chem. Soc.* **2019**, *141*, 2878-2883. https://pubs.acs.org/doi/10.1021/jacs.8b12568

The reuse of material from this article has been permitted, Copyright 2019 American Chemical Society (ACS). Permission for further reuse should be directed to the ACS.

- *Data-Mining the Diaryl(thio)urea Conformational Landscape: Understanding the Contrasting Behavior of Ureas and Thioureas with Quantum Chemistry*, G. Luchini, **D. M. H. Ascough**, J. V. Alegre-Requena, V. Gouverneur, R. S. Paton *Tetrahedron* **2019**, *75*, 697-702. https://doi.org/10.1016/j.tet.2018.12.033

The reuse of material from this article is permitted by Elsevier.

Other Publications:

- *Stereospecific 1,3-H Transfer of Indenols Proceeds via Persistent Ion-Pairs Anchored by NH•••π Interactions*, **D. M. H. Ascough**, F. Duarte, R. S. Paton *J. Am. Chem. Soc.* **2018**, *140*, 16740-16748.

- *Chemical Epigenetics: The Impact of Chemical- and Chemical Biology Techniques on Bromodomain Target Validation*, M. Schiedel, M. Moroglu, **D. M. H. Ascough**, A. E. R. Chamberlain, J. J. A. G. Kamps, A. R. Sekirnik, S. J. Conway *Angew. Chem. Int. Ed.* **2019**, *Accepted Article,* DOI: 10.1002/anie.201812164

- *Enantioselective Rhodium-Catalyzed Insertion of Trifluorodiazoethanes into Tin Hydrides*, S. Hyde, J. Veliks, **D. M. H. Ascough**, R. Szpera, R. S. Paton, V. Gouverneur *Tetrahedron*, **2019**, *75*, 17-25.

Abbreviations

Å	Ångström (1×10^{-10} M)
AIM	atoms in molecules
AO	atomic orbital
Ar	aryl
BACCA	bis-*tert*-alcohol-functionalized crown-6-calix[4]arene
BINAM	2,2′-Bis(amino)-1,1′-binaphthyl
bmim	1-butyl-3-methylimidazolium
Bn	benzyl, $C_6H_5CH_2$
BO	Born–Oppenheimer
BTC5A	bis-triethylene glycolic crown-5-calix[4]arene
CBS	complete basis set
CC	coupled cluster
CCSD	coupled cluster singles doubles
CCSD(T)	coupled cluster singles doubles perturbative triples
CI	configuration-interaction
COSMO	conductor-like screening model
CPCM	conductor-like polarizable continuum model
DAST	diethylaminosulfur trifluoride
DCM	dichloromethane
DFB	1,2-difluorobenzene
DFT	density functional theory
DI-AS	distortion/interaction-activation strain method
DLPNO	domain-based local pair natural orbital
DMPU	*N,N'*-dimethylpropyleneurea
DMSO	dimethyl sulfoxide
DNA	deoxyribonucleic acid
E2	elimination, bimolecular
ECP	effective core potential
EDA	energy decomposition analysis
ee	enantiomeric excess
er	enantiomeric ratio
Et	ethyl
fs	femtosecond
GGA	generalized gradient approximation
GIAO	gauge-independent atomic orbital
HB	hydrogen bond
HB PTC	hydrogen bonding phase-transfer catalysis
HF	hydrogen fluoride
HFT	Hartree–Fock theory
HFIP	hexafluoroisopropanol
HOMO	highest occupied molecular orbital
iPr	isopropyl
IR	infra-red
IRC	intrinsic reaction coordinate
IUPAC	International Union of Pure and Applied Chemistry
LCAO	linear combination of atomic orbitals
LDA	local density approximation
LFER	linear free energy relationship
LINCS	linear constraint solver algorithm
LUMO	lowest unoccupied molecular orbital
MD	molecular dynamics

Me	methyl
mGGA	meta-generalized gradient approximation
MM	molecular mechanics
MMFF	Merck molecular force field
MO	molecular orbital
Ms	mesylate, methanesulfonate
NBO	natural bond orbitals
NCI	non-covalent interaction
NFSI	*N*-fluorobenzenesulfonimide
NMR	nuclear magnetic resonance
NPA	natural population analysis
NPT	ensemble at constant number, pressure and temperature
ns	nanosecond
NVT	ensemble at constant number, volume and temperature
OPLS	optimized potential for liquid simulations
PBC	periodic boundary condition
PES	potential energy surface
PET	positron emission tomography
Ph	phenyl group
Piv	pivalate, COO^tBu
PMB	*para*-methoxybenzyl
Pr	propyl
ps	picosecond
PT	phase-transfer
PTC	phase-transfer catalysis
QM	quantum mechanics
RESP	restrained electrostatic potential
RMSD	root-mean squared deviation
RT	room temperature, 298.15 K
SAM	*S*-adenosyl methionine
SCF	self-consistent field
SCRF	self-consistent reaction field
SM	starting material
SMD	solvation model based on density
S_N2	substitution, nucleophilic, bimolecular
TBA	tetrabutylammonium
TBAB	tetrabutylammonium bromide
TBAF	tetrabutylammonium fluoride
TBAT	tetrabutylammonium (triphenylsilyl)difluorosilicate
TBS	$^tBuMe_2Si$
TCA	trichloroacetimidate
TDI	turnover frequency determining intermediate
TDTS	turnover frequency determining transition state
Tf	triflate, trifluoromethanesulfonate
TMAF	tetramethylammonium fluoride
TOF	turnover frequency
TS	transition state structure
TST	transition state theory
VDW	van der Waals
WFT	wave function theory
ZPE	zero-point energy

1 Introduction

1.1 The Significance of Fluorine

Fluorine is the lightest of the halogens, located at the top of group 17 in the periodic table, with atomic number 9. It has an estimated abundance in the Earth's continental crust of 525 ppm, making it approximately the 15th most abundant element, though estimates vary.[1] Despite this, fluorine is rarely found incorporated into organic natural products, with an estimated ~5-15 isolations;[2–5] a figure obscured by misidentifications, such as through contamination with synthetic fluorinated compounds.[6,7] This is in contrast to the rest of the halogens, with more than 5000 halogenated natural products known in total,[8] including over 110 iodinated metabolites despite iodine's low abundance.[9] A plausible explanation for the dearth of organofluorine compounds is the low solubility of naturally occurring inorganic fluoride salts, and that the process of incorporating fluorine into an organic molecule using an inorganic fluoride source is challenging. Only one natural enzyme, the fluorinase, is known to synthesize a carbon-fluorine bond in nature.[10]

In contrast to the lack of fluorinated natural products, fluorine is well-known to impart desirable biological properties on organic molecules, such as by improving affinity, efficacy, metabolic properties and modulating lipophilicity and pKa.[11–17] Approximately 25 % of drugs[18] and 25 % of agrochemicals[19] contain at least one fluorine atom. Over 150 fluorinated drugs have been approved to date, on an upward trajectory that's set to continue, with approximately 40 % of pharmaceuticals entering phase III clinical trials containing organic fluorine.[20] Fluorine may be incorporated into pharmaceuticals in one of many functional groups, including a fluorine atom itself (aliphatic or aromatic), the difluoromethyl group and the trifluoromethyl group, each with a unique set of properties (Figure 1.1). The prevalence of fluorine in medicinal chemistry may also be attributed to

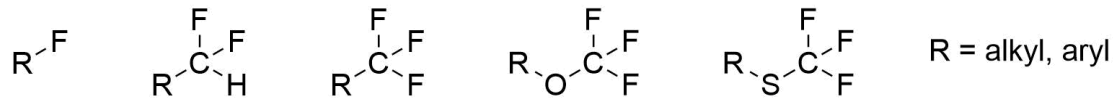

Figure 1.1: Common fluorinated motifs.

the fact that it can act as an (bio)isostere for common functional groups, such as hydrogen and hydroxyl, meaning that a molecule may be fluorinated without significantly changing its steric properties.[21] More exotic (bio)isosteres include replacement of an amide for an α,α-difluoro ketone,[22] ketones for a C–F bond, and enols for alkenyl fluorides.[23] Chemical methods for the conversion of abundant "inorganic fluorine" to "organic fluorine" are therefore highly sought after.[24–26]

The remarkable effects of fluorine on molecules ultimately stems from the properties of the element itself. Fluorine is the most electronegative element, with a Pauling electronegativity of 3.98. Fluorine is also one of the smallest elements, with a covalent radius of 50-60 pm,[27,28] behind only hydrogen and helium, due to a low number of electron shells (valence electrons have principal quantum number of 2) and high effective nuclear charge. Its anionic form, fluoride, has a charge of -1, formed by gaining a single electron with electron affinity second only to chlorine,[29] and is the smallest singly charged anion with ionic radius of 117 pm and 119 pm for four-coordinate and six-coordinate fluoride respectively.[30] The small radius of fluoride results in the anion having one of the highest anionic charge densities, 24 C/mm^3, despite carrying only a single negative charge.[31] This is exceeded by the oxide, O^{2-} (40 C/mm^3), and nitride, N^{3-} (50 C/mm^3), anions however the extreme basicity of these ions means they are rarely encountered in solution. The charge density of fluoride greatly exceeds that of chloride (8 C/mm^3) and multiply charged anions such as phosphide, P^{3-} (14 C/mm^3), and sulfide, S^{2-} (16 C/mm^3). Fluoride therefore is highly hydrophilic, with a hydration enthalpy of

515 kJ/mol,[32] and forms salts with high lattice energies, such as its naturally occurring form, fluorite, CaF_2, with lattice energy of 2640 kJ/mol.[29] Fluoride forms strong hydrogen bonds, and when uncoordinated, is highly basic with pK_{aH} = 3.2 in water and 15 in dimethyl sulfoxide (DMSO).[33]

When incorporated into organic molecules, the properties of fluorine change dramatically. The carbon-fluorine bond is the strongest single bond to carbon, with bond dissociation energy of 460 kJ/mol in fluoromethane.[34] Perfluorocarbons, most notably poly(tetrafluoroethylene) (Teflon), are renowned for their inertness to chemical attack and their thermal stability.[35] The strength of the C–F bond is the primary reason behind fluorine's high metabolic stability, although there are certain structural motifs that may be susceptible to metabolism.[36] The C–F bond also has a strong dipole moment due to the large electronegativity difference. Despite this, fluorine substitution is often associated with lipophilicity.[37] Mono-, or di- substitution of aliphatic chains often decreases lipophilicity due to the polarity of the bond, whereas aromatic fluorination increases lipophilicity due to the bond's non-polarizable nature.[38] Organic fluorine is generally a poor hydrogen bond acceptor in contrast to its anionic form.[39] Fluorine can also alter lipophilicity indirectly, for example by lowering amine basicity, or through conformational effects.[12,13]

1.2 Fluorination Methods and Reagents

Due to the ubiquity of fluorine in high-value molecules, developing novel methods for fluorination has been actively pursued. Besides radical fluorination,[40,41] these methods can be divided into two classes – those that use electrophilic sources of fluorine and those that use nucleophilic sources of fluorine. The former are formal sources of "F^+", including F_2 itself, and have established an exquisite toolbox of bench-stable electrophilic

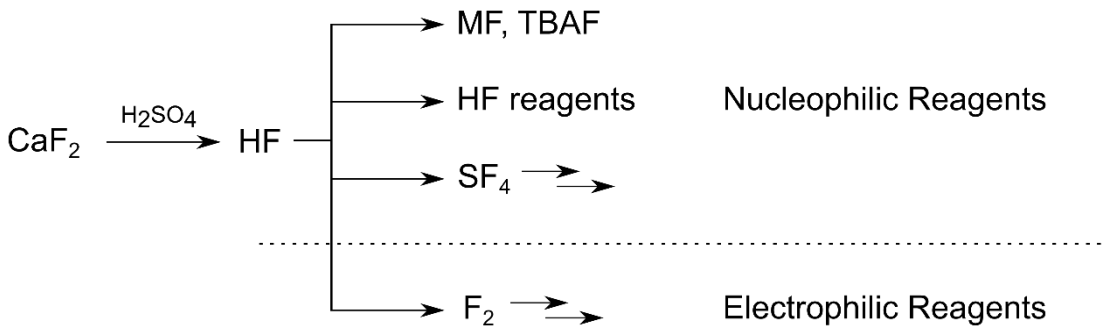

Figure 1.2: Tracing the origins of fluorine. All fluorine is ultimately derived from fluorite, with varying degrees of processing. Data from Harsanyi and Sanford. Ref 42.

fluorinating reagents. The latter are formal sources of "F^-", including the F^- anion itself, which are generally cheap, abundant and easy to handle, however use of fluoride for fluorination is not as trivial as it first appears. All fluorinating reagents are ultimately derived from fluorite (CaF_2) with varying degrees of processing[42] – use of fluorite directly is a holy grail of fluorination chemistry (Figure 1.2).

Whilst most syntheses incorporate fluorine by using fluorinated starting materials,[24] thereby avoiding the need for a fluorination step, there is high demand for late-stage fluorination methods for incorporating fluorine into an already elaborated molecule.[43] Such techniques can be useful in medicinal chemistry where an intermediate can be diversified by fluorination at various positions, without having to repeat the whole synthesis. An application where late-stage fluorination is essential is for ^{18}F positron emission tomography (PET).[44,45] PET is a medical imaging technique used to aid diagnosis and requires injection of a patient with a radionuclide labelled tracer molecule. The radionuclide is a positron emitter, most commonly ^{18}F, which allows location of the PET tracer in the body from coincident gamma rays emitted by positron-electron annihilation events. Due to the relatively short half-life of ^{18}F of 110 minutes, the radioisotope must be incorporated, late-stage, into an already elaborated tracer molecule,

before purification and administration to the patient. Due to the high synthetic demands of such a procedure, the (in)ability to synthesize PET tracers is a current limitation to research.[46]

The following sections outline common reagents and reactions for fluorination, with particular focus on methods suitable for asymmetric fluorination.

1.2.1 Electrophilic Fluorination

Electrophilic fluorination uses reagents that act as sources of "F^+" – the simplest of which is $F_{2\,(g)}$ – but this is notoriously hazardous, reactive and unselective, with few facilities in the world able to handle it. $F_{2\,(g)}$ can, however, be used to derive alternative electrophilic fluorinating reagents with improved properties. XeF_2 retains high reactivity, however as a white solid it is easier to handle and doesn't require specialist facilities.[48] A major class of reagents contain an N–F bond,[49] including *N*-fluoropyridinium salts,[50,51] Selectfluor™ [52,53], Synfluor™ [54] and *N*-fluorobenzenesulfonimide (NFSI)[55] (Figure 1.3). Such reagents

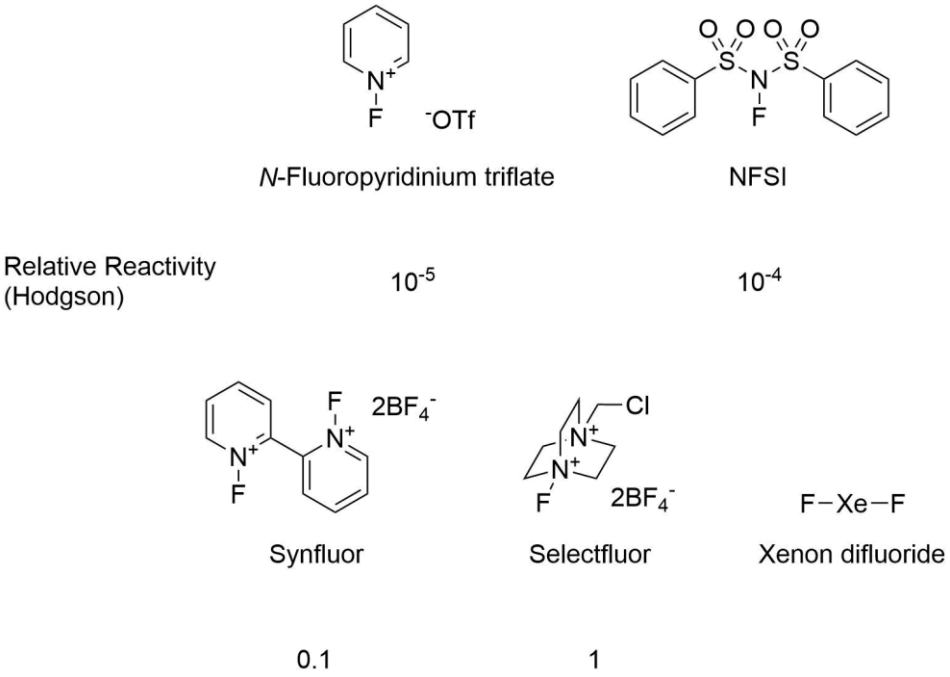

Figure 1.3: Common electrophilic fluorinating reagents, with their relative reactivity as determined by Hodgson and co-workers, Ref 47.

are surprisingly safe and easy to handle, being bench stable and commercially available and have been successfully applied to asymmetric fluorination. The scaffold supporting the "F^+" provides a means of controlling reactivity, which may be quantified by redox potentials, or through kinetic experiments. Whilst such reagents represent a source of "F^+", reactions may also proceed via a radical pathway. Selected electrophilic fluorination reactions are summarized in Scheme 1.1. Successful fluorination reactions have also been achieved with electrophilic fluorine sources under ion pairing catalysis, notably by Maruoka and Toste (see section 1.4).

Electrophilic fluorinating reagents, however, are often fine chemicals, with many step syntheses from natural resources and often have poor atom economy, with a significant

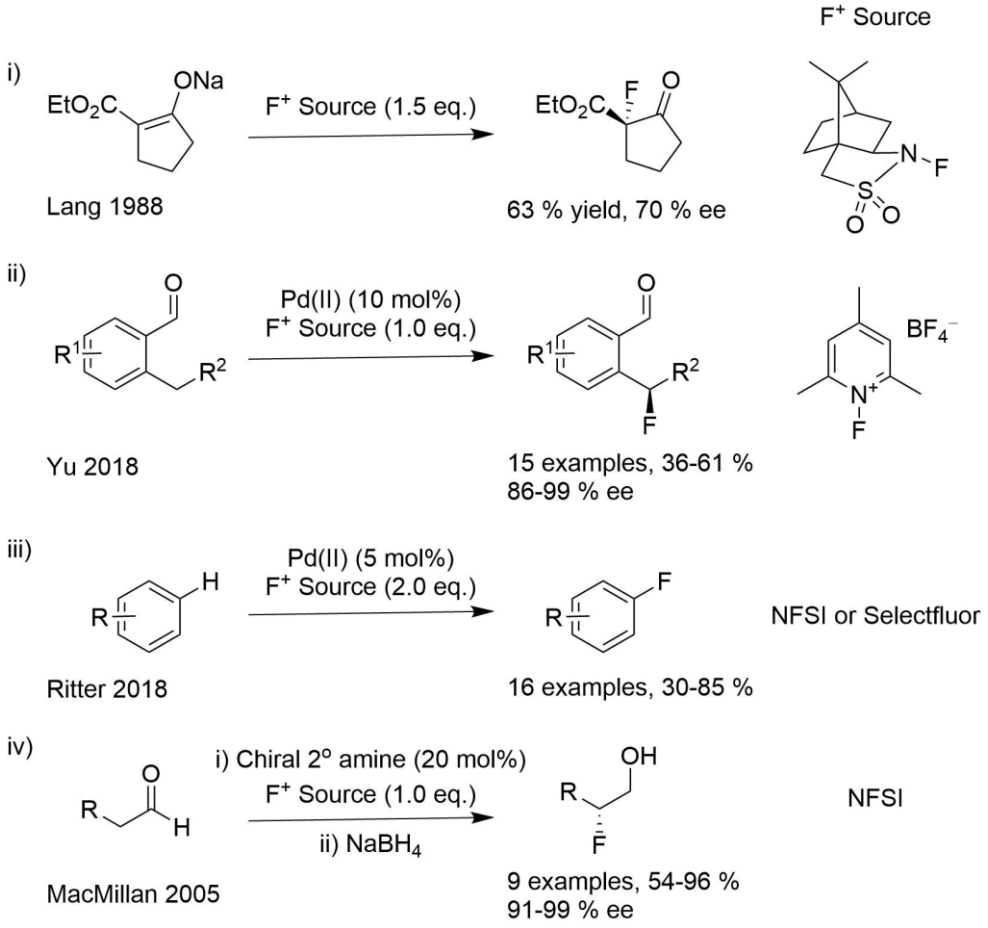

Scheme 1.1: Selected fluorination reactions involving electrophilic fluorinating reagents. i) First enantioselective fluorination reaction[56] ii) enantioselective Pd(II) catalyzed benzylic C–H fluorination[57] iii) Pd(II) catalyzed aromatic C–H fluorination[58] iv) enantioselective organocatalyzed α-fluorination of aldehydes.[59]

organic scaffold to support a single fluorine atom. Nucleophilic fluorination has an inherent advantage in this regard – using simple fluoride salts is appealing, whereas using simple $F_{2\,(g)}$ is not.

1.2.2 Nucleophilic Fluorination

1.2.2.1 Reactivity of Fluoride

Nucleophilic fluorination uses sources of "F^-", for creation of a carbon-fluorine bond. Reagents include inorganic fluoride salts and hydrogen fluoride (HF), as well as more specialist reagents such as diethylaminosulfur trifluoride (DAST) for deoxyfluorination.[60] Fluoride is a charge dense ion, due to its small ionic radius, and as such, it is strongly coordinating. Once fluoride is in solution, its reactivity and selectivity profile is highly sensitive to its coordination environment. When strongly solvated, particularly by hydrogen bond donating solvents, fluoride becomes unreactive, as reaction would involve breaking one or more of the strong interactions with the solvent. Conversely, when poorly solvated or in gas phase, fluoride is highly basic, favoring elimination reactions over substitution, making incorporation of fluorine into a molecule challenging.[61–65]

1.2.2.2 Hydrogen Fluoride

Hydrogen fluoride (HF), forming hydrofluoric acid in aqueous solution, is a nucleophilic fluorinating reagent, readily soluble in a variety of solvents.[66] This reagent has excellent atom economy, with 95 % of the reagent mass in the fluorine atom, and the realistic possibility that the hydrogen atom may also be incorporated. Hydrogen fluoride is a weak acid, with pKa of 3.17 in water,[33] comparable to that of a carboxylic acid rather than other hydrogen halides, testament to the charge density of the conjugate base, fluoride.[67] HF is highly toxic and hazardous, readily penetrating tissue and causing severe burns due to

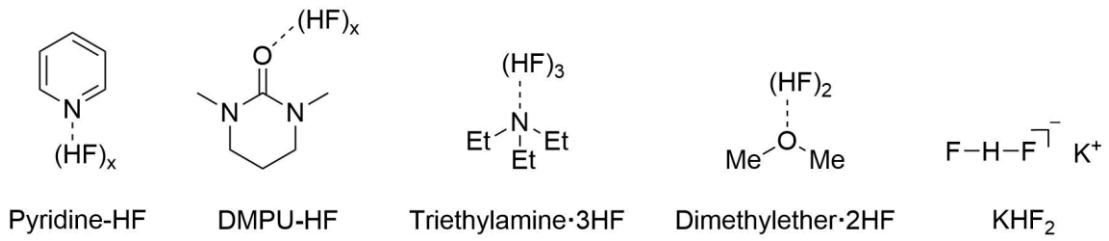

Figure 1.4: Hydrogen fluoride-based reagents for nucleophilic fluorination.

fluoride content, rather than acidity, with risk increased by the volatility of the reagent. HF sequesters calcium ions the body, potentially causing cardiac arrest.[68] As a result of these hazards, multiple hydrogen fluoride reagents have been developed, not just to reduce toxicity and increase ease of handling, but also to allow tunability of the reagent. Tunability, however, is far more challenging than with electrophilic reagents. Examples of HF reagents include pyridine-HF (Olah's reagent),[69] DMPU-HF,[70] triethylamine•3HF,[71] dimethylether•2HF,[72] KHF_2. (Figure 1.4). These reagents have enjoyed much success, however do not fully negate the drawbacks of HF and may reduce advantages such as atom economy.

1.2.2.3 Reagents Containing the Fluoride Ion

Inorganic fluoride salts are bench-stable, easy to handle, abundant and cheap, and therefore appear the obvious choice of fluorination reagent. However, their use is hindered by high lattice energies, low solubility in organic solvents and reactivity/selectivity problems depending on the degree of solvation of the fluoride anion, typically requiring harsh conditions (*vide supra*). The low solubility of inorganic fluoride salts can largely be attributed to the high lattice energies of the salts which cannot be overcome by solvation. This is typical for organic solvents (particularly aprotic solvents) where the solvation of the fluoride is poor. Alternative fluoride sources, designed to overcome the drawbacks of simple metal fluoride salts, have seen enormous success,

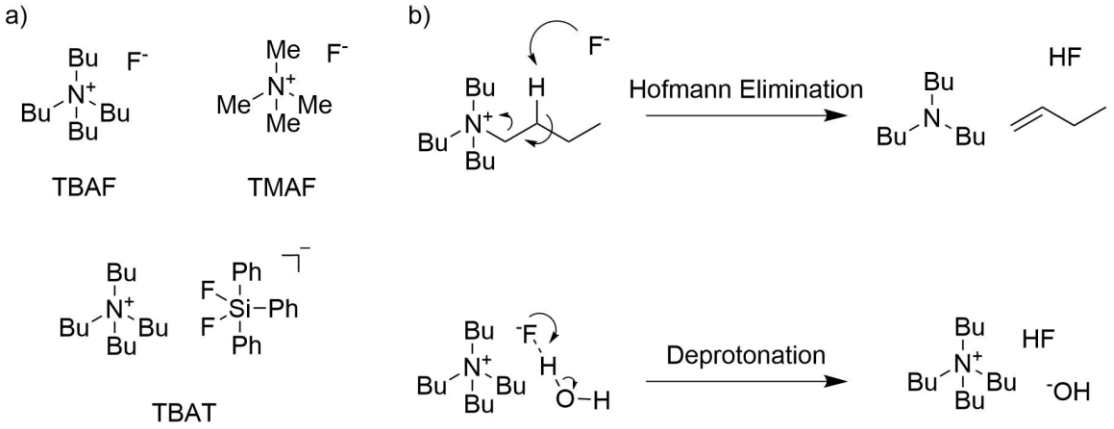

Figure 1.5: a) Examples of organic soluble fluoride sources b) problems caused by water of hydration in TBAF. Hofmann elimination upon drying, and hydroxide formation *in situ*.

particularly tetrabutylammonium fluoride hydrate (TBAF) – an organic-soluble fluoride source. Tetramethylammonium fluoride (TMAF)[73] and tetrabutylammonium (triphenylsilyl)difluorosilicate (TBAT)[74] were designed to overcome the limitations originating from water of hydration in TBAF, namely hydroxide formation and Hofmann elimination induced by drying (Figure 1.5). These reagents don't provide direct control over fluoride reactivity and selectivity, however. Asymmetric fluorination using nucleophilic fluorine sources has lagged behind those using electrophilic fluorine sources,[75] however, several successful protocols have been developed with metal catalysts (Scheme 1.2). Organocatalytic asymmetric nucleophilic fluorination remained a challenge.[75,76]

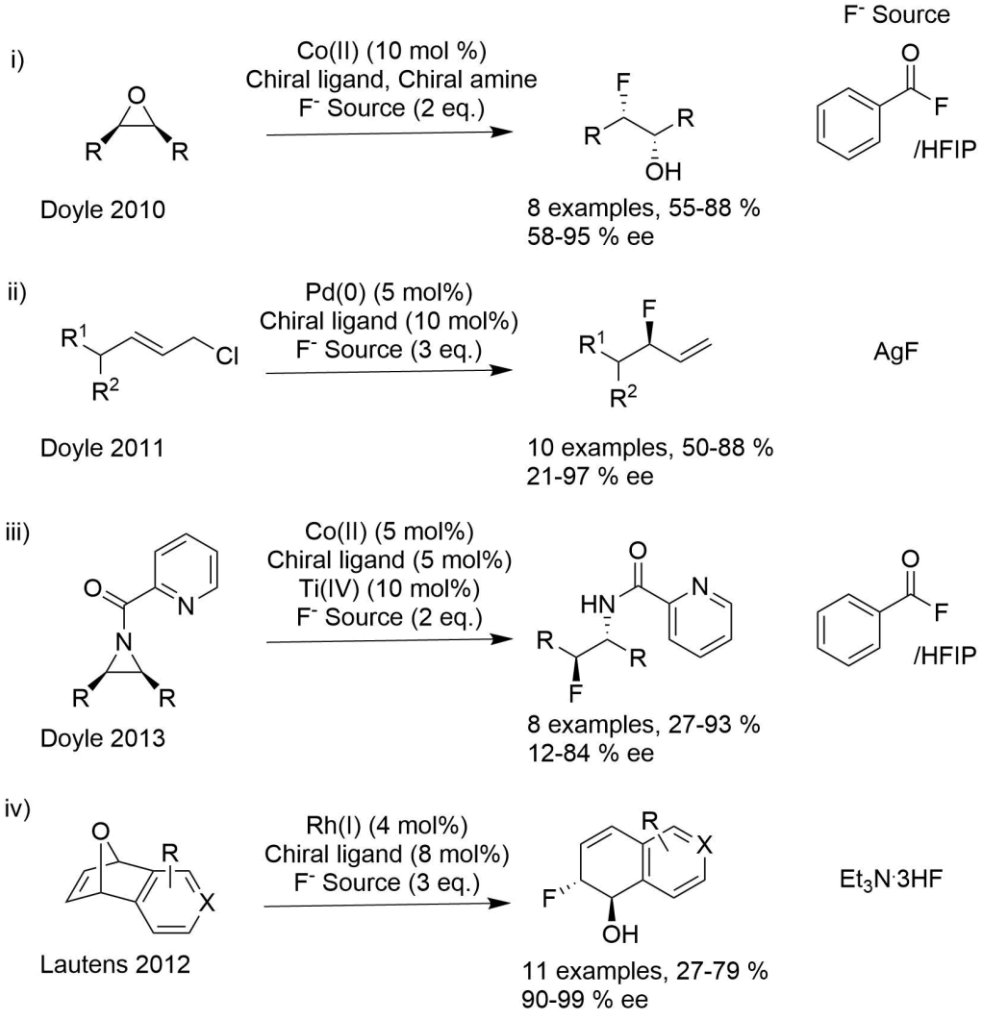

Scheme 1.2: Selected asymmetric nucleophilic fluorination reactions. All require transition metal catalysts. i) Co(II) catalyzed enantioselective ring opening of epoxides[77] ii) Pd(0) catalyzed regio- and enantio- selective allylic fluorination[78] iii) Co(II) catalyzed enantioselective ring opening of aziridines with Ti(IV) co-catalyst[79] iv) Rh(II) catalyzed enantioselective ring opening of oxabicyclic alkenes.[80]

1.2.2.4 The Fluorinase

The fluorinase enzyme is the only known enzyme in nature that synthesizes a product containing a carbon-fluorine bond.[7,10] The fluorinase mediates reaction of *S*-Adenosyl methionine (SAM) with the fluoride anion under aqueous conditions – the latter may be derived from group 1 metal salts. The mechanism of the fluorinase enzyme has been extensively studied since being reported in 2002 and established to proceed *via* an S_N2 reaction at the sulfonium ion, mediated by hydrogen bonding to fluoride (Scheme 1.3).[81,82] Initially, fluoride is weakly bound to the enzyme through hydrogen bonding,

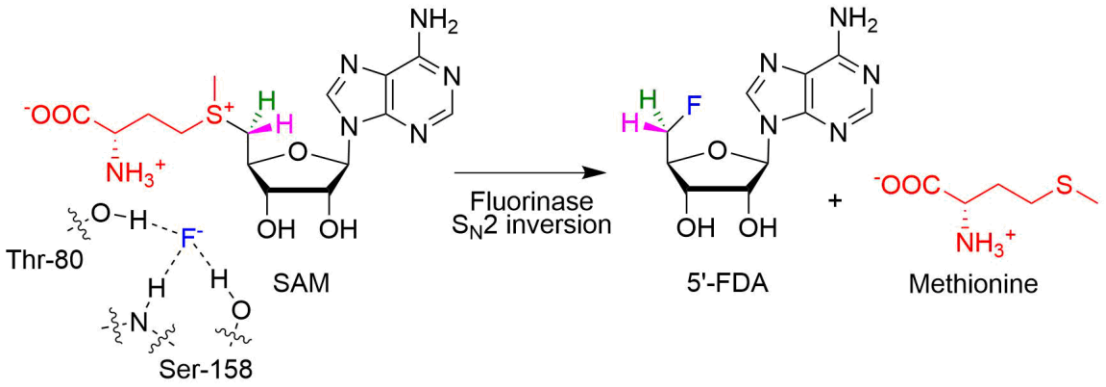

Scheme 1.3: Fluorinase mediated S_N2 reaction of SAM with fluoride to produce 5'-fluoro-5'-deoxyadenosine. Amino acids involved in fluoride binding determined by Senn *et al.*[82]

releasing two of the four water molecules solvating the fluoride anion. The positively charged SAM substrate binds strongly to the fluorinase-fluoride complex, displacing the final two waters of solvation coordinated to the fluoride. SAM binds to fluoride in a reactive conformation, with the fluoride anion pre-organized to attack the substrate C-S σ*. Fluoride substitution is then rapid, with inversion at carbon, producing 5'-fluoro-5'-deoxyadenosine and L-methionine as products, which are released to turn over the enzyme. Limited progress has been made at broadening the substrate scope of the fluorinase in nearly two decades since its discovery, suggesting that it is an extremely challenging task.[5,83–86]

1.2.2.5 Activating Simple Metal Fluoride Salts

Due to their highly attractive potential as fluoride sources, considerable research has focused on the "activation" of metal fluoride salts, without requiring harsh conditions. Such attempts have aimed to i) solubilize the fluoride source in synthetically useful, typically organic, solvents, ii) tune the reactivity profile of the solvated fluoride towards productive substitution reactions, rather than elimination, iii) create a chiral environment for asymmetric fluorination.

Many attempts have aimed at solubilizing the salts by binding the metal cation with crown ethers (Figure 1.6a).[87–93] This approach, however, does not provide control over the solubilized fluoride, causing selectivity problems, and making asymmetric fluorination challenging. Further, the crown ether is often a promoter, rather than a catalyst. Chiral crown ethers have successfully been employed for trifluoromethylation.[94] Hybrid approaches have been developed, by incorporating hydrogen bond donors to bind fluoride, giving more control over the anion (*vide infra*).[95–97] An elegant approach, by Song and co-workers, involves cleaving the crown ether and introducing terminal hydroxyl groups which bind fluoride (Figure 1.6b).[98] This promoter has also been combined with electrochemical methods,[99] and a similar promoter used under ion pairing catalysis for kinetic resolution of alcohols (Section 1.4).

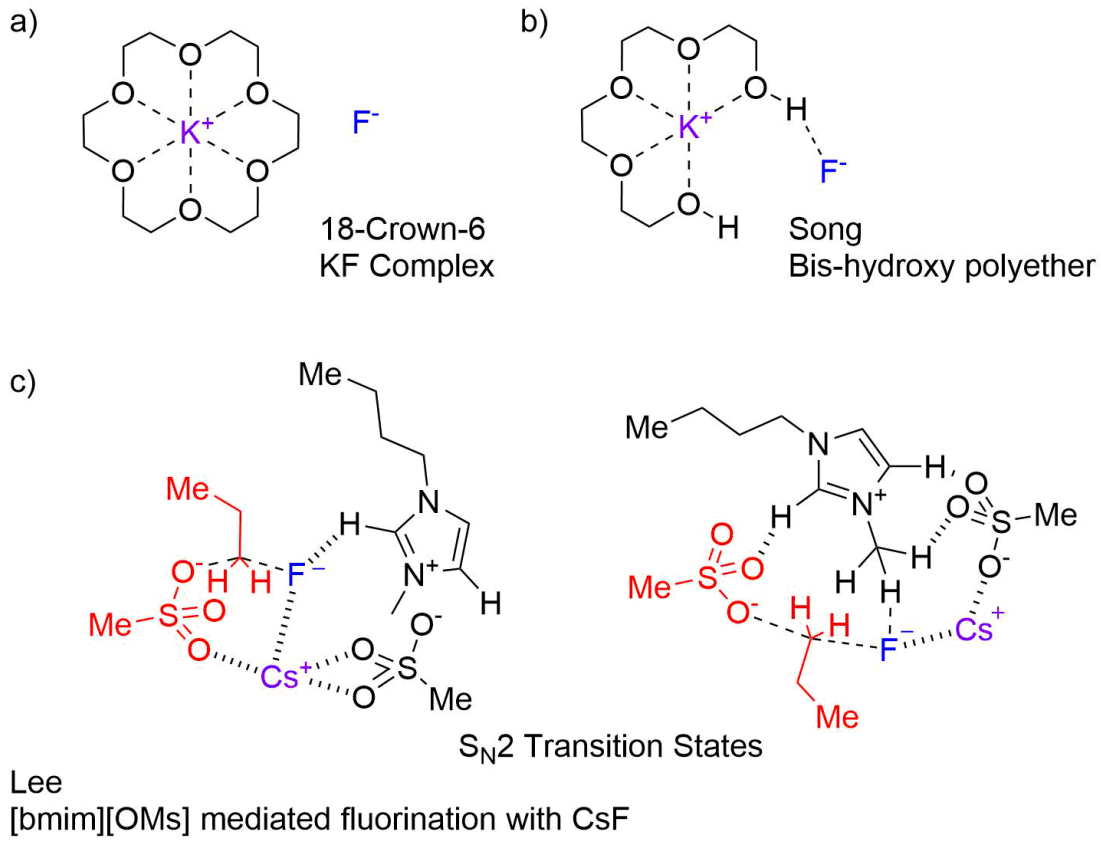

Figure 1.6: Selected methods for fluorination using metal fluorides. a) 18-Crown-6 bound potassium fluoride, b) Bis-hydroxy polyether promotor of Song and co-workers. Terminal hydrogen bonds bond fluoride and electrophile,[98] c) S_N2 transition state structures for ionic liquid ([bmim][OMs]) mediated fluorination with CsF.[100]

An alternative approach is to solubilize the metal fluoride in ionic liquid solvents.[101–103] Koguchi has also used an ionic liquid to support a crown ether.[104] Mechanistic study of ionic liquid promoted fluorinations reveals key interactions with both the metal cation and the fluoride anion, as well as binding of the leaving group in some circumstances (Figure 1.6c).[100]

1.2.2.6 Hydrogen Bonding Promoted Fluorination

Hydrogen bonding has long been exploited as a key interaction for the recognition of fluoride, with large quantities of literature describing hydrogen bonding sensors for fluoride.[105–111] Inspired by the fluorinase, many, including the Gouverneur group, have realized the potential of hydrogen bonding to activate fluoride and control its reactivity and selectivity. Examples of hydrogen bonding promoted nucleophilic fluorination have been achieved and have been well reviewed.[112,113] One approach is to use hydrogen bonding solvents, breaking the dogma that protic solvents are universally detrimental for S_N2 reactions of anions.[114,115] Inspired by these advances, Gouverneur and co-workers. extensively characterized numerous stoichiometric hydrogen bonded alcohol and urea fluoride complexes, synthesized from TBAF, in the solid state, revealing striking structural diversity (Figure 1.7a).[116,117] Further, kinetic studies of an S_N2:E2 competition reaction with primary bromide substrate were performed, establishing decreased reactivity, but increased S_N2 over E2 selectivity with increasing hydrogen bond donor strength.

Attempts have been made to exploit hydrogen bonding to aid in the solubilization of metal fluorides including the method of Song (*vide supra*). More elaborate structures have been developed with explicit cation binding groups and hydrogen bonds for fluorine binding, such as BACCA and BTC5A of Kim and co-workers (Figure 1.7b).[96,118,119]

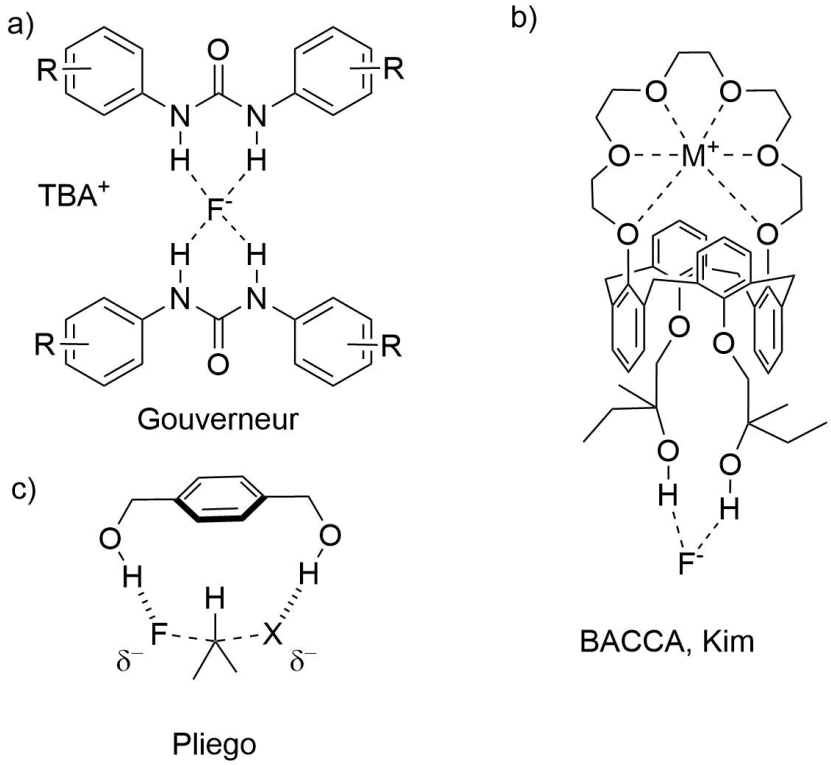

Figure 1.7: Selected examples of hydrogen bonding promoted fluorination. a) stoichiometric urea-fluoride complexes of Gouverneur and co-workers.[117] b) Bis-tert-Alcohol-Functionalized Crown-6-Calix[4]arene of Kim and co-workers. incorporating metal and fluoride binding groups[118] c) Transition state structure "receptor" of Pliego, designed to bind fluoride and leaving group in the S_N2 TS.[120]

A distinct approach, partly theory led by Pliego and co-workers., develops the idea of a transition state structure (TS) "receptor" to achieve catalysis mediated by hydrogen bonding (Figure 1.7c).[97,120–122] Both the fluoride nucleophile, and the leaving group are bound by hydrogen bonds, lowering the energy of the TS. This method has the potential to work with solvated fluoride, as well as for insoluble metal fluoride salts by the addition of a metal binding group to the catalyst, however no catalyst for asymmetric fluorination has been proposed.

1.3 Hydrogen Bonding

A hydrogen bond is a type of non-covalent interaction first reported over 100 years ago, [123,124] and now pervasive in our understanding of biology and chemistry, explaining fundamental concepts such as DNA base pairing and the anomalous properties of water.

Despite being well-known, our understanding of hydrogen bonds has changed significantly during that time period. In 2011 the International Union of Pure and Applied Chemistry (IUPAC) recommended the definition of *"The hydrogen bond is an attractive interaction between a hydrogen atom from a molecule or a molecular fragment X–H in which X is more electronegative than H, and an atom or a group of atoms in the same or a different molecule, in which there is evidence of bond formation"* which may be denoted as X–H•••Y–Z where X–H is the hydrogen bond *donor* and Y–Z is the hydrogen bond *acceptor*.[125] Intriguingly, this definition requires "*evidence"* to support the assignment of a hydrogen bond, rather than being defined simply on the basis of the species involved, testament to the difficulties and controversies in defining the interaction[126]

Many traditional definitions require X (of the hydrogen bond donor) to be electronegative, such as N, O and F (not just *more electronegative* than hydrogen), with the broadening of the definition now including C–H bonds as hydrogen bond donors, which were formerly controversial.[127–131] Hydrogen bond acceptors require electron density (commonly a lone pair of electrons) to interact with the δ^+ hydrogen, with both charged and neutral acceptors commonplace. Hydrogen bonds that fall within the traditional definition may be referred to as *classical* and those that don't as *non-classical*. Hydrogen bond strengths may range from 1 to 170 kJ/mol, depending on the system, but are typically up to ~20 kJ/mol.[132–135] Naturally, the strength of a hydrogen bond is also strongly dependent on the medium in which it is determined. Hydrogen bonds are directional interactions,[126,132,136] influencing molecular geometry.

Besides the species that can form a hydrogen bond, the exact nature of the bonding is also controversial. Because of the definition of the X–H bond as polar, there is naturally an electrostatic contribution, with debate surrounding the degree of covalent

contribution.[137,138] Observations in favour of a covalent contribution are the overlap of van der Waals radii and the directionality of the interaction.[139] "Covalent" hydrogen bonds have been reported[140] and studies using natural bond orbital analysis have concluded that electrostatics are a minor component after charge-transfer.[141] A much more recent study by Stone, however, has disputed the latter as fundamentally flawed.[142] Other recent studies, including one published recently by Galbraith, support covalency as the dominant factor.[136,143]

Whilst the nature of hydrogen bonding remains controversial, there appears consensus that the factors involved in hydrogen bonding are varied, and dependent on the species involved and the geometry of the bond formed.

1.3.1 Hydrogen Bonding Catalysis

Hydrogen bonding catalysis is a major subdiscipline of organocatalysis, focusing on the use of small molecule hydrogen bond donors to accelerate the rate of a reaction. Hydrogen bonding catalysis is closely related to Brønsted acid catalysis, with the distinction lying in whether the catalyst fully protonates the substrate in the mechanism – a distinction that is not always clear.[146] Hydrogen bond donors may be one of a diverse

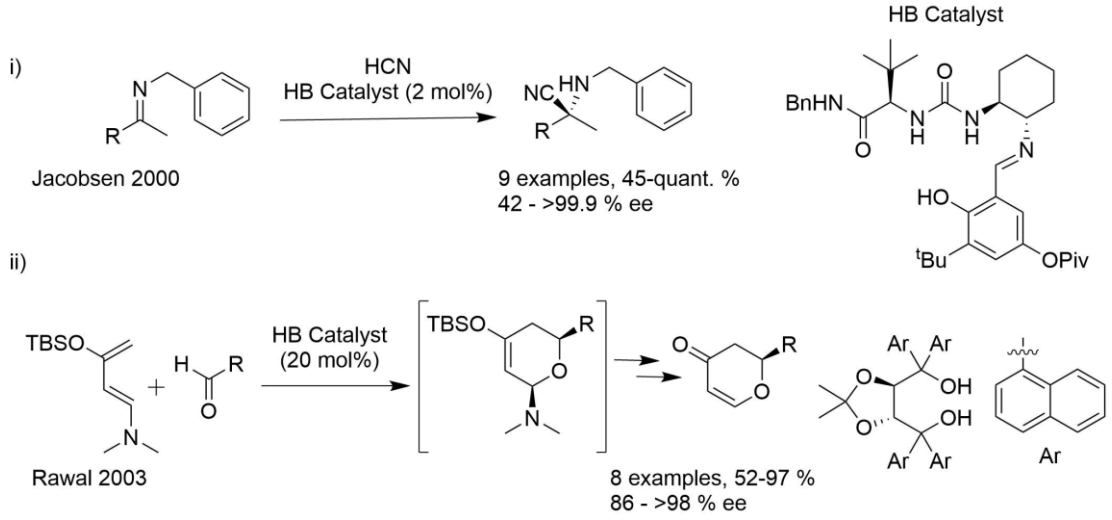

Scheme 1.4: Selected example of hydrogen bonding catalysis a) Urea catalyzed enantioselective hydrocyanation of ketoimines[144] b) Alcohol catalyzed enantioselective Diels–Alder reaction.[145]

array of species including alcohols, amines, (thio)ureas and phosphoric acids which are typically used to bind an electrophile, lowering its LUMO, and thus increasing its reactivity towards nucleophiles.[147,148] Use of a chiral hydrogen bond donor can facilitate an asymmetric transformation by providing a chiral environment. Typical hydrogen bonding promoted reactions are shown in Scheme 1.4.

1.3.2 Hydrogen Bonding Promoted Activation of Carbon–Fluorine Bonds

It has long been established that acidic and/or hydrogen bonding conditions can assist in the activation of carbon-fluorine bonds, particularly with *β*-unsaturation, by binding of the fluorine leaving group.[149,150] More recently in 2013, Paquin and co-workers demonstrated that water co-solvent accelerated the rate of substitution of a benzylic fluoride with morpholine through hydrogen bonding, forming a carbon-nitrogen bond.[151] This was followed by a report that stoichiometric quantities of a small molecule hydrogen bond donor could promote the same transformation, including in aprotic solvents (Scheme 1.5).[152] DFT and isotopic labelling studies support an S_N2 mechanism.[153,154] Further, the strong hydrogen bonding to fluoride permits activation of C–F bonds, in contrast to other carbon-halogen bonds. Other examples of the activation of carbon-fluorine bonds include for Friedel–Crafts, which likely proceeds *via* a more S_N1 type mechanism with strong hydrogen bond donors.[154–157]

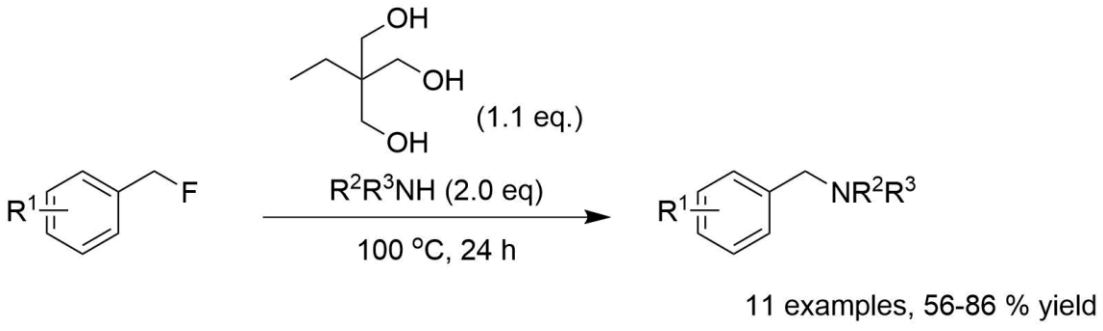

Scheme 1.5: Hydrogen bonding promoted activation of a benzylic carbon–fluorine bond by a stoichiometric alcohol promoter, under neat conditions.[152]

1.4 Asymmetric Ion Pairing Catalysis

Asymmetric ion pairing catalysis is a contemporary field of catalysis, where a chiral catalyst takes part in an ion pair, generating an asymmetric environment for an ensuing transformation. The field can be broadly split into four mechanisms – chiral cation-/anion- directed catalysis and cation/anion binding catalysis.[158] Generation of the chiral ion pair for ion pairing catalysis may be done through phase-transfer catalysis (PTC) – a mechanistic concept where a reaction is run with multiple phases, which separate the reagents, and a catalyst mediates the transfer of one or more reagents between the phases, allowing them to react. Typical chiral cations include quaternary ammonium salts and chiral anions include chiral borates or phosphates. Good enantioselectivity requires tight ion pairing and therefore, typically, low polarity solvents.

The cation-binding mechanism often involves binding of a metal cation with a chiral crown ether or polyether, which may solubilize a group 1 metal fluoride.[159] Anion-binding catalysis typically involves a hydrogen bonding catalyst binding an anion, rather than an electrophile as in classical hydrogen bonding catalysis. This anion may be formed by direct removal of a leaving group *in situ*, referred to as anion-abstraction catalysis.[160–162] With a chiral hydrogen bond donor, this anionic complex can ion pair with a cationic substrate, providing a chiral environment for the ensuing transformation. Examples of the four principal asymmetric ion pairing catalysis mechanisms are given in Scheme 1.6. Fluorinations have been performed under chiral anion-directed catalysis by Toste and co-workers[163] and chiral cation-directed catalysis by Maruoka and co-workers[164] using electrophilic fluorine sources (Scheme 1.6i and ii).

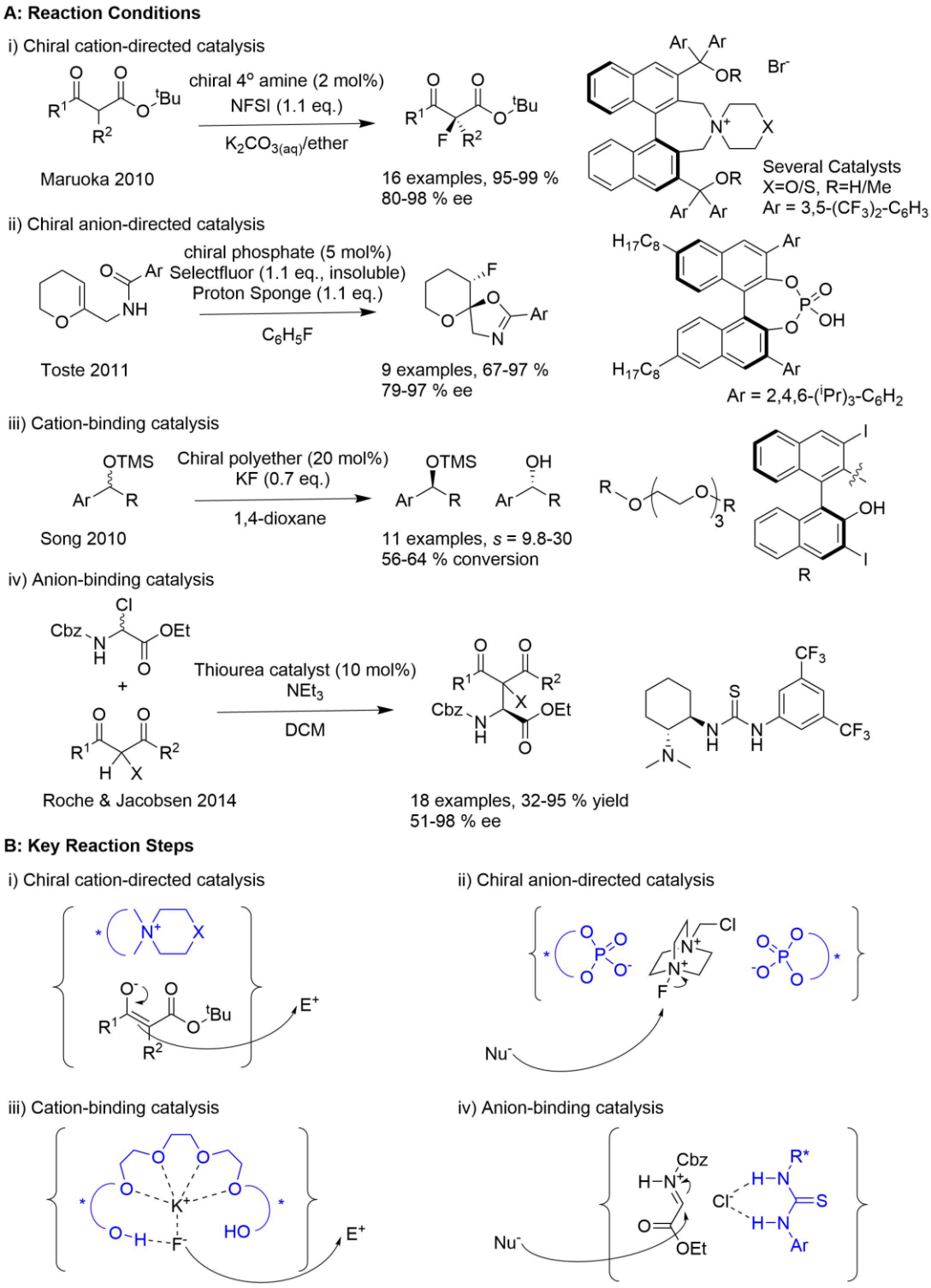

Scheme 1.6: Selected examples of the four main types of anion-binding catalysis. i) Chiral cation-directed catalysis. Asymmetric electrophilic fluorination under liquid-liquid phase-transfer catalysis with a chiral cationic quaternary amine catalyst[164] ii) Chiral anion-directed catalysis. Asymmetric electrophilic fluorination under solid-liquid phase-transfer catalysis with a chiral anionic phosphate catalyst[163] iii) Cation-binding catalysis. Deprotective kinetic resolution of silyl protected alcohols with a chiral polyether catalyst for binding of potassium ion[159] iv) Anion-binding catalysis. Asymmetric Mannich reaction with a chiral thiourea catalyst. Thiourea abstracts chloride leaving group to form a chiral-anion.[165] Section A: Reaction conditions. Section B: Key reaction step (enantiodetermining/enantioselective) involving the chiral ion pair. Ion pair enclosed within curly braces. Chiral catalyst is highlighted in blue.

1.5 Computational Organic Chemistry

The roots of computational organic chemistry stretch back over 60 years with the advent of semi-empirical methods, however the widespread application of density functional theory (DFT) to small molecules in the 1990s has led to the surge of the field that defines modern computational organic chemistry.[166,167] The hybrid functional, B3LYP (Becke 3-parameters, Lee, Yang, Parr), was developed over the course of the 1980s and early 1990s, and rapidly implemented in quantum chemistry software packages – a functional that still sees widespread use to this day.[168–171] Advancing theory and models, more efficient algorithms and vastly increased computational power have seen this discipline rapidly become a practical tool for organic chemistry.

It is the case, and likely will remain so, that exquisitely accurate computational methods are reserved for a small number of systems that have little practical importance for organic chemistry – small, conformationally inflexible molecules, in the gas phase. However, there is a large appetite for computational assistance and insight into the study of 'real' reactions, optimized for their experimental significance rather than computational convenience.[172] The ultimate goal is for computation to alleviate the burden of experimental screening (*aka* trial and error) by performing accurate calculations on the same timescale as experiment, ideally in a predictive capacity. Computational organic chemistry has been highly successful in explaining chemical phenomena,[173–177] and is coming of age with increasing reports of computational prediction.[178–182]

1.5.1 Common Computational Methods

A computational organic chemist has many methods at their disposal, implemented in various software packages. These methods can be broadly separated into those that depend upon quantum mechanics and those that depend upon classical mechanics.

1.5.1.1 Quantum Mechanical Methods

Quantum mechanics (QM) famously came to prominence at the turn of the 19th/20th century, when experimental observations came to light that could not be explained with classical mechanics, including Young's slits, the photoelectric effect, black-body radiation and atomic emission spectra. In 1926, Schrödinger published his eponymous equation – an equation that underpins all wave function theory (WFT) computational methods (Equation 1.1 – the time independent Schrödinger equation).[183] In this equation, Ψ represents the wave function of a system – a mathematical function that contains all of the dynamical information, $\hat{H}$ represents the Hamiltonian operator – a quantum mechanical operator for energy, and E is the energy of the wave function, Ψ. Despite the simple form of the equation, solution is challenging for all but the simplest systems, requiring a number of approximations.

As nuclei are much more massive than electrons, it can be assumed that electrons can instantly adapt to movement of the nuclei, thus their motions can be deconvoluted – the Born-Oppenheimer (BO) approximation.[184] This allows the electronic wave function to be solved for a given set of atomic coordinates, returning the energy of the system. If these energies are considered as a function of the positions of the nuclei, the result is a potential energy surface (PES), a fundamental concept in computational chemistry and frequently used to rationalize the kinetics and thermodynamics of organic reactions.

$$\hat{H}\Psi = E\Psi \qquad (1.1)$$

One of the earliest approximate methods for solving the Schrödinger equation is Hartree–Fock theory (HFT), also known as the self-consistent field (SCF) method. In the linear combination of atomic orbitals (LCAO) approach, a trial solution is constructed where each molecular orbital is described as a linear combination of atomic orbitals. Finding the optimum solution set then becomes synonymous with optimizing the coefficients of the linear combinations to find the lowest energy. The trial solutions are successively optimized in the average field of all the others until a converged, "self-consistent" solution is obtained. HFT has been highly successful, however, its key limitations, notably incomplete treatment of electron correlation and subsequent lack of dispersion, have led it to become obsolete for computational organic chemistry as a method in itself. Its exact treatment of exchange leads it to be included in *hybrid* density functionals, in varying proportions. Successive theoretical methods have been based upon HFT, referred to as *post-Hartree–Fock* methods, which generally improve on accuracy, but at increased computational cost. Such methods include configuration-interaction (CI), many-body perturbation theory – including the Møller–Plesset perturbation methods[185] (MP2,[186–190] MP3,[191,192] MP4[193]) and coupled cluster theory (CC).[194,195] The MP*n* methods and coupled cluster methods remain in widespread use. The accuracy of coupled cluster can be increased by treating excitations – singles (S), doubles (D), triples (T), quadruples (Q) – with methods denoted, for example, as CCSD. The most commonly used method includes singles, doubles and perturbative triples, denoted CCSD(T).

CCSD(T) is frequently referred to as the "gold-standard" of computational chemistry,[196–198] however its high computational cost, and very strong scaling with system size (~$O(N^7)$ where N is system size)[199] renders it impractical for most systems. Recent developments

have established a more efficient form of CCSD(T) known as DLPNO-CCSD(T) (domain-based local pair natural orbitals), which achieves a remarkable near-linear scaling with system size, making it a practical method for typical organic systems.[200]

A popular alternative to WFT approaches are those based upon density functional theory (DFT). DFT has its origins back in the 1970s, when Hohenberg and Kohn proved the existence of the exact density functional,[201] however it only became suitable for small molecule chemistry 20 years later in the 1990s. DFT bypasses the difficulties associated with WFT methods, where the latter involves solving equations in 4N variables (3 spatial coordinates and spin coordinate for each electron), by using a *density functional* that acts upon the electron density of a system (itself a function of only 3 spatial coordinates) and returns energy. Thus, the need to solve the Schrödinger equation is bypassed in exchange for a much less costly calculation – it is this substantial decrease in computational cost that has led to the ubiquity of DFT in computational organic chemistry. Further, DFT methods scale much more favorably with system size than WFT methods at ~$O(N^3)$, where N is system size.[199]

Whilst it is proved that such an exact functional exists to return the energy, this functional is unknown, resulting in the development of a large number of functionals, pejoratively referred to as the "functional zoo", with different functionals optimized for different tasks. As DFT is not variational, there is no certain way of knowing whether one functional returns a more accurate energy than another, leading to the necessity to benchmark DFT methods against WFT methods or experiment. Further, whilst the initial trend in density functional design was increasing both the accuracy of the electron density and the energy, more recently functionals have sacrificed the former in favor of the latter – a trend away from the exact functional.[202]

Kohn and Sham proposed conversion of a conventional DFT system to an equivalent but fictitious system of non-interacting electrons with the same electron density,[203] yielding *Kohn–Sham density functional theory* (KS-DFT, Equation 1.2). Each term in equation 1.2 can be computed exactly, with the exception of the exchange-correlation functional, E_{XC}, which is not exactly known – different approximations to the E_{XC} result in different density functionals.

$$E[\rho] = T[\rho] + V[\rho] + J[\rho] + E_{xc}[\rho] \quad (1.2)$$

$E[\rho]$ is the KS-DFT ground state energy; $T[\rho]$ the electron kinetic energy; $V[\rho]$ the electron-nuclear interaction potential; $J[\rho]$ the Coulombic interaction and $E_{xc}[\rho]$ the exchange-correlation functional.

Whilst there are no guarantees about the relative accuracies of the final energies, approximations to the exchange-correlation functional can be ranked in a hierarchy, commonly referred to as "Jacob's Ladder".[204] Key approximations include i) the local-density approximation (LDA), where E_{XC} is described solely by the electron density at a given point in space (first rung), ii) the generalized gradient approximation (GGA), where E_{XC} may also depend upon the gradient of the electron density, with respect to position (second rung), iii) the meta-generalized gradient approximation (mGGA), where E_{XC} may also be dependent on the second derivative of the density with respect to position (equivalent to the kinetic energy density – third rung). The fourth rung is defined by inclusion of 'exact' Hartree–Fock exchange, with the fifth rung reached by dependence on *virtual orbitals* yielding a *double hybrid* functional.

Two functionals used extensively in this work are M06-2X and ωB97X-D3. M06-2X is a hybrid mGGA exchange correlation functional incorporating 'double' Hartree–Fock exchange ('2X' – giving a total of 54 %),[205] therefore sitting on the fourth rung of the ladder. M06-2X is a highly parametrized functional, with 32 parameters fitted to known

data. M06-2X describes dispersion well in the medium range, due to the mGGA and the functional's parametrization, however it fails to reproduce long range dispersion with $1/r^6$ range dependence.[206] ωB97X-D3 is a range-separated hybrid GGA functional, also located on the fourth rung, consisting of the ωB97X functional[207] and an empirical dispersion correction (D3).[208,209] ωB97X is built up from the B97 GGA functional (rung 2),[210] with range-separation (ω) and incorporation of exact exchange (X). Range-separation (long-range correction) is designed to overcome inaccurate long-range behavior by treating long- and short-range interactions differently. To describe dispersion, Grimme's empirical pairwise atom-atom DFT-D3 dispersion correction is added.[211] This treats dispersion as an add-on to DFT, with minimal increase in computational cost, by considering the dispersion interaction between pairwise and 3-body groups of atoms, enforcing the correct $1/r^6$ distance dependence at long range. The dispersion correction is damped at short range, such as by the method of Becke and Johnson (BJ).[212–215] No knowledge of electronic structure, nor atom connectivity is required for the DFT-D approach.

With both WFT or DFT methods, a *basis set* is used to describe the solutions of an electronic structure computation. A basis set is a series of *basis functions* typically located on each atom, with the solution described as a linear combination of these functions. A basis function typically has a similar form to an atomic orbital, though use of gaussian-type basis functions, with e^{-r^2} behavior, far exceed the use of Slater type basis functions with the "correct" e^{-r} dependence, due to their computational efficiency. A basis set that has one basis function per (partially) filled atomic orbital is referred to as a single-ζ basis set, however this is inadequate for most chemistry. Double-ζ and triple-ζ

basis sets double and triple the number of basis functions respectively and are both in common use.

Basis set size has a large effect on the cost and accuracy of a computation – the ideal of an infinite basis set is unachievable, however extrapolation techniques can be used to estimate the complete basis set (CBS) limit.[216] Too small a basis set and the electrons do not have the freedom required to reach a realistic solution, with loss of accuracy in the chemistry. A basis set superposition error (BSSE) is also introduced when calculating complexation energies, as each fragment in the complex is also described by the basis functions of the other fragment, leading to a lowering in energy of the complex. BSSE may be reduced by increasing basis set size, or by employing a correction such as the counterpoise correction.[217] Larger basis sets give a lower energy, and a more theoretically correct solution than smaller basis sets. The error induced by using a finite basis set is smaller for DFT methods than WFT methods, meaning that a smaller basis set can be used for DFT, for a given accuracy, resulting in further relative performance benefit. As chemistry largely affects the valence electrons, basis sets are biased towards their description over core electrons – core electrons may even be replaced by an effective core potential (ECP). Notable exceptions to the importance of valence electrons are nuclear magnetic resonance calculations (NMR) where the behavior of the electrons around the nuclei is most important, and contracted basis sets give a superior description. Quantum mechanical methods are implemented in many quantum chemical software packages including Gaussian,[218] Jaguar,[219] Orca,[220,221] Turbomole[222] and ADF.[223]

1.5.1.2 Classical Mechanical Methods

Classical mechanical methods aim to describe the energy, geometry and mechanics of molecules using classical mechanics, necessarily without understanding the fundamental

quantum mechanics that determines the behavior of the system. Such models may be described as "ball and stick", with each atom treated as a (charged) particle, and the forces involved described by a *force field*. Common force fields include AMBER,[224] CHARMM,[225] MMFF,[226] OPLS[227,228] and UFF.[229] The total energy of a system is partitioned into contributions from bonded and non-bonded interactions – E_{bonded} and $E_{non\text{-}bonded}$ respectively. The bonded term is further composed of contributions from distortion of bonds (E_{bond}), angles (E_{angle}), and dihedrals ($E_{dihedral}$), from their equilibrium values. Non-bonded interactions are composed of van der Waals (E_{VDW}) and electrostatic ($E_{electrostatic}$) terms. The energy of the system is the sum of these terms over all atoms/groups of atoms. Their functional form varies between force fields (Equation 1.3).

$$E_{MM} = \underbrace{E_{bond} + E_{angle} + E_{dihedral}}_{E_{bonded}} + \underbrace{E_{VDW} + E_{electrostatic}}_{E_{non\text{-}bonded}} \quad (1.3)$$

Static optimizations using a force field are referred to as *molecular mechanics* (MM). Whilst classical methods obviously compromise on theoretical rigor, computation is trivial and has favorable scaling with system size, allowing large systems solvated in a box of solvent to be simulated over time in *molecular dynamics* (MD) simulations. Simulation of such large systems is inaccessible to QM methods.

The accuracy of MM and MD calculations depends entirely on the validity of the force field used. Parameters may be assigned to a given molecule on the basis of its molecular connectivity, or a system may be parametrized against quantum mechanical methods, to generate parameters specific to an individual system. Further, chemical reactivity cannot be studied using traditional force fields, as bonds cannot be broken and formed.

1.5.2 Conformational Flexibility, Sampling and Scaling

A consideration before computing a system is the amount of computational time it will take. When a molecule is subjected to a geometry optimization, the algorithm will optimize the molecule to the local minimum geometry – a single, structurally similar, conformer. It is the global minimum conformer, however, that most greatly influences the properties and chemistry of a molecule, and an unfortunate fact is that it is not possible to verify whether a particular conformer is the global minimum.[172,177,230] Finding the dominant conformers for a system is essential to accurately describing it.[231–235] For a conformationally inflexible molecule, it may be possible to compute all of the conformers systematically, thereby identifying the global minimum. However, conformational space increases rapidly with the number of rotatable bonds in a molecule, rapidly becoming infeasible. For example, *n*-butane has 1 rotatable bond (Me–C–C–Me dihedral), forming 3 conformers (1 *anti*, 2 *gauche*, though the *gauche* conformers are degenerate). Doubling the chain length to *n*-octane results in 5 rotatable bonds with a predicted $3^5 = 243$ conformers ignoring degeneracy. In reality, the situation is much more complex, with 347 conformers;[236] clash of the ends of the alkyl chain when brought into proximity invalidates the assumption of only three minima for the rotation of an individual bond. Complete computation of octane would therefore take approximately 1000× more computer time than butane using a DFT method – a factor of ~100 arising from increased conformational space, and a factor of ~10 arising from DFT scaling. Common practice in computational chemistry is therefore to truncate "extraneous" substituents, such as a propyl substituent to a methyl substituent, to reduce conformational space. Conformational searching may be done manually – using chemical intuition, however, software exists to automate the exploration of conformational space, by rotating rotatable bonds in a molecule.[237] Classical molecular mechanics tends to be used for energy

evaluations due to low computational cost. Conformational search may be done systematically; using a search algorithm such as Monte-Carlo;[238] or simulation using MD.[239,240] Due to the relatively low accuracy of force field energies, the energy of a large number of conformers must be computed using QM methods before conformers may be discarded. State of the art, efficient QM methods are currently being developed for conformational sampling, notably Grimme's XTB tight binding.[241–243]

1.5.2.1 Ion Pairing

A related issue occurs with non-covalently bonded systems such as ion pairs. Ion pairing occurs between ions of different charge, in low polarity solvents, creating a net neutral species in solution. Whilst not strictly speaking conformers, ion pairs can adopt many different geometries depending on the relative positions of the ions, each with a different energy.[244,245] The importance of counterions in modern ion pairing catalysis is in contrast to the approach traditionally taken in computational chemistry of neglecting counterions – though this remains an appropriate approximation in polar solvents and with non-coordinating counterions. Favorable error cancellation (due to the systematic nature of the approximation) also increases its applicability.

Sampling of ion pairs is more challenging than typical conformational sampling as the relative positioning of the ions can't easily be described in terms of internal coordinates (*i.e.* bond dihedral angles). Further, as the dominant coulombic interaction is of low directionality, the resulting potential energy surface is often very flat. Though, in situations where the ion pair is formed in a particular orientation, by chemical reaction, the ion pair may be able to maintain its orientation on a reasonable timescale, such as in the proton-slide mechanism.[246–249] Besides manual sampling, methods for sampling of ion pairs have been developed including those based upon semi-empirical methods,[250,251]

or using MD simulations.[239] Note that the conformers of the individual ions themselves must be considered simultaneously with the relative orientation of the ions in the ion pair. Several recent examples of computation gaining useful insight into ion pairing reactions have been published.[252–256]

1.5.3 Solvation Models – Implicit and Explicit

When a molecule is solvated for a typical organic reaction, there are typically on the order of 100-1000 solvent molecules per solvated molecule (0.1 moles/kg, solvent 10-100 Da). This poses the problem of system size and also 'conformations', where the solvent molecules can rearrange in a near infinite number of ways. Modelling of such *explicitly solvated* systems is possible using classical methods (MD) due to the low computational cost of the method (Figure 1.8a). This brings the benefit that explicit solvent-molecule interactions are included and can be studied – a particularly important factor in protic solvents, where hydrogen bonding interactions are critical.

Explicitly solvated systems cannot be modeled using QM methods due to the high computational cost of the methods and poor scaling. Solvent, however is a very important factor in organic reactivity, with large differences to energetics in the gas phase, particularly with polar or ionic interactions. A solution to this conundrum is provided by *implicit solvation* models, whereby a molecule is located in a solvent cavity, and the solvent is modelled as a continuum by its bulk dielectric constant, ε, at minimal additional computational cost (Figure 1.8b).[257–260] No solvent molecules are explicitly modelled, trading loss of specific solvent-molecule interactions for computational feasibility. Implicit solvation models are ubiquitous in computational organic chemistry and may be applied to optimization/frequency calculations or just as a single point energy correction. The *self-consistent reaction field* (SCRF) method is used whereby the charges on the

species polarize the surrounding continuum, which in turn alters the charge distribution of the molecule. Calculation is iterated until a self-consistent solution is obtained.[261] Examples of implicit solvation models include CPCM,[262–264] IEFPCM,[265–267] COSMO[268] and SMD.[269] This approach has been developed further by COSMO-RS, whereby the properties of the solvent are derived from QM calculations, such as the screening charge density.[270–273] This keeps computational cost low, however, describes to some extent, explicit solvent-molecule interactions.

A compromise approach is the concept of *microsolvation*, where only "key" solvent molecules, adjacent to the molecule of interest, are modelled (Figure 1.8c).[63,274–282] An implicit solvation model is typically applied to the whole system, including the explicit solvent molecules. This has the advantage that explicit solvent-molecule interactions are modelled using QM, at the same level of theory as the molecule of interest. However, even a complete first solvation shell does not accurately describe the behaviour of bulk

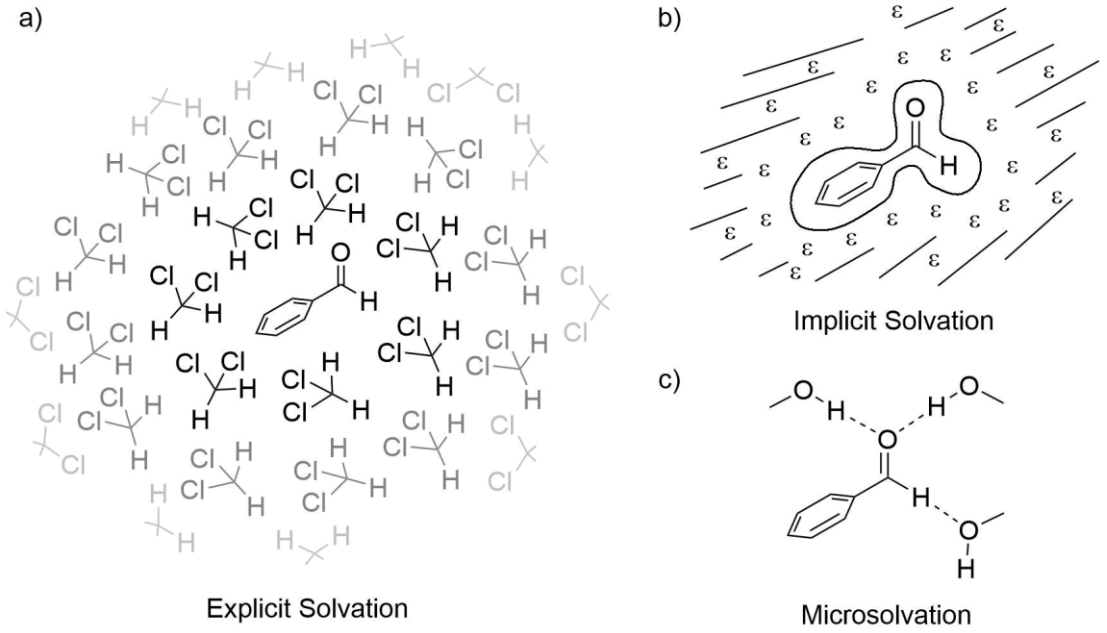

Figure 1.8: Three common models of solvation for computational chemistry. a) modelling of solvent molecules explicitly, at a low level of theory b) implicit solvation, with solvent modelled by a continuum with relative permittivity, ε. The molecule of interest is enclosed within a cavity c) microsolvation by a small number of explicit solvent molecules, at a high level of theory. This approach may be combined with an implicit solvation model (b) to the whole system, including the explicit solvent molecules.

solvent – it neglects the interaction of these solvent molecules with the second solvation shell and so on. The unavoidable question, therefore, is how many solvent molecules are required to accurately describe solvation. Further, even with a small number of solvent molecules, the number of possible orientations of the solvent molecules is high, rapidly becoming implausible to consider and compute. It is therefore subjective where the solvent molecules are added. The microsolvation approach is not in common use for the general study of organic reactivity due to the high computational cost and the additional problems entailed, however it can give qualitative theoretical insight into the importance of solvation effects in some systems.

1.5.4 Transition State Theory

To investigate reaction rates, computational methods can be readily used to calculate Gibbs free energies of activation, ($\Delta G^{\ddagger}$), by calculation of ground state and transition state structures. Experimental kinetic measurements, however, yield rate constants, *k*. Transition state theory provides the means for interconverting between energy barriers and rate constants for elementary reactions.

The fundamental premise of TST is that the activated complex (a transient structure near to the TS, with lifetime of less than a vibration) and the reactants may be regarded as in equilibrium. The activated complex can then proceed to products. A statistical mechanical or thermodynamics-based derivation yields the Eyring equation (1.4), relating *k* and $\Delta G^{\ddagger}$,

$$k = \kappa \frac{k_B T}{h} \exp\left(\frac{-\Delta G^{\ddagger}}{RT}\right) \qquad (1.4)$$

where κ is the *transmission coefficient* and the other constants have their usual definitions.[283–285] The transmission coefficient represents the probability that an activated complex proceeds to product, and is usually set to 1, assuming no re-crossing of the TS.

The Eyring equation is of a similar form to the Arrhenius equation that preceded it (equation 1.5), but they describe distinct concepts. The Arrhenius equation refers to the macroscopic activation energy and rate constant for a reaction (i.e. one of each for a multi-step reaction), whereas the Eyring equation refers to an individual elementary step.

$$k = A \exp\left(\frac{-E_a}{RT}\right) \tag{1.5}$$

An intimate understanding of reaction mechanism is required to relate the rate constants of individual steps in the mechanism to the macroscopic rate constant of the whole reaction.

A practical application of the Eyring equation in computational organic chemistry is for calculating kinetic selectivity, for example for two competing mechanisms, or transition state structures to enantiomeric products. Under kinetic control, the ratio of the products is equal to the ratio of the rates of their formation (Equation 1.6).

$$\frac{k_1}{k_2} = \frac{\frac{k_B T}{h}\exp\left(\frac{-\Delta G_1^{\ddagger}}{RT}\right)}{\frac{k_B T}{h}\exp\left(\frac{-\Delta G_2^{\ddagger}}{RT}\right)} = \frac{\exp\left(\frac{-\Delta G_1^{\ddagger}}{RT}\right)}{\exp\left(\frac{-\Delta G_2^{\ddagger}}{RT}\right)} = \exp\left(\frac{\Delta\Delta G^{\ddagger}}{RT}\right) \quad \Delta\Delta G^{\ddagger} = \Delta G_2^{\ddagger} - \Delta G_1^{\ddagger} \tag{1.6}$$

The ratio of products therefore depends on the difference in Gibbs free energy of activation for the two processes. When k_1 and k_2 represent formation of enantiomeric products, equation 1.6 relates the enantiomeric ratio (e.r.) to the Gibbs free energy difference of the competing diastereomeric TSs. In general, however, there are multiple

TSs to each enantiomeric product, arising from conformational flexibility, resulting in an ensemble of transition state structures. In this case, the enantiomeric ratio is the ratio of the sum of the rates to each enantiomeric product *via* each TS in the ensemble (Equation 1.7).

$$e.r. = \frac{k_{\mathrm{Major}}}{k_{Minor}} = \frac{\sum_{Major\ TSs} \frac{\mathrm{k_B T}}{\mathrm{h}} \exp\left(\frac{-\Delta \mathrm{G_i}^{\ddagger}}{\mathrm{RT}}\right)}{\sum_{Minor\ TSs} \frac{\mathrm{k_B T}}{\mathrm{h}} \exp\left(\frac{-\Delta \mathrm{G_j}^{\ddagger}}{\mathrm{RT}}\right)} = \frac{\sum_{Major\ TSs} \exp\left(\frac{-\Delta \mathrm{G_i}^{\ddagger}}{\mathrm{RT}}\right)}{\sum_{Minor\ TSs} \exp\left(\frac{-\Delta \mathrm{G_j}^{\ddagger}}{\mathrm{RT}}\right)} \qquad (1.7)$$

Besides the validity of the underlying TST, a challenge for computation is that *k* depends exponentially on Gibbs free energy differences, amplifying uncertainty in the computed value.

1.5.5 Energy Decomposition Methods

Computational results tend to directly give numbers, rather than insight.[286] Converting numbers into chemically useful conclusions can be challenging, however successful approaches include natural bond orbital analysis (NBO)[287,288], the non-covalent interaction index (NCI)[289,290] and atoms in molecule (AIM).[291] To explain the origins of energy differences, various energy decomposition analyses (EDA) have been developed, attempting to assign contributions of an energy difference to chemically meaningful factors.[292–296] Several successful approaches have been devised, including truncated/fragmented models[253,297–299] and the distortion/interaction-activation strain method.[297,300–303] Truncated models involve the deletion of part of the two structures of interest and reevaluating the energy difference. If necessary, loose valence is plugged with hydrogen atoms in a consistent manner. How the energy difference between the two

structures changes upon truncation highlights the relative contribution of that structural feature to the energy difference.

1.5.5.1 The Distortion/Interaction-Activation Strain Method

The distortion/interaction-activation strain model (DI-AS) was developed independently in the labs of Bickelhaupt and Houk and partitions the activation barrier of a reaction into the "distortion" and "interaction" of the components of the reaction. This model has been successfully applied to many systems, including rationalizing S_N2 vs E2 competition.[293,304]

An intrinsic reaction coordinate (IRC) calculation is run for each system of interest, from reactants to TS. The system is partitioned into different components, typically the reactants. For each point on the IRC, the energy of each component is evaluated individually (*i.e.* by deleting all other atoms), without changing the geometry. The energy of each component in its distorted geometry, for a given point on the pathway, relative to its energy when undistorted defines the *distortion energy* of that component. For a given point on the IRC, the distortion of the individual components can be summed to give the total distortion energy. The hypothetical energy released when the distorted components are brought together, is referred to as the *interaction energy* – mathematically the difference between the total energy of the system at that point and the total distortion energy. Comparison of the relative contributions of the distortion and interactions terms between multiple systems can then give insight into the origins of selectivity. An outline of this approach is given in Figure 1.9. One significant advantage of DI-AS analysis is that it can be run using any quantum chemistry package capable of running an IRC calculation.

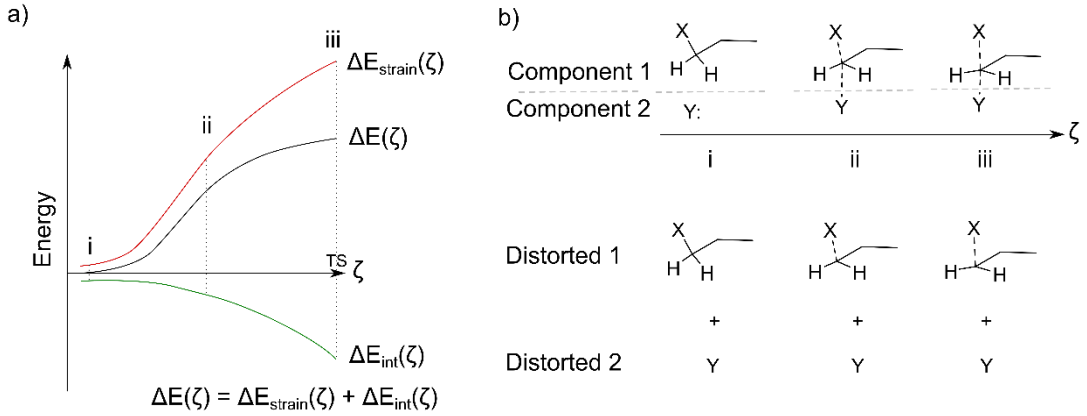

Figure 1.9: The distortion/interaction-activation strain method for decomposing contributions to an activation barrier. An S_N2 reaction is used as example. The system is separated into component 1 (substrate) and component 2 (nucleophile). a) Plot of energies over the reaction coordinate, up to the TS. Total distortion energy ($\Delta E_{strain}(\zeta)$), interaction energy ($\Delta E_{int}(\zeta)$) and total energy ($\Delta E(\zeta)$). b) Structures over the reaction coordinate, illustrated by the three points, i-iii. At each point, the system is separated into the two components and the energies evaluated in the distorted geometry – the difference in energy from the equilibrium geometry defines $\Delta E_{strain}(\zeta)$. In this particular example, as Y is an atom, it has 0 distortion energy at all points. Interaction energy can then be calculated as $\Delta E_{int}(\zeta) = \Delta E(\zeta) - \Delta E_{strain}(\zeta)$.

1.5.6 Hammett Equations

Hammett equations are a type of linear free energy relationship (LFER) where Gibbs free energies (or logarithms of rate/equilibrium constants), for a series of molecules with differently substituted aromatics, are correlated against a Hammett substituent constant, σ. Providing there are no changes to the underlying chemical mechanism, the plot is expected to be linear – indeed a plot with a discontinuity is indicative of a change in mechanism for activation barriers/rate constants. Hammett substituent constants have been derived for common functional groups, substituted at the *para* and *meta* positions of an aromatic – σ_p and σ_m respectively.[305–307] Hammett substituent constants were originally derived from the equilibrium constants of benzoic acid derivatives and the relative rates of hydrolysis of their esters, however demonstrate remarkable generality.[308,309]

1.6 Thesis Summary

This work describes the computational investigation of the effects of hydrogen bonding on the reactivity and selectivity of fluoride, with a focus on developing novel fluorination methodology in collaboration with experimental chemistry. The computational work described herein is solely my own, except where otherwise acknowledged, whereas all experimental work was performed by co-workers in the Gouverneur Group.

This work begins with an investigation into the reactivity and selectivity of stoichiometric urea-fluoride complexes in a model S_N2 vs E2 reaction with primary bromide substrate, using published experimental data (Chapter 2). Computational methods are benchmarked against high level quantum mechanical benchmarks and experimental data to establish an appropriate level of theory for describing fluoride. The experimental results are reproduced and rationalized, revealing the fundamental influences of hydrogen bonding on fluoride reactivity and selectivity. Applying this knowledge, computation alongside experiment, exploits hydrogen bonding to fluoride in a catalytic process – hydrogen bonding phase-transfer catalysis (HB PTC, Chapter 3-4). Computation investigates mechanism and guides chiral catalyst design for asymmetric fluorination. Investigation of the key factors for reactivity and selectivity reveal the strengths and weaknesses of the transformation, with a view to expanding the synthetic benefits of the mechanism, such as by increasing substrate scope. The thesis concludes by discussing the implications of using hydrogen bonding to fluoride as a means of controlling reactivity and selectivity, by applying kinetic models, and uses this knowledge to propose novel reactions (Chapter 5).

This thesis also demonstrates how using computation can aid experimental reaction development in real-time, and how theoretical insight into fundamental reactivity can be

used practically in developing novel reactions. Further, how close collaboration of computation and experiment can create a synergy, achieving an outcome greater than either could achieve alone.

1.7 References

(1) Wedepohl, K. H. The Composition of the Continental Crust. *Geochim. Cosmochim. Acta* **1995**, *59*, 1217–1232.

(2) Harper, D. B.; O'Hagan, D. The Fluorinated Natural Products. *Nat. Prod. Rep.* **1994**, *11*, 123–133.

(3) O'Hagan, D.; Harper, D. B. Fluorine-Containing Natural Products. *J. Fluor. Chem.* **1999**, *100*, 127–133.

(4) Chan, K. K. J.; O'Hagan, D. The Rare Fluorinated Natural Products and Biotechnological Prospects for Fluorine Enzymology. *Methods Enzymol.* **2012**, *516*, 219–235.

(5) O'Hagan, D.; Deng, H. Enzymatic Fluorination and Biotechnological Developments of the Fluorinase. *Chem. Rev.* **2015**, *115*, 634–649.

(6) Aldemir, H.; Kohlhepp, S. V.; Gulder, T.; Gulder, T. A. M. Structure of a Putative Fluorinated Natural Product from Streptomyces Sp. TC1. *J. Nat. Prod.* **2014**, *77*, 2331–2334.

(7) Deng, H.; O'Hagan, D.; Schaffrath, C. Fluorometabolite Biosynthesis and the Fluorinase from Streptomyces Cattleya. *Nat. Prod. Rep.* **2004**, *21*, 773–784.

(8) Gribble, G. W. A Recent Survey of Naturally Occurring Organohalogen Compounds. *Environ. Chem.* **2015**, *12*, 396–405.

(9) Dembitsky; Valery M. Biogenic Iodine and Iodine-Containing Metabolites. *Nat. Prod. Commun.* **2006**, *1*, 139–175.

(10) O'Hagan, D.; Schaffrath, C.; Cobb, S. L.; Hamilton, J. T. G.; Murphy, C. D. Biosynthesis of an Organofluorine Molecule. *Nature* **2002**, *416*, 279.

(11) Bégué, J. P.; Bonnet-Delpon, D. Recent Advances (1995-2005) in Fluorinated Pharmaceuticals Based on Natural Products. *J. Fluor. Chem.* **2006**, *127*, 992–1012.

(12) Shah, P.; Westwell, A. D. The Role of Fluorine in Medicinal Chemistry. *J. Enzyme Inhib. Med. Chem.* **2007**, *22*, 527–540.

(13) Bohm, H.-J.; Banner, D.; Bendels, S.; Kansy, M.; Kuhn, B.; Muller, K.; Obst-Sander, U.; Stahl, M. Fluorine in Medicinal Chemistry. *ChemBioChem* **2004**, *5*, 637–643.

(14) Isanbor, C.; O'Hagan, D. Fluorine in Medicinal Chemistry: A Review of Anti-Cancer Agents. *J. Fluor. Chem.* **2006**, *127*, 303–319.

(15) Gillis, E. P.; Eastman, K. J.; Hill, M. D.; Donnelly, D. J.; Meanwell, N. A. Applications of Fluorine in Medicinal Chemistry. *J. Med. Chem.* **2015**, *58*, 8315–8359.

(16) Kirk, K. L. Fluorine in Medicinal Chemistry: Recent Therapeutic Applications of Fluorinated Small Molecules. *J. Fluor. Chem.* **2006**, *127*, 1013–1029.

(17) Hagmann, W. K. The Many Roles for Fluorine in Medicinal Chemistry. *J. Med. Chem.* **2008**, *51*, 4359–4369.

(18) Wang, J.; Sánchez-Roselló, M.; Aceña, J. L.; Del Pozo, C.; Sorochinsky, A. E.; Fustero, S.; Soloshonok, V. A.; Liu, H. Fluorine in Pharmaceutical Industry: Fluorine-Containing Drugs Introduced to the Market in the Last Decade (2001-2011). *Chem. Rev.* **2014**, *114*, 2432–2506.

(19) Fujiwara, T.; O'Hagan, D. Successful Fluorine-Containing Herbicide Agrochemicals. *J. Fluor. Chem.* **2014**, *167*, 16–29.

(20) Zhou, Y.; Wang, J.; Gu, Z.; Wang, S.; Zhu, W.; Luis, J.; Soloshonok, V. A.; Izawa, K.; Liu, H. Next Generation of Fluorine-Containing Pharmaceuticals, Compounds Currently in Phase II − III Clinical Trials of Major Pharmaceutical Companies : New Structural Trends and Therapeutic Areas. *Chem. Rev.* **2016**, *116*, 422–518.

(21) Patani, G. A.; LaVoie, E. J. Bioisosterism : A Rational Approach in Drug Design. *Chem. Rev.* **1996**, *96*, 3147–3176.

(22) Damon, D. B.; Hoover, D. J. Synthesis of the Ketodifluoromethylene Dipeptide Isostere. *J. Am. Chem. Soc.* **1990**, *112*, 6439–6442.

(23) Meanwell, N. A. Fluorine and Fluorinated Motifs in the Design and Application of Bioisosteres

for Drug Design. *J. Med. Chem.* **2018**, *61*, 5822–5880.
(24) Yerien, D. E.; Bonesi, S.; Postigo, A. Fluorination Methods in Drug Discovery. *Org. Biomol. Chem.* **2016**, *14*, 8398–8427.
(25) Kirk, K. L. Fluorination in Medicinal Chemistry: Methods, Strategies, and Recent Developments. *Org. Process Res. Dev.* **2008**, *12*, 305–321.
(26) Liang, T.; Neumann, C. N.; Ritter, T. Introduction of Fluorine and Fluorine-Containing Functional Groups. *Angew. Chem. Int. Ed.* **2013**, *52*, 8214–8264.
(27) Slater, J. C. Atomic Radii in Crystals. *J. Chem. Phys.* **1964**, *41*, 3199–3204.
(28) Cordero, B.; Gómez, V.; Platero-Prats, A. E.; Revés, M.; Echeverría, J.; Cremades, E.; Barragán, F.; Alvarez, S. Covalent Radii Revisited. *J. Chem. Soc. Dalt. Trans.* **2008**, 2832–2838.
(29) Haynes, W. M.; Lide, D. R.; Bruno, T. J. *CRC Handbook of Chemistry and Physics*, 97th editi.; Taylor & Francis Inc., 2017.
(30) Shannon, R. D. Revised Effective Ionic Radii and Systematic Studies of Interatomie Distances in Halides and Chalcogenides. *Acta Crystallogr.* **1976**, *A32*, 751.
(31) Rayner-Canham, G.; Overton, T. *Descriptive Inorganic Chemistry*, 5th Editio.; W. H. Freeman and Company: New York, NY, 2010.
(32) Smith, D. W. Ionic Hydration Enthalpies. *J. Chem. Educ.* **1977**, *54*, 540–542.
(33) Bordwell, F. G. Equilibrium Acidities in Dimethyl Sulfoxide Solution. *Acc. Chem. Res.* **1988**, *21*, 456–463.
(34) Liebman, J. F.; Greenberg, A. *In Molecular Structure and Energetics*; VCH Publishers: Deerfield Beach, FL, 1986.
(35) Lemal, D. M. Perspective on Fluorocarbon Chemistry. *J. Org. Chem.* **2004**, *69*, 1–11.
(36) Pan, Y. The Dark Side of Fluorine. *ACS Med. Chem. Lett.* **2019**, *10*, 1016–1019.
(37) Biffinger, J. C.; Kim, H. W.; DiMagno, S. G. The Polar Hydrophobicity of Fluorinated Compounds. *ChemBioChem* **2004**, *5*, 622–627.
(38) Purser, S.; Moore, P. R.; Swallow, S.; Gouverneur, V. Fluorine in Medicinal Chemistry. *Chem. Soc. Rev* **2008**, *37*, 320–330.
(39) Howard, J. A. K.; Hoy, V. J.; O'Hagan, D.; Smith, G. T. How Good Is Fluorine as a Hydrogen Bond Acceptor? *Tetrahedron* **1996**, *52*, 12613–12622.
(40) Sibi, M. P.; Landais, Y. $C_{Sp}{}^3$-F Bond Formation: A Free-Radical Approach. *Angew. Chem. Int. Ed.* **2013**, *52*, 3570–3572.
(41) Chatalova-Sazepin, C.; Hemelaere, R.; Paquin, J.-F.; Sammis, G. M. Recent Advances in Radical Fluorination. *Synthesis* **2015**, *47*, 2554–2569.
(42) Harsanyi, A.; Sandford, G. Organofluorine Chemistry: Applications, Sources and Sustainability. *Green Chem.* **2015**, *17*, 2081–2086.
(43) Neumann, C. N.; Ritter, T. Late-Stage Fluorination: Fancy Novelty or Useful Tool? *Angew. Chem. Int. Ed.* **2015**, *54*, 3216–3221.
(44) Miller, P. W.; Long, N. J.; Vilar, R.; Gee, A. D. Synthesis of ^{11}C, ^{18}F, ^{15}O, and ^{13}N Radiolabels for Positron Emission Tomography. *Angew. Chem. Int. Ed.* **2008**, *47*, 8998–9033.
(45) Deng, X.; Rong, J.; Wang, L.; Vasdev, N.; Zhang, L.; Josephson, L.; Liang, S. H. Chemistry for Positron Emission Tomography: Recent Advances in ^{11}C-, ^{18}F-, ^{13}N-, and ^{15}O-Labeling Reactions. *Angew. Chem. Int. Ed.* **2019**, *58*, 2580–2605.
(46) Campbell, M. G.; Ritter, T. Late-Stage Fluorination: From Fundamentals to Application. *Org. Process Res. Dev.* **2014**, *18*, 474–480.
(47) Rozatian, N.; Ashworth, I. W.; Sandford, G.; Hodgson, D. R. W. A Quantitative Reactivity Scale for Electrophilic Fluorinating Reagents. *Chem. Sci.* **2018**, *9*, 8692–8702.
(48) Tius, M. A. Xenon Difluoride in Synthesis. *Tetrahedron* **1995**, *51*, 6605–6634.
(49) Lal, G. S.; Pez, G. P.; Syvret, R. G. Electrophilic NF Fluorinating Agents. *Chem. Rev.* **2002**, *96*, 1737–1756.
(50) Umemoto, T.; Tomita, K. N-Fluoropyridinium Triflate and Its Analogs, the First Stable 1:1 Salts of Pyridine Nucleus and Halogen Atom. *Tetrahedron Lett.* **1986**, *27*, 3271–3274.
(51) Umemoto, T.; Kawada, K.; Tomita, K. N-Fluoropyridinium Triflate and Its Derivatives: Useful Fluorinating Agents. *Tetrahedron Lett.* **1986**, *27*, 4465–4468.
(52) Banks, E. R.; Mohialdin-Khaffaf, S. N.; Lal, G. S.; Sharif, I.; Syvret, R. G. 1-Alkyl-4-Fluoro-1,4-Diazoniabicyclo[2.2.2]Octane Salts: A Novel Family of Electrophilic Fluorinating Agents. *J. Chem. Soc., Chem. Commun.* **1992**, 595–596.
(53) Nyffeler, P. T.; Durón, S. G.; Burkart, M. D.; Vincent, S. P.; Wong, C. H. Selectfluor: Mechanistic Insight and Applications. *Angew. Chem. Int. Ed.* **2004**, *44*, 192–212.
(54) Singh, R. P.; Umemoto, T. 1,1'-Difluoro-2,2'-Bipyridinium Bis(Tetrafluoroborate). *Encycl.*

Reagents Org. Synth. **2008**.
(55) Differding, E.; Ofner, H. N-Fluorobenzenesulfonimide: A Practical Reagent for Electrophilic Fluorinations. *Synlett* **1991**, *3*, 187–189.
(56) Differding, E.; Lang, R. W. New Fluorinating Reagents - I. The First Enantioselective Fluorination Reaction. *Tetrahedron Lett.* **1988**, *29*, 6087–6090.
(57) Park, H.; Verma, P.; Hong, K.; Yu, J. Q. Controlling Pd(IV) Reductive Elimination Pathways Enables Pd(II)-Catalysed Enantioselective C(Sp^3)-H Fluorination. *Nat. Chem.* **2018**, *10*, 755–762.
(58) Yamamoto, K.; Li, J.; Garber, J. A. O.; Rolfes, J. D.; Boursalian, G. B.; Borghs, J. C.; Genicot, C.; Jacq, J.; Van Gastel, M.; Neese, F.; Ritter, T. Palladium-Catalysed Electrophilic Aromatic C-H Fluorination. *Nature* **2018**, *554*, 511–514.
(59) Beeson, T. D.; MacMillan, D. W. C. Enantioselective Organocatalytic α-Fluorination of Aldehydes. *J. Am. Chem. Soc.* **2005**, *127*, 8826–8828.
(60) Middleton, W. J. New Fluorinating Reagents. Dialkylaminosulfur Fluorides. *J. Org. Chem.* **1975**, *40*, 574–578.
(61) Bickelhaupt, F. M.; Nibbering, N. M. M.; Baerends, E. J.; Ziegler, T. Theoretical Investigation on Base-Induced 1,2-Eliminations in the Model System F^- + CH_3CH_2F. The Role of the Base as a Catalyst. *J. Am. Chem. Soc.* **1993**, *115*, 9160–9173.
(62) Bento, A. P.; Solà, M.; Bickelhaupt, F. M. E2 and S_N2 Reactions of X^- + CH_3CH_2X (X = F, Cl); an Ab Initio and DFT Benchmark Study. *J. Chem. Theory Comput.* **2008**, *4*, 929–940.
(63) Bickelhaupt, F. M.; Baerends, E. J.; Nibbering, N. M. M. The Effect of Microsolvation on E2 and S_N2 Reactions: Theoretical Study of the Model System F^- + C_2H_5F +nHF. *Chem. Eur. J.* **1996**, *2*, 196–207.
(64) O'Hair, R. a J.; Davico, G. E.; Hacaloglu, J.; Dang, T. T.; DePuy, C. H.; Bierbaum, V. M. Measurements of Solvent and Secondary Kinetic Isotope Effects for the Gas-Phase S_N2 Reactions of Fluoride with Methyl Halides. *J. Am. Chem. Soc.* **1994**, *116*, 3609–3610.
(65) Vincent, M. A.; Hillier, I. H. The Solvated Fluoride Anion Can Be a Good Nucleophile. *Chem. Commun.* **2005**, 5902–5903.
(66) National Center for Biotechnology Information. Hydrofluoric acid, CID=14917 https://pubchem.ncbi.nlm.nih.gov/compound/Hydrofluoric-acid (accessed Jul 24, 2019).
(67) Giguère, P. A.; Turrell, S. The Nature of Hydrofluoric Acid. A Spectroscopic Study of the Proton-Transfer Complex $H_3O^+.F^-$. *J. Am. Chem. Soc.* **1980**, *102*, 5473–5477.
(68) Agency for Toxic Substances & Disease Registry. *Hydrogen Fluoride (HF), CAS 7664-39-3; UN 1052 (Anhydrous), UN 1790 (Solution)*; 2019.
(69) Olah, G. A.; Welch, J. T.; Vankar, Y. D.; Nojima, M.; Kerekes, I.; Olah, J. A. Synthetic Methods and Reactions. 63. Pyridinium Poly(Hydrogen Fluoride)(30% Pyridine-70% Hydrogen Fluoride): A Convenient Reagent for Organic Fluorination Reactions. *J. Org. Chem.* **1979**, *44*, 3872–3881.
(70) Okoromoba, O. E.; Han, J.; Hammond, G. B.; Xu, B. Designer HF-Based Fluorination Reagent: Highly Regioselective Synthesis of Fluoroalkenes and Gem -Difluoromethylene Compounds from Alkynes. *J. Am. Chem. Soc.* **2014**, *136*, 14381–14384.
(71) Haufe, G. Triethylamine Trishydrofluoride in Synthesis. *J. fur Prakt. Chemie/Chemiker-Zeitung* **1996**, *338*, 99–113.
(72) Bucsi, I.; Török, B.; Marco, A. I.; Rasul, G.; Prakash, G. K. S.; Olah, G. A. Stable Dialkyl Ether/Poly(Hydrogen Fluoride) Complexes: Dimethyl Ether/Poly(Hydrogen Fluoride), a New, Convenient, and Effective Fluorinating Agent. *J. Am. Chem. Soc.* **2002**, *124*, 7728–7736.
(73) Christe, K. O.; Wilson, W. W.; Wilson, R. D.; Bau, R.; Feng, J. an. Syntheses, Properties, and Structures of Anhydrous Tetramethylammonium Fluoride and Its 1:1 Adduct with Trans-3-Amino-2-Butenenitrile. *J. Am. Chem. Soc.* **1990**, *112*, 7619–7625.
(74) Pilcher, A. S.; Ammon, H. L.; DeShong, P. Utilization of Tetrabutylammonium (Triphenylsilyl)Difluorosilicate as a Fluoride Source for Nucleophilic Fluorination. *J. Am. Chem. Soc.* **1995**, *117*, 5166–5167.
(75) Yang, X.; Wu, T.; Phipps, R. J.; Toste, F. D. Advances in Catalytic Enantioselective Fluorination, Mono-, Di-, and Trifluoromethylation, and Trifluoromethylthiolation Reactions. *Chem. Rev.* **2015**, *115*, 826–870.
(76) Lin, J. H.; Xiao, J. C. Recent Advances in Asymmetric Fluorination and Fluoroalkylation Reactions via Organocatalysis. *Tetrahedron Lett.* **2014**, *55*, 6147–6155.
(77) Kalow, J. A.; Doyle, A. G. Enantioselective Ring Opening of Epoxides by Fluoride Anion Promoted by a Cooperative Dual-Catalyst System. *J. Am. Chem. Soc.* **2010**, *132*, 3268–3269.
(78) Katcher, M. H.; Sha, A.; Doyle, A. G. Palladium-Catalyzed Regio- and Enantioselective Fluorination of Acyclic Allylic Halides. *J. Am. Chem. Soc.* **2011**, *133*, 15902–15905.

(79) Kalow, J. A.; Doyle, A. G. Enantioselective Fluoride Ring Opening of Aziridines Enabled by Cooperative Lewis Acid Catalysis. *Tetrahedron* **2013**, *69*, 5702–5709.
(80) Zhu, J.; Tsui, G. C.; Lautens, M. Rhodium-Catalyzed Enantioselective Nucleophilic Fluorination: Ring Opening of Oxabicyclic Alkenes. *Angew. Chem. Int. Ed.* **2012**, *51*, 12353–12356.
(81) Zhu, X.; Robinson, D. A.; McEwan, A. R.; O'Hagan, D.; Naismith, J. H. Mechanism of Enzymatic Fluorination in Streptomyces Cattleya. *J. Am. Chem. Soc.* **2007**, *129*, 14597–14604.
(82) Senn, H. M.; O'Hagan, D.; Thiel, W. Insight into Enzymatic C-F Bond Formation from QM and QM/MM Calculations. *J. Am. Chem. Soc.* **2005**, *127*, 13643–13655.
(83) Deng, H.; Cobb, S. L.; McEwan, A. R.; McGlinchey, R. P.; Naismith, J. H.; O'Hagan, D.; Robinson, D. A.; Spencer, J. B. The Fluorinase from Streptomyces Cattleya Is Also a Chlorinase. *Angew. Chem. Int. Ed.* **2006**, *45*, 759–762.
(84) O'Hagan, D. Recent Developments on the Fluorinase from Streptomyces Cattleya. *J. Fluor. Chem.* **2006**, *127*, 1479–1483.
(85) Eustáquio, A. S.; O'Hagan, D.; Moore, B. S. Engineering Fluorometabolite Production: Fluorinase Expression in Salinispora Tropica Yields Fluorosalinosporamide. *J. Nat. Prod.* **2010**, *73*, 378–382.
(86) Sun, H.; Yeo, W. L.; Lim, Y. H.; Chew, X.; Smith, D. J.; Xue, B.; Chan, K. P.; Robinson, R. C.; Robins, E. G.; Zhao, H.; Ang, E. L. Directed Evolution of a Fluorinase for Improved Fluorination Efficiency with a Non-Native Substrate. *Angew. Chem. Int. Ed.* **2016**, *55*, 1–5.
(87) Pliego Jr, J. R.; Riveros, J. M. New Insights on Reaction Pathway Selectivity Promoted by Crown Ether Phase-Transfer Catalysis: Model Ab Initio Calculations of Nucleophilic Fluorination. *J. Mol. Catal. A Chem.* **2012**, *363–364*, 489–494.
(88) Wynn, D. A.; Roth, M. M.; Pollard, B. D. The Solubility of Alkali-Metal Fluorides in Non-Aqueous Solvents with and without Crown Ethers, as Determined by Flame Emission Spectrometry. *Talanta* **1984**, *31*, 1036–1040.
(89) Jadhav, V. H.; Jeong, H. J.; Choi, W.; Kim, D. W. Crown Ether Metal Complex Fluoride Salt as a Facile and Low Hygroscopic Fluoride Source for Nucleophilic Fluorination. *Chem. Eng. J.* **2015**, *270*, 36–40.
(90) Yie-Shun, C.; Jagur-Grodzinski, J.; Vofsi, D. Heterogeneous Fluorination of Chlorine Containing Polymers with 18-Crown-6 as Phase Transfer Agent. *Polymer* **1985**, *26*, 786–792.
(91) Kawakami, Y.; Yamashita, Y. Reaction Modes of Fluorination of Cyclic Ethers by Potassium Fluoride-18-Crown-6. *J. Org. Chem.* **1980**, *45*, 3930–3932.
(92) Makino, K.; Yoshioka, H. Selective Fluorination of Substituted Methanols with Methanesulfonyl Fluoride and Cesium Fluoride as Modified with Crown Ethers. *J. Fluor. Chem.* **1987**, *35*, 677–683.
(93) Gingras, M.; N. Harpp, D. New Anhydrous Fluorinating Systems: The Combination of Crown-Ethers and Cesium Fluoride. A Relative Rate Study. *Tetrahedron Lett.* **1988**, *29*, 4669–4672.
(94) Kawai, H.; Kusuda, A.; Mizuta, S.; Nakamura, S.; Funahashi, Y.; Masuda, H.; Shibata, N. Synthesis of Novel C2-Symmetric Chiral Crown Ethers and Their Application to Enantioselective Trifluoromethylation of Aldehydes and Ketones. *J. Fluor. Chem.* **2009**, *130*, 762–765.
(95) Pliego Jr, J. R. Potassium Fluoride Activation for the Nucleophilic Fluorination Reaction Using 18-Crown-6, [2.2.2]-Cryptand, Pentaethylene Glycol and Comparison with the New Hydro-Crown Scaffold: A Theoretical Analysis. *Org. Biomol. Chem.* **2018**, *16*, 3127–3137.
(96) Kang, S. M.; Kim, C. H.; Lee, K. C.; Kim, D. W. Bis-Triethylene Glycolic Crown-5-Calix[4]Arene: A Promoter of Nucleophilic Fluorination Using Potassium Fluoride. *Org. Lett.* **2019**, *21*, 3062–3066.
(97) Carvalho, N. F.; Pliego Jr, J. R. Theoretical Design and Calculation of a Crown Ether Phase-Transfer-Catalyst Scaffold for Nucleophilic Fluorination Merging Two Catalytic Concepts. *J. Org. Chem.* **2016**, *81*, 8455–8463.
(98) Lee, J. W.; Yan, H.; Jang, H. Bin; Kim, H. K.; Park, S. W.; Lee, S.; Chi, D. Y.; Song, C. E. Bis-Terminal Hydroxy Polyethers as All-Purpose, Multifunctional Organic Promoters: A Mechanistic Investigation and Applications. *Angew. Chem. Int. Ed.* **2009**, *48*, 7683–7686.
(99) Sawamura, T.; Takahashi, K.; Inagi, S.; Fuchigami, T. Electrochemical Fluorination Using Alkali-Metal Fluorides. *Angew. Chem. Int. Ed.* **2012**, *51*, 4413–4416.
(100) Oh, Y. H.; Jang, H. Bin; Im, S.; Song, M. J.; Kim, S. Y.; Park, S. W.; Chi, D. Y.; Song, C. E.; Lee, S. S_N2 Fluorination Reactions in Ionic Liquids: A Mechanistic Study towards Solvent Engineering. *Org. Biomol. Chem.* **2011**, *9*, 418–422.
(101) Kim, D. W.; Song, C. E.; Chi, D. Y. New Method of Fluorination Using Potassium Fluoride in

Ionic Liquid: Significantly Enhanced Reactivity of Fluoride and Improved Selectivity. *J. Am. Chem. Soc.* **2002**, *124*, 10278–10279.
(102) Shinde, S. S.; Patil, S. N.; Ghatge, A.; Kumar, P. Nucleophilic Fluorination Using Imidazolium Based Ionic Liquid Bearing Tert-Alcohol Moiety. *New J. Chem.* **2015**, *39*, 4368–4374.
(103) Chen, Z.; Tonouchi, Y.; Matsumoto, K.; Saimura, M.; Atkin, R.; Nagata, T.; Katahira, M.; Hagiwara, R. Partially Naked Fluoride in Solvate Ionic Liquids. *J. Phys. Chem. Lett.* **2018**, *9*, 6662–6667.
(104) Koguchi, S. An Ionic-Liquid-Supported 18-Crown-6 Ether: Recyclable Catalyst for Acetylation and Fluorination in an Ionic Liquid. *Trans. Mat. Res. Soc. Japan* **2013**, *38*, 35–36.
(105) Bhardwaj, V. K.; Sharma, S.; Singh, N.; Hundal, M. S.; Hundal, G. New Tripodal and Dipodal Colorimetric Sensors for Anions Based on Tris/Bis-Urea/Thiourea Moieties. *Supramol. Chem.* **2011**, *23*, 790–800.
(106) Zhang, P.; Li, C.; Zhang, H.; Li, Y.; Yu, X.; Geng, L.; Wang, Y.; Zhen, X.; Ma, Z. Fluorogenic and Chromogenic Detection of Biologically Important Fluoride Anion in Aqueous Media with a Fluorescein-Linked Hydrogen-Bonding Receptor via "off-on" Approach. *J. Incl. Phenom. Macrocycl. Chem.* **2015**, *81*, 295–300.
(107) Ghosh, K.; Adhikari, S.; Fröhlich, R.; Petsalakis, I. D.; Theodorakopoulos, G. Experimental and Theoretical Anion Binding Studies on Coumarin Linked Thiourea and Urea Molecules. *J. Mol. Struct.* **2011**, *1004*, 193–203.
(108) Atta, A. K.; Ahn, I. H.; Hong, A. Y.; Heo, J.; Kim, C. K.; Cho, D. G. Fluoride Indicator That Functions in Mixed Aqueous Media: Hydrogen Bonding Effects. *Tetrahedron Lett.* **2012**, *53*, 575–578.
(109) Jo, Y.; Chidalla, N.; Cho, D. G. Bis-Ureidoquinoline as a Selective Fluoride Anion Sensor through Hydrogen-Bond Interactions. *J. Org. Chem.* **2014**, *79*, 9418–9422.
(110) Parthiban, C.; Ciattini, S.; Chelazzi, L.; Elango, K. P. Selective Colorimetric Sensing of Fluoride in an Aqueous Solution by Amino-Naphthoquinone and Its Co(II), Ni(II), Cu(II) and Zn(II) Complexes-Effect of Complex Formation on Sensing Behaviour. *RSC Adv.* **2016**, *6*, 91265–91274.
(111) Cao, X.; Zhao, N.; Lv, H.; Gao, A.; Shi, A.; Wu, Y. 4-Nitrobenzene Thiourea Self-Assembly System and Its Transformation upon Addition of Hg^{2+} Ion: Applications as Sensor to Fluoride Ion. *Sensors Actuators, B* **2018**, *266*, 637–644.
(112) Liang, S.; Hammond, G. B.; Xu, B. Hydrogen Bonding: Regulator for Nucleophilic Fluorination. *Chem. Eur. J.* **2017**, *23*, 17850–17861.
(113) Lee, J.-W. W.; Oliveira, M. T.; Jang, H. Bin; Lee, S.; Chi, D. Y.; Kim, D. W.; Song, C. E. Hydrogen-Bond Promoted Nucleophilic Fluorination: Concept, Mechanism and Applications in Positron Emission Tomography. *Chem. Soc. Rev.* **2016**, *45*, 4638–4650.
(114) Kim, D. W.; Jeong, H.; Lim, S. T.; Sohn, M.; Katzenellenbogen, J. A.; Chi, D. Y. Facile Nucleophilic Fluorination Reactions Using *Tert*-Alcohols as a Reaction Medium: Significantly Enhanced Reactivity of Alkali Metal Fluorides and Improved Selectivity. *J. Org. Chem.* **2008**, *73*, 957–962.
(115) Yang, L.; Dong, T.; Revankar, H. M.; Zhang, C.-P. P. Recent Progress on Fluorination in Aqueous Media. *Green Chem.* **2017**, *19*, 3951–3992.
(116) Engle, K. M.; Pfeifer, L.; Pidgeon, G. W.; Giuffredi, G. T.; Thompson, A. L.; Paton, R. S.; Brown, J. M.; Gouverneur, V. Coordination Diversity in Hydrogen-Bonded Homoleptic Fluoride-Alcohol Complexes Modulates Reactivity. *Chem. Sci.* **2015**, *6*, 5293–5302.
(117) Pfeifer, L.; Engle, K. M.; Pidgeon, G. W.; Sparkes, H. A.; Thompson, A. L.; Brown, J. M.; Gouverneur, V. Hydrogen-Bonded Homoleptic Fluoride–Diarylurea Complexes: Structure, Reactivity and Coordinating Power. *J. Am. Chem. Soc.* **2016**, *138*, 13314–13325.
(118) Jadhav, V. H.; Choi, W.; Lee, S. S.; Lee, S.; Kim, D. W. Bis-*Tert*-Alcohol-Functionalized Crown-6-Calix[4]Arene: An Organic Promoter for Nucleophilic Fluorination. *Chem. Eur. J.* **2016**, *22*, 4515–4520.
(119) Pliego Jr, J. R. Mechanism of Nucleophilic Fluorination Promoted by Bis-*Tert*-Alcohol-Functionalized Crown-6-Calix[4]Arene. *Int. J. Quantum Chem.* **2018**, *118*, 1–9.
(120) Pliego Jr, J. R. Design of an Organocatalyst for Ion-Molecule S_N2 Reactions: A New Solvent Effect on the Reaction Rate Predicted by Ab Initio Calculations. *J. Mol. Catal. A Chem.* **2005**, *239*, 228–234.
(121) Pliego Jr, J. R.; Piló-Veloso, D. Chemoselective Nucleophilic Fluorination Induced by Selective Solvation of the S_N2 Transition State. *J. Phys. Chem. B* **2007**, *111*, 1752–1758.
(122) Pliego Jr., J. R. Chemical Reactions inside Structured Nano-Environment: S_N2 vs. E2 Reactions

for the F^- + CH_3CH_2Cl System. *Phys. Chem. Chem. Phys.* **2011**, *13*, 779–782.
(123) Moore, T. S.; Winmill, T. F. The State of Amines in Aqueous Solution. *J. Chem. Soc. Trans.* **1912**, *101*, 1635–1676.
(124) Goymer, P. 100 Years of the Hydrogen Bond. *Nat. Chem.* **2012**, *4*, 863–864.
(125) Arunan, E.; Desiraju, G. R.; Klein, R. A.; Sadlej, J.; Scheiner, S.; Alkorta, I.; Clary, D. C.; Crabtree, R. H.; Dannenberg, J. J.; Hobza, P.; Kjaergaard, H. G.; Legon, A. C.; Mennucci, B.; Nesbitt, D. J. Definition of the Hydrogen Bond (IUPAC Recommendations 2011). *Pure Appl. Chem.* **2011**, *83*, 1637–1641.
(126) Arunan, E.; Desiraju, G. R.; Klein, R. A.; Sadlej, J.; Scheiner, S.; Alkorta, I.; Clary, D. C.; Crabtree, R. H.; Dannenberg, J. J.; Hobza, P.; Kjaergaard, H. G.; Legon, A. C.; Mennucci, B.; Nesbitt, D. J. Defining the Hydrogen Bond: An Account (IUPAC Technical Report). *Pure Appl. Chem.* **2011**, *83*, 1619–1636.
(127) Desiraju, G. R. The C-H···O Hydrogen Bond in Crystals: What Is It? *Acc. Chem. Res.* **1991**, *24*, 290–296.
(128) Koch, U.; Popelier, P. L. A. Characterization of C-H-O Hydrogen Bonds on the Basis of the Charge Density. *J. Phys. Chem.* **1995**, *99*, 9747–9754.
(129) Desiraju, G. R. C-H···O and Other Weak Hydrogen Bonds. From Crystal Engineering to Virtual Screening. *Chem. Commun.* **2005**, 2995–3001.
(130) Johnston, R. C.; Cheong, P. H. Y. C-H···O Non-Classical Hydrogen Bonding in the Stereomechanics of Organic Transformations: Theory and Recognition. *Org. Biomol. Chem.* **2013**, *11*, 5057–5064.
(131) Liu, Y.; Zhao, W.; Chun-Hsing, C.; Flood, A. H. Chloride Capture Using a C-H Hydrogen-Bonding Cage. *Science* **2019**, *365*, 159–161.
(132) Steiner, T. The Hydrogen Bond in the Solid State. *Angew. Chem. Int. Ed.* **2002**, *41*, 48–76.
(133) Calhorda, M. J. Weak Hydrogen Bonds: Theoretical Studies. *Chem. Commun.* **2000**, 801–809.
(134) Emsley, J. Very Strong Hydrogen Bonding. *Chem. Soc. Rev.* **1980**, *9*, 91–124.
(135) Anslyn, E. V.; Dougherty, D. A. *Modern Physical Organic Chemistry*; Murdzek, J., Ed.; University Science Books: Mill Valley, CA, 2006.
(136) Martín Pendás, A.; Blanco, M. A.; Francisco, E. The Nature of the Hydrogen Bond: A Synthesis from the Interacting Quantum Atoms Picture. *J. Chem. Phys.* **2006**, *125*, 184112.
(137) Kollman, P. A.; Allen, L. C. The Theory of the Hydrogen Bond. *Chem. Rev.* **1972**, *72*, 283–303.
(138) Grabowski, S. J. What Is the Covalency of Hydrogen Bonding? *Chem. Rev.* **2011**, *111*, 2597–2625.
(139) Herschlag, D.; Pinney, M. M. Hydrogen Bonds: Simple after All? *Biochemistry* **2018**, *57*, 3338–3352.
(140) Minyaev, R. M.; Orlova, G. V. Covalent Nature of the Hydrogen Bond. *J. Struct. Chem.* **1985**, *26*, 157–164.
(141) Reed, A. E.; Weinhold, F.; Curtiss, L. A.; Pochatko, D. J. Natural Bond Orbital Analysis of Molecular Interactions: Theoretical Studies of Binary Complexes of HF, H_2O, NH_3, N_2, O_2, F_2, CO and CO_2 with HF, H_2O, and NH_3. *J. Chem. Phys.* **1986**, *84*, 5687–5705.
(142) Stone, A. J. Natural Bond Orbitals and the Nature of the Hydrogen Bond. *J. Phys. Chem. A* **2017**, *121*, 1531–1534.
(143) Nemes, C. T.; Laconsay, C. J.; Galbraith, J. M. Hydrogen Bonding from a Valence Bond Theory Perspective: The Role of Covalency. *Phys. Chem. Chem. Phys.* **2018**, *20*, 20963–20969.
(144) Vachal, P.; Jacobsen, E. N. Enantioselective Catalytic Addition of HCN to Ketoimines. Catalytic Synthesis of Quaternary Amino Acids. *Org. Lett.* **2000**, *2*, 867–870.
(145) Huang, Y.; Unni, A. K.; Thadani, A. N.; Rawal, V. H. Single Enantiomers from a Chiral-Alcohol Catalyst. *Nature* **2003**, *424*, 146.
(146) Fleischmann, M.; Drettwan, D.; Sugiono, E.; Rueping, M.; Gschwind, R. M. Brønsted Acid Catalysis: Hydrogen Bonding versus Ion Pairing in Imine Activation. *Angew. Chem. Int. Ed.* **2011**, *50*, 6364–6369.
(147) Doyle, A. G.; Jacobsen, E. N. Small-Molecule H-Bond Donors in Asymmetric Catalysis. *Chem. Rev.* **2007**, *107*, 5713–5743.
(148) Taylor, M. S.; Jacobsen, E. N. Asymmetric Catalysis by Chiral Hydrogen-Bond Donors. *Angew. Chem. Int. Ed.* **2006**, *45*, 1520–1543.
(149) Swain, C. G.; Spalding, R. E. T. III. Mechanism of Acid Catalysis of the Hydrolysis of Benzyl Fluoride. *J. Am. Chem. Soc.* **1960**, *82*, 6104–6107.
(150) Miller, W. T.; Bernstein, J. The Relative Reactivities of Some Substituted Benzyl Fluorides. *J. Am. Chem. Soc.* **1948**, *70*, 3600–3604.

(151) Champagne, P. A.; Pomarole, J.; Thérien, M. È.; Benhassine, Y.; Beaulieu, S.; Legault, C. Y.; Paquin, J. F. Enabling Nucleophilic Substitution Reactions of Activated Alkyl Fluorides through Hydrogen Bonding. *Org. Lett.* **2013**, *15*, 2210–2213.
(152) Champagne, P. A.; Saint-Martin, A.; Drouin, M.; Paquin, J. F. Triol-Promoted Activation of C-F Bonds: Amination of Benzylic Fluorides under Highly Concentrated Conditions Mediated by 1,1,1-Tris(Hydroxymethyl) Propane. *Beilstein J. Org. Chem.* **2013**, *9*, 2451–2456.
(153) Champagne, P. A.; Drouin, M.; Legault, C. Y.; Audubert, C.; Paquin, J. F. Revised Mechanistic Explanation for the Alcohol-Promoted Amination of Benzylic Fluorides under Highly Concentrated Conditions: Computational and Experimental Evidence on a Model Substrate. *J. Fluor. Chem.* **2015**, *171*, 113–119.
(154) Keddie, N. S.; Champagne, P. A.; Desroches, J.; Paquin, J. F.; O'Hagan, D. Stereochemical Outcomes of C-F Activation Reactions of Benzyl Fluoride. *Beilstein J. Org. Chem.* **2017**, *14*, 106–113.
(155) Hemelaere, R.; Champagne, P. A.; Desroches, J.; Paquin, J. F. Faster Initiation in the Friedel-Crafts Reaction of Benzyl Fluorides Using Trifluoroacetic Acid as Activator. *J. Fluor. Chem.* **2016**, *190*, 1–6.
(156) Champagne, P. A.; Benhassine, Y.; Desroches, J.; Paquin, J. F. Friedel-Crafts Reaction of Benzyl Fluorides: Selective Activation of C-F Bonds as Enabled by Hydrogen Bonding. *Angew. Chem. Int. Ed.* **2014**, *53*, 13835–13839.
(157) Hamel, J. D.; Paquin, J. F. Activation of C-F Bonds α to C-C Multiple Bonds. *Chem. Commun.* **2018**, *54*, 10224–10239.
(158) Brak, K.; Jacobsen, E. N. Asymmetric Ion-Pairing Catalysis. *Angew. Chem. Int. Ed.* **2013**, *52*, 534–561.
(159) Yan, H.; Jang, H. Bin; Lee, J. W.; Kim, H. K.; Lee, S. W.; Yang, J. W.; Song, C. E. A Chiral-Anion Generator: Application to Catalytic Desilylative Kinetic Resolution of Silyl-Protected Secondary Alcohols. *Angew. Chem. Int. Ed.* **2010**, *49*, 8915–8917.
(160) Ford, D. D.; Lehnherr, D.; Kennedy, C. R.; Jacobsen, E. N. Anion-Abstraction Catalysis: The Cooperative Mechanism of α-Chloroether Activation by Dual Hydrogen-Bond Donors. *ACS Catal.* **2016**, *6*, 4616–4620.
(161) Kennedy, C. R.; Lehnherr, D.; Rajapaksa, N. S.; Ford, D. D.; Park, Y.; Jacobsen, E. N. Mechanism-Guided Development of a Highly Active Bis-Thiourea Catalyst for Anion-Abstraction Catalysis. *J. Am. Chem. Soc.* **2016**, *138*, 13525–13528.
(162) Raheem, I. T.; Thiara, P. S.; Peterson, E. A.; Jacobsen, E. N. Enantioselective Pictet−Spengler-Type Cyclizations of Hydroxylactams: H-Bond Donor Catalysis by Anion Binding. *J. Am. Chem. Soc.* **2007**, *129*, 13404–13405.
(163) Rauniyar, V.; Lackner, A. D.; Hamilton, G. L.; Toste, F. D. Asymmetric Electrophilic Fluorination Using an Anionic Chiral Phase-Transfer Catalyst. *Science* **2011**, *334*, 1681–1684.
(164) Wang, X.; Lan, Q.; Shirakawa, S.; Maruoka, K. Chiral Bifunctional Phase Transfer Catalysts for Asymmetric Fluorination of β-Keto Esters. *Chem. Commun.* **2010**, *46*, 321–323.
(165) Wasa, M.; Liu, R. Y.; Roche, S. P.; Jacobsen, E. N. Asymmetric Mannich Synthesis of α-Amino Esters by Anion-Binding Catalysis. *J. Am. Chem. Soc.* **2014**, *136*, 12872–12875.
(166) Bachrach, S. M. *Computational Organic Chemistry*, 1st ed.; John Wiley & Sons, Inc.: Hoboken, NJ, 2007.
(167) Burke, K. Perspective on Density Functional Theory. *J. Chem. Phys.* **2012**, *136*, 150901.
(168) Becke, A. D. Density-Functional Thermochemistry. III. The Role of Exact Exchange. *J. Chem. Phys.* **1993**, *98*, 5648–5652.
(169) Lee, C.; Yang, W.; Parr, R. G. Development of the Colle-Salvetti Correlation-Energy Formula into a Functional of the Electron Density. *Phys. Rev. B* **1988**, *37*, 785–789.
(170) Vosko, S. H.; Wilk, L.; Nusair, M. Accurate Spin-Dependent Electron Liquid Correlation Energies for Local Spin Density Calculations: A Critical Analysis. *Can. J. Phys.* **1980**, *58*, 1200–1211.
(171) Hertwig, R. H.; Koch, W. On the Parameterization of the Local Correlation Functional . What Is Becke-3-LYP. *Chem. Phys. Lett.* **1997**, *268*, 345–351.
(172) Houk, K. N.; Liu, F. Holy Grails for Computational Organic Chemistry and Biochemistry. *Acc. Chem. Res.* **2017**, *50*, 539–543.
(173) Lodewyk, M. W.; Siebert, M. R.; Tantillo, D. J. Computational Prediction of ^{1}H and ^{13}C Chemical Shifts: A Useful Tool for Natural Product, Mechanistic, and Synthetic Organic Chemistry. *Chem. Rev.* **2012**, *112*, 1839–1862.
(174) Szymkuc, S.; Gajewska, E. P.; Klucznik, T.; Molga, K.; Dittwald, P.; Startek, M.; Bajczyk, M.;

Grzybowski, B. A. Computer-Assisted Synthetic Planning: The End of the Beginning. *Angew. Chem. Int. Ed.* **2016**, *55*, 5904–5937.
(175) Hopmann, K. H. Quantum Chemical Studies of Asymmetric Reactions: Historical Aspects and Recent Examples. *Int. J. Quantum Chem.* **2015**, *115*, 1232–1249.
(176) Sperger, T.; Sanhueza, I. A.; Schoenebeck, F. Computation and Experiment: A Powerful Combination to Understand and Predict Reactivities. *Acc. Chem. Res.* **2016**, *49*, 1311–1319.
(177) Peng, Q.; Duarte, F.; Paton, R. S. Computing Organic Stereoselectivity – from Concepts to Quantitative Calculations and Predictions. *Chem. Soc. Rev.* **2016**, *45*, 6093–6107.
(178) Luo, S. X.; Engle, K. M.; Dong, X.; Hejl, A.; Takase, M. K.; Henling, L. M.; Liu, P.; Houk, K. N.; Grubbs, R. H. An Initiation Kinetics Prediction Model Enables Rational Design of Ruthenium Olefin Metathesis Catalysts Bearing Modified Chelating Benzylidenes. *ACS Catal.* **2018**, *8*, 4600–4611.
(179) Picazo, E.; Houk, K. N.; Garg, N. K. Computational Predictions of Substituted Benzyne and Indolyne Regioselectivities. *Tetrahedron Lett.* **2015**, *56*, 3511–3514.
(180) Cao, Y.; Osuna, S.; Liang, Y.; Haddon, R. C.; Houk, K. N. Diels-Alder Reactions of Graphene: Computational Predictions of Products and Sites of Reaction. *J. Am. Chem. Soc.* **2013**, *135*, 17643–17649.
(181) Liu, F.; Liang, Y.; Houk, K. N. Bioorthogonal Cycloadditions: Computational Analysis with the Distortion/Interaction Model and Predictions of Reactivities. *Acc. Chem. Res.* **2017**, *50*, 2297–2308.
(182) Houk, K. N.; Cheong, P. H. Y. Computational Prediction of Small-Molecule Catalysts. *Nature* **2008**, *455*, 309–313.
(183) Schrödinger, E. An Undulatory Theory of the Mechanics of Atoms and Molecules. *Phys. Rev.* **1926**, *28*, 1049–1070.
(184) Born, M.; Oppenheimer, R. Zur Quantentheorie Der Molekeln. *Ann. Phys.* **1927**, *389*, 457–484.
(185) Møller, C.; Plesset, M. S. Note on an Approximation Treatment for Many-Electron Systems. *Phys. Rev.* **1934**, *46*, 618–622.
(186) Head-Gordon, M.; Pople, J. A.; Frisch, M. J. MP2 Energy Evaluation by Direct Methods. *Chem. Phys. Lett.* **1988**, *153*, 503–506.
(187) Sæbø, S.; Almlöf, J. Avoiding the Integral Storage Bottleneck in LCAO Calculations of Electron Correlation. *Chem. Phys. Lett.* **1989**, *154*, 83–89.
(188) Frisch, M. J.; Head-Gordon, M.; Pople, J. A. Semi-Direct Algorithms for the MP2 Energy and Gradient. *Chem. Phys. Lett.* **1990**, *166*, 281–289.
(189) Frisch, M. J.; Head-Gordon, M.; Pople, J. A. A Direct MP2 Gradient Method. *Chem. Phys. Lett.* **1990**, *166*, 275–280.
(190) Head-Gordon, M.; Head-Gordon, T. Analytic MP2 Frequencies without Fifth-Order Storage. Theory and Application to Bifurcated Hydrogen Bonds in the Water Hexamer. *Chem. Phys. Lett.* **1994**, *220*, 122–128.
(191) Pople, J. A.; Binkley, J. S.; Seeger, R. Theoretical Models Incorporating Electron Correlation. *Int. J. Quantum Chem.* **1976**, *10*, 1–19.
(192) Pople, J. A.; Seeger, R.; Krishnan, R. Variational Configuration Interaction Methods and Comparison with Perturbation Theory. *Int. J. Quantum Chem.* **1977**, *12*, 149–163.
(193) Krishnan, R.; Pople, J. A. Approximate Fourth-order Perturbation Theory of the Electron Correlation Energy. *Int. J. Quantum Chem.* **1978**, *14*, 91–100.
(194) Bartlett, R. J.; Purvis, G. D. Many-body Perturbation Theory, Coupled-pair Many-electron Theory, and the Importance of Quadruple Excitations for the Correlation Problem. *Int. J. Quantum Chem.* **1978**, *14*, 561–581.
(195) Raghavachari, K.; Trucks, G. W.; Pople, J. A.; Head-gordon, M. A Fifth-Order Perturbation Comparison of Electron Correlation Theories. *Chem. Phys. Lett.* **1989**, *157*, 479–483.
(196) Ramabhadran, R. O.; Raghavachari, K. Extrapolation to the Gold-Standard in Quantum Chemistry: Computationally Efficient and Accurate CCSD(T) Energies for Large Molecules Using an Automated Thermochemical Hierarchy. *J. Chem. Theory Comput.* **2013**, *9*, 3986–3994.
(197) Řezáč, J.; Hobza, P. Describing Noncovalent Interactions beyond the Common Approximations: How Accurate Is the "Gold Standard," CCSD(T) at the Complete Basis Set Limit? *J. Chem. Theory Comput.* **2013**, *9*, 2151–2155.
(198) Sengupta, A.; Ramabhadran, R. O.; Raghavachari, K. Breaking a Bottleneck: Accurate Extrapolation to "Gold Standard" CCSD(T) Energies for Large Open Shell Organic Radicals at Reduced Computational Cost. *J. Comput. Chem.* **2016**, *37*, 286–295.
(199) Ochsenfeld, C.; Kussmann, J.; Lambrecht, D. S. Linear-Scaling Methods in Quantum Chemistry.

Rev. Comput. Chem. **2007**, *23*, 1–82.
(200) Riplinger, C.; Neese, F. An Efficient and near Linear Scaling Pair Natural Orbital Based Local Coupled Cluster Method. *J. Chem. Phys.* **2013**, *138*, 034106.
(201) Hohenberg, P.; Kohn, W. Inhomogeneous Electron Gas. *Phys. Rev.* **1964**, *136*, B864–B871.
(202) Medvedev, M. G.; Bushmarinov, I. S.; Lyssenko, K. A.; Sun, J.; Perdew, J. P. Density Functional Theory Is Straying from the Path toward the Exact Functional. *Science* **2017**, *355*, 49–52.
(203) Kohn, W.; Sham, L. J. Self-Consistent Equations Including Exchange and Correlation Effects. *Phys. Rev.* **1965**, *140*, A1133–A1138.
(204) Perdew, J. P.; Schmidt, K. Jacob's Ladder of Density Functional Approximations for the Exchange-Correlation Energy. *AIP Conf. Proc.* **2001**, *577*, 1–20.
(205) Zhao, Y.; Truhlar, D. G. The M06 Suite of Density Functionals for Main Group Thermochemistry, Thermochemical Kinetics, Noncovalent Interactions, Excited States, and Transition Elements: Two New Functionals and Systematic Testing of Four M06-Class Functionals and 12 Other Function. *Theor. Chem. Acc.* **2008**, *120*, 215–241.
(206) Grimme, S. Density Functional Theory with London Dispersion Corrections. *Wiley Interdiscip. Rev. Comput. Mol. Sci.* **2011**, *1*, 211–228.
(207) Chai, J. Da; Head-Gordon, M. Systematic Optimization of Long-Range Corrected Hybrid Density Functionals. *J. Chem. Phys.* **2008**, *128*, 084106.
(208) Chai, J.-D.; Head-Gordon, M. Long-Range Corrected Hybrid Density Functionals with Damped Atom–Atom Dispersion Corrections. *Phys. Chem. Chem. Phys.* **2008**, *10*, 6615–6620.
(209) Lin, Y.-S.; Li, G.-D.; Mao, S.-P.; Chai, J.-D. Long-Range Corrected Hybrid Density Functionals with Improved Dispersion Corrections You-Sheng. *J. Chem. Theory Comput.* **2013**, *9*, 263–272.
(210) Becke, A. D. Density-Functional Thermochemistry. V. Systematic Optimization of Exchange-Correlation Functionals. *J. Chem. Phys.* **1997**, *107*, 8554.
(211) Grimme, S.; Antony, J.; Ehrlich, S.; Krieg, H. A Consistent and Accurate Ab Initio Parametrization of Density Functional Dispersion Correction (DFT-D) for the 94 Elements H-Pu. *J. Chem. Phys.* **2010**, *132*, 154104.
(212) Grimme, S.; Ehrlich, S.; Goerigk, L. Effect of the Damping Function in Dispersion Corrected Density Functional Theory. *J. Comput. Chem.* **2011**, *32*, 1456–1465.
(213) Johnson, E. R.; Becke, A. D. A Post-Hartree-Fock Model of Intermolecular Interactions. *J. Chem. Phys.* **2005**, *123*, 024101.
(214) Becke, A. D.; Johnson, E. R. A Density-Functional Model of the Dispersion Interaction. *J. Chem. Phys.* **2005**, *123*, 154101.
(215) Johnson, E. R.; Becke, A. D. A Post-Hartree-Fock Model of Intermolecular Interactions: Inclusion of Higher-Order Corrections. *J. Chem. Phys.* **2006**, *124*, 174104.
(216) Truhlar, D. G. Basis-Set Extrapolation. *Chem. Phys. Lett.* **1998**, *294*, 45–48.
(217) Boys, S. F.; Bernardi, F. The Calculation of Small Molecular Interactions by the Differences of Separate Total Energies. Some Procedures with Reduced Errors. *Mol. Phys.* **1970**, *19*, 553–566.
(218) Frisch, M. J.; Trucks, G. W.; Schlegel, H. B.; Scuseria, G. E.; Robb, M. A.; Cheeseman, J. R.; Scalmani, G.; Barone, V.; Petersson, G. A.; Nakatsuji, H.; Li, X.; Caricato, M.; Marenich, A.; Bloino, J.; Janesko, B. G.; Gomperts, R.; Mennucci, B.; Hratchian, H. P.; Ortiz, J. V.; Izmaylov, A. F.; Sonnenberg, J. L.; Williams-Young, D.; Ding, F.; Lipparini, F.; Egidi, F.; Goings, J.; Peng, B.; Petrone, A.; Henderson, T.; Ranasinghe, D.; Zakrzewski, V. G.; Gao, J.; Rega, N.; Zheng, G.; Liang, W.; Hada, M.; Ehara, M.; Toyota, K.; Fukuda, R.; Hasegawa, J.; Ishida, M.; Nakajima, T.; Honda, Y.; Kitao, O.; Nakai, H.; Vreven, T.; Throssell, K.; Montgomery Jr., J. A.; Peralta, J. E.; Ogliaro, F.; Bearpark, M.; Heyd, J. J.; Brothers, E.; Kudin, K. N.; Staroverov, V. N.; Keith, T.; Kobayashi, R.; Normand, J.; Raghavachari, K.; Rendell, A.; Burant, J. C.; Iyengar, S. S.; Tomasi, J.; Cossi, M.; Millam, J. M.; Klene, M.; Adamo, C.; Cammi, R.; Ochterski, J. W.; Martin, R. L.; Morokuma, K.; Farkas, O.; Foresman, J. B.; Fox, D. J. Gaussian 16. Gaussian Inc: Wallingford, CT 2016.
(219) Bochevarov, A. D.; Harder, E.; Hughes, T. F.; Greenwood, J. R.; Braden, D. A.; Philipp, D. M.; Rinaldo, D.; Halls, M. D.; Zhang, J.; Friesner, R. A. Jaguar: A High-Performance Quantum Chemistry Software Program with Strengths in Life and Materials Sciences. *Int. J. Quantum Chem.* **2013**, *113*, 2110–2142.
(220) Neese, F. The ORCA Program System. *Wiley Interdiscip. Rev. Comput. Mol. Sci.* **2012**, *2*, 73–78.
(221) Neese, F. Software Update: The ORCA Program System, Version 4.0. *Wiley Interdiscip. Rev. Comput. Mol. Sci.* **2018**, *8*, e1237.
(222) Turbomole GmbH. TURBOMOLE V7.3. Karlsruhe 2018.
(223) Te Velde, G.; Bickelhaupt, F. M.; Baerends, E. J.; Fonseca Guerra, C.; van Gisbergen, S. J. A.;

Snijders, J. G.; Ziegler, T. Chemistry with ADF. *J. Comput. Chem.* **2001**, *22*, 931–967.
(224) Cornell, W. D.; Cieplak, P.; Bayly, C. I.; Gould, I. R.; Merz Jr., K. M.; Ferguson, D. M.; Spellmeyer, D. C.; Fox, T.; Caldwell, J. W.; Kollman, P. A. A Second Generation Force Field for the Simulation of Proteins, Nucleic Acids, and Organic Molecules. *J. Am. Chem. Soc.* **1995**, *117*, 5179–5197.
(225) Brooks, B. R.; Bruccoleri, R. E.; Olafson, B. D.; States, D. J.; Swaminathan, S.; Karplus, M. CHARMM A Program for Macromolecular Energy, Minimization, and Dynamics Calculations, Journal of Computational Chemistry Volume 4, Issue 2. *J Comput Chem* **1983**, *4*, 187–217.
(226) Halgren, T. Merck Molecular Force Field. *J. Comput. Chem.* **1996**, *17*, 490–519.
(227) Jorgensen, W. L.; Tirado-Rives, J. The OPLS Potential Functions for Proteins. Energy Minimizations for Crystals of Cyclic Peptides and Crambin. *J. Am. Chem. Soc.* **1988**, *110*, 1657–1666.
(228) Jorgensen, W. L.; Maxwell, D. S.; Tirado-Rives, J. Development and Testing of the OPLS All-Atom Force Field on Conformational Energetics and Properties of Organic Liquids. *J. Am. Chem. Soc.* **1996**, *118*, 11225–11236.
(229) Rappé, A. K.; Casewit, C. J.; Colwell, K. S.; Goddard, W. A.; Skiff, W. M. UFF, a Full Periodic Table Force Field for Molecular Mechanics and Molecular Dynamics Simulations. *J. Am. Chem. Soc.* **1992**, *114*, 10024–10035.
(230) Lam, Y.-H.; Grayson, M. N.; Holland, M. C.; Simon, A.; Houk, K. N. Theory and Modeling of Asymmetric Catalytic Reactions. *Acc. Chem. Res.* **2016**, *49*, 750–762.
(231) Besora, M.; Braga, A. A. C.; Ujaque, G.; Maseras, F.; Lledós, A. The Importance of Conformational Search: A Test Case on the Catalytic Cycle of the Suzuki-Miyaura Cross-Coupling. *Theor. Chem. Acc.* **2011**, *128*, 639–646.
(232) Cook, T. C.; Andrus, M. B.; Ess, D. H. Quantum Mechanical Transition-State Analysis Reveals the Precise Origin of Stereoselectivity in Chiral Quaternary Cinchonidinium Phase-Transfer Catalyzed Enolate Allylation. *Org. Lett.* **2012**, *14*, 5836–5839.
(233) Grayson, M. N.; Yang, Z.; Houk, K. N. Chronology of CH···O Hydrogen Bonding from Molecular Dynamics Studies of the Phosphoric Acid-Catalyzed Allylboration of Benzaldehyde. *J. Am. Chem. Soc.* **2017**, *139*, 7717–7720.
(234) Seguin, T. J.; Wheeler, S. E. Stacking and Electrostatic Interactions Drive the Stereoselectivity of Silylium-Ion Asymmetric Counteranion-Directed Catalysis. *Angew. Chem. Int. Ed.* **2016**, *55*, 15889–15893.
(235) Xue, X. S.; Li, X.; Yu, A.; Yang, C.; Song, C.; Cheng, J. P. Mechanism and Selectivity of Bioinspired Cinchona Alkaloid Derivatives Catalyzed Asymmetric Olefin Isomerization: A Computational Study. *J. Am. Chem. Soc.* **2013**, *135*, 7462–7473.
(236) Goto, H.; Osawa, E.; Yamato, M. How Many Conformers Are There for Small N-Alkanes? Consequences of Asymmetric Deformation in GG′ Segment. *Tetrahedron* **1993**, *49*, 387–396.
(237) Wavefunction Inc. Spartan '16. Irvine, CA.
(238) Chang, G.; Guida, W. C.; Still, W. C. An Internal Coordinate Monte Carlo Method for Searching Conformational Space. *J. Am. Chem. Soc.* **1989**, *111*, 4379–4386.
(239) Duarte, F.; Paton, R. S. Molecular Recognition in Asymmetric Counteranion Catalysis: Understanding Chiral Phosphate-Mediated Desymmetrization. *J. Am. Chem. Soc.* **2017**, *139*, 8886–8896.
(240) Jorgensen, W. L.; Tirado-Rives, J. Monte Carlo vs Molecular Dynamics for Conformational Sampling. *J. Phys. Chem.* **1996**, *100*, 14508–14513.
(241) Grimme, S.; Bannwarth, C.; Shushkov, P. A Robust and Accurate Tight-Binding Quantum Chemical Method for Structures, Vibrational Frequencies, and Noncovalent Interactions of Large Molecular Systems Parametrized for All Spd-Block Elements (Z = 1-86). *J. Chem. Theory Comput.* **2017**, *13*, 1989–2009.
(242) Bannwarth, C.; Ehlert, S.; Grimme, S. GFN2-XTB - An Accurate and Broadly Parametrized Self-Consistent Tight-Binding Quantum Chemical Method with Multipole Electrostatics and Density-Dependent Dispersion Contributions. *J. Chem. Theory Comput.* **2019**, *15*, 1652–1671.
(243) Bursch, M.; Hansen, A.; Grimme, S. Fast and Reasonable Geometry Optimization of Lanthanoid Complexes with an Extended Tight Binding Quantum Chemical Method. *Inorg. Chem.* **2017**, *56*, 12485–12491.
(244) Lu, T.; Wheeler, S. E. Harnessing Weak Interactions for Enantioselective Catalysis. *Science* **2015**, *347*, 719–720.
(245) Raskatov, J. A.; Thompson, A. L.; Cowley, A. R.; Claridge, T. D. W.; Brown, J. M. Chiral Recognition in Contact Ion-Pairs; Observation, Characterization and Analysis. *Chem. Sci.* **2013**,

4, 3140.
(246) Ascough, D. M. H.; Duarte, F.; Paton, R. S. Stereospecific 1,3-H Transfer of Indenols Proceeds via Persistent Ion-Pairs Anchored By NH···π Interactions. *J. Am. Chem. Soc* **2018**, *140*, 16740–16748.
(247) Bruice, P. Y.; Bruice, T. C. Aminolysis of Substituted Phenyl Quinoline-8- and -6-Carboxylates with Primary and Secondary Amines. Involvement of Proton-Slide Catalysis. *J. Am. Chem. Soc.* **1974**, *96*, 5533–5542.
(248) Simón, L.; Paton, R. S. Phosphazene Catalyzed Addition to Electron-Deficient Alkynes: The Importance of Nonlinear Allenyl Intermediates upon Stereoselectivity. *J. Org. Chem.* **2017**, *82*, 3855–3863.
(249) Cannizzaro, C. E.; Strassner, T.; Houk, K. N. The Origin of 1,4-Asymmetric Induction in the Additions of Chiral Alcohols to Ketenes. *J. Am. Chem. Soc.* **2001**, *123*, 2668–2669.
(250) Kamachi, T.; Yoshizawa, K. Low-Mode Conformational Search Method with Semiempirical Quantum Mechanical Calculations: Application to Enantioselective Organocatalysis. *J. Chem. Inf. Model.* **2016**, *56*, 347–353.
(251) Kamachi, T.; Yoshizawa, K. Enantioselective Alkylation by Binaphthyl Chiral Phase-Transfer Catalysts: A DFT-Based Conformational Analysis. *Org. Lett.* **2014**, *16*, 472–475.
(252) Tsuji, N.; Kennemur, J. L.; Buyck, T.; Lee, S.; Prévost, S.; Kaib, P. S. J.; Bykov, D.; Farès, C.; List, B. Activation of Olefins via Asymmetric Bronsted Acid Catalysis. *Science* **2018**, *359*, 1501–1505.
(253) Maji, R.; Mallojjala, S. C.; Wheeler, S. E. Chiral Phosphoric Acid Catalysis: From Numbers to Insights. *Chem. Soc. Rev.* **2018**, *47*, 1142–1158.
(254) Gheewala, C. D.; Hirschi, J. S.; Lee, W. H.; Paley, D. W.; Vetticatt, M. J.; Lambert, T. H. Asymmetric Induction via a Helically Chiral Anion: Enantioselective Pentacarboxycyclopentadiene Brønsted Acid-Catalyzed Inverse-Electron-Demand Diels-Alder Cycloaddition of Oxocarbenium Ions. *J. Am. Chem. Soc.* **2018**, *140*, 3523–3527.
(255) Uraguchi, D.; Yamada, K.; Sato, M.; Ooi, T. Catalyst-Directed Guidance of Sulfur-Substituted Enediolates to Stereoselective Carbon–Carbon Bond Formation with Aldehydes. *J. Am. Chem. Soc.* **2018**, *140*, 5110–5117.
(256) Haines, B. E.; Nelson, B. M.; Grandner, J. M.; Kim, J.; Houk, K. N.; Movassaghi, M.; Musaev, D. G. Mechanism of Permanganate-Promoted Dihydroxylation of Complex Diketopiperazines: Critical Roles of Counter-Cation and Ion-Pairing. *J. Am. Chem. Soc.* **2018**, *140*, 13375–13386.
(257) Mennucci, B. Polarizable Continuum Model. *Wiley Interdiscip. Rev. Comput. Mol. Sci.* **2012**, *2*, 386–404.
(258) Cramer, C. J.; Truhlar, D. G. Implicit Solvation Models: Equilibria, Structure, Spectra, and Dynamics. *Chem. Rev.* **1999**, *99*, 2161–2200.
(259) Tomasi, J.; Mennucci, B.; Cammi, R. Quantum Mechanical Continuum Solvation Models. *Chem. Rev.* **2005**, *105*, 2999–3093.
(260) Young Lee, G.; Bay, K. L.; Houk, K. N. Evaluation of DFT Methods and Implicit Solvation Models for Anion-Binding Host-Guest Systems. *Helv. Chim. Acta* **2019**, *102*, e1900032.
(261) Chen, J. L.; Noodleman, L.; Case, D. A.; Bashford, D. Incorporating Solvation Effects into Density Functional Electronic Structure Calculations. *J. Phys. Chem.* **1994**, *98*, 11059–11068.
(262) Barone, V.; Cossi, M. Quantum Calculation of Molecular Energies and Energy Gradients in Solution by a Conductor Solvent Model. *J. Phys. Chem. A* **1998**, *102*, 1995–2001.
(263) Cossi, M.; Rega, N.; Scalmani, G.; Barone, V. Energies, Structures, and Electronic Properties of Molecules in Solution with the C-PCM Solvation Model. *J. Comput. Chem.* **2003**, *24*, 669–681.
(264) Takano, Y.; Houk, K. N. Benchmarking the Conductor-like Polarizable Continuum Model (CPCM) for Aqueous Solvation Free Energies of Neutral and Ionic Organic Molecules. *J. Chem. Theory Comput.* **2005**, *1*, 70–77.
(265) Cancès, E.; Mennucci, B.; Tomasi, J. A New Integral Equation Formalism for the Polarizable Continuum Model: Theoretical Background and Applications to Isotropic and Anisotropic Dielectrics. *J. Chem. Phys.* **1997**, *107*, 3032–3041.
(266) Mennucci, B.; Cancès, E.; Tomasi, J. Evaluation of Solvent Effects in Isotropic and Anisotropic Dielectrics and in Ionic Solutions with a Unified Integral Equation Method: Theoretical Bases, Computational Implementation, and Numerical Applications. *J. Phys. Chem. B* **1997**, *101*, 10506–10517.
(267) Cancès, E.; Mennucci, B. New Applications of Integral Equations Methods for Solvation Continuum Models: Ionic Solutions and Liquid Crystals. *J. Math. Chem.* **1998**, *23*, 309–326.
(268) Klamt, A.; Schüürmann, G. COSMO: A New Approach to Dielectric Screening in Solvents with

Explicit Expressions for the Screening Energy and Its Gradient. *J. Chem. Soc. Perkin Trans. 2* **1993**, 799–805.
(269) Marenich, A. V.; Cramer, C. J.; Truhlar, D. G. Universal Solvation Model Based on Solute Electron Density and on a Continuum Model of the Solvent Defined by the Bulk Dielectric Constant and Atomic Surface Tensions. *J. Phys. Chem. A* **2009**, *113*, 6378–6396.
(270) Klamt, A. The COSMO and COSMO-RS Solvation Models. *Wiley Interdiscip. Rev. Comput. Mol. Sci.* **2011**, *1*, 699–709.
(271) Mu, T.; Rarey, J.; Gmehling, J. Performance of COSMO-RS with Sigma Profiles from Different Model Chemistries. *Ind. Eng. Chem. Res.* **2007**, *46*, 6612–6629.
(272) Klamt, A.; Jonas, V.; Bürger, T.; Lohrenz, J. C. W. Refinement and Parametrization of COSMO-RS. *J. Phys. Chem. A* **1998**, *102*, 5074–5085.
(273) Klamt, A.; Eckert, F. Fast Solvent Screening via Quantum Chemistry: COSMO-RS Approach. *AIChE J.* **2002**, *48*, 369–385.
(274) Chen, X. H.; Luo, S. W.; Tang, Z.; Cun, L. F.; Mi, A. Q.; Jiang, Y. Z.; Gong, L. Z. Organocatalyzed Highly Enantioselective Direct Aldol Reactions of Aldehydes with Hydroxyacetone and Fluoroacetone in Aqueous Media: The Use of Water to Control Regioselectivity. *Chem. Eur. J.* **2007**, *13*, 689–701.
(275) Blom, M. N.; Compagnon, I.; Polfer, N. C.; Von Helden, G.; Meijer, G.; Suhai, S.; Paizs, B.; Oomens, J. Stepwise Solvation of an Amino Acid: The Appearance of Zwitterionic Structures. *J. Phys. Chem. A* **2007**, *111*, 7309–7316.
(276) Feller, D. *Ab Initio* Study of M^+:18-Crown-6 Microsolvation. *J. Phys. Chem. A* **1997**, *101*, 2723–2731.
(277) Bachrach, S. M. Microsolvation of Glycine: A DFT Study. *J. Phys. Chem. A* **2008**, *112*, 3722–3730.
(278) Pan, Y.; McAllister, M. A. Characterization of Low-Barrier Hydrogen Bonds. 1. Microsolvation Effects. An Ab Initio and DFT Investigation. *J. Am. Chem. Soc.* **1997**, *119*, 7561–7566.
(279) Tachikawa, H. Direct Ab Initio Dynamics Study on a Gas Phase Microsolvated S_N2 Reaction of $F^-(H_2O)$ with CH_3Cl. *J. Phys. Chem. A* **2000**, *104*, 497–503.
(280) Merrill, G. N.; Fletcher, G. D. A Microsolvation Approach to the Prediction of the Relative Enthalpies and Free Energies of Hydration for Ammonium Ions. *Theor. Chem. Acc.* **2008**, *120*, 5–22.
(281) Singh, N. J.; Min, S. K.; Kim, D. Y.; Kim, K. S. Comprehensive Energy Analysis for Various Types of π-Interaction. *J. Chem. Theory Comput.* **2009**, *5*, 515–529.
(282) Aikens, C. M.; Gordon, M. S. Incremental Solvation of Nonionized and Zwitterionic Glycine. *J. Am. Chem. Soc.* **2006**, *128*, 12835–12850.
(283) Eyring, H. The Activated Complex in Chemical Reactions. *J. Chem. Phys.* **1935**, *3*, 107–115.
(284) Evans, M. G.; Polanyi, M. Some Applications of the Transition State Method to the Calculation of Reaction Velocities, Especially in Solution. *Trans. Faraday Soc.* **1935**, *31*, 875–894.
(285) Laidler, K. J.; King, M. C. The Development of Transition-State Theory. *J. Phys. Chem.* **1983**, *87*, 2657–2664.
(286) Neese, F.; Atanasov, M.; Bistoni, G.; Maganas, D.; Ye, S. Chemistry and Quantum Mechanics in 2019: Give Us Insight and Numbers. *J. Am. Chem. Soc.* **2019**, *141*, 2814–2824.
(287) Foster, J. P.; Weinhold, F. Natural Hybrid Orbitals. *J. Am. Chem. Soc.* **1980**, *102*, 7211–7218.
(288) Reed, A. E.; Weinstock, R. B.; Weinhold, F. Natural Population Analysis. *J. Chem. Phys.* **1985**, *83*, 735–746.
(289) Johnson, E. R.; Keinan, S.; Mori Sánchez, P.; Contreras García, J.; Cohen, A. J.; Yang, W. NCI : Revealing Non-Covalent Interactions. *J. Am. Chem. Soc.* **2010**, *132*, 6498–6506.
(290) Contreras-García, J.; Johnson, E. R.; Keinan, S.; Chaudret, R.; Piquemal, J. P.; Beratan, D. N.; Yang, W. NCIPLOT: A Program for Plotting Noncovalent Interaction Regions. *J. Chem. Theory Comput.* **2011**, *7*, 625–632.
(291) Bader, R. F. W. Atoms in Molecules. *Atoms Mol.* **1985**, *18*, 9–15.
(292) Zhao, L.; Hopffgarten, M. von; Andrada, D. M.; Frenking, G. Energy Decomposition Analysis. *Wiley Interdiscip. Rev. Comput. Mol. Sci.* **2018**, *8*, e1345.
(293) Bickelhaupt, F. M.; Houk, K. N. Analyzing Reaction Rates with the Distortion/Interaction-Activation Strain Model. *Angew. Chem. Int. Ed.* **2017**, *56*, 10070–10086.
(294) Fernández, I.; Bickelhaupt, F. M. The Activation Strain Model and Molecular Orbital Theory: Understanding and Designing Chemical Reactions. *Chem. Soc. Rev.* **2014**, *43*, 4953.
(295) Coulson, C. A. Present State of Molecular Structure Calculations. *Rev. Mod. Phys.* **1960**, *32*, 170–177.

(296) Andrés, J.; Ayers, P. W.; Boto, R. A.; Carbó-Dorca, R.; Chermette, H.; Cioslowski, J.; Contreras-García, J.; Cooper, D. L.; Frenking, G.; Gatti, C.; Heidar-Zadeh, F.; Joubert, L.; Martín Pendás, Á.; Matito, E.; Mayer, I.; Misquitta, A. J.; Mo, Y.; Pilmé, J.; Popelier, P. L. A.; Rahm, M.; Ramos-Cordoba, E.; Salvador, P.; Schwarz, W. H. E.; Shahbazian, S.; Silvi, B.; Solà, M.; Szalewicz, K.; Tognetti, V.; Weinhold, F.; Zins, É.-L. Nine Questions on Energy Decomposition Analysis. *J. Comput. Chem.* **2019**, *accepted*, DOI: 10.1002/jcc.26003.
(297) Maji, R.; Champagne, P. A.; Houk, K. N.; Wheeler, S. E. Activation Mode and Origin of Selectivity in Chiral Phosphoric Acid-Catalyzed Oxacycle Formation by Intramolecular Oxetane Desymmetrizations. *ACS Catal.* **2017**, *7*, 7332–7339.
(298) Seguin, T. J.; Wheeler, S. E. Electrostatic Basis for Enantioselective Brønsted-Acid-Catalyzed Asymmetric Ring Openings of Meso-Epoxides. *ACS Catal.* **2016**, *6*, 2681–2688.
(299) Nguyen, Q. N. N.; Lodewyk, M. W.; Bezer, S.; Gagné, M. R.; Waters, M. L.; Tantillo, D. J. Effects of Helix Macrodipole and Local Interactions on Catalysis of Acyl Transfer by α-Helical Peptides. *ACS Catal.* **2015**, *5*, 1617–1622.
(300) Chen, S.; Zheng, Y.; Cui, T.; Meggers, E.; Houk, K. N. Arylketone π-Conjugation Controls Enantioselectivity in Asymmetric Alkynylations Catalyzed by Centrochiral Ruthenium Complexes. *J. Am. Chem. Soc.* **2018**, *140*, 5146–5152.
(301) Chen, S.; Houk, K. N. Origins of Stereoselectivity in Mannich Reactions Catalyzed by Chiral Vicinal Diamines. *J. Org. Chem.* **2018**, *83*, 3171–3176.
(302) Chen, S.; Huang, X.; Meggers, E.; Houk, K. N. Origins of Enantioselectivity in Asymmetric Radical Additions to Octahedral Chiral-at-Rhodium Enolates: A Computational Study. *J. Am. Chem. Soc.* **2017**, *139*, 17902–17907.
(303) Zhang, S. Q.; Taylor, B. L. H.; Ji, C.-L.; Gao, Y.; Harris, M. R.; Hanna, L. E.; Jarvo, E. R.; Houk, K. N.; Hong, X. Mechanism and Origins of Ligand-Controlled Stereoselectivity of Ni-Catalyzed Suzuki-Miyaura Coupling with Benzylic Esters: A Computational Study. *J. Am. Chem. Soc.* **2017**, *139*, 12994–13005.
(304) Wolters, L. P.; Ren, Y.; Bickelhaupt, F. M. Understanding E2 versus S_N2 Competition under Acidic and Basic Conditions. *ChemistryOpen* **2014**, *3*, 29–36.
(305) Hansch, C.; Rockwell, S. D.; Jow, P. Y. C.; Leo, A.; Steller, E. E. Substituent Constants for Correlation Analysis. *J. Med. Chem.* **1977**, *20*, 304–306.
(306) Hansch, C.; Leo, A.; Taft, R. W. A Survey of Hammett Substituent Constants and Resonance and Field Parameters. *Chem. Rev.* **1991**, *91*, 165–195.
(307) McDaniel, D. H.; Brown, H. C. An Extended Table of Hammett Substituent Constants Based on the Ionization of Substituted Benzoic Acids. *J. Org. Chem.* **1958**, *23*, 420–427.
(308) Hammett, L. P. The Effect of Structure upon the Reactions of Organic Compounds. Benzene Derivatives. *J. Am. Chem. Soc.* **1937**, *59*, 96–103.
(309) Jaffé, H. H. A Reëxamination of the Hammett Equation. *Chem. Rev.* **1953**, *53*, 191–261.

2 Establishing the Fundamentals of Fluoride Reactivity and S_N2:E2 Selectivity in Hydrogen Bonded Complexes

2.1 Introduction

To extend the understanding of the effects of hydrogen bonding on the reactivity and selectivity of fluoride, Gouverneur and co-workers synthesized stoichiometric hydrogen bonded fluoride complexes from TBAF with various alcohol and urea hydrogen bond donors.[1,2] These fluoride complexes were used as stoichiometric fluoride reagents for a model S_N2 vs E2 reaction with primary bromide substrate (**1**), with select results summarized in Table 2.1. S_N2 is the desired reactivity of fluoride, producing a fluorinated product (**2**), whereas E2 reactivity is undesired, producing alkenes not containing fluorine (**3**). The general trends are that reaction rate decreases with increasing urea hydrogen bond donor strength (increasing substituent Hammett σ_p), but S_N2 over E2 selectivity increases. Ureas provide superior selectivity over alcohols, achieving up to an 8.7 selectivity ratio in favor of S_N2, unprecedented at the time of publication.

The motivation for investigating such complexes was ultimately to use hydrogen bonding for catalytic fluorination, inspired by the mechanism of the fluorinase enzyme. This chapter describes initial computational work to reproduce and rationalize the observed kinetic and selectivity data of stoichiometric urea-fluoride complexes. In the process, a level of theory is established to accurately describe hydrogen bonding to fluoride, to apply to future work. Further, the origins of the change in S_N2 over E2 selectivity are probed. This chapter focuses on the reactivity and selectivity of 6 para-disubstituted diarylurea complexes (**U**X), with X = CF_3, H, F, Cl, Me and OMe substituents. All experimental results refer to those published in the two papers cited above.

Table 2.1: SN2:E2 Reactivity and Selectivity of Stoichiometric Hydrogen Bonded Fluoride Complexes of Formula U_2F with Primary Bromide Substrate.

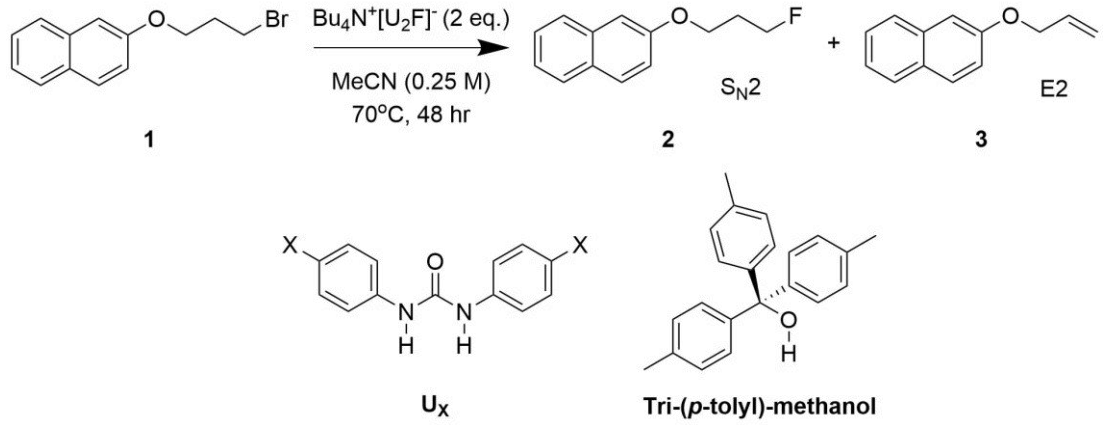

Donor Type	X	Rate Constant / 10^{-5} M^{-1} s^{-1}		Selectivity (S_N2/E2)
		S_N2	E2	
Diarylurea (U_X)	**OMe**†	12.7	2.45	5.2
	Me†	9.8	1.65	5.7
	H†	5.76	0.85	6.8
	F†	5.67	0.80	7.1
	Cl†	5.83	0.84	6.9
	CF_3†	1.65	0.19	8.7
Tri-(*p*-tolyl)-methanol*‡		1700	810	2.1

* 0.5 M concentration. ‡/† Results of Gouverneur and co-workers. ‡: ref 1. †: ref 2.

2.2 Computational Methods and Benchmarking

2.2.1 Density Functional Theory

Geometry optimizations and frequency calculations were performed in Gaussian 09, rev D.01.[3] Single point energy calculations were performed in Orca 3.0.3 due to superior implementation of *ab initio* methods.[4] Calculations in Gaussian with Minnesota type functionals were performed using the 99,590 ultrafine integration grid.[5] Solvation in Gaussian was modeled using the conductor-like polarizable continuum model (CPCM)[6–8] and in ORCA by the conductor-like screening model (COSMO).[9] Stationary points were classified by vibrational frequencies – those with no imaginary frequencies as minima, and those with a single imaginary frequency as transition state structures (TSs). Thermochemistry was calculated from frequency analysis using *GoodVibes* python

script.[10] A free-rotor approximation was applied to vibrational modes below 50 cm^{-1}, as proposed by Grimme.[11] Gibbs free energies were evaluated at 1 M concentration and 298.15 K for equilibrium constants, and 0.5 M/343.15 K for kinetic studies in accordance with the experimental conditions. Charges were calculated using natural population analysis (NPA) in natural bond order calculations (NBO).[12] 1-Bromopropane is used as model primary bromide nucleophile.

2.2.2 Benchmarking

The TS benchmarking described herein is based upon preliminary work performed by Paton and co-workers.[13] Geometries of S_N2, *anti*-E2 and *syn*-E2 TSs were benchmarked relative to Møller–Plesset perturbation theory (MP2)[14] method with quadruple-ζ def2-QZVPPD basis set.[15,16] Single point energy accuracy was benchmarked through reproducing activation barrier heights for the three mechanisms relative to domain based local pair natural orbital coupled cluster singles, doubles, perturbative triples (DLPNO-CCSD(T))[17,18] with ma-def2-TZVPP basis set.[15,19] Wavefunction theory (WFT) methods such as MP2 and DLPNO-CCSD(T) are suitable for benchmarking against due to their general accuracy and the fact that they do not depend on the arbitrary choice of a density functional, unlike DFT approaches. Calculations were performed in acetonitrile solvent in both cases.

Benchmarking of computational methods can be separated into two branches: a) comparison of methods to high-level theoretical calculations and b) comparison to experimental observables.[20] The former has the advantage that no experimental data is required, increasing practicality, but also enabling benchmarking of properties that are challenging, or impossible to observe experimentally, such as solution phase geometries and TS geometries. Even high-level theoretical methods, however, employ

approximations and have uncertainty, with the results of the benchmark depending completely on their validity. Further, the high computational cost of the methods limits benchmarking to small systems. Benchmarking against experimental values is often preferred due to the definitiveness of the experimental results, subject to the experiments being correctly carried out. These results, however, must be measured experimentally, requiring appropriate laboratory equipment. Further, it may be non-trivial to construct a computational model that is directly comparable to the experimental conditions, leading to some uncertainty in the comparison.

Once a system has been computed at a given level of theory, further comparison with experimental data can be used to support that computation is getting the right results for the right reasons. Examples of comparisons include i) experimental observation of computed low energy intermediates, or catalyst resting state, ii) explanation of relative substrate yields (including unreactive substrates), iii) explanation of relative substrate selectivities, iv) kinetic isotope effects and v) side reactions.

Initial benchmarking is performed relative to high-level WFT calculations to ensure accurate TS geometries (unobservable experimentally) and fluoride delivery barrier heights (difficult to deconvolute from experimental data). The rest of this chapter involves the application of the chosen method to reproduce experimental data (*e.g.* fluoride binding energies, S_N2:E2 selectivity), which may be considered as benchmarking of the method against experimental data, for the work in future chapters. The close interplay of computation and experiment in Chapters 3 and 4 also ensures that computational results and hypotheses are regularly compared with experimental results.

2.2.2.1 Geometry Benchmarking

The key bond lengths of TSs for S_N2, *anti*-E2 and *syn*-E2 mechanisms were measured and compared to the MP2/def2-QZVPPD benchmark (Figure 2.1). The root-mean-square deviation (RMSD) of the bond lengths was used as a measure of the accuracy of each method (Table 2.2).

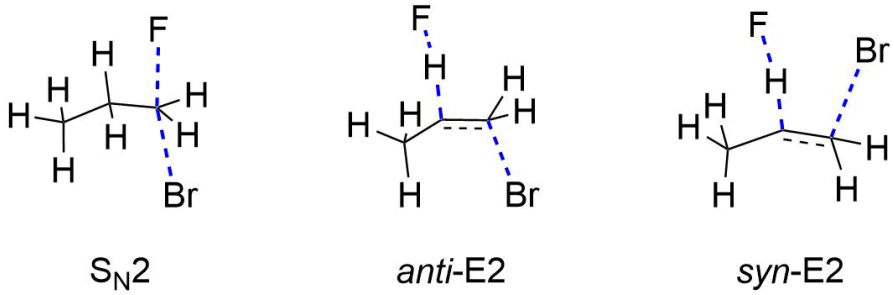

Figure 2.1: Transition state structures used for geometry and energy barrier benchmarking. Bonds used in calculation of geometry RMSD are highlighted in blue. Energy barriers are the energies of the TSs relative to the energy of the reactants.

Table 2.2: Geometry Optimization Benchmarking of TSs Relative to MP2 Benchmark Geometries.

Functional/ Method	Basis Set	S_N2		*anti*-E2			*syn*-E2			RMSD
		C-F	C-Br	H-F	C-H	C-Br	H-F	C-H	C-Br	
MP2	QZVPPD	2.00	2.36	1.21	1.35	2.28	1.18	1.35	2.29	0
ωB97X-D[21,22]	Small	2.12	2.43	1.30	1.28	2.50	1.32	1.26	2.56	0.15
	TZVPPD	2.09	2.41	1.27	1.31	2.38	1.26	1.29	2.43	0.08
	QZVPPD	2.09	2.41	1.26	1.31	2.38	1.26	1.29	2.43	0.08
OLYP[23]	Small	2.18	2.48	1.31	1.29	2.52	1.36	1.25	2.61	0.18
	TZVPPD	2.13*	2.46	1.29	1.30	2.39	1.30	1.28	2.47	0.11
	QZVPPD	2.14	2.46	1.29	1.30	2.39	1.30	1.28	2.47	0.11
B3LYP-D3[24–28]	Small	2.15	2.45	1.32	1.29	2.54	1.34	1.25	2.62	0.18
	TZVPPD	2.12	2.43	1.30	1.29	2.43	1.31	1.26	2.50	0.12
	QZVPPD	2.12	2.43	1.30	1.29	2.43	1.31	1.26	2.50	0.12
M06-2X[29]	Small	2.06	2.41	1.25	1.32	2.36	1.25	1.31	2.40	0.06
	TZVPP(D)	2.04	2.39	1.25	1.32	2.30	1.22	1.33	2.33	0.03
	TZVPPD	2.04	2.39	1.25	1.32	2.30	1.22	1.33	2.32	0.03
	QZVPPD	2.04	2.39	1.24	1.32	2.30	1.21	1.33	2.32	0.03
M06-L[30]	TZVPP(D)	2.14	2.36	1.26	1.35	2.28	1.23	1.36	2.60	0.15
TPSSTPSS[31]	TZVPP(D)	2.15	2.38	1.29	1.31	2.42	1.27	1.32	2.50	0.11

Ahlrichs type basis sets have been abbreviated by removing def2 prefix. Figures highlighted in light blue indicate results by Paton and co-workers.[13] *Corrected value. The basis set referred to as 'small' consists of 6-31+G(d) on fluorine,[32–35] LANL08(d)/LANL2DZ on bromine[36,37] and 6-31G(d) on all other atoms. def2-TZVPP(D) refers to def2-TZVPPD on fluorine and bromine, with def2-TZVPP otherwise.

All functionals show good basis set convergence by the time triple-ζ quality is reached, with RMSD indistinguishable at 0.01 Å resolution, and a significant deterioration in geometry quality when the small basis set is used. Comparing the def2-TZVPP(D) and def2-TZVPPD basis sets with M06-2X functional demonstrates that diffuse basis functions are only required on the electronegative atoms, which have a net negative charge in the TSs. The best performing functional by some margin is M06-2X, with RMSD of 0.03 Å with triple-ζ basis set, compared to the next best, ωB97X-D with RMSD of 0.08 Å.

The geometry of urea-fluoride complexes with unsubstituted diphenylurea, $\mathbf{U_H}$, were also benchmarked to ensure accurate description of fluoride hydrogen bonding (Table 2.3). Due to the size of the system, geometries were benchmarked against MP2/def2-TZVPPD, rather than the larger def2-QZVPPD basis set. Further, quadruple-ζ basis sets were not benchmarked due to the degree of basis set convergence seen with the TS benchmarking, and the impractical computational cost.

Again, the larger basis set is found to produce geometries closer to the benchmark geometry for all functionals, notably in the length of the hydrogen bonds to fluoride themselves. The best performing functionals were M06-2X and TPSSTPSS, both with RMSDs of 0.01 Å. Given the high performance of the former, and the poor performance of the latter in TS benchmarking, M06-2X with def2-TZVPP(D) basis set was selected to study the reactivity and selectivity of urea-fluoride complexes.

Table 2.3: Geometry Benchmarking of Urea-Fluoride Complexes Relative to MP2 Geometries.

Functional / Method	Basis Set	Bond Distances / Å			RMSD
		N–F	N–H	H–F	
MP2	def2-TZVPP(D)	2.635	1.038	1.648	0
ωB97X-D	Small	2.697	1.034	1.716	0.05
	def2-TZVPP(D)	2.660	1.034	1.676	0.02
M06-2X	Small	2.683	1.035	1.703	0.04
	def2-TZVPP(D)	2.647	1.035	1.664	0.01
OLYP	Small	2.747	1.039	1.755	0.09
	def2-TZVPP(D)	2.702	1.040	1.707	0.05
B3LYP-D3	Small*	2.701	1.035	1.718	0.06
	def2-TZVPP(D)*	2.661	1.036	1.675	0.02
M06-L	Small	2.683	1.035	1.703	0.04
	def2-TZVPP(D)	2.661	1.034	1.675	0.02
TPSSTPSS	Small	2.685	1.048	1.688	0.04
	def2-TZVPP(D)	2.647	1.050	1.645	0.01

*Single low imaginary frequency. The basis set referred to as 'small' consists of 6-31+G(d) on fluorine and 6-31G(d) on all other atoms. Def2-TZVPP(D) refers to def2-TZVPPD on fluorine and bromine, with def2-TZVPP otherwise.

2.2.2.2 Activation Barrier Benchmarking

To assess the performance of different functionals at computing activation barriers, DLPNO-CCSD(T)/ma-def2-TZVPP single points were evaluated on MP2/def2-QZVPPD geometries, for the S_N2, *anti*-E2 and *syn*-E2 mechanisms and used as a benchmark for DFT methods. The barrier heights are tabulated in Table 2.4. The basis set denoted (ma)-def2-TZVPP was used to benchmark methods, corresponding to def2-TZVPP on carbon and hydrogen, and ma-def2-TZVPP otherwise. A mixed basis set was used to remove diffuse functions from carbon, which prevented reliable SCF convergence in some cases, due to linear dependence of the basis functions.

TS barrier benchmarking demonstrates that the functional used for optimization, M06-2X, is inferior for barrier heights, with RMSD of 15 kJ/mol. However, ωB97X-D3, similar to ωB97X-D used for optimization, but with updated dispersion correction,

Table 2.4: Activation Barrier Benchmarking Relative to DLPNO-CCSD(T).

Functional / method	$\Delta E^{\ddagger}$ (S_N2)	$\Delta E^{\ddagger}$ (*anti*-E2)	$\Delta E^{\ddagger}$ (*syn*-E2)	RMSD	$\Delta\Delta E^{\ddagger}$ (S_N2–E2)
DLPNO-CCSD(T)	68.2	82.2	124.3	0.0	-13.9
RI-SCS-MP2	78.9	92.0	136.2	10.9	-13.1
ωB97X-D3	66.6	78.9	118.3	4.0	-12.3
M06-2X	60.2	66.0	104.8	15.3	-5.8
OLYP	78.3	63.8	102.4	17.5	14.6
B3LYP-D3	51.9	60.2	99.5	21.3	-8.3

All calculations were performed with the (ma)-def2-TZVPP basis set. Energies are given in kJ/mol.

performs very well for activation barriers, reproducing both the benchmark barrier heights (4.0 kJ/mol RMSD) and the S_N2:E2 selectivity (-12.3 kJ/mol *c.f.* -13.9 kJ/mol). Single point energy corrections were therefore chosen to be performed using ωB97X-D3/(ma)-def2-TZVPP. Interestingly, OLYP uniquely calculates the opposite selectivity to the benchmark, with S_N2:E2 $\Delta\Delta E^{\ddagger}$ 28.5 kJ/mol off the benchmark. This result is surprising given the successes of OLYP in describing the geometries and energy barriers in similar systems in gas-phase.[38–40] Its inaccurate description of hydrogen bonding, as reproduced in urea-fluoride complex benchmarking is, however, documented.[39]

2.2.3 Optimized Level of Theory

The optimized level of theory used for the remainder of this work uses the hybrid meta-GGA exchange-correlation functional M06-2X, with a mixed triple-ζ basis set, referred to as def2-TZVPP(D), consisting of def2-TZVPPD on fluoride ion and substrate bromide, and def2-TZVPP otherwise for geometry and frequency calculations. The use of diffuse functions assists in describing anions but are generally superfluous for other atoms.[41,42] Augmenting a basis set with diffuse functions on specific atoms is an efficient way to increase accuracy with minimal increase in basis set size.[19,43] The M06-2X

functional is well established to accurately describe non-covalent interactions[29,44–47] and incorporates dispersion through the parametrization of the functional.[48] All calculations were performed in implicit acetonitrile solvent. Single point energy corrections were performed using the range-separated hybrid functional, ωB97X-D3, incorporating Grimme's D3 dispersion correction,[28] with the full ma-def2-TZVPP basis set.

2.3 Selectivity for S_N2 vs E2 Reactivity

Experimentally, Gouverneur and co-workers used homoleptic $NBu_4[U_2F]$ complexes as stoichiometric fluoride sources, where U represents a para-disubstituted diarylurea. A urea with X para-disubstitution is referred to as **U**$_X$. Figure 2.2 outlines the potential reactivity of the $[U_2F]^-$ complexes. Firstly, one, or both of the ureas in the complex can dissociate producing alternative potential fluoride sources, $[UF]^-$ and F^-. Each one of these species can potentially react productively *via* S_N2 to form fluorinated product, or unproductively *via* E2 to form undesired alkene product. Experimentally, kinetic experiments demonstrate that the bis urea-fluoride complexes, $[U_2F]^-$, were unreactive.

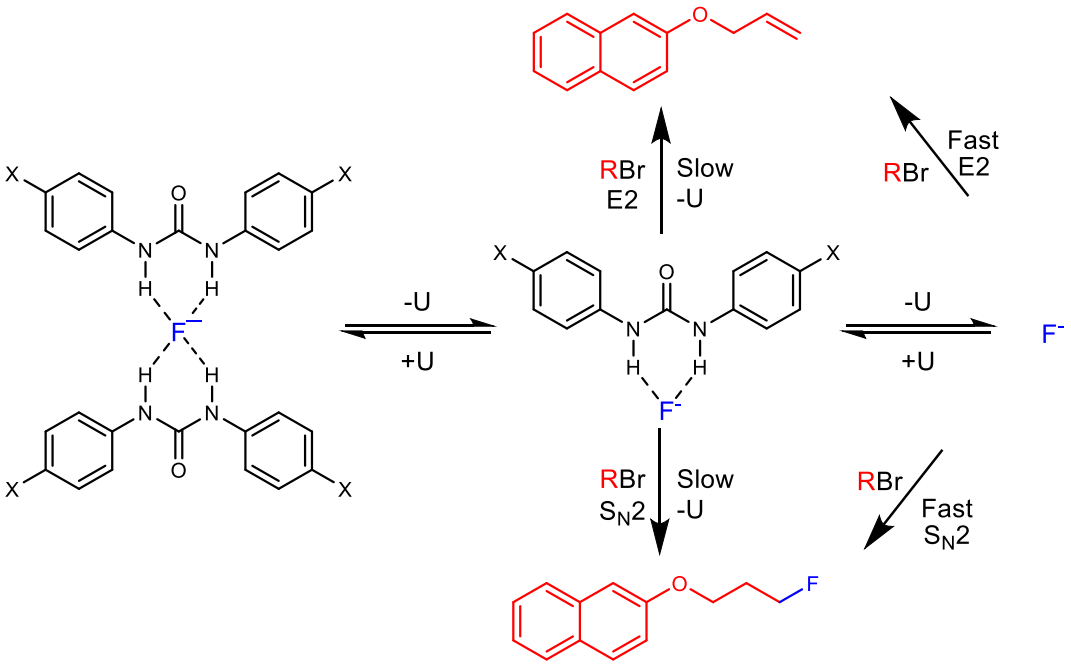

Figure 2.2: Possible reactive pathways of stoichiometric $[U_2F]^-$ complexes as fluoride source with primary substrate, RBr. Experimental substrate is shown, PrBr is computed as surrogate.

Additionally, F^-, where both ureas have dissociated, would be expected to behave similarly to TBAF in terms of both reactivity and selectivity. The focus of this study is therefore on the mono urea-fluoride complexes, $[UF]^-$.

2.3.1 Fluoride Complexes and Binding Energies

Experimental fluoride binding energies were determined by UV-vis and NMR titrations. Computational binding energies were evaluated by taking the Gibbs free energy difference between urea-fluoride complex, and separated urea and fluoride. This gives a reasonable model, however the influence of the cation, explicit solvent interactions and solvent entropy changes are neglected. As the binding constants were determined in MeCN with TBAF fluoride source, neglect of the cation is reasonable as the polar solvent facilitates dissociation of ion pairs, and the TBA cation is relatively non-coordinating. Neglect of explicit solvent interactions and solvent entropy are standard approximations in computational chemistry due to the impracticality of computing explicit solvation with quantum mechanical methods (see Chapter 1).

All ureas studied are non-planar due to steric clash of the aromatic groups and urea oxygen, resulting in two low energy conformers, with approximate symmetries of C_s and C_2 (Figure S1). The lowest energy C_2 conformers are used for further study. Ureas with substituents with larger σ_p generally adopt a structure closer to planarity and, upon fluoride binding, all ureas adopt a planar structure. A plot of computed binding energies against experimental binding energies is given in Figure 2.3. BSSE was confirmed to be small at 1.2 kJ/mol for $\mathbf{U_H}$, using the counterpoise method, and will affect all ureas similarly. The computed binding energies correlate well with experimental values, with $R^2 = 0.96$, however the trend with changing urea substituent is stronger than seen experimentally, with gradient of 3.66. Complexation is enthalpically dominated,

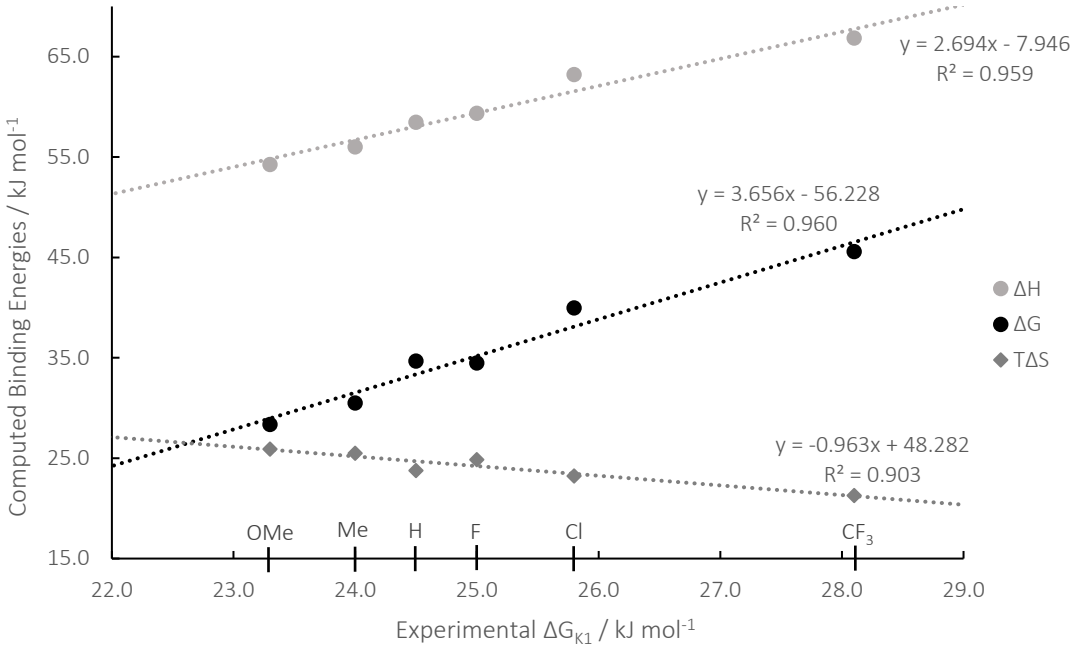

Figure 2.3: Computed Gibbs free energies, enthalpies and entropies of binding for $[UF]^-$ complexes, plotted against experimentally determined Gibbs free energies of binding (298.15 K, computed concentration of 1 M). Points from left to right represent $\mathbf{U_X}$ where X = OMe, Me, H, F, Cl, CF_3.

contributing the largest term to ΔG and dominating the trend with urea substituent. Good correlations are also achieved against Hammett σ_p (Figure S4, $R^2 = 0.99$ for ΔG). Whilst both ΔG and ΔH increase with Hammett σ_p, the entropy term, TΔS becomes generally less unfavorable. This is despite stronger hydrogen bonding with σ_p, and is consistent with a smaller loss in vibrational entropy upon binding by ureas that adopt a geometry closer to the planar structure enforced upon fluoride binding (Table S2). Good correlation is seen between a measure of this distortion from planarity (represented by the dihedral between aromatic ring and urea) and entropy of binding (Figure S5).

Bis urea complex, $[U_2F]^-$, geometries computationally optimized in solution all favor a π-π stacked geometry (Figure 2.4). This contrasts strongly with the solid-state crystal structures where a diverse array of coordination geometries is seen. It may be inferred from this result that the diversity of solid-state structures arises from packing forces rather than an intrinsic geometric preference of fluoride with different hydrogen bond donors.

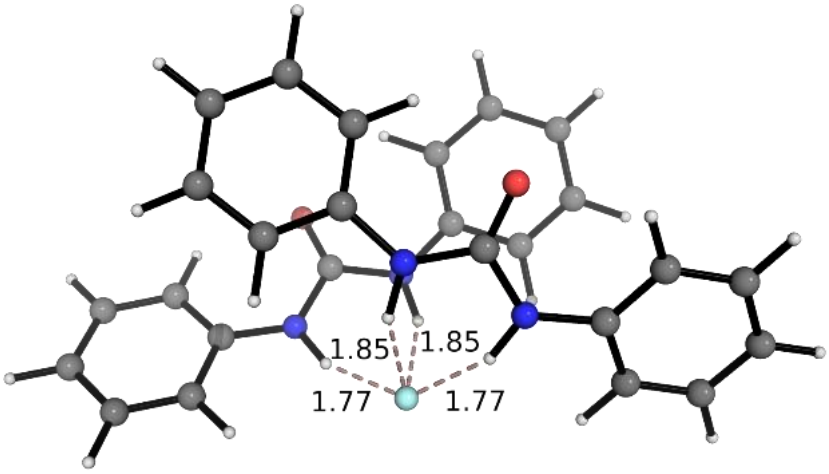

Figure 2.4: Bis urea-fluoride complex geometry, exhibiting interurea π-π stacking (**[U$_{H\ 2}$F]$^-$** illustrated).

Correlation of N–F distances (indicative of hydrogen bond length) in both mono and bis complexes is strong against substituent Hammett constant, σ_p, with R^2 of 0.99 and 0.98 respectively. This is in contrast to the average N–F distances measured in the solid-state which do not illustrate a clear trend with σ_p, likely as a result of the dominance of packing forces, and lie intermediate in length between the solution phase mono and bis complexes (Figure 2.5). Hydrogen bond lengths are longer in the bis complexes over the mono by

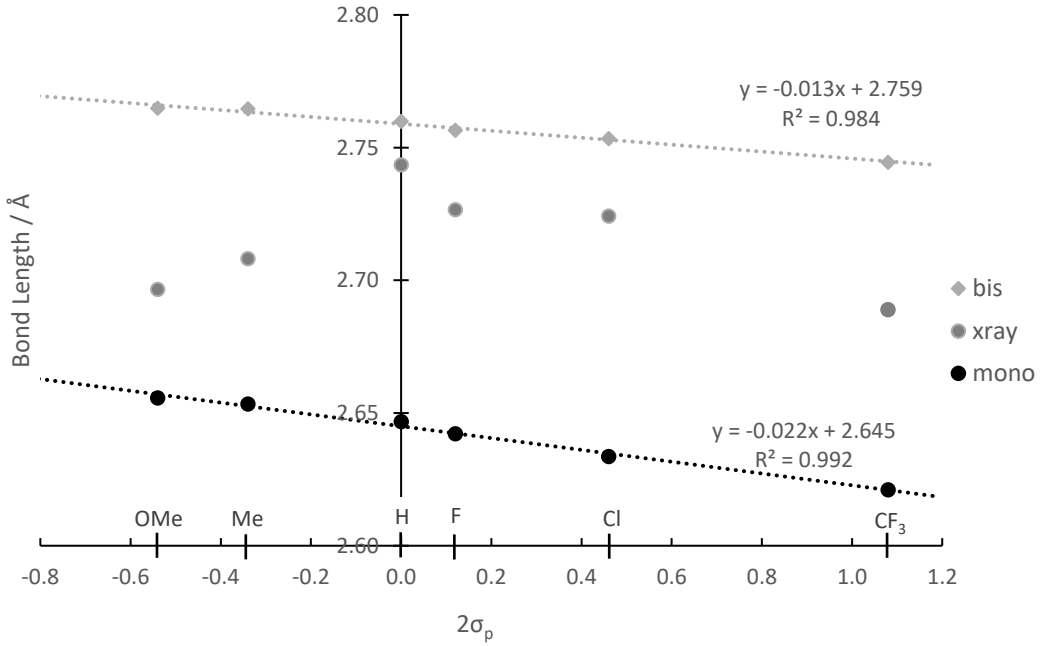

Figure 2.5: Hydrogen bond distances (N–F distance) in mono ($[UF]^-$) and bis ($[U_2F]^-$) computed structures compared to experimental distances in crystal structure. Note that $2\sigma_p$ is plotted as each urea has 2 *para* substituents. Points from left to right represent **U**x where X = OMe, Me, H, F, Cl, CF_3.

approximately 0.1 Å, as expected from the competition of a larger number of hydrogen bonds for fluoride. This difference in hydrogen bond length becomes greater as σ_p increases.

The charge on fluoride in the hydrogen bonded complexes display a strong correlation against substituent σ_p, with R^2 of 0.98 and 1.00 for mono and bis complexes respectively (Figure 2.6). As the hydrogen bond strength increases (increasing σ_p), the charge on fluoride is lowered on the order of 0.01 *e*. Mono complexes have more negative charge on fluoride, due to the formation of fewer hydrogen bonds, with charge on fluoride becoming less negative more strongly with σ_p than with the bis complexes. In the calculation of the urea-fluoride complexes, density functional theory calculations are sensitive enough to display clear trends in Gibbs free energies, geometries and atomic charges, laying the groundwork for study of the reactivity of the complexes.

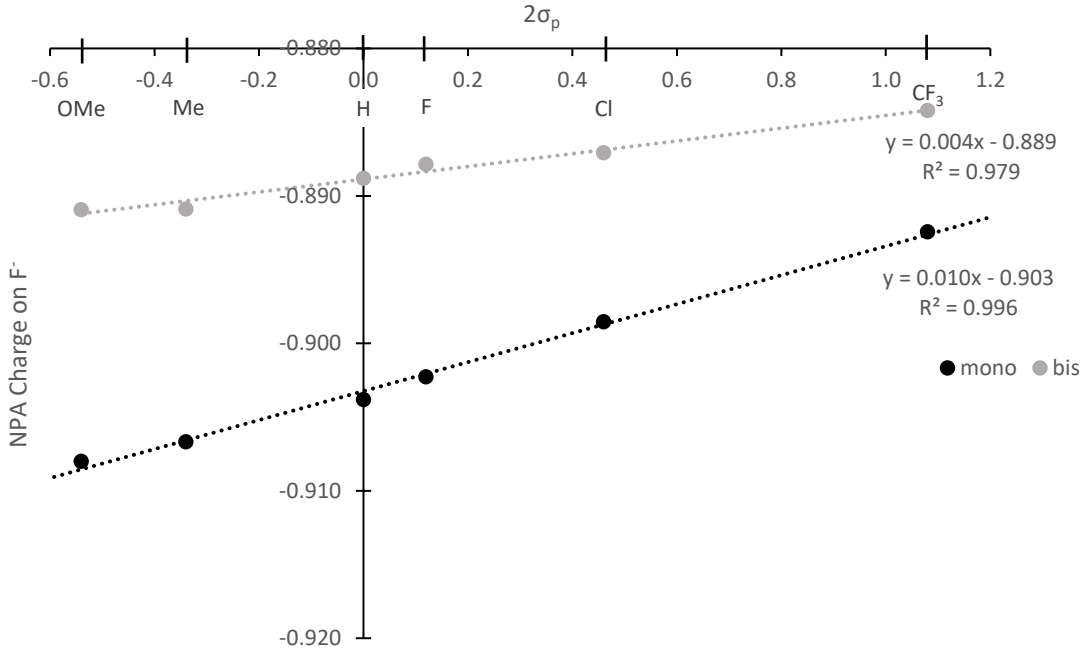

Figure 2.6: NPA charges on fluoride for mono and bis urea-fluoride complexes against Hammett Constant. Points from left to right represent **U**X where X = OMe, Me, H, F, Cl, CF_3.

2.3.2 Transition State Structures and Kinetics

Transition state structures (TSs) for S_N2, *anti*-E2 and *syn*-E2 mechanisms were computed with the non-hydrogen bonded fluoride anion (Figure 2.7), with Gibbs free energy barriers of $\Delta G^{\ddagger}$ = 90.7, 86.0 and 124.9 kJ/mol respectively. These barriers demonstrate a modest preference for *anti*-E2 over S_N2 mechanism by 4.7 kJ/mol, highlighting the high basicity of uncoordinated fluoride. The *syn*-E2 mechanism is uncompetitive, with a barrier exceeding *anti*-E2 by 38.9 kJ/mol and is therefore not considered further – future reference to the E2 mechanism thus implicitly refers to *anti*-E2. The energy barriers, $\Delta E^{\ddagger}$, for the 3 mechanisms are 66.6, 78.9 and 118.3 kJ/mol respectively, and enthalpy barriers of 62.2, 60.1 and 98.6 kJ/mol respectively. The large changes in relative barrier heights highlights the importance of enthalpic and entropic corrections in comparing the relative favorability of the substitution and elimination pathways, rather than using electronic energies.

S_N2 and *anti*-E2 TSs were calculated with each of the 6 $[UF]^-$ complexes. Conformational sampling established that Van der Waal's contact of the urea with the PrBr substrate was favored in all cases. Example TSs with unsubstituted urea, $\mathbf{U_H}$, are shown in Figure 2.8. Key distances are plotted in Figure 2.9 and tabulated in Table S3.

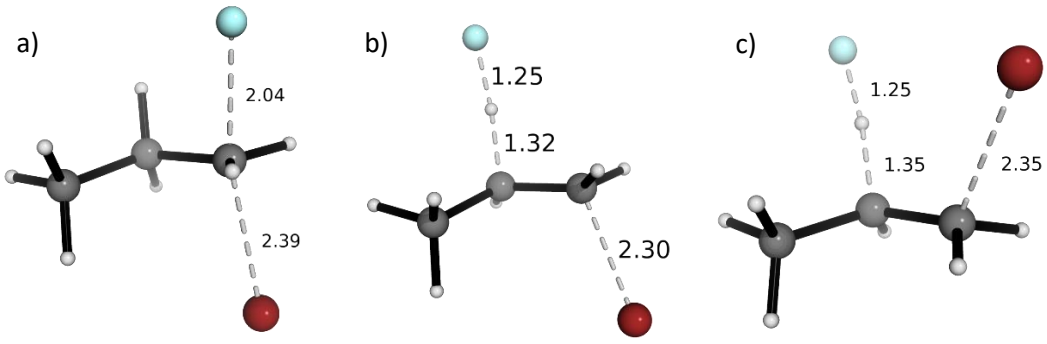

Figure 2.7: Computed transition state structures for a) S_N2 b) anti-E2 c) syn-E2 mechanisms.

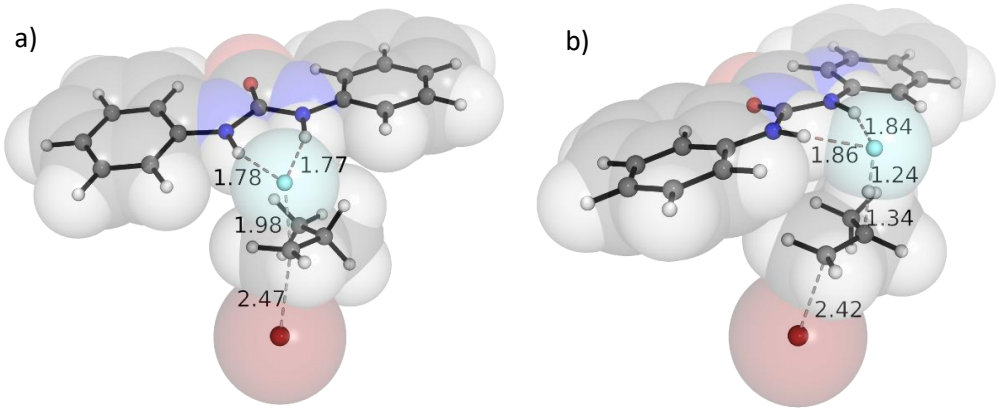

Figure 2.8: Transition state structures for urea mediated fluoride delivery for a) S_N2 reaction b) E2 reaction. Exemplified by unsubstituted urea-fluoride complex, $\mathbf{[U_HF]^-}$. TSs with other ureas are given in the Appendix, Figures S6 and S7.

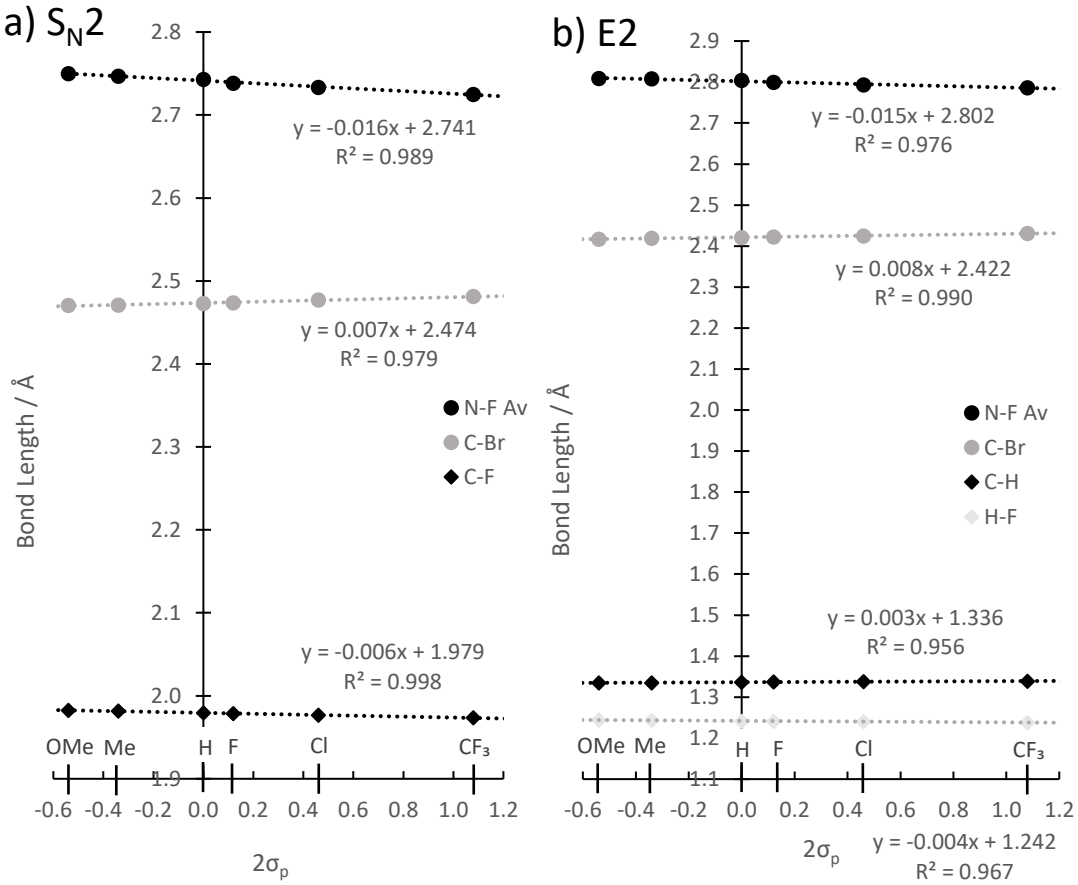

Figure 2.9: Key distances in transition state structures for a) S_N2 and b) E2 reactivity plotted against Hammett constant σ_p. Points from left to right represent $\mathbf{U_X}$ where X = OMe, Me, H, F, Cl, CF_3.

Plots of key TS distances against σ_p shows that all follow a strong linear correlation (R^2 > 0.96), though the overall changes in distances are small, on the order of 0.1 Å. As σ_p increases, TS positions for both S_N2 and E2 mechanisms become later, demonstrated by elongating C–Br distance, and shortening C–F or H–F distances respectively. Activation barriers are tabulated in Table 2.5 and plotted against σ_p in Figure 2.10.

Table 2.5: Activation Barriers to S_N2 and E2 Mechanisms.

Species	**Sub^n**	**S_N2 / kJ/mol**				**E2 / kJ/mol**			
		ΔE‡	**ΔH‡**	**TΔS‡**	**ΔG‡**	**ΔE‡**	**ΔH‡**	**TΔS‡**	**ΔG‡**
No urea	n/a	64.7	62.3	-28.5	90.7	76.7	60.1	-26.0	86.1
U	**OMe**	63.0	67.5	-52.0	119.5	86.5	77.0	-52.1	129.0
	Me	62.9	67.6	-54.5	122.1	86.8	77.5	-50.8	128.3
	H	63.4	68.4	-54.6	123.0	87.8	78.6	-53.6	132.2
	F	64.2	69.2	-55.2	124.3	88.5	79.3	-52.3	131.6
	Cl	65.2	70.1	-54.9	125.0	89.7	80.8	-53.6	134.3
	CF_3	65.7	71.3	-59.3	130.6	90.9	82.3	-56.4	138.7
R^2 vs σ_p		0.91	0.98	0.85	0.96	0.98	0.98	0.81	0.96

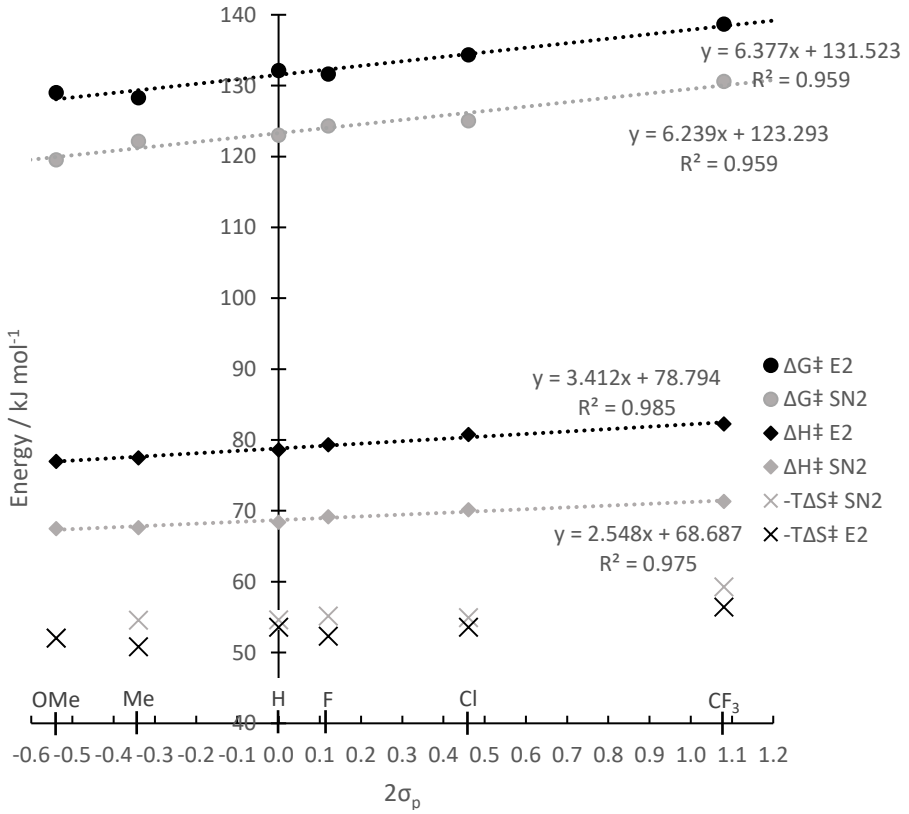

Figure 2.10: Key energy barriers for S_N2 and E2 reactivity plotted against Hammett constant σ_p. Points from left to right represent $\mathbf{U_X}$ where X = OMe, Me, H, F, Cl, CF_3.

All activation parameters correlate strongly against Hammett σ_p, with increasing activation barrier as the Hammett σ_p increases (*i.e.* as the urea becomes a stronger hydrogen bond donor). This correlation is particularly strong in the case of activation enthalpies, with R^2 of 0.98 for both S_N2 and E2 mechanisms. Entropy ($-T\Delta S^{\ddagger}$), however, correlates more weakly, with R^2 of 0.85 and 0.81 for S_N2 and E2 respectively, and contains considerably more noise. The largest (absolute) residuals are 1.4 kJ/mol and 0.92 kJ/mol for S_N2 and E2 respectively, with an overall change of 4.8 kJ/mol and 6.0 kJ/mol between $\mathbf{U_{OMe}}$ and $\mathbf{U_{CF3}}$ read from the regression line. The uncertainty in the entropic term is thus significant relative to the degree of change caused by changing urea substituents. Generally, the low degree of noise in the calculations is remarkable, with kJ/mol precision in the trends – particularly as the trends involve comparison of systems containing different ureas, reducing the potential for favorable error cancellation. Gibbs free energies show a slightly weaker correlation than enthalpy, with R^2 of 0.96 for both mechanisms, due to the addition of the entropic term, but demonstrate a clear increase in activation barriers with Hammett constant. Note that the activation barriers themselves cannot yet be directly compared with experiment, as they do not account for the formation of the $[UF]^-$ complex.

2.3.2.1 S_N2:E2 Selectivity

S_N2:E2 selectivity depends on the difference in $\Delta G^{\ddagger}$ for the S_N2 and E2 mechanisms ($\Delta\Delta G^{\ddagger}$). When looking at the enthalpic contributions, the barrier to E2 reaction is significantly higher than to S_N2 for all substituents. The regression lines show that $\Delta H^{\ddagger}$ for the E2 reaction increases more rapidly with σ_p than the S_N2 barrier with gradients of 3.41 and 2.55 respectively. Ignoring entropic changes, this corresponds to increasing S_N2:E2 selectivity as σ_p increases, in agreement with experimental kinetics.

Table 2.6: S_N2:E2 Selectivity Calculated by Various Methods.

		U					
		OMe	**Me**	**H**	**F**	**Cl**	**CF_3**
$2\sigma_p$		-0.54	-0.34	0	0.12	0.46	1.08
$\Delta\Delta G^{\ddagger}$ / kJ/mol	Experimental*	4.7	5.0	5.5	5.6	5.5	6.2
	Approach 1	9.5	6.1	9.2	7.3	9.3	8.1
	Approach 2†	8.16	8.18	8.23	8.25	8.29	8.38
	Approach 3	7.5	7.9	8.2	8.2	8.7	9.0
S_N2/E2	Experimental	5.2	5.7	6.8	7.1	6.9	8.7
	Approach 1*	28.0	8.6	24.7	12.9	26.1	17.0
	Approach 2*	17.4	17.6	17.9	18.0	18.3	18.9
	Approach 3*	14.0	16.0	17.8	17.7	20.9	23.1

* Conversion between S_N2/E2 ratios and $\Delta\Delta G^{\ddagger}$ assumes that all reactivity results from reaction of the $[UF]^-$ complexes. Background reactivity is likely to influence the values. †Higher precision values are reflective of the regression method used but do not imply higher accuracy – see text.

Due to the uncertainty in the entropy values, calculation of the S_N2:E2 ratios requires care. Three distinct approaches were taken to convert the computed energy values into the kinetic representation, specifically, the ratio of S_N2 product to E2 product for each urea, summarized as:

Approach 1: direct calculation from the $\Delta\Delta G^{\ddagger}$ with each urea.

Approach 2: estimation of $\Delta\Delta G^{\ddagger}$ from the lines of best fit of $\Delta G^{\ddagger}(S_N2)$ and $\Delta G^{\ddagger}(E2)$ against σ_p.

Approach 3: use of an averaged entropic contribution, $\Delta\Delta S^{\ddagger}$.

The energy values and selectivities calculated through the three approaches are summarized in Table 2.6.

The first approach, with direct calculation of $\Delta\Delta G^{\ddagger}$ for each urea, is unsuccessful, leading to scattered values with no correlation of selectivity with σ_p. The strength of this approach is that it uses the calculated Gibbs free energies without further processing. This,

however, forgoes the opportunity to reduce uncertainty through averaging, leading to erratic results.

The second approach exploits the correlation of the activation barriers with σ_p to reduce the uncertainty arising from the entropy calculation. Necessarily this approach *assumes* that such a correlation exists (a reasonable approximation given the strong correlations, but omits the opportunity to explain anomalies, such as $\mathbf{U_{Cl}}$ vs $\mathbf{U_F}$). From the equations of the trend lines for $\Delta G^{\ddagger}(S_N2)$ and $\Delta G^{\ddagger}(E2)$, equations can be derived for $\Delta\Delta G^{\ddagger}$ and S_N2/E2 ratio (Equations 2.1 and 2.2).

$$\Delta\Delta G^{\ddagger} = \Delta G^{\ddagger}(S_N2) - \Delta G^{\ddagger}(E2) = -\left(0.275\sigma_p + 8.23\right) \tag{2.1}$$

$$\frac{k_{S_N2}}{k_{E2}} = e^{\frac{0.275\ \sigma_p\ +\ 8.23}{343.15\ R}} \tag{2.2}$$

Using this equation with the σ_p values of the substituents leads to very uniform selectivities (17.4 → 18.9), with an increasing trend with σ_p. The selectivities are higher than seen experimentally, though no account is made for the competing background reaction which lowers selectivity. Further, the change in selectivity with σ_p is weaker than seen experimentally. The strengths of this method are that it reproduces the smooth trend in selectivities seen experimentally, whilst still using the calculated Gibbs free energies directly. The method, however, assumes a correlation with σ_p, which enforces the smooth trend. The fitting of the trendlines to the points and noise in the energies themselves can still have a large influence on the equations, and therefore on accuracy, particularly how strongly selectivity changes with σ_p. High precision Gibbs free energies are given in Table 2.6 to reflect that this method necessarily yields values where the relative ordering is known to high precision (reflected at the second decimal place), but this should not be interpreted as high accuracy of the values themselves.

The final method targets the uncertainty in the entropy values directly, by assuming that $\Delta\Delta S^{\ddagger}$ (that is, $\Delta S^{\ddagger}(S_N2) - \Delta S^{\ddagger}(E2)$) is independent of σ_p. Whilst the individual $\Delta S^{\ddagger}$ would be expected to be dependent on σ_p – as σ_p increases, the TS positions get later, and thus more 'ordered', so $\Delta S^{\ddagger}$ increases – it is reasonable to assume that the effect is similar for both the S_N2 and the E2 TSs thus largely cancelling out and $\Delta\Delta S^{\ddagger}$ remaining roughly constant. The appropriateness of this approximation is supported by the fact that $-T\Delta S^{\ddagger}(S_N2)$ correlates with σ_p with gradient of 3.70 and $R^2 = 0.85$, as does $-T\Delta S^{\ddagger}(E2)$ with gradient of 2.96 and $R^2 = 0.81$. $-T\Delta\Delta S^{\ddagger}$ however, has no correlation with σ_p, with $R^2 = 0.09$. The averaged value of $-T\Delta\Delta S^{\ddagger} = 2.0 \pm 1.3$ kJ/mol is added to $\Delta\Delta H^{\ddagger}$ for each urea and used to calculate selectivity (Table 2.6). The computed $\Delta\Delta G^{\ddagger}$ and S_N2/E2 selectivity values correlate well with σ_p (which has not been assumed) and show an increase in selectivity with σ_p from 14.0 to 23.1. The computed values are plotted against the experimental values in Figure 2.11.

Both the $\Delta\Delta G^{\ddagger}$ values and the derived S_N2/E2 selectivities correlate well against experimental values, with R^2 of 0.87 and 0.86 respectively. The largest residuals occur

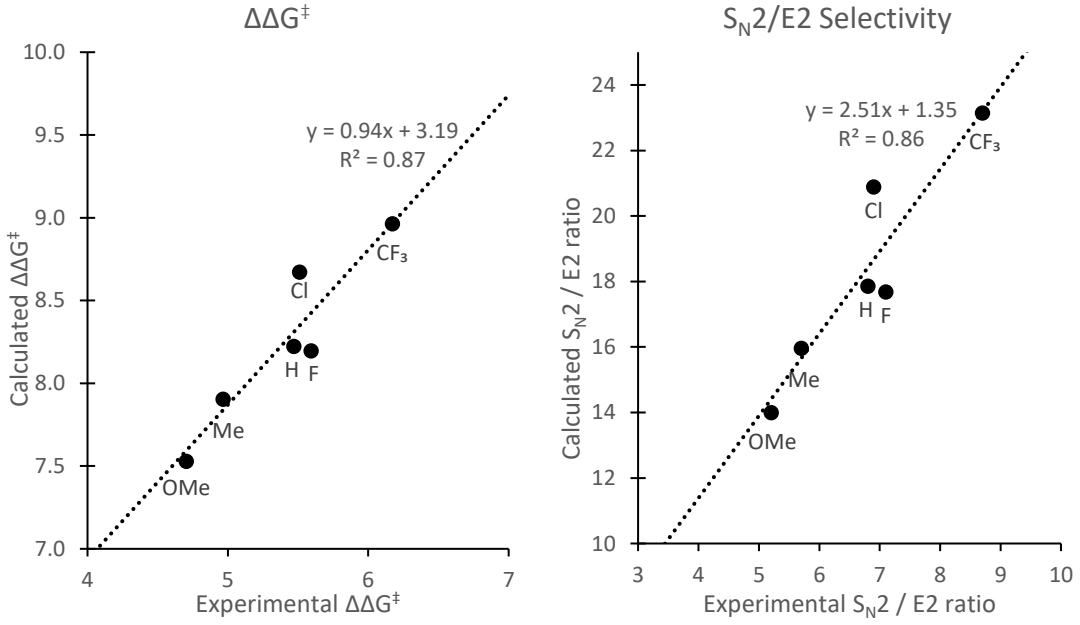

Figure 2.11: Correlation of computed selectivity vs experimental selectivity, assuming only reactivity of $[UF]^-$ complexes.

with **U**$_{F}$ and **U**$_{Cl}$, partly arising from the apparently anomalous experimental results which don't correlate with σ_p. $\Delta\Delta G^{\ddagger}$ has approximately unit gradient, however computation consistently overestimates by 3 kJ/mol, assuming reactivity only by $[UF]^-$. These computed results are in agreement with experiment in terms of the effects of σ_p on selectivity and are consistent with competition between $[UF]^-$ reactivity and the uncoordinated background reaction. The experimental reversal in selectivity of Cl and F as inferred from their σ_p values is not reproduced computationally, suggesting that this arises from factors not accounted for in the model – this is further supported by the strong correlation of experimental fluoride binding energies with σ_p. Possible reasons for this could be interactions with the naphthyl substrate specifically, or solubility related factors. As the energy change involved is less than 1 kJ/mol it is unrealistic for computation to provide an explanation with any degree of certainty.

2.3.2.2 Comparison with Alcohol-Fluoride Complexes

In addition to urea-fluoride complexes, Gouverneur and co-workers previously studied the reactivity of various alcohol-fluoride complexes.[1] Monodentate donor, tri-(*p*-tolyl)-methanol (**Ar$_3$COH**), was used to generate a bis alcohol-fluoride complex, which was used as fluoride source for S_N2:E2 competition (Table 2.1). The corresponding mono alcohol-fluoride complex ($[AF]^-$), in addition to TSs for S_N2 and E2 reactivity, were calculated and are illustrated in Figure 2.12. Experimentally, the bis complex is also seen to be reactive, however the size of this system makes computation impractical at this level of theory. Conformational sampling and preliminary calculations were performed by Paton and co-workers.[13] Key bond distances are tabulated in Table 2.7 and key energies in Table 2.8, with selected urea data for comparison.

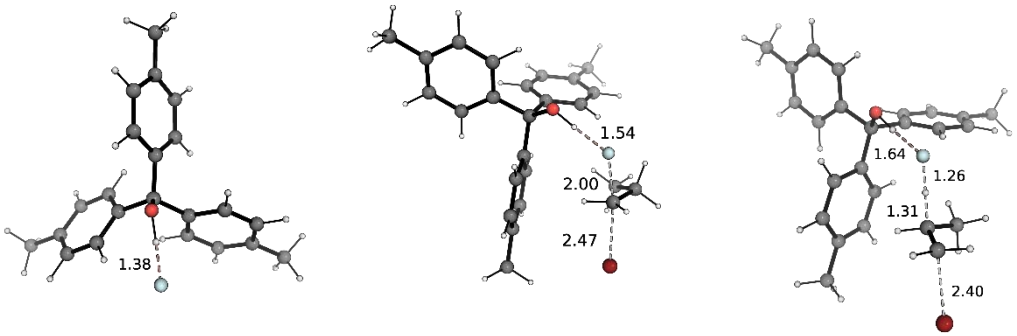

Figure 2.12: Structure of **Ar_3COH**-fluoride complexes and transition state structures for S_N2 and E2 mechanisms.

Table 2.7: Key Bond Distances.

Species		**S_N2**			**E2**				**$[AF]^-$**
		C-F	**C-Br**	**X-F**	**H-F**	**C-H**	**C-Br**	**X-F**	**X-F**
Fluoride	n/a	2.045	2.394	n/a	1.247	1.319	2.299	n/a	n/a
Ar_3COH	**$[AF]^-$**	1.995	2.472	2.536	1.265	1.314	2.403	2.624	2.422
U	**OMe**	1.983	2.471	2.750	1.244	1.335	2.417	2.809	2.656
	H	1.979	2.473	2.743	1.241	1.337	2.421	2.804	2.647
	CF_3	1.973	2.481	2.725	1.238	1.339	2.431	2.786	2.621
PrBr		n/a	1.968	n/a	n/a	1.094	1.968	n/a	n/a
PrF		1.400	n/a	n/a	n/a	n/a	n/a	n/a	n/a
HF		n/a	n/a	n/a	0.923	n/a	n/a	n/a	n/a

Bond lengths reported in Å. N-F distances are reported as an average.

Table 2.8: Activation Barriers to S_N2 and E2 Mechanisms.

Species		**S_N2 / kJ/mol**				**E2 / kJ/mol**			
		$\Delta E^‡$	**$\Delta H^‡$**	**$T\Delta S^‡$**	**$\Delta G^‡$**	**$\Delta E^‡$**	**$\Delta H^‡$**	**$T\Delta S^‡$**	**$\Delta G^‡$**
Fluoride	n/a	64.7	62.3	-28.5	90.7	76.7	60.1	-26.0	86.1
Ar_3COH	**$[AF]^-$**	44.2	49.1	-56.4	105.5	67.1	58.6	-50.7	109.3
MeOH		67.6	72.7	-45.5	118.1	87.5	78.6	-39.9	118.5
U	**OMe**	63.0	67.5	-52.0	119.5	86.5	77.0	-52.1	129.0
	H	63.4	68.4	-54.6	123.0	87.8	78.6	-53.6	132.2
	CF_3	65.7	71.3	-59.3	130.6	90.9	82.3	-56.4	138.7

Bond distances show that fluoride delivery by a single alcohol, **Ar_3COH**, as $[AF]^-$ complex, makes the S_N2 TS later than with uncoordinated fluoride. Compared with fluoride delivery by **U_H** the C–Br distances are similar, however the forming C–F bond is significantly longer with the alcohol, indicating a looser TS. For the E2 mechanism, compared to free fluoride, the H–F and C–Br distances are elongated, however the C–H distance is shorter. Comparing to **U_H**, the **Ar_3COH** TS is significantly earlier, consistent with the effects of a weaker hydrogen bond donor.

There are several influences on the activation barriers. For S_N2 reactivity, the **Ar_3COH**-fluoride complex results in a *lowering* of $\Delta E^‡$ by 20 kJ/mol relative to free fluoride. This contrasts with the ureas where $\Delta E^‡$ is essentially unchanged. Coordination by more hydrogen bond donors increases $\Delta E^‡$, however this is opposed by donor-substrate interactions which stabilize the TS relative to the reactants. The energetic barrier to fluoride delivery with the **Ar_3COH**-fluoride complex is therefore lowered relative to uncoordinated fluoride by interaction of the alcohol aromatic rings that envelope the substrate. For comparison, the S_N2 and E2 TSs were reoptimized with MeOH as hydrogen bond donor (Figure S8), leading to an increase in $\Delta E^‡$ to 67.6 kJ/mol and 87.5 kJ/mol for S_N2 and E2 mechanisms respectively, an effect exceeding the difference in fluoride complexation strength (ΔE of -35.6 kJ/mol compared with -37.9 kJ/mol for MeOH).

The entropic barrier, $\Delta S^‡$, is consistent for alcohol and urea-fluoride complexes, however both are approximately double the penalty for uncoordinated fluoride. In both situations, the molecularity of the reactions are the same (fluoride source + substrate), resulting in a similar contribution from loss of translational entropy, however only in the case of the hydrogen bonded complexes is rotational entropy lost in the TS. Fluoride itself is

therefore an intrinsically entropically favored fluoride source as there is no loss of rotational entropy on substrate attack. This difference can be quantified using statistical thermodynamics, where the rotational partition functions of linear and non-linear molecules have the following form in the high temperature limit:[49]

$$q^R_{Linear} = \frac{k_B T}{\sigma h c \tilde{B}} \qquad q^R_{Non-linear} = \frac{1}{\sigma}\left(\frac{k_B T}{hc}\right)^{\frac{3}{2}}\left(\frac{\pi}{\tilde{A}\tilde{B}\tilde{C}}\right)^{\frac{1}{2}} \tag{2.3}$$

where $\tilde{A}$, $\tilde{B}$, $\tilde{C}$ are the rotational constants of the molecule and σ is the *symmetry number* – the number of orientations of a molecule that can superimpose upon itself – equal to 1, in a molecule with no symmetry. Rotational partition functions can be used to compute the rotational entropy using:[50]

$$S^R = R\ln(q^R) + R\mathrm{T}\left(\frac{\partial \ln(q^R)}{\partial T}\right)_v \tag{2.4}$$

resulting in the following expressions

$$\Rightarrow \quad S^R_{Linear} = Rln(q^R) + R \qquad S^R_{Non-linear} = Rln(q^R) + \frac{3}{2}R \tag{2.5}$$

As the rotational entropy, S^R, is a function of the rotational constants of a molecule, and therefore its molecular composition and geometry, S^R can take a range of values. In this case, as the urea-fluoride complexes have lower rotational constants than the substrate, the rotational entropy loss in the TSs with coordinated fluoride is approximately the rotational entropy of the substrate, with TΔS = 32 kJ/mol (PrBr, rotational constants of 11.1, 2.3 and 2.0 GHz => S^R(343.15 K) = 92 J/K/mol). In principle, using a linear hydrogen bonded fluoride complex is entropically superior to a non-linear complex, however this significantly limits the possible hydrogen bond donors.

Overall, the balance of entropy and enthalpy leads to larger activation barriers for all hydrogen bonded fluoride sources over uncoordinated fluoride. The effect on the entropic contribution is similar for both S_N2 and E2 mechanisms, however the energetic barrier for E2 is raised, in contrast to the S_N2 energy barrier which remains approximately constant, leading to an increase in S_N2:E2 selectivity.

2.4 The Origins of Tuning Fluoride S_N2:E2 Selectivity with Hydrogen Bonds

2.4.1 Background

The origins of the relative favorability of S_N2 and E2 reactivity with different potential nucleophiles/bases has been extensively studied,[51–54] including the effects of hydrogen bonding on fluoride in the context of solvation.[55] A summary of these results has recently been incorporated into a review on the distortion/interaction-activation strain analysis – a method that has proved particularly fruitful for this type of system.[56] The distortion/interaction-activation strain model (DI-AS) is herein applied to probe the origins of the differing reactivity and S_N2/E2 selectivity of urea-fluoride complexes with primary bromide substrate, in a solvated environment.

2.4.2 Distortion/Interaction-Activation Strain Analysis

Distortion/interaction-activation strain (DI-AS) analysis was undertaken over the intrinsic reaction coordinate (IRC) for a representative subset of ureas (**U**$_{\mathbf{OMe}}$, **U**$_{\mathbf{H}}$ and **U**$_{\mathbf{CF3}}$). To enable comparison of the different ureas, the IRC was projected as breaking C–Br distance minus forming F–C distance for S_N2 reactions, and breaking C–Br distance minus forming F–H distance for E2.[57]

In the first analysis, the system was treated as being composed of $[UF]^-$ and PrBr. Thus, the zero point on the energy scale is of these two species infinitely separated; distortion

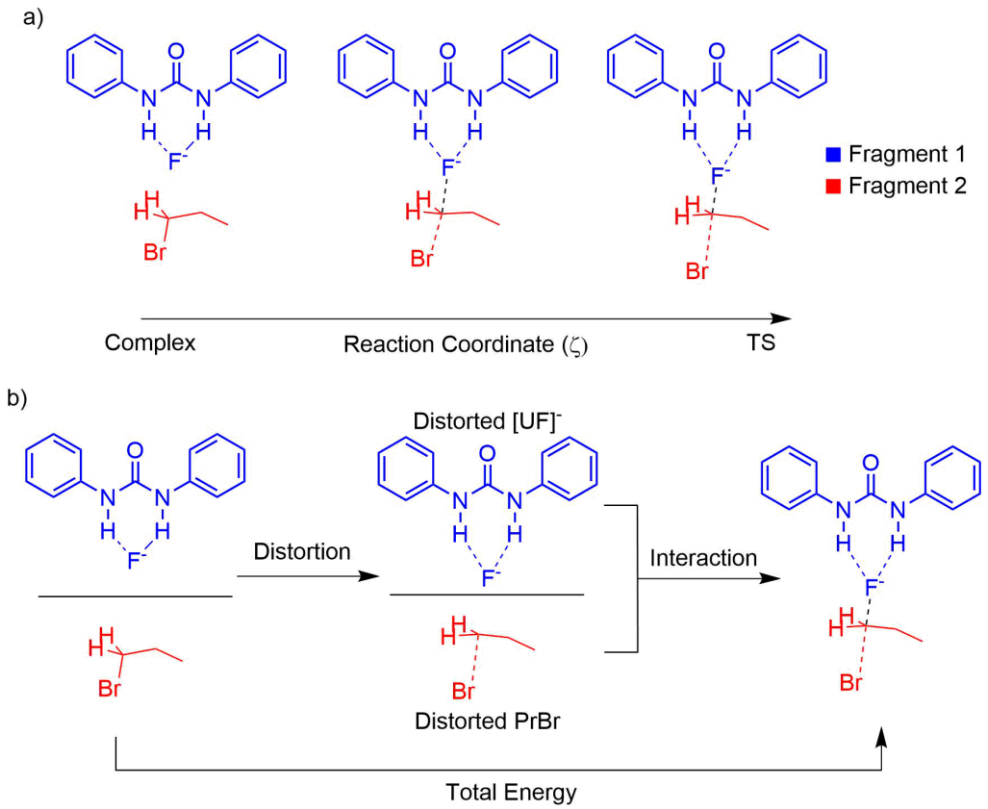

Figure 2.13: Graphical illustration of distortion/interaction-activation strain model with urea-fluoride complex and PrBr substrate – S_N2 reaction used as example. a) schematic illustration of the evolution of the system from reactive complex to TS over the IRC pathway. The system is partitioned into two fragments, illustrated by different coloring. b) Overview of the energy decomposition of the DI-AS approach. Left: Separated undistorted fragments, used as energy zero point. Middle: Separated fragments are distorted to their geometry for a given point on the IRC pathway, costing the *distortion energy*. Right: Distorted fragments are brought together into the reactive geometry, releasing the *interaction energy*.

is the sum of the distortion of the $[UF]^-$, and of PrBr, relative to their equilibrium geometries; and interaction is the energy of bringing these distorted fragments together (Figure 2.13). The profiles for E2 and S_N2 reactions are given in Figure 2.14.

For both the E2 and S_N2 mechanism, changes in urea substituent have little effect on distortion, which is dominated by distortion of PrBr substrate. In contrast, interaction is significantly weakened as the hydrogen bond strength of the urea donor is increased, particularly later along the IRC pathway. The balance of these two factors leads to the total energy being higher for stronger hydrogen bond donors consistently over the IRC

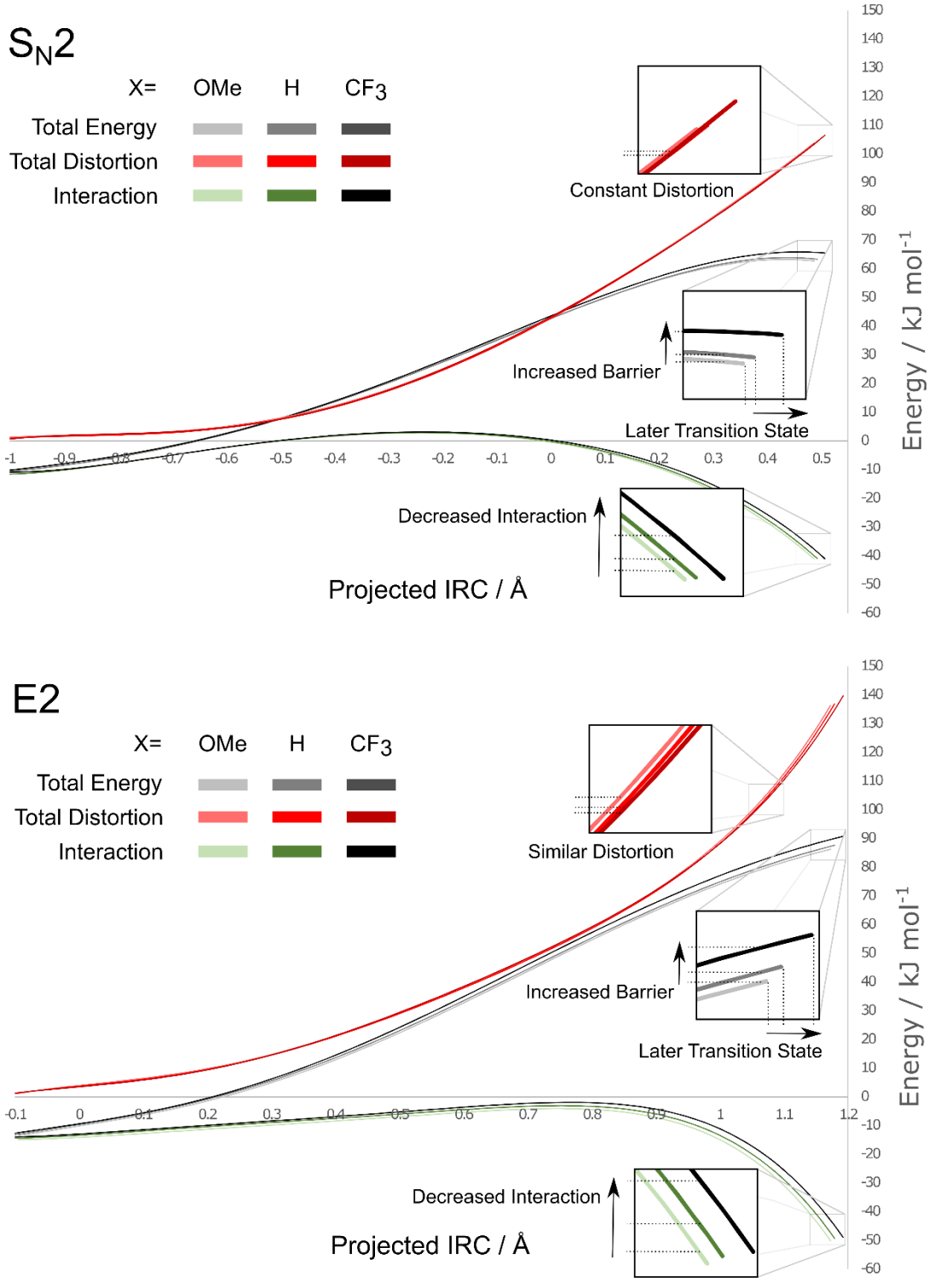

Figure 2.14: Distortion/interaction-activation strain analysis where the system is treated as consisting of $[UF]^-$ and PrBr fragments. Annotations refer to the effect of increasing hydrogen bond donor strength (increasing substituent σ_p). In both cases, changes in urea substituent have a dominant effect on interaction, whilst distortion is approximately invariant.

for both mechanisms. A secondary effect of the weaker interaction is that the TS position becomes later, causing a further increase in the activation barrier. This analysis suggests that the strength of interaction is a larger effect than the position of the TS, however the energy differences are too small to be conclusive.

The E2 mechanism has higher distortion than the S_N2 mechanism due to more bonds breaking (~110 *c.f.* ~140 kJ/mol distortion at TS). Distortion of the substrate leads to LUMO lowering in both mechanisms, but to a greater degree in the E2 mechanism, creating a better HOMO-LUMO match and therefore stronger interaction. This only partially compensates for greater distortion, however, resulting in a higher barrier for the E2 mechanism.[56] An additional factor is that the hydrogen bonding between urea and fluoride is weakened over the IRC as fluoride is neutralized – contained in the interaction term. The charges on fluoride in the E2 TSs are lower than the corresponding S_N2 TSs, indicating more charge transfer, consistent with the stronger interaction terms. This is despite the resulting decrease in hydrogen bond strength, suggesting this is a minor factor.

The origins of increased S_N2 over E2 selectivity with stronger hydrogen bond donors can also be understood. The difference in interaction strength between different ureas is larger in the E2 mechanism than for S_N2. This originates from the greater LUMO lowering in the E2 mechanism, creating a better HOMO-LUMO energy match and therefore greater discrimination in interaction strength based on the energy of the nucleophile HOMO.[53,54,56,58] A stronger hydrogen bond donor therefore weakens interaction for both mechanisms, but to a greater degree for the E2 mechanism, causing the difference in activation barriers to increase. A further point of interest is that if DI-AS analysis is only performed at the TSs for this system, it would be erroneously concluded that interaction is invariant with urea substitution and the differing activation barriers result from

different levels of substrate distortion – a potential pitfall that has been previously highlighted for the model.[56]

DI-AS analysis can also be performed by treating the system as being composed of urea, fluoride and PrBr fragments. The zero point on the energy scale now corresponds to infinite separation of these three species (Figure 2.15). A strength of fragmenting the system in this way is that the zero point is consistent between the different ureas – *i.e.* transitioning from the Total Energy curve of one urea to another corresponds energetically to dissociation of the first urea, and association of the second. The energy profiles for the E2 and S_N2 reactions are given in Figure 2.16.

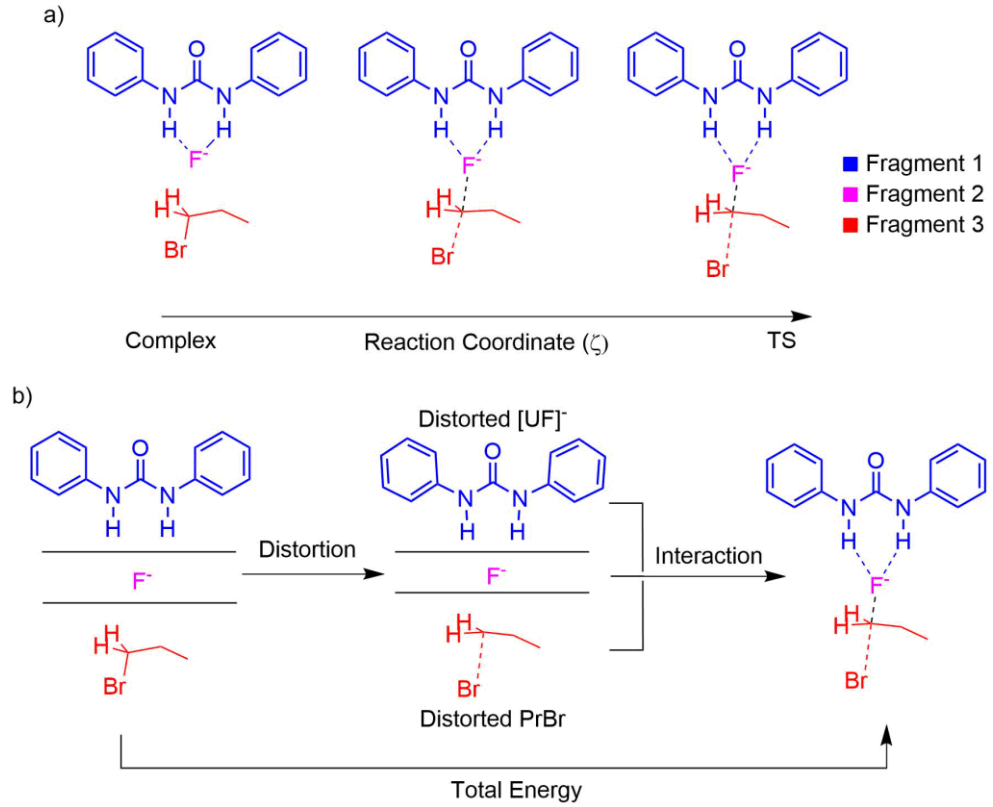

Figure 2.15: Graphical illustration of distortion/interaction-activation strain model with urea, fluoride and PrBr substrate – S_N2 reaction used as example. a) schematic illustration of the evolution of the system from reactive complex to TS over the IRC pathway. The system is partitioned into three fragments, illustrated by different coloring. b) Overview of the energy decomposition of the DI-AS approach. Left: Separated undistorted fragments, used as energy zero point. Middle: Separated fragments are distorted to their geometry for a given point on the IRC pathway, costing the *distortion energy*. Distortion energy of fluoride is necessarily 0. Right: Distorted fragments are brought together into the reactive geometry, releasing the *interaction energy*.

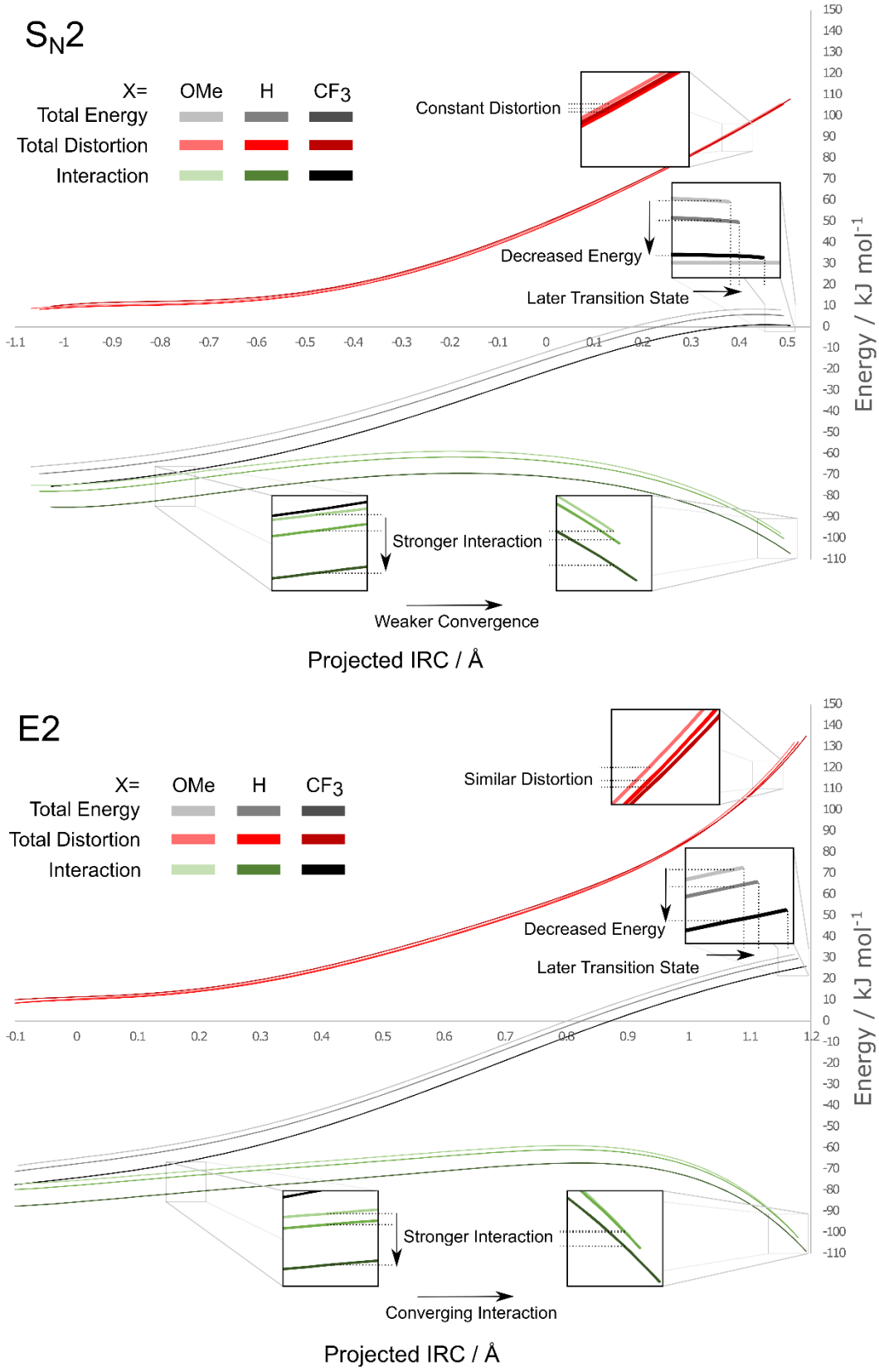

Figure 2.16: Distortion/interaction-activation strain analysis where the system is treated as consisting of Urea, F^- and PrBr fragments. Annotations refer to the effect of increasing hydrogen bond donor strength (increasing substituent σ_p). In both cases, changes in urea substituent have a dominant effect on interaction, whilst distortion is approximately invariant.

In all cases, both the total energy curve and the interaction curve begin strongly negative, dominated by the formation of hydrogen bonds between urea and fluoride. Distortion remains approximately consistent (dominated by PrBr distortion, as in previous analysis), and differences in interaction energy are the origin of the differences between the ureas.

A significant change from the previous analysis is that the order of the Total Energy and Interaction curves is reversed, with stronger hydrogen bond donors leading to a lower total energy and stronger interaction. As the zero point of this analysis is consistent between ureas, this reflects the 'true' energy ordering, where a stronger hydrogen bond donor leads to a *lower* energy TS. This fact can be reconciled with a slower reaction by recognizing that the stronger hydrogen bond donor stabilizes the starting materials to a greater degree, creating a larger barrier (highlighted by the previous DI-AS analysis where the zero point was taken as the reactants, $[UF]^-$ + PrBr). If the system is mentally partitioned into the core TS unit (fluoride attacking PrBr) and the urea, coordination of a stronger hydrogen bonding urea to the TS unit resulting in a lower total energy is consistent with chemical intuition.

In the E2 mechanism, interaction of the stronger hydrogen bond donor begins as significantly more favorable than with the weaker donor. This originates from the formation of stronger hydrogen bonds to fluoride with the stronger hydrogen bond donor. Along the IRC pathway, however, the distinction between the 3 interaction curves diminishes strongly due to a larger HOMO-LUMO mismatch for the stronger donor (*vide supra*). This trend in interaction also occurs for the S_N2 mechanism, however the curves converge to a much lesser degree due to a larger HOMO-LUMO mismatch intrinsic to the mechanism.

The different contributions to the distortion term are illustrated in Figure 2.17. Early along the IRC, distortion is dominated by distortion of the urea, caused by hydrogen bonding to fluoride. As fluoride is delivered to the substrate, urea distortion decreases due to the weakening hydrogen bonding. This occurs to a greater extent in the E2 mechanism, with urea distortion approaching zero at the TSs. In contrast, PrBr distortion increases rapidly over the IRC pathway, becoming the dominant factor. No significant differences in distortion with different urea substituents can be determined, with distortion of all components relatively consistent.

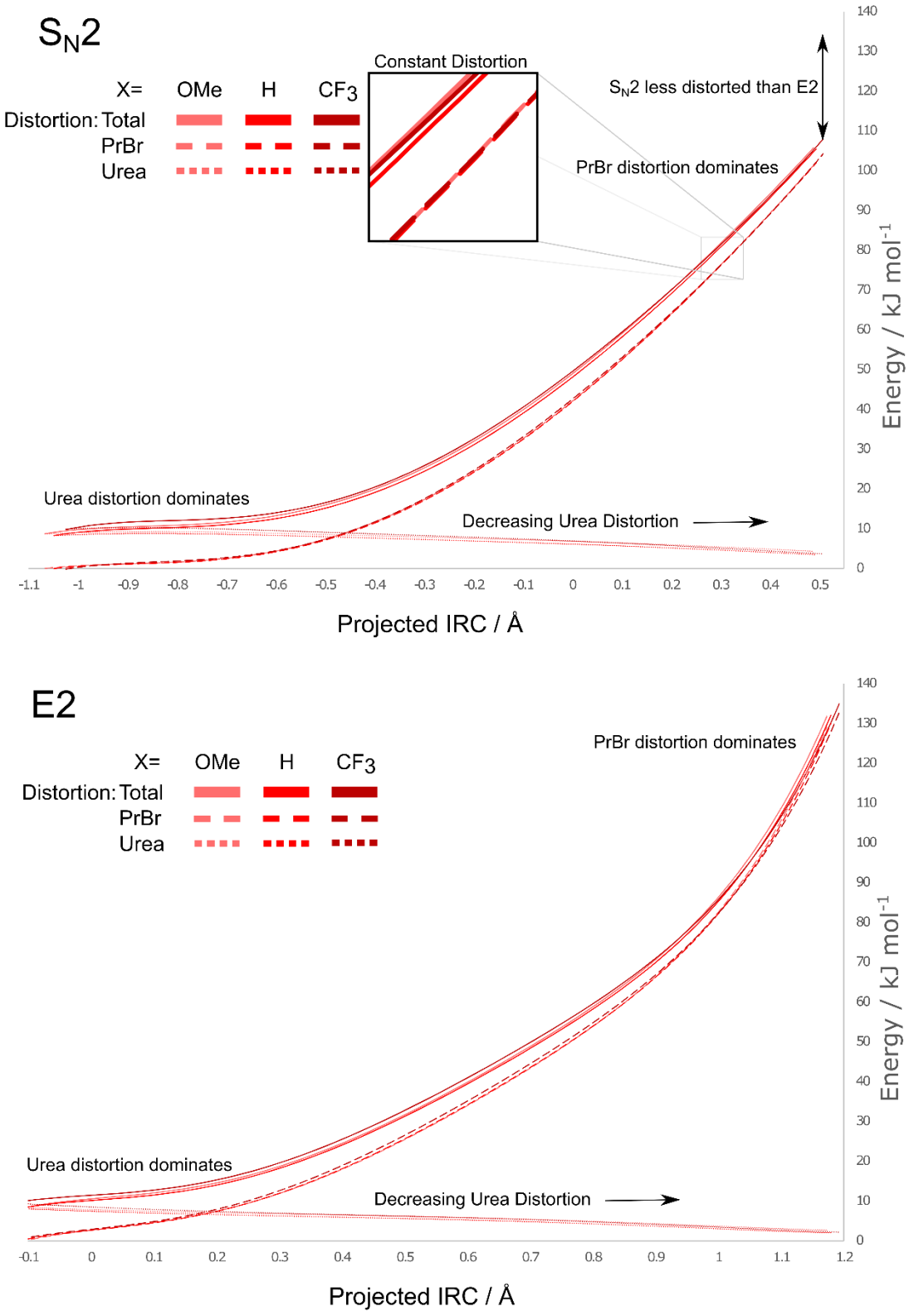

Figure 2.17: Distortion/interaction-activation strain analysis where the system is treated as consisting of Urea, F^- and PrBr fragments. Distortion only is shown, including separated contributions from urea and PrBr fragments (fluoride distortion is necessarily zero). Early on the IRC pathway, distortion is dominated by the urea, however this is dwarfed by PrBr distortion later along the IRC pathway.

2.4.3 Choosing the Right "Zero"

The importance of the choice of zero point is illustrated in Figure 2.18 with a schematic depiction of the Gibbs free energy profiles for an S_N2 reaction for a stronger hydrogen bond donor, $\mathbf{U}_{\mathbf{Strong}}$, and a weaker hydrogen bond donor, $\mathbf{U}_{\mathbf{Weak}}$. The inclusion of entropy does not affect the schematic shape of the profiles, nor does the exact identity of the hydrogen bond donor (all factors not relating to hydrogen bonding of fluoride are assumed constant). In most cases, entropy differences between different hydrogen bond donors are a minor factor compared to the differences in enthalpic contributions, particularly when comparing similar donors. The S_N2 mechanism is used to illustrate the concept, however it is equally applicable to E2.

In the first case, Figure 2.18 a), the reactants for each respective reaction are set to a Gibbs free energy of zero. The stronger the hydrogen bond donor, the higher the activation barrier to reaction. The overall exergonicity of the reaction (*i.e.* the relative energy of the products) is dependent on the urea-fluoride reagent, as it includes the breaking of the hydrogen bonds in the complex, overall resulting in a more exergonic process with a weaker hydrogen bond donor. This way of viewing the reaction can, however, be misleading as comparing the energies of the pathways with different ureas (*i.e.* the relative heights of the blue and red curves) is meaningless, and it may erroneously be concluded that a weaker hydrogen bond donor lowers the energy of the TS, leading to faster reaction. Each curve is shifted by the Gibbs free energy of complexation of fluoride with the respective urea, on the order of 30-40 kJ/mol.

In the second case, Figure 2.18 b), the zero point is set with the urea dissociated. As illustrated, the products of the reaction ($\mathbf{U}_\mathbf{X}$ + PrF + Br^-) are at equal energy and, similarly, hypothetical reactants of $\mathbf{U}_\mathbf{X}$ + F^- + PrBr, are also at equal energy. As the urea is

dissociated at the zero-point, transition between the red and blue curves corresponds to dissociation and association of the respective ureas. That is, that the pathway of the red curve may be regarded as occurring with $\mathbf{U}_{\mathbf{Strong}}$ spectating the reaction at infinite separation, and the pathway of the blue curve may be regarded as occurring with $\mathbf{U}_{\mathbf{Weak}}$ spectating the reaction at infinite separation. The activation barriers are, of course, unchanged and the kinetics implied by both profiles is consistent.

At all points of the profile with urea coordinated, the energy of the system is lower when coordinated by a stronger hydrogen bond donor – naturally, due to the formation of stronger hydrogen bonds. This difference is however less pronounced at the TS than in the reactants and reactive complex, as discussed extensively in the DI-AS analyses, resulting in a higher activation barrier and slower kinetics, despite stabilizing all species on the Gibbs free energy profile relative to the weaker donor.

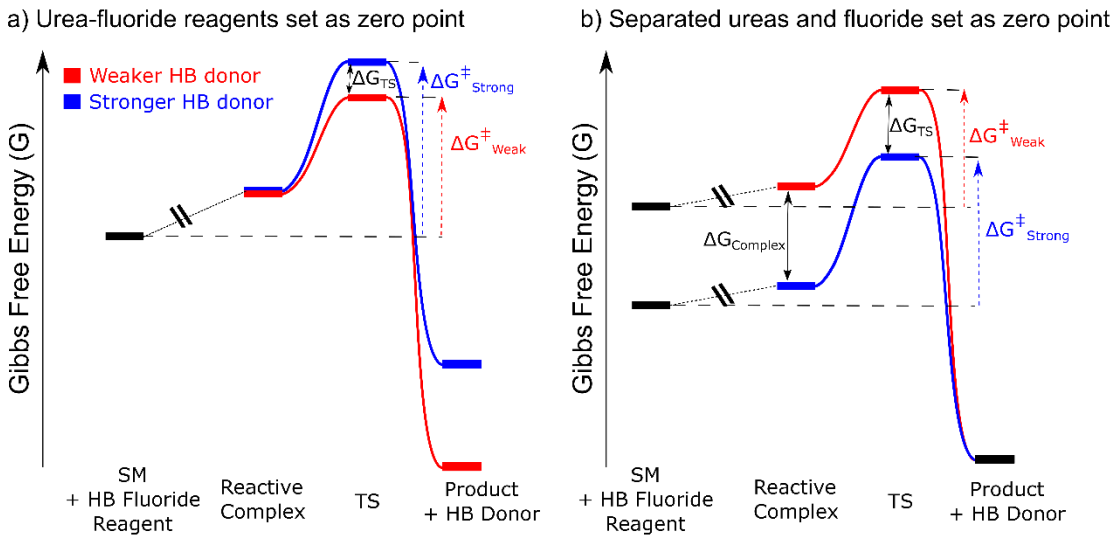

Figure 2.18: Illustration of the choice of energy zero point for S_N2 fluorination with different hydrogen bonded fluoride complexes. a) The reactants of each fluorination ($[UF]^-$ + PrBr) are set to 0. This viewpoint prominently illustrates the relative reaction barriers that dictate the reaction kinetics. b) The products of each fluorination ($\mathbf{U}$x + PrF + Br^-) are set to 0. This viewpoint accurately depicts the relative thermodynamic stability of the pathways with different ureas, with transition between the red and blue curves corresponding to dissociation and association of the respective ureas.

2.5 Fluoride Geometric Preference

Fluoride has four valence electron pairs and may therefore be expected to preferentially form four hydrogen bonds, with greatest angular separation between donors, resulting in a tetrahedral geometry. Both experimental x-ray structures and computed solvated fluoride donor complexes, however, deviate substantially from this 'ideal' geometry due to packing forces, or Van der Waals contacts, suggesting that the intrinsic preference of fluoride for a particular coordination geometry is low. The geometries of small fluoride hydrogen bond donor complexes have been investigated before by both experiment and theory, establishing favored geometries with up to 6 hydrogen bond donors. HF complexes with 2-4 donors adopt bent, trigonal planar and tetrahedral geometries respectively, whilst complexes with water adopt geometries where the water donors can interact with each other.[59–62] To our knowledge, there is no study that investigates the energetic penalty on distortion of these complexes from the ideal geometry. Herein, a model system of complexes of the form $[F(HF)_n]^-$ where n=1-6 are optimized, and then distorted to assess the energetic penalty of distorting hydrogen bond donor geometry around fluoride. In order for the results to have practical application, both optimizations and single point energy evaluations are performed in solvent (acetonitrile). Calculations were performed at the DLPNO-CCSD(T)/ma-def2-QZVPP/COSMO(MeCN)// MP2/def2-TZVPP(D)/CPCM(MeCN) level of theory and energies are quoted as electronic energies.

The geometries of the hydrogen bonded complexes are shown in Figure 2.19, in agreement with published work. Geometric data are tabulated in Table S4. Fluoride complexed by 2 HF molecules was subjected to a bend of the H-F-H angle and the energy computed. Similarly, the tridentate complex was subjected to an in-plane bend and an

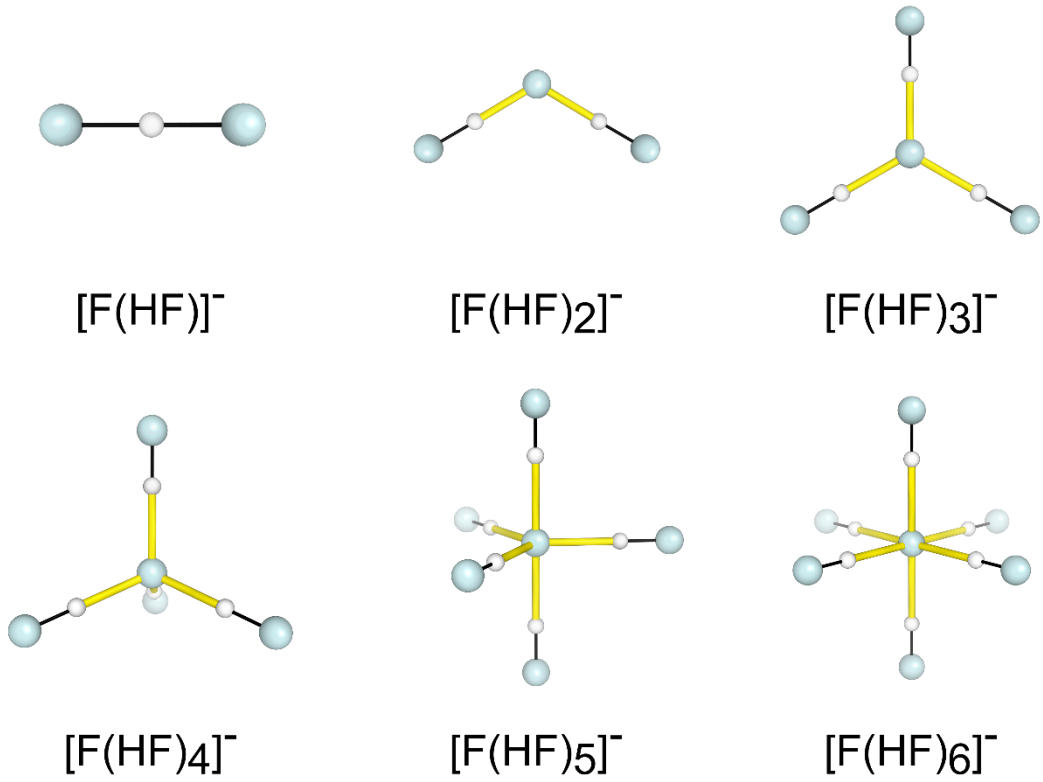

Figure 2.19: Ground state geometries of HF complexes of fluoride, of formula $[F(HF)_n]^-$ where n=1–6.

umbrella distortion. The tetradentate complex was distorted by increase of one H-F-H angle, similar to an E symmetry bend, as well as flattening towards planar geometry, through reduction of the H-H-H-H dihedral angle. The energy profiles are given in Figure 2.20.

It can be seen in all cases that the energy profiles are very flat for small distortions, indicating a low preference for the precise equilibrium geometry. In the cases of the in-plane bends for $[F(HF)_n]^-$ n=2-4 (Figure 2.20a), all three potential energy curves are very similar. At small angles (a state far from equilibrium – indicating close angular separation of two hydrogen bond donors), the energetic penalty of distortion increases rapidly once this angle in smaller than approximately 75°. Donors can approach slightly closer with increasing numbers of hydrogen bond donors due to the longer hydrogen bond distances.

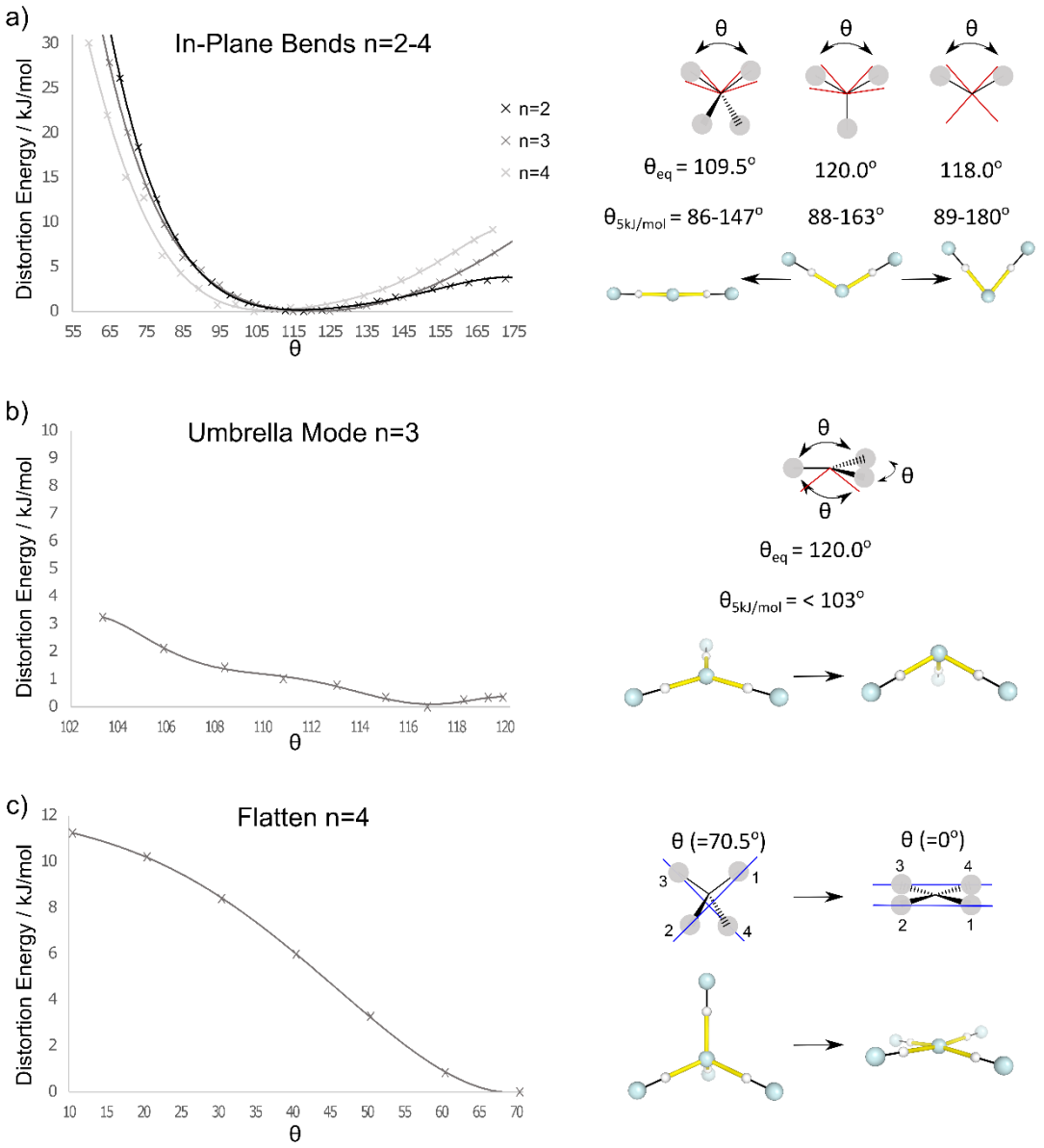

Figure 2.20: Energy profiles for distortion of HF fluoride hydrogen bonded complexes subject to various geometric distortions. a) In-plane distortion, where the angle between two of the hydrogen bond donors is varied. b) Umbrella distortion of 3 donor complex. The angle denotes the angle between any two of the hydrogen bond donors. c) Flattening of tetrahedral complex. Angle denotes that of dihedral 1,2,3,4 as depicted in the figure.

For the n=2 complex, the energy profile is very flat for angles greater than 75°. From an equilibrium angle of 118°, distortion to linear $D_{\infty h}$ geometry (θ=180°) results in an energetic penalty of only 3.8 kJ/mol, suggesting little intrinsic geometric preference arising from hydrogen bonding. For n=3, the profile is very similar to that with 2 donors, indicating little geometric preference for the D_{3h} trigonal planar structure (θ=120°) over,

for example, a T-shape structure (θ=180°, ΔE < 10 kJ/mol). Similarly, with 4 donors, the penalty of forming a seesaw geometry (θ=180°) is approximately 10 kJ/mol. The increasing penalty of linearizing the in-plane angle with increasing number of hydrogen bond donors is consistent with closer angular approach to the other donors.

An umbrella distortion was applied to the n=3 complex, resulting in C_{3v} structures. A low energetic penalty is paid for this distortion, with a preference of approximately 2.5 kJ/mol for a planar structure (θ=120°) over pyramidal. The n=4 complex was also subjected to a flattening distortion, towards a D_{4h} square planar geometry (θ=0°), found to be accompanied by an energetic penalty of approximately 12 kJ/mol – a small amount considering the degree of geometric distortion involved.

Whilst the above analysis is not exhaustive, it demonstrates that fluoride does not have a strong geometric preference for the arrangement of hydrogen bond donors around it. At least moderate distortion of all modes investigated is tolerated with less than a 5 kJ/mol energetic penalty. Significant energetic penalties are only encountered when ligands are forced into Van der Waal's contact. Such small energetic terms are likely to be overwhelmed by other factors in most systems, consistent with the π-π stacked geometries observed for bis urea-fluoride complexes in solution. When considering assigning small energy differences, for example in explaining the origins of enantioselectivity, small distortions of the hydrogen bond donors from the ideal geometry can be safely neglected as the source of energetic difference. Larger distortions, particularly if hydrogen bond donors are forced into close Van der Waal's contact, do however, require investigation.

2.6 Conclusions

This chapter explores the fundamental effects of hydrogen bonding on the reactivity and selectivity of fluoride. The behavior of diarylurea-fluoride complexes, with different *para* substituents on the urea, as nucleophilic reagents in an S_N2 vs E2 competition reaction is investigated, based upon experimental results. Complexation energies, urea-fluoride hydrogen bond lengths and charge on fluoride in the reactive mono urea-fluoride complexes correlate strongly with the Hammett σ_p of the diarylurea substituents. For S_N2 and E2 reactivity, the transition state structures of both mechanisms smoothly becomes later with increasing hydrogen bond donor strength. Experimental results are reproduced, where activation barriers and S_N2:E2 selectivity increase with hydrogen bond donor strength. Using distortion/interaction-activation strain analysis, it is established that the different reactivity and selectivity of the urea-fluoride complexes arises from changes in interaction energy between complex and substrate, whilst distortion remains constant. The lowering of the nucleophile HOMO with stronger hydrogen bond donors leads to a poorer energy match with the LUMO of the substrate, resulting in weaker interaction. This effect is greater for the E2 mechanism than the S_N2, causing an increasing preference for S_N2 reactivity with increasing hydrogen bond donor strength.

Coordination of both the fluoride complexes and the S_N2 and E2 TSs by stronger hydrogen bond donors results in a lower energy species than with a weaker donor, due to the formation of stronger hydrogen bonds. Stabilization of the TS, however, is exceeded by stabilization of the complex, resulting in a larger kinetic barrier to fluorination.

Comparison of urea-fluoride complexes with an alcohol-fluoride complex establishes that donor-substrate interactions are significant in lowering the energy of the alcohol TS and are a potential vector for increasing the reactivity of hydrogen bonded fluoride

complexes. Further, the reactivity of all complexed fluoride is inherently disadvantaged over free fluoride due to the loss of rotational entropy on fluoride delivery, with a penalty on the order of 20-30 kJ/mol.

An investigation into the energy required to distort the coordination geometry around fluoride, complexed by hydrogen bond donors in solution, demonstrates that fluoride does not have a strong preference for the ideal geometries. When coordinated by 2 HF molecules, the angle between the donors can be varied by approximately 90^{o} with less than a 5 kJ/mol energy penalty. All other modes investigated tolerate moderate distortion for similar energy penalties. Larger distortions, such as flattening of the tetrahedral tetracoordinate complex to a planar D_{4h} geometry incurs an energy penalty of just over 10 kJ/mol. These results rationalize the preference of bis urea-fluoride complexes to adopt a geometry where the two ureas π-π stack, as well as the structural diversity of homoleptic urea-fluoride complexes in the solid state, where packing forces override the geometric preference of fluoride.

A level of theory appropriate to the study of hydrogen bonding to fluoride is established to underpin future work on catalytic fluorination, particularly the use of a large, triple-ζ, basis set on fluoride. The M06-2X functional most accurately reproduces geometry benchmarks for S_N2 and E2 transition state structures, as well as hydrogen bond lengths in urea-fluoride complexes. Barrier heights and S_N2:E2 selectivity computed with DLPNO-CCSD(T) is most accurately reproduced with the ωB97X-D3 functional, which is used for single point energy corrections. Remarkably, this level of theory is sensitive enough to reproduce the relative reactivity of differently substituted ureas with accuracy down to the kJ/mol level, supporting the use of this level of theory for enantioselective catalysis, where selectivity is governed by small energy differences.

2.7 References

(1) Engle, K. M.; Pfeifer, L.; Pidgeon, G. W.; Giuffredi, G. T.; Thompson, A. L.; Paton, R. S.; Brown, J. M.; Gouverneur, V. Coordination Diversity in Hydrogen-Bonded Homoleptic Fluoride-Alcohol Complexes Modulates Reactivity. *Chem. Sci.* **2015**, *6*, 5293–5302.

(2) Pfeifer, L.; Engle, K. M.; Pidgeon, G. W.; Sparkes, H. A.; Thompson, A. L.; Brown, J. M.; Gouverneur, V. Hydrogen-Bonded Homoleptic Fluoride-Diarylurea Complexes: Structure, Reactivity, and Coordinating Power. *J. Am. Chem. Soc.* **2016**, *138*, 13314–13325.

(3) Frisch, M. J.; Trucks, G. W.; Schlegel, H. B.; Scuseria, G. E.; Robb, M. A.; Cheeseman, J. R.; Scalmani, G.; Barone, V.; Petersson, G. A.; Nakatsuji, H.; Li, X.; Caricato, M.; Marenich, A.; Bloino, J.; Janesko, B. G.; Gomperts, R.; Mennucci, B.; Hratchian, H. P.; Ortiz, J. V.; Izmaylov, A. F.; Sonnenberg, J. L.; Williams-Young, D.; Ding, F.; Lipparini, F.; Egidi, F.; Goings, J.; Peng, B.; Petrone, A.; Henderson, T.; Ranasinghe, D.; Zakrzewski, V. G.; Gao, J.; Rega, N.; Zheng, G.; Liang, W.; Hada, M.; Ehara, M.; Toyota, K.; Fukuda, R.; Hasegawa, J.; Ishida, M.; Nakajima, T.; Honda, Y.; Kitao, O.; Nakai, H.; Vreven, T.; Throssell, K.; Montgomery Jr., J. A.; Peralta, J. E.; Ogliaro, F.; Bearpark, M.; Heyd, J. J.; Brothers, E.; Kudin, K. N.; Staroverov, V. N.; Keith, T.; Kobayashi, R.; Normand, J.; Raghavachari, K.; Rendell, A.; Burant, J. C.; Iyengar, S. S.; Tomasi, J.; Cossi, M.; Millam, J. M.; Klene, M.; Adamo, C.; Cammi, R.; Ochterski, J. W.; Martin, R. L.; Morokuma, K.; Farkas, O.; Foresman, J. B.; Fox, D. J. Gaussian 09. Gaussian Inc: Wallingford, CT 2009.

(4) Neese, F. The ORCA Program System. *Wiley Interdiscip. Rev. Comput. Mol. Sci.* **2012**, *2*, 73–78.

(5) Wheeler, S. E.; Houk, K. N. Integration Grid Errors for Meta-GGA-Predicted Reaction Energies: Origin of Grid Errors for the M06 Suite of Functionals. *J. Chem. Theory Comput.* **2010**, *6*, 395–404.

(6) Barone, V.; Cossi, M. Quantum Calculation of Molecular Energies and Energy Gradients in Solution by a Conductor Solvent Model. *J. Phys. Chem. A* **1998**, *102*, 1995–2001.

(7) Cossi, M.; Rega, N.; Scalmani, G.; Barone, V. Energies, Structures, and Electronic Properties of Molecules in Solution with the C-PCM Solvation Model. *J. Comput. Chem.* **2003**, *24*, 669–681.

(8) Takano, Y.; Houk, K. N. Benchmarking the Conductor-like Polarizable Continuum Model (CPCM) for Aqueous Solvation Free Energies of Neutral and Ionic Organic Molecules. *J. Chem. Theory Comput.* **2005**, *1*, 70–77.

(9) Klamt, A.; Schüürmann, G. COSMO: A New Approach to Dielectric Screening in Solvents with Explicit Expressions for the Screening Energy and Its Gradient. *J. Chem. Soc. Perkin Trans. 2* **1993**, 799–805.

(10) Funes-Ardoiz, I.; Paton, R. S. Goodvibes v2.0. **2018**, http://doi.org/10.5281/zenodo.3346166.

(11) Grimme, S. Supramolecular Binding Thermodynamics by Dispersion-Corrected Density Functional Theory. *Chem. Eur. J.* **2012**, *18*, 9955–9964.

(12) Foster, J. P.; Weinhold, F. Natural Hybrid Orbitals. *J. Am. Chem. Soc.* **1980**, *102*, 7211–7218.

(13) Ardkhean, R.; Gouverneur, V.; Paton, R. Unpublished Results.

(14) Møller, C.; Plesset, M. S. Note on an Approximation Treatment for Many-Electron Systems. *Phys. Rev.* **1934**, *46*, 618–622.

(15) Weigend, F.; Ahlrichs, R. Balanced Basis Sets of Split Valence, Triple Zeta Valence and Quadruple Zeta Valence Quality for H to Rn: Design and Assessment of Accuracy. *Phys. Chem. Chem. Phys.* **2005**, *7*, 3297–3305.

(16) Rappoport, D.; Furche, F. Property-Optimized Gaussian Basis Sets for Molecular Response Calculations. *J. Chem. Phys.* **2010**, *133*, 134105.

(17) Riplinger, C.; Sandhoefer, B.; Hansen, A.; Neese, F. Natural Triple Excitations in Local Coupled Cluster Calculations with Pair Natural Orbitals. *J. Chem. Phys.* **2013**, *139*, 134101.

(18) Riplinger, C.; Neese, F. An Efficient and near Linear Scaling Pair Natural Orbital Based Local Coupled Cluster Method. *J. Chem. Phys.* **2013**, *138*, 034106.

(19) Zheng, J.; Xu, X.; Truhlar, D. G. Minimally Augmented Karlsruhe Basis Sets. *Theor. Chem. Acc.* **2011**, *128*, 295–305.

(20) Mata, R. A.; Suhm, M. A. Benchmarking Quantum Chemical Methods: Are We Heading in the Right Direction? *Angew. Chem. Int. Ed.* **2017**, *56*, 11011–11018.

(21) Chai, J.-D.; Head-Gordon, M. Long-Range Corrected Hybrid Density Functionals with Damped Atom–Atom Dispersion Corrections. *Phys. Chem. Chem. Phys.* **2008**, *10*, 6615–6620.

(22) Grimme, S. Semiempirical GGA-Type Density Functional Constructed with a Long-Range Dispersion Correction. *J. Comput. Chem.* **2006**, *27*, 1787–1799.

(23) Handy, N. C.; Cohen, A. J. Left-Right Correlation Energy. *Mol. Phys.* **2001**, *99*, 403–412.
(24) Becke, A. D. Density-Functional Thermochemistry. III. The Role of Exact Exchange. *J. Chem. Phys.* **1993**, *98*, 5648–5652.
(25) Lee, C.; Yang, W.; Parr, R. G. Development of the Colle-Salvetti Correlation-Energy Formula into a Functional of the Electron Density. *Phys. Rev. B* **1988**, *37*, 785–789.
(26) Vosko, S. H.; Wilk, L.; Nusair, M. Accurate Spin-Dependent Electron Liquid Correlation Energies for Local Spin Density Calculations: A Critical Analysis. *Can. J. Phys.* **1980**, *58*, 1200–1211.
(27) Stephens, P. J.; Devlin, F. J.; Chabalowski, C. F.; Frisch, M. J. Ab Initio Calculation of Vibrational Absorption and Circular Dichroism Spectra Using Density Functional Force Fields. *J. Phys. Chem.* **1994**, *98*, 11623–11627.
(28) Grimme, S.; Antony, J.; Ehrlich, S.; Krieg, H. A Consistent and Accurate Ab Initio Parametrization of Density Functional Dispersion Correction (DFT-D) for the 94 Elements H-Pu. *J. Chem. Phys.* **2010**, *132*, 154104.
(29) Zhao, Y.; Truhlar, D. G. The M06 Suite of Density Functionals for Main Group Thermochemistry, Thermochemical Kinetics, Noncovalent Interactions, Excited States, and Transition Elements: Two New Functionals and Systematic Testing of Four M06-Class Functionals and 12 Other Function. *Theor. Chem. Acc.* **2008**, *120*, 215–241.
(30) Zhao, Y.; Truhlar, D. G. A New Local Density Functional for Main-Group Thermochemistry, Transition Metal Bonding, Thermochemical Kinetics, and Noncovalent Interactions. *J. Chem. Phys.* **2006**, *125*, 194101.
(31) Tao, J.; Perdew, J. P.; Staroverov, V. N.; Scuseria, G. E. Climbing the Density Functional Ladder : Nonempirical Meta – Generalized Gradient Approximation Designed for Molecules and Solids. *Phys. Rev. Lett.* **2003**, *91*, 146401.
(32) Ditchfield, R.; Hehre, W. J.; Pople, J. A. Self-Consistent Molecular-Orbital Methods. IX. An Extended Gaussian-Type Basis for Molecular-Orbital Studies of Organic Molecules. *J. Chem. Phys.* **1971**, *54*, 724–728.
(33) Hehre, W. J.; Ditchfield, K.; Pople, J. A. Self-Consistent Molecular Orbital Methods. XII. Further Extensions of Gaussian-Type Basis Sets for Use in Molecular Orbital Studies of Organic Molecules. *J. Chem. Phys.* **1972**, *56*, 2257–2261.
(34) Hariharan, P. C.; Pople, J. A. The Influence of Polarization Functions on Molecular Orbital Hydrogenation Energies. *Theor. Chim. Acta* **1973**, *28*, 213–222.
(35) Rassolov, V. A.; Ratner, M. A.; Pople, J. A.; Redfern, P. C.; Curtiss, L. A. 6-31G* Basis Set for Third-Row Atoms. *J. Comput. Chem.* **2001**, *22*, 976–984.
(36) Roy, L. E.; Hay, P. J.; Martin, R. L. Revised Basis Sets for the LANL Effective Core Potentials. *J. Chem. Theory Comput.* **2008**, *4*, 1029–1031.
(37) Wadt, W. R.; Hay, P. J. Ab Initio Effective Core Potentials for Molecular Calculations. Potentials for Main Group Elements Na to Bi. *J. Chem. Phys.* **1985**, *82*, 284–298.
(38) Swart, M.; Solà, M.; Bickelhaupt, F. M. Energy Landscapes of Nucleophilic Substitution Reactions: A Comparison of Density Functional Theory and Coupled Cluster Methods. *J. Comput. Chem.* **2007**, *28*, 1551–1560.
(39) Xu, X.; Goddard, W. A. Assessment of Handy-Cohen Optimized Exchange Density Functional (OPTX). *J. Phys. Chem. A* **2004**, *108*, 8495–8504.
(40) Bento, A. P.; Solà, M.; Bickelhaupt, F. M. Ab Initio and DFT Benchmark Study for Nucleophilic Substitution at Carbon (S_N2@C) and Silicon (S_N2@Si). *J. Comput. Chem.* **2005**, *26*, 1497–1504.
(41) Bauzá, A.; Quiñonero, D.; Deyaì, P. M.; Frontera, A. Is the Use of Diffuse Functions Essential for the Properly Description of Noncovalent Interactions Involving Anions? *J. Phys. Chem. A* **2013**, *117*, 2651–2655.
(42) Lynch, B. J.; Zhao, Y.; Truhlar, D. G. Effectiveness of Diffuse Basis Functions for Calculating Relative Energies by Density Functional Theory. *J. Phys. Chem. A* **2003**, *107*, 1384–1388.
(43) Papajak, E.; Truhlar, D. G. Efficient Diffuse Basis Sets for Density Functional Theory. *J. Chem. Theory Comput.* **2010**, *6*, 597–601.
(44) Mardirossian, N.; Head-Gordon, M. How Accurate Are the Minnesota Density Functionals for Noncovalent Interactions, Isomerization Energies, Thermochemistry, and Barrier Heights Involving Molecules Composed of Main-Group Elements? *J. Chem. Theory Comput.* **2016**, *12*, 4303–4325.
(45) Mardirossian, N.; Head-Gordon, M. Thirty Years of Density Functional Theory in Computational Chemistry: An Overview and Extensive Assessment of 200 Density Functionals. *Mol. Phys.* **2017**, *115*, 2315–2372.

(46) DiLabio, G. a; Johnson, E. R.; Otero-de-la-Roza, A. Performance of Conventional and Dispersion-Corrected Density-Functional Theory Methods for Hydrogen Bonding Interaction Energies. *Phys. Chem. Chem. Phys.* **2013**, *15*, 12821–12828.
(47) Kozuch, S.; Martin, J. M. L. Halogen Bonds: Benchmarks and Theoretical Analysis. *J. Chem. Theory Comput.* **2013**, *9*, 1918–1931.
(48) Grimme, S. Density Functional Theory with London Dispersion Corrections. *Wiley Interdiscip. Rev. Comput. Mol. Sci.* **2011**, *1*, 211–228.
(49) Atkins, P.; De Paula, J. *Atkins' Physical Chemistry*, 9th ed.; Oxford University Press: Oxford, 2010.
(50) Ochterski, J. W. *Thermochemistry in Gaussian*; 2000.
(51) Bickelhaupt, F. M.; Nibbering, N. M. M.; Baerends, E. J.; Ziegler, T. Theoretical Investigation on Base-Induced 1,2-Eliminations in the Model System F^- + CH_3CH_2F. The Role of the Base as a Catalyst. *J. Am. Chem. Soc.* **1993**, *115*, 9160–9173.
(52) Bento, A. P.; Solà, M.; Bickelhaupt, F. M. E2 and S_N2 Reactions of X^- + CH_3CH_2X (X = F, Cl); an Ab Initio and DFT Benchmark Study. *J. Chem. Theory Comput.* **2008**, *4*, 929–940.
(53) Wolters, L. P.; Ren, Y.; Bickelhaupt, F. M. Understanding E2 versus S_N2 Competition under Acidic and Basic Conditions. *ChemistryOpen* **2014**, *3*, 29–36.
(54) Bickelhaupt, F. M. Understanding Reactivity with Kohn-Sham Molecular Orbital Theory: E2-S_N2 Mechanistic Spectrum and Other Concepts. *J. Comput. Chem.* **1999**, *20*, 114–128.
(55) Bickelhaupt, F. M.; Baerends, E. J.; Nibbering, N. M. M. The Effect of Microsolvation on E2 and S_N2 Reactions: Theoretical Study of the Model System F^- + C_2H_5F +nHF. *Chem. Eur. J.* **1996**, *2*, 196–207.
(56) Bickelhaupt, F. M.; Houk, K. N. Analyzing Reaction Rates with the Distortion/Interaction-Activation Strain Model. *Angew. Chem. Int. Ed.* **2017**, *56*, 10070–10086.
(57) Van Zeist, W. J.; Koers, A. H.; Wolters, L. P.; Bickelhaupt, F. M. Reaction Coordinates and the Transition-Vector Approximation to the IRC. *J. Chem. Theory Comput.* **2008**, *4*, 920–928.
(58) Bickelhaupt, F. M.; Bento, A. P. Nucleophilicity and Leaving-Group Ability in Frontside and Backside S_N2 Reactions. *J. Org. Chem.* **2008**, *73*, 7290–7299.
(59) Aiken, K.; Bunn, J.; Sutton, S.; Christianson, M.; Winder, D.; Freeman, C.; Padgett, C.; McMillen, C.; Ghosh, D.; Landge, S. Nuclear Magnetic Resonance Spectroscopy Investigations of Naphthalene-Based 1,2,3-Triazole Systems for Anion Sensing. *Magnetochemistry* **2018**, *4*, 15.
(60) Bajaj, P.; Riera, M.; Lin, J. K.; Mendoza Montijo, Y. E.; Gazca, J.; Paesani, F. Halide Ion Microhydration: Structure, Energetics, and Spectroscopy of Small Halide-Water Clusters. *J. Phys. Chem. A* **2019**, *123*, 2843–2852.
(61) Zhan, C. G.; Dixon, D. A. Hydration of the Fluoride Anion: Structures and Absolute Hydration Free Energy from First-Principles Electronic Structure Calculations. *J. Phys. Chem. A* **2004**, *108*, 2020–2029.
(62) Gerken, M.; Boatz, J.; Kornath, A.; Haiges, R.; Schneider, S.; Schroer, T.; Christe, K. The ^{19}F NMR Shifts Are Not a Measure for the Nakedness of the Fluoride Anion. *J. Fluor. Chem.* **2002**, *116*, 49–58.

3 Nucleophilic Fluorination Mediated by Hydrogen Bonding Phase-Transfer Catalysis

3.1 Introduction

Building on the successes of work with stoichiometric complexes, we looked to exploit hydrogen bonding of fluoride in a catalytic reaction. As hydrogen bonding of fluoride decreases its reactivity, a prerequisite to catalytic fluorination using this activation mode is to ensure that uncoordinated fluoride is unable to react with the substrate. The solution developed in the Gouverneur group was to use an insoluble source of fluoride, specifically an alkali metal fluoride in organic solvent, and exploit the strength of hydrogen bonding to fluoride to render the fluoride soluble, if and only if, coordinated by catalyst. In the case of a chiral urea, this would render fluoride available in a chiral environment, thus opening the door to asymmetric fluorination. Proof of concept was demonstrated with catalytic quantities of simple achiral urea **1**, commonly referred to as 'Schreiner's urea', in dichloromethane for the desymmetrization of *in situ* generated episulfonium ions with cesium fluoride (Scheme 3.1). The reaction occurs in very good yield at room temperature, without exclusion of air or rigorous exclusion of water.

Episulfonium ions were chosen as the reactive electrophile through inspiration from the fluorinase enzyme, which fluorinates an (acyclic) sulfonium ion, *S*-adenosyl methionine

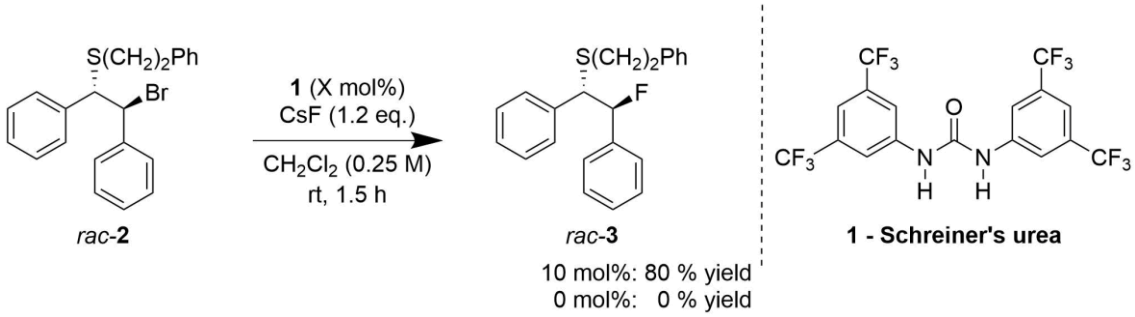

Scheme 3.1: Simple reaction demonstrating the HB PTC concept. In the absence of hydrogen bonding catalyst, **1**, no reaction is observed between CsF and the episulfonium precursor. When catalytic quantities are added, very good yields of fluorinated product are formed.

(SAM). Sulfonium ions are highly reactive electrophiles, with episulfonium ions having additional ring strain, ensuring that the reaction of fluoride with the electrophile is facile once fluoride is rendered available by the catalyst.

The activation of insoluble nucleophiles with hydrogen bonding catalysts through phase-transfer constitutes a novel catalytic mechanism that we call hydrogen bonding phase-transfer catalysis (HB PTC). This concept is not specific to the nucleophile, electrophile nor hydrogen bonding catalyst used, however, we demonstrate the utility of this mechanism in this context, by performing an unprecedented organocatalytic asymmetric nucleophilic fluorination.

The experimental work in this chapter was performed by members of the Gouverneur group, notably Gabriele Pupo, Francesco Ibba and Anna Chiara Vicini. Initial experimental mechanistic work was performed by Lukas Pfeifer. All computation in this publication was performed by me with supervision from R. S. Paton, concurrently with the experimental development of HB PTC. The work described in this chapter features in the publication *Asymmetric nucleophilic fluorination under hydrogen bonding phase-transfer catalysis*, G. Pupo*, F. Ibba*, D. M. H. Ascough*, A. C. Vicini, P. Ricci, K. E. Christensen, L. Pfeifer, J. R. Morphy, J. M. Brown, R. S. Paton, V. Gouverneur, *Science* **2018**, *360*, 638-642.[1] This work been reused in accordance with the AAAS License to Publish.

3.2 Computational Methods

3.2.1 Density Functional Theory

Geometry optimizations and frequency calculations were performed in Gaussian 09, revision D.01.[2] The M06-2X[3] hybrid functional with ultrafine (99,590) integration grid[4] was used with a mixed basis set, denoted def2-SVP(TZVPPD). This basis set consists of the triple-ζ quality def2-TZVPPD[5,6] basis set on heteroatoms (including ECP for cesium[7]), excluding those of the urea catalyst, and the split-valence def2-SVP[5] basis set on all other atoms. Use of such a mixed basis set is necessary for feasible computation on a system size of ~100s of atoms, whilst adequately describing the behavior of fluoride. Benchmarking demonstrates negligible change in critical bond lengths compared to use of def2-TZVPP in place of def2-SVP. (See 3.2.3, benchmarking). Solvation in dichloromethane (DCM) was modelled using the conductor-like polarizable continuum model (CPCM).[8–10] Stationary points with all real frequencies were classified as minima, and those with a single imaginary frequency as transition state structures (TSs). Thermochemistry was evaluated using *GoodVibes* python script[11] at 298.15 K and 1 mol/dm^3 concentration, implementing a quasi-harmonic approximation for entropy calculation and a free-rotor description for low frequency vibrational modes (v < 100 cm^{-1}).[12] Single point energy corrections were performed in the ORCA 3.0.3 software package.[13] The ωB97X-D3[14,15] functional, incorporating Grimme's D3 dispersion correction[16] was used in combination with the (ma)-def2-TZVPP basis set, consisting of ma-def2-TZVPP[17] on heteroatoms, with corresponding ECP for cesium, and def2-TZVPP on carbon and hydrogen. Solvation in DCM was modelled using the conductor-like screening model (COSMO).[18] The optimization density was used to compute non-covalent interactions (NCIs) using the non-covalent interaction index.[19,20] The Spartan '16 software package[21] was used for conformational sampling of small molecules, by

systematic scanning of rotatable dihedrals, using the Merck molecular force field (MMFF).[22] Density functional theory (DFT) single point calculations were performed on all conformers in Gaussian and those within a 40 kJ/mol window were optimized.

3.2.2 Molecular Dynamics

Due to the nature of the reaction, involving ion pairing, and a highly conformationally flexible catalyst, conformational sampling was performed in explicit solvent using molecular dynamics (MD) in the GROMACS v. 5.1.4 software package.[23–28] The optimized potential for liquid simulations (OPLS-AA 2005)[29,30] forcefield was used, with compatible parameters generated from Schrödinger Maestro,[31] corrected for restrained electrostatic potential (RESP) charges.[32,33] RESP charges were fitted to HF/6-31G(d) electrostatic potential map using Ambertools.[34] Parameters for the episulfonium ion were generated by analogy to the aziridinium ion. DCM solvent topology was obtained from virtualchemistry.org.[35,36]

The species of interest was centered in a cubic box, with 3-dimensional periodic boundary conditions (PBC), and minimum distance to the boundary of 15 Å. The *genion* command was used to insert a cesium counterion in a random position in the box where applicable. System temperature was maintained by the velocity rescaling method (time constant of 100 fs),[37] and constant pressure was maintained (NPT simulations) using the Parrinello–Rahman barostat (time constant of 2 ps, reference pressure of 1 bar, compressibility of 4.5×10^{-5} bar^{-1}).[38,39] Van der Waals interactions and the particle mesh Ewald method were used with 1 nm cut-off.[40] Simulations used the linear constraint solver algorithm (LINCS).[41]

Systems were minimized by steepest-descents method for 5000 steps. Initial random velocities were generated according to a 173 K Maxwell-Boltzmann distribution to initiate equilibration under constant volume (NVT), with 1 fs timestep, and heavy atom position restraints. System temperature was raised to that required for the NPT production run over the course of the NVT simulation, followed by an equilibration period, totaling 200 ps. The timestep was increased to 2 fs under constant pressure equilibration (NPT), with a total equilibration time of 400 ps, during which time it was verified that system volume was stabilized. A continuation of NPT simulation was used for the production run, from which results were derived.

Conformers were generated from the production run through heavy atom root-mean-squared deviation (RMSD) clustering of frames using the GROMOS algorithm.[42] Molecular symmetry was accounted for in calculation of the RMSD values using an in-house python script written by the author. Fluorine atoms in CF_3 groups were omitted from RMSD calculation.

Use of classical MD simulations for conformational sampling of ion pairs has been demonstrated by Duarte and Paton.[43] We investigated catalyst-fluoride binding modes and reactive ion pair (catalyst-fluoride-episulfonium) conformations using a similar classical MD approach. To accelerate conformational sampling, the catalyst and its complexes were simulated at elevated temperature of 373 K. Simulations of the reactive ion pair were performed at reaction temperature of 298 K. When investigating fluoride binding modes, it was further found that the presence of an explicit Cs^+ cation was essential for efficient equilibration of binding modes on the simulation timescale.

3.2.3 Density Functional Theory Basis Set Benchmarking

Due to the large size of the experimental bis-urea catalysts used for asymmetric HB PTC, the use of a triple-ζ basis set is prohibitive for optimizations. A large basis set is, however, essential for accurately describing the reactivity of fluoride due to its high charge density (Chapter 2 benchmarking), particularly with strong hydrogen bond donors that are susceptible to deprotonation, and highly reactive electrophiles (episulfonium ions) that react with low activation barriers. A mixed basis set, denoted def2-SVP(TZVPPD), and defined above was therefore essential, retaining a large basis set on critical heteroatoms, such as fluoride, but using a smaller basis on, for example, the catalyst backbone which would tremendously increase computational cost for minimal increase in accuracy if described with the triple-ζ basis set. A full triple-ζ basis set was used for single point energy corrections, so the impact was assessed on the quality of the geometries produced.

Benchmarking of the urea-fluoride complex and key TSs are given in Table 3.1 and Table 3.2 respectively. In both cases, the mixed def2-SVP(TZVPPD) basis set performs comparably to the full def2-TZVPP(D) basis set benchmark with RMSDs of 0.01 Å and 0.01 Å. Use of a small basis set on all atoms (def2-SVP), however, is detrimental, with RMSD of 0.06 Å for the TSs, but complete deprotonation of the urea catalyst in the fluoride complex. The latter result is qualitatively incorrect, compared to experimental results, demonstrating that this basis set is too small to accurately describe the hydrogen bonding interactions to fluoride.

Further benchmarking of the uncoordinated TSs for bromide loss and fluoride delivery (**TS_{Br}** and **TS_F** respectively) was undertaken to probe the effects of the basis set size on individual atoms in more detail (Figure 3.1). It is readily seen for both TSs that the mixed def2-SVP(TZVPPD) basis set performs virtually indistinguishably from the full def2-

TZVPP(D) basis set. Reduction in size of the basis set on the leaving group (sulfur) to def2-SVP from the def2-SVP(TZVPPD) basis set (orange), significantly decreases performance. Ironically, the C-S bond length in both examples is little changed, with the change occurring in the forming/breaking C-X bond distances. Of similar performance is the smaller def2-SVP(D) basis set, with diffuse functions on sulfur and bromide/fluoride. The worst performing basis set by some margin was the smallest, def2-SVP basis set on all atoms with large deviations in all distances benchmarked.

Benchmarking therefore confirms that def2-SVP(TZVPPD) is an accurate basis set, capable of reproducing the geometries of a full triple-ζ basis set without the prohibitive computational cost. The smaller split-valence def2-SVP(D) basis set performs slightly worse, however, would be sufficiently accurate for many purposes – inclusion of diffuse basis functions on critical heteroatoms is essential.

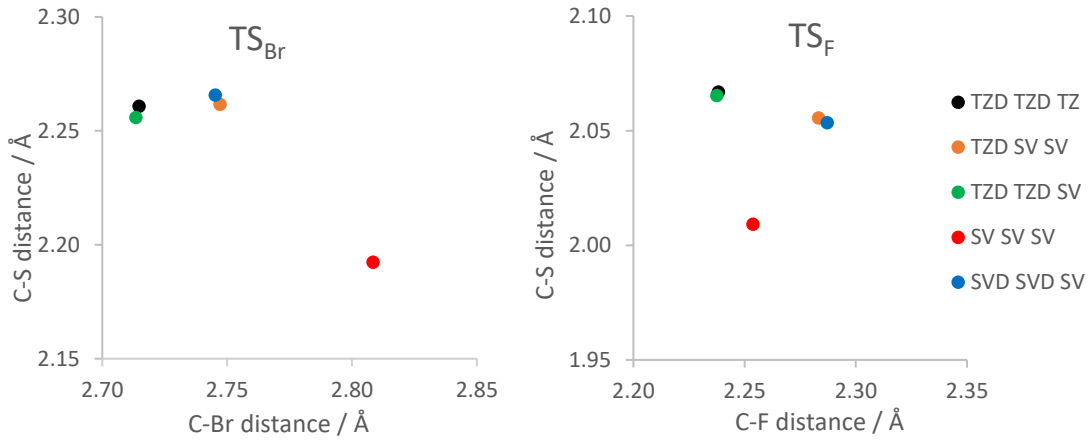

Figure 3.1: Comparison of key bond lengths in bromide removal (**TS$_{Br}$**) and fluoride delivery (**TS$_{F}$**) transition state structures. In both cases the mixed def2-SVP(TZVPPD) basis set performs near identically to the full def2-TZVPP(D) basis set. Names in the legend take the format of (basis on fluoride/bromine, basis on sulfur, basis on other atoms). TZD = def2-TZVPPD, TZ = def2-TZVPP, SVD = def2-SVPD, SV = def2-SVP.

Table 3.1: Benchmarking of Mixed Basis Set on Urea-Fluoride Complex Geometry.

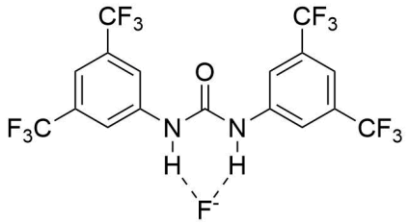

Functional	Basis Set	Key Bond Lengths (Average) / Å			RMSD
		N-F	N-H	H-F	
M06-2X	def2-TZVPP(D)	2.589	1.045	1.599	-
M06-2X	def2-SVP(TZVPPD)	2.587	1.051	1.591	0.006
M06-2X	def2-SVP	Deprotonated			(0.115)

Table 3.2: Benchmarking of Mixed Basis Set on Key Transition State Structure Geometries.

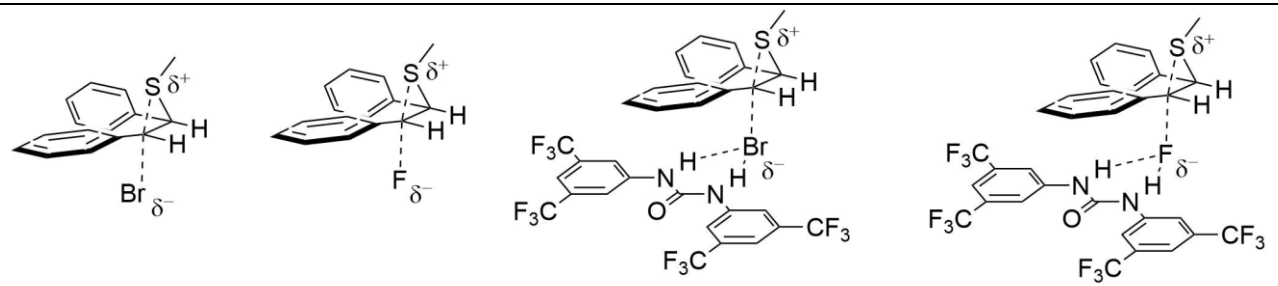

TS_{Br} TS_{F} $TS_{Br}(cat)$ $TS_{F}(cat)$

Functional	Basis Set	Uncoordinated / Å				Coordinated / Å										RMSD
		TS_{Br}		TS_{F}		$TS_{Br}(cat)$					$TS_{F}(cat)$					
		C-Br	C-S	C-F	C-S	C-Br	C-S	N-Br	N-H	H-Br	C-F	C-S	N-F	N-H	H-F	
M06-2X	def2-TZVPP(D)	2.715	2.261	2.238	2.067	2.670	2.296	3.453	1.016	2.471	2.093	2.233	2.700	1.027	1.734	-
M06-2X	def2-SVP(TZVPPD)	2.713	2.256	2.238	2.065	2.672	2.283	3.431	1.021	2.499	2.099	2.229	2.690	1.034	1.719	0.011
M06-2X	def2-SVP	2.809	2.192	2.254	2.009	2.727	2.248	3.420	1.023	2.461	2.180	2.163	2.630	1.042	1.649	0.059

3.2.4 Naming and Numbering Conventions

The following naming and numbering conventions are adhered to for describing the catalyst-fluoride complex (Figure 3.2) and the episulfonium substrate (Figure 3.3).

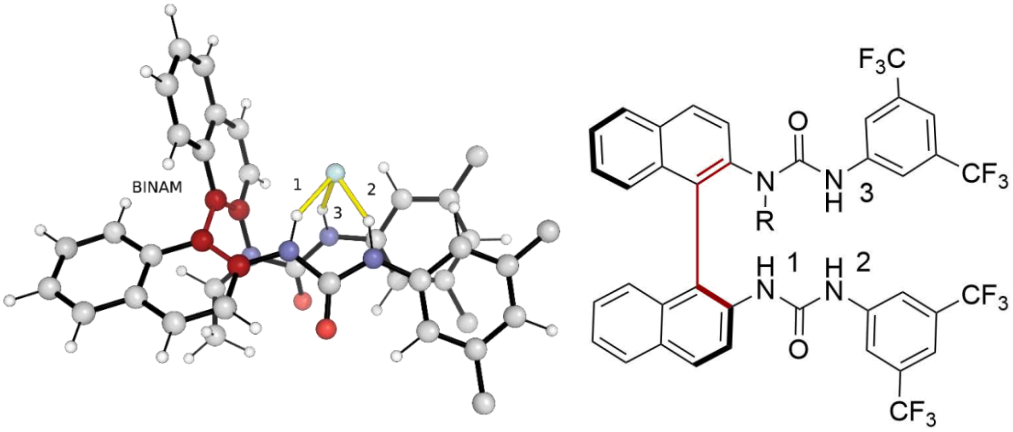

Figure 3.2: Naming and numbering conventions for tridentate BINAM-based catalyst fluoride complexes. Hydrogen bonds are numbered 1-3. Atoms used to define the BINAM dihedral are emphasized in dark red.

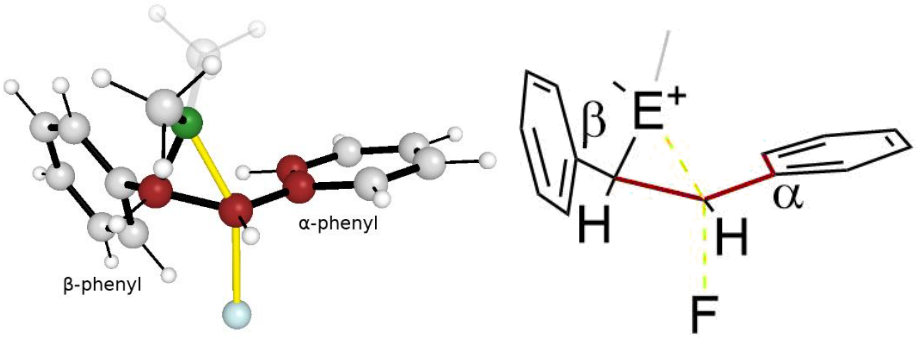

Figure 3.3: Naming and numbering conventions for meso cationic substrates (episulfonium and aziridinium. S/N atom colored in green – Additional alkyl group for aziridinium transparent). The phenyl groups are named by their relative positioning to the forming and breaking bonds. Atoms used to define the α-dihedral (dihedral of the α-phenyl ring) are emphasized in dark red. The β-dihedral is defined analogously. As drawn, a positive dihedral angle is defined as a clockwise rotation about the α-dihedral and a counter-clockwise rotation about the β-dihedral.

3.3 Results and Discussion

3.3.1 Hydrogen Bonding Phase-Transfer Catalysis with an Achiral Urea – Mechanistic Investigation

3.3.1.1 Proposed Catalytic Cycle

After the initial result, given in Scheme 3.1, evidence was sought to support the HB PTC mechanistic hypothesis and to rule out plausible competing mechanisms, notably anion-binding catalysis pioneered by Jacobsen. The substrate used for the following

calculations, in anticipation of an asymmetric variant of the reaction, was stilbene-derived substrate **4**, generating *meso*-episulfonium ions **6**. The initially proposed mechanistic hypothesis is given in Scheme 3.2, using achiral Schreiner's urea catalyst **1** (Figure S9).

Formation of episulfonium **6**, could potentially be urea promoted, by binding of the bromide leaving group. The plausibility of this is a balance between the unfavorable entropic loss from coordination of the catalyst versus the favorable enthalpy of hydrogen bonding to the bromide. Urea may then be involved in the transport of the bromide leaving group, through apolar solvent, to the solid. The critical mechanistic step is phase-transfer, modelled by an exchange of the bromide leaving group for fluoride nucleophile in solution in an 'anion-exchange' step. As solids cannot be computed in the same way as small molecules, a different approach must be taken for this step. Once fluoride is brought into solution, ostensibly due to catalyst binding, this complex can ion pair with the episulfonium ion and deliver fluoride in an S_N2 reaction, generating product **5** and regenerating catalyst.

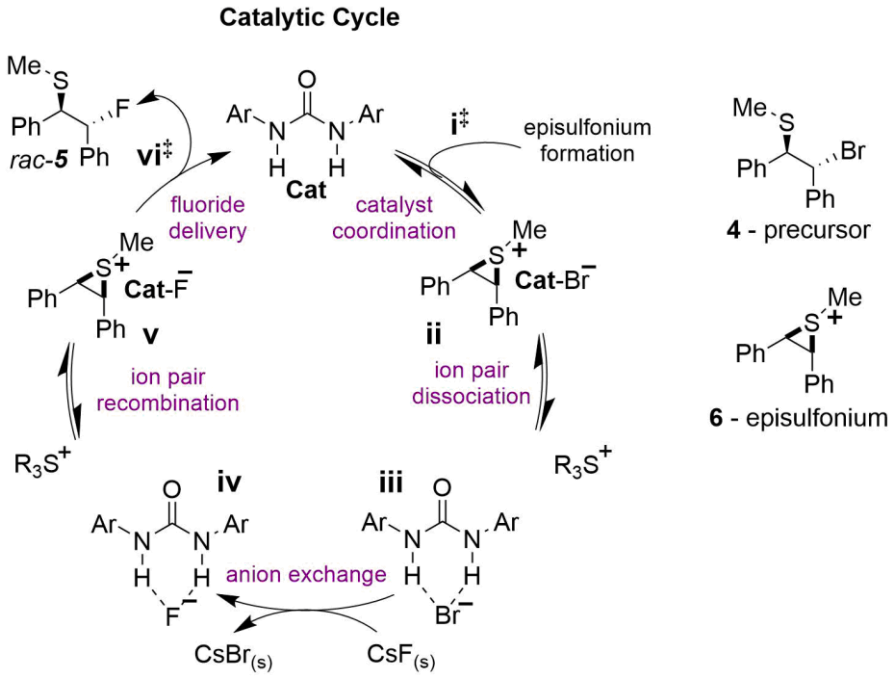

Scheme 3.2: Proposed catalytic cycle for fluorination of *in situ* formed episulfonium ions, using CsF under hydrogen bonding phase-transfer catalysis. Own work adapted from Ref. 1.

3.3.1.2 Modelling Phase-Transfer

The thermodynamics of the anion-exchange phase-transfer step was modelled by incorporating experimental thermodynamic enthalpies, such as enthalpies of formation, in a thermodynamic cycle and combining this with entropy data to obtain a Gibbs free energy change (Figure 3.4, Tables S11-13). A similar approach has been taken in the context of crown-ether binding.[44,45]

By combining enthalpy changes of formation, an experimentally derived 112 kJ/mol for the process $CsF_{(s)} + Br^-_{(g)} \rightarrow CsBr_{(s)} + F^-_{(g)}$ can be evaluated. Experimental molar entropies are available for all species in the equation, resulting in an associated entropy change of 2.3 J/K/mol, from which the Gibbs free energy change of 111 kJ/mol is derived. This process is highly unfavorable, primarily due to the high lattice energy of CsF manifesting in a highly favorable free energy of formation ($\Delta H_f(CsF_{(s)})$ = -533.5 kJ/mol *c.f.* $\Delta H_f(CsBr_{(s)})$ = -405.8 kJ/mol) which is not recovered by any other factors in the process. Upon inclusion of solvation effects in dichloromethane, modelled computationally, formation of fluoride ion is still unfavored, but to a lesser degree, with ΔG_{PT} =

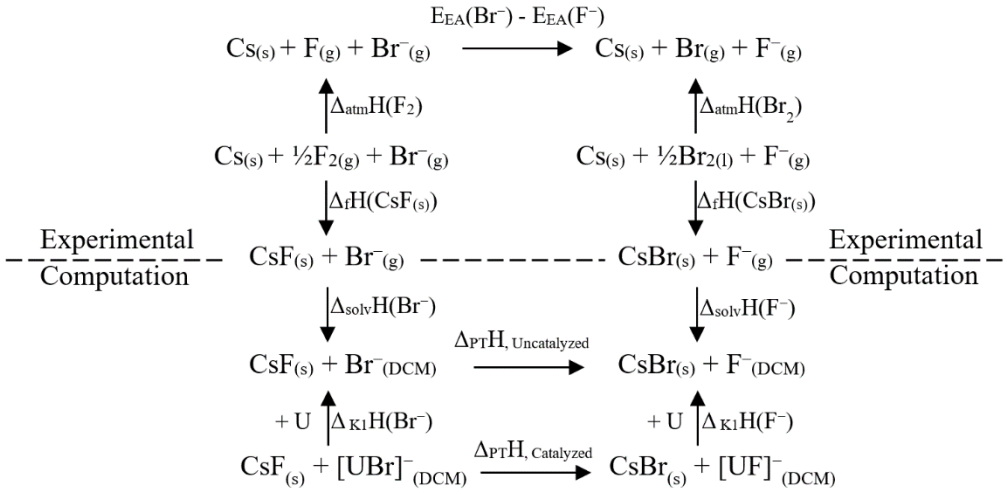

Figure 3.4: Thermodynamic cycle for calculation of the thermodynamics of phase-transfer. All values above the horizontal score are experimentally derived, and those below are computed. Own work reproduced from Ref. 1.

+33.7 kJ/mol due to the much higher solvation energy of fluoride ($\Delta G_{solv}(F^-)$ = -310 kJ/mol *c.f.* $\Delta G_{solv}(Br^-)$ = -233 kJ/mol). This value describes the unfavorability of bringing fluoride into solution in the hypothetical uncatalyzed pathway. Inclusion of urea binding to both fluoride and bromide results in a favorable ΔG_{PT} = -16.7 kJ/mol, due to the much stronger binding of the urea to fluoride over bromide, indicating that the hydrogen bonding catalyst can make this step thermodynamically plausible.

Evaluation of the thermodynamics of phase-transfer for different catalysts and group 1 metal salts are given in Table 3.3. With Schreiner's urea, phase-transfer becomes progressively less favorable for the group 1 metal salts CsF, KF and NaF. This is due to the increasing lattice energy with decreasing metal ion radius. Specifically, breaking apart the MF lattice is compensated to a lesser degree by formation of the corresponding MBr lattice as the cation decreases in size. The trend in Gibbs free energy for this process qualitatively correlates with the trend in experimental yields with the different salts. In the case of the unsubstituted urea **7** – a weaker hydrogen bond donor – weaker hydrogen bonds are formed to both fluoride and bromide, however this has a greater effect on fluoride binding, leading to the process being thermodynamically less favorable. A further notable result in that Schreiner's thiourea, **8**, is expected to be a competent HB PTC catalyst on the basis of hydrogen bond donor strength, however experimentally, no yield is obtained due to reaction of the catalyst, through sulfur, with the *in situ* formed episulfonium. Computationally, therefore, we predict that thioureas are capable HB PTC catalysts if such deactivation pathways are avoided, such as by introducing steric bulk around the thiourea sulfur atom.

There are several limitations of the model used to model phase-transfer. Firstly, the model does not provide mechanistic insight into the process. Secondly, the description is purely thermodynamic – the model cannot exclude large kinetic barriers for processes that are thermodynamically favored. The thermodynamics of the model can, however, have direct implication on kinetics – the endergonicity of the process in the absence of urea stipulates a minimum Gibbs free energy barrier for this process. Thirdly, bulk properties are used. The values from this process assume consumption of bulk MF lattice and formation of bulk MBr lattice due to the use of experimental molar Gibbs free energies of formation. During the reaction, phase-transfer occurs at the surface of the solid, and $MF_{(s)}$ and $MBr_{(s)}$ lattices may become mixed. This description, however, adequately describes the overall process at molar quantities. A further practical limitation is that the method can only be applied to salts where the relevant experimental thermodynamic quantities are known. As

Table 3.3: Computed Gibbs Free Energies of Anion-Exchange Phase-Transfer for Different (Thio)urea Catalysts and Group I Metal Salts Compared to Experimental Reaction Yield.

Catalyst	Salt	$\Delta_{PT}G$ / kJ/mol	Yield / % *
Uncatalyzed	CsF	+33.7	0
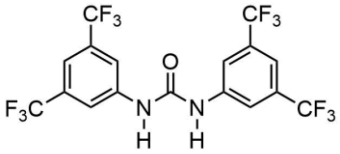 **1**	CsF	-16.7	80
	KF	+7.0	55†
	NaF	+43.1	0
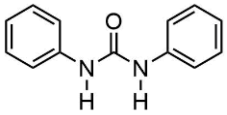 **7**	CsF	-7.0	5
	KF	+16.7	*n.d.*
	NaF	+52.8	*n.d.*
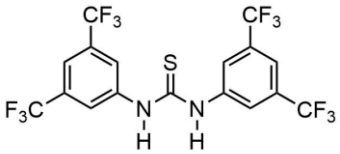 **8**	CsF	-21.0	0

* 10 mol% thio(urea) loading, 1.2 eq MF, 1.5 h, rt, DCM (0.25 M). † 24 h. Experimental work performed by co-workers.

such, the method requires adapting to more exotic salts, such as through estimation of lattice energies using, for example, the Kapustinskii equation.

3.3.1.3 The Gibbs Free Energy Profile

Computation of the rest of the pathway results in the free energy profile in Figure 3.5. Formation of the episulfonium ion in the presence and absence of urea have comparable barriers, with the barrier in the absence of urea favored by 10 kJ/mol. The barrier height of 90 kJ/mol to auto-ionization (**i**‡) is achievable at room temperature, corresponding to a rate constant of approximately $k_{TST} = 1 \times 10^{-3}$ s^{-1} at 298.15 K. This result is initially surprising, however the entropic penalty of coordination is significant and the hydrogen bonding to bromine, with only partially formed negative charge, is weak. Considering the uncertainty in the computational methods, and the concentration dependence of Gibbs free energies for the bimolecular catalyzed TS, an unqualified assertion that Schreiner's urea does not catalyze this step is difficult to justify, however the result is inconsistent with anion binding catalysis, where the catalyzed process would need to be significantly lower than the uncatalyzed process to rationalize the experimentally observed catalytic effect. Once bromide is fully formed, coordination of the urea to the anion in the ion pair is favorable (**ii→ii.Cat**). The charge on the bromide is now sufficient to form hydrogen bonds to the catalyst that overcome the entropic penalty of coordination.

Steps **ii→iv** concern anion transport and phase-transfer, and are the steps at which the catalyzed and uncatalyzed pathways diverge in Gibbs free energy. Initially, the ions are separated (**ii→iii**) – after which urea coordination of the separated bromide leads to 26 kJ/mol lower Gibbs free energy. Phase-transfer, described by the anion-exchange step (**iii→iv**), leads to further divergence in energy, with the hypothetical uncatalyzed pathway reaching a prohibitive energetic span of 122 kJ/mol. Meanwhile, the catalyzed

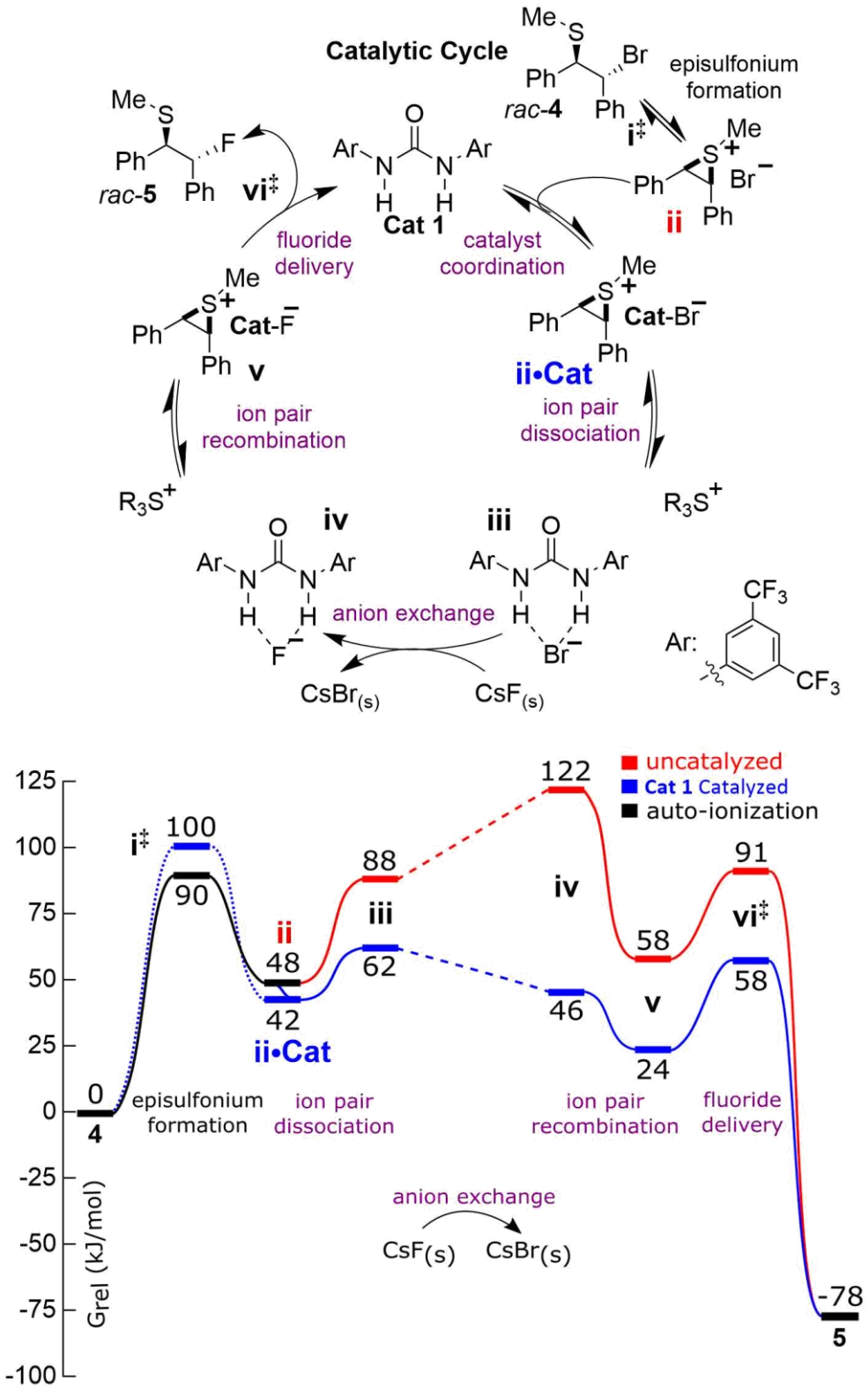

Figure 3.5: Computed reaction profile for HB PTC fluorination of *in situ* formed episulfonium ion catalyzed by Schreiner's urea, **1**. Gibbs free energies are evaluated at reaction temperature of 298.15 K. Own work adapted from Ref. 1.

pathway remains at plausible energies, stabilized by the strong coordination of fluoride by urea catalyst.

Formation of an ion pair between episulfonium and (urea) fluoride occurs (**iv**→**v**) followed by formation of fluorinated product *via* transition state structure (**vi**‡). From the ion pair, the barrier to fluoride delivery (**v**→**vi**‡) is increased minimally when fluoride is bound by urea ($\Delta G_{cat}^{\ddagger}$ = 34 kJ/mol *c.f.* $\Delta G_{uncat}^{\ddagger}$ = 33 kJ/mol). Product is formed irreversibly with a barrier to the reverse process in the absence of catalyst of 169 kJ/mol. This barrier remains prohibitive in the presence of catalyst at 136 kJ/mol despite being reduced significantly. The large effect of catalyst coordination on episulfonium formation with loss of fluoride (**vi**‡) is in stark contrast to the inability of the catalyst to lower the barrier with loss of bromide (**i**‡). The origin of this effect is the catalyst forming much stronger hydrogen bonds to the forming fluoride anion than the forming bromide anion, due to the former's much higher charge density.

The reaction profile makes it clear that the critical difference between the two profiles is in the steps describing anion-transport and phase-transfer (**ii**→**iv**), and that these steps are prohibitive in the absence of catalyst. This is further supported by computing the profile with unsubstituted urea **7** (Figure 3.6), experimentally found to be poorly active (5 % yield). Comparison of the profiles reveals little difference in solution-phase barriers, consistent with work on stoichiometric urea-fluoride complexes in Chapter 2. Much larger differences in the profiles emerge during phase-transfer, reflecting the experimental reactivity observed and supporting the hypothesis that the urea acts through accelerating the phase-transfer process, thereby supporting the HB PTC mechanistic hypothesis.

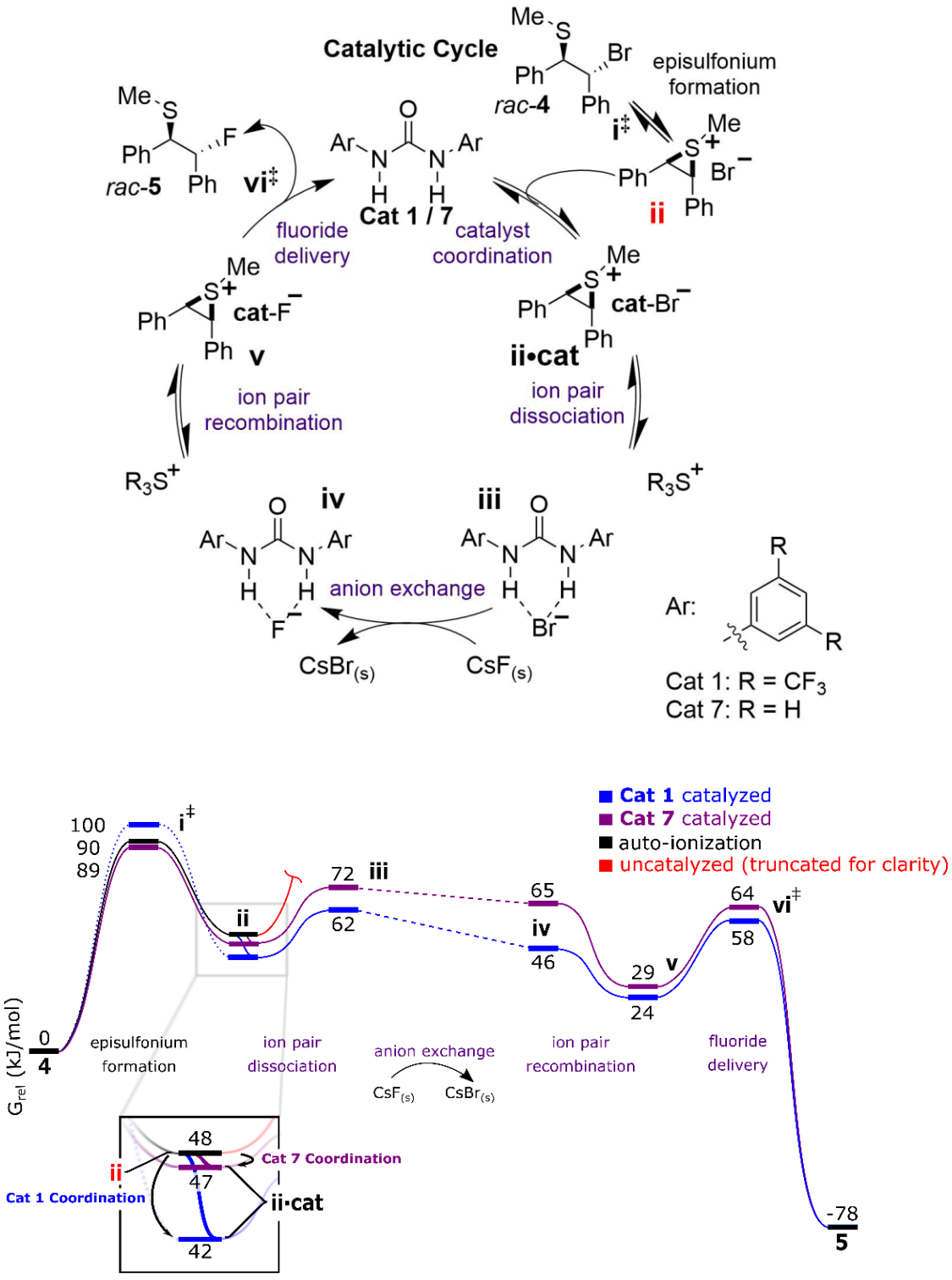

Figure 3.6: Computed reaction profile for unsubstituted urea catalyst **7** (purple), compared with superior Schreiner's urea catalyst, **1**, (blue). Own work adapted from Ref. 1.

3.3.1.4 Insight

Transition state structures for bromide removal and fluoride delivery with, and without, urea catalyst are shown in Figure 3.7a. In all cases, there is a preference for the α-phenyl ring to conjugate with the forming and breaking bonds, as typical for a benzylic substitution. This preference is more pronounced with fluoride than bromide. In the cases with urea hydrogen bond donor, the urea favors π-π stacking with the aromatic groups of the substrate. If both $\mathbf{TS_{Br}}$ and $\mathbf{TS_F}$ are viewed from the perspective of anion delivery, urea coordination makes both TS positions later, consistent with work on alkyl bromide substrates in Chapter 2. In the lowest energy geometry of the reactive fluoride-episulfonium ion pair, fluoride is bound on the *exo*-face of the episulfonium 3-membered ring, interacting with the acidified C–H bonds. In order to react, the fluoride must align with one of the episulfonium C–S σ*. This ion pair, with fluoride aligned, is

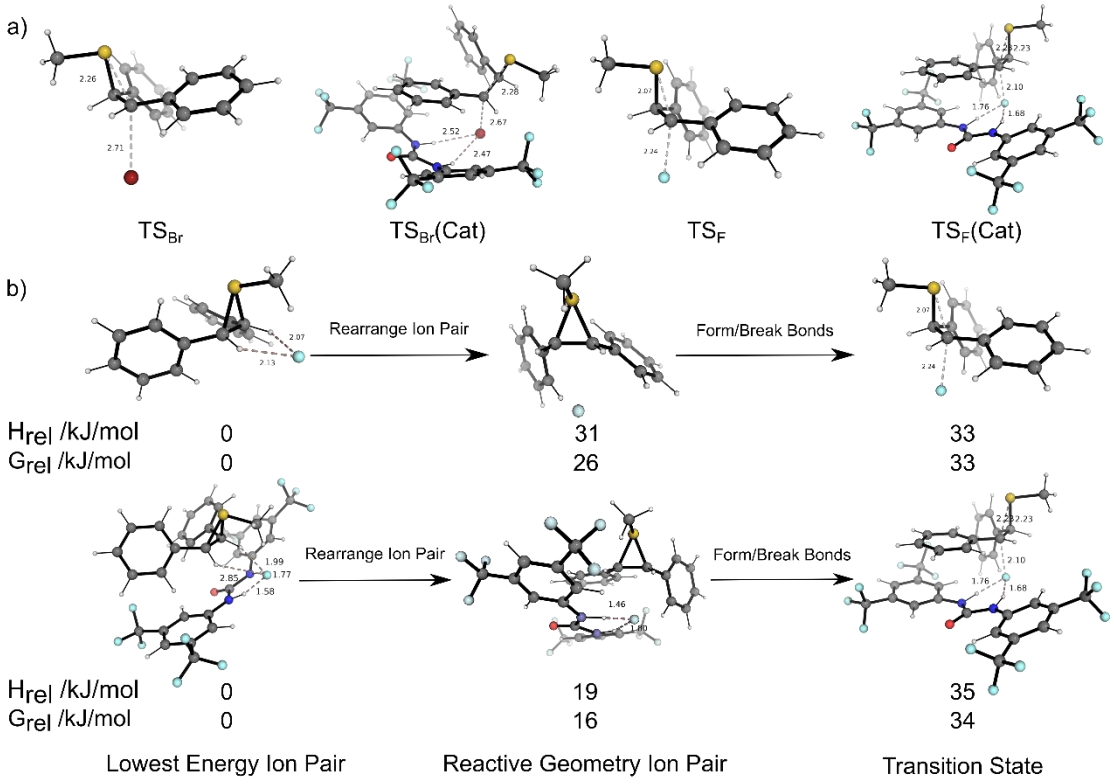

Figure 3.7: a) Transition state structures for bromide removal and fluoride delivery, with and without urea hydrogen bond donor (**1**). The α-phenyl ring favors conjugation with the forming and breaking bonds. b) relative Gibbs free energies of the lowest energy fluoride ion pair and the reactive conformation of the ion pair.

a shallow energy minimum, with $\Delta G = +26$ kJ/mol relative to the minimum energy geometry and resides 7 kJ/mol lower in Gibbs free energy than the fluoride delivery TS. Therefore, remarkably, just 20 % of the barrier from minimum energy ion pair to TS originates from the breaking of the C–S bond, with the rest arising from the loss of C–H and ionic interactions with fluoride in the ion pair (Figure 3.7b). This effect remains but is diminished when fluoride is coordinated by urea. Destabilizing the reactive ion pair by preventing fluoride from sitting next to the *exo*-face of the episulfonium ring is therefore the approach with the most potential to influence the kinetics of this step. Key geometric parameters of the species are tabulated in Table 3.4.

When considering asymmetric catalysis, the computed free energy profile allows some insight into whether asymmetric HB PTC is plausible with a chiral urea. The profile shows that the enantiodetermining TS is not the rate-limiting TS. The rate-limiting process being either episulfonium formation, or phase-transfer (the model does not quantify the kinetics of the latter process), and the enantiodetermining TS being fluoride delivery. Once episulfonium product is formed, loss of fluoride is prohibitive. Thus, if product is formed enantioenriched, it will not racemize, even in the presence of urea catalyst. Also, once the catalyst brings fluoride into solution, it will not readily dissociate (steps **iv**→**vi**‡) prior to the fluoride delivery TS. This is crucial to prevent a racemic background reaction from reducing enantiocontrol.

Table 3.4: Key Geometric Data for Episulfonium Containing Species.

Species	**Key Distances / Å**				**Key Angles / º**	
	C–X	**C–S**	**H Bond 1**	**H Bond 2**	**α-dihedral**	**β-dihedral**
TS_{Br}	2.713	2.256	-	-	3.4	-41.0
TS_{Br}(Cat 1)	2.672	2.283	2.523	2.475	-41.2	83.9
TS_{F}	2.238	2.065	-	-	18.2	-53.3
TS_{F}(Cat 1)	2.099	2.229	1.760	1.678	-4.8	-66.5
IP_{Br}(Cat 1)	-	-	2.378	2.507	-	-
IP_{F}(Cat 1)	-	-	1.580	1.771	-	-

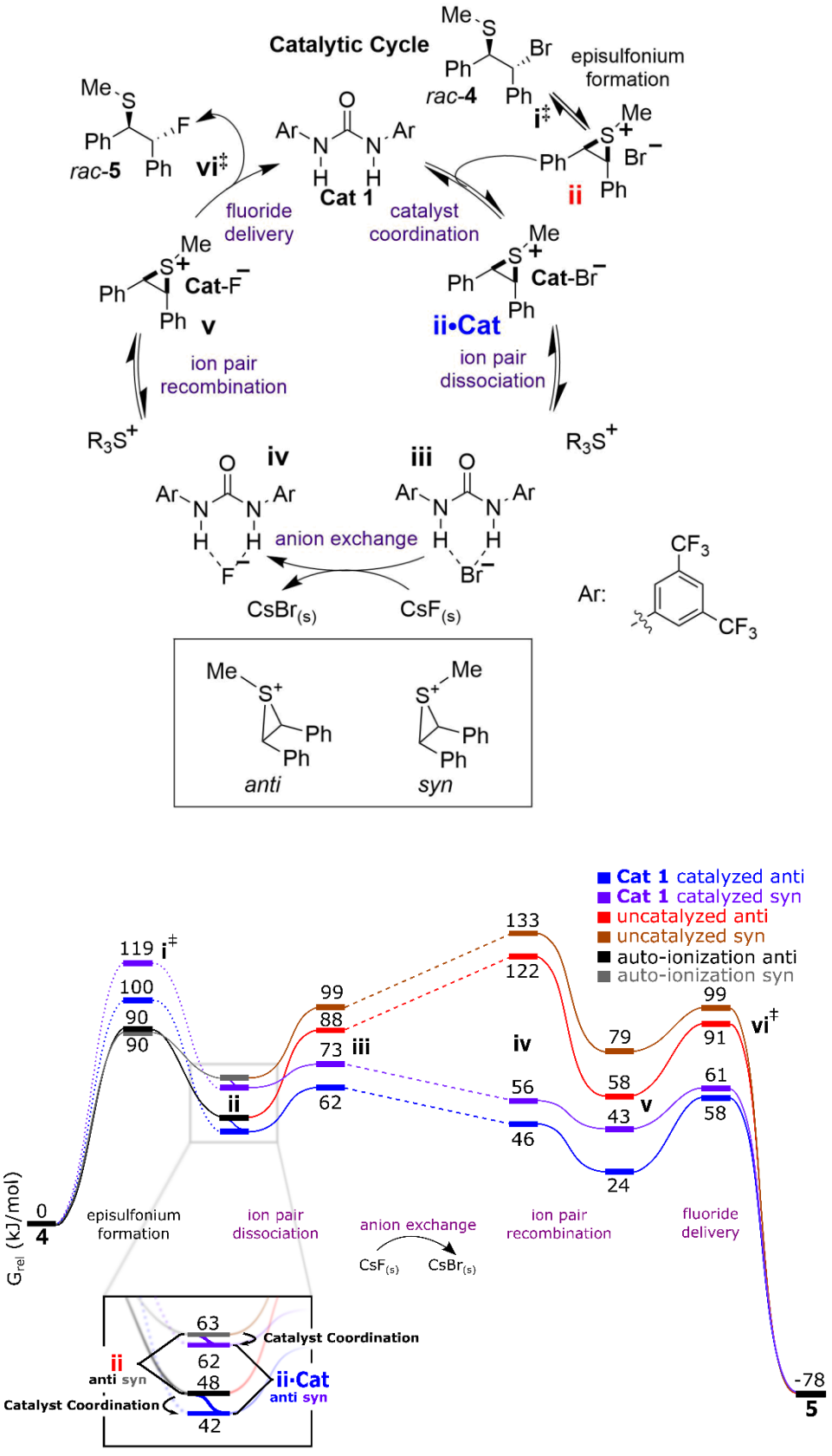

Figure 3.8: Computed reaction profile comparing the *anti* (blue, red) and *syn* (purple, orange) isomers of episulfonium. *Anti* is consistently thermodynamically favored and so will be the dominant isomer. Own work adapted from Ref. 1.

3.3.1.5 Episulfonium Isomers

The bromide episulfonium precursor, **4**, can form one of two episulfonium isomers. Thus far, only the *anti*-isomer has been considered, however the *syn*-isomer is also plausible. The reaction profile was recalculated with the *syn*-isomer of episulfonium intermediate, **6**, formed in step **i**‡. This isomer of episulfonium is then maintained until fluoride delivery in step **vi**‡. The Gibbs free energy profile for *syn* episulfonium is shown in Figure 3.8, superimposed with the *anti* profile for clarity. Formation of the episulfonium ion is favored without coordination of urea **1**, with equal kinetic favorability to the *syn* and *anti*-isomers. The formed ion pair is however significantly more favored for the *anti*-isomer both uncoordinated (ΔG = 14 kJ/mol) and when coordinated by urea catalyst (ΔG = 20 kJ/mol). An energy difference of 14 kJ/mol manifests as a preference of *anti* over *syn* by a factor of 300 at 298.15 K – a preference increased when coordinated by catalyst. As formation of the episulfonium occurs prior to the enantiodetermining TS, in the case of a chiral urea, the *anti*-isomer will dominate and so is considered for future work. Stationary points are illustrated in Figure S11, with geometric data in Table S15.

3.3.1.6 Leaving Group Effects

The effect of changing leaving group of the episulfonium precursor was investigated for chloride and trichloroacetimidate (TCA). The barriers to auto-ionization are given in Figure 3.9. The height of the free energy barriers agrees well with the experimental reactivity at room temperature. Reaction with bromide leaving group is rapid. Reaction with chloride is slower, but still achievable with barrier of 104 kJ/mol, and reaction with unactivated TCA leaving group is prohibitive at 143 kJ/mol. The full Gibbs free energy profile of the reaction with chloride leaving group was computed for comparison to the bromide leaving group (Figure 3.10). The favorability of the overall reaction, as well as

the anion-exchange process is largely unchanged with the leaving group due to cancellation of effects. The overall exergonicity of the reaction is reduced by 15 kJ/mol with the chloride leaving group – a stronger C-Cl bond is broken on formation of the episulfonium, however this is largely compensated for by the formation of the higher lattice energy CsCl salt. Similarly, the favorability of the anion-exchange process is reduced by only 1 kJ/mol indicating near complete compensation of the stronger urea-chloride hydrogen bonds by the formation of the CsCl salt. Stationary points are illustrated in Figure S12, with geometric data in Table S16.

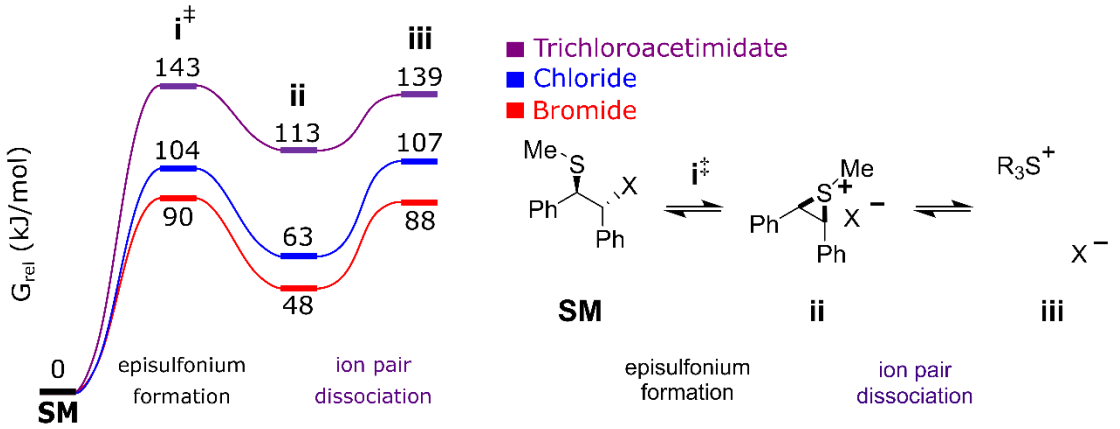

Figure 3.9: Computed barriers to auto-ionization of substrates with different leaving groups. Computed barriers correlate well with experimental reactivity. Own work reproduced from Ref. 1.

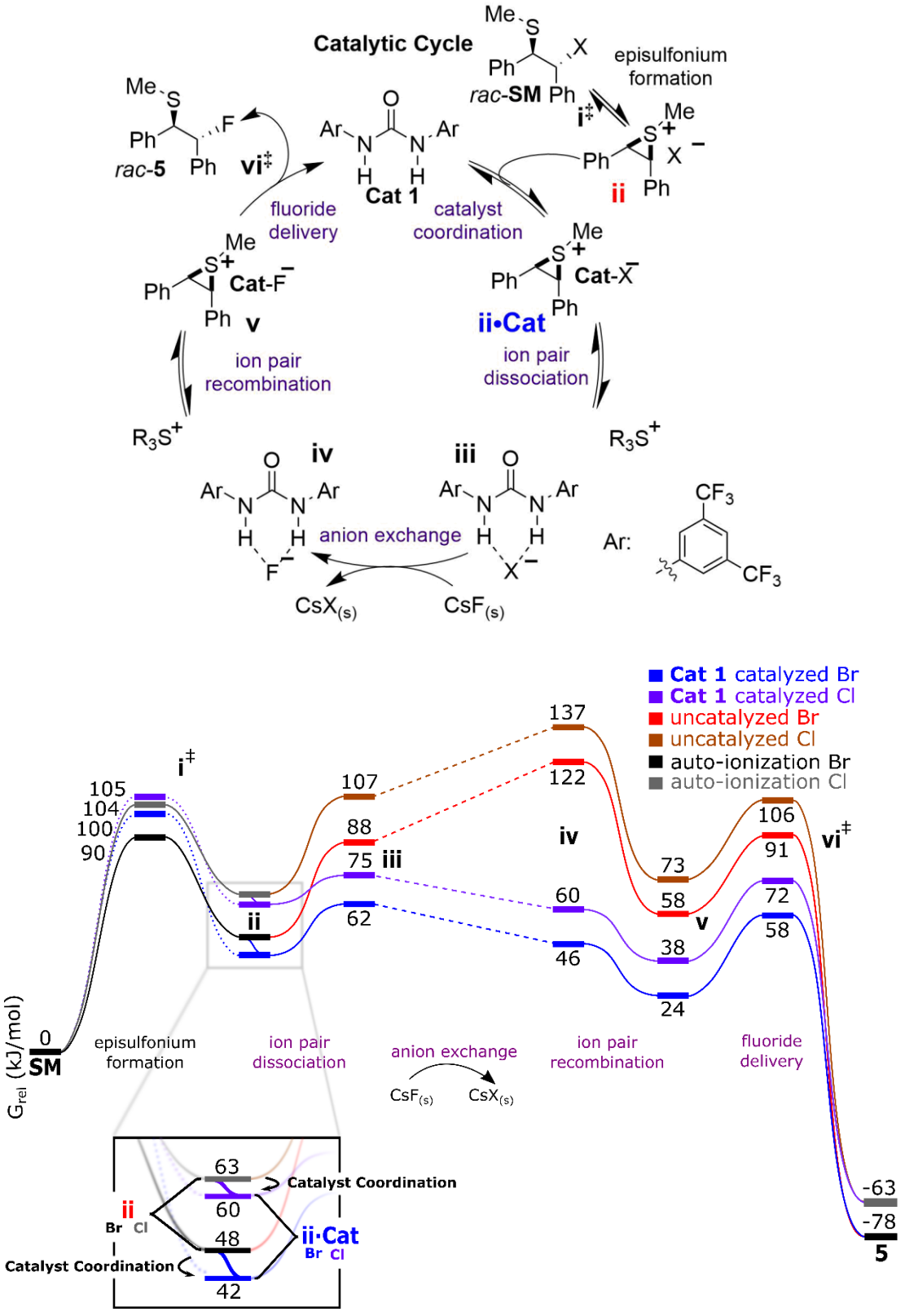

Figure 3.10: Full reaction profile comparing substrate with chloride and bromide leaving group, with and without Schreiner's urea catalyst. Own work adapted from Ref. 1.

3.3.2 Hydrogen Bonding Phase-Transfer Catalysis with a Chiral Urea for Asymmetric Fluorination

3.3.2.1 Determining Catalyst-Fluoride Binding Mode

Calculations on the mechanism of fluorination of *meso*-episulfonium ions using an achiral catalyst supports the HB PTC hypothesis and the proposal that use of a chiral urea should be capable of performing the desymmetrization enantioselectively. Experimentally, several classes of chiral urea catalyst were screened before identification of bis-ureas based on the BINAM scaffold as most promising and synthetically tractable to modification (Figure 3.11). These catalysts are highly active, however, enantioselectivity is low (Scheme 3.3). Synthetic modification of many positions, leading to a library of tens of catalysts, failed to find a catalyst with improved enantioselectivity over the prototypical catalyst, **9**.

As the BINAM based catalysts are of moderate size, have many rotatable bonds and are highly flexible, this system presents a significant computational challenge. The most important factor to determine is how the bis-urea catalyst family binds fluoride. With four hydrogen bond donors, there are many potential binding modes of fluoride – those initially considered were a 'bis' tetracoordinate complex and a 'co-operative' dicoordinate complex (Figure 3.12) as both binding modes have been implicated previously in hydrogen bonding catalysis.[46–49] To probe the plausibility of these binding

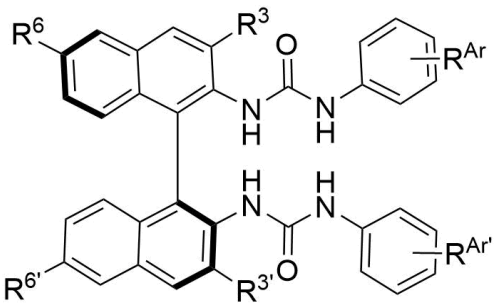

Figure 3.11: Chiral urea catalysts based upon the BINAM scaffold, with positions of easiest synthetic modification indicated.

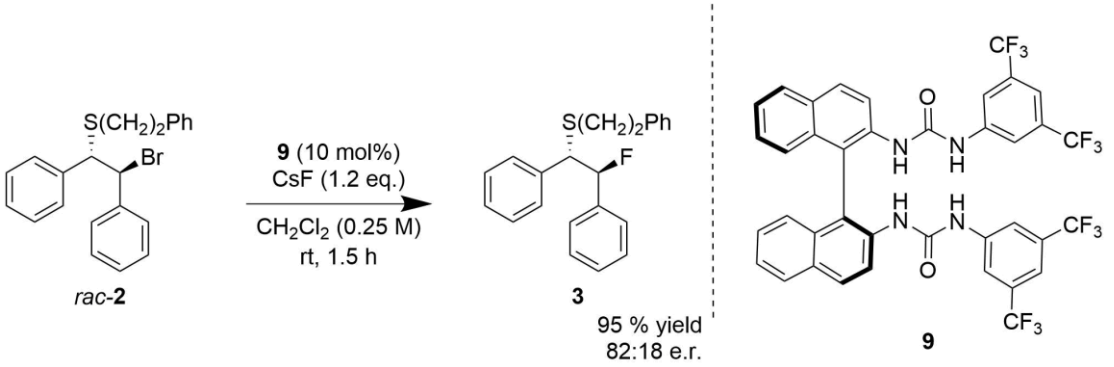

Scheme 3.3: Enantioselective desymmetrization of episulfonium ions using prototypical BINAM based bis-urea, **9**. Yields are excellent, however enantioselectivity is poor.

modes, molecular dynamics simulations were performed of the catalyst-fluoride complex, in explicit dichloromethane solvent. Initial simulations were performed without an explicit cesium counterion. Simulations at 298.15 K showed no interconversion of binding modes after 100 ns of simulation time. To enhance sampling, simulation temperature was raised to 373.15 K and an explicit cesium counterion included in the simulation. 6 simulations of 20 ns were run, 3 beginning from co-operative binding and 3 with bis binding. In the combined 120 ns of simulation, 0 % of frames were in the co-operative binding mode, whereas 58 % were binding via the tetracoordinate bis binding mode. An unexpected result was that the remaining 42 % of frames were for a tricoordinate binding mode, resulting from the isomerization of one of the urea groups from *anti-anti* to *anti-syn* (Figure 3.13, Table S17).

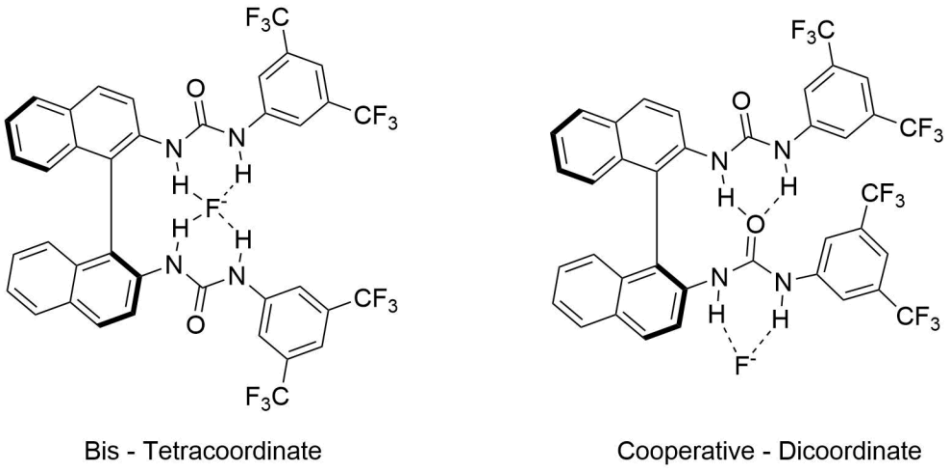

Figure 3.12: Plausible fluoride binding modes for BINAM based bis-urea catalysts. Own work adapted from Ref. 1.

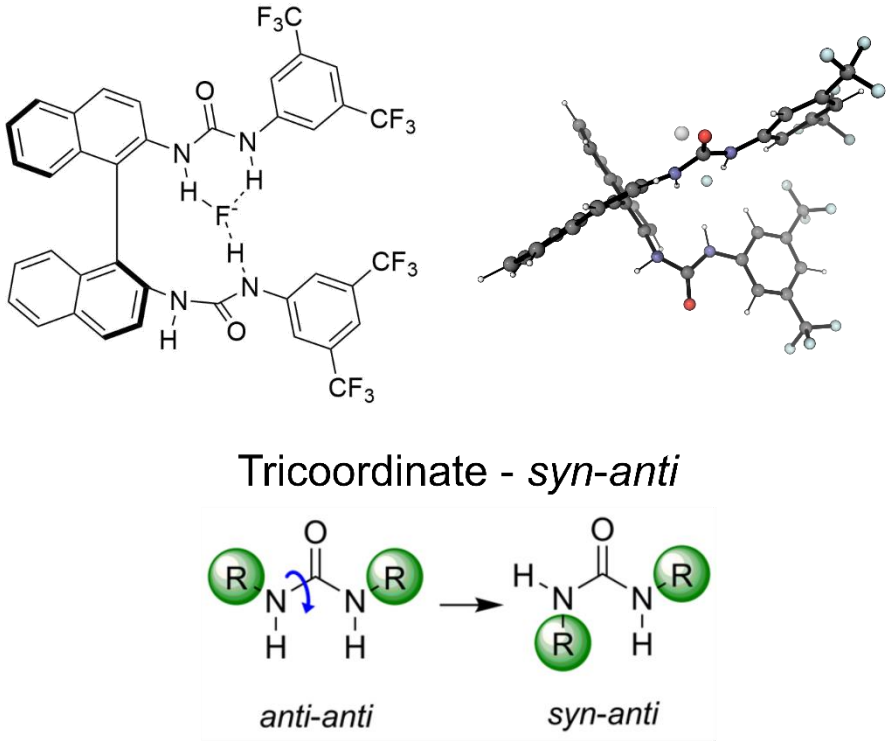

Figure 3.13: Molecular dynamics predicted tricoordinate fluoride binding mode with anti-syn urea. Left: ChemDraw representation. Right: Ball and stick representation of MD frame. Bottom: Illustration of urea isomerization. Figure adapted in part from own work in Ref. 50.

The driving force behind this isomerization is the geometric improvement of hydrogen bonding in the tricoordinate complex and increased conjugation of the ureas with the BINAM backbone, rather than an intrinsic preference of the urea functional group. It is not geometrically possible for the catalyst to form 4 non-elongated hydrogen bonds to fluoride and maintain full conjugation of one or more ureas with the BINAM backbone. Conversely, *syn-anti* isomerization of one urea permits the formation of 3 non-elongated hydrogen bonds and maintains full conjugation of the other urea with the BINAM.

Permitting isomerization of the urea functional groups vastly increases the number of plausible fluoride binding modes of the catalyst that must be considered computationally, to the extent that it is impractical to compute. To further investigate this result, two transition state structures were computed using catalyst **9** to deliver fluoride to episulfonium ion **6** – one with catalyst forming four hydrogen bonds to fluoride, and one

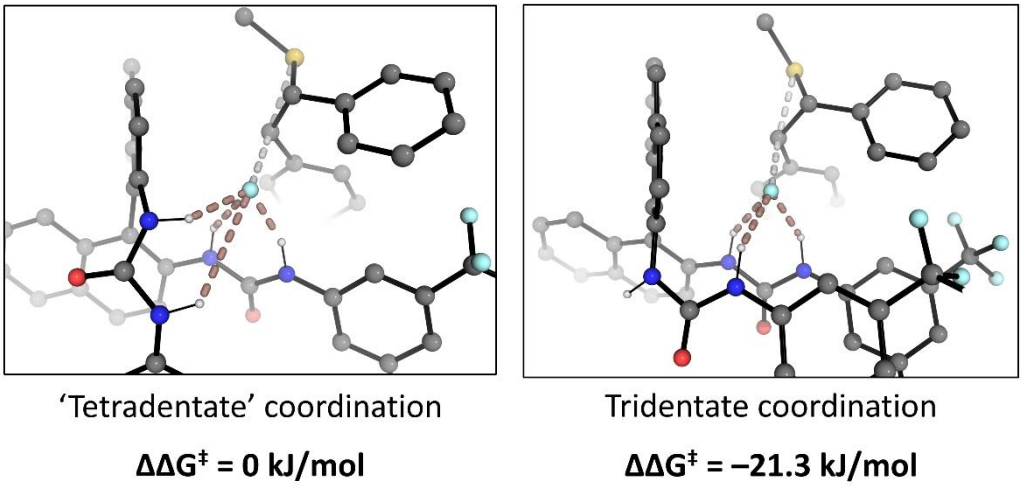

Figure 3.14: Trial TSs for fluorination of episulfonium ion with tetracoordinate and tricoordinate fluoride binding. The tetracoordinate TS cannot maintain all four hydrogen bonds, however the tricoordinate TS maintains all three, with a pyramidal geometry around fluorine. The distortion in hydrogen bonding is reflected in the relative Gibbs free energies. Figure adapted in part from own work in Ref. 50.

forming three hydrogen bonds, with *syn-anti* isomerized urea. A plausible TS geometry was chosen using chemical intuition. In the resulting TSs, the tricoordinate TS is favored over the tetracoordinate TS by 21.3 kJ/mol – a very large Gibbs free energy difference, corresponding to a ratio of 5.4×10^3 at 298.15 K. Additionally, in the tetracoordinate TS, the catalyst cannot maintain all four hydrogen bonds to fluoride (Figure 3.14, Table S18).

Despite the preliminary DFT calculations supporting the tricoordinate binding mode, other binding modes (including tetradentate) contributing to selectivity through low energy TSs cannot be ruled out unreservedly, and full conformational sampling would need to be undertaken to pursue this conclusion. The ability of the catalyst to bind fluoride in numerous ways is a plausible origin of the experimental difficulty in optimizing the substituents of BINAM based bis-urea catalysts for high enantioselectivity. The computation does, however, predict that one hydrogen bond donor is superfluous to catalyst activity. Alkylation of this nitrogen, preventing it from acting as a hydrogen bond donor, should maintain catalyst activity and vastly reduce the conformational flexibility of the catalyst, most notably when binding fluoride where only a single binding mode is

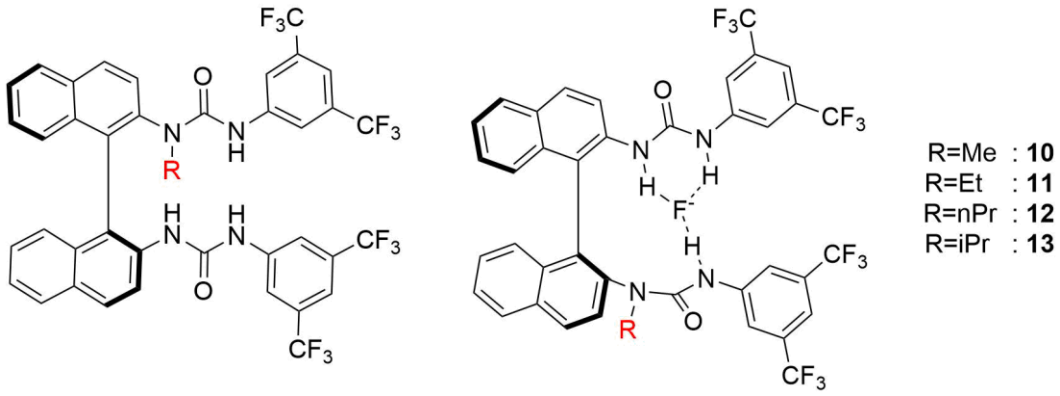

Figure 3.15: LHS: Improved catalyst proposed on the basis of computation, with mono-alkylated urea highlighted in red. RHS: Single, tricoordinate fluoride binding mode predicted for the alkylated catalyst.

anticipated (Figure 3.15). Molecular dynamics simulations of the *N*-methylated catalyst **10** were performed, binding fluoride in the presence of cesium counterion. After 100 ns of simulation, the tridentate binding mode dominated (96 % of frames) and was stable once formed, supporting the hypothesized binding mode, and resulting in only 2 conformationally similar high-weighted clusters (1.1 Å RMSD), both with tridentate binding (Figure S14).

This vastly reduced conformational space has large benefits for computational investigation of the system, and also experimentally as structure-activity relationships should become more tractable. Of note is that alkylation of the catalyst (**9→10**) may have a positive or negative effect on enantioselectivity – the resulting system should, however be more rationalizable and therefore easier to optimize to high enantioselectivities through modification of the catalyst or conditions.

Methylation studies of the catalyst were undertaken experimentally to investigate the computational hypothesis and to probe the role of the individual hydrogen bond donors. The results of the methylation study are shown in Table 3.5.

Table 3.5: Experimental Catalyst Methylation Studies.

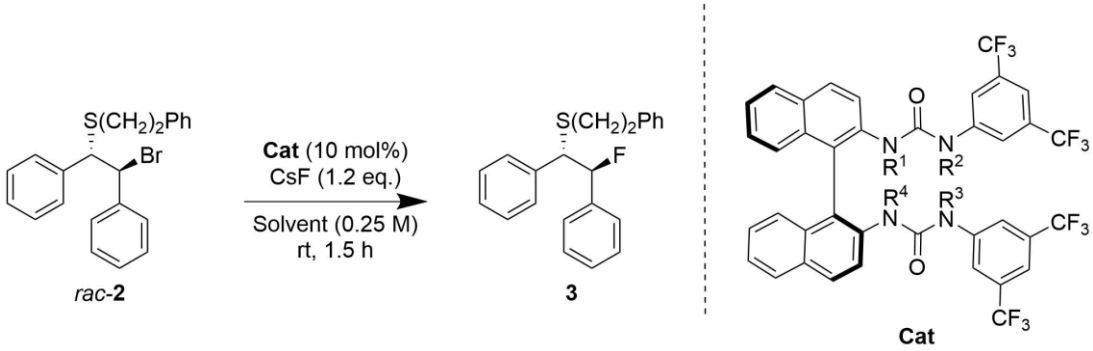

Cat #	R^1	R^2	R^3	R^4	Solvent	Yield / %	e.r.
9	H	H	H	H	CH_2Cl_2	>95	82:18
9	H	H	H	H	1,2-DFB	>95	86:14
10	H	H	H	Me	1,2-DFB	>95	88:12
-	H	H	Me	H	1,2-DFB	15	53:47
-	Me	H	H	Me	1,2-DFB	0	n/a
-	H	Me	Me	H	1,2-DFB	0	n/a
11	H	H	H	Et	1,2-DFB	>95	91:9
13	H	H	H	^{i}Pr	1,2-DFB	>95	90:10
13	H	H	H	^{i}Pr	CH_2Cl_2	>95	88:12

DFB = difluorobenzene. Experimental work performed by co-workers.

Notably, the computational prediction is borne out, with alkylation of position 4 preserving catalyst activity, and simultaneously increasing enantioselectivity. As the size of the alkyl group is increased to iPr, enantioselectivity increases, achieving acceptably high levels when the temperature is reduced. Interestingly, the enantioselectivity of the unalkylated catalyst does not increase as the temperature is reduced, possibly due to catalyst aggregation or the behavior of the complex ensemble of TSs.

3.3.2.2 Computing the Transition State Structure Ensemble

Substrate scope was performed with the optimized catalyst and is shown in (Figure 3.16). Simultaneously, we turned our attention to rationalizing the observed enantioselectivity. Key outstanding questions included i) which is the major enantiomer (at this point

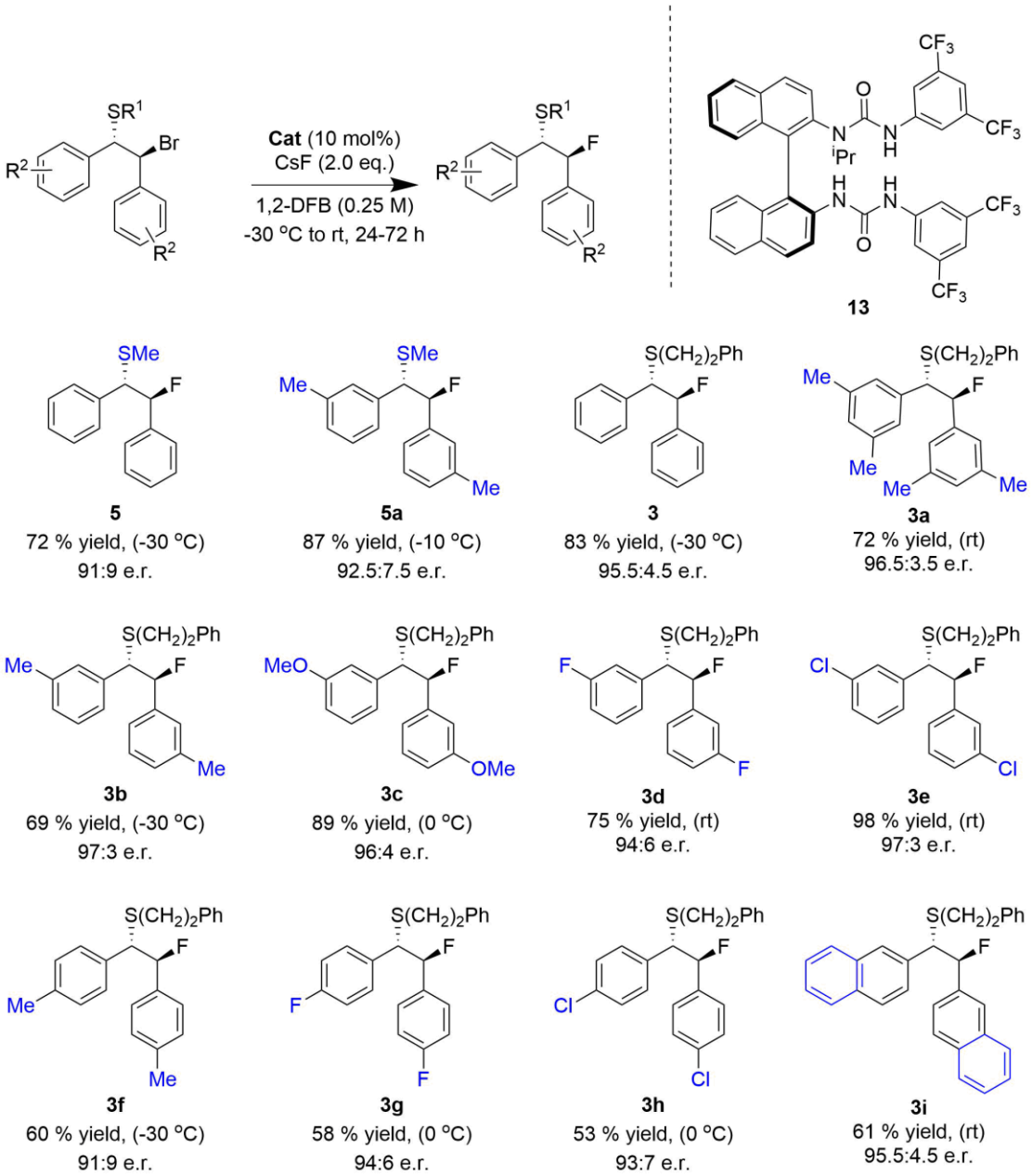

Figure 3.16: Substrate scope for asymmetric desymmetrization of meso-episulfonium ions. Substrate scope is limited to stilbene derived episulfonium ions, however a broad range of substituents are tolerated on the aromatic rings. Experimental work performed by co-workers.

unknown), ii) what are the key factors and interactions that determine enantioselectivity and iii) why is good enantioselectivity only achieved with stilbene derived substrates?

To begin to answer these questions, the lowest energy TSs to major and minor product must be located. A molecular dynamics (MD) sampling protocol was performed on *N*-methylated catalyst, **10**, to locate the lowest energy TS conformations. From previous

MD simulations, this catalyst has only 2 binding modes for CsF; both of which bind fluoride in a tricoordinate manner and rapidly interconvert. The cesium cation was replaced by the stilbene derived episulfonium ion, **6**, (corresponding to product **5** in Figure 3.16) forming the "reactive ion pair" between tricoordinate catalyst-fluoride complex and episulfonium. This ion pair was simulated for 100 ns at reaction temperature of 298 K to sample conformations. The resulting output was clustered by RMSD (cut-off = 1.0 Å, every fifth frame, clusters taken with weighting > 1.5 %), with the 12 most populated ion pairs retained. To ensure that novel conformations were retained, the lower weighted clusters were manually inspected before being discarded. Clustering of the frames was performed with hydrogen and CF_3 fluorines removed, with awareness of the symmetry of the system (16 ways of superimposing the system on itself). The use of every fifth frame in the trajectory was a result of practical limitations in the calculation of the symmetry aware RMSD matrix.

Each of the 12 ion pairs were optimized using DFT and used as the starting point for TS searches (Figure 3.17). The episulfonium substrate was advanced forward to align either of the C–S σ* with fluoride nucleophile, generating TSs to both products. After optimization, a total of 16 unique DFT optimized TSs were obtained, with 9 to (*S*,*S*) product and 7 to (*R*,*R*) product with (*S*) catalyst, with a total Gibbs free energy span of 42.2 kJ/mol (Figure S15). The distribution of Gibbs free energies of the ensemble is illustrated in Figure 3.18, with key geometric parameters in Table 3.6.

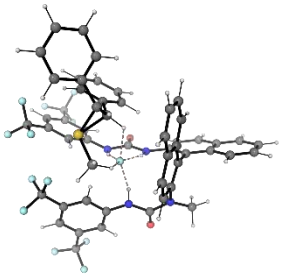

IP Cat 10 F epi 1
0.0 kJ/mol

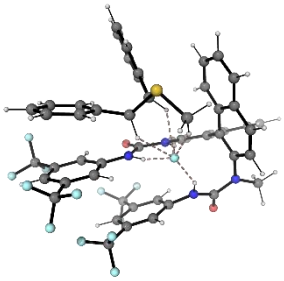

IP Cat 10 F epi 2
+ 1.2 kJ/mol

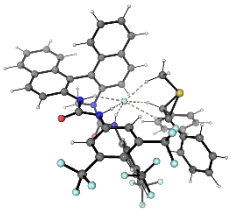

IP Cat 10 F epi 3
+ 2.3 kJ/mol

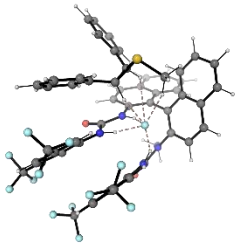

IP Cat 10 F epi 4
+ 6.0 kJ/mol

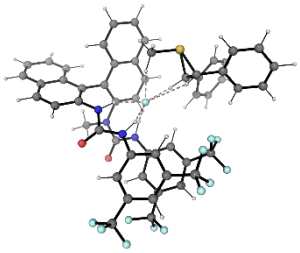

IP Cat 10 F epi 5
+ 7.2 kJ/mol

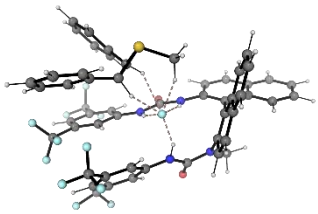

IP Cat 10 F epi 6
+ 9.7 kJ/mol

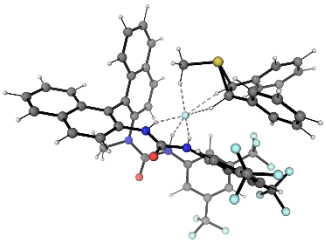

IP Cat 10 F epi 7
+ 12.3 kJ/mol

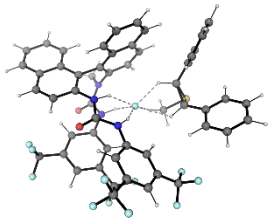

IP Cat 10 F epi 8
+ 13.7 kJ/mol

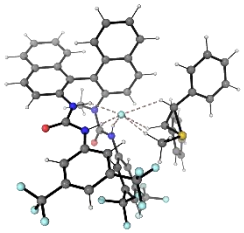

IP Cat 10 F epi 9
+ 19.2 kJ/mol

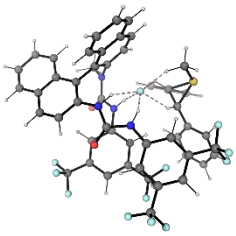

IP Cat 10 F epi 10
+ 21.5 kJ/mol

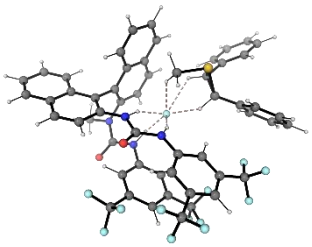

IP Cat 10 F epi 11
+ 26.1 kJ/mol

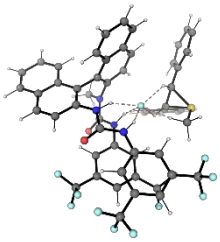

IP Cat 10 F epi 12
+ 28.3 kJ/mol

Figure 3.17: DFT optimized ensemble of episulfonium-fluoride-catalyst reactive ion pair. Relative Gibbs free energies evaluated at 298.15 K. Own work reproduced from Ref. 1.

Table 3.6 Key Geometric Parameters for Transition State Structures with Me Catalyst.

TS Cat 10	imag	Key Distances / Å						Key Angles / º			
		C-F	C-S	α-C-H	H-bond 1	H-bond 2	H-bond 3	H-bond 3	α-Dihedral†	β-Dihedral†	Backbone
major 1	-418.30	2.070	2.210	1.091	1.734	1.839	1.854	149.5	-20.5	-71.4	68.4
major 2	-387.71	2.071	2.268	1.089	1.840	1.795	1.871	152.8	4.7	-59.4	113.2
major 3	-406.05	2.083	2.205	1.091	1.679	1.906	1.879	149.4	-19.6	-72.3	67.6
major 4	-292.68	2.186	2.240	1.091	1.778	1.749	1.933	151.7	-8.6	-76.5	73.2
major 5	-426.00	2.058	2.253	1.090	1.761	1.841	1.898	146.9	13.1	-33.2	64.0
major 6	-424.89	2.066	2.265	1.089	1.938	1.683	2.021	145.5	22.0	-35.4	67.3
major 7	-398.95	2.097	2.205	1.090	1.743	1.633	2.788	140.8	-14.7	-57.5	69.7
major 8	-452.00	2.027	2.289	1.090	1.944	1.658	1.921	165.6	-2.8	-49.1	66.8
major 9	-433.42	2.053	2.277	1.087	2.002	1.643	1.927	152.9	26.4	-26.3	111.6
minor 1	-365.95	2.109	2.225	1.090	1.800	1.728	1.711	172.8	-6.3	90.6	76.9
minor 2	-429.11	2.055	2.243	1.090	1.827	1.803	1.793	148.2	22.2	-26.1	73.6
minor 3	-415.48	2.075	2.196	1.089	1.728	1.808	1.880	147.9	-40.7	86.6	65.2
minor 4	-397.02	2.075	2.224	1.088	1.771	1.877	1.800	151.2	-4.1	-63.2	112.4
minor 5	-438.90	2.068	2.184	1.093	1.748	1.789	1.889	148.1	-52.7	50.9	69.1
minor 6	-426.40	2.068	2.252	1.090	1.734	1.872	2.131	137.0	15.6	-34.0	64.6
minor 7	-412.25	2.068	2.252	1.088	1.902	1.715	1.839	159.2	-21.0	-64.8	112.3

†Phenyl ring dihedrals measured relative to C-C bond.

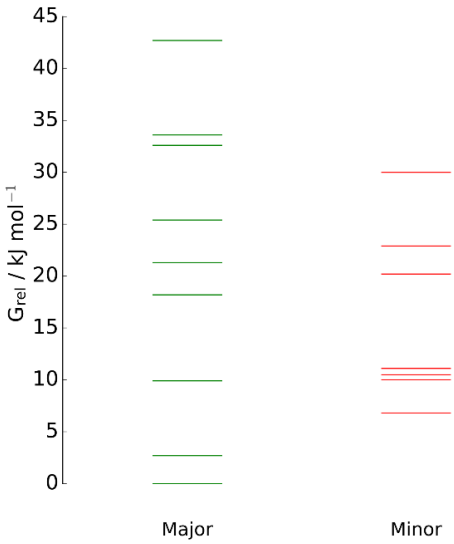

Figure 3.18: Gibbs Free energy distribution of transition state structures to major (*S*,*S*) and minor (*R*,*R*) product at 243.15 K. Own work reproduced from Ref. 1.

To enable direct comparison with experimental work, the structures were reoptimized with *N*-^{i}Pr group (catalyst **13**) on the catalyst in place of Me. Dihedral scanning of the iPr group revealed a favored conformer with hydrogen pointing towards the BINAM core. The lowest energy catalyst-fluoride complex was superimposed with the subsequently determined solid-state structure from x-ray crystallography and excellent agreement was found, including fluoride binding geometry and catalyst conformation (Figure 3.19).

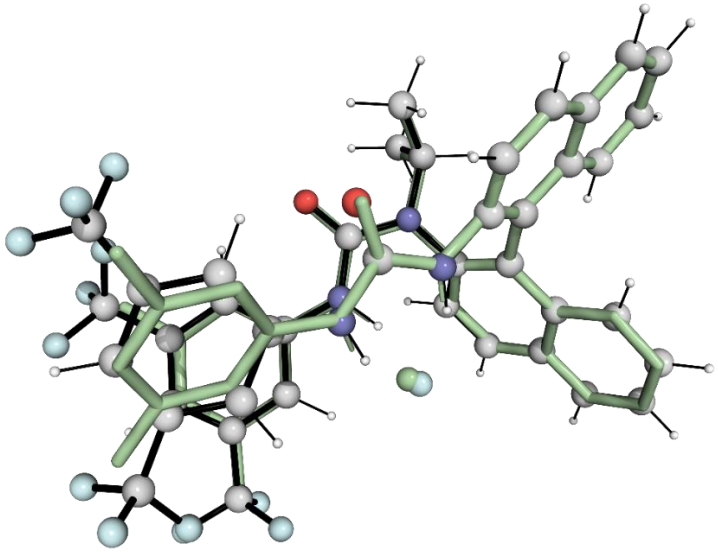

Figure 3.19: Overlay of the computed minimum energy geometry for catalyst **13**-fluoride complex with Cs cation (conventional coloring) with subsequently determined solid-state structure from crystallography with TBA cation (green wireframe), demonstrating excellent agreement. Cations are removed for clarity.

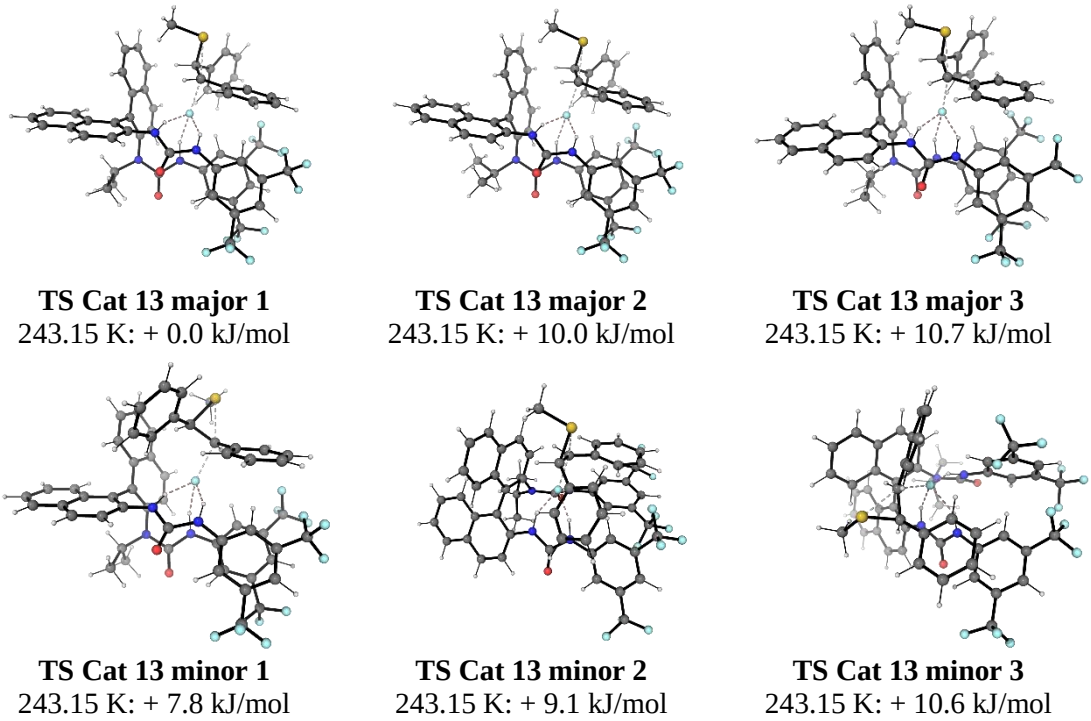

Figure 3.20: DFT optimized ensemble of transition state structures with N-^{i}Pr catalyst **13**. Own work adapted from Ref. 1.

The lowest energy TSs in the ensemble were reoptimized with iPr group on the catalyst. Due to an absence of TSs between 11.0 and 18.0 kJ/mol and the limited contribution of higher energy TSs, only TSs within the 11.0 kJ/mol window were reoptimized. Different conformers of the iPr group were considered but were not found to be energetically competitive. A total of 17 TSs with iPr catalyst **13** were located, however only six were within the original 11.0 kJ/mol window and are used for further analysis (Figure 3.20). Boltzmann weighting of the TSs at 243.15 K in dichloromethane gives an e.r. of 96.5:3.5, aligning well with the experimental e.r. of 91:9 in 1,2-difluorobenzene. Key geometric data for all 17 optimized TSs is given in Table 3.7 and geometries of TSs not included in the final ensemble are given in Figure S17.

Table 3.7: Key Geometric Parameters for Transition State Structures with iPr Catalyst.

TS	imag	Key Distances / Å						Key Angles / º			
		C-F	C-S	α-C-H	H-bond 1	H-bond 2	H-bond 3	H-bond 3	α-Dihedral	β-Dihedral	Backbone
TS Cat 13 major 1	-415.39	2.069	2.213	1.090	1.728	1.831	1.870	150.4	-20.9	-70.6	71.7
TS Cat 13 major 2	-408.62	2.078	2.208	1.090	1.706	1.855	1.888	146.5	-18.0	-72.3	68.5
TS Cat 13 major 3	-406.40	2.082	2.208	1.091	1.680	1.887	1.903	150.4	-20.6	-70.6	71.3
TS Cat 13 major 4	-385.12	2.073	2.272	1.088	1.857	1.785	1.865	153.0	5.5	-59.1	111.0
TS Cat 13 major 5	-408.30	2.077	2.211	1.090	1.705	1.856	1.884	147.5	-17.5	-73.2	68.0
TS Cat 13 major 6	-375.93	2.082	2.273	1.088	1.840	1.787	1.918	150.3	5.2	-59.2	111.7
TS Cat 13 major 7	-398.20	2.091	2.202	1.091	1.655	1.938	1.901	147.4	-17.1	-73.0	67.7
TS Cat 13 minor 1	-416.48	2.073	2.195	1.089	1.726	1.800	1.884	149.5	-40.5	86.6	68.2
TS Cat 13 minor 2	-364.96	2.113	2.227	1.090	1.791	1.732	1.724	171.0	-7.1	90.2	79.9
TS Cat 13 minor 3	-421.87	2.060	2.248	1.090	1.811	1.807	1.802	148.9	22.3	-25.4	76.7
TS Cat 13 minor 4	-416.62	2.066	2.238	1.090	1.771	1.852	1.804	145.8	24.0	-21.9	71.9
TS Cat 13 minor 5	-418.25	2.075	2.198	1.089	1.731	1.796	1.922	143.9	-41.8	-87.8	65.2
TS Cat 13 minor 6	-338.12	2.136	2.219	1.090	1.765	1.751	1.713	170.7	-4.2	-91.3	74.3
TS Cat 13 minor 7	-395.39	2.078	2.227	1.088	1.797	1.852	1.795	150.9	-4.6	-61.7	109.3
TS Cat 13 minor 8	-417.88	2.075	2.203	1.089	1.734	1.791	1.925	144.1	-41.6	-86.7	64.6
TS Cat 13 minor 9	-392.96	2.084	2.226	1.088	1.778	1.863	1.838	149.2	-3.5	-67.6	110.4
TS Cat 13 minor 10	-391.12	2.088	2.236	1.088	1.875	1.789	1.851	144.3	-8.6	-54.6	95.2

[†]Phenyl ring dihedrals measured relative to C-C bond.

3.3.2.3 Transition State Structure Analysis

For more detailed analysis, we focus on the two highest contributing transition state structures – the lowest energy TS to major product (**TS Cat 13 major 1** herein referred to as **TS_{Major}**) and the lowest energy TS to minor product (**TS Cat 13 minor 1** herein referred to as **TS_{Minor}**), with $\Delta\Delta G^{\ddagger}$ = 7.8 kJ/mol.

The conformation of the catalyst in both the major and minor is similar and is in very good agreement with the subsequently determined single-crystal x-ray structure of the ground state fluoride complex (Figure 3.21). The following compare favorably i) tricoordinate binding of fluoride, ii) catalyst conformation including urea conformation and BINAM angle, iii) isopropyl group orientation, iv) episulfonium substrate superimposes on the position of the TBA cation in the x-ray structure.

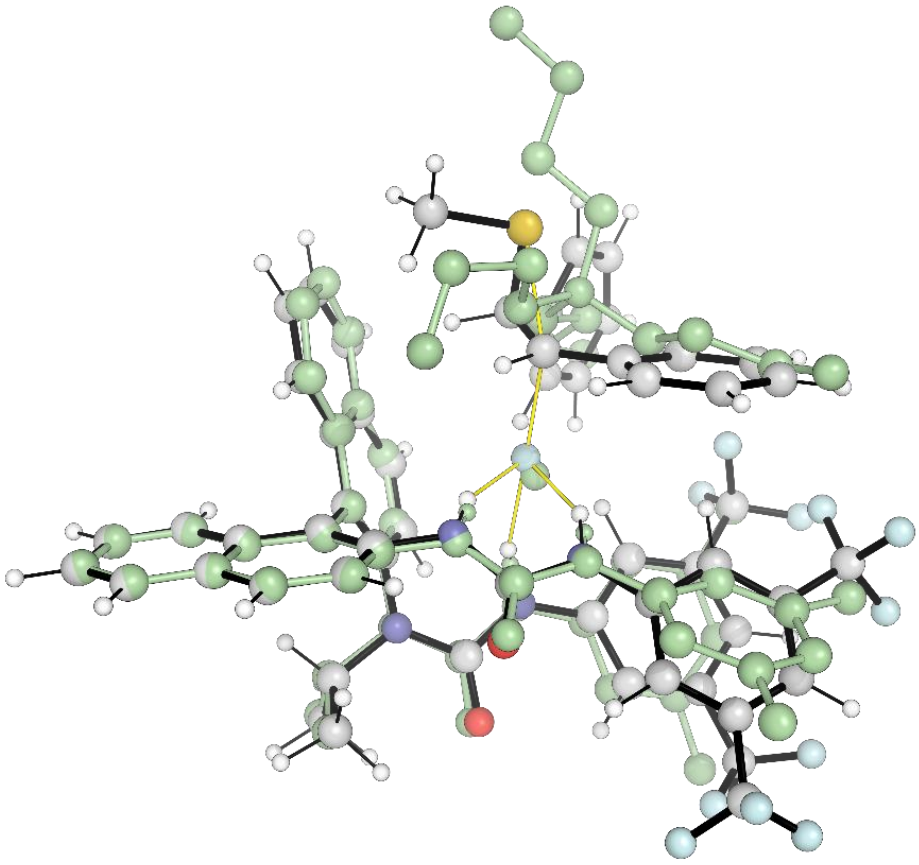

Figure 3.21: Overlay of TS_{Major} (conventional coloring) with experimentally determined crystal structure (green). The episulfonium substrate in the TS overlays well with TBA in the crystal structure.

Substrate conformation plays a key role in determining selectivity. When studying the system with achiral Schreiner's type urea, we noted a preference for the stilbene derived substrates to maintain conjugation of the α-phenyl ring with the forming and breaking bonds. This can be attributed to the fact that the S_N2 is benzylic and favors conjugation of the aromatic ring. In **TS_{Major}** this dihedral is 21° whereas in **TS_{Minor}** it is further from conjugation at 40°, measured relative to the C–C bond of the episulfonium ring. For the ensemble of optimized TSs, nearly all low energy TSs have a dihedral angle close to conjugation (the notable exception being **TS_{Minor}**), demonstrating the ubiquity of this effect. In order to estimate the energetic contribution to selectivity, a dihedral scan of the TS with achiral Schreiner's urea (**TS_F(Cat 1)**) was run at fixed C–S and C–F distance (Figure 3.22).

The scan confirms that **TS_{Major}** is closer to the energetic minimum than **TS_{Minor}**, with an energetic difference of ~4 kJ/mol, contributing approximately half of $\Delta\Delta G^{\ddagger}$ of 7.8 kJ/mol. A complementary approach was taken where the two TSs were separated into episulfonium-fluoride + catalyst units and the distortion of the former group evaluated. Distortion was greater in **TS_{Minor}**, by 4 kJ/mol, concurring with the dihedral scan.

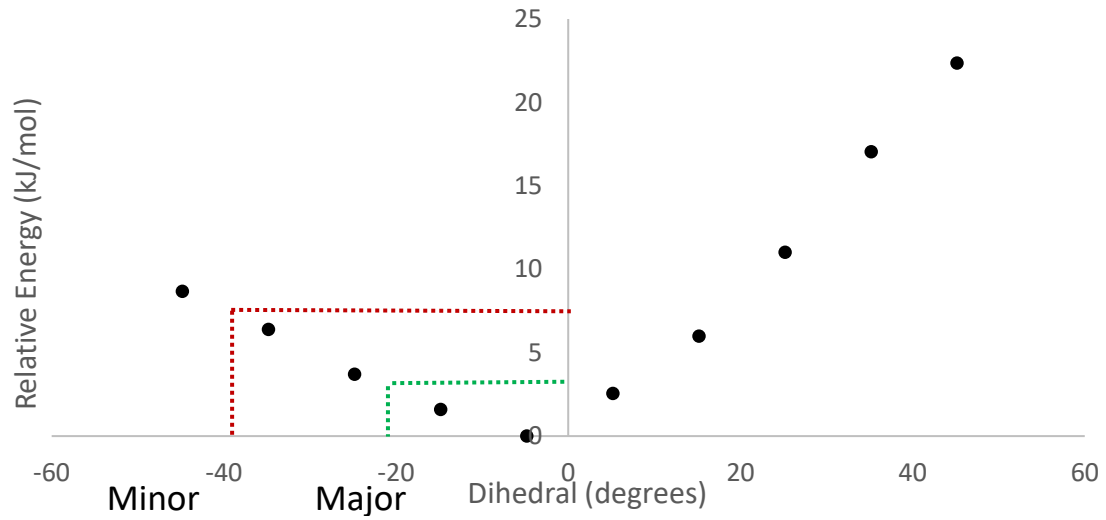

Figure 3.22: Dihedral scan of α-phenyl ring in fluoride delivery TS with Schreiner's urea, **1**. Dihedral angles for **TS_{Major}** (green) and **TS_{Minor}** (red) are indicated. Own work adapted from Ref. 1.

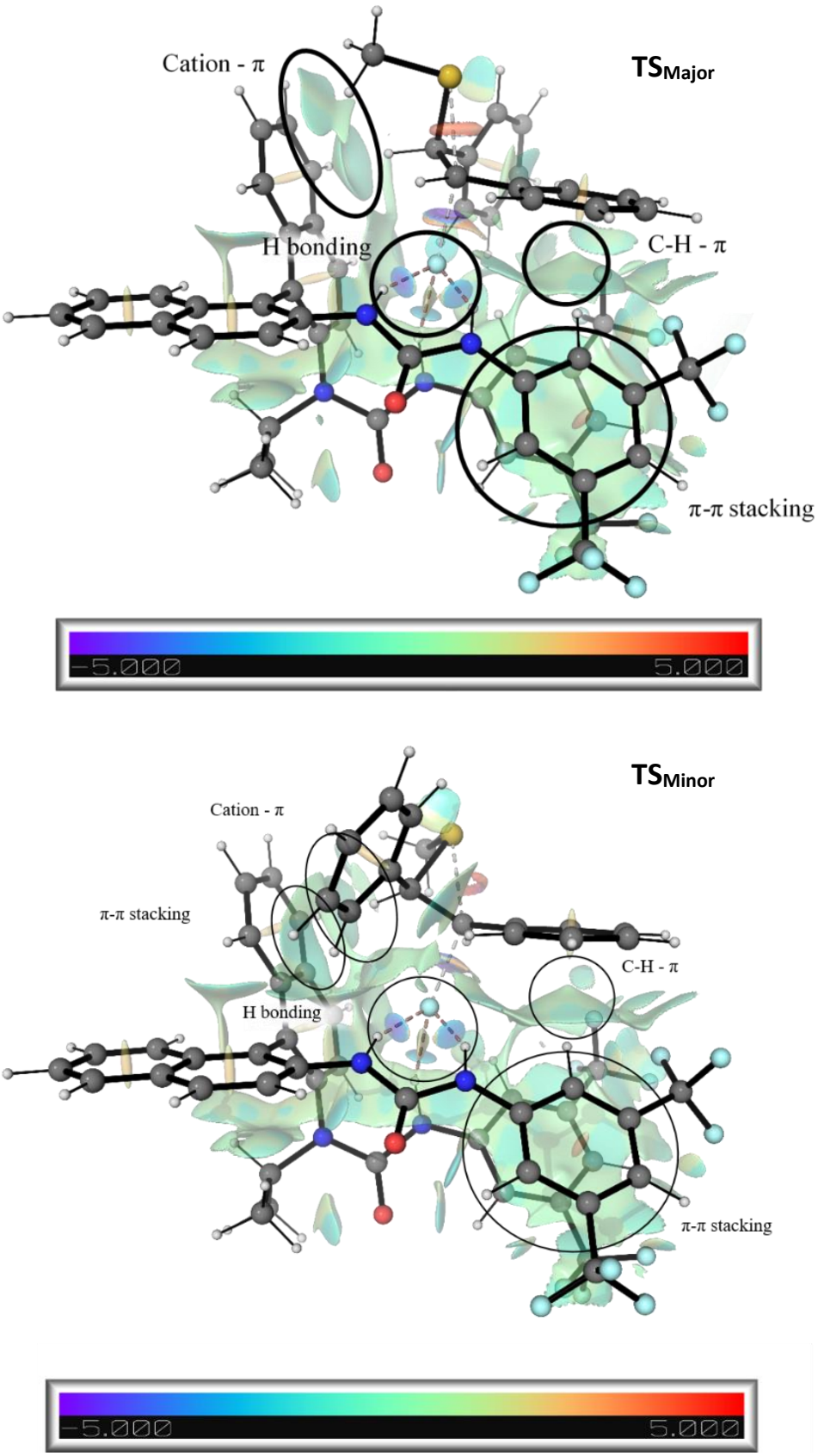

Figure 3.23: Non-covalent interaction plots for **TS$_{Major}$** (top) and **TS$_{Minor}$** (bottom), with key NCIs labelled. Own work adapted from Ref. 1.

Non-covalent interactions are responsible for the positioning of the substrate in the catalyst pocket and are similar for both $\mathbf{TS_{Major}}$ and $\mathbf{TS_{Minor}}$. All TSs in the ensemble form three hydrogen bonds to fluoride. Additionally, a key cation-π interaction docks the episulfonium into the naphthyl backbone of the BINAM catalyst. The catalyst adopts intramolecular π-π stacking and also a C–H - π interaction between catalyst *o*-C–H and substrate phenyl ring. Key differences between $\mathbf{TS_{Major}}$ and $\mathbf{TS_{Minor}}$ are that the cation-π interaction is 0.05 Å shorter in $\mathbf{TS_{Major}}$, consistent with a stronger interaction, however $\mathbf{TS_{Minor}}$ has some additional π-π stacking, between stilbene and BINAM backbone. The non-covalent interactions were visualized using the non-covalent interaction index and are annotated in Figure 3.23.

Evolution of the system over the intrinsic reaction coordinate (IRC) pathway was examined with methylated catalyst, **10**, for the pathway leading to major product ($\mathbf{IRC_{Major}}$) and pathway leading to minor product ($\mathbf{IRC_{Minor}}$), revealing similar evolution of bond distances from reactant to product in both pathways (Figure 3.24).

In order to compare the IRCs for the two pathways, the IRC was reduced to C–S distance minus C–F distance. The plot of key distances can be interpreted in two domains: $-0.5 < \text{IRC} < 1.2$, describing main bond forming and breaking, and $1.2 < \text{IRC} < 1.3$ primarily describing substrate relaxation (note approximately constant C–F distance in this region). Changes in distances in the first domain are all approximately linear with respect to the IRC; gradients for this region are evaluated for $-0.5 < \text{IRC} < 1.0$. The TS positions for $\mathbf{TS_{Major}}$ and $\mathbf{TS_{Minor}}$ are 0.14 Å and 0.12 Å respectively, with the y-axis intercepting at the position of $\mathbf{TS_{Major}}$.

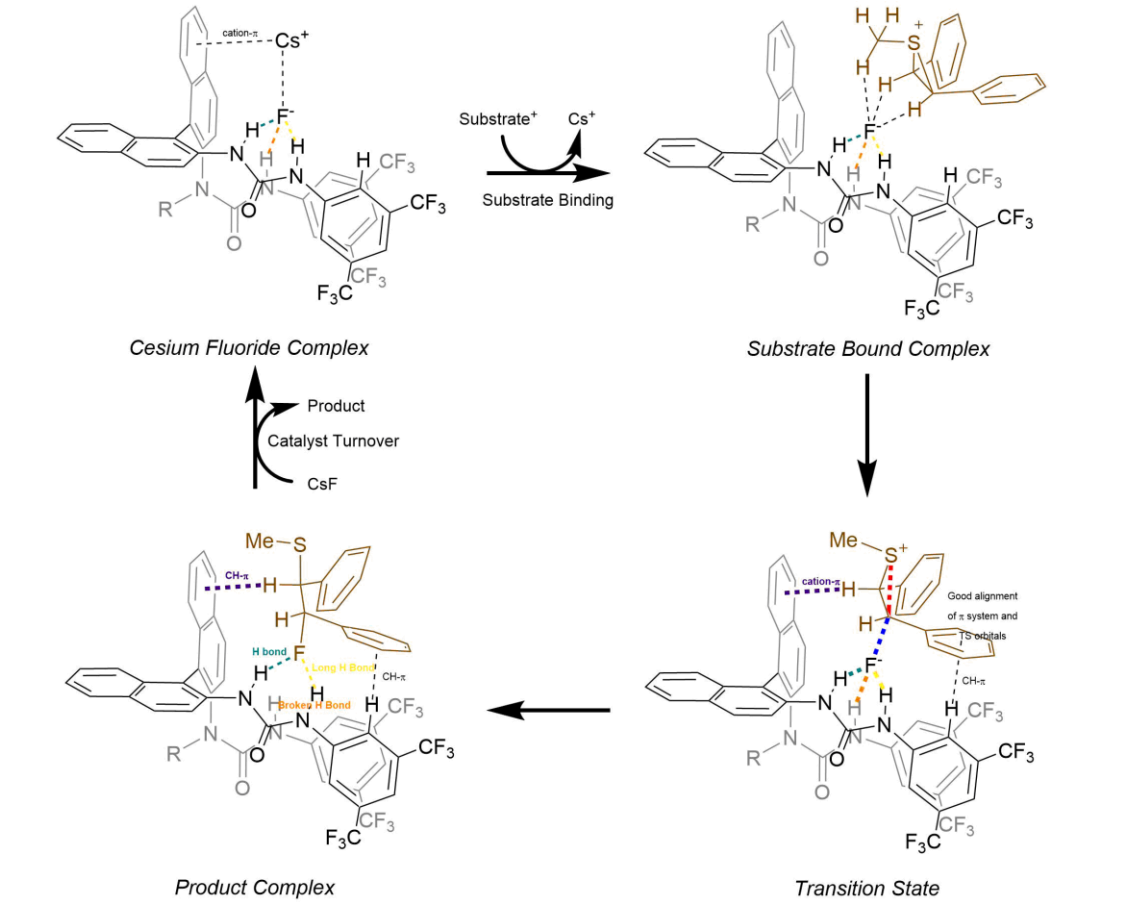

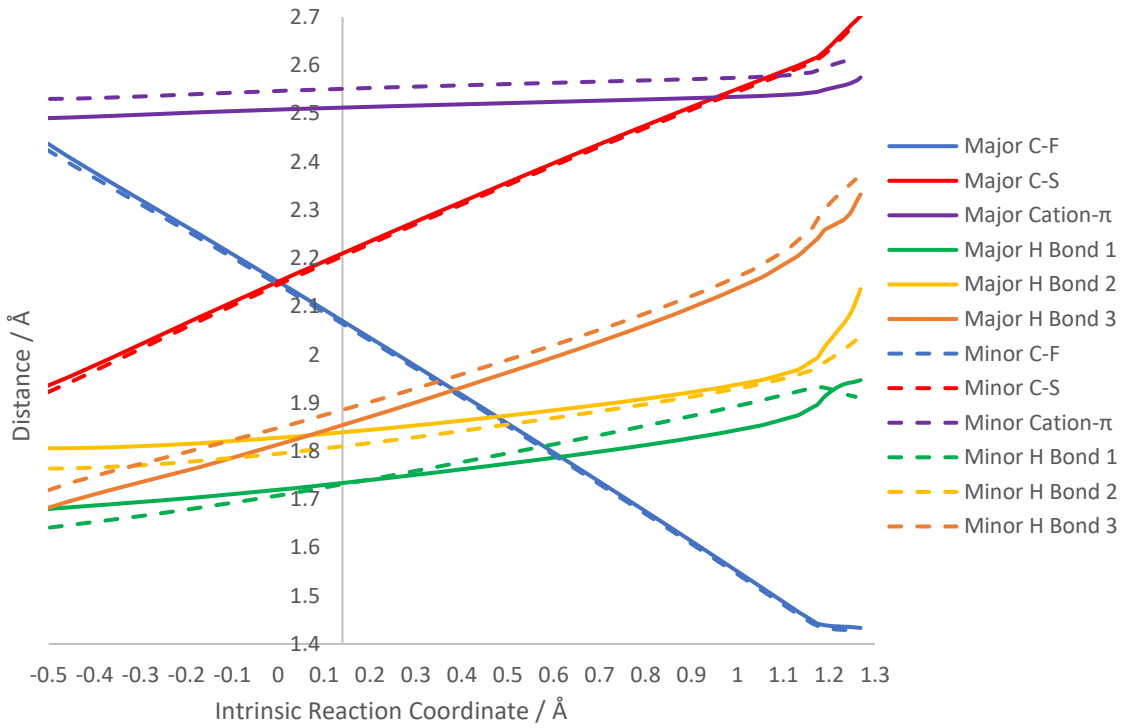

Figure 3.24: Evolution of key bond distances over the intrinsic reaction coordinate pathway to major (solid lines) and minor (dashed lines) product. Own work adapted from Ref. 1.

The forming and breaking bonds (C–S and C–F) evolve similarly over **IRC$_{Major}$** and **IRC$_{Minor}$**, with **IRC$_{Major}$** marginally looser prior to the TS. The cation-π in **IRC$_{Major}$** is consistently shorter than that in **IRC$_{Minor}$**. The evolution of the 3 hydrogen bonds for both IRCs is similar.

At the TS, all hydrogen bonds remain (< 1.9 Å), however all elongate over the IRC pathway due to neutralization of the charge on fluoride. Notably H-bond 3, corresponding to the N–H on the monodentate alkylated urea, elongates much more rapidly than the other two hydrogen bonds (gradient of 0.30 compared to 0.12 average for the other H-bonds) and is broken in the product complex. Further, for **IRC$_{Major}$**, H-bond 2 elongates once the C–F bond is formed. This behavior of hydrogen bonds over the IRC pathway parallels the behavior of the hydrogen bonds in the fluorinase enzyme. Fluorinase binds fluoride with a bidentate Ser-158 residue and forms a third hydrogen bond contact, on substrate binding, with a monodentate Thr-80 residue. In our system, the catalyst binds fluoride primarily through a bidentate urea, with a third hydrogen bond formed to the monodentate *syn-anti* isomerized alkylated urea. In the fluorinase, the hydrogen bond to monodentate Thr-80 is broken over the reaction coordinate and is no longer present in the product complex, similar to the behavior of our system where the third hydrogen bond to the monodentate urea is broken over the IRC pathway.[51–53]

3.3.3 BINAM-Based Catalyst Mechanism

The chiral BINAM-based ureas can solubilize CsF stoichiometrically – in contrast to the achiral Schreiner's urea – determined experimentally by stirring urea and fluoride salt, before filtration and evaporation of the solvent.[54] Further, the tricoordinate binding is sufficiently strong to catalyze formation of the episulfonium ion through coordination of the bromide leaving group. This was demonstrated by taking the lowest energy TS for

fluoride delivery to the episulfonium ion and replacing fluoride with bromide (Figure S16). Whilst thorough conformational sampling was not undertaken, the barrier to bromide loss was lowered from 90.2 kJ/mol to 82.7 kJ/mol. Under reaction conditions, this effect is expected to be of minimal importance, however, as the sub-stoichiometric levels of catalyst bind much more favorably to fluoride than bromide, demonstrated computationally ($\Delta G_{K1}(Br^-)$ = -21.9 kJ/mol and $\Delta G_{K1}(F^-)$ = -76.1 kJ/mol, methylated catalyst **10**) and experimentally ($K1(Br^-) = 3.3 \pm 0.3 \times 10^5\ M^{-1}$ and $K1(F^-) = 1.7 \pm 0.2 \times 10^6\ M^{-1}$, measured with TBAB and TBAF respectively, iPr catalyst **13**). The binding and solubilization of fluoride is therefore expected to outcompete the removal of the bromide leaving group, however challenging microkinetic modelling for the heterogeneous system would need to be undertaken to gain further insight.

Regardless of the precise nature of its formation, the overall neutral reactive ion pair, consisting of catalyst-fluoride-episulfonium, undergoes the enantiodetermining transformation. This is supported by the independence of enantioselectivity from leaving group identity (Br^- or Cl^-) and cation identity (Cs^+ or K^+) and the absence of non-linear effects confirming the involvement of only one molecule of catalyst in the enantiodetermining step.

3.3.4 Role of the *ortho*-CH in 3,5-Bis(trifluoromethyl)phenyl Substituted Ureas

The role of the *ortho*-CH of the 3,5-Bis(trifluoromethyl)phenyl group have led to this group being regarded as 'privileged' in the context of (thio)urea catalysis.[55] This group features in our preferred catalysts, both for the achiral HB PTC reaction (Schreiner's urea, **1**) and also the final chiral catalysts (**10-13**). The role of this group is potentially 2-fold; the inductive nature of the CF_3 groups increases the acidity of the urea and thus increases the strength of the hydrogen bonding to fluoride. Alternatively, the *ortho*-CH

can directly participate *via* non-classical hydrogen bonding, due to its acidity, again arising from the inductive properties of the CF_3 groups.

Firstly, the HB PTC reaction does not *require* this group, as the reaction proceeds with unsubstituted diphenylurea, **7**, however yield is significantly reduced. In the case of Schreiner's urea, there is evidence of interaction of the *o*-CH protons, however this interaction is intramolecular, with the oxygen of the urea itself. Interaction with bound fluoride is hindered geometrically and is not detected by the non-covalent interaction index (Figure 3.25). The former intramolecular interaction can strengthen hydrogen bonding through acidifying the urea, as well as reduce entropy loss from aryl group rotation on binding, by rigidifying the free urea.[55] Comparison of the urea-fluoride complexes for the unsubstituted urea, **7**, and Schreiner's urea reveal that it is the *o*-CH--

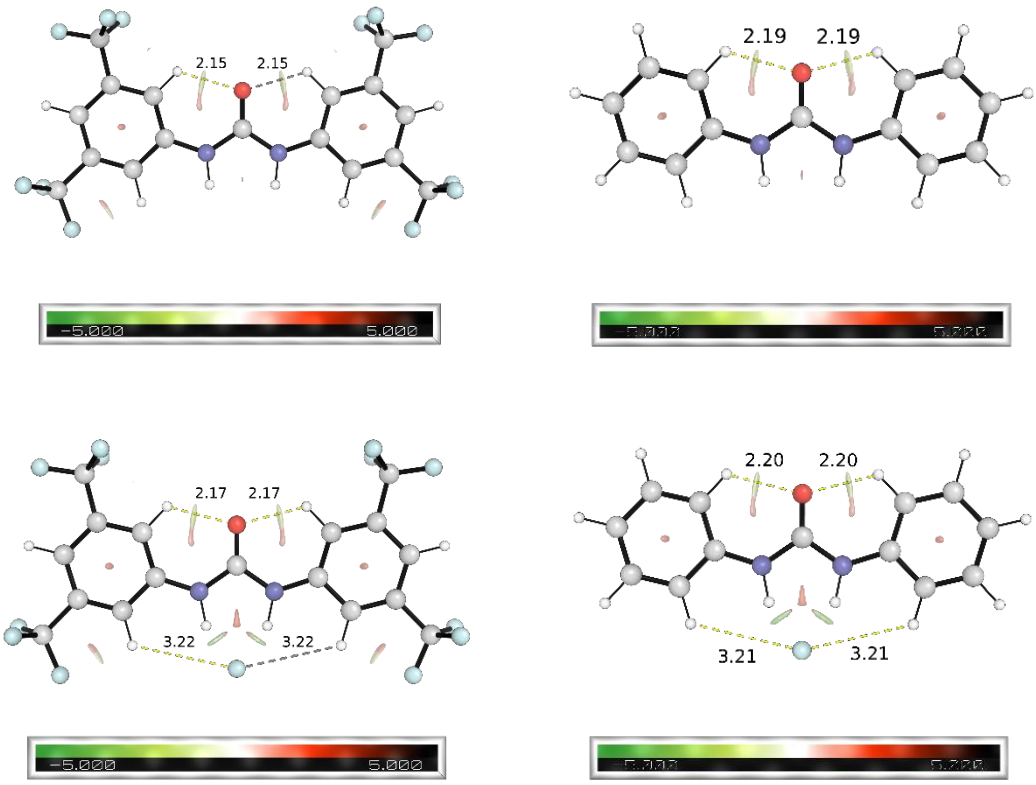

Figure 3.25: Geometry of achiral ureas and fluoride complexes. Left: urea **1**, Right: urea **7**. NCI plot and distance analysis suggest stronger interaction of the *o*-CH in the CF_3 substituted urea, **1**, with urea oxygen rather than fluoride.

Table 3.8: Shortest *o*-CH–F^- Distances in Reactive Ion Pairs (Me catalyst, **10**) and Transition State Structures (iPr catalyst, **13**).

Ion Pair	*o*-CH–F^- / Å	TS	*o*-CH–F^- / Å
IP Cat 10 F epi 1	2.140	**TS Cat 13 Minor 4**	2.286
IP Cat 10 F epi 7	2.233	**TS Cat 13 Minor 3**	2.308
IP Cat 10 F epi 3	2.465	**TS Cat 13 Major 6**	2.345
IP Cat 10 F epi 5	2.510	**TS Cat 13 Major 4**	2.387
IP Cat 10 F epi 4	2.512	**TS Cat 13 Major 7**	2.481

-O(urea) distance that shortens (2.20 Å compared to 2.17 Å) on addition of the CF_3 groups, rather than the *o*-CH---F^- distance (3.21 Å compared to 3.32 Å). Interaction of the *o*-CH bond with substrate is also infeasible as the positively charged episulfonium ion has no Lewis basic sites. Therefore, the *o*-CH bonds in Schreiner's urea do not play a major direct role in HB PTC but may play an indirect role *via* intramolecular hydrogen bonding to the urea oxygen.

In the case of the chiral BINAM based bis-urea catalysts, the situation is different, primarily down to the alkylated urea. This urea is *anti-syn* isomerized and can only form one N–H hydrogen bond but plausibly forms another hydrogen bond with the *o*-CH bond. Analysis of the catalyst-fluoride complexes optimized with methylated catalyst **10**,

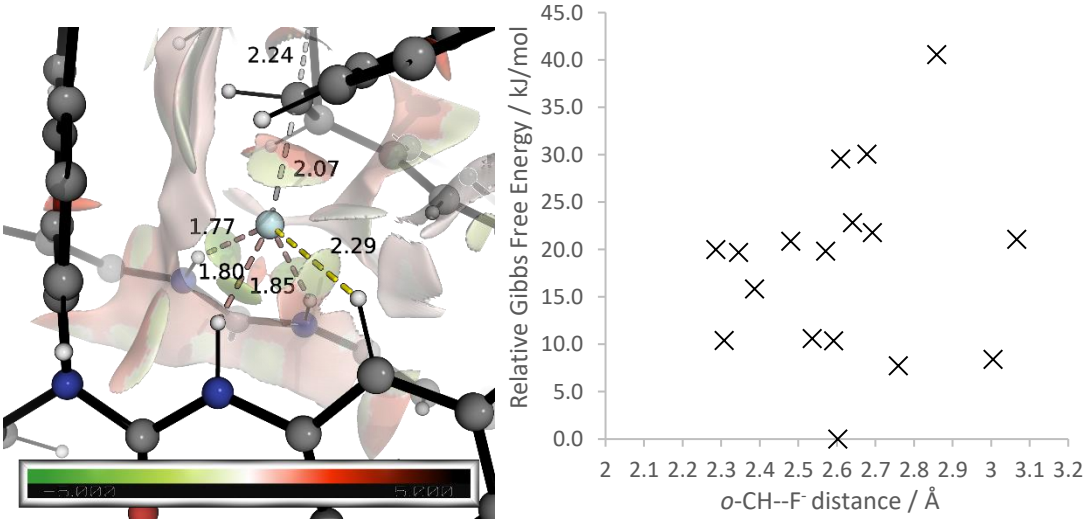

Figure 3.26: LHS: Non-covalent interaction plot for **TS Cat 13 Minor 4**, visualizing the interaction between *o*-CH and fluoride. RHS: Plot of relative transition state structure Gibbs free energies with iPr catalyst against length of *o*-CH---F^- interaction, showing a lack of correlation ($R^2 = 0.02$).

however, show no such interaction, with π-π stacking of the aryl groups favored. The reactive ion pairs show some involvement of the *o*-CH proton, with 3 ion pairs (**IP Cat 10 F epi 1**, **3**, **7**) having *o*-CH---F^- distances of below 2.5 Å, as do the TSs with ^{i}Pr catalyst **13** (Table 3.8). The distance of this interaction does not correlate with TS Gibbs free energy, suggesting that the interaction is of minor importance, likely down to the steric congestion that results around fluoride (Figure 3.26).

3.3.5 On the Stability of β-Fluorosulfides

An initial concern with using episulfonium ions as substrate for proving the HB PTC concept was that the products of the reaction – β-fluorosulfides – are reported to be unstable, decomposing to form fluoroepisulfuranes, containing an S–F bond, at room temperature (Scheme 3.4).[56] This could result in inaccurate yields, through conversion of the product to another compound, and inaccurate enantioselectivities, through facilitating racemization of the product. The existence of fluoroepisulfuranes has, however, not been confirmed, prompting some skepticism in the literature but no rebuttal.[57,58] The chloride analog, chloroepisulfuranes have long been proposed as high energy intermediates in the addition of sulfenyl chlorides to alkenes, which decompose to the thermodynamically more stable β-chlorosulfide products.[57–59] The selenium analog with chloride –

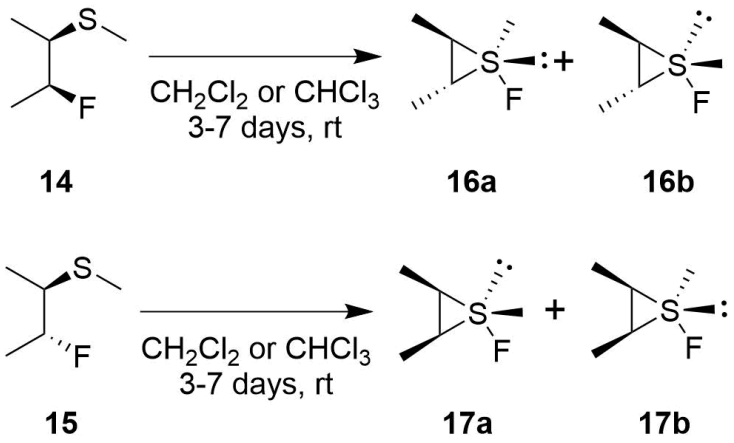

Scheme 3.4: Reported room temperature decomposition of β-fluorosulfides to fluoroepisulfuranes in dichloromethane/chloroform at room temperature.

chloroepiselenuranes – were reportedly isolated as a thermodynamically unstable intermediate that decomposed to the corresponding β-chloroselenide, however this assignment was subsequently refuted.[60,61]

3.3.5.1 Energetics

Initial calculations cast doubt on the feasibility of the decomposition, with computed energies of the fluoroepisulfuranes corresponding to product **5** having energies of +143 kJ/mol and +156 kJ/mol relative to the product for methyl *anti* and *syn* respectively in DCM (diphenyl analogues of **17b** and **17a** respectively) – inconceivable for a thermodynamic decomposition product. This result in hand, we attempted to verify the characterization data provided in the initial report by computing the NMR spectra of the fluoroepisulfurane structure.

3.3.5.2 Computational Methods

All calculations were performed in Gaussian 09, Rev. D.01 software package.[2] Optimization and single point calculations used the M06-2X functional[3] and NMR calculations used the mPW1PW91 functional.[62,63] All calculations were performed with the triple-ζ Pople type 6-311+G(2d,p) basis set.[64–68] Optimization and frequency calculations were performed in gas phase. NMR and single point energy corrections were calculated in chloroform solvent, using the solvation model based on density (SMD).[69] This level of theory was chosen based upon the performance of the M06-2X functional for the calculation of the episulfonium system and the availability and performance of NMR scaling factors in the Cheshire CCAT database ($^{1}H_{Slope}$ = -1.0951, $^{1}H_{Intercept}$ = 31.9773, $^{13}C_{Slope}$ = -1.0379, $^{13}C_{Intercept}$ = 187.2065).[70] ^{19}F chemical shifts were referenced relative to MeCHFMe for aliphatic compounds[71] and SF_6 for fluoroepisulfuranes.[72] NMR chemical shifts were computed using the gauge-independent

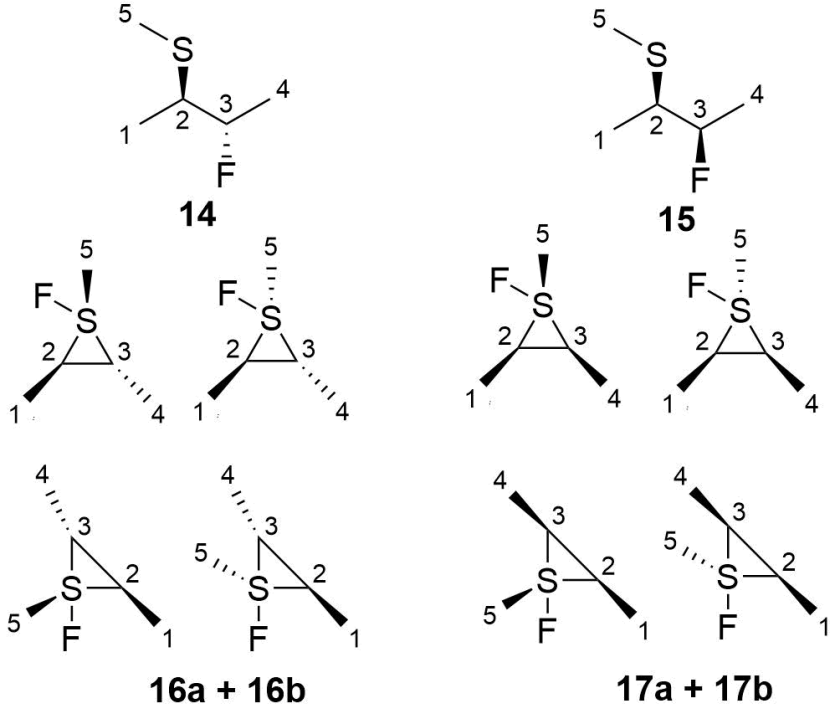

Figure 3.27: Numbering conventions used for fluoroepisulfuranes and precursors.

atomic orbitals (GIAO) method[73–77] and spin-spin coupling constants via the two-step procedure of Frisch.[78] A scaling factor of 0.944 was used for vibrational frequencies for thermochemistry, based on the value for M06-2X/6-311+G(d,p).[79] Boltzmann weighting of conformers was performed using Gibbs free energies, evaluated at 298.15 K employing a rigid-rotor approximation for vibrational modes below 100 cm^{-1} cut-off and vibrational scaling.[11,12] Numbering conventions used in this section are given in Figure 3.27. Geometries are given in Figure S18 and shielding constants in Tables S21-22.

3.3.5.3 NMR Calculations

NMR chemical shifts were computed for the two β-fluorosulfide starting materials, **14** and **15**, and the 4 proposed fluoroepisulfurane products, **16a-b** and **17a-b** (Table 3.9). Experimentally, fluoroepisulfuranes were reported as mixtures of **16a+b** and **17a+b**, however coupling and 2D NMR allows disentanglement of the spectra of the individual species. These individual spectra were not assigned to a particular species, however, so

Table 3.9: Computed ^{1}H NMR Chemical Shifts (C) Compared to Experimental Chemical Shifts (E), ^{1}H Coupling Constants and ^{19}F Chemical Shifts.

Structure		^{1}H Chemical Shift / ppm					^{3}J / Hz			^{19}F / ppm
		1	**2**	**3**	**4**	**5**	**1/2**	**2/3**	**3/4**	
16a+b 1	E	1.22	3.59	2.74	1.30	2.13	6.2	4.7	6.9	71.5
16a+b 2	E	1.22	3.56	2.67	1.27	2.13	6.2	5.0	7.1	71.5
16a	C	1.61	2.50	1.33	1.11	2.47	6.9	6.4	6.5	39.2
16b	C	1.45	2.43	1.23	1.31	2.55	7.1	7.7	6.7	41.2
17a+b 1	E	1.17	3.61	2.77	1.25	2.13†	6.3	4.2	6.9	71.4/71.5
17a+b 2	E	1.17	3.58	2.79	1.25	2.12†	6.3	4.4	5.9	71.4/71.5
17a	C	1.52	2.86	1.64	1.20	2.31	7.2	11.0	7.1	28.7
17b	C	1.45	2.87	1.75	1.09	2.65	7.4	10.3	6.8	38.2
14	C	1.28	2.74	4.58	1.38	2.13	7.4	5.8	6.4	-168.9
15	C	1.29	2.73	4.65	1.37	2.14	7.5	4.9	6.5	-169.7

are labelled as '1' and '2' respectively. The largest deviations between experimental and computed NMR shifts occur with hydrogens 2 and 3, with deviations up to 1.51 ppm. Computed NMR spectra for the precursors, **14** and **15** are included for completeness (experimental spectra not reported).

The RMSD between computed and experimental structures are given in Table 3.10 along with maximum absolute deviations in parentheses. The alignment can be improved by permitting reassignment but remains too high for a correct assignment.

Coupling constants are generally less diagnostic, however the coupling constant for protons 2 and 3 in structures **17a** and **17b** show marked disagreement, with experimental

Table 3.10: Comparison of Computed ^{1}H NMR Chemical Shifts and Experimentally Reported Values. RMSD values given, with maximum absolute deviation given in parentheses.

Experimental

Computed	**Reported Assignment**		**Reassignment Permitted**	
	16a+b 1	**16a+b 2**	**16a+b 1**	**16a+b 2**
16a	0.83 (1.41)	0.80 (1.34)	0.56 (1.09)	0.54 (1.06)
16b	0.88 (1.51)	0.85 (1.44)	0.57 (1.04)	0.56 (1.01)
	17a+b 1	**17a+b 2**	**17a+b 1**	**17a+b 2**
17a	0.63 (1.13)	0.63 (1.15)	0.47 (0.75)	0.46 (0.72)
17b	0.63 (1.02)	0.63 (1.04)	0.39 (0.74)	0.38 (0.71)

Table 3.11: Comparison of Reported Fluoroepisulfurane Shifts with Computed Shifts for the Precursors. Fluoroepisulfurane peaks are reassigned for best fit.

Structure		^{1}H Chemical Shift / ppm					RMSD / ppm	
		1	2	3	4	5	All Peaks	Excluding 3
14	C	1.28	2.74	4.58	1.38	2.13	-	-
16a+b 1	E	1.22	2.74	3.59	1.30	2.13	0.44	0.05
16a+b 2	E	1.22	2.67	3.56	1.27	2.13	0.46	0.07
15	C	1.29	2.73	4.65	1.37	2.14	-	-
17a+b 1	E	1.17	2.77	3.61	1.25	2.13	0.47	0.09
17a+b 2	E	1.17	2.79	3.58	1.25	2.12	0.49	0.09

values of 4.2 Hz and 4.4 Hz compared to computed values of 11.0 Hz and 10.3 Hz. This coupling corresponds to cis protons on the 3-membered ring with near-zero dihedral angle. The computed shifts align with Karplus values in contrast to the experimental shifts where the coupling constant is far too low, demonstrating an inconsistency in the experimental assignment. Interestingly, when the experimentally reported spectra for the fluoroepisulfuranes are compared to the computed spectra for the precursors, **14** and **15**, allowing reassignment, much better agreement is seen with the exception of hydrogen 3, as assigned in the precursors. When comparing all peaks, all RMSD values are below 0.49 ppm. When excluding peak 3, all RMSD values fall to 0.09 ppm or below. These results suggest that the experimental spectra correspond to structures that are more structurally similar to the precursors, with the exception of substitution about carbon 3 (bonded to fluorine). A significant change in fluorine environment is also expected from the large change in ^{19}F chemical shift.

Table 3.12: Computed ^{13}C NMR Chemical Shifts (C) Compared to Experimental Chemical Shifts (E).

Structure		^{13}C Chemical Shift / ppm				
		1	2	3	4	5
16a+b 1	E	18.32	47.67	78.03	16.90	14.55
16a+b 2	E	17.24	47.43	76.40	16.57	14.37
16a	C	11.81	40.87	42.16	15.15	31.40
16b	C	16.38	47.35	37.37	13.69	31.19
17a+b 1	E	16.08	45.88	75.98	15.19	14.56
17a+b 2	E	15.70	45.54	75.82	15.19	14.43
17a	C	5.48	35.17	33.27	8.44	23.35
17b	C	10.80	46.83	36.65	10.09	39.51

Table 3.13: Comparison of Computed ^{13}C NMR Chemical Shifts and Experimentally Reported Values. RMSD values given, with maximum absolute deviation given in parentheses.

Experimental

Computed	**Reported Assignment**		**Reassignment Permitted**	
	16a+b 1	**16a+b 2**	**16a+b 1**	**16a+b 2**
16a	18.2 (35.9)	17.5 (34.2)	17.4 (35.9)	16.9 (34.2)
16b	19.7 (40.7)	19.1 (39.0)	15.6 (30.7)	15.1 (29.0)
	17a+b 1	**17a+b 2**	**17a+b 1**	**17a+b 2**
17a	20.9 (42.7)	20.7 (42.6)	20.0 (40.8)	19.9 (40.7)
17b	21.1 (39.3)	21.0 (39.2)	16.4 (29.2)	16.5 (29.0)

Analysis of carbon chemical shifts paints a similar picture, with large deviations, particularly for carbon 3 (Table 3.12), with maximum absolute deviations of 34.2 ppm or above. The RMSD agreement and maximum absolute deviations are given in Table 3.13.

Comparison of the reported chemical shifts to those computed for the precursor allowing for reassignment, shows much better agreement (RMSD < 7.6 ppm), as for the ^{1}H shifts. ^{13}C shifts also have the largest deviation for the shift assigned to carbon 3, bonded to fluorine. If this is excluded, RMSD drops below 2.2 ppm in all cases, in good agreement, and well below the deviation for the proposed fluoroepisulfurane structures (Table 3.14). The peaks are, however, reassigned in a different ordering to those for the ^{1}H shifts, raising the possibility that the correlations between experimental ^{1}H and ^{13}C shifts have been misassigned.

Table 3.14: Comparison of Reported Fluoroepisulfurane Shifts with Computed Shifts for the Precursors. Fluoroepisulfurane peaks are reassigned for best fit.

Structure		**^{13}C Chemical Shift / ppm**					**RMSD / ppm**	
		1	**2**	**3**	**4**	**5**	**All**	**Excluding 3**
14	C	14.87	49.91	92.49	17.05	17.49	-	-
16a+b 1	E	14.55	47.67	78.03	16.90	18.32	6.6	1.2
16a+b 2	E	14.37	47.43	76.4	16.57	17.24	7.3	1.3
15	C	14.59	49.36	92.32	16.58	17.42	-	-
17a+b 1	E	14.56	45.88	75.98	15.19	16.08	7.5	2.0
17a+b 2	E	14.43	45.54	75.82	15.19	15.7	7.6	2.2

3.3.5.4 Summary of β-Fluorosulfide Stability

The evidence against the proposed fluoroepisulfurane assignment is overwhelming, with infeasibly high Gibbs free energies and NMR data inconsistent with computed values, demonstrating the power of modern computational techniques in structural (re)assignment. None the less, whilst the structural assignment, and existence of fluoroepisulfuranes is refuted, it is not disproved that β-fluorosulfides decompose under the stated conditions to another product consistent with the characterization data. Computed NMR spectra for the β-fluorosulfide precursors suggests structural similarity with the decomposition products, but a significant change of environment in and around fluorine. No decomposition of the stilbene derived β-fluorosulfides was observed during the course of the HB PTC work, suggesting that the decomposition is specific to the compounds, **14** and **15**, reported. Experimental verification of the decomposition in the initial report is required and provides an opportunity to gather additional characterization data to aid structural reassignment.

3.4 Conclusion

We have developed a novel catalytic mechanism that we call hydrogen bonding phase-transfer catalysis (HB PTC) and applied it to asymmetric fluorination with CsF, through collaboration between computation (author's work) and experiment (co-workers' work). Computation supports the proposed mechanism for HB PTC, where binding of fluoride by a hydrogen bonding catalyst enables fluoride solubilization and anion-transport. Alternative mechanisms, such as anion-abstraction catalysis to form the episulfonium, are ruled out. Accounting for phase-transfer required a model that combined tabulated experimental data with computed results, and qualitatively describes the performance of achiral catalysts for HB PTC. Important mechanistic insight is gained,

paving the way for use of chiral ureas for asymmetric fluorination, including recognizing that the enantiodetermining TS may not be turnover-limiting. Computation demonstrates that, once fluoride is in solution, fluorination of the episulfonium ion is trivial, with most of the energetic barrier originating from rearrangement of the ion pair. The relative reactivity of episulfonium ion precursors with different leaving groups is consistent with computed barriers to auto-ionization.

Computation assisted chiral catalyst design by suggesting alkylation of a superfluous N–H hydrogen bond donor on the basis of MD simulations, resulting in a catalyst with a single persistent tridentate fluoride binding mode, which was later proved experimentally. Catalyst alkylation maintained catalyst efficiency, as predicted computationally, and increased enantioselectivity. The vast reduction in conformational space enabled computational study of the system. The TS ensemble was generated through unbiased MD-based conformational sampling, with enantioselectivity and sense of induction consistent with experiment. Analysis of the lowest energy TSs reveals the key role of the aromatic rings in stilbene derived substrates for achieving high enantioselectivity, by favorable conjugation of the α-aryl ring with the forming and breaking bonds. Analysis of bond lengths over the IRC pathway reveals that the hydrogen bond between fluoride and the monodentate urea donor is broken over the IRC, and does not persist in the product complex, paralleling the behavior of hydrogen bonds in the fluorinase enzyme. Understanding the origins of enantioselectivity and the limitations of the substrate scope underpins future work on catalyst design.

The reported instability of the β-fluorosulfide products through room temperature thermodynamic decomposition to fluoroepisulfuranes was challenged. The energies of the proposed structures are infeasibly high, particularly as a thermodynamic product.

Calculation of NMR chemical shifts for the proposed structures shows significant disagreement with the reported experimental spectra, casting doubt on the assignment. No decomposition of the products of the HB PTC reaction was seen experimentally, suggesting that the decomposition is not general to all β-fluorosulfides.

3.5 References

(1) Pupo, G.; Ibba, F.; Ascough, D. M. H.; Vicini, A. C.; Ricci, P.; Christensen, K. E.; Pfeifer, L.; Morphy, J. R.; Brown, J. M.; Paton, R. S.; Gouverneur, V. Asymmetric Nucleophilic Fluorination under Hydrogen Bonding Phase-Transfer Catalysis. *Science* **2018**, *360*, 638–642.

(2) Frisch, M. J.; Trucks, G. W.; Schlegel, H. B.; Scuseria, G. E.; Robb, M. A.; Cheeseman, J. R.; Scalmani, G.; Barone, V.; Petersson, G. A.; Nakatsuji, H.; Li, X.; Caricato, M.; Marenich, A.; Bloino, J.; Janesko, B. G.; Gomperts, R.; Mennucci, B.; Hratchian, H. P.; Ortiz, J. V.; Izmaylov, A. F.; Sonnenberg, J. L.; Williams-Young, D.; Ding, F.; Lipparini, F.; Egidi, F.; Goings, J.; Peng, B.; Petrone, A.; Henderson, T.; Ranasinghe, D.; Zakrzewski, V. G.; Gao, J.; Rega, N.; Zheng, G.; Liang, W.; Hada, M.; Ehara, M.; Toyota, K.; Fukuda, R.; Hasegawa, J.; Ishida, M.; Nakajima, T.; Honda, Y.; Kitao, O.; Nakai, H.; Vreven, T.; Throssell, K.; Montgomery Jr., J. A.; Peralta, J. E.; Ogliaro, F.; Bearpark, M.; Heyd, J. J.; Brothers, E.; Kudin, K. N.; Staroverov, V. N.; Keith, T.; Kobayashi, R.; Normand, J.; Raghavachari, K.; Rendell, A.; Burant, J. C.; Iyengar, S. S.; Tomasi, J.; Cossi, M.; Millam, J. M.; Klene, M.; Adamo, C.; Cammi, R.; Ochterski, J. W.; Martin, R. L.; Morokuma, K.; Farkas, O.; Foresman, J. B.; Fox, D. J. Gaussian 09. Gaussian Inc: Wallingford, CT 2009.

(3) Zhao, Y.; Truhlar, D. G. The M06 Suite of Density Functionals for Main Group Thermochemistry, Thermochemical Kinetics, Noncovalent Interactions, Excited States, and Transition Elements: Two New Functionals and Systematic Testing of Four M06-Class Functionals and 12 Other Functionals. *Theor. Chem. Acc.* **2008**, *120*, 215–241.

(4) Wheeler, S. E.; Houk, K. N. Integration Grid Errors for Meta-GGA-Predicted Reaction Energies: Origin of Grid Errors for the M06 Suite of Functionals. *J. Chem. Theory Comput.* **2010**, *6*, 395–404.

(5) Weigend, F.; Ahlrichs, R. Balanced Basis Sets of Split Valence, Triple Zeta Valence and Quadruple Zeta Valence Quality for H to Rn: Design and Assessment of Accuracy. *Phys. Chem. Chem. Phys.* **2005**, *7*, 3297–3305.

(6) Rappoport, D.; Furche, F. Property-Optimized Gaussian Basis Sets for Molecular Response Calculations. *J. Chem. Phys.* **2010**, *133*, 134105.

(7) Leininger, T.; Nicklass, A.; Küchle, W.; Stoll, H.; Dolg, M.; Bergner, A. The Accuracy of the Pseudopotential Approximation: Non-Frozen-Core Effects for Spectroscopic Constants of Alkali Fluorides XF (X = K, Rb, Cs). *Chem. Phys. Lett.* **1996**, *255*, 274–280.

(8) Barone, V.; Cossi, M. Conductor Solvent Model. *J. Phys. Chem. A* **1998**, *102*, 1995–2001.

(9) Cossi, M.; Rega, N.; Scalmani, G.; Barone, V. Energies, Structures, and Electronic Properties of Molecules in Solution with the C-PCM Solvation Model. *J. Comput. Chem.* **2003**, *24*, 669–681.

(10) Takano, Y.; Houk, K. N. Benchmarking the Conductor-like Polarizable Continuum Model (CPCM) for Aqueous Solvation Free Energies of Neutral and Ionic Organic Molecules. *J. Chem. Theory Comput.* **2005**, *1*, 70–77.

(11) Funes-Ardoiz, I.; Paton, R. S. Goodvibes v2.0. **2018**, http://doi.org/10.5281/zenodo.3346166.

(12) Grimme, S. Supramolecular Binding Thermodynamics by Dispersion-Corrected Density Functional Theory. *Chem. Eur. J.* **2012**, *18*, 9955–9964.

(13) Neese, F. The ORCA Program System. *Wiley Interdiscip. Rev. Comput. Mol. Sci.* **2012**, *2*, 73–78.

(14) Chai, J.-D.; Head-Gordon, M. Long-Range Corrected Hybrid Density Functionals with Damped Atom–Atom Dispersion Corrections. *Phys. Chem. Chem. Phys.* **2008**, *10*, 6615–6620.

(15) Lin, Y.-S.; Li, G.-D.; Mao, S.-P.; Chai, J.-D. Long-Range Corrected Hybrid Density Functionals with Improved Dispersion Corrections You-Sheng. *J. Chem. Theory Comput.* **2013**, *9*, 263–272.

(16) Grimme, S.; Antony, J.; Ehrlich, S.; Krieg, H. A Consistent and Accurate Ab Initio Parametrization of Density Functional Dispersion Correction (DFT-D) for the 94 Elements H-Pu.

J. Chem. Phys. **2010**, *132*, 154104.
(17) Zheng, J.; Xu, X.; Truhlar, D. G. Minimally Augmented Karlsruhe Basis Sets. *Theor. Chem. Acc.* **2011**, *128*, 295–305.
(18) Klamt, A.; Schüürmann, G. COSMO: A New Approach to Dielectric Screening in Solvents with Explicit Expressions for the Screening Energy and Its Gradient. *J. Chem. Soc. Perkin Trans. 2* **1993**, 799–805.
(19) Johnson, E. R.; Keinan, S.; Mori Sánchez, P.; Contreras García, J.; Cohen, A. J.; Yang, W. NCI : Revealing Non-Covalent Interactions. *J. Am. Chem. Soc.* **2010**, *132*, 6498–6506.
(20) Contreras-García, J.; Johnson, E. R.; Keinan, S.; Chaudret, R.; Piquemal, J. P.; Beratan, D. N.; Yang, W. NCIPLOT: A Program for Plotting Noncovalent Interaction Regions. *J. Chem. Theory Comput.* **2011**, *7*, 625–632.
(21) Wavefunction Inc. Spartan '16. Irvine, CA.
(22) Halgren, T. Merck Molecular Force Field. *J. Comput. Chem.* **1996**, *17*, 490–519.
(23) Berendsen, H. J. C.; van der Spoel, D.; van Drunen, R. GROMACS: A Message-Passing Parallel Molecular Dynamics Implementation. *Comput. Phys. Commun.* **1995**, *91*, 43–56.
(24) Lindahl, E.; Hess, B.; van der Spoel, D. GROMACS 3.0: A Package for Molecular Simulation and Trajectory Analysis. *J. Mol. Model.* **2001**, *7*, 306–317.
(25) Van Der Spoel, D.; Lindahl, E.; Hess, B.; Groenhof, G.; Mark, A. E.; Berendsen, H. J. C. GROMACS: Fast, Flexible, and Free. *J. Comput. Chem.* **2005**, *26*, 1701–1718.
(26) Hess, B.; Kutzner, C.; Van Der Spoel, D.; Lindahl, E. GROMACS 4: Algorithms for Highly Efficient, Load-Balanced, and Scalable Molecular Simulation. *J. Chem. Theory Comput.* **2008**, *4*, 435–447.
(27) Pronk, S.; Pall, S.; Schulz, R.; Larsson, P.; Bjelkmar, P.; Apostolov, R.; Shirts, M. R.; Smith, J. C.; Kasson, P. M.; Van Der Spoel, D.; Hess, B.; Lindahl, E. GROMACS 4.5: A High-Throughput and Highly Parallel Open Source Molecular Simulation Toolkit. *Bioinformatics* **2013**, *29*, 845–854.
(28) Abraham, M. J.; Murtola, T.; Schulz, R.; Pall, S.; Smith, J. C.; Hess, B.; Lindahl, E. Gromacs: High Performance Molecular Simulations through Multi-Level Parallelism from Laptops to Supercomputers. *SoftwareX* **2015**, *1–2*, 19–25.
(29) Jorgensen, W. L.; Tirado-Rives, J. The OPLS Potential Functions for Proteins. Energy Minimizations for Crystals of Cyclic Peptides and Crambin. *J. Am. Chem. Soc.* **1988**, *110*, 1657–1666.
(30) Jorgensen, W. L.; Maxwell, D. S.; Tirado-Rives, J. Development and Testing of the OPLS All-Atom Force Field on Conformational Energetics and Properties of Organic Liquids. *J. Am. Chem. Soc.* **1996**, *118*, 11225–11236.
(31) Schrodinger LLC. Schrodinger Release 2017-2. MS Jaguar: New York, NY 2017.
(32) Bayly, C. I.; Cieplak, P.; Cornell, W. D.; Kollman, P. A. A Well-Behaved Electrostatic Potential Based Method Using Charge Restraints for Deriving Atomic Charges: The RESP Model. *J. Phys. Chem.* **1993**, *97*, 10269–10280.
(33) Comell, W. D.; Cieplak, P.; Bayly, C. I.; Kollman, P. A. Application of RESP Charges To Calculate Conformational Energies, Hydrogen Bond Energies, and Free Energies of Solvation. *J. Am. Chem. Soc.* **1993**, *115*, 9620–9631.
(34) D.A. Case, D.S. Cerutti, T.E. Cheatham, III, T.A. Darden, R.E. Duke, T.J. Giese, H. Gohlke, A.W. Goetz, D. Greene, N. Homeyer, S. Izadi, A. Kovalenko, T.S. Lee, S. LeGrand, P. Li, C. Lin, J. Liu, T. Luchko, R. Luo, D. Mermelstein, K.M. Merz, G. Monard, H., D. M. Y. and P. A. K. AMBER 2017. University of California: San Francisco 2017.
(35) van der Spoel, D.; van Maaren, P. J.; Caleman, C. GROMACS Molecule & Liquid Database. *Bioinformatics* **2012**, *28*, 752–753.
(36) Chen, S.; Yi, S.; Gao, W.; Zuo, C.; Hu, Z. Force Field Development for Organic Molecules: Modifying Dihedral and 1-n Pair Interaction Parameters. *J. Comput. Chem.* **2015**, *36*, 376–384.
(37) Bussi, G.; Donadio, D.; Parrinello, M. Canonical Sampling through Velocity Rescaling. *J. Chem. Phys.* **2007**, *126*, 014101.
(38) Parrinello, M.; Rahman, A. Crystal Structure and Pair Potentials: A Molecular Dynamics Study. *Phys. Rev. Lett.* **1980**, *45*, 1196–1199.
(39) Parrinello, M.; Rahman, A. Polymorphic Transitions in Single Crystals: A New Molecular Dynamics Method. *J. Appl. Phys.* **1981**, *52*, 7182–7190.
(40) Essmann, U.; Perera, L.; Berkowitz, M. L.; Darden, T.; Lee, H.; Pedersen, L. G. A Smooth Particle Mesh Ewald Method. *J. Chem. Phys.* **1995**, *103*, 8577–8593.
(41) Hess, B.; Bekker, H.; Berendsen, H. J. C.; Fraaije, J. G. E. M. LINCS: A Linear Constraint

Solver for Molecular Simulations. *J. Comput. Chem.* **1997**, *18*, 1463–1472.
(42) Daura, X.; Gademann, K.; Jaun, B.; Seebach, D.; van Gunsteren, W. F.; Mark, A. E. Peptide Folding: When Simulation Meets Experiment. *Angew. Chem. Int. Ed.* **1999**, *38*, 236–240.
(43) Duarte, F.; Paton, R. S. Molecular Recognition in Asymmetric Counteranion Catalysis: Understanding Chiral Phosphate-Mediated Desymmetrization. *J. Am. Chem. Soc.* **2017**, *139*, 8886–8896.
(44) Pliego Jr, J. R.; Riveros, J. M. New Insights on Reaction Pathway Selectivity Promoted by Crown Ether Phase-Transfer Catalysis: Model Ab Initio Calculations of Nucleophilic Fluorination. *J. Mol. Catal. A Chem.* **2012**, *363–364*, 489–494.
(45) Carvalho, N. F.; Pliego Jr, J. R. Theoretical Design and Calculation of a Crown Ether Phase-Transfer-Catalyst Scaffold for Nucleophilic Fluorination Merging Two Catalytic Concepts. *J. Org. Chem.* **2016**, *81*, 8455–8463.
(46) Kennedy, C. R.; Lehnherr, D.; Rajapaksa, N. S.; Ford, D. D.; Park, Y.; Jacobsen, E. N. Mechanism-Guided Development of a Highly Active Bis-Thiourea Catalyst for Anion-Abstraction Catalysis. *J. Am. Chem. Soc.* **2016**, *138*, 13525–13528.
(47) Ford, D. D.; Lehnherr, D.; Kennedy, C. R.; Jacobsen, E. N. On- and off-Cycle Catalyst Cooperativity in Anion-Binding Catalysis. *J. Am. Chem. Soc.* **2016**, *138*, 7860–7863.
(48) Ford, D. D.; Lehnherr, D.; Kennedy, C. R.; Jacobsen, E. N. Anion-Abstraction Catalysis: The Cooperative Mechanism of α-Chloroether Activation by Dual Hydrogen-Bond Donors. *ACS Catal.* **2016**, *6*, 4616–4620.
(49) Jones, C. R.; Dan Panto, G.; Morrison, A. J.; Smith, M. D. Plagiarizing Proteins: Enhancing Efficiency in Asymmetric Hydrogen-Bonding Catalysis through Positive Cooperativity. *Angew. Chem. Int. Ed.* **2009**, *48*, 7391–7394.
(50) Luchini, G.; Ascough, D. M. H.; Alegre-Requena, J. V.; Gouverneur, V.; Paton, R. S. Data-Mining the Diaryl(Thio)Urea Conformational Landscape: Understanding the Contrasting Behavior of Ureas and Thioureas with Quantum Chemistry. *Tetrahedron* **2019**, *75*, 697–702.
(51) Dong, C.; Dong, C.; Huang, F.; Huang, F.; Deng, H.; Deng, H.; Schaffrath, C.; Schaffrath, C.; Spencer, J. B.; Spencer, J. B.; Naismith, J. H.; Naismith, J. H. Crystal Structure and Mechanism of a Bacterial Fluorinating Enzyme. *Nature* **2004**, *427*, 561–565.
(52) Zhu, X.; Robinson, D. A.; McEwan, A. R.; O'Hagan, D.; Naismith, J. H. Mechanism of Enzymatic Fluorination in Streptomyces Cattleya. *J. Am. Chem. Soc.* **2007**, *129*, 14597–14604.
(53) O'Hagan, D. Recent Developments on the Fluorinase from Streptomyces Cattleya. *J. Fluor. Chem.* **2006**, *127*, 1479–1483.
(54) Pupo, G.; Vicini, A. C.; Ascough, D. M. H.; Ibba, F.; Christensen, K. E.; Thompson, A. L.; Brown, J. M.; Paton, R. S.; Gouverneur, V. Hydrogen Bonding Phase-Transfer Catalysis with Potassium Fluoride: Enantioselective Synthesis of β-Fluoroamines. *J. Am. Chem. Soc.* **2019**, *141*, 2878–2883.
(55) Lippert, K. M.; Hof, K.; Gerbig, D.; Ley, D.; Hausmann, H.; Guenther, S.; Schreiner, P. R. Hydrogen-Bonding Thiourea Organocatalysts: The Privileged 3,5-Bis(Trifluoromethyl)Phenyl Group. *European J. Org. Chem.* **2012**, 5919–5927.
(56) Carretero, J. C.; Ruano, J. L. G.; Rodriguez, J. H. Stable Episulphuranes. *Tetrahedron Lett.* **1987**, *28*, 4593–4596.
(57) Pasquato, L.; Destro, R.; Lucchini, V.; Modena, G. Sulfur Electrophiles as Mechanistic Probe . New Insight in the Electrophilic Additions. *Phosphorus, Sulfur and Silicon* **1999**, *153*, 235–245.
(58) Fachini, M.; Lucchini, V.; Modena, G.; Pasi, M.; Pasquato, L. Nucleophilic Reactions at the Sulfur of Thiiranium and Thiirenium Ions. New Insight in the Electrophilic Additions to Alkenes and Alkynes. Evidence for an Episulfurane Intermediate. *J. Am. Chem. Soc.* **1999**, *121*, 3944–3950.
(59) Csizmadia, B. V. M.; Schmid, G. H.; Mezey, P. G.; Csizmadia, I. G. Ab Initio SCF-MO Study of the Reaction Intermediates Formed by Addition of Thiohypochlorous Acid to Ethylene. *J. Chem. Soc. Perkin Trans. 2* **1977**, 1019–1024.
(60) Garratt, D. G.; Schmid, G. H. The Isolation of an Episelenurane from the Reaction of 4-Tolueneselenenyl Chloride with Ethylene. *Can. J. Chem.* **1974**, *52*, 1027.
(61) Reich, H. J.; Trend, J. E. Organoselenium Chemistry. Addition of Tolueneselenenyl Chloride to Ethylene: Concerning the Reported Isolation of a Stable Episelenurane. *Can. J. Chem.* **1975**, *53*, 1922–1927.
(62) Adamo, C.; Barone, V. Exchange Functionals with Improved Long-Range Behavior and Adiabatic Connection Methods without Adjustable Parameters: The MPW and MPW1PW Models. *J. Chem. Phys.* **1998**, *108*, 664–675.

(63) Adamo, C.; Barone, V. Toward Reliable Adiabatic Connection Models Free from Adjustable Parameters. *Chem. Phys. Lett.* **1997**, *274*, 242–250.
(64) Krishnan, R.; Binkley, J. S.; Seeger, R.; Pople, J. A. Self-Consistent Molecular Orbital Methods. XX. A Basis Set for Correlated Wave Functions. *J. Chem. Phys.* **1980**, *72*, 650–654.
(65) McLean, A. D.; Chandler, G. S. Contracted Gaussian Basis Sets for Molecular Calculations. I. Second Row Atoms, Z=11-18. *J. Chem. Phys.* **1980**, *72*, 5639–5648.
(66) Francl, M. M.; Pietro, W. J.; Hehre, W. J.; Binkley, J. S.; Gordon, M. S.; DeFrees, D. J.; Pople, J. A. Self-Consistent Molecular Orbital Methods. XXIII. A Polarization-Type Basis Set for Second-Row Elements. *J. Chem. Phys.* **1982**, *77*, 3654–3665.
(67) Clark, T.; Chandrasekhar, J.; Spitznagel, G. W.; Schleyer, P. V. R. Efficient Diffuse Function-Augmented Basis Sets for Anion Calculations. III.* The 3-21+G Basis Set for First-Row Elements, Li-F. *J. Comput. Chem.* **1983**, *4*, 294–301.
(68) Spitznagel, G. W.; Clark, T.; von Ragué Schleyer, P.; Hehre, W. J. An Evaluation of the Performance of Diffuse Function-augmented Basis Sets for Second Row Elements, Na-Cl. *J. Comput. Chem.* **1987**, *8*, 1109–1116.
(69) Marenich, A. V.; Cramer, C. J.; Truhlar, D. G. Universal Solvation Model Based on Solute Electron Density and on a Continuum Model of the Solvent Defined by the Bulk Dielectric Constant and Atomic Surface Tensions. *J. Phys. Chem. A* **2009**, *113*, 6378–6396.
(70) Lodewyk, M. W.; Siebert, M. R.; Tantillo, D. J. CHESHIRE Chemical Shift Repository http://cheshirenmr.info/ (accessed Jan 11, 2017).
(71) Dmowski, W.; Kamiński, M. Dialkyl-α,α-Difluorobenzylamines and Dialkyl(Trifluoromethyl)-Amines - Novel Fluorinating Reagents. *J. Fluor. Chem.* **1983**, *23*, 219–228.
(72) Dungan, C. H.; van Wazer, J. R. *Compilation of Reported F19 NMR Chemical Shifts 1951 to Mid-1967*, 1st ed.; Wiley-Interscience: New York, NY, 1970.
(73) London, F. The Quantic Theory of Inter-Atomic Currents in Aromatic Combinations. *J. Phys. Radium* **1937**, *8*, 397–409.
(74) McWeeny, R. Pertubation Theory for the Fock-Dirac Density Matrix. *Phys. Rev.* **1962**, *126*, 1028–1034.
(75) Ditchfield, R. Self-Consistent Perturbation Theory of Diamagnetism. *Mol. Phys.* **1974**, *27*, 789–807.
(76) Wolinski, K.; Hinton, J. F.; Pulay, P. Efficient Implementation of the Gauge-Independent Atomic Orbital Method for NMR Chemical Shift Calculations. *J. Am. Chem. Soc.* **1990**, *112*, 8251.
(77) Cheeseman, J. R. A Comparison of Models for Calculating Nuclear Magnetic Resonance Shielding Tensors. *J. Chem. Phys.* **1996**, *104*, 5497–5509.
(78) W. Deng and M. J. Frisch, J. R. C. Calculation of Nuclear Spin-Spin Coupling Constants of Molecules with First and Second Row Atoms in Study of Basis Set Dependence. *J. Chem. Theory Comput.* **2006**, *2*, 1028–1037.
(79) Bao, J. L.; Zheng, J.; Alecu, I. M.; Lynch, B. J.; Zhao, Y.; Truhlar, D. G. Database of Frequency Scale Factors for Electronic Model Chemistries https://comp.chem.umn.edu/freqscale/version3b2.htm (accessed Jan 11, 2017).

4 Hydrogen Bonding Phase-Transfer Catalysis for Asymmetric Fluorination of Aziridinium Ions

4.1 Introduction

Alongside the pioneering HB PTC work on enantioselective desymmetrization of episulfonium ions, experimental work on the desymmetrization of the more synthetically useful aziridinium ion was ongoing. Enantioselective desymmetrization of aziridinium ions with fluoride yields enantioenriched *β*-fluoroamines, which feature prominently in medicinal chemistry, and have unique stereoelectronic effects.[1–7] Several methods for catalytic enantioselective synthesis exist, including strategies requiring fluorinated precursors,[8–12] as well as those involving formation of a carbon-fluorine bond directly.[13–18] The latter has the advantage of incorporating fluorine late-stage. The prototypical *β*-fluoroamine structures for the HB PTC transformation are given in Scheme 4.1.

Initial screening of chiral urea catalysts focused on the BINAM scaffold, analogous to the catalysts used for desymmetrization of episulfonium ions (Chapter 3). The original tetradentate bis-urea, **6**, failed to attain high levels of enantioselectivity, however the computationally predicted alkylation of one of the donors, yielding a tridentate catalyst, significantly increased the enantioselectivity of the reaction (**7**-**9**). Further experimental optimization yielded a final catalyst with larger aromatic substituents – a polytrifluoromethylated terphenyl π-system (**12**), and N-ethyl alkylation.[19]

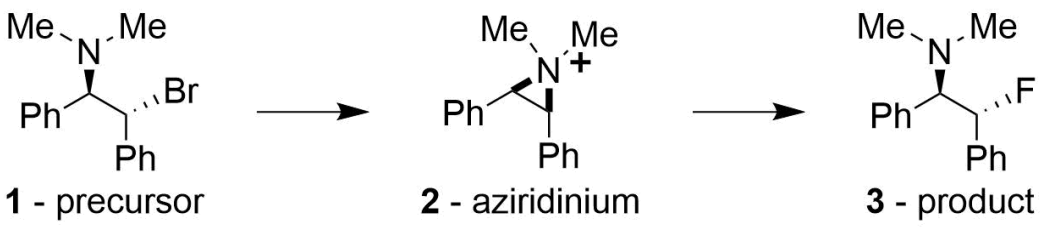

Scheme 4.1: Aziridinium ion and *β*-fluoro amine product formed from desymmetrization with fluoride.

A key finding of the experimental work was that potassium fluoride could be used as fluoride source, as well as cesium fluoride – a pleasing result given the higher lattice energy of potassium fluoride over cesium fluoride (lattice energies of 829 kJ/mol and 759 kJ/mol respectively).[20] To achieve comparable yields to CsF, reactions with KF were run at higher concentration (0.5 M compared to 0.25 M) and with a greater excess of the fluoride salt (5 eq. compared to 3 eq.). Potassium fluoride has several advantages over cesium fluoride, notably its lower cost ($8/mol and $72/mol respectively) and lower molecular weight (58.1 g/mol vs 151.9 g/mol respectively). Fluorination was successfully

Table 4.1: Desymmetrization of meso-Aziridinium Ions with Potassium Fluoride.

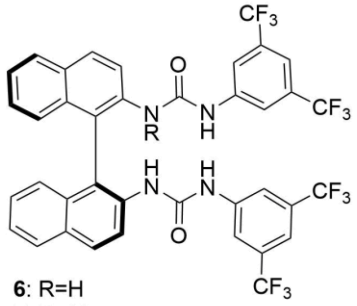

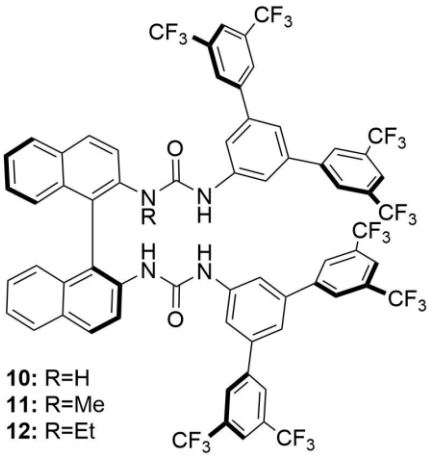

Catalyst	Solvent	Temperature	Yield / %	e.r.
6	CH_2Cl_2	rt	>99	55:45
7	CH_2Cl_2	rt	98	85:15
8	CH_2Cl_2	rt	99	86:14
9	CH_2Cl_2	rt	83	86:14
10	CH_2Cl_2	rt	77	55:45
11	CH_2Cl_2	rt	72	88:12
12	CH_2Cl_2	rt	80	90.5:9.5
12*	$CHCl_3$	-15ºC	71	95:5

* 10 mol% of catalyst, 5 eq. KF, 0.5 M, 72 h. Experimental work performed by co-workers.

performed on up to 50 g scale, requiring 502 mmol of potassium fluoride. A summary of experimental work is given in Table 4.1.

The experimental work in this chapter was performed by members of the Gouverneur group, notably Anna Chiara Vicini, Gabriele Pupo and Francesco Ibba. Experimental work on desymmetrization of aziridinium ions overlaps with the development of HB PTC for desymmetrization of episulfonium ions – experiment and computation were performed concurrently. Given the background to this work was already covered through the study of episulfonium ions – both mechanistic background and rational improvement of the catalysts through alkylation – computation focuses primarily on rationalizing the origins of enantioselectivity and substrate scope and underlines the challenges of using potassium fluoride for nucleophilic fluorination. The work described in this chapter features in the publication *Hydrogen Bonding Phase-Transfer Catalysis with Potassium Fluoride: Enantioselective Synthesis of β-Fluoroamines*, G. Pupo*, A. C. Vicini*, D. M. H. Ascough, F. Ibba, K. E. Christensen, A. L. Thompson, J. M. Brown, R. S. Paton, V. Gouverneur, *J. Am. Chem. Soc.* **2019**, *141*, 2878-2883.[19] All computation in this publication was performed by me with supervision from R. S. Paton. This work has been reused in accordance with the ACS AuthorChoice Creative Commons Attribution (CC-BY) License, Copyright 2019 American Chemical Society.

4.2 Computational Methods

4.2.1 Density Functional Theory

The methods used for this chapter are based upon those used in Chapter 3 for the desymmetrization of episulfonium ions.[21] All calculations were performed on the *N,N*-dimethyl aziridinium ion **2**. Optimization, frequency and single point calculations were performed in dichloromethane (DCM) for the achiral Gibbs free energy profiles,

and chloroform for investigation of the system with chiral catalyst. Gibbs free energies were evaluated at 298.15 K and 1 M concentration unless otherwise stated.

Reference to the intrinsic reaction coordinate (IRC) refers to the geometrically meaningful reduction of the IRC onto the forming and breaking bonds – defined as the breaking C–N bond distance minus the forming C–F distance.[22,23]

Energy differences between transition state structures (TSs) were partially rationalized through the use of truncated (fragmented) models – where part of the TS structure in both major and minor TSs is deleted – and the single point energy evaluated, without geometry optimization.[24–27] Any unsatisfied valence was satisfied by adding hydrogen atoms, in a consistent geometry.

4.2.2 Molecular Dynamics

The molecular dynamics (MD) simulation methods were based upon those used in Chapter 3, with explicit solvation in chloroform, obtained from virtualchemistry.org.[28,29] Minimization, NVT equilibration and NPT equilibration were performed using the same parameters. Data was derived from a further 300 ns of NPT simulation.

Catalyst-fluoride binding modes were investigated with cesium cation, and were explored at elevated temperature of 373 K, with simulations of the reactive ion pair (catalyst-fluoride-aziridinium) performed at the reaction temperature of 298 K.

4.2.3 Naming and Definitions

Naming and numbering conventions, as well as angle definitions are defined consistently with Chapter 3 on the desymmetrization of episulfonium ions and are reproduced below (Figure 4.1, Figure 4.2).

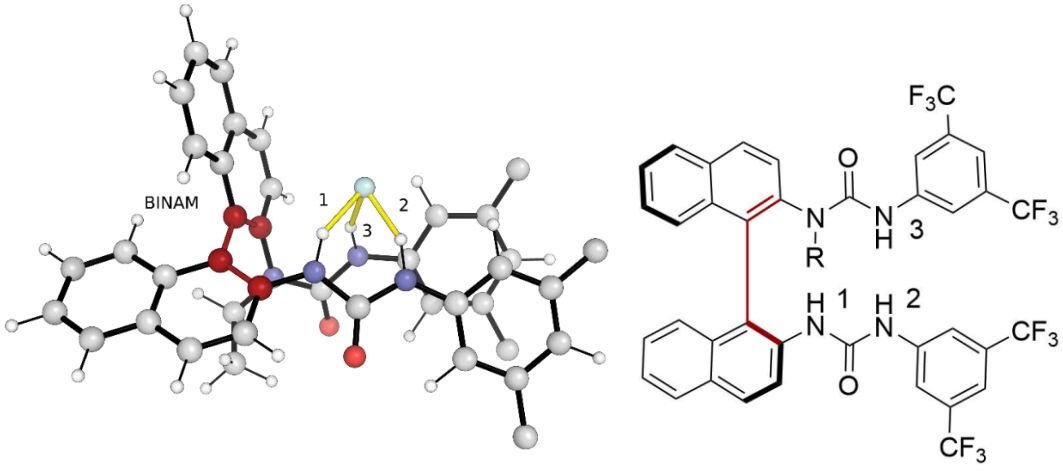

Figure 4.1: Naming and numbering conventions for tridentate BINAM-based catalyst fluoride complexes. Hydrogen bonds are numbered 1-3. Atoms used to define the BINAM dihedral are emphasized in dark red.

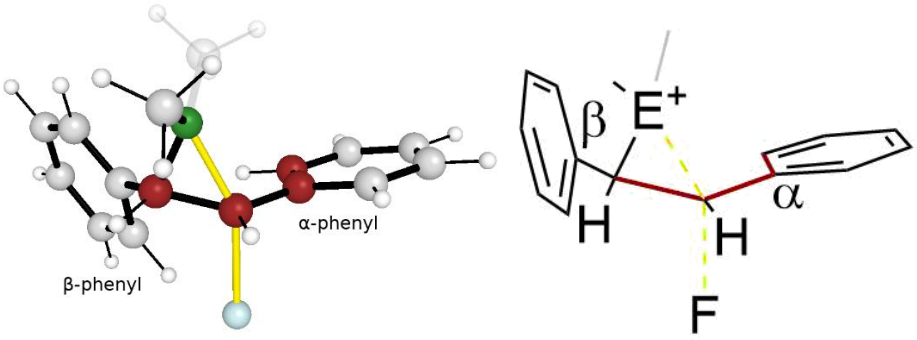

Figure 4.2: Naming and numbering conventions for meso cationic substrates (episulfonium and aziridinium. S/N atom colored in green – Additional alkyl group for aziridinium transparent). The phenyl groups are named by their relative positioning to the forming and breaking bonds. Atoms used to define the α-dihedral (dihedral of the α-phenyl ring) are emphasized in dark red. The β-dihedral is defined analogously. As drawn, a positive dihedral angle is defined as a clockwise rotation about the α-dihedral and a counter-clockwise rotation about the β-dihedral.

4.3 Results and Discussion

4.3.1 Fluorination of Aziridinium Ions with Achiral Urea Catalyst

Initial experimental studies on fluorination of aziridinium ions used achiral Schreiner's urea, **15**, with CsF salt in dichloromethane (Scheme 4.2). Quantitative yields are achieved with 10 mol% of Schreiner's urea, **15**, in dichloromethane solvent – in contrast, in the absence of catalyst, no background reactivity is seen. A Gibbs free energy profile comparing the uncatalyzed process with that catalyzed by Schreiner's urea, using the thermodynamic model of solubility described in Chapter 3, is given in Figure 4.3 with bromide aziridinium ion precursor, **1**. Barrier to formation of the aziridinium ion is relatively high (**i**‡), with auto-ionization barrier of 87 kJ/mol, and barrier with urea coordinated of 94 kJ/mol. Urea hydrogen bonding to the bromide leaving group is weak, and unable to overcome the entropy penalty of coordination, resulting in a comparable barrier height. The aziridinium-bromide ion pair (**ii**) formed is only marginally less stable than the starting materials, with Gibbs free energies of 9 kJ/mol and 2 kJ/mol in the absence and presence of Schreiner's urea catalyst respectively. Whilst an energy difference of 9 kJ/mol is small, it corresponds to an equilibrium ionization of only 3 % at room temperature. The cost of separating the ion pair (**ii-iii**) is reduced from 34 kJ/mol to 15 kJ/mol when the bromide anion is coordinated by the urea, resulting in ions at 43 kJ/mol and 17 kJ/mol relative to starting materials respectively (**iii**). The relative

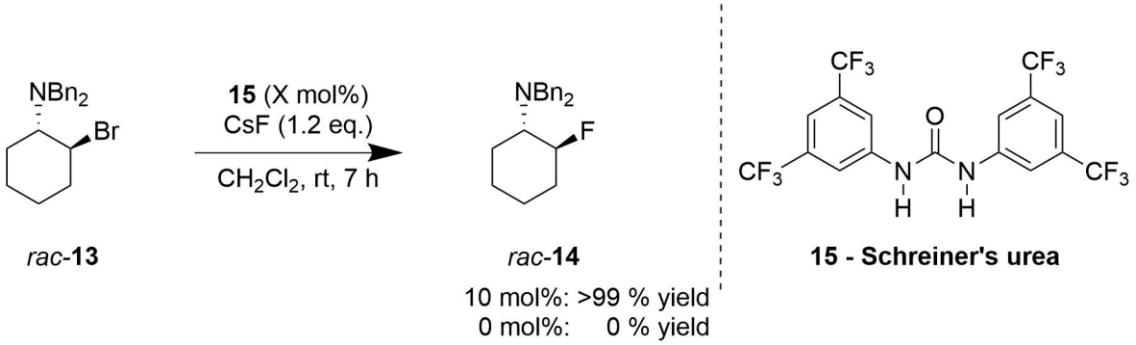

Scheme 4.2: Racemic fluorination of aziridinium ion with fluoride under HB PTC with achiral Schreiner's urea. Experimental work performed by co-workers.

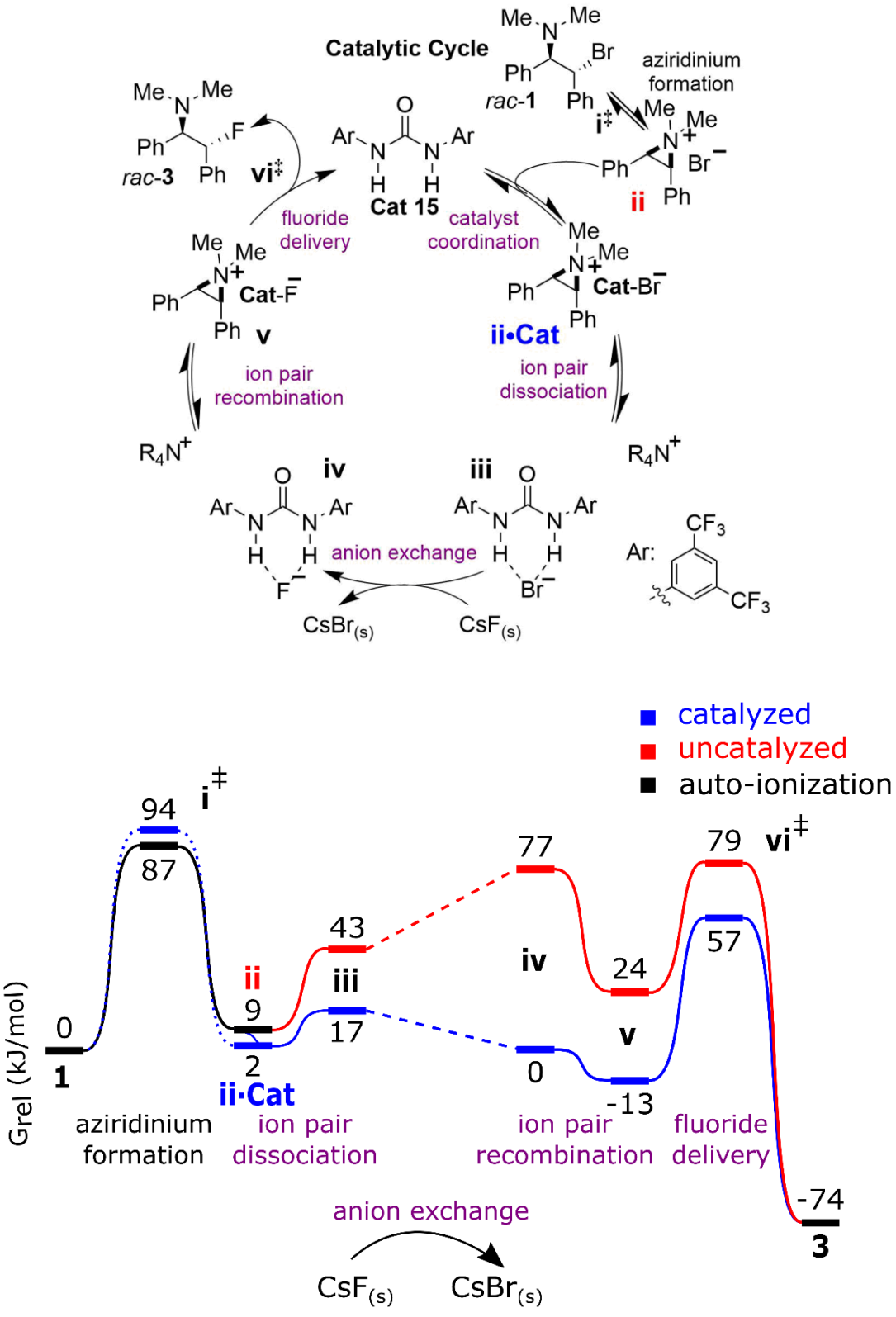

Figure 4.3: Gibbs free energy profile for desymmetrization of aziridinium ions derived from bromide substrate, **1**, with fluoride. The profile is computed for the hypothetical uncatalyzed reaction, and that catalyzed by Schreiner's urea **15**.

stability of the ion pair, **ii**, can therefore be attributed to the formed carbon-nitrogen bond in the strained aziridinium ion largely compensating for the breaking of the carbon-bromine bond (ΔG = 43 kJ/mol to the separated ions), with a similar amount (34 kJ/mol) recovered from interaction with the bromide leaving group in the ion pair.

After phase-transfer, modelled by anion exchange (**iii-iv**), the separation between catalyzed and uncatalyzed pathways reaches a maximum, at 77 kJ/mol (**iv**), demonstrating the critical role of the urea in these processes, consistent with the HB PTC mechanism. Combination of fluoride with the aziridinium ion results in reactive ion pairs with energies relative to starting materials of 24 kJ/mol and -13 kJ/mol for the uncatalyzed and catalyzed processes respectively (**v**).

Fluoride delivery to form the product (**vi**‡) then proceeds via a modest barrier of 55 kJ/mol and 70 kJ/mol for uncatalyzed and catalyzed pathways respectively, forming products at -74 kJ/mol. In neither case is the fluoride delivery transition state structure expected to be turnover/rate limiting, surpassed by the TS to auto-ionization of the substrate. No kinetic information is known about the phase-transfer process, however.

The barrier to fluorination, from ion pair to TS (**v-vi**‡), may be partitioned into contributions from rearranging the ion pair, and the process of forming/breaking covalent bonds (Figure 4.4). In the uncatalyzed case, 27 kJ/mol of the barrier arises from rearrangement of the ion pair, with the remaining 28 kJ/mol arising from bond forming/breaking, indicating a roughly 50:50 contribution. In contrast, with urea, rearrangement of the ion pair costs only 6 kJ/mol, however the bond forming/breaking process is associated with a significantly increased barrier of 64 kJ/mol, corresponding

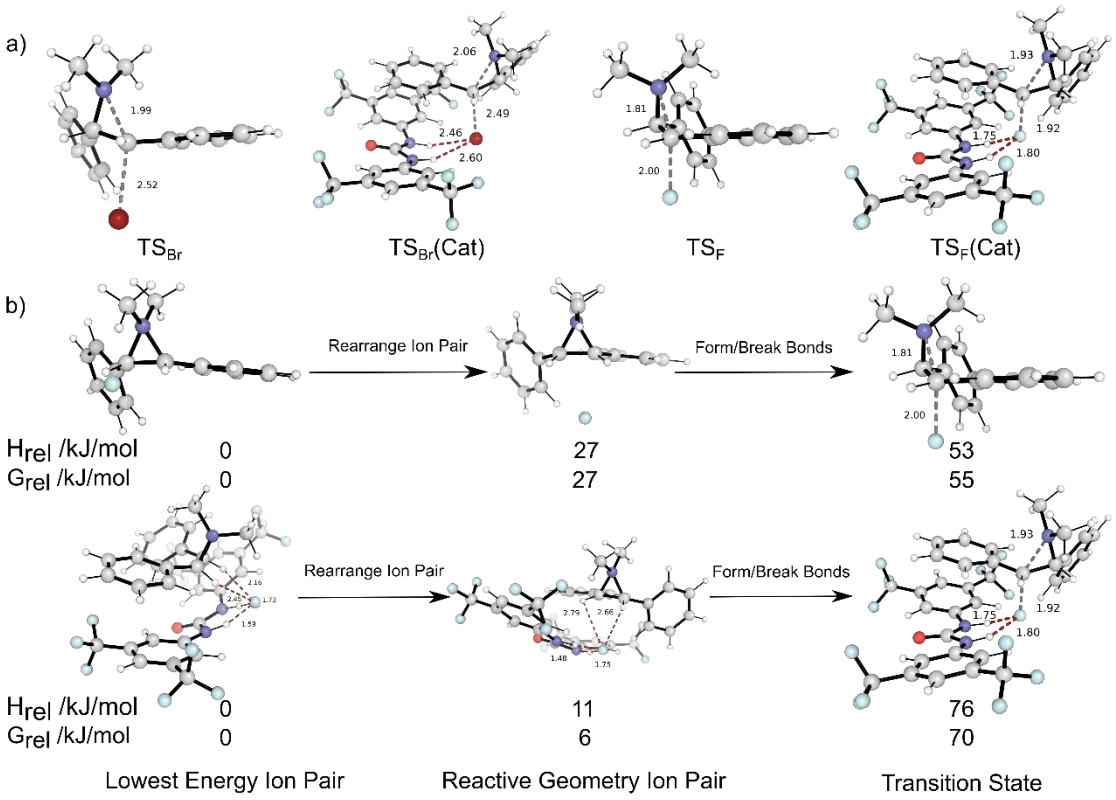

Figure 4.4: a) Key transition state structures for bromide removal and fluoride delivery. b) Relative contributions to the fluoride delivery energy barrier from ion pair rearrangement and bond forming/breaking.

to 91 % from bond forming/breaking. Key geometric data for the species is tabulated in Table 4.2.

Subsequently, aziridinium precursors with chlorine leaving group were used synthetically due to ease of handling relative to their bromine counterparts. The Gibbs free energy profile for the same HB PTC fluorination with chlorine substrate analog, **16**, is given in Figure 4.5. The profiles for the two leaving groups are qualitatively similar, with the same general profile shape. The exergonicity of the reaction is reduced from -74 kJ/mol to -60 kJ/mol on changing from Br to Cl leaving group, due to the stronger bond broken to the leaving group outweighing the higher lattice energy of the salt by-product. Formation of the aziridinium ion proceeds via a higher barrier with the Cl leaving group at 99 kJ/mol for auto-ionization and 101 kJ/mol for urea assisted ionization. The

Table 4.2: Key Geometric Data for Aziridinium Containing Species.

Species	Key Distances / Å				Key Angles / º	
	C–X	C–N	H Bond 1	H Bond 2	α-dihedral	β-dihedral
TS_{Br}	2.518	1.989	-	-	27.9	33.7
TS_{Br}(Cat)	2.487	2.059	2.457	2.604	23.0	26.3
TS_{Cl}	2.377	1.958	-	-	28.0	36.8
TS_{Cl}(Cat)	2.337	2.034	2.283	2.437	24.2	29.0
TS_{F}	1.997	1.809	-	-	27.2	47.8
TS_{F}(Cat)	1.918	1.934	1.752	1.804	24.2	42.5
IP_{Br}(Cat)	-	-	2.515	2.366	-	-
IP_{Cl}(Cat)	-	-	2.339	2.186	-	-
IP_{F}(Cat)	-	-	1.729	1.591	-	-

difference between catalyzed and uncatalyzed ionization is reduced compared to the bromine leaving group, from 7 kJ/mol to 2 kJ/mol, due to the urea forming stronger hydrogen bonds to chlorine. The two barrier heights are within computational uncertainty and the competition of the two pathways will depend upon the experimental conditions. The formed ion pairs with chloride leaving group (**ii**) have relative Gibbs free energies of 24 kJ/mol and 10 kJ/mol relative to starting materials when uncoordinated and coordinated respectively. These are slightly less thermodynamically favored compared to the starting material, than with Br leaving group (G_{rel} of 24 kJ/mol and 9 kJ/mol respectively), due to the breaking of a stronger carbon-halogen bond (contributing ~18 kJ/mol), despite the formation of a stronger ionic interaction (~3 kJ/mol). A larger separation between catalyzed and uncatalyzed processes is seen for steps **ii→iii** with chloride leaving group due to the formation of stronger hydrogen bonds to the catalyst. Once fluoride is brought into solution, the influence of the leaving group has concluded, and the profiles are identical. This part of the profile is, however, shifted, due to the relative favorability of forming the aziridinium ions, however fluoride delivery is still not turnover limiting in the catalyzed mechanism with chloride leaving group.

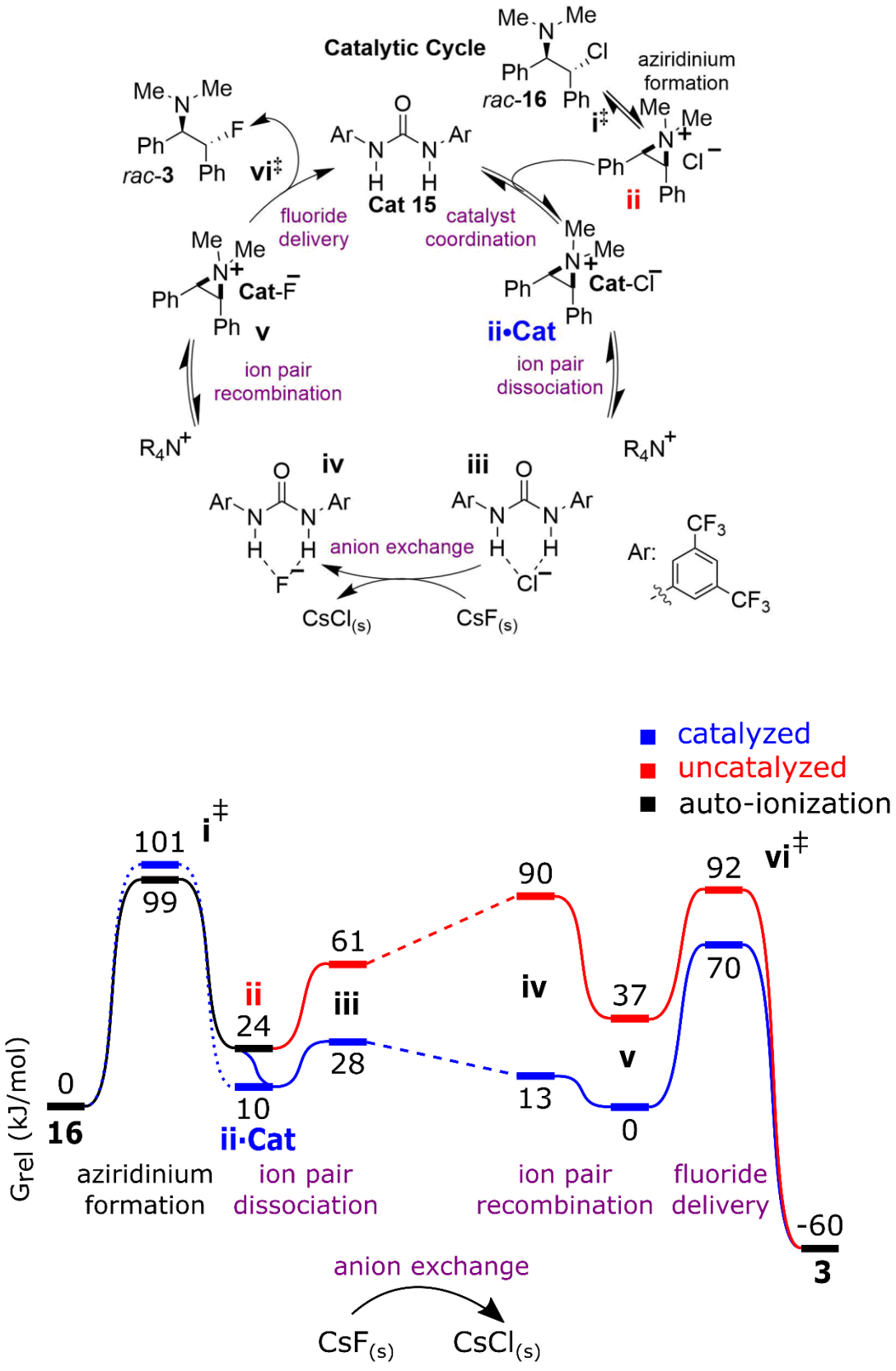

Figure 4.5: Gibbs free energy profile for desymmetrization of aziridinium ions derived from chloride precursor, **16**, with fluoride. The profile is computed for the hypothetical uncatalyzed reaction, and that catalyzed by Schreiner's urea **15**.

4.3.2 Enantioselective Desymmetrization of Aziridinium Ions with a Chiral Urea Catalyst

Early in the development of the transformation for the fluorination of aziridinium ions, we wanted to assess the possibility of activating KF as a fluoride source using HB PTC. Preliminary calculations were performed using the prototypical methylated tricoordinate catalyst, **7**, and are described in section 4.3.2.1. Experimental screening determined that alkylated, tridentate BINAM based urea catalysts remained suitable HB PTC catalysts and that larger aromatic substituents achieved higher enantioselectivities, before settling on catalyst **12** in chloroform solvent (Figure 4.6). The enantioselectivity achieved with this catalyst is rationalized by computing the TS ensemble. The final substrate scope for the reaction is given in Figure 4.7.

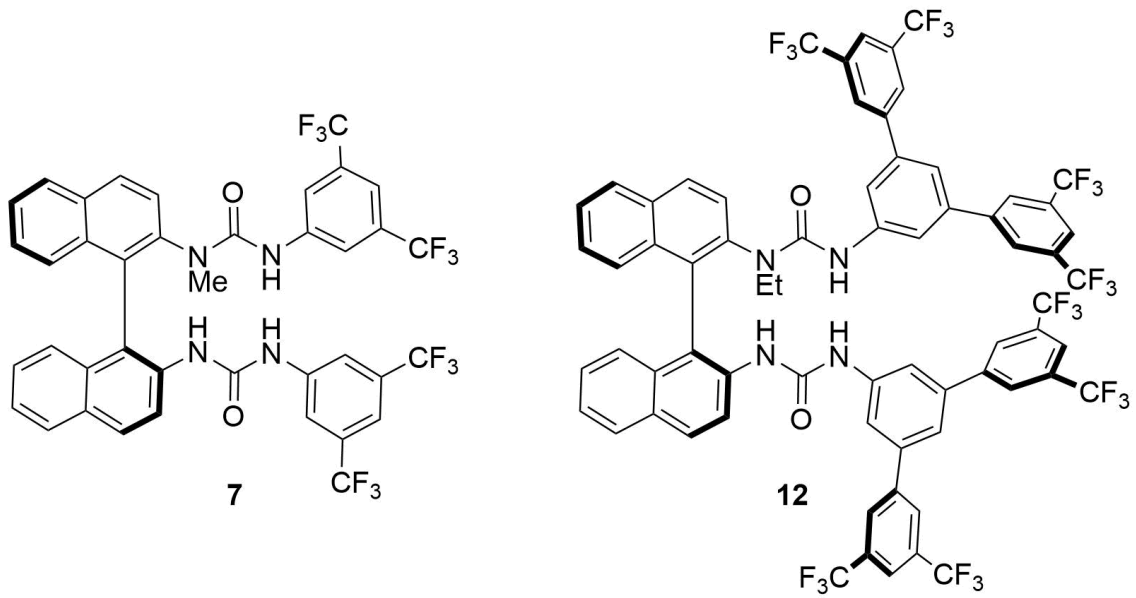

Figure 4.6: Chiral catalysts for HB PTC. Left: Prototypical alkylated tricoordinate BINAM catalyst, **7**. Right: Catalyst optimized for asymmetric fluorination of aziridinium ions under HB PTC, **12**.

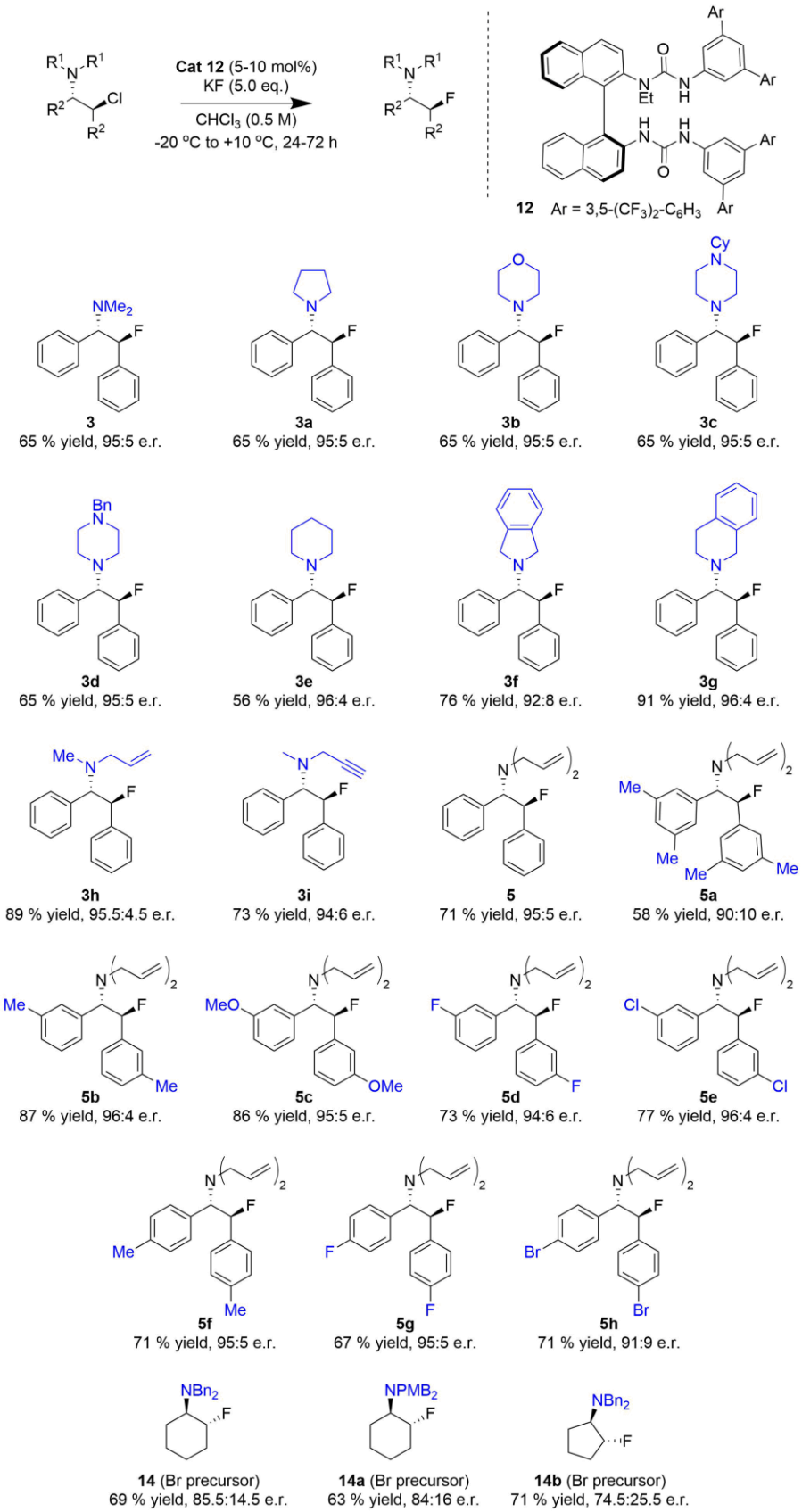

Figure 4.7: Substrate scope of asymmetric desymmetrization of aziridinium ions with potassium fluoride under HB PTC. Non-stilbene derived products (**14x**) have opposite absolute configuration to stilbene derived products (**3x** and **5x**). Experimental work performed by co-workers.

4.3.2.1 Metal Fluoride Solubilization

A key question about using KF as fluoride source is whether the higher lattice energy, compared to CsF, can be compensated for. Preliminary calculations were undertaken to investigate the feasibility of tridentate, methylated BINAM based urea catalyst, **7**, for solvating KF. As BINAM catalysts are known experimentally to dissolve CsF in dichloromethane,[19] a thermodynamic approach based upon the solubilization of a MF formula unit was considered appropriate, using tabulated experimental data (Tables S33-34). Experimental values by Chase Jr.[30] from the NIST chemistry WebBook SRD 69.[31] By combining experimental tabulated thermodynamic data with computed values, the process $MF_{(s)} \rightarrow MF_{(DCM)}$ was computed for CsF and KF, giving Gibbs free energy changes of 35.8 kJ/mol and 70.2 kJ/mol in the absence of urea hydrogen bond donor (Table 4.3). Note that MF refers to a formula unit in gas and solution phase, whereas it refers to a giant ionic lattice in the solid phase. The higher value for KF originates from the higher Gibbs free energy of formation of $KF_{(g)}$ over $CsF_{(g)}$ (194 kJ/mol vs 152 kJ/mol respectively), with free energy of solvation of the ion pairs being relatively similar.

Table 4.3: Derived Gibbs Free Energies at 298.15 K.

Process	**ΔG (kJ/mol)**
$CsF_{(s)}$ -> $CsF_{(g)}$	152
$KF_{(s)}$ -> $KF_{(g)}$	194
$CsF_{(g)}$ -> $CsF_{(DCM)}$	-116
$KF_{(g)}$ -> $KF_{(DCM)}$	-124
$CsF_{(s)}$ -> $CsF_{(DCM)}$	35.8
$KF_{(s)}$ -> $KF_{(DCM)}$	70.2
$\mathbf{7}_{(DCM)}$ + $CsF_{(DCM)}$ -> $\mathbf{7}FCs_{(DCM)}$	-35.4
$\mathbf{7}_{(DCM)}$ + $KF_{(DCM)}$ -> $\mathbf{7}FK_{(DCM)}$	-37.2
$\mathbf{7}_{(DCM)}$ + $CsF_{(s)}$ -> $\mathbf{7}FCs_{(DCM)}$	0.4
$\mathbf{7}_{(DCM)}$ + $KF_{(s)}$ -> $\mathbf{7}FK_{(DCM)}$	33.0

In the presence of methylated tridentate urea catalyst, **7**, the catalyst is able to bind the solvated ion pair, decreasing the energetic penalty to solvation. Solvation of a formula unit of CsF, in the presence of urea **7** is lowered to 0.4 kJ/mol, and solvation of KF, with **7** is lowered to 33.0 kJ/mol. The near zero value for CsF is consistent with the experimental observation that the catalyst can solvate this salt. The higher value with KF implies that this salt cannot be solvated in large quantities by the catalyst, but enough can be solvated to react at room temperature. Further, the values demonstrate that coordination of a solvated KF formula unit by the hydrogen bonding catalyst in DCM can significantly thermodynamically stabilize it and underlines the fact that KF is significantly more challenging to solubilize than CsF.

4.3.2.2 Catalyst-Fluoride Binding Mode

The fluoride binding modes of catalyst **12** were investigated by simulating the catalyst, bound to fluoride in the presence of cesium counterion in explicit chloroform solvent. 300 ns of simulation at 373 K demonstrated persistent tridentate binding of fluoride. The frames of the trajectory were clustered using a cut-off of 0.6 Å and the 11 highest weighted clusters were optimized with DFT. A substructure of the complex was used for calculation of the mutual RMSDs to ensure that the structures were clustered in a chemical meaningful way (Figure 4.8). For example, isomers of each urea group involve the direct movement of 6 atoms, over a relatively short distance, but have large chemical implications. In contrast, translation/rotation of a distal aryl group involves the movement of on the order of 10-20 atoms (depending on substitution), potentially by much larger displacements, particularly in rotation, with much smaller chemical implication.

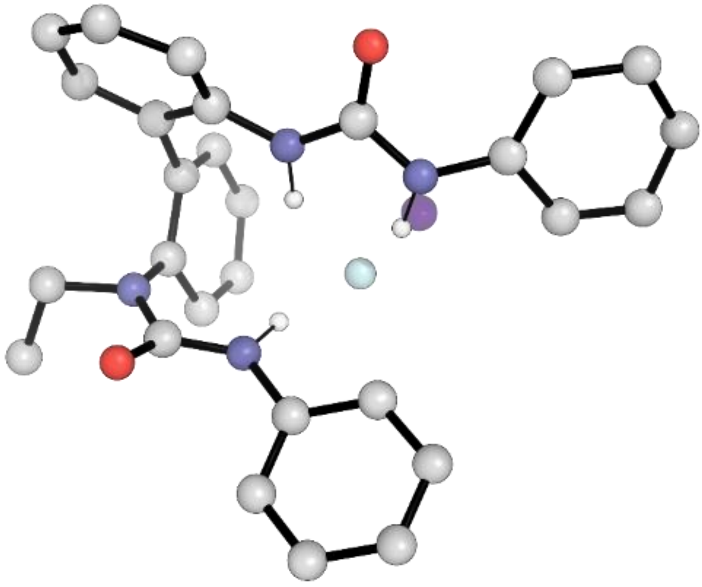

Figure 4.8: Substructure used for RMSD alignment of MD trajectory for catalyst-fluoride complex, to emphasize conformation of chemically relevant groups. Own work reproduced from Ref. 19.

DFT optimizations were performed in the absence of cation, and with a potassium counterion replacing the cesium cation. Complexes in the absence of cation are illustrated in Figure 4.9 and complexes in the presence of potassium cation are illustrated in Figure 4.10. Key geometric parameters are tabulated in Table 4.4 and Table 4.5 respectively. In the lowest energy conformer, pairing of the potassium cation leads to an increase in mean hydrogen bond length from 1.72 Å to 1.80 Å. Averaging over all conformers, H Bond 1 increases in length by 0.00 Å, H Bond 2 by 0.11 Å and H bond 3 by 0.13 Å, highlighting a tendency for the fluoride to move towards the BINAM backbone. Potassium-fluoride separation is consistent between conformers, with mean separation of 2.44 Å and standard deviation of 0.01 Å.

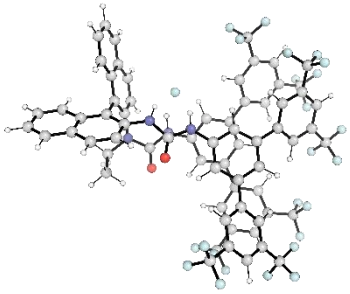

Cat 12-F-1
0.0 kJ/mol

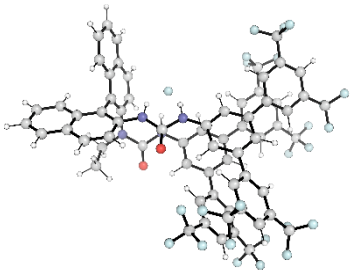

Cat 12-F-2
+1.5 kJ/mol

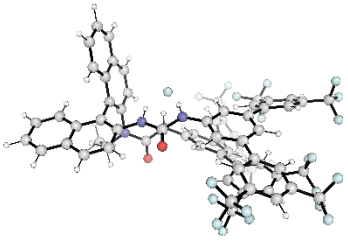

Cat 12-F-3
+1.7 kJ/mol

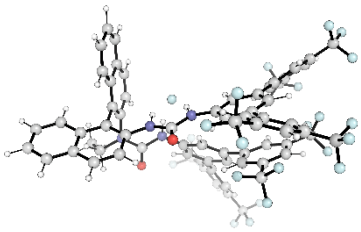

Cat 12-F-4
+4.3 kJ/mol

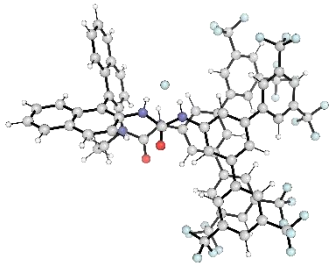

Cat 12-F-5
+5.5 kJ/mol

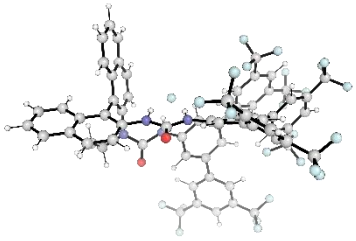

Cat 12-F-6
+6.1 kJ/mol

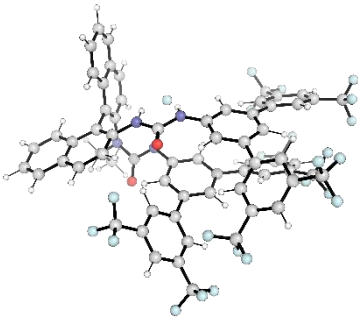

Cat 12-F-7
+6.8 kJ/mol

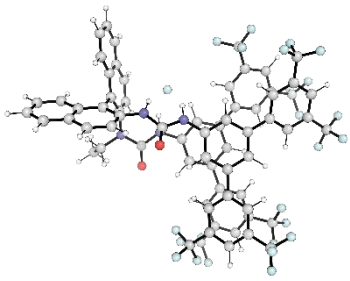

Cat 12-F-8
+8.8 kJ/mol

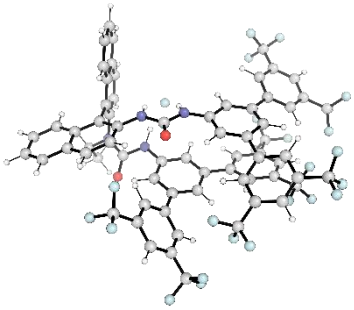

Cat 12-F-9
+9.0 kJ/mol

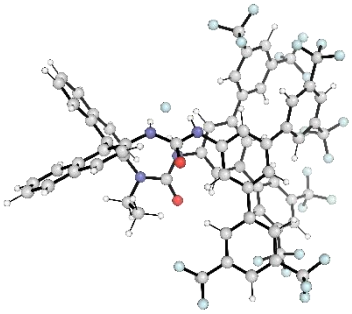

Cat 12-F-10
+9.5 kJ/mol

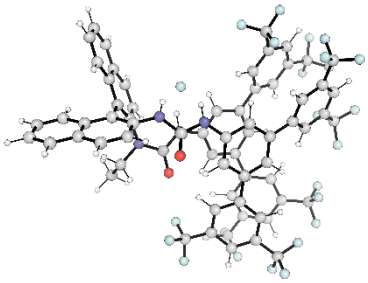

Cat 12-F-11
+17.1 kJ/mol

Figure 4.9: Conformers of Catalyst **12-F** complex with relative Gibbs free energies. Own work adapted from Ref. 19.

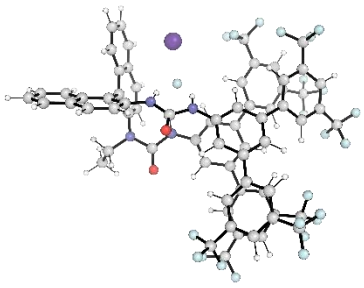

Cat 12-F•K-1
0.0 kJ/mol

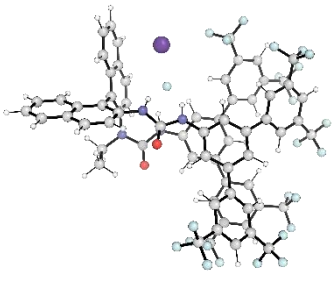

Cat 12-F•K-2
+1.0 kJ/mol

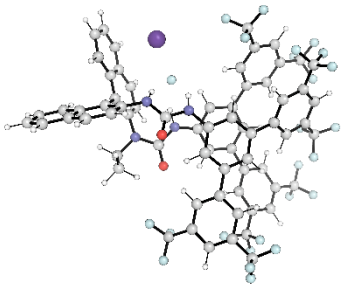

Cat 12-F•K-3
+5.5 kJ/mol

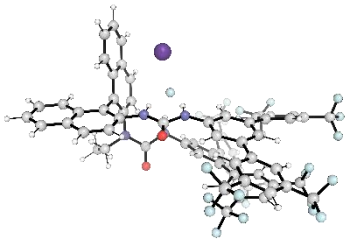

Cat 12-F•K-4
+6.1 kJ/mol

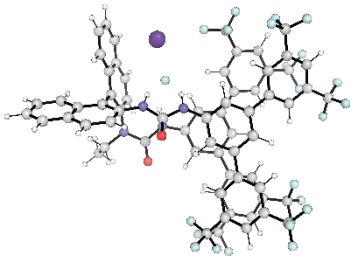

Cat 12-F•K-5
+6.2 kJ/mol

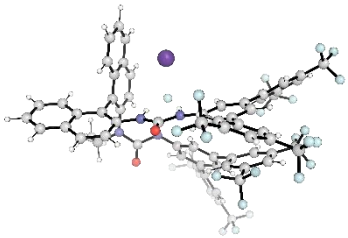

Cat 12-F•K-6
+7.4 kJ/mol

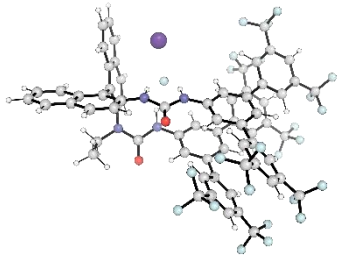

Cat 12-F•K-7
+7.8 kJ/mol

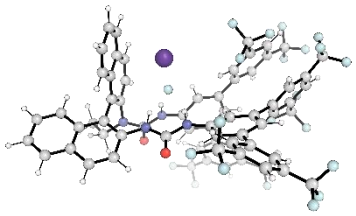

Cat 12-F•K-8
+9.8 kJ/mol

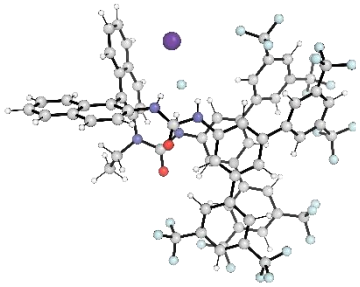

Cat 12-F•K-9
+13.6 kJ/mol

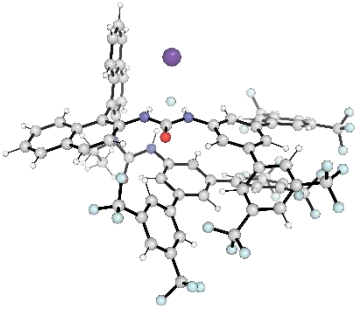

Cat 12-F•K-10
+22.6 kJ/mol

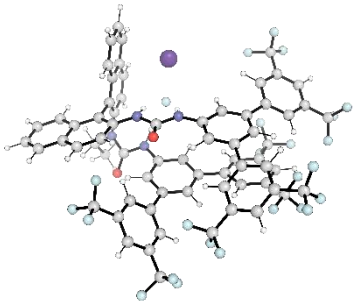

Cat 12-F•K-11
+23.2 kJ/mol

Figure 4.10: Conformers of **Cat 12-F•K** complex with relative Gibbs free energies. Potassium is illustrated as a purple sphere. Own work adapted from Ref. 19.

Table 4.4: Key Geometric Parameters for Complexes of **12** with Fluoride.

	Key Distances / Å				Key Angles / ◦	
	H-Bond 1	**H-Bond 2**	**H-Bond 3**	**M-F**	**H-Bond 3**	**Backbone**
Cat 12-F-1	1.719	1.693	1.733	-	153.8	71.5
Cat 12-F-2	1.812	1.576	1.709	-	156.7	73.2
Cat 12-F-3	1.862	1.514	1.589	-	168.9	79.2
Cat 12-F-4	1.785	1.544	1.619	-	164.8	86.4
Cat 12-F-5	1.740	1.670	1.712	-	155.0	70.4
Cat 12-F-6	1.792	1.603	1.597	-	164.7	79.9
Cat 12-F-7	1.874	1.539	1.698	-	155.3	105.1
Cat 12-F-8	1.696	1.699	1.798	-	155.7	72.6
Cat 12-F-9	1.852	1.566	1.708	-	155.4	108.6
Cat 12-F-10	1.714	1.748	1.670	-	161.7	71.6
Cat 12-F-11	1.714	1.757	1.691	-	160.7	67.7

Table 4.5: Key Geometric Parameters for Complexes of **12** with Potassium Fluoride.

	Key Distances / Å				Key Angles / ◦	
	H-Bond 1	**H-Bond 2**	**H-Bond 3**	**M-F**	**H-Bond 3**	**Backbone**
Cat 12-F•K 1	1.744	1.794	1.872	2.427	153.0	72.6
Cat 12-F•K 2	1.729	1.811	1.895	2.427	151.4	74.4
Cat 12-F•K 3	1.732	1.858	1.804	2.433	160.8	74.7
Cat 12-F•K 4	1.845	1.650	1.696	2.442	168.0	77.5
Cat 12-F•K 5	1.743	1.785	1.939	2.424	153.6	74.4
Cat 12-F•K 6	1.808	1.637	1.714	2.461	166.1	85.4
Cat 12-F•K 7	1.801	1.698	1.827	2.429	153.9	74.8
Cat 12-F•K 8	1.803	1.731	1.715	2.444	162.3	83.7
Cat 12-F•K 9	1.734	1.878	1.810	2.429	159.9	69.5
Cat 12-F•K 10	1.837	1.643	1.851	2.449	150.3	107.7
Cat 12-F•K 11	1.820	1.662	1.870	2.447	151.2	110.0

4.3.2.3 Computing the Transition State Structure Ensemble

In order to conformationally sample the transition state structures, the reactive ion pair (*i.e.* **Cat 12**-fluoride-aziridinium) was simulated by molecular dynamics in explicit chloroform solvent, for 300 ns. A substructure of the system was then clustered by symmetry aware RMSD calculation using a cut-off of 0.8 Å (Figure 4.11). Clusters with

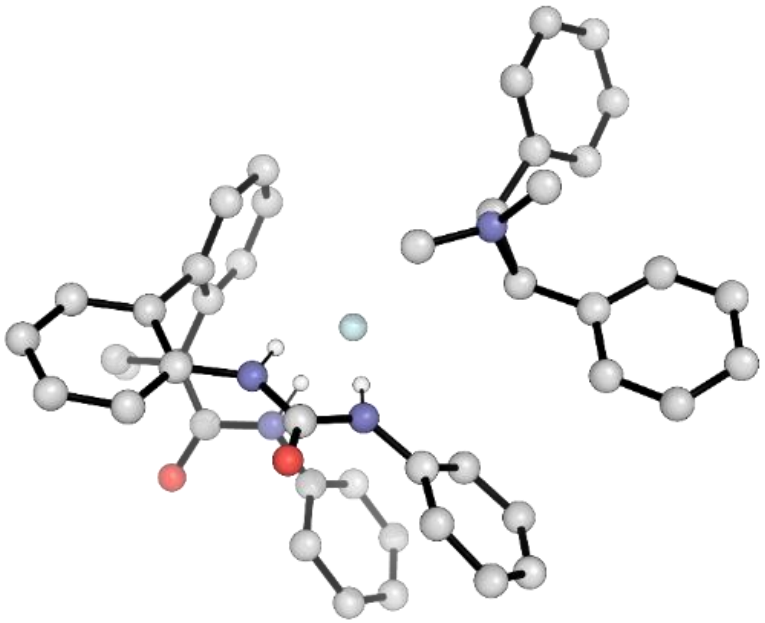

Figure 4.11: Substructure used for RMSD alignment of MD trajectory to emphasize conformation of chemically relevant groups. Own work reproduced from Ref. 19.

greater than 1 % weighting were retained, giving a total of 7 clusters for DFT optimization.

To ensure that the clusters were sufficiently converged within the simulation timeframe, and therefore sufficient conformational sampling had been undertaken: i) the cluster weightings at 150 ps (half the simulation duration) were verified to compare favorably with the cluster weightings for the total 300 ps simulation time ii) a duplicate simulation with different starting geometry was run, and verified to produce similar high weighted clusters after 300 ns simulation. The evolution of the cluster weightings over the course of each of the runs is shown in Figure 4.12.

Whilst there remains some movement in the precise weighting of each cluster at 300 ns simulation time, each cluster has converged towards a final value, and the simulations demonstrate a good rate of interconversion of the various binding modes. The ordering of the low weighted clusters continues to change due to the small differences in cluster

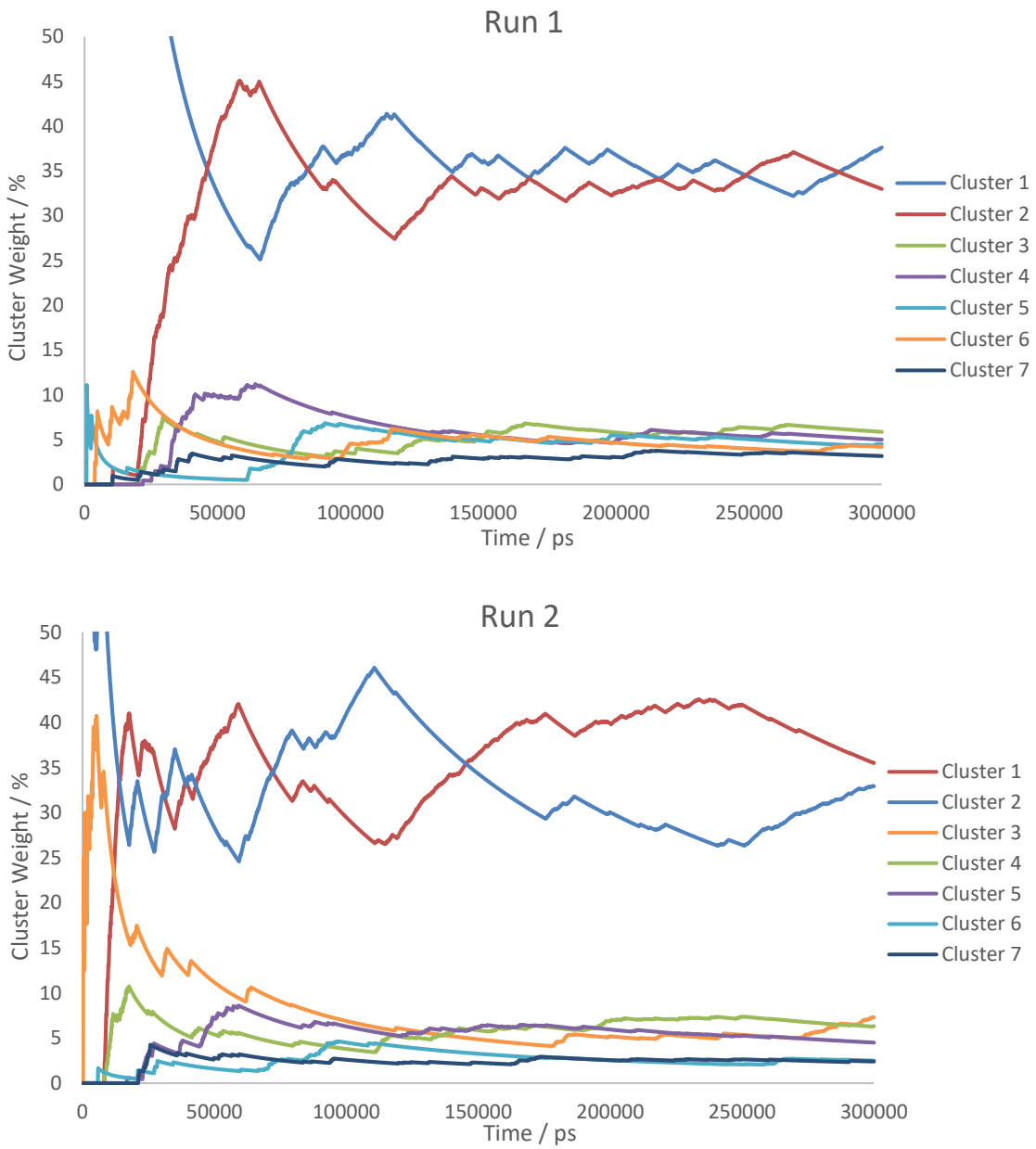

Figure 4.12: Evolution of the percentage weight of each high-weighted cluster over the course of two duplicate 300 ns runs. Clusters are numbered according to their final weighting in the respective simulations. The color of each cluster in run 2 matches the color of the cluster in run 1 that it matches structurally.

weight, however the ordering is not used directly when optimizing the clusters with DFT. For both runs, the 7 clusters with weighting over 1 % have qualitatively the same structures, demonstrating good agreement between the two simulations. They do, however, have different relative weightings with the correspondence between clusters in run 1 and run 2 as (1↔2, 2↔1, 3↔4, 4↔5, 5↔6, 6↔3, 7↔7). At half simulation time of

150 ns, the clusters in both simulations are qualitatively the same as at the end of the simulations, with minor changes in the ordering of the low weighted clusters. From this, it can be inferred that extending the simulation time would not result in any significant changes to cluster weightings or identity. The 7 highest weighted clusters from the MD simulation are illustrated in Figure 4.13, with cluster members drawn in wireframe over the median frame drawn in ball and stick. The 7 ion pair geometries after optimization by DFT are given in Figure 4.14.

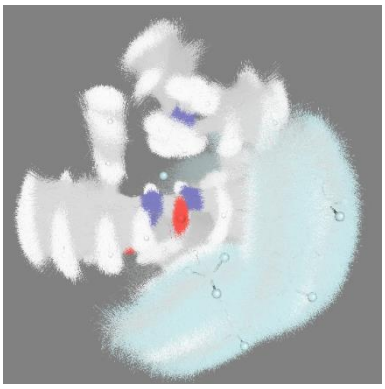

Cluster 1 – 11344 (9734)

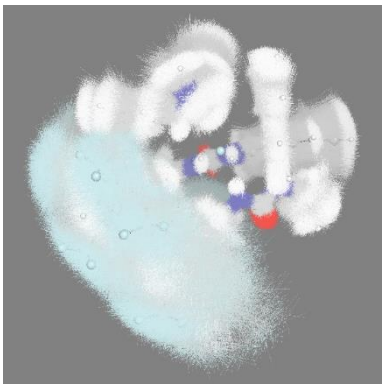

Cluster 2 – 10075 (10461)

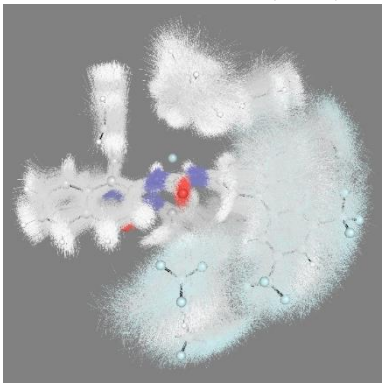

Cluster 3 – 1645 (1898)

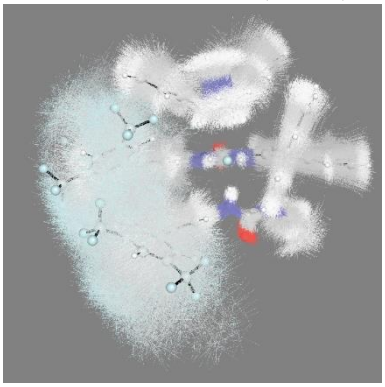

Cluster 4 – 1427 (1435)

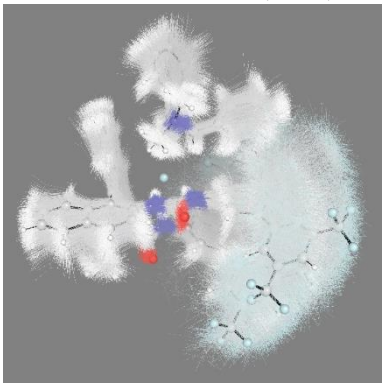

Cluster 5 – 1384 (901)

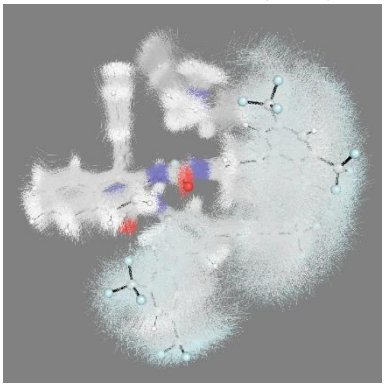

Cluster 6 – 1200 (2136)

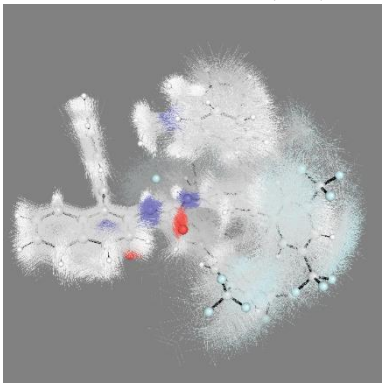

Cluster 7 – 833 (799)

Figure 4.13: Illustration of the 7 highest weighted clusters from the MD simulation of the reactive ion pair. The central frame is drawn in conventional ball and stick representation, and all other frames belonging to the cluster are superimposed as wireframe. Number of contributing frames (from 30,000) given for the two simulations underneath.

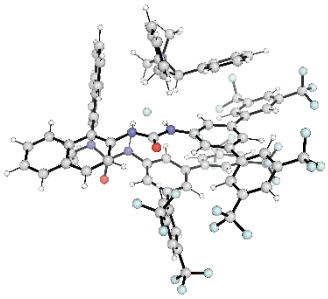

Cat 12-F-Azir-1
0.0 kJ/mol

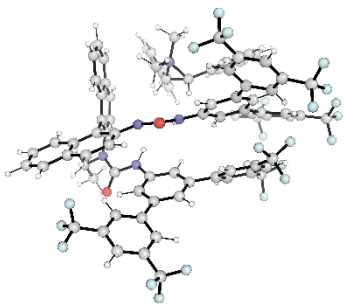

Cat 12-F-Azir-2
+0.8 kJ/mol

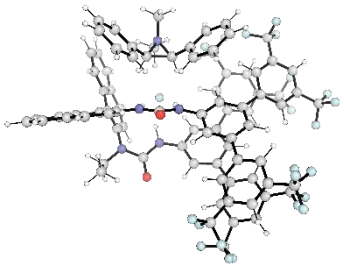

Cat 12-F-Azir-3
+7.4 kJ/mol

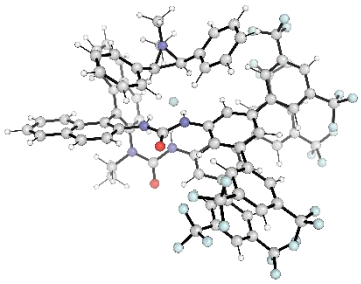

Cat 12-F-Azir-4
+7.9 kJ/mol

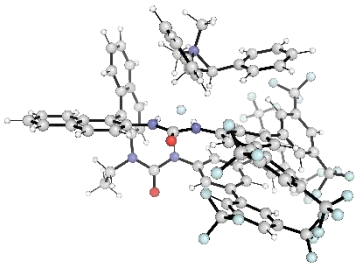

Cat 12-F-Azir-5
+8.4 kJ/mol

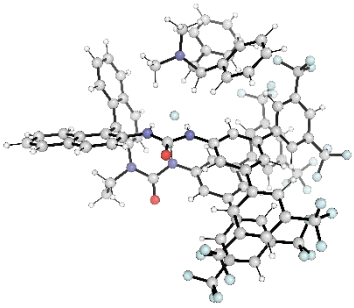

Cat 12-F-Azir-6
+14.0 kJ/mol

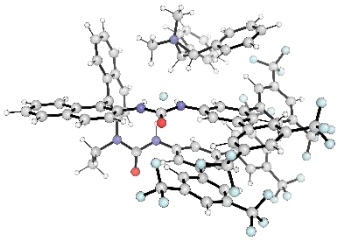

Cat 12-F-Azir-7
+24.8 kJ/mol

Figure 4.14: Conformers of the reactive ion pair, **Cat 12-F** with aziridinium, with relative Gibbs free energies. Own work adapted from Ref. 19.

Each DFT optimized reactive ion pair was then used as the starting point for generating TSs, by advancing the aziridinium ion forward to align the C–N σ* with fluoride. A total of 11 TSs were optimized, with 5 to (*S*,*S*) product and 6 to (*R*,*R*) product with (*S*) catalyst. Rotamers caused by the catalyst N-ethyl group were checked for the lowest Gibbs free energy conformers, within 14 kJ/mol of the lowest energy TS, generating a further 3 conformers within the energy window. The resulting ensemble of 7 lowest Gibbs free

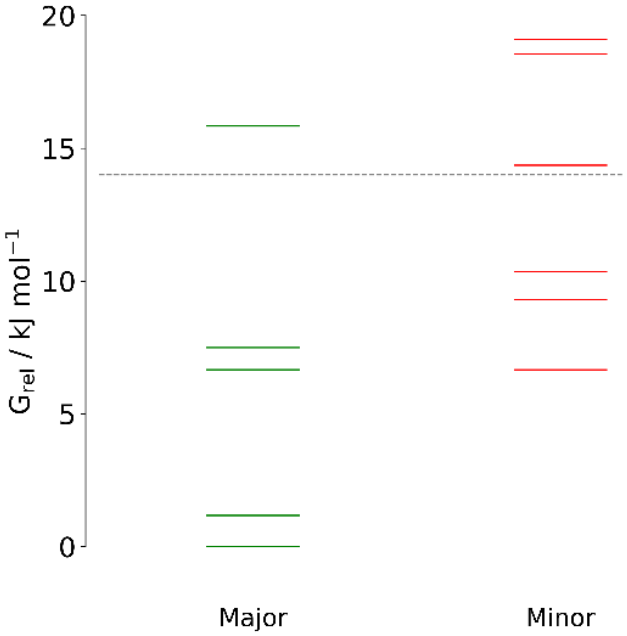

Figure 4.15: Relative Gibbs free energies of the TS ensemble at 278.15 K. Own work reproduced from Ref. 19.

energy TSs is used for further analysis. The relative Gibbs free energies of the lowest energy TSs are shown in Figure 4.15.

From the TS ensemble, it can be inferred that (*S*) catalyst affords (*S*,*S*) product, with an e.r. of 95:5. The major enantiomer is in agreement with single crystal x-ray crystallography and the enantioselectivity agrees favorably with the experimental value of 95:5 e.r., with potassium fluoride salt. The structures and relative Gibbs free energies of the TSs are given in Figure 4.16 with tabulated geometric data in Table 4.6.

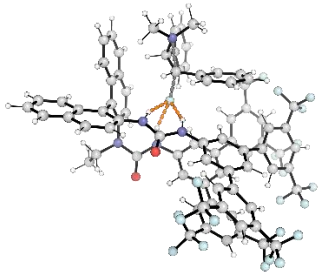

TS Cat 12-F-Azir-major1
0.0 kJ/mol

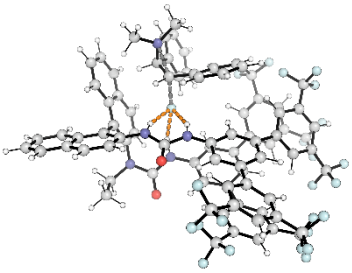

TS Cat 12-F-Azir-major2
+1.2 kJ/mol

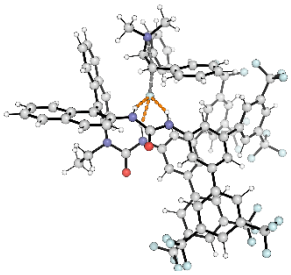

TS Cat 12-F-Azir-major3
+6.7 kJ/mol

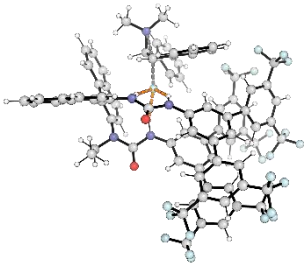

TS Cat 12-F-Azir-major4
+7.5 kJ/mol

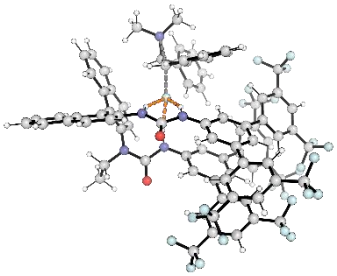

TS Cat 12-F-Azir-major5
+15.8 kJ/mol

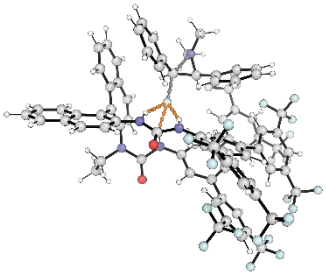

TS Cat 12-F-Azir-major6
+20.3 kJ/mol

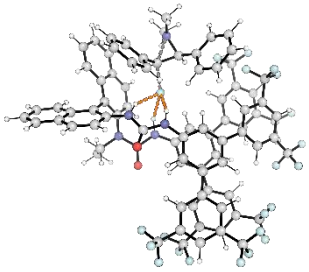

TS Cat 12-F-Azir-major7
+48.1 kJ/mol

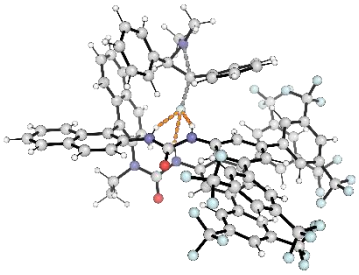

TS Cat 12-F-Azir-minor1
+6.7 kJ/mol

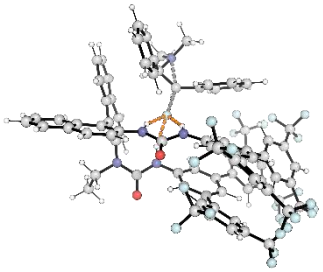

TS Cat 12-F-Azir-minor2
+9.3 kJ/mol

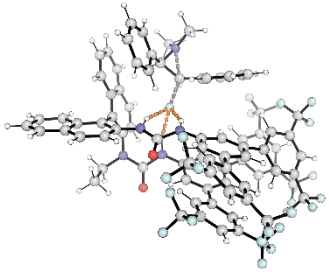

TS Cat 12-F-Azir-minor3
+10.4 kJ/mol

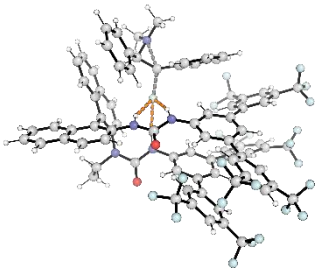

TS Cat 12-F-Azir-minor4
+14.4 kJ/mol

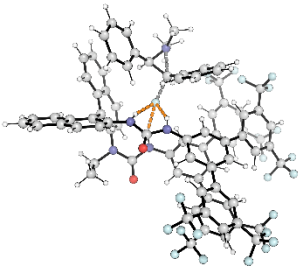

TS Cat 12-F-Azir-minor5
+18.6 kJ/mol

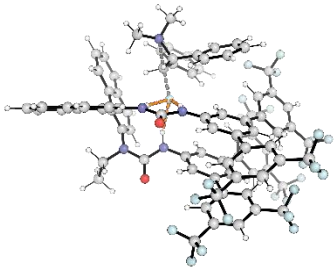

TS Cat 12-F-Azir-minor6
+19.2 kJ/mol

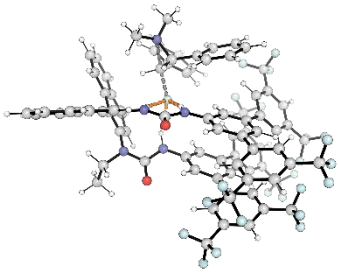

TS Cat 12-F-Azir-minor7
+20.5 kJ/mol

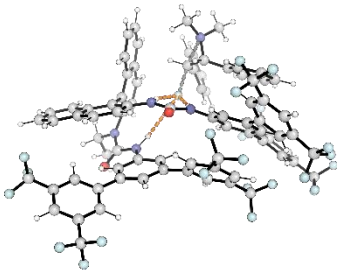

TS Cat 12-F-Azir-minor8
+46.4 kJ/mol

Figure 4.16: Transition state structures to major and minor product. Relative Gibbs free energies at 278.15 K. Own work adapted from Ref. 19.

Table 4.6**:** Key Geometric Parameters for TSs

TS	Freq. imag.	Key Distances / Å					Key Angles / º			
		C-F	C-N	H bond 1	H bond 2	H bond 3	H bond 3	α-Dihedral†	β-Dihedral†	Backbone
TS Cat 12-F-Azir-major1	-553.0	1.914	1.932	1.801	1.813	2.012	142.5	-34.5	-43.5	70.7
TS Cat 12-F-Azir-major2	-553.0	1.912	1.935	1.790	1.823	1.987	145.3	-34.2	-44.1	71.3
TS Cat 12-F-Azir-major3	-553.1	1.916	1.940	1.738	1.860	2.053	152.0	-27	-34.0	67.3
TS Cat 12-F-Azir-major4	-553.1	1.915	1.940	1.737	1.867	2.045	154.7	-27.2	-34.1	68.5
TS Cat 12-F-Azir-major5	-554.0	1.915	1.942	1.857	1.775	1.976	151.2	-21.2	-43.4	68.4
TS Cat 12-F-Azir-major6	-580.6	1.896	1.876	1.857	1.810	1.875	144.5	-86.3	-21.8	70.9
TS Cat 12-F-Azir-major7	-569.6	1.891	1.892	1.925	1.724	1.990	149.0	-72.5	-38.1	65.4
TS Cat 12-F-Azir-minor1	-567.3	1.908	1.904	1.887	1.739	2.115	139.9	-54.2	-46.4	67.5
TS Cat 12-F-Azir-minor2	-566.1	1.906	1.898	1.827	1.794	2.022	145.0	-49.8	-43.1	69.4
TS Cat 12-F-Azir-minor3	-565.5	1.904	1.899	1.820	1.799	1.992	148.3	-50.7	-43.0	70.4
TS Cat 12-F-Azir-minor4	-562.8	1.910	1.922	1.894	1.692	2.281	150.9	-42.6	-43.5	69.6
TS Cat 12-F-Azir-minor5	-570.7	1.890	1.895	1.837	1.785	2.061	145.7	-65.6	-42.2	67.5
TS Cat 12-F-Azir-minor6	-571.9	1.897	1.892	1.960	1.680	2.012	145.8	-71.8	37.4	68.7
TS Cat 12-F-Azir-minor7	-571.9	1.897	1.892	1.959	1.679	2.014	145.8	-71.8	37.5	68.8
TS Cat 12-F-Azir-minor8	-579.6	1.915	1.872	1.873	1.642	3.035	169.9	-78.3	26.0	112.3

4.3.2.4 Transition State Structure Analysis

The two highest contributing TSs – the lowest energy TS to major product, **TS Cat 12-F-Azir-major1**, and the lowest energy TS to minor product, **TS Cat 12-F-Azir-minor1** – are further analyzed to reveal the origins of enantioselectivity. These two TSs are herein referred to as $\mathbf{TS_{Major}}$ and $\mathbf{TS_{Minor}}$ respectively, with $\Delta\Delta G^{\ddagger}$ = -6.7 kJ/mol and $\Delta\Delta E^{\ddagger}$ = -7.1 kJ/mol. The key results are summarized in Figure 4.17, including the origins of substituent tolerance, and the origins of enantioselectivity.

In both TSs, catalyst **12** adopts a similar conformation – forming intramolecular π-π stacking interactions (Figure 4.18). Catalyst conformation is therefore not a significant factor in enantioselectivity. The π-π stacking interactions in general reduce the accessible conformers of the catalyst, making catalyst **12** less conformationally flexible that its analog, catalyst **8**, with smaller aromatic substituents.

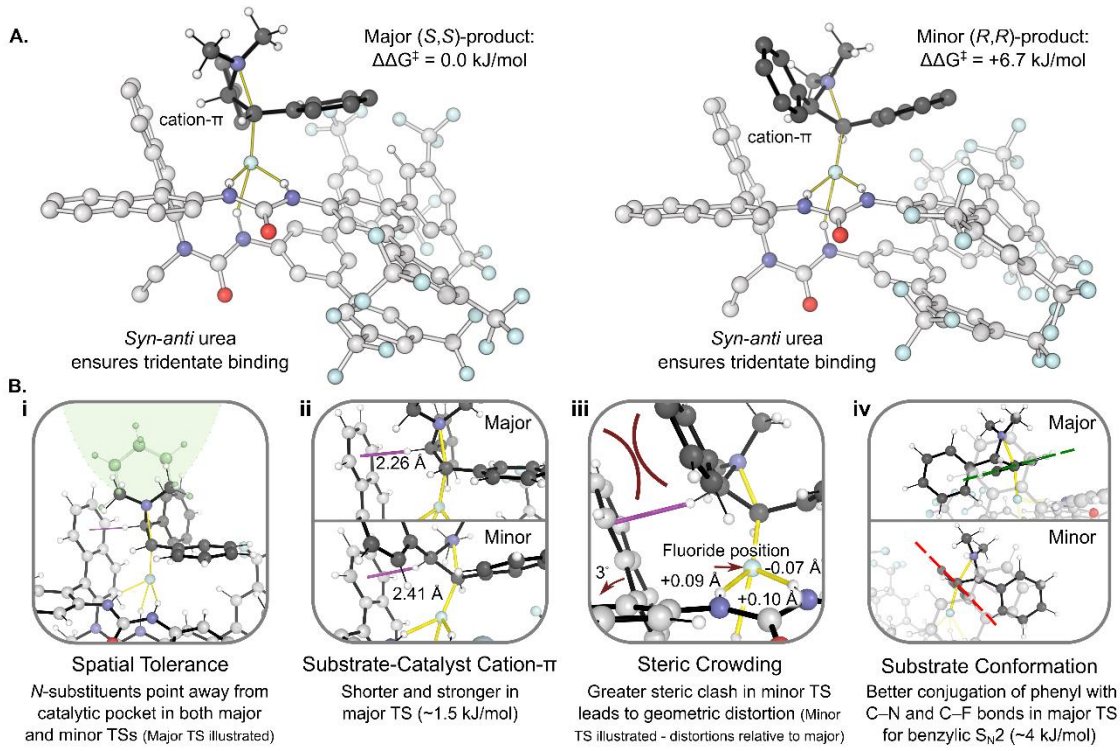

Figure 4.17: A) Geometries of the lowest energy TSs to major and minor product. B) Summary of the key factors influencing substrate tolerance and origins of enantioselectivity. Own work reproduced with permission, Copyright 2019 American Chemical Society.[19]

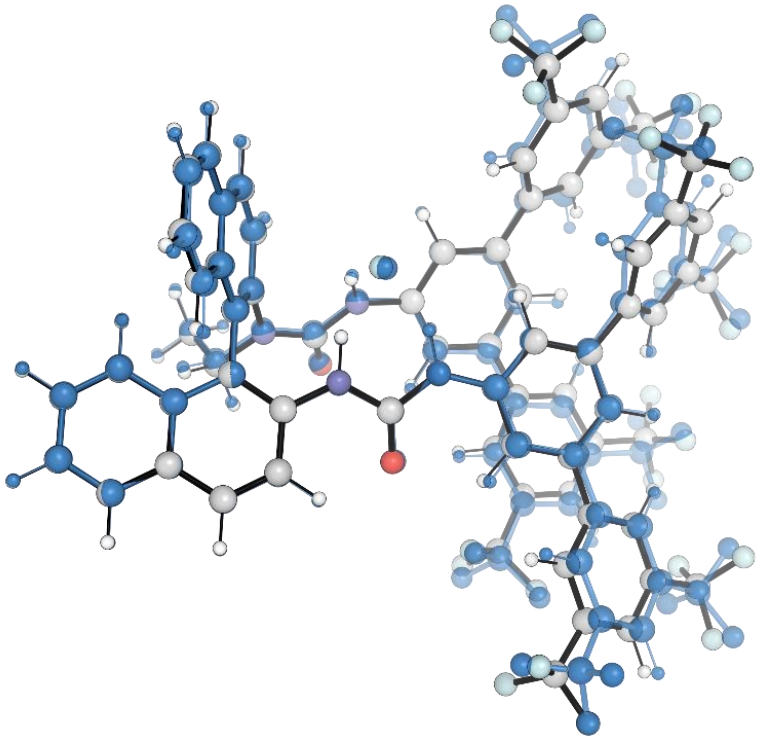

Figure 4.18: Superposition of catalyst geometry in **TS_{Major}** and **TS_{Minor}** (conventional coloring and blue coloring respectively) showing conformational similarity. Substrate is removed for clarity. Own work reproduced from Ref. 19.

Substrate conformation is a key factor, favoring conjugation of the α-phenyl ring with the forming and breaking bonds, as expected for a benzylic S_N2 substitution. The α-dihedral in **TS_{Major}** has a value of -34.5°, and in **TS_{Minor}** has a value of -54.2° – further from conjugation (Figure 4.17Biv). To estimate the energetic contribution of this conformational difference on enantioselectivity, a dihedral scan of the fluoride delivery TS with achiral Schreiner's urea was performed (**TS_F(cat)**, Figure 4.19). The scan estimates an energetic contribution of approximately 4 kJ/mol to $\Delta\Delta G^{\ddagger}$.

A quartic polynomial fit to the points -65° < dihedral < 25° identifies the favored α-dihedral as -27.6°, from which it can be inferred that **TS_{Major}** is approximately 7° from the optimum geometry, and **TS_{Minor}** approximately 27° away.

To further probe the contribution of α-phenyl conjugation, truncated models were used. Single point energy evaluation of the core TS unit (*i.e.* aziridinium ion + fluoride) reveals

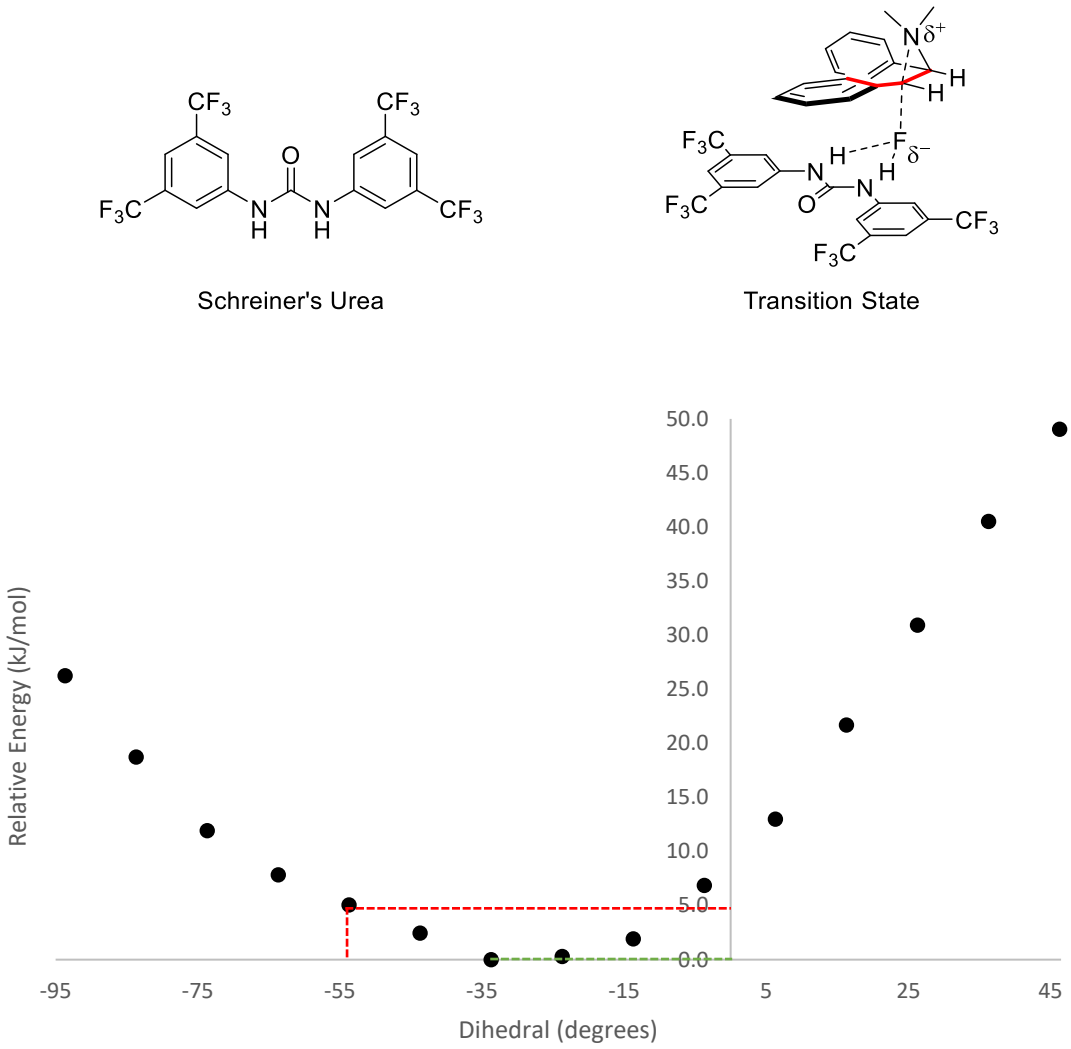

Figure 4.19: Energy plot for α-dihedral scan of aziridinium in fluoride delivery TS with Schreiner's urea catalyst. The dihedral angles for **TS$_{Major}$** and **TS$_{Minor}$** are illustrated in green and red respectively. Own work reproduced from Ref. 19.

that **TS$_{Major}$** is lower in energy by 4.9 kJ/mol, consistent with the dominant difference being α-phenyl group conjugation, when compared with the results of the dihedral scan. Additionally, replacing the α-phenyl ring with a methyl group in both TS substructures reduces the energy difference to 1.7 kJ/mol. **TS$_{Major}$** is looser than **TS$_{Minor}$** (both C–N and C–F distances longer), consistent with increased conjugation of the α-phenyl ring (Figure 4.20).

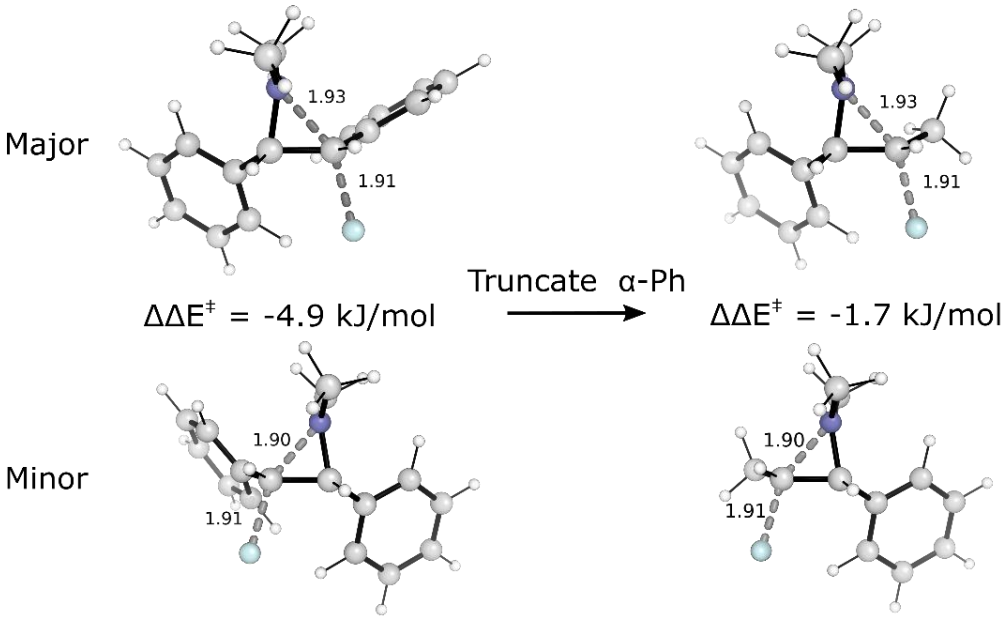

Figure 4.20: Substructure of **TS$_{Major}$** and **TS$_{Minor}$** formed from truncated models, with catalyst removed. LHS: Geometry in **TS$_{Major}$** is favored over **TS$_{Minor}$** by 4.9 kJ/mol. RHS: On truncating the α-phenyl group to methyl group, the energetic preference for **TS$_{Major}$** drops to 1.7 kJ/mol, demonstrating the α-phenyl's key role in stabilizing **TS$_{Major}$**. Own work reproduced from Ref. 19.

Non-covalent interactions help to orient the substrate in the catalytic pocket. Notably, the aziridinium ion forms a cation-π interaction with the catalyst backbone in both **TS$_{Major}$** and **TS$_{Minor}$**, with distances of 2.26 Å and 2.41 Å respectively (Figure 4.17Bii). The shorter distance in **TS$_{Major}$** is consistent with a stronger interaction. To quantify this, the BINAM aromatic group was truncated in both TSs and the single point energies evaluated, returning an approximate energy difference of 1.5 kJ/mol (Figure 4.21).

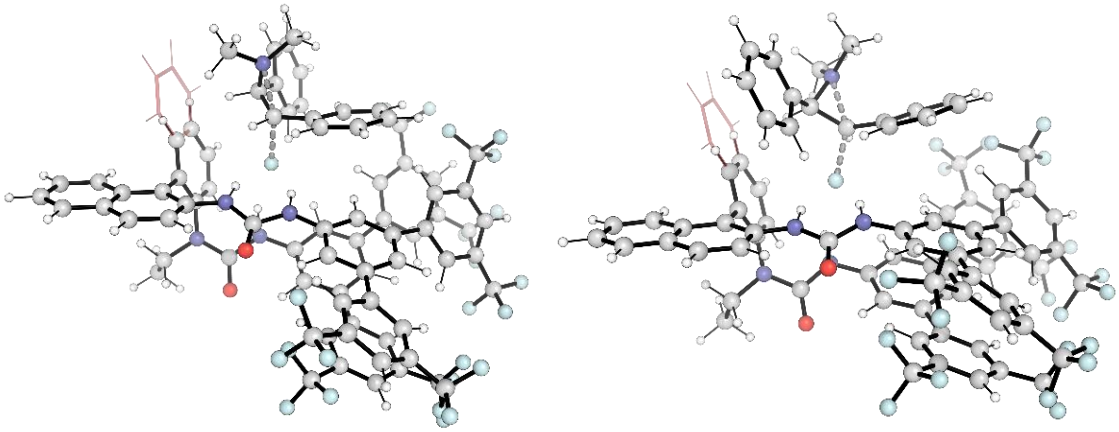

Figure 4.21: Estimated contribution of the cation-π interaction to enantioselectivity through truncated models. The removed aromatic ring is shown in red wireframe. The energy difference between the TSs is reduced from 7.1 kJ/mol to 5.5 kJ/mol implying a stronger cation-π interaction in **TS$_{Major}$** by approximately 1.5 kJ/mol. Own work reproduced from Ref. 19.

The extensive non-covalent interactions in the two TSs are plotted using the non-covalent interaction index, based on the optimization density, in Figure 4.22.

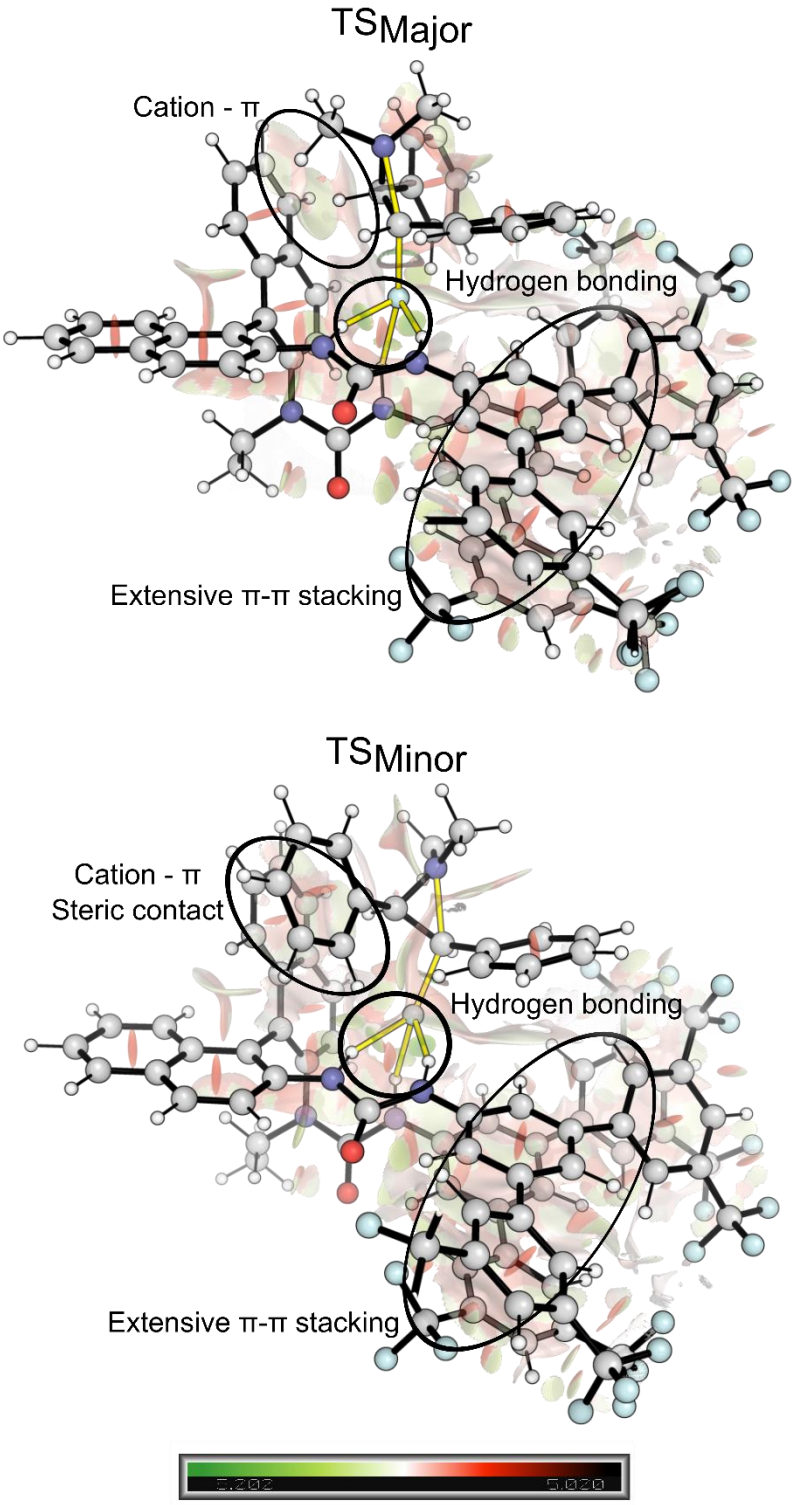

Figure 4.22: Non-covalent interaction plots for **TS$_{Major}$** (top) and **TS$_{Minor}$** (bottom). Key NCIs are annotated. Own work adapted from Ref. 19.

The lowest energy TSs in the ensemble all feature three hydrogen bonds between catalyst and fluoride, though hydrogen bond 3 varies widely in length and is often elongated. For the two lowest energy TSs, in **TS_{Minor}** fluoride is bound further from the catalyst BINAM backbone as evidenced by longer hydrogen bonds 1 and 3, as well as shorter hydrogen bond 2 (Figure 4.17Biii, Figure S22). Single point energy evaluation of the TSs with substrate removed (*i.e.* catalyst-fluoride complexes) show that **TS_{Major}** has slightly favored fluoride binding (energy difference of 2.5 kJ/mol).

Evidence of increased steric clash in **TS_{Minor}** comes from analysis of the geometry over the intrinsic reaction coordinate (IRC) pathway. The IRC pathway to major and minor product are herein referred to as **IRC_{Major}** and **IRC_{Minor}** respectively. Key distances and angles are plotted against a physically meaningful projection of the IRC (Figure 4.23). The IRC falls into two key regions: Region 1: -0.9 < IRC < 0.9, during which the main bond forming and breaking takes place, Region 2: IRC > 0.9, primarily describing substrate relaxation, where the projection of the IRC becomes less physically meaningful. The IRC plot begins with fluoride aligned with the C–N σ*, at approximately double the equilibrium bond length. The plot ends with C–F bond fully formed and C–N bond fully broken, and is augmented by plotting of points corresponding to the optimized product complex geometry.

The main points can be summarized as follows: i) **IRC_{Major}** is looser than **IRC_{Minor}** over region 1 (*i.e.* longer C–N and C–F distances), consistent with greater conjugation of the α-phenyl ring. The later position of **TS_{Major}** results in C–F bonds formed to a similar extent at the respective TSs. ii) Early along the IRC, all hydrogen bonds have roughly equal length, however hydrogen bond 3 elongates quickly along both pathways, reaching 2.11 Å in **TS_{Minor}**. iii) Fluoride moves away from the BINAM backbone along **IRC_{Minor}**,

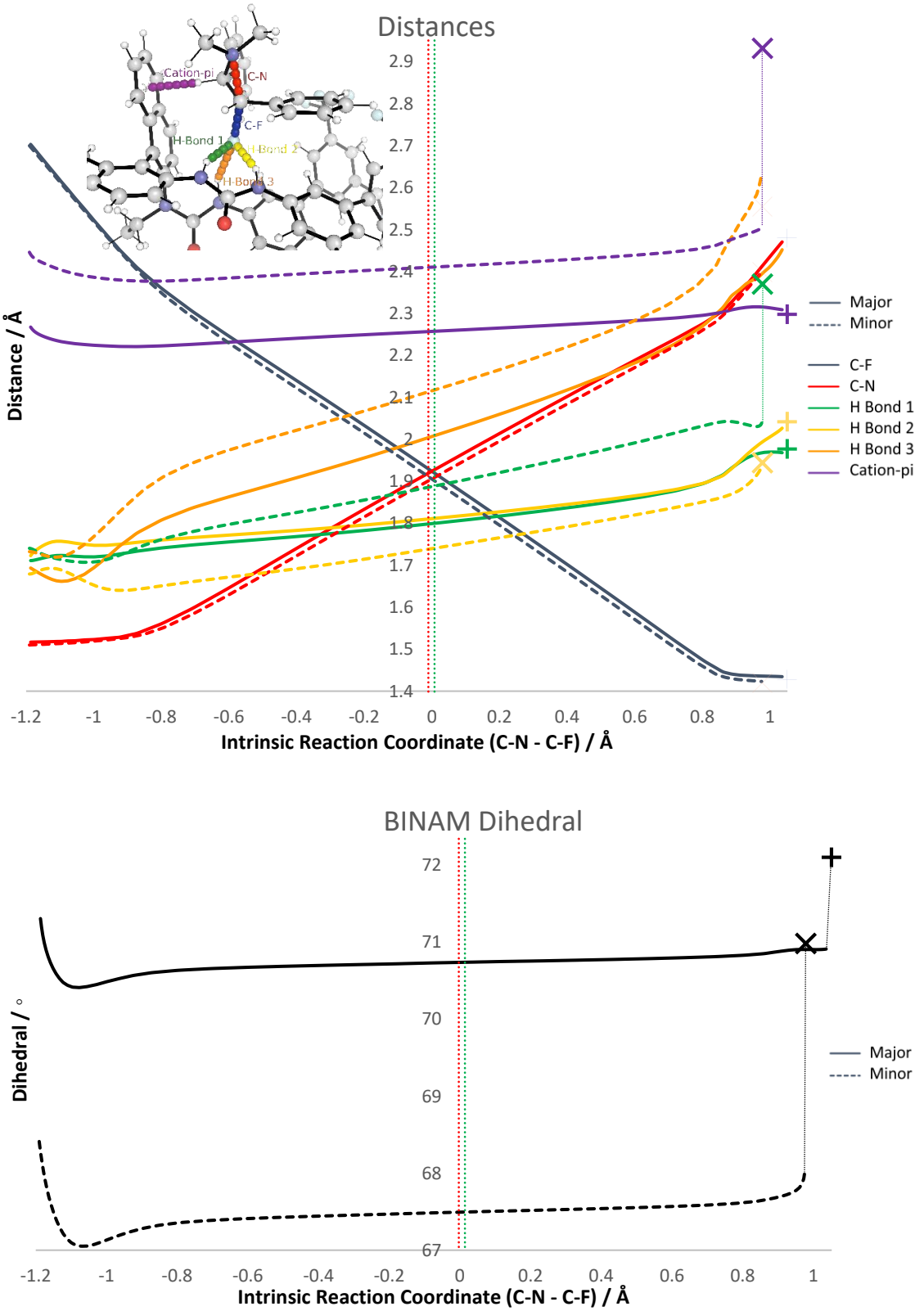

Figure 4.23: Plots of key geometric parameters over the IRC pathway for **TS$_{Major}$** (solid) and **TS$_{Minor}$** (dashed). The positions of the two TSs are indicated by green (**TS$_{Major}$**) and red (**TS$_{Minor}$**) vertical dashed lines. The geometries of product complexes are also plotted - (major: +, minor: X) – the sometimes large vertical displacement of these points should not be interpreted as an abrupt change in geometry. Own work reproduced from Ref. 19.

evidenced by elongation of hydrogen bond 1, and relative shortening of hydrogen bond 2. Hydrogen bond 1 is broken in the product complex. iv) The cation-π interaction in **IRC$_{Major}$** is consistently shorter than in **IRC$_{Minor}$** in region 1. Both cation-π interactions elongate as the aziridinium charge is neutralized, transitioning to a CH-π interaction. In region 2, the CH-π in **IRC$_{Minor}$** elongates significantly, indicating product moving away from the BINAM aromatic rings, whereas it remains constant length in **IRC$_{Major}$**. v) The BINAM dihedral angle is consistently smaller along **IRC$_{Minor}$**, indicating a more open catalytic site. As bond forming begins, the BINAM angle decreases along both **IRC$_{Major}$** and **IRC$_{Minor}$**. In region 2, once bonds are formed, the dihedrals increase, but to a much larger extent for **IRC$_{Minor}$** over **IRC$_{Major}$** (3.5^{o} and 1.5^{o} respectively).

Points iii-v are consistent with greater steric congestion in **TS$_{Minor}$**, that builds up over the IRC to accommodate the substrate, before relaxing in the product complex.

Experimentally, the transformation demonstrates good substituent tolerance on aziridinium nitrogen, supporting many pharmaceutically relevant motifs. The identity of these substituents typically has little effect on enantioselectivity (92:8 to 97:3 e.r. for 11 substrates **3-3i**, and **5,** with CsF and KF), corresponding to $\Delta\Delta G^{\ddagger}$ values of approximately 6 - 9 kJ/mol. The majority of which fall within 94:6 to 96:4 e.r., corresponding to $\Delta\Delta G^{\ddagger}$ values of approximately 7 - 8 kJ/mol. The low range of $\Delta\Delta G^{\ddagger}$ values is consistent with the transition state structure models, where the nitrogen substituents project out of the catalytic pocket into solvent in both TSs, resulting in similar $\Delta\Delta G^{\ddagger}$ despite the diversity of substituents (Figure 4.17bi). Substitution on the aromatic rings themselves leads to larger changes in enantioselectivity (9 substrates **5-5h**, 90:10 to 97.5:2.5 e.r. with CsF and KF), consistent with the TSs, where the substituents of these rings are in closer proximity to the catalyst and likely to influence enantioselectivity.

Several cycloalkyl substrates, not derived from stilbene, were also fluorinated experimentally (**14-14b,** Figure 4.7). Enantioselectivity is poor compared to stilbene derived substrates, ranging from 74.5:25.5 to 85.5:14.5 e.r. and results in a major product of opposite absolute configuration, as determined by derivatization. The TSs with cycloalkyl substrates cannot be directly inferred from those of the stilbene derived substrate, **1**, due to the importance of the stilbene rings in determining the substrate docking pose. To investigate the key differences between the two substrate classes, the two lowest energy TSs with stilbene substrate were reoptimized after converting the substrate to the cyclopentene derived analog (**19**). The resulting TSs are shown in Figure 4.24.

The significant change in substrate docking pose is unsurprising given the established role of the stilbene substrate's aromatic rings in returning half of $\Delta\Delta G^{\ddagger}$, and results in the Gibbs free energies of the two TSs swapping ($\Delta\Delta G^{\ddagger}$ = 1.6 kJ/mol, corresponding to 66:34 e.r.). There is, of course, no good reason why these two TSs remain the lowest two TSs for the cyclopentene substrate, which could only be determined through full conformational sampling. Additionally, the energy difference between the TSs is too small to say, with reasonable certainty, which is lower in energy. It is, however, demonstrated with certainty that the stilbene rings are important in influencing enantioselectivity and substrate docking pose to a level where selectivity may be reversed. Further analysis of the TSs and their application to design of improved catalysts is undertaken in Chapter 5.

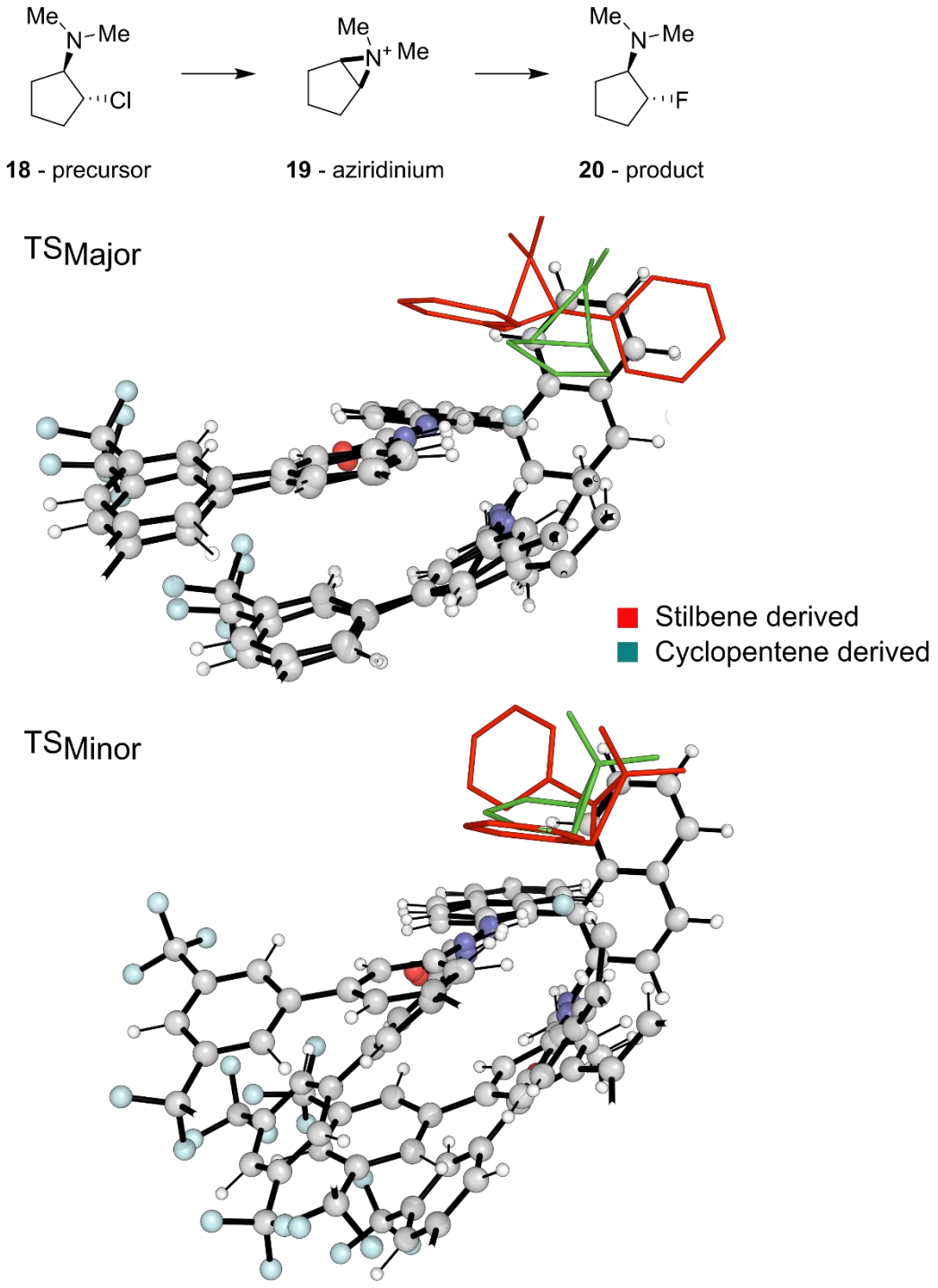

Figure 4.24: Transition state structures optimized with cyclopentene derived aziridinium ion (green). TSs are superimposed with the TSs with stilbene derived aziridinium ion (red) that were used as starting points. Catalyst geometry superimposes almost perfectly in both cases (ball and stick), whereas substrate shifts position (wireframe).

4.3.3 Comparison with the Desymmetrization of Episulfonium Ions

4.3.3.1 Mechanism

Aziridinium ions and episulfonium ions have the same connectivity, except sulfur is swapped for nitrogen, which brings an additional alkyl group. Using stilbene derived ions as examples, the C–N bonds in the aziridinium ion are shorter than the C–S bond in the episulfonium ion (1.50 Å compared to 1.83 Å), resulting in a more compact ion – further, the forming C–F bond distance is shorter in the fluoride delivery TSs for aziridinium ions (2.00 Å compared to 2.24 Å with free fluoride), leading to an overall more compact TS unit. Specifically for stilbene derived ions, the aziridinium has reduced conformational freedom due to the additional *syn* alkyl group on nitrogen clashing with the phenyl rings, restricting rotation.

Formation of both the aziridinium and episulfonium ions in the HB PTC reactions proceeds via similar auto-ionization barriers. With bromide leaving group, episulfonium ion formation proceeds with barrier of 90 kJ/mol and formation of the aziridinium ion with barrier of 87 kJ/mol. The situation with chloride leaving group is similar, with barriers of 104 kJ/mol and 99 kJ/mol respectively. The thermodynamic stability of the ion pairs formed, however, differ greatly with episulfonium-bromide ion pair having a Gibbs free energy relative to precursor of +48 kJ/mol, whereas with the aziridinium ion it is +9 kJ/mol. With chloride leaving group, the ion pairs have relative energies of 60 kJ/mol and 24 kJ/mol respectively. The marked difference in relative ion pair stability originates from the greater ability of the nitrogen lone pair to stabilize the positive charge, over sulfur (Figure 4.25a).

This behavior is similar for the fluorinated product, when viewed from the perspective of fluoride loss. Relative to the fluorinated product, the fluoride ion pairs have Gibbs free

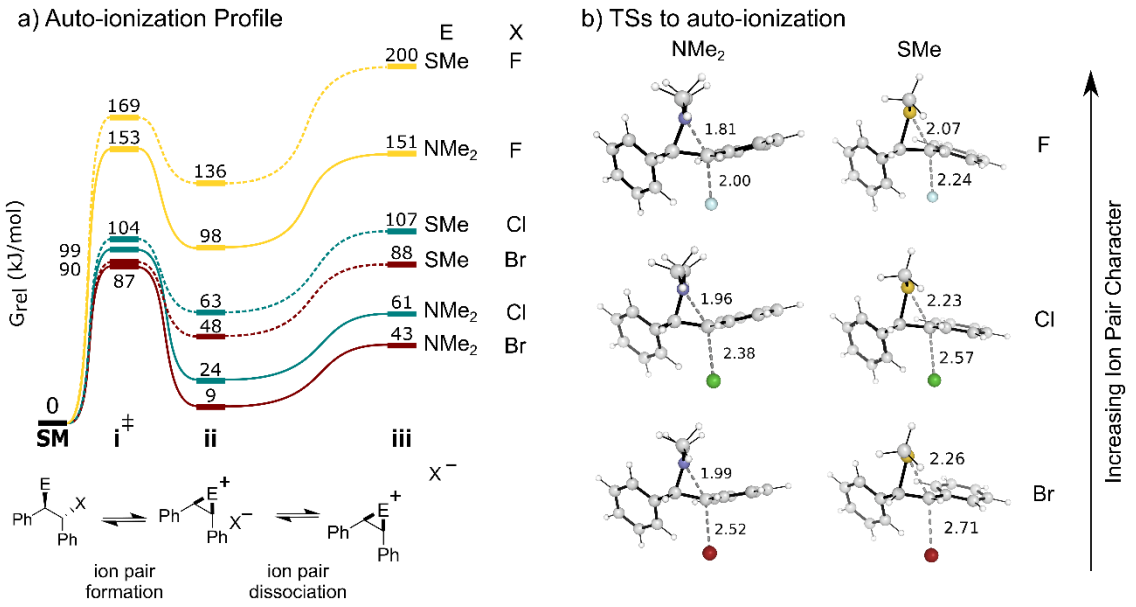

Figure 4.25: Comparison of the auto-ionization behavior of stilbene derived episulfonium and aziridinium precursors with halogen leaving groups. Note that ionization with fluoride leaving group is the reverse reaction of fluorination, described in this work. a) Gibbs free energy profile for auto-ionization and separation of the formed ion pair in DCM, 298.15 K, 1M. Connecting lines are schematic. b) Corresponding TSs for auto-ionization, showing increasing ion pair character as leaving group is changed from bromide, through chloride, to fluoride.

energies of +136 kJ/mol and +98 kJ/mol for episulfonium and aziridinium ions respectively. The barrier to formation of the ion pairs from the fluorinated products are 169 kJ/mol and 153 kJ/mol respectively, showing a greater difference between the barriers than with chloride and bromide leaving groups. This is consistent with the Hammond postulate – changing leaving group from Br to Cl to F leads to a less stable ion pair, thus the TSs adopt increasing ion pair character, where there is discrimination between the stabilization afforded by sulfur and nitrogen. For the aziridinium ion, the C–N distance in the TSs with Br, Cl and fluoride are 1.99 Å, 1.96 Å and 1.81 Å, showing a much more developed bond with fluoride over the other halogens. Similarly, for the episulfonium ion, the C–S distances are 2.26 Å, 2.23 Å and 2.07 Å respectively (Figure 4.25b).

Considering the reverse process of fluoride delivery, the Gibbs free energy barrier from the fluoride ion pair to the fluoride delivery TS is much larger for the aziridinium ion (55 kJ/mol) over the episulfonium ion (33 kJ/mol). Further, a larger proportion of the barrier for the aziridinium ion occurs from bond forming/breaking – 28 kJ/mol compared to 7 kJ/mol – largely accounting for this difference.

Apart from the relative stabilities of the ion pairs, the Gibbs free energy profiles for the complete HB PTC mechanism with episulfonium ions and aziridinium ions are qualitatively similar, with the largest differences between catalyzed and uncatalyzed processes occurring in steps concerning anion-transport and phase-transfer.

4.3.3.2 Enantioselectivity

The enantioselective desymmetrization of episulfonium ions (Chapter 3) and of aziridinium ions (this chapter) are undertaken under similar HB PTC conditions, with tricoordinate alkylated urea catalysts, facilitating comparison between the two. However, it should be noted that the solvents (CH_2Cl_2 vs. $CHCl_3$) and catalyst are slightly different.

Despite using an unbiased conformational sampling protocol, the lowest energy TSs for desymmetrization of episulfonium ions and aziridinium ions bear striking similarity (Figure 4.26). This is due to the key factors that determine substrate docking pose and TS energy being unchanged – broad catalyst conformation, including the position of the three hydrogen bond donors, and the shape of the stilbene derived substrate, characterized by the twist of the aromatic rings.

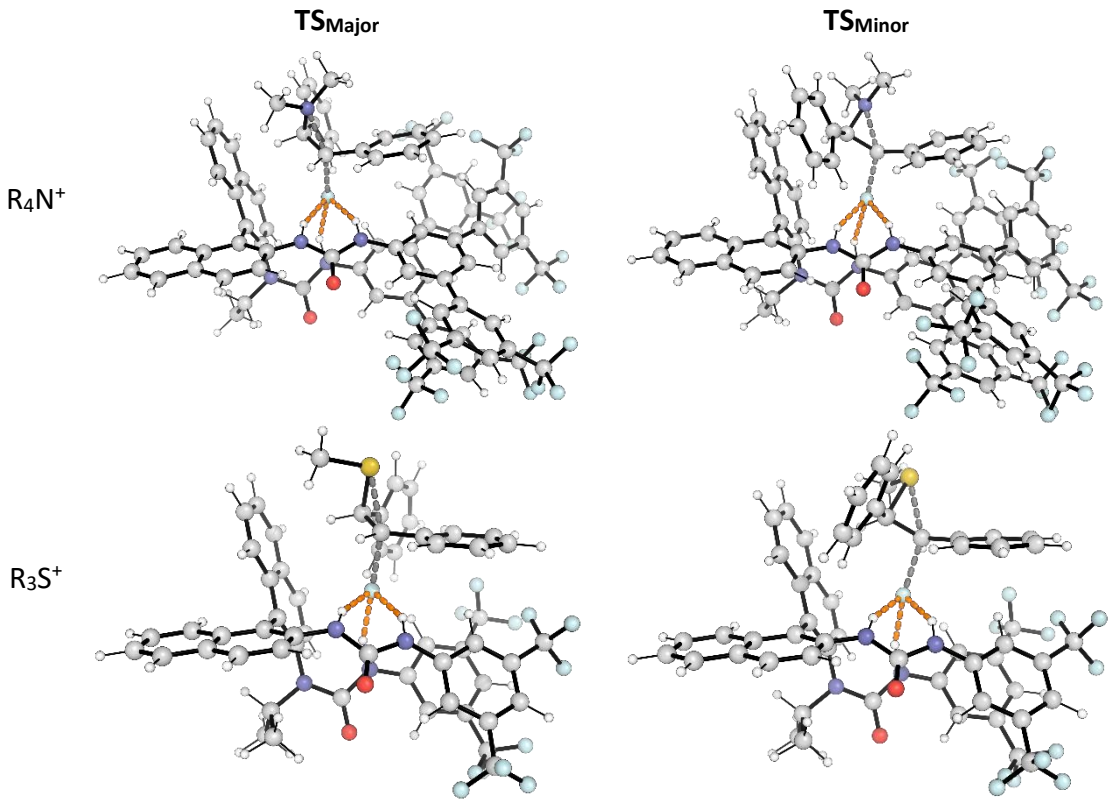

Figure 4.26: Lowest energy transition state structures to major and minor product with aziridinium and episulfonium ions, with respective catalysts in dichloromethane (aziridinium TSs were reoptimized). Despite the different catalysts and substrates, the transition state structures are clearly analogous in geometry.

The preference of the substrate α-aryl ring for conjugation with the forming and breaking bonds is similar for episulfonium ions and aziridinium ions and contributes roughly half of $\Delta\Delta G^{\ddagger}$ in both cases. An α-phenyl dihedral scan of **TS_F(Cat)** in dichloromethane, with achiral Schreiner's urea is shown in Figure 4.27 for both cations. The stability afforded through conjugation of the α-phenyl ring is similar in both cases close to the minimum of the curve. At larger rotations, the energy of the aziridinium starts to exceed that of the episulfonium ion due to steric clash of the phenyl ring with the additional *syn* nitrogen substituent.

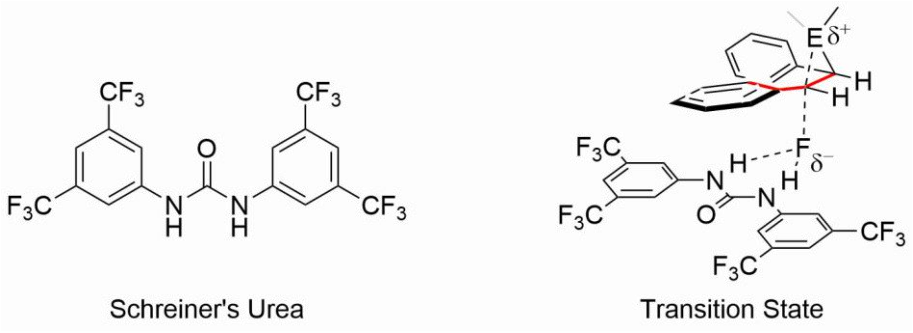

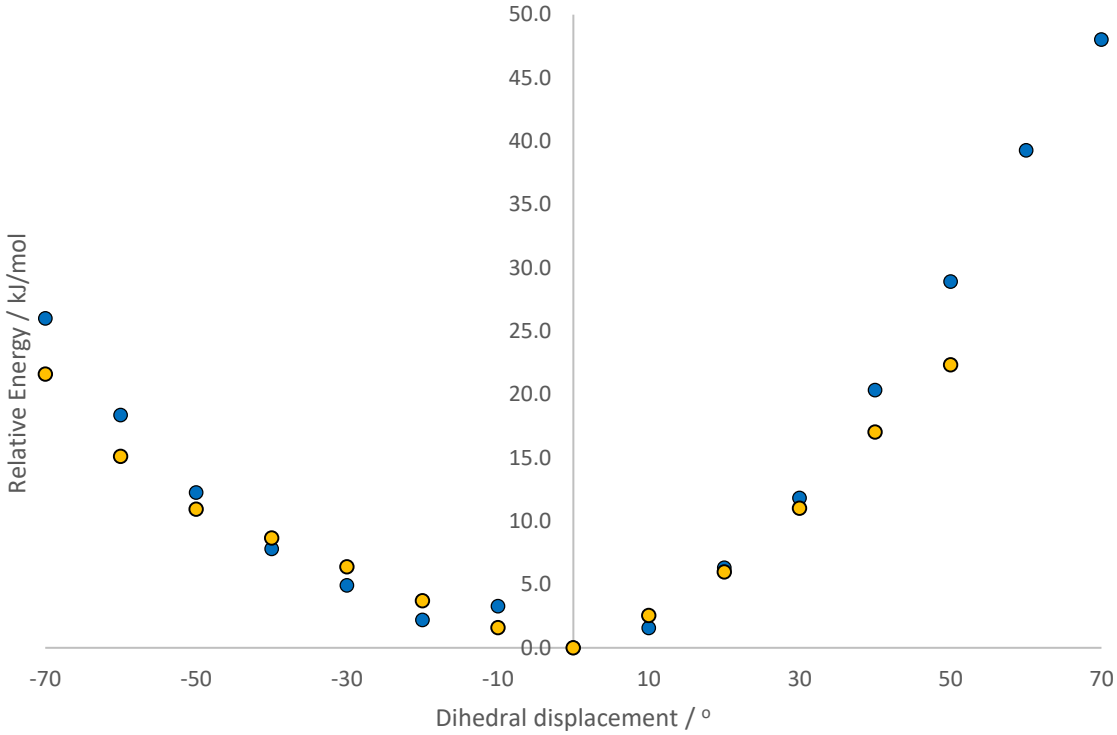

Figure 4.27: Energy plot for the α-dihedral of stilbene derived episulfonium (yellow) and aziridinium (blue) ions. Angle is plotted as the displacement of the dihedral angle from their respective minima.

Despite the superficial similarity of the TSs, the remainder of the origins of enantioselectivity for the two cations is different. In the case of the aziridinium ion, there is evidence of steric clash in the minor TS, supported by the difference in key distances between **IRC$_{Major}$** and **IRC$_{Minor}$** over the IRC. In contrast, the two IRCs for the episulfonium ion have remarkably similar distances across the IRC (Figure 4.28).

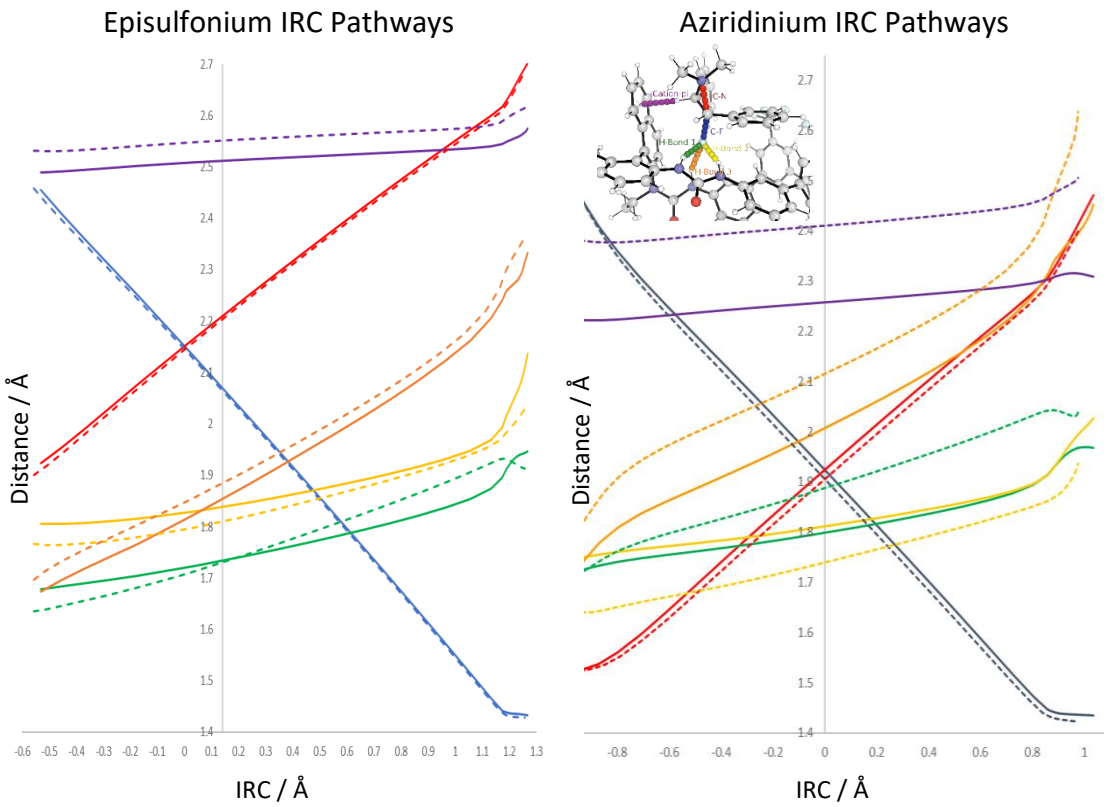

Figure 4.28: Comparison of distances over the intrinsic reaction coordinate pathways for major (solid line) and minor (dashed line) pathways with episulfonium (Left) and aziridinium (Right) ions. Note that the catalyst and solvent are slightly different and that the scales on the x-axis are not directly comparable.

The x-coordinates of the IRC pathways for aziridinium ion and episulfonium ion cannot be compared directly, however broad comparisons can be made over the region of C–F bond formation. The cation-π interactions are shorter in both cases with the aziridinium ion over the episulfonium ions, likely down to the smaller size of the N/S substituents in the aziridinium, from the shorter C–N bond. Notably, the aziridinium IRC_{Major} cation-π is much shorter than the other three. A consistent hypothesis is that the S-Me group prevents formation of a short cation-π with episulfonium ions – this is not the case with aziridinium ions, however only in the major can this short cation-π actually form. The closer approach of the aziridinium ion leads to greater differences in bond distances between the major and minor pathways than is seen with episulfonium ions.

4.4 Conclusion

We have applied the concept of hydrogen bonding phase-transfer catalysis to the enantioselective desymmetrization of aziridinium ions using potassium fluoride as fluorine source, through computation (author's work) and experiment (co-workers' work). Computation of the Gibbs free energy profile for the HB PTC mechanism reveals that the auto-ionization of aziridinium ion precursors with bromide or chloride leaving group is plausible at room temperature, forming an ion pair only slightly less thermodynamically favored than the precursor, at +9 kJ/mol with bromide leaving group. Auto-ionization is favored over catalyst involvement, however the barriers are within computational error. The largest differences between the catalyzed and uncatalyzed pathways occurs during the steps describing anion-transport and phase-transfer, supporting the operation of the HB PTC mechanism. Once the reactive azetidinium-fluoride ion pair is formed, the barrier to fluorination is moderate at 70 kJ/mol when mediated by Schreiner's urea.

Computation provides insight into why the use of potassium fluoride is significantly more challenging than cesium fluoride, by comparing the energetics of solubilization in the presence and absence of catalyst. Hydrogen bonding of the metal fluoride ion pair by catalyst affords significant thermodynamic stabilization, of around 35 kJ/mol, enhancing solubility. With cesium fluoride, solubilization of the ion pair becomes roughly thermodynamically neutral, consistent with experiments that demonstrate that the catalyst can solubilize this salt.

MD simulations demonstrate that the chiral, alkylated, tricoordinate BINAM-based urea catalyst forms a stable and persistent ion pair with fluoride, in accordance with the computational design of this class of catalysts for HB PTC. Alkylation of the catalyst,

compared to the unalkylated tetracoordinate catalyst, leads to a greater improvement in enantioselectivity than was seen with episulfonium substrates. An MD based, unbiased sampling protocol is employed to generate the ensemble of TSs from which enantioselectivity is rationalized. This ensemble is consistent with experiment in both the absolute configuration of the product and the degree of enantioinduction. Approximately half of enantioselectivity originates from substrate conformational preference, with stilbene derived substrates favoring conjugation of the α-aryl ring with the forming and breaking bonds. The rest occurs from increased steric clash in the minor TS and higher strength non-covalent interactions in the major TS. The importance of substrate conformational preference in enantioselectivity underpins the ubiquity of stilbene derived substrates for enantioselective HB PTC fluorinations to this point. Reoptimization of the lowest energy TSs with a cyclopentene derived aziridinium ion shows significant change in substrate docking pose and is accompanied by a swap in Gibbs free energy ordering, highlighting reasons behind the inversion of enantioselectivity seen experimentally.

The chapter concludes with a detailed comparison of the behavior of aziridinium and episulfonium ions. Whilst there are many similarities, there are some differences arising from the greater ability of nitrogen to stabilize the positive charge, notably the much-enhanced thermodynamic stability of the ion and ion pairs from auto-ionization relative to the halide precursors. With bromide and chloride leaving groups, this has relatively little influence on the kinetic barrier to ion pair formation, as the TSs have little ion pair character. With fluorine as a leaving group, the ion pair is much higher in energy, and the TS is more ion pair-like, with much larger kinetic barrier to formation. As the TSs have more ion pair character, the difference between episulfonium and aziridinium barrier heights is increased over that seen with bromide and chloride leaving groups. With

regards to the asymmetric reaction, both stilbene derived episulfonium and aziridinium ions demonstrate a similar preference for conjugation of the α-phenyl ring with the forming and breaking bonds, however, the conformational flexibility of the aziridinium ion is reduced due to steric clash of the additional *syn* alkyl group on nitrogen with the substrate's aryl rings. Additionally, whilst distances along the IRC pathways to major and minor product show similar behavior in the case of the episulfonium ion, the two pathways with aziridinium ion have significant differences consistent with steric congestion on the pathway to minor product, building up towards the TS.

4.5 References

(1) Percy, J. M. Product Class 10: β-Fluoroamines. In *Science of Synthesis, 34: Category 5, Compounds with One Carbon Heteroatom Bond*; 2006; pp 379–386.

(2) Briggs, C. R. S.; O'Hagan, D.; Howard, J. A. K.; Yufit, D. S. The C-F Bond as a Tool in the Conformational Control of Amides. *J. Fluor. Chem.* **2003**, *119*, 9–13.

(3) Morgenthaler, M.; Schweizer, E.; Hoffmann-Röder, A.; Benini, F.; Martin, R. E.; Jaeschke, G.; Wagner, B.; Fischer, H.; Bendels, S.; Zimmerli, D.; Schneider, J.; Diederich, F.; Kansy, M.; Müller, K. Predicting and Tuning Physicochemical Properties in Lead Optimization: Amine Basicities. *ChemMedChem* **2007**, *2*, 1100–1115.

(4) Sato, K.; Hoshino, K.; Tanaka, M.; Hayakawa, I.; Osada, Y. Antimicrobial Activity of DU-6859, a New Potent Fluoroquinolone, against Clinical Isolates. *Antimicrob. Agents Chemother.* **1992**, *36*, 1491–1498.

(5) Murray, T. K.; Whalley, K.; Robinson, C. S.; Ward, M. A.; Hicks, C. A.; Lodge, D.; Vandergriff, J. L.; Baumbarger, P.; Siuda, E.; Gates, M.; Ogden, A. M.; Skolnick, P.; Zimmerman, D. M.; Nisenbaum, E. S.; Bleakman, D.; O'Neill, M. J. LY503430, a Novel α-Amino-3-Hydroxy-5-Methylisoxazole-4-Propionic Acid Receptor Potentiator with Functional, Neuroprotective and Neurotrophic Effects in Rodent Models of Parkinson's Disease. *J. Pharmacol. Exp. Ther.* **2003**, *306*, 752–762.

(6) Nag, S.; Lehmann, L.; Heinrich, T.; Thiele, A.; Kettschau, G.; Nakao, R.; Gulyás, B.; Halldin, C. Synthesis of Three Novel Fluorine-18 Labeled Analogues of L-Deprenyl for Positron Emission Tomography (PET) Studies of Monoamine Oxidase B (MAO-B). *J. Med. Chem.* **2011**, *54*, 7023–7029.

(7) Sofia, M. J.; Bao, D.; Chang, W.; Du, J.; Nagarathnam, D.; Rachakonda, S.; Reddy, P. G.; Ross, B. S.; Wang, P.; Zhang, H. R.; Bansal, S.; Espiritu, C.; Keilman, M.; Lam, A. M.; Steuer, H. M. M.; Niu, C.; Otto, M. J.; Furman, P. A. Discovery of a β-D-2'-Deoxy-2'-α-Fluoro-2′-β-C-Methyluridine Nucleotide Prodrug (PSI-7977) for the Treatment of Hepatitis C Virus. *J. Med. Chem.* **2010**, *53*, 7202–7218.

(8) Guan, Y. Q.; Han, Z.; Li, X.; You, C.; Tan, X.; Lv, H.; Zhang, X. A Cheap Metal for a Challenging Task: Nickel-Catalyzed Highly Diastereo- and Enantioselective Hydrogenation of Tetrasubstituted Fluorinated Enamides. *Chem. Sci.* **2019**, *10*, 252–256.

(9) Vaithiyanathan, V.; Kim, M. J.; Liu, Y.; Yan, H.; Song, C. E. Direct Access to Chiral β-Fluoroamines with Quaternary Stereogenic Center through Cooperative Cation-Binding Catalysis. *Chem. Eur. J.* **2017**, *23*, 1268–1272.

(10) Vara, B. A.; Johnston, J. N. Enantioselective Synthesis of β-Fluoro Amines via β-Amino α-Fluoro Nitroalkanes and a Traceless Activating Group Strategy. *J. Am. Chem. Soc.* **2016**, *138*, 13794–13797.

(11) Trost, B. M.; Saget, T.; Lerchen, A.; Hung, C. I. Catalytic Asymmetric Mannich Reactions with

Fluorinated Aromatic Ketones: Efficient Access to Chiral β-Fluoroamines. *Angew. Chem. Int. Ed.* **2016**, *55*, 781–784.
(12) Cosimi, E.; Engl, O. D.; Saadi, J.; Ebert, M. O.; Wennemers, H. Stereoselective Organocatalyzed Synthesis of α-Fluorinated β-Amino Thioesters and Their Application in Peptide Synthesis. *Angew. Chem. Int. Ed.* **2016**, *55*, 13127–13131.
(13) Lu, D. F.; Zhu, C. L.; Sears, J. D.; Xu, H. Iron(II)-Catalyzed Intermolecular Aminofluorination of Unfunctionalized Olefins Using Fluoride Ion. *J. Am. Chem. Soc.* **2016**, *138*, 11360–11367.
(14) Suzuki, S.; Kamo, T.; Fukushi, K.; Hiramatsu, T.; Tokunaga, E.; Dohi, T.; Kita, Y.; Shibata, N. Iodoarene-Catalyzed Fluorination and Aminofluorination by an Ar-I/HF·pyridine/MCPBA System. *Chem. Sci.* **2014**, *5*, 2754–2760.
(15) O'Reilly, M. C.; Lindsley, C. W. A General, Enantioselective Synthesis of β- And γ-Fluoroamines. *Tetrahedron Lett.* **2013**, *54*, 3627–3629.
(16) Kong, W.; Feige, P.; De Haro, T.; Nevado, C. Regio- and Enantioselective Aminofluorination of Alkenes. *Angew. Chem. Int. Ed.* **2013**, *52*, 2469–2473.
(17) Fadeyi, O. O.; Lindsley, C. W. Rapid, General Access to Chiral β-Fluoroamines and β,β-Difluoroamines via Organocatalysis. *Org. Lett.* **2009**, *11*, 943–946.
(18) Kalow, J. A.; Doyle, A. G. Enantioselective Fluoride Ring Opening of Aziridines Enabled by Cooperative Lewis Acid Catalysis. *Tetrahedron* **2013**, *69*, 5702–5709.
(19) Pupo, G.; Vicini, A. C.; Ascough, D. M. H.; Ibba, F.; Christensen, K. E.; Thompson, A. L.; Brown, J. M.; Paton, R. S.; Gouverneur, V. Hydrogen Bonding Phase-Transfer Catalysis with Potassium Fluoride: Enantioselective Synthesis of β-Fluoroamines. *J. Am. Chem. Soc.* **2019**, *141*, 2878–2883.
(20) Haynes, W. M.; Lide, D. R.; Bruno, T. J. *CRC Handbook of Chemistry and Physics*, 97th editi.; Taylor & Francis Inc., 2017.
(21) Pupo, G.; Ibba, F.; Ascough, D. M. H.; Vicini, A. C.; Ricci, P.; Christensen, K. E.; Pfeifer, L.; Morphy, J. R.; Brown, J. M.; Paton, R. S.; Gouverneur, V. Asymmetric Nucleophilic Fluorination under Hydrogen Bonding Phase-Transfer Catalysis. *Science* **2018**, *360*, 638–642.
(22) Bickelhaupt, F. M.; Houk, K. N. Analyzing Reaction Rates with the Distortion/Interaction-Activation Strain Model. *Angew. Chem. Int. Ed.* **2017**, *56*, 10070–10086.
(23) Van Zeist, W. J.; Koers, A. H.; Wolters, L. P.; Bickelhaupt, F. M. Reaction Coordinates and the Transition-Vector Approximation to the IRC. *J. Chem. Theory Comput.* **2008**, *4*, 920–928.
(24) Maji, R.; Mallojjala, S. C.; Wheeler, S. E. Chiral Phosphoric Acid Catalysis: From Numbers to Insights. *Chem. Soc. Rev.* **2018**, *47*, 1142–1158.
(25) Maji, R.; Champagne, P. A.; Houk, K. N.; Wheeler, S. E. Activation Mode and Origin of Selectivity in Chiral Phosphoric Acid-Catalyzed Oxacycle Formation by Intramolecular Oxetane Desymmetrizations. *ACS Catal.* **2017**, *7*, 7332–7339.
(26) Seguin, T. J.; Wheeler, S. E. Electrostatic Basis for Enantioselective Brønsted-Acid-Catalyzed Asymmetric Ring Openings of Meso-Epoxides. *ACS Catal.* **2016**, *6*, 2681–2688.
(27) Nguyen, Q. N. N.; Lodewyk, M. W.; Bezer, S.; Gagné, M. R.; Waters, M. L.; Tantillo, D. J. Effects of Helix Macrodipole and Local Interactions on Catalysis of Acyl Transfer by α-Helical Peptides. *ACS Catal.* **2015**, *5*, 1617–1622.
(28) van der Spoel, D.; van Maaren, P. J.; Caleman, C. GROMACS Molecule & Liquid Database. *Bioinformatics* **2012**, *28*, 752–753.
(29) Chen, S.; Yi, S.; Gao, W.; Zuo, C.; Hu, Z. Force Field Development for Organic Molecules: Modifying Dihedral and 1-n Pair Interaction Parameters. *J. Comput. Chem.* **2015**, *36*, 376–384.
(30) Chase Jr., M. W. NIST-JANAF Thermochemical Tables, Fourth Edition. *J. Phys. Chem. Ref. Monogr. 9* **1998**, 1–1951.
(31) Linstrom, P. J.; Mallard, W. G. *NIST Chemistry WebBook, NIST Standard Reference Database Number 69*; National Institute of Standards and Technology: Gaithersburg MD, 20899.

5 Insight, Theory and Conclusions

5.1 Introduction

The unifying theme of this work is how hydrogen bonding to fluoride with different hydrogen bond donors affects the reactivity and selectivity of fluoride. Initially, the purpose was to rationalize already determined experimental results, as in the case of work in Chapter 2 on stoichiometric fluoride complexes, where it had been established experimentally that stronger hydrogen bonding to fluoride led to decreased reactivity. Using this knowledge, and having established an appropriate level of theory, computational insight was used concurrently with experiment to establish, and ultimately support, the mechanistic hypothesis of hydrogen bonding phase-transfer catalysis (HB PTC). After experimental screening of chiral catalysts proved a challenging task for asymmetric fluorination, computation played a pivotal role in the optimization of the successful catalyst. Despite the successes of HB PTC, including the use of potassium fluoride for asymmetric fluorination, much potential remains to be exploited. Computation can now take a leading role in broadening the scope of existing reactions, and developing new reactivity, plausibly in a predictive capacity.

Whilst I am not the first to recognize the complexity of the effect of hydrogen bonding on fluoride, it is still commonly perceived as a situation of '*hydrogen bonded fluoride is unreactive whilst uncoordinated fluoride is highly reactive'*. Several studies have argued that the situation is more nuanced, with several publications of hydrogen bonding promoted fluorination from a synthetic perspective, that have been well reviewed.[1–7]

I would like to contribute by exploring different case studies based upon our approach – catalyzing a reaction with a small molecule hydrogen bond donor, through fluoride

binding. This demonstrates that the effect of hydrogen bonding on fluoride reactivity is complex, but rational, depending on a number of intricately balanced factors.

This chapter discusses my overall perspective on the effect of hydrogen bonding to fluoride; a conundrum of apparent contradictions where 'Chapter 2' fluoride decreases in reactivity when coordinated by hydrogen bonds, but 'Chapter 3' fluoride increases in reactivity when coordinated. I will discuss how hydrogen bonding to fluoride can both increase and decrease the reactivity of fluoride, sometimes do both, and sometimes do neither. I will also discuss extensions of our existing work, to broaden substrate scope for enantioselective fluorination beyond stilbene derived substrates. A broader goal is to increase mechanistic understanding of HB PTC in general, particularly of the phase-transfer step, to extend reactivity to neutral substrates and to intricately understand the mechanism of the transformation. I would like to acknowledge Dr. Alex Durr and Dr. Nhu Nguyen for useful discussions.

5.2 Catalyst Designs for Improved Substrate Scope in the Fluorination of Episulfonium and Aziridinium Ions

5.2.1 Current System

Despite the successes of HB PTC, including its applicability to a variety of substrates and nucleophiles, achieving high levels of asymmetric induction remains challenging. Specifically, for fluorination, high enantioselectivity (>90 % *ee*) with episulfonium and aziridinium ions can only be achieved with stilbene derived substrates, with two aromatic rings. The ensuing S_N2 reaction is benzylic, favoring conjugation of the α-aryl ring with the forming and breaking bonds. This induces a twist in the β-aromatic ring, creating a distinct shape for the substrate depending on whether fluoride attacks at one carbon or the other, facilitating discrimination (Chapter 3, 4). For non-stilbene derived substrates,

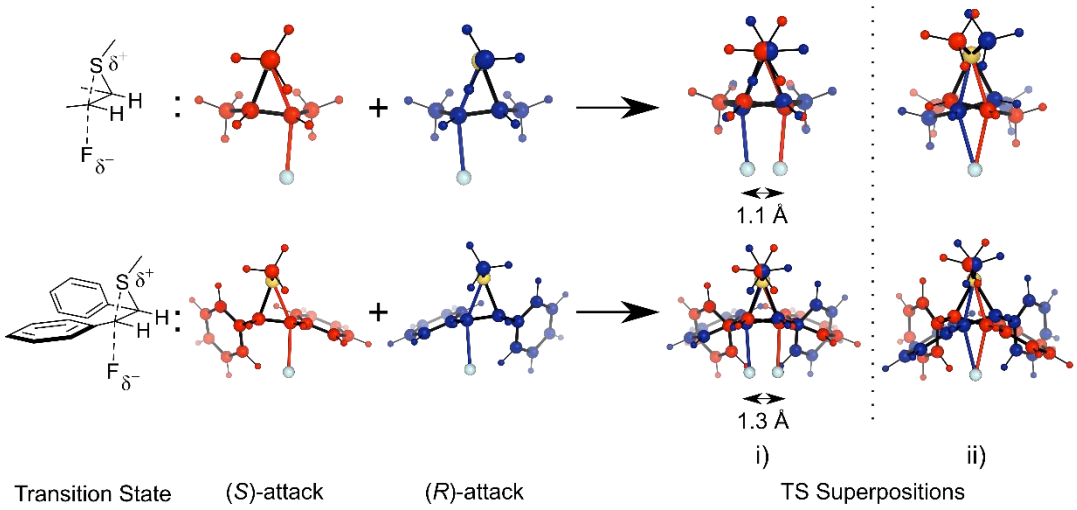

Figure 5.1: Illustration of the challenges of episulfonium/aziridinium desymmetrization (episulfonium illustrated). Top: without specific substitution, the TSs to enantiomeric products superimpose almost perfectly, making discrimination challenging. Bottom: stilbene derived ions sport a propeller like twist of the two aromatic rings. The TSs to enantiomeric product no longer superimpose well, enabling easier discrimination. Two TS superpositions are given. i) cations superimposed, highlighting a 1.1-1.3 Å shift in fluoride resulting in reversal of selectivity. ii) superposition of fluoride, highlighting the different shapes that the cation presents to catalyst-bound fluoride. Geometries computed at the CPCM(DCM)/M06-2X/def2-SVP(TZVPPD) level of theory.

the difference between attack at either carbon in the desymmetrization is subtle and can be thought of as i) a shift of the fluoride anion by approximately 1 Å, or equivalently, ii) a small twist of the substrate around fluoride (Figure 5.1). This is accompanied by a subtle change in transition state structure (TS) shape, depending on which C–S/C–N bond is elongated. Overall, these correspond to an incredibly minor geometric change between the two TSs to enantiomeric products. In order to develop a transformation with high enantioselectivity across broad substrate scope, it is these subtle differences that should be exploited (or amplified) as the origin of enantioselectivity, rather than changes specific to a particular subset of substrates.

A further consideration for the transformation is that the intrinsic stereoelectronic requirements are relatively unrestrictive. The only requirement of the S_N2 mechanism is alignment of the fluoride (lone pair) with the C–X σ*, with an ideal angle of 180°. Fluoride itself has little geometric preference for its coordination geometry (notably, no

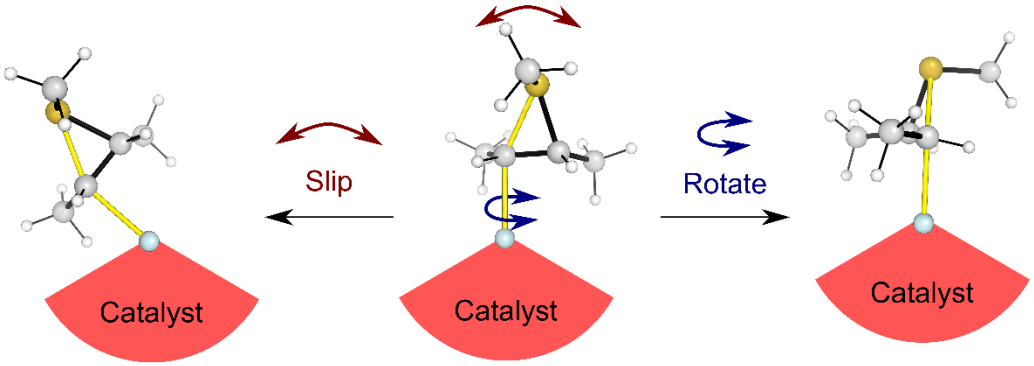

Figure 5.2: Illustration of the main degrees of freedom of episulfonium/aziridinium ions in the catalytic pocket (episulfonium illustrated). Left – Due to the low preference of fluoride for a tetrahedral geometry, substrate can 'slip' side to side. Right – The stereoelectronic requirements of the S_N2 reaction do not restrict substrate rotation about the forming C–F bond.

strong preference for a tetrahedral arrangement, Chapter 2), allowing the substrate to 'slip' across the surface of the fluoride. Further, the substrate itself can rotate about the axis of the forming C–F bond. These degrees of freedom give the substrate the flexibility to adopt a docking pose that avoids unfavorable interactions and makes discrimination between enantiomers difficult in the absence of further interactions (Figure 5.2). The docking pose of stilbene substrates for the fluorination of episulfonium and aziridinium ions is dominated by the steric requirements of the aromatic groups, rather than any part of the molecule directly related to reactivity. Once these groups are removed, enantioselectivity is lost, and indeed, inverted in the case of cycloalkene derived aziridinium ions.

A more general point that can be drawn are guidelines for the assignment of stereochemistry by analogy. In papers describing enantioselective methodology, commonly the absolute configuration of one product will be determined (*e.g.* by x-ray crystallography), and the rest of the substrate scope assumed to have the same absolute configuration induced in the transformation, by analogy. Assignment by analogy, however, assumes that the 'extraneous' groups that are changed between molecules in

the substrate scope, are not responsible for the enantioselectivity induced. Clearly, in order for all substrates to be reactive, the key functional groups for *reactivity* must be retained. Assignment by analogy is therefore only generally applicable where the same groups are responsible for both reactivity and selectivity. Determination of the TSs is therefore essential for safe assignment by analogy, as this allows determination of the groups responsible for selectivity, and whether these are retained across the substrate scope.

In the case of HB PTC fluorination, the unrestrictive stereoelectronic requirements of the S_N2 mechanism means that it is different groups that enable reactivity (episulfonium/aziridinium ring) and enantioselectivity (stilbene rings). Changing from a stilbene derived substrate to a cycloalkene derived substrate in the substrate scope therefore means that the sense of enantioinduction cannot be inferred by analogy. This is, however, also a strength as it gives a high degree of flexibility in catalyst design and potentially enables reactivity with a broader range of functional groups

5.2.2 Limitations of Current Alkylated BINAM Catalysts

The current generation of alkylated BINAM catalysts achieve high levels of enantioselectivity for stilbene derived episulfonium and aziridinium substrates. The enantioselectivity is consistent across substrates with different steric and electronic demands on the stilbene rings, in keeping with enantioselectivity arising primarily from the complementarity of substrate shape (arising from the aromatic rings) and catalyst shape (arising from the shape of the BINAM backbone).

Substrates favor forming a cation-π interaction with the BINAM backbone, reducing the number of accessible conformations (‘Rotation’, Figure 5.2), however this interaction

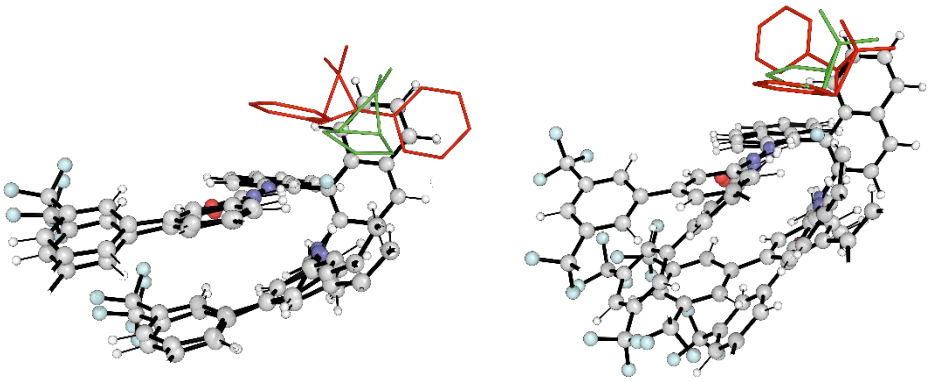

Figure 5.3: Transition state structures to major (Left) and minor (Right) product with stilbene derived aziridinium cation (red). Overlaid are the same TSs optimized with cyclopentene derived substrate (green). Both TSs show slipping of the aziridinium cation across the BINAM π-face of the catalyst on changing substrate, sufficient to reverse the energy ordering of the two TSs.

still allows the substrate to slip across the face of the aromatic ring ('Slip', Figure 5.2). The catalytic pocket of the alkylated BINAM catalysts is very open, meaning that many TS conformations are possible (requiring thorough conformational sampling). With aziridinium cations (Chapter 4), moving from stilbene-derived substrates to cyclopentene-derived substrates sees a significant slip of the cation across the BINAM π-system (Figure 5.3). In order to achieve high enantioselectivity for non-stilbene-derived substrates, additional directional interactions are required to bind and orient the substrate in the catalytic pocket.

5.2.3 Proposed Second-Generation Design Principles and Catalyst Designs

Design of a second-generation of catalyst therefore revolves around replacing or augmenting the substrate-catalyst cation-π interaction with more directional interactions. In the TSs, enantioselectivity originates from the docking of the substrate into the catalyst BINAM core, whereas the bis-CF_3 substituted aromatic rings on the periphery have a much smaller function for enantioselectivity. *Ortho* substitution on one of these rings provides a means to close up the catalytic pocket of the catalyst and is a plausible location to include a specific substrate binding group (Figure 5.4).

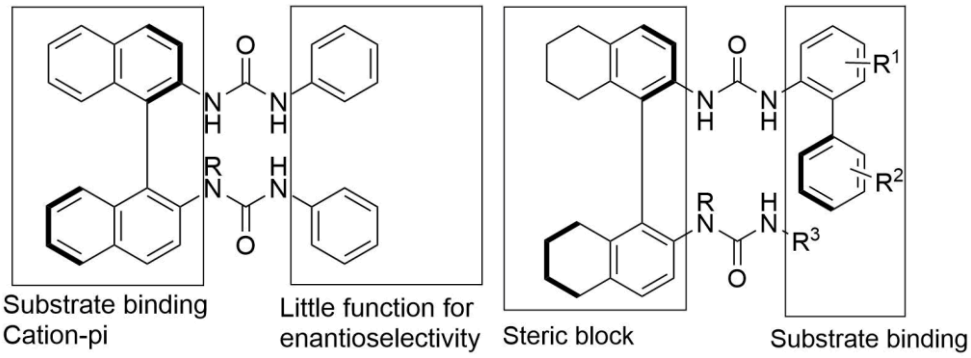

Figure 5.4: Left: Broad assignment of function to first-generation catalyst structures. Right: Proposed second-generation catalysts with designed group for substrate binding. R^2 can be one of many electron rich functional groups capable of interacting with positively charged cations.

Distinguishing between enantiomers remains challenging, even with a bespoke binding group. A specific design was therefore conceived with a sterically hindered ortho pyridine group (Figure 5.5), designed such that the pyridine sp^2 lone pair can interact with the acidic C–H bonds of the substrate only when fluoride attacks one of the two carbon atoms. This interaction was validated by the optimization of plausible TSs with cyclopentene derived aziridinium, with the lowest Gibbs free energy TS optimized exhibiting the proposed interaction, but it being absent in the lowest energy minor (Figure 5.6, truncated catalyst used for simplicity). Despite full conformational sampling not being undertaken, the TSs suggest possible discrimination of the diastereomeric TSs by approximately 9 kJ/mol, sufficient for high enantioselectivity. Further, the electron rich pyridine group

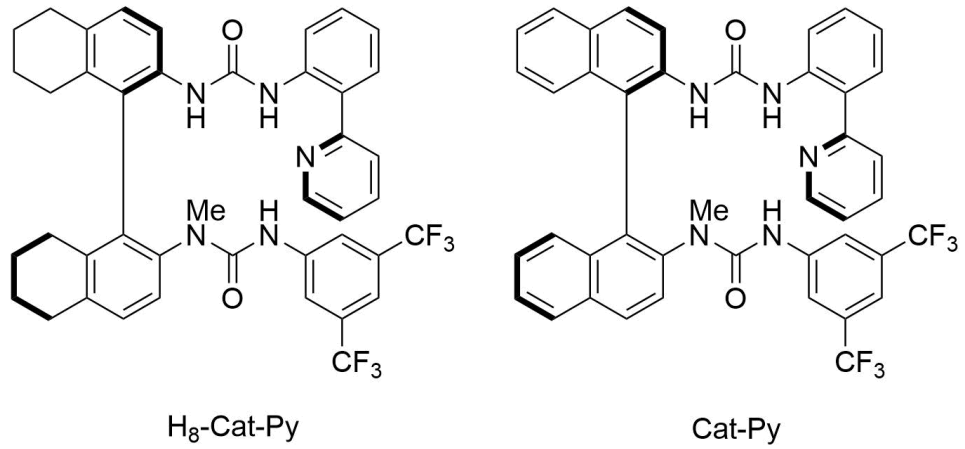

Figure 5.5: Specific second-generation design with ortho-pyridine substrate binding group. LHS – Preferred catalyst with H_8-BINAM backbone to prevent binding via cation-π. RHS – Synthetically easier catalyst with unsaturated backbone, but with reduced predicted enantioselectivity.

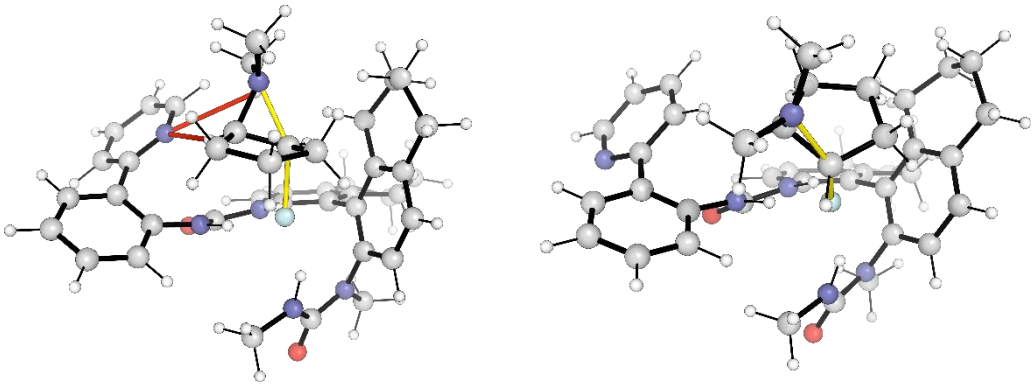

$\Delta\Delta G^{\ddagger}$ = 8.6 kJ/mol

Figure 5.6: Lowest computed Gibbs free energy transition state structures to major (left) and minor (right) product with **H_8-cat-py** second-generation catalyst and cyclopentene aziridinium substrate. Substrate interacts with the pyridine only in the major TS, with the designed interaction (red lines). Calculations performed at the COSMO(DCM)/ωB97X-D3/(ma)-def2-TZVPP//CPCM(DCM)/ M06-2X/def2-SVP(TZVPPD) level of theory.

can bind the cesium cation, potentially increasing the efficiency of phase-transfer (Figure S23-S24).

Due to the conceivably short synthesis, it was decided to synthesize the catalyst experimentally. Unfortunately, the synthesis was not as simple as originally anticipated, with the pyridine lone pair complicating cross-coupling – somewhat negating an advantage of this design. Further, synthesis of the catalyst with H_8-BINAM backbone was unachievable, with the unsaturated variant, **Cat-py**, ultimately synthesized. Whilst this catalyst could plausibly achieve selectivity with cycloalkyl substrates, the model was computed to be inferior, as the presence of the unsaturated BINAM backbone allows the minor TS to form a cation-π interaction, ubiquitous for the first-generation catalysts, as an alternative to interaction with the pyridine, reducing $\Delta\Delta G^{\ddagger}$ to 6.8 kJ/mol (Figure 5.7).

Upon testing, **Cat-py** demonstrated low activity (11 % yield) and 11 % ee with benzyl protected cyclohexyl aziridinium substrate – substantially less than the first-generation catalyst (Scheme 5.1). Given the low yield of product, it is plausible that the pyridine group decreased the activity of the catalyst to such an extent that racemic background

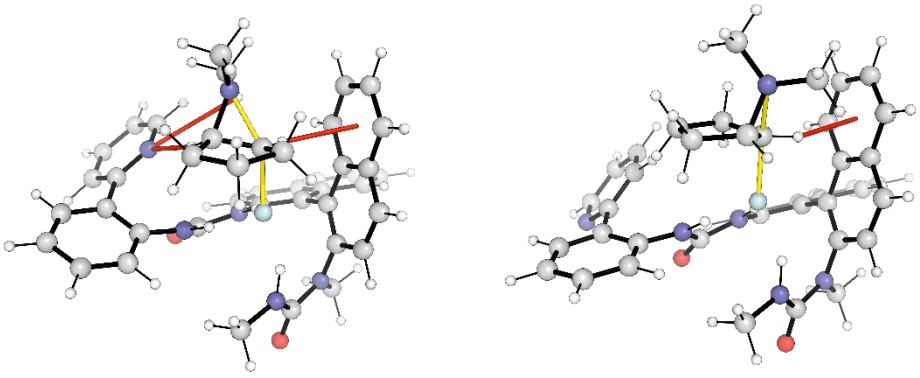

$\Delta\Delta G^{\ddagger}$ = 6.8 kJ/mol

Figure 5.7: Lowest computed Gibbs free energy transition state structures to major (left) and minor (right) product with second-generation catalyst, **cat-py**, and cyclopentene aziridinium substrate. Substrate interacts with the pyridine only in the major TS (red lines) but can form a cation-π interaction instead in the minor. Calculations performed at the COSMO(DCM)/ωB97X-D3/(ma)-def2-TZVPP//CPCM(DCM)/ M06-2X/def2-SVP(TZVPPD) level of theory.

reaction became competitive, possibly through poor solubility. The increased potential for the catalyst to bind the cesium cation does not appear to assist phase-transfer, highlighting an area for future investigation.

Whilst this specific example was unsuccessful, the H_8 variant of the catalyst is computed to have higher selectivity, however is likely to suffer similar activity problems and the challenging synthesis of the catalyst makes this statement of little practical interest. Design of further catalysts is ongoing, with a focus on identifying alternative electron-rich substrate binding groups, that do not have a detrimental effect on catalyst activity. As the design principles for the second-generation are broad, and many of the catalysts accessible by a short synthesis, computational investigation and experimental screening of plausible candidates is likely a fruitful area of research.

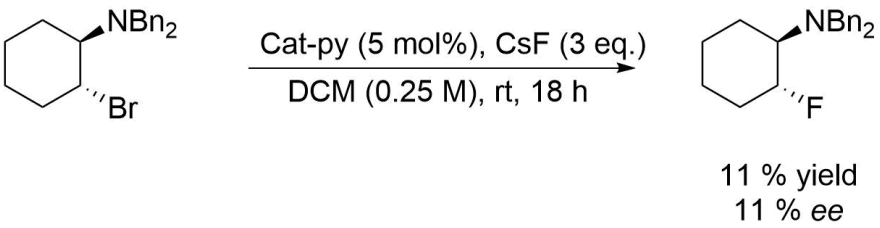

Scheme 5.1: Experimental reactivity and selectivity of **cat-py**.

5.3 The Effect of Hydrogen Bonding on the Reactivity of Fluoride for Catalytic Fluorination

This section focusses on the effect of hydrogen bond donor strength on catalyst efficacy in systems where the dominant interaction is hydrogen bonding between catalyst and fluoride. This has been our approach from stoichiometric hydrogen bond donor-fluoride complexes, through to HB PTC. Several other complimentary approaches have been taken to activating fluoride for nucleophilic fluorination (Chapter 1), each with a distinct set of advantages and disadvantages.

For example, fluorinase based approaches work efficiently under aqueous conditions, however have severely limited substrate scope and are challenging to engineer. Hydrogen bonding solvent promoted approaches, including ionic liquids, facilitate efficient and selective fluorination, however are limited in 'tunability' for *e.g.* enantioselective fluorination or changing regioselectivity, due to requiring super-stoichiometric quantities of a bespoke (chiral) hydrogen bonding solvent. Cation binding promoted approaches, with *e.g.* crown ethers or oligoethylene glycol derivatives, are effective at solubilizing metal fluoride, however don't give direct control over fluoride. Additionally, the favorable cation binding interaction cannot be exploited repeatedly to achieve catalytic turnover. The transition state structure 'receptor' based approach can selectively stabilize the TS for an S_N2 reaction, by binding the leaving group, as well as fluoride. This lowers the activation barrier, however limits substrate leaving group scope and doesn't address solubility challenges with the fluoride source. Further, care must be taken to ensure that the product doesn't sequester the catalyst.

This section explores the kinetic implications, scope and limitations, of our complimentary approach of using a sub-stoichiometric hydrogen bonding catalyst, to bind fluoride, for catalytic nucleophilic fluorination.

5.3.1 General Factors

In Chapter 2, distortion/interaction-activation strain analysis was used to identify the origins of the increase in activation barrier for S_N2 reactions with more strongly hydrogen bonded stoichiometric fluoride complexes. Whilst stronger donors lower the energy of the TS, relative to a weaker donor, they also lower the energy of the reactants to a greater degree, resulting in a higher barrier. The origin of this effect is from modulating the energy of the fluoride source HOMO and the charge on fluoride. Thus, all other things being equal, a stronger hydrogen bond donor creates a larger kinetic barrier to fluorination, decreasing the reactivity of fluoride. The change in the position of the TS was determined to be a minor factor in determining relative barrier height, and this is assumed to be generalizable in the following analysis.

Entropy becomes an important factor when comparing the reactivity of hydrogen bonded fluoride with uncoordinated fluoride. In all cases where fluoride is hydrogen bonded by a small molecule donor there is the possibility of dissociation of the donor (though this may be prohibitively unfavorable). This is a particularly important consideration for asymmetric catalysis where the uncoordinated pathway is the racemic background reaction. When the donor coordinates to fluoride, there is a favorable enthalpy change, however it is accompanied by an unfavorable entropy cost of association, from loss of translational and possibly rotational degrees of freedom (Chapter 2), on the order of 30-50 kJ/mol at 298.15 K. Whether coordination of the hydrogen bond donor is favorable, and therefore whether the coordinated pathway may outcompete the

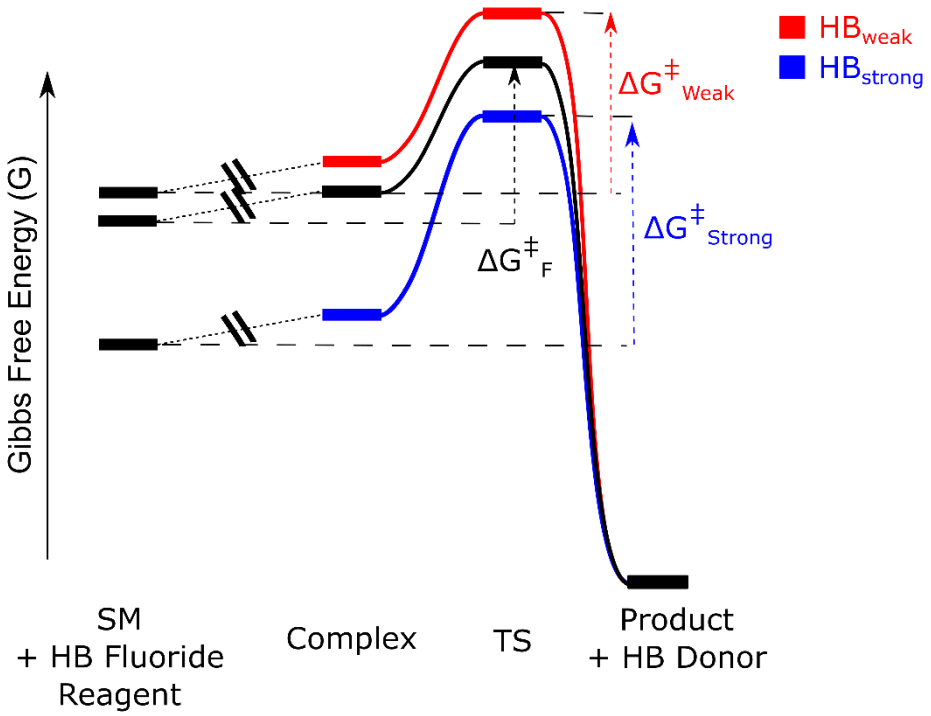

Figure 5.8: Schematic Gibbs free energy profile for fluorination with a stoichiometric fluorine source. Black: Fluorination with uncoordinated fluoride. Red: Fluorination with a weak hydrogen bond donor (**HB**$_{weak}$), insufficient to overcome the entropic penalty of coordination. Blue: Fluorination with a strong hydrogen bond donor (**HB**$_{strong}$).

background reaction, depends on whether the enthalpic term is larger than the entropic penalty. Figure 5.8 illustrates this point with a schematic Gibbs free energy profile, where donor, **HB**$_{Weak}$ is too weak to overcome the entropy penalty, whereas **HB**$_{Strong}$ is sufficiently strong under a given set of conditions. As fluoride is an acceptor that forms some of the strongest hydrogen bonds compared to other acceptors, this is more likely to be a concern for other anions (see Chapter 4.3.3).

Enthalpically, hydrogen bonding of **HB**$_{Weak}$ and **HB**$_{Strong}$ lower the enthalpy of both the complex and the TS relative to the uncoordinated pathway. The enthalpy of the complex is lowered to a greater degree, increasing the barrier. Once entropy is accounted for, the Gibbs free energy of the pathways with hydrogen bond donor are increased relative to the uncoordinated pathway, due to the entropy of coordination, possibly leading to a higher free energy pathway than when uncoordinated (illustrated by **HB**$_{Weak}$). If this step

forms part of a catalytic cycle, **HB$_{Weak}$** would not act as a catalyst (for fluorination) as dissociation of the catalyst reveals an alternative pathway of lower free energy. As the entropy term is dependent on reaction conditions, however, such as concentration and temperature, it may be possible to achieve catalysis by changing the conditions. The situation is more nuanced in the case of **HB$_{Strong}$** as the TS is lowered relative to the uncoordinated pathway, but so are the intermediate complexes, resulting in larger barriers. These two opposing factors underpin the complex behavior of hydrogen bonding on fluoride reactivity, and sensitivity to the precise reaction conditions – the implications of which are explored in the following case studies. All other factors are initially assumed constant (an ideal often not achievable in practice), the effects of which are discussed afterwards. Ureas are used in explicit examples in the following analysis, however the principles can be extended to other hydrogen bond donors.

5.3.2 Stoichiometric Reactions and Catalysis

The effect of the strength of hydrogen bond donors on fluoride reactivity is different depending on whether a pre-formed hydrogen bonded fluoride reagent is used in a stoichiometric reaction, or whether the hydrogen bonded complex is formed in situ in a catalytic cycle (Figure 5.9).

In the stoichiometric case, the hydrogen bonds are already formed prior to the reaction, and must therefore be broken over the course of the reaction. This is reflected in different Gibbs free energies of reaction where weaker hydrogen bonded reagents undergo a more exergonic reaction. This is also significant in the case of the kinetic barriers, where stronger hydrogen bonded reagents result in higher kinetic barriers, relative to separated starting materials, or reactive complex. All things equal, the reactive complex formed has the same components as in the catalytic case but is formed as a binary complex of

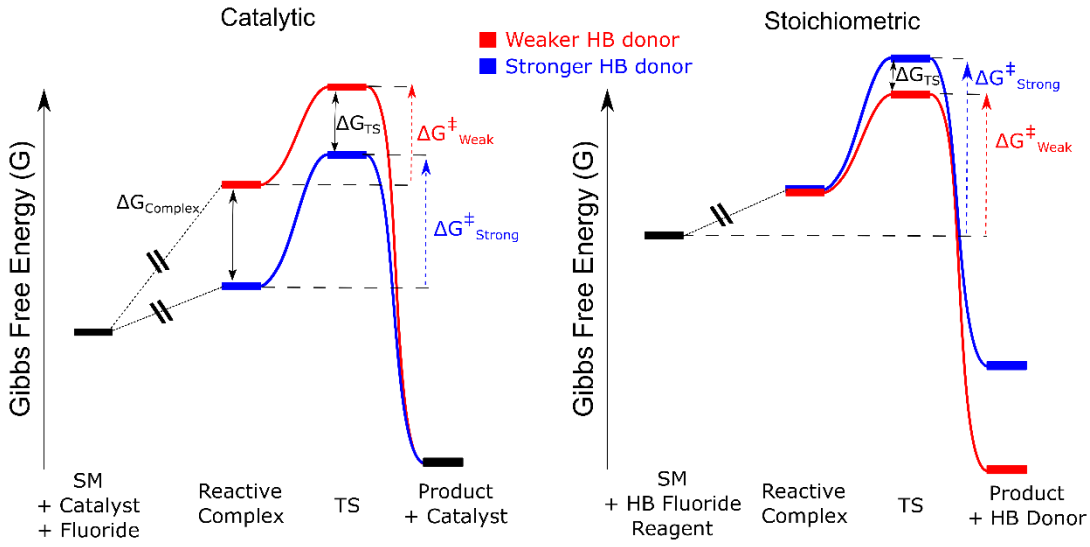

Figure 5.9: The effect of hydrogen bond donor strength on reactivity of fluoride, for catalytic and stoichiometric reactions. The starting materials for each profile are set to zero to highlight the important features for each scenario (note that both catalyzed and stoichiometric reactions can be drawn in either representation). In the stoichiometric case, the barrier height is responsible for the observed kinetics. In the catalyzed case, it is the Gibbs free energy of the individual states (e.g. TS, Complex etc.) that influence turnover, not the barrier height of individual steps.

hydrogen bonded fluoride reagent and the substrate. The energy of the reactive complexes, relative to the starting materials, will not differ strongly between ureas as no hydrogen bonds are formed or broken.

In the catalytic case, the reaction begins with starting material, fluoride source (not coordinated to catalyst) and free catalyst. These species ultimately form the ternary 'reactive complex' where catalyst binds fluoride, and this is associated with the substrate. Fluoride delivery can then ensue. The energy of these complexes varies strongly depending on the strength of hydrogen bonds formed by the catalyst. The exergonicity of the reaction is necessarily unaffected by the identity of the catalyst, as the catalyst must be released to facilitate turnover. At all points on the profile where HB catalyst is bound, the stronger donor leads to a structure lower in Gibbs free energy, due to formation of stronger hydrogen bonds. The profile is not, however, necessarily lower than that for uncoordinated fluoride due to the entropic penalty of catalyst coordination (*vide supra*).

The barrier for fluoride delivery from the reactive complex is increased with stronger HB donors ($\Delta G^{\ddagger}_{Strong} > \Delta G^{\ddagger}_{Weak}$), however the TS itself is stabilized to a greater degree with the stronger donor (ΔG_{TS}). As the turnover frequency of a catalytic cycle cannot be interpreted in terms of individual barrier heights – rather the Gibbs free energy of certain individual states – the effect of hydrogen bond donor strength on catalytic kinetics depends on the rest of the reaction profile.

5.3.3 The Energetic Span Model

Interpreting the turnover frequency (TOF) of a catalytic cycle from the Gibbs free energy profile is not intuitive. Figure 5.10 illustrates several plausible (but incorrect) proposals for the critical factors that could limit TOF i) highest energy point, ii) largest barrier to an individual step, and iii) energy of the individual states, as well as the correct 'Energetic span'. The energetic span model, formulated by Kozuch and Shaik, states that the kinetics of catalytic cycles cannot be interpreted in terms of the barriers to individual steps, instead being interpreted in terms of the *energetic span* of the reaction, which depends on the energy of individual states.[8,9] In Figure 5.10, the purple profile represents the faster reaction, due to having a smaller energetic span, despite all states on the blue profile being the same, or lower in energy. The energetic span model has been successfully applied to many systems, [10–13] providing a practical way to convert from the energy representation (Gibbs free energy profile) to the *k* representation (turnover frequency), potentially with high-throughput.[14]

The energetic span is defined as the Gibbs free energy difference between the turnover frequency determining transition state (TDTS) and the turnover frequency determining intermediate (TDI). The TDI is commonly referred to as the resting state of a catalyst. The TDI and TDTS are determined as the intermediate and transition state structure that

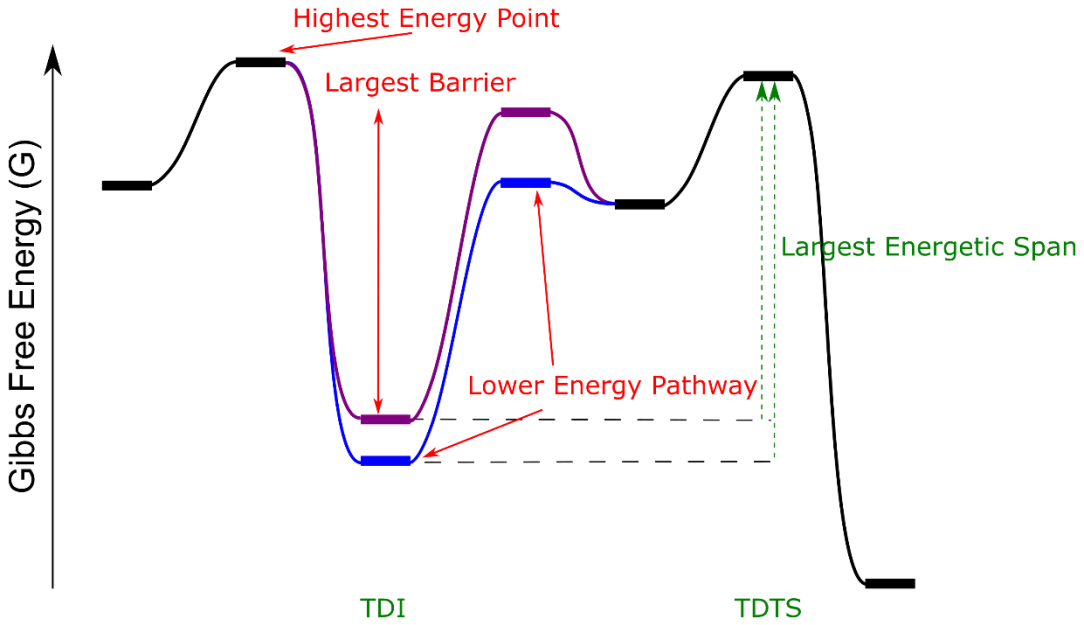

Figure 5.10: Schematic Gibbs free energy profile for a catalytic reaction, annotated with plausible TOF determining factors (red: incorrect, green: correct). Incorrect: The turnover frequency of a reaction cannot be attributed to the barrier height for individual steps, the overall highest point on the profile, nor whether a profile has high or low energy states in general. Correct: The energetic span, between TDI and TDTS determines the TOF of a reaction.

maximize the energetic span, accounting for the cyclic nature of the energy profile i.e. they are not necessarily the low and high points on an energy profile as drawn.

Provided that i) the reaction is exergonic, ii) the energetic span is much larger for the TDI and TDTS than any other combination of intermediates and transition state structures, and iii) that energy redistribution is rapid, no other states of the energy profile (significantly) affects TOF. Though species that enter or exit the catalytic cycle between TDI and TDTS can influence turnover through concentration effects. The effect of hydrogen bond donors on catalytic fluorination with fluoride therefore depends primarily on whether either, or both, of the TDI and TDTS involves the donor hydrogen bonding to fluoride. The energetic span, δG, is related to TOF and rate by the following expressions:[15]

$$TOF = \frac{k_B T}{h} e^{-\frac{\delta G}{RT}} \qquad Rate = TOF \times [cat] \tag{1.1}$$

5.3.4 Case Studies for Catalysis

The following examples explore how the strength of the hydrogen bond donor influences the turnover frequency of a catalytic fluorination, depending on how the key steps feature in the Gibbs free energy profile for the whole catalytic cycle. Additionally, the behavior of energetic barriers and species energies are assumed to follow the behavior established in Chapter 2, where stronger hydrogen bonding stabilizes the intermediate more than the TS. For simplicity, in the following examples, the intermediate may be viewed as a complex that features the catalyst binding to fluoride (such as the reactive complex with or without substrate), and the TS as corresponding to the fluoride delivery process, although the principles are generalizable to other situations where fluoride is less strongly bound by catalyst in the TS than in the intermediate. The dashed line connecting the two states highlights that there may be intermediate states, however their Gibbs free energies are bounded between the two states, and are therefore of little consequence to TOF.

The only factor being changed between hydrogen bond donors is the strength of the hydrogen bonding interaction with fluoride. As the Gibbs free energy profile for a turnover of a catalytic cycle can be drawn with any starting point, all profiles show the TDTS following the TDI with no loss in generality. Details about the black states on the Gibbs free energy profiles are unimportant, providing a framework for the key steps of the cycle. If these states are not identified as turnover determining, they are not required to have the same energy with the different catalysts.

5.3.4.1 Hydrogen Bonded Fluoride in both the TDTS and TDI

In a mechanism where catalyst hydrogen bonds to fluoride in both the TDI and TDTS, increasing the strength of the hydrogen bond donor lowers the Gibbs free energy of both of these states. The TDI is lowered to a greater extent (Chapter 2), resulting in an increase in energetic span and a decrease in turnover frequency with the stronger hydrogen bond donor (Figure 5.11). This is despite all points on the energy profile being the same energy, or lowered in energy by the stronger donor, highlighting the importance of the energetic span model. This can be summarized as the dominant effect of the stronger hydrogen bond donor is to stabilize the resting state of the catalyst (TDI), thereby reducing TOF.

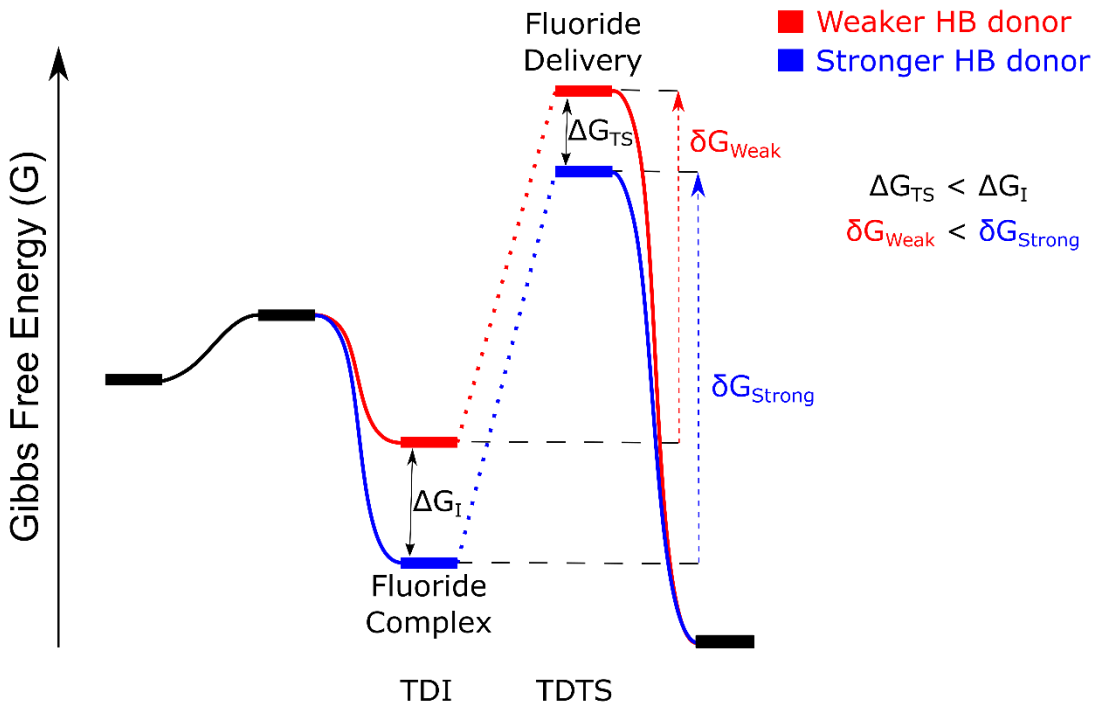

Figure 5.11: Schematic Gibbs free energy profile illustrating that the energetic span, δG, is increased by stronger hydrogen bond donors, when HB catalyst binds fluoride in both the TDI and TDTS. This results from the greater stabilization of the fluoride complex (TDI) than the fluoride delivery TS (TDTS).

5.3.4.2 Hydrogen Bonded Fluoride in the TDI

In a mechanism where the catalyst hydrogen bonds to fluoride in the TDI, but not the TDTS (*i.e.* the fluoride delivery TS is not turnover limiting), increasing the strength of the HB donor stabilizes the TDI, but has no effect on the TDTS, resulting in an increased energetic span, and decreased TOF (Figure 5.12). This can be summarized as the stronger hydrogen bond donor stabilizing the resting state of the catalyst.

Whilst this scenario is possible, it is unlikely to occur in a simple fluorination as the TDTS is a high energy state that does not involve fluoride delivery by the catalyst, implying another significant process occurring in the mechanism. It is unlikely that such a TDTS will follow fluoride delivery, as the formation of a strong carbon-fluorine bond leads to a low Gibbs free energy for the following states. The TDTS may precede fluoride delivery and could perhaps originate from a significant rearrangement of the substrate that is required prior to reaction with fluoride.

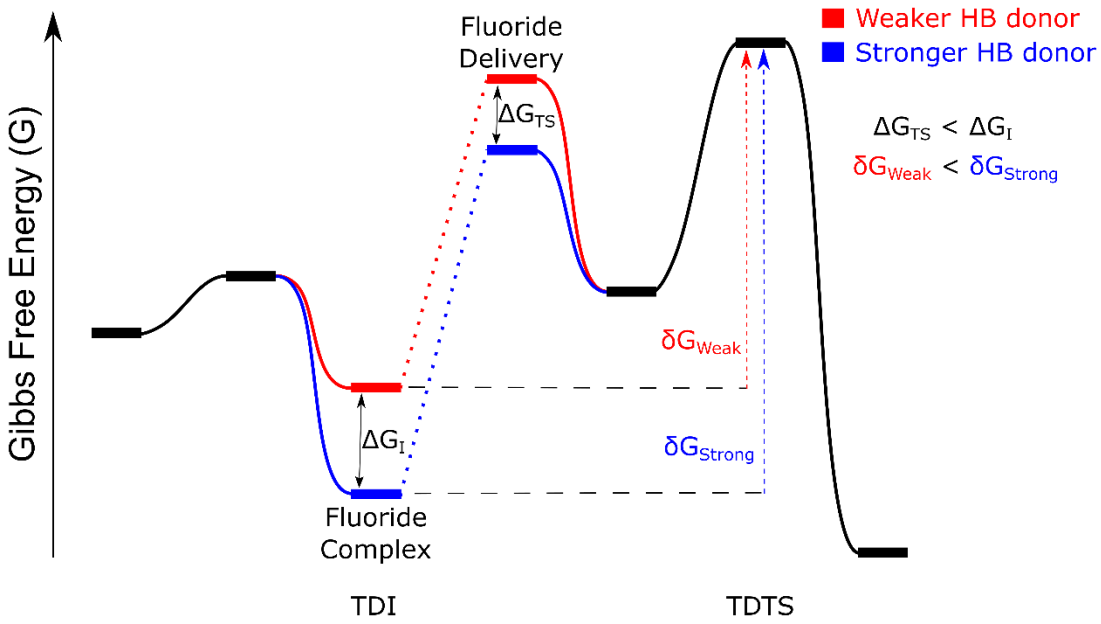

Figure 5.12: Schematic Gibbs free energy profile illustrating that the energetic span, δG, is increased by stronger hydrogen bond donors, when HB catalyst binds fluoride in the TDI, but not the TDTS. The TDTS is drawn after the fluoride delivery TS, however the argument is unchanged if it comes before.

5.3.4.3 Hydrogen Bonded Fluoride in the TDTS

In a mechanism where the catalyst hydrogen bonds to fluoride in the TDTS, but not in the TDI, increasing the strength of the hydrogen bond donor stabilizes the TDTS, reducing the energetic span and leading to an increase in TOF (Figure 5.13). The resting state of the catalyst therefore does not involve it binding fluoride, suggesting a situation where fluoride is 'unavailable', potentially through use of an *in situ* fluoride releasing reagent, or with fluoride isolated in a different phase. In this scenario, hydrogen bonding to fluoride, alone, is capable of catalyzing fluorination.

The same kinetic behavior will also occur if the catalyst hydrogen bonds to fluoride more weakly in the TDI than the TDTS, so weak coordination of the catalyst to the fluoride source in the TDI need not be completely excluded.

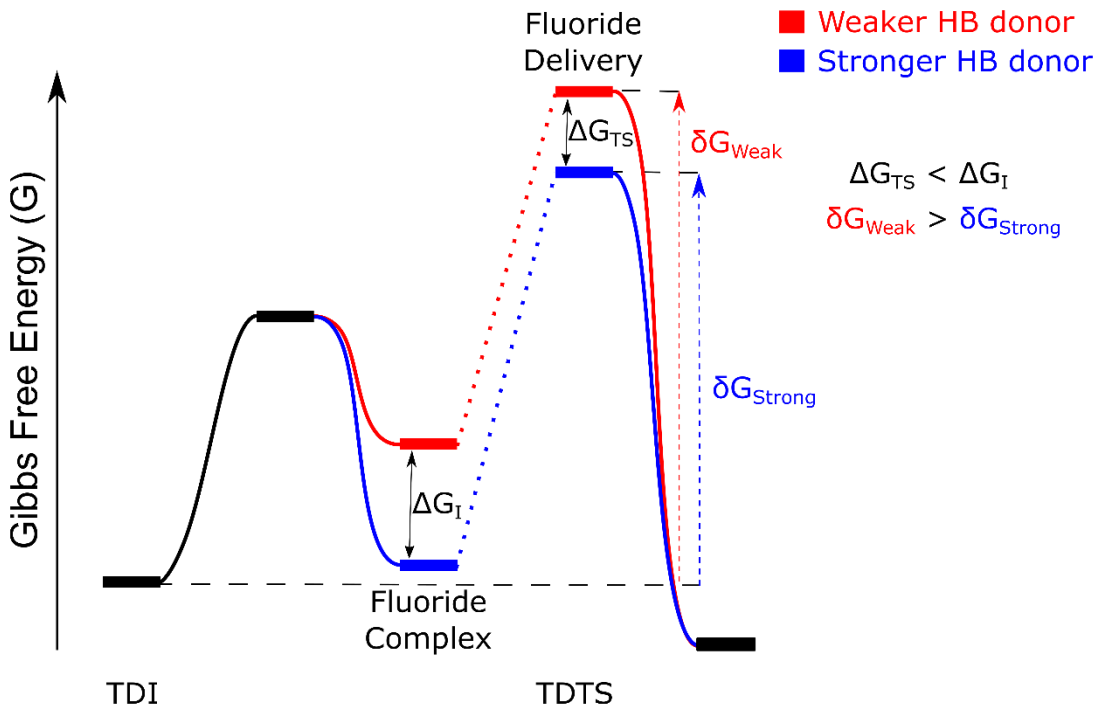

Figure 5.13: Schematic Gibbs free energy profile illustrating that the energetic span, δG, is decreased by stronger hydrogen bond donors, when HB catalyst binds fluoride in the TDTS, but not the TDI.

5.3.4.4 Hydrogen Bonded Fluoride in Neither the TDTS nor TDI

In a mechanism where the catalyst hydrogen bonds to fluoride in neither the TDI nor the TDTS, changing the strength of the donor will have no effect on the energetic span of the reaction, and therefore little effect on catalytic turnover (Figure 5.14). Such a situation is more likely to occur as part of a complex reaction mechanism, rather than a simple hydrogen bonding mediated fluorination. Despite the strength of the donor not affecting the TOF of the catalytic reaction, the donor may still be acting as a catalyst by preventing a higher TDTS from occurring.

The same kinetic behavior will occur if the catalyst hydrogen bonds to both the TDI and TDTS with the same strength, lowering both equally, however this is not a typical situation (5.3.4.1).

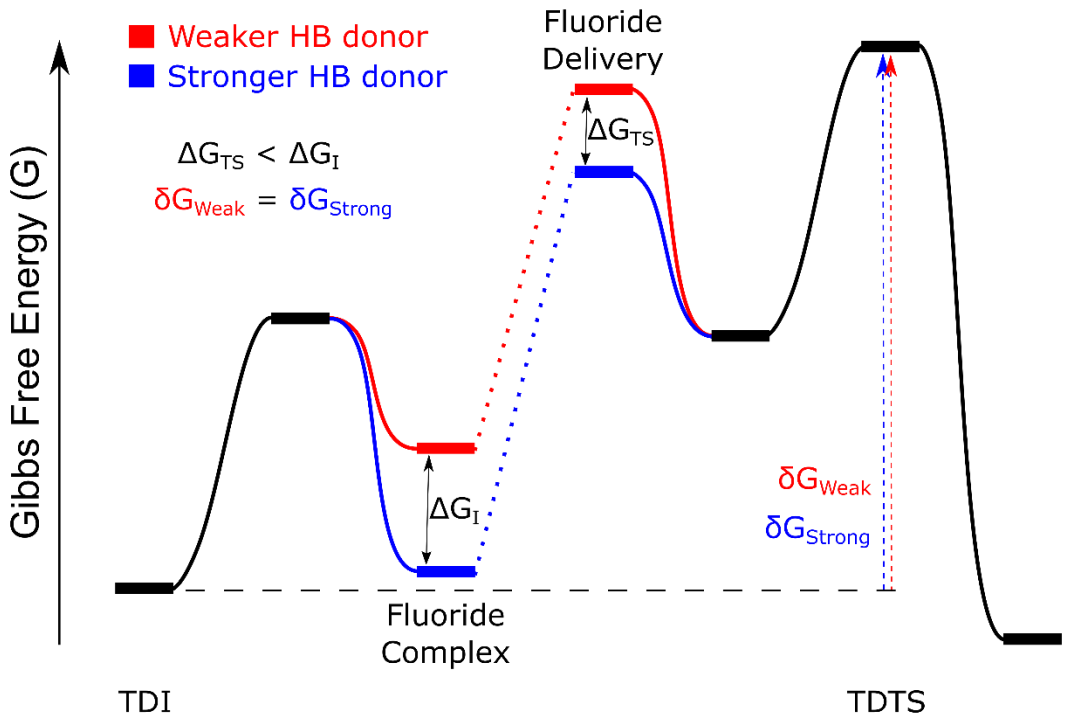

Figure 5.14 Schematic Gibbs free energy profile illustrating that the energetic span, δG, is unchanged by different hydrogen bond donor strengths, when HB catalyst binds fluoride in neither the TDI, nor TDTS.

5.3.4.5 Multidentate Hydrogen Bond Donors

In the case of multidentate hydrogen bond donors, the lowest energy species (complexes or TSs) are expected to form the largest number of hydrogen bonds geometrically possible. Once the HB donor is coordinated, formation of subsequent hydrogen bonds is associated with minimal entropic penalty, which is easily compensated for by the favorable enthalpic interaction. Overcoming the entropy penalty of association, in order to outcompete the background reaction, is therefore more easily achieved by multidentate HB donors. Adopting the highest coordination number possible is found to be the case for the tricoordinate urea catalysts used for HB PTC where all of the lowest energy TSs form three hydrogen bonds to fluoride. In the lowest energy complexes, the catalyst also forms three hydrogen bonds to fluoride. If the hydrogen bond donor dissociates one (or more) of its donors, both the energy of the reactive complex and the TS will be raised in energy, the former to a greater degree (Figure 5.15).

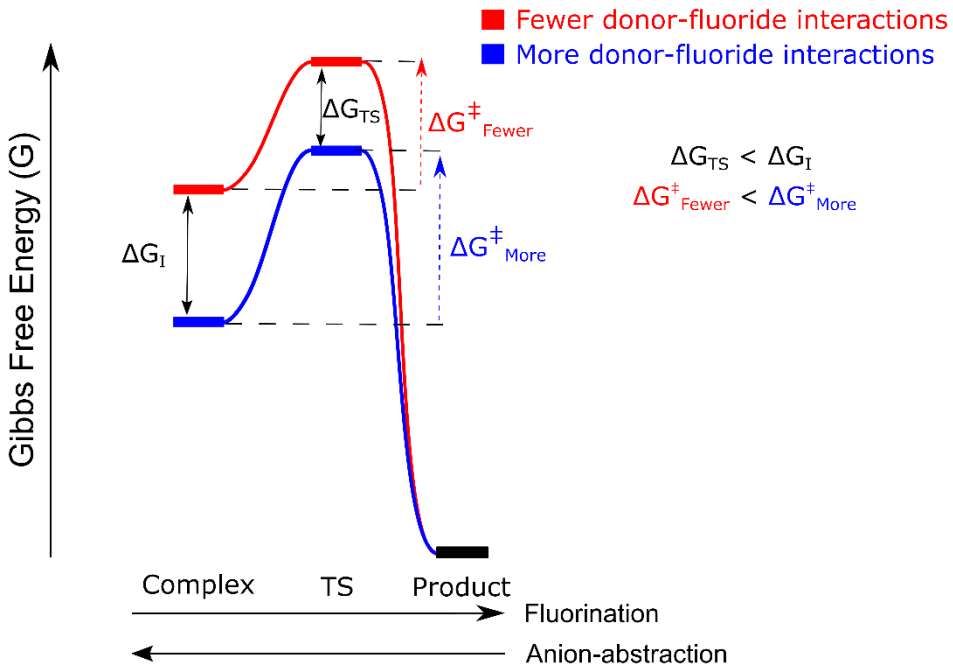

Figure 5.15: In both the reactive complex and the fluoride delivery TS, a higher catalyst-fluoride coordination number results in a lower Gibbs free energy relative to when unbound. The stabilization is greater for the reactive complex than the TS, leading to an increased barrier. When comparing different binding modes of the same catalyst, the binding modes will likely interconvert, resulting in the lowest energy (blue) pathway being followed at all points.

All other things equal, the barrier from reactive complex to TS is reduced by decreasing coordination number (similar to the effect of hydrogen bond strength), consistent with the superficial interpretation that less coordinated fluoride is more reactive. This is the case whether comparing two separate catalysts with different numbers of hydrogen bond donors, or whether comparing different binding modes of a multidentate catalyst. In the latter case, however, binding modes are likely to interconvert, and the lowest energy species are relevant, resulting in the complexes of maximum coordination number dominating.

Figure 5.15 can also be interpreted in the context of the reverse reaction – fluoride abstraction. The more hydrogen bonds a donor can form, the lower the free energy barrier to fluoride removal, and the lower the energy of the formed ion pair.

An important assumption so far is that all complexes that the catalyst can form with fluoride are reactive. Once a certain coordination number of fluoride is reached, one or more donors must dissociate prior to fluoride delivery (and possibly formation of the reactive complex) to sterically accommodate the substrate. This significantly increases the barrier to fluoride delivery which is likely to increase the energetic span of the reaction.

5.3.4.6 Coordination Saturation of Fluoride

With high concentrations of hydrogen bond donors, such as in hydrogen bonding solvents, saturation of fluoride with hydrogen bond donors must be considered. As fluoride forms strong hydrogen bonds, it is likely that the saturated fluoride complex will be the TDI. In order to react, at least one hydrogen bond donor must dissociate for fluoride to attack the substrate, accompanied by a large energetic penalty. The fluoride delivery

TS will be strongly stabilized by the high degree of hydrogen bonding remaining to the other donors, relative to the uncoordinated TS, however, the energetic span is large due to the dissociation, restricting catalytic turnover. Whether the fluoride delivery TS is the TDTS or not, increasing the hydrogen bond donor strength will increase the energetic span by stabilizing the TDI to the greatest degree, consistent with conventional wisdom about the low reactivity of fluoride in strongly hydrogen bonding solvents.

5.3.4.7 Limitations and Caveats

The above profiles illustrate the contrasting ways in which hydrogen bonding to fluoride can affect the turnover of nucleophilic fluorination reactions, using the energetic span model. Naturally, the conclusions are dependent upon the validity of this model. Whilst the case studies have been presented as distinct examples, the identity of the TDI and TDTS can be changed, for example by changing the catalyst, and a reaction may switch scenarios based upon the exact conditions. Gibbs free energy is also dependent on the concentration of species, with profiles commonly (as here) drawn at a standard state of 1 M. Changing the initial concentration of species, or as they change over the reaction, can change the shape of the profile. In an experimental system, it may be possible to measure the steady state concentrations of the different species and use this to tune the computed profile. Imperfections in the experimental setup, such as the presence of water traces (particularly in the case of fluoride sources such as TBAF, or hygroscopic fluoride salts), can also cause deviation between the ideal computed profiles and experimental kinetics.

5.3.5 Beyond Hydrogen Bonding to Fluoride

The scenarios discussed so far isolate the effect of hydrogen bonding to fluoride. In general, a hydrogen bonding catalyst will also interact directly with the substrate and

cause a deviation from the profiles shown above. The strength of these interactions can tune the energetic span if catalyst and substrate are involved in either, or both, of the TDI and TDTS. Such interactions are commonly non-covalent interactions such as van der Waal's forces and π-stacking effects, but possibly more specific interactions such as hydrogen bonds and cation/anion-π interactions. In aqueous solution, the hydrophobic effect may be exploited. If both catalyst and substrate are involved in both the TDI and TDTS, a differential in the strength of catalyst-substrate interactions is required to lower the energetic span, otherwise both will be modulated in Gibbs free energy in a similar manner. This can be achieved, for example, through pre-organization of the catalyst or substrate in a higher energy, but reactive conformation, or leaving group binding. Both have been exploited previously in other fields of catalysis, and leaving group binding has previously been proposed for catalyzing S_N2 reactions with fluoride (Chapter 1).

Conversely, if both catalyst and substrate are involved in the TDTS, but not the TDI, no differential is required as only the TDTS is lowered in Gibbs free energy by increasing the strength of interaction. The likelihood of this scenario is increased by the fact that formation of the reactive complex, by association of substrate, incurs a significant, but unavoidable entropic penalty – substrate-catalyst interactions that partially offset this penalty stabilize the TS relative to the uncatalyzed pathway, but will not cause the reactive complex to become TDI.

Considerations when looking to exploit catalyst-substrate interactions are to ensure that the binding is not too strong that the pre-reactive complex, or the product complex becomes the TDI, thereby inhibiting turnover. As catalyst-fluoride hydrogen bonding is so strong, it is unlikely that a complex of substrate and catalyst alone will become TDI (*i.e.* without fluoride bound). Further, as fluoride is neutralized in the product complex,

this significantly reduces the chance of the product inhibiting turnover. An approach such as leaving group binding, or creating a transition state structure 'receptor', however, makes the latter a realistic consideration.

5.3.6 Towards Homogeneous Catalytic Fluorination with Fluoride Mediated by a Small Molecule Hydrogen Bond Donor

5.3.6.1 Introduction

The distortion/interaction-activation strain analysis of Chapter 2, coupled with the experimental work upon which it is based, provides a compelling argument for hydrogen bonding decreasing the reactivity of fluoride in homogeneous solution. Use of fluoride bound by increasingly strong hydrogen bond donors leads to slower fluorination compared to uncoordinated fluoride by stabilizing the fluoride to a greater degree than the TS (5.3.4.1). This seemingly precludes the use of hydrogen bonding to catalyze homogeneous fluorination, as the TDI involves stronger hydrogen bonding to fluoride than the TS. Whilst it is true that hydrogen bonding to fluoride *alone* cannot catalyze homogenous fluorination from fluoride ion (nor indeed be responsible for the catalytic effect, so far as such an effect can be partitioned), catalyst-substrate interactions may be exploited to lower the Gibbs free energy of the fluoride delivery TDTS relative to the fluoride complex TDI, and thus lead to hydrogen bonding mediated catalytic fluorination from fluoride in homogeneous solution.

To illustrate this concept, a model system was devised, consisting of the fluorination of 9-(bromomethyl)anthracene (**Ar$_3$Br**) in acetonitrile solution with soluble fluoride (such as TBAF). The substrate was chosen so that diarylurea catalysts, such as Schreiner's urea, can form favorable π-π stacking interactions. Key species for the model system are given in Figure 5.16.

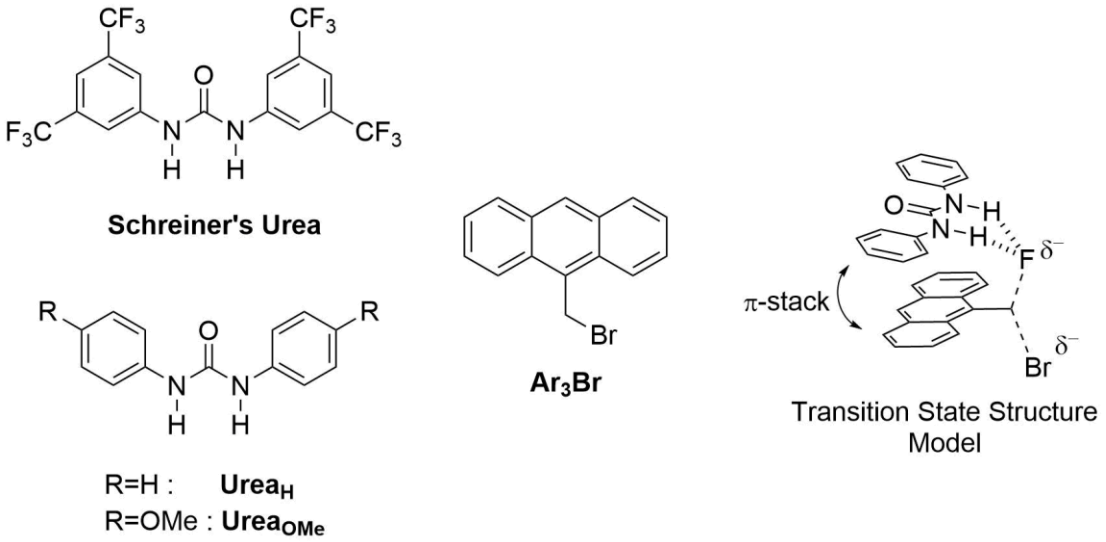

Figure 5.16: Key species computed in model system.

5.3.6.2 Level of Theory

Geometry optimizations and frequency calculations were performed in Gaussian 16, rev. A. 03[16] using the M06-2X[17] hybrid functional with ultrafine (99,590) integration grid. A mixed basis set, denoted def2-SVP(D) was used consisting of def2-SVPD[18] on electronegative atoms and def2-SVP[19] otherwise. This basis set incorporates an ECP for cesium.[20] Solvation in the stated solvents was modeled using the conductor-like polarizable continuum model (CPCM).[21–23] Stationary points with all real frequencies were classified as minima, and those with a single imaginary frequency as transition state structures (TS). Thermochemistry was evaluated using *GoodVibes* python script[24] at 298.15 K and 1 mol/dm^3 concentration unless otherwise stated, implementing a quasi-harmonic approximation for entropy calculation and a free-rotor description for low frequency vibrational modes (ν < 100 cm^{-1}).[25] Single point energy corrections were performed in the ORCA 4.1.0 software package[26,27]. The ωB97X-D3[28,29] functional, incorporating Grimme's D3 dispersion correction[30] was used in combination with the (ma)-def2-TZVPP basis set, consisting of ma-def2-TZVPP[31] on heteroatoms, with corresponding ECP for cesium, and def2-TZVPP on carbon and hydrogen. Integration

utilized the Lebedev302 grid for SCF cycles and the Levedev590 grid for final energy evaluation. Solvation in the stated solvents was modelled using the CPCM model.

5.3.6.3 Results

The computed Gibbs free energy profile with **Schreiner's urea** and unsubstituted diphenylurea (**Urea$_H$**) in acetonitrile is illustrated in Figure 5.17, with Gibbs free energies in Table 5.1. Geometries shown in Figure S25. The fluorination reaction is significantly thermodynamically favored, ruling out the reverse reaction of C–F bond activation.

In this model system, no urea is ultimately able to reduce the effective barrier for the reaction (but achieving within 8 kJ/mol of the uncatalyzed barrier height in the case of **Urea$_H$**), however the principles described are still illustrated. In the presence of a urea, the TDI of the reaction is significantly lowered, becoming the urea-fluoride complex (**II**). In contrast, for the uncatalyzed case, the lowest Gibbs free energy state is separated substrate and fluoride (**I**). When uncatalyzed, complexation of fluoride and substrate is unfavorable due to the entropy penalty (**I→III**). With urea, this coordination remains unfavorable, (rotational entropy is also lost– Chapter 2) but is partially compensated by catalyst-substrate interactions. Comparing the coordinated pathways to the uncatalyzed pathway, urea dissociation at this point is highly unfavorable as it involves loss of interactions with both fluoride and substrate (**III** vertical transitions). The TDTS in all

Table 5.1: Gibbs free energies for hydrogen bonding mediated fluorination under homogeneous conditions in MeCN.

	Gibbs Free Energy / kJ/mol						
	II	**III**	**IV‡**	**V**	**VI**	**II'**	**Span**
Uncoordinated	n/a	21.0	76.9	-62.1	n/a	n/a	76.9
Urea$_H$	-28.9	-6.5	55.9	-40.7	-77.2	18.8	84.8
Schreiner's Urea	-44.6	-23.3	50.4	-43.0	-84.5	12.0	95.0

II' refers to the catalyst-**Ar$_3$Br** complex, without fluoride coordinated. Formation of this complex is less favorable than coordination of fluoride to the catalyst, so it is not the TDI.

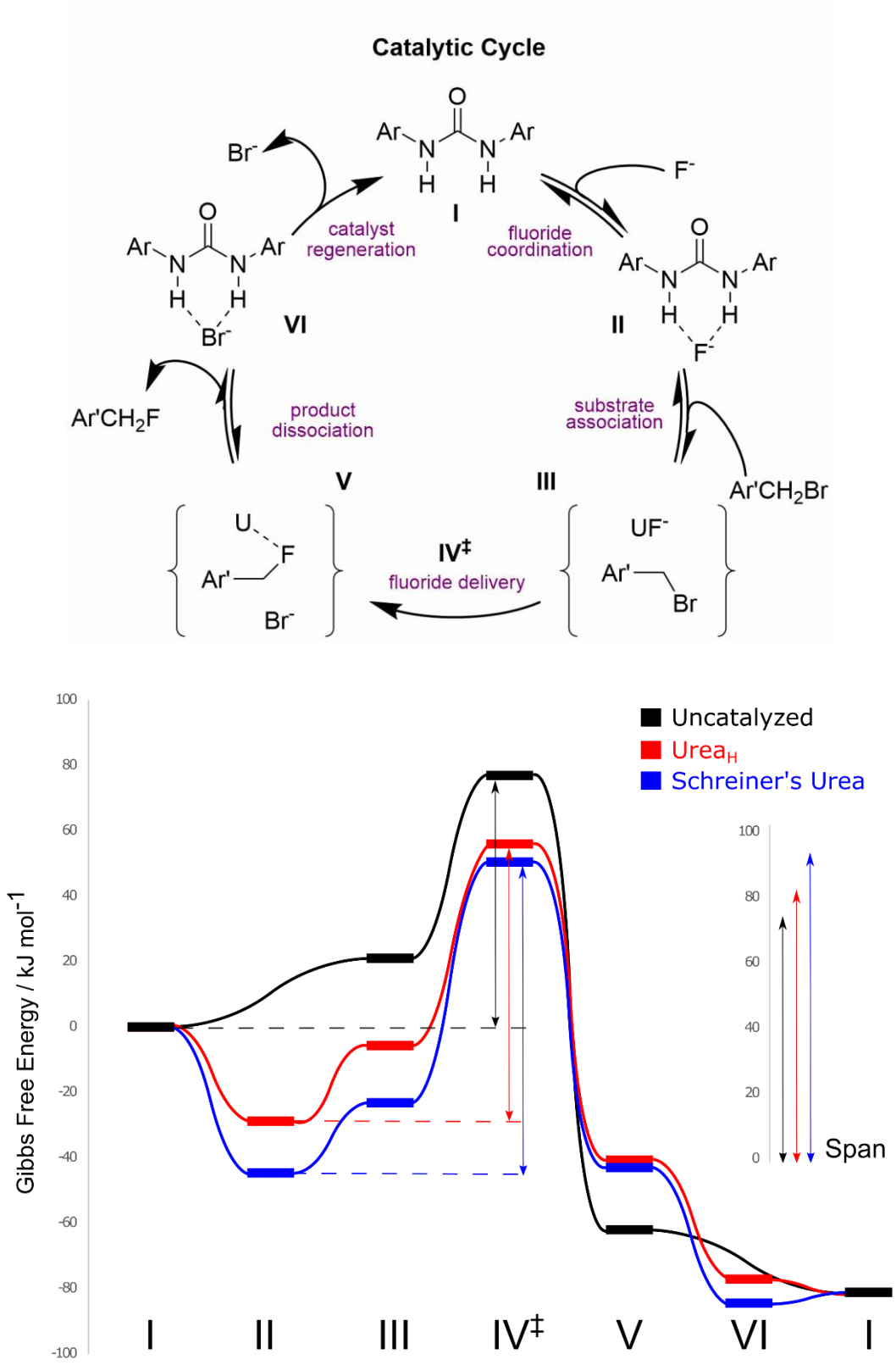

Figure 5.17: Towards homogeneous fluorination with fluoride catalyzed by small hydrogen bond donors. Gibbs free energy profile for fluorination of 9-(bromomethyl)anthracene in acetonitrile with different diarylurea hydrogen bond donors.

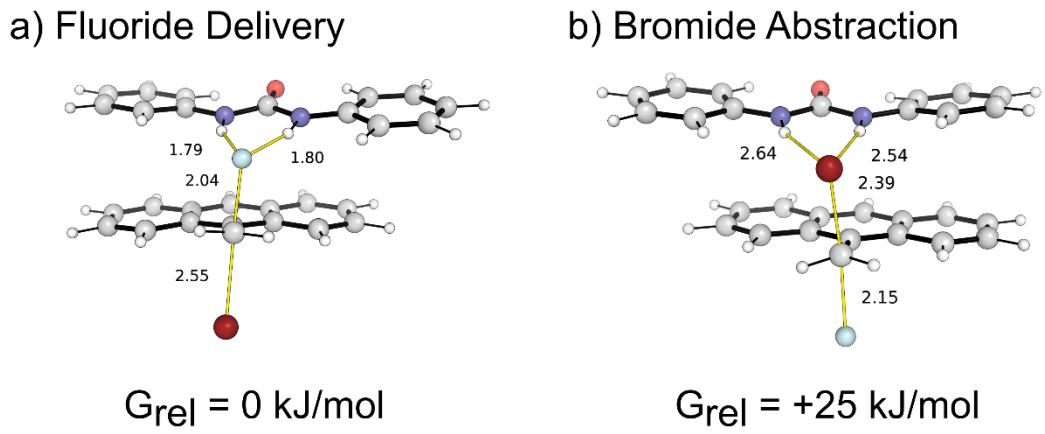

Figure 5.18: Transition state structures for a) fluoride delivery (favored) and b) bromide abstraction.

cases is fluoride delivery, **IV**‡, which is stabilized in the presence of all ureas relative to the uncatalyzed pathway. Binding of the leaving group by the urea was also investigated but is uncompetitive, resulting in a transition state structure 25 kJ/mol higher in Gibbs free energy than binding of fluoride, due to the weaker hydrogen bonding (Figure 5.18). The bromide binding TS is also 4 kJ/mol higher than without the urea coordinated.

After fluoride delivery, no species are found to influence the energetic span (**V**-**VI**). With all ureas, the energetic span of the reaction exceeds the barrier of the uncatalyzed reaction, by stabilizing the solvated fluoride (**II** – TDI) to a greater degree than the fluoride delivery TS (**IV**‡ – TDTS). The energetic span is larger for the stronger hydrogen bond donor, demonstrating that strong hydrogen bonding is not the key to achieving catalysis, and indeed weaker hydrogen bonding is beneficial. The profiles illustrate that the system has room for further optimization of substrate-catalyst interactions. By increasing catalyst-substrate interactions, steps **III** and **IV**‡ of the cycle are reduced in Gibbs free energy, whilst the TDI, **II**, is unaffected, reducing the energetic span. An increase in interaction on the order of 20 kJ/mol for the unsubstituted urea would facilitate catalysis. Equally importantly, increasing the strength of the π-stack is unlikely to change the TDI

to any other state, including off-cycle states. Catalyst binding to substrate (without fluoride) is almost necessarily higher in Gibbs free energy than the complex where fluoride is also bound, as hydrogen bonds to fluoride are strong and will overcome the entropic penalty of coordination (**II'**). With **Urea$_H$** and **Schreiner's Urea**, this complex has relative Gibbs free energies of 18.8 kJ/mol and 12.0 kJ/mol respectively. Further, the product complexes, (**V-VI**) are also unlikely to be turnover limiting. The lowest energy product complex involves hydrogen bonding catalyst binding the anionic leaving group, with product dissociated. Although this complex may be lower in energy than free catalyst, **I**, it will not be lower than the TDI, **II**, where the catalyst binds fluoride much more strongly. Thus, unless there are significant concentration effects, product inhibition is not a major consideration. Additionally, the barrier to the reverse reaction (hydrogen bonding mediated fluoride abstraction) is high (> 120 kJ/mol), and significantly higher than the forward reaction, implying that this is unlikely to be an issue. For the investigation of modifications of this system, therefore, it is only necessary to compute states **I** – **IV**‡ to assess turnover frequency and catalytic viability.

Weaker hydrogen bond donor, with *para*-OMe disubstitution (**Urea$_{OMe}$**), failed to show any significant improvement over **Urea$_H$**, so the latter is used as the preferred donor (Table 5.2). The leaving group was changed from bromide to chloride (**Ar$_3$Cl**) to decrease the background reaction at manageable temperatures but led to little change in catalytic

Table 5.2: Critical Gibbs Free Energies and Energetic Spans for Urea Mediated Fluorination of 9-(chloromethyl)anthracene with Fluoride in Acetonitrile Solution.

	Gibbs Free Energy / kJ/mol			
	II	**III**	**IV**‡	**Span**
Uncoordinated	n/a	n.d.	87.2	87.2
Urea$_H$	-28.9	-5.2	67.9	96.7
Urea$_{OMe}$	-27.0	-4.4	69.1	96.0

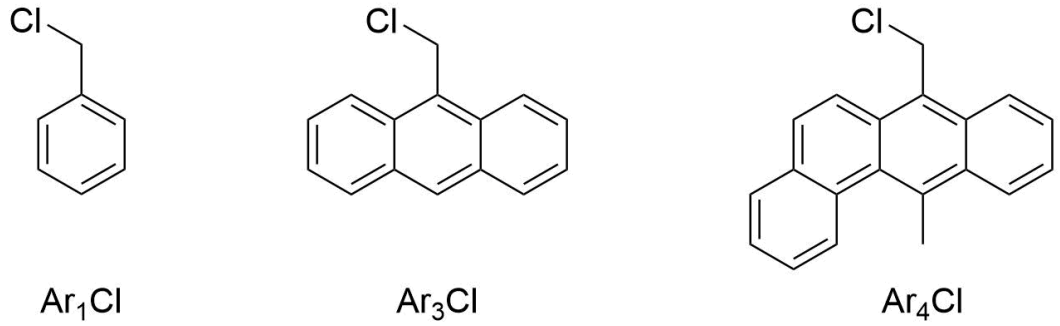

Figure 5.19: Model substrates with different numbers of aromatic rings as backbone. These modulate the strength of catalyst-substrate interactions through π-π stacking.

potential. Chloride abstraction by the catalyst, rather than fluoride delivery, in the TS is unfavorable by 24 kJ/mol – comparable to the bromide leaving group.

To probe the role of interaction between catalyst and substrate, substrates with different numbers of aromatic rings were computed (Figure 5.19, with names **Ar$_x$Cl** where the aromatic skeleton is based upon x aromatic rings). The critical Gibbs free energies are given in Table 5.3, with partial Gibbs free energy profile plotted in Figure 5.20. The barrier to uncatalyzed fluoride delivery is relatively consistent between the 3 substrates, perhaps due to increased stabilization of the TS through conjugation with a larger π system, balanced with 1,3-allylic strain in **Ar$_3$Cl** and **Ar$_4$Cl**. The relative electronic energies of the species are tabulated in Table 5.4 for comparison.

Table 5.3: Critical Gibbs Free Energies with Different Aromatic Groups on Substrate at 298.15 K.

		Gibbs Free Energy / kJ/mol			
	Catalyst	**II**	**III**	**IV‡**	**Span**
Ar$_1$Cl	–	n/a	n.d.	87.2	87.2
	Urea$_H$	-28.9	2.3	79.4	108.3
Ar$_3$Cl	–	n/a	n.d.	87.2	87.2
	Urea$_H$	-28.9	-5.2	67.9	96.7
Ar$_4$Cl	–	n/a	n.d.	86.4	86.4
	Urea$_H$	-28.9	-7.5	58.8	87.6

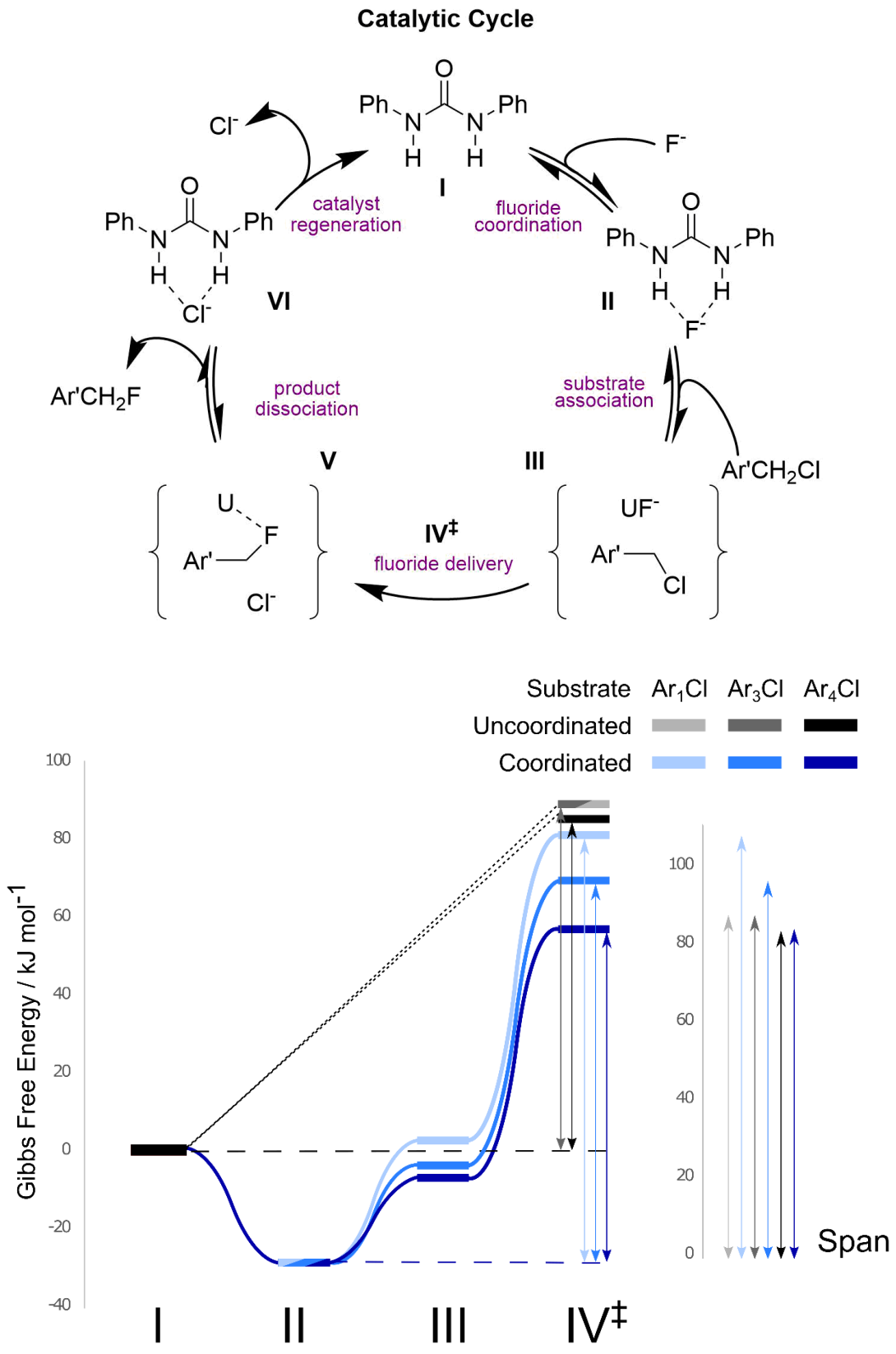

Figure 5.20: Gibbs free energy profile for fluorination of chloride substrates, **Ar$_x$Cl**, with increasing catalyst-substrate π-stacking with increasing x. Energetic span is decreased as the number of substrate aromatic rings increases. Structures are given in Figures S26-28.

Table 5.4: Critical Energies with Different Aromatic Groups on Substrate.

		Energy / kJ/mol		
	Catalyst	**II**	**III**	**IV‡**
Ar_1Cl	–	n/a	n.d.	64.2
	$Urea_H$	-55.7	-81.4	-2.8
Ar_3Cl	–	n/a	n.d.	64.3
	$Urea_H$	-55.7	-94.2	-18.4
Ar_4Cl	–	n/a	n.d.	64.5
	$Urea_H$	-55.7	-97.6	-28.7

With **$Urea_H$**, the TDI remains the urea-fluoride complex for all substrates (**I**). Coordination of substrate remains unfavorable due to the entropic penalty, however, becomes more favorable as the π system becomes larger (**II**: **Ar_1Cl**: 2.3 kJ/mol → **Ar_4Cl**: -7.5 kJ/mol). The greater catalyst-substrate interaction with larger π systems is also reflected in stabilization of the fluoride delivery TS (**IV‡**) by up to 21 kJ/mol (**Ar_1Cl**: 79.4 kJ/mol → **Ar_4Cl**: 58.8 kJ/mol). Interestingly, the barrier to fluoride delivery (**III-IV‡**) is also decreased with the larger π system – this arises as the chloride favors CH interactions, and the catalyst favors π-stacking with the substrate. These two interactions cannot both be optimal in the ion pair (Figure S26). Whilst this is of little consequence here, achieving such a differential is useful if the reactive complex is tightly bound.

Under standard conditions, none of the substrates achieve a lower effective barrier for urea mediated fluorination over the uncoordinated background reaction, however, in the case of the largest π-system (**Ar_4Cl**), this difference is within computational error (Uncoordinated: 86 kJ/mol, Coordinated: 88 kJ/mol). Biasing the conditions in favor of the coordinated reaction by lowering the temperature to 258.15 K (feasible for a reaction of this kinetic barrier) to reduce the unfavorable entropic terms, results in a lower barrier to the coordinated reaction, achieving catalysis (Table 5.5). Changing overall

Table 5.5: Critical Gibbs Free Energies for Fluorination of **Ar_4Cl** Substrate at Reduced Temperature (258.15 K).

		Gibbs Free Energy / kJ/mol			
	Catalyst	**II**	**III**	**IV‡**	**Span**
Ar_4Cl	–	n/a	n.d.	81.8	83.3
	$Urea_H$	-32.7	-18.9	47.4	80.1

concentration will not significantly affect the relative rates of the catalyzed and uncatalyzed pathways as the change in molecularity between the rate limiting states is the same, despite the molecularity of the catalyzed reaction being higher.

An alternative system was also investigated, with catalyst-substrate interactions augmented by a weak hydrogen bond. This has the effect of stabilizing the TDTS for the catalyzed pathway through coordination of the urea oxygen, but also serves to stabilize the intermediate ion pair by coordinating fluoride directly, potentially decreasing rate for both catalyzed and uncatalyzed pathways (Figure 5.21).

The degree to which this affects the uncatalyzed reaction depends upon the degree of equilibration of the reactive complex prior to fluoride attack, leading to an inherent complexity to this approach. At decreased temperature of 258.15 K, the system demonstrates potential for catalysis, reducing the effective barrier from 96 to 91 kJ/mol,

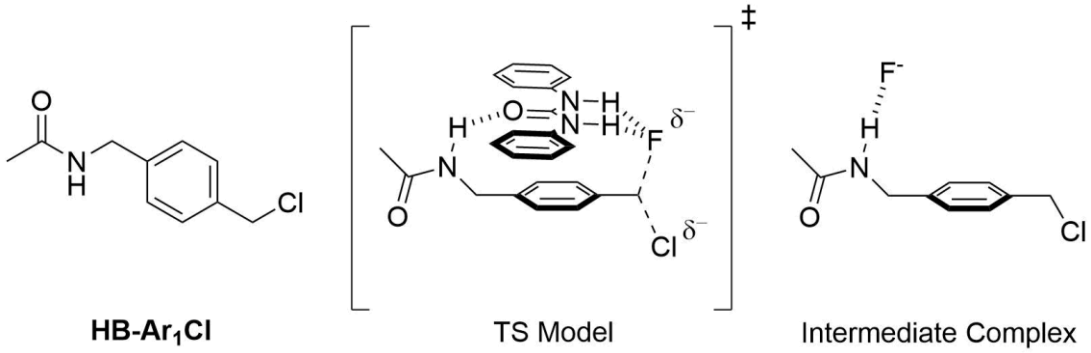

Figure 5.21: Substrate designed to interact with urea catalyst through a weak hydrogen bond. The primary effect is hydrogen bonding of the urea oxygen atom in the TS, however a secondary effect is a possible increase in barrier for the uncatalyzed pathway by formation of a more stable intermediate.

Table 5.6: Critical Gibbs Free Energies with Hydrogen Bonding Substrate.

			Gibbs Free Energy / kJ/mol			
	Catalyst	T/K	**II**	**III**	**IV‡**	**Span**
HB-Ar$_1$Cl	–	298.15	n/a	-8.1	88.4	96.4
	Urea$_H$	298.15	-28.9	-22.1	69.9	98.8
	–	258.15	n/a	-11.3	85.0	96.3
	Urea$_H$	258.15	-32.7	-33.4	58.7	91.4

from complex to TS (Table 5.6). The Gibbs free energy profile at 298.15 K is plotted in Figure 5.22 with comparison to non-hydrogen bonding **Ar$_1$Cl** substrate.

As computed, the hydrogen bonding system, **HB-Ar$_1$Cl**, achieves a lower barrier compared to background than the π-stacking based system **Ar$_1$Cl**. However, of note is that **HB-Ar$_1$Cl** can also hydrogen bond with the fluoride itself, whereas π-stacking is an orthogonal interaction. A result of this is that at reduced temperature, the catalyst-fluoride-substrate complex becomes TDI. Increasing the strength of the hydrogen bond is therefore unlikely to lower the energetic span further, as both TDI and TDTS will be lowered by similar amounts. Binding of the chloride leaving group in the TS, instead of fluoride is less favored by 26 kJ/mol (Figure S29).

Whilst in devising these systems, with the potential for catalysis, there is a degree of substrate engineering, the systems are a proof of principle. Further, it is theoretically necessary for catalyst-substrate interactions to be optimized and should not therefore be interpreted as a weakness of implementation. However, in devising synthetically useful reactions, the nature of these interactions should be kept as broad as possible to avoid unnecessarily narrow substrate scope. With the limits of computational accuracy in mind, experimental tweaking is expected before this principle is proved experimentally, notably the relative favorability of the coordinated and uncoordinated reactions depends upon

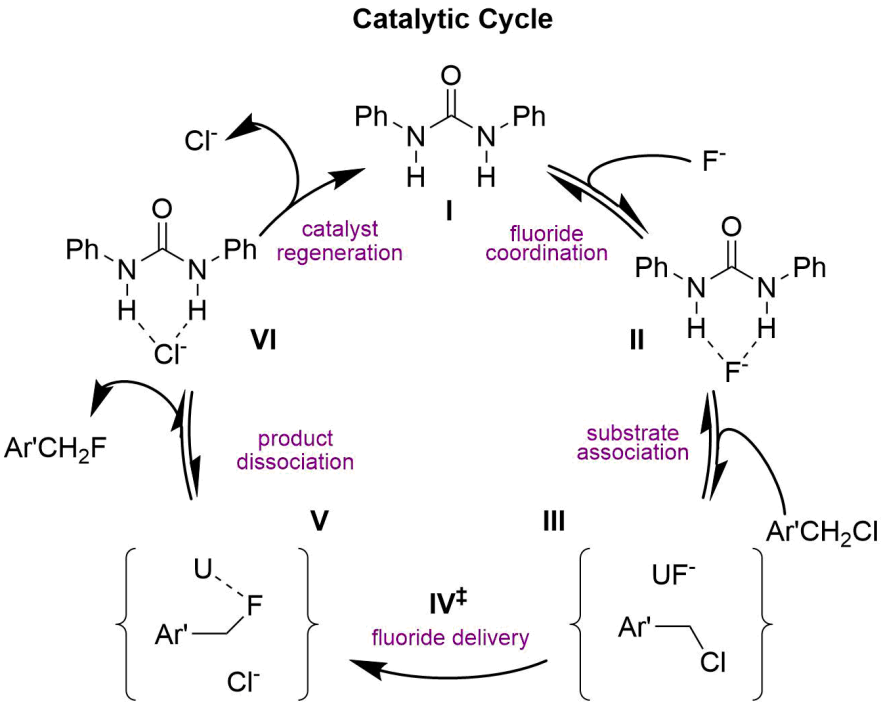

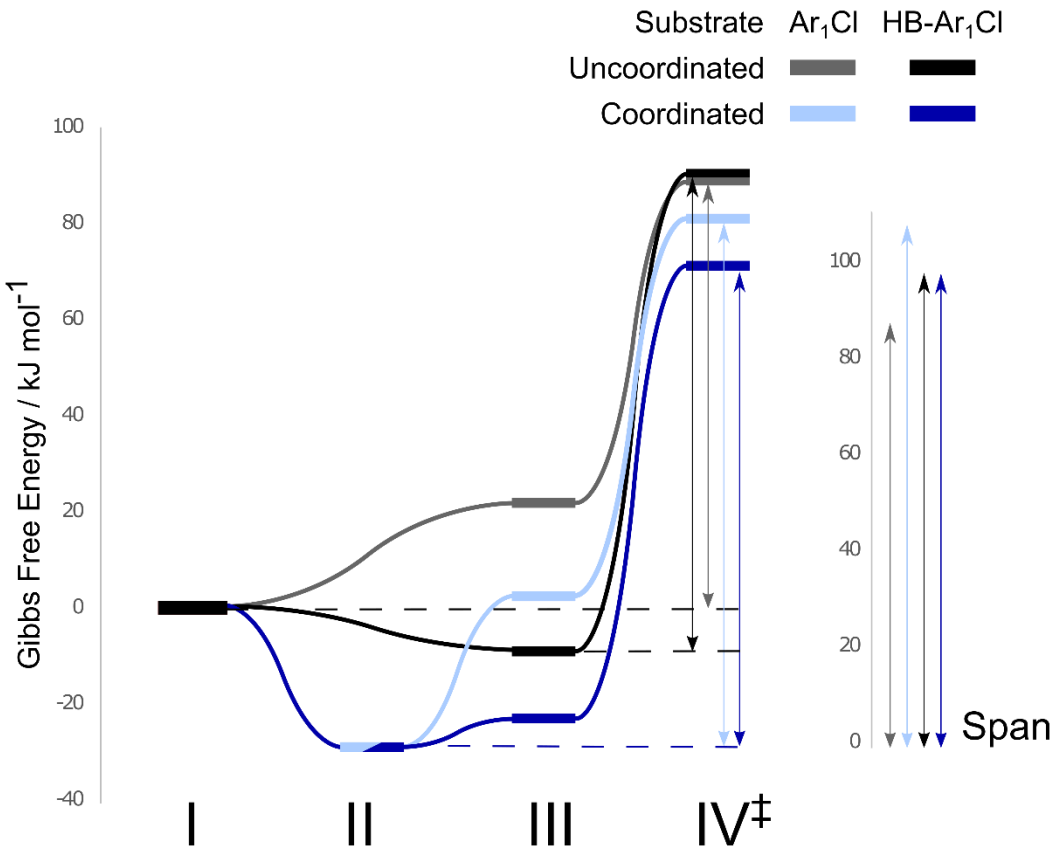

Figure 5.22: Gibbs free energy profile for fluorination of chloride substrates with, and without, substrate hydrogen bond donor group. Energetic span is decreased by formation of a catalyst-substrate hydrogen bond. The uncatalyzed reaction is also slowed by stabilization of the reactive complex.

accurate computation of the entropy of coordination, which is a recognized computational challenge.

The principles demonstrated here for neutral halide substrate can also be applied to charged substrates with a few additional considerations, such as the intrinsically more favorable complexation (ion pairing) energies. Further, as polar solvents are compatible, and indeed, sometimes favored, the principles should also be applicable to hydrogen bonding solvents when hydrophobic interactions are exploited. Experimentally, the lowering in energy of the TS through hydrogen bond donor-substrate interactions could initially be demonstrated using stoichiometric hydrogen bonded complexes by competition experiments between a substrate capable of forming strong catalyst-substrate interactions and one that is not.

Homogeneous catalysis with fluoride and hydrogen bonding catalysts leads to a much simpler reaction mechanism than HB PTC, providing a framework for experimental mechanistic investigation without the challenges of heterogeneous reactions (*e.g.* reactions can be monitored in real time by NMR). Synthetically, such an approach is complimentary to HB PTC, providing the potential for (enantio)selective fluorination, such as kinetic resolutions, in more polar solvents and providing an incremental route to small-molecule catalyzed fluorination in hydrogen bonding solvents with simple fluoride salts, and ultimately water.

5.3.7 Towards Fluorination under Aqueous Conditions

Nucleophilic fluorination in water is well understood to be challenging due to the lack of reactivity of fluoride when strongly solvated. None the less, nature's only fluorination enzyme, the fluorinase, does so using fluoride under aqueous conditions. Synthetically,

selective fluorination under aqueous conditions is desirable for several reasons i) to fluorinate molecules with poor solubility in organic solvents (or that denature, such as biomolecules), ii) water is a persistent impurity in commercial fluoride sources, iii) ^{18}F for radiochemistry is generated as an aqueous solution, with a significant proportion of activity lost during drying, iv) water is safe to handle and environmentally friendly.

A scenario can be envisaged using a small molecule hydrogen bonding catalyst in a hydrogen bonding solvent, similar to the conditions of the fluorinase. Using fluoride in water follows the same principles outlined earlier in this chapter but introduces a few constraints, i) strong solvent-fluoride hydrogen bonds and high solvent concentration make solvated fluoride likely the TDI and ii) multiple fluoride-water hydrogen bonds must be broken for fluoride to interact with catalyst and substrate, increasing the energetic span. In the absence of additional interactions, hydrogen bonding to fluoride cannot catalyze fluorination in water from aqueous fluoride. In the case that the HB donor binds fluoride more strongly than the solvent, it will lower both the TDI (becoming solvated catalyst-fluoride complex) and the fluoride delivery TDTS – the former to a greater degree, increasing the energetic span of the reaction. On the other hand, if the donor binds fluoride less strongly than the solvent, it will stabilize neither and have no effect on the reaction (Figure 5.23). Achieving catalysis, *i.e.* decreasing the energetic barrier of the reaction relative to coordination by solvent, must therefore be achieved by stabilizing the TDTS using interactions other than catalyst-fluoride hydrogen bonds.

Catalysis can be achieved by sufficiently favorable catalyst-substrate interactions, lowering the TDTS relative to the TDI, as these interactions are not present in the TDI. Additionally, having a positively charged electrophile allows the system to benefit from

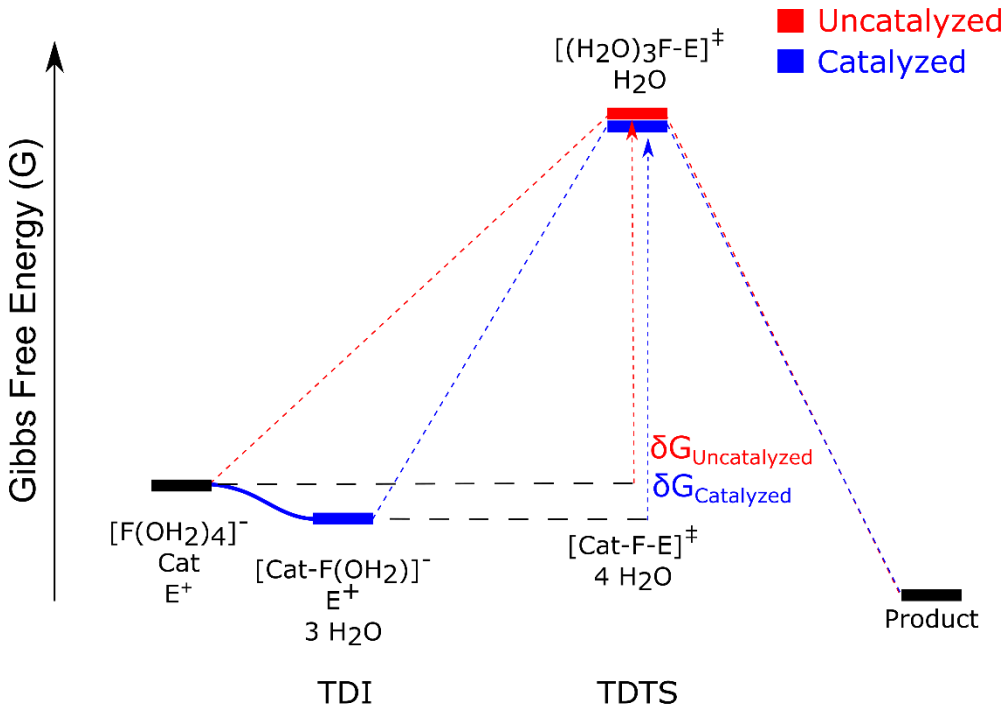

Figure 5.23: A catalyst that interacts only through hydrogen bonding to fluoride cannot catalyze a simple fluorination in water. If the HB donor outcompetes water (blue), both TDI and TDTS are lowered in Gibbs free energy, but the former to a greater degree, increasing the energetic span. If the HB donor cannot outcompete water, neither the TDI nor TDTS is lowered in Gibbs free energy and the energetic barrier is unchanged.

the Coulombic interaction. Weaker hydrogen bonding to fluoride is advantageous to prevent the intermediates from becoming too low in energy and increasing the energetic span. As previously stated, it must be ensured that catalyst-product interactions are not too strong as to inhibit turnover. Further, exploiting Coulombic interactions ensures that substrate binding to catalyst in the absence of fluoride is not too favorable, making this complex the TDI. A hypothetical Gibbs free energy profile where catalysis is achieved is shown in Figure 5.24.

Hydrogen bonding of the catalyst to fluoride is comparable in strength to binding of the catalyst to the substrate (bearing in mind the strong solvation of the fluoride). The ternary reactive complex (**III**) is therefore only marginally higher in free energy than the starting materials due to a balance of strong binding energy and the entropic loss on coordination.

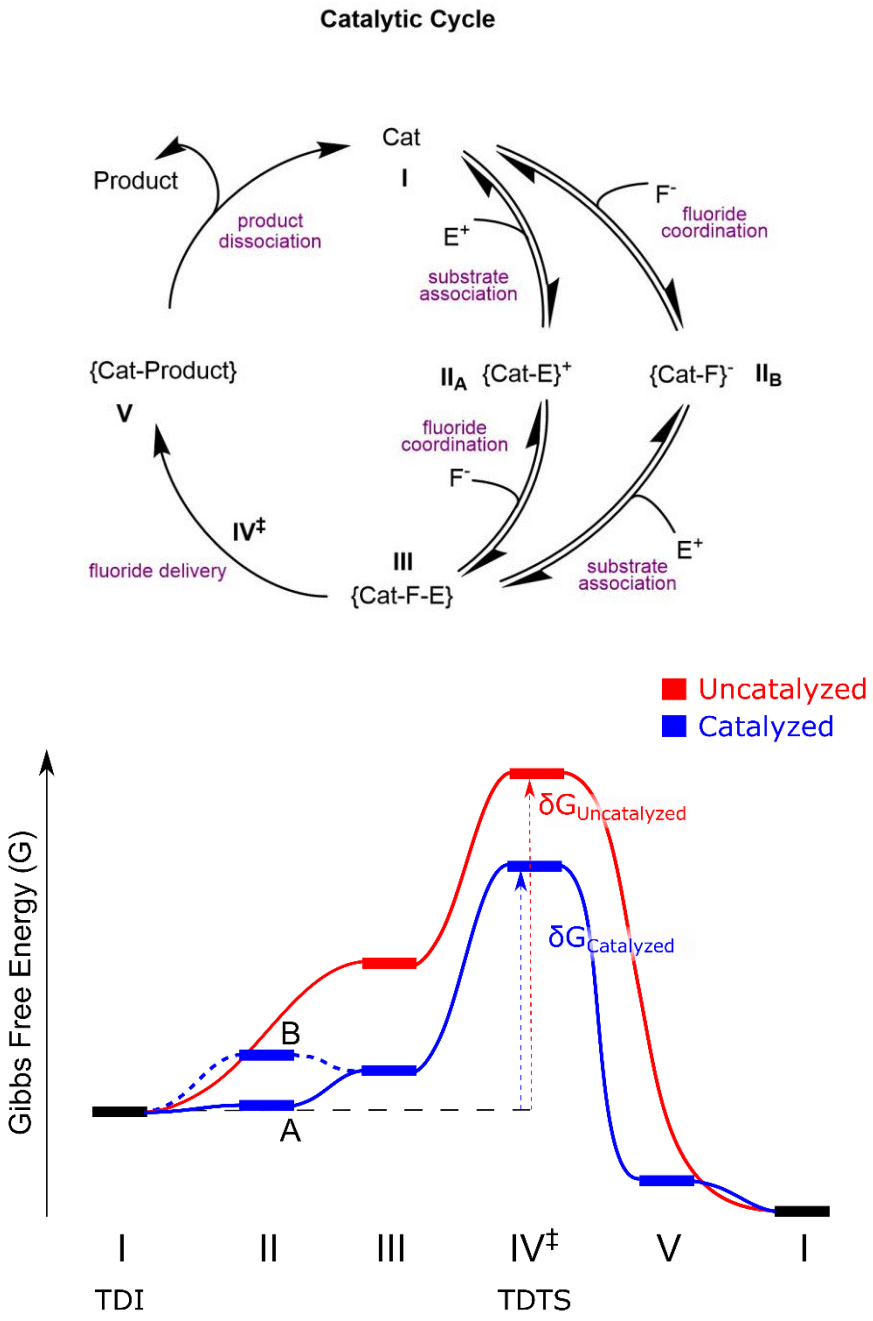

Figure 5.24: Hypothetical Gibbs free energy profile achieving catalysis under aqueous conditions. Binding of fluoride by the hydrogen bonding catalyst (**II$_B$**) is weaker than binding of electrophile (**II$_A$**). Strong catalyst-electrophile interactions are maintained from the reactive complex to the transition state structure.

This contrasts with the higher Gibbs free energy complex in the uncatalyzed pathway, where fluoride-substrate interactions are weak. The barrier from complex **(III**) to TS (**IV**‡) is comparable for both the catalyzed and uncatalyzed pathways as the hydrogen bonding strengths of catalyst and solvent are comparable.

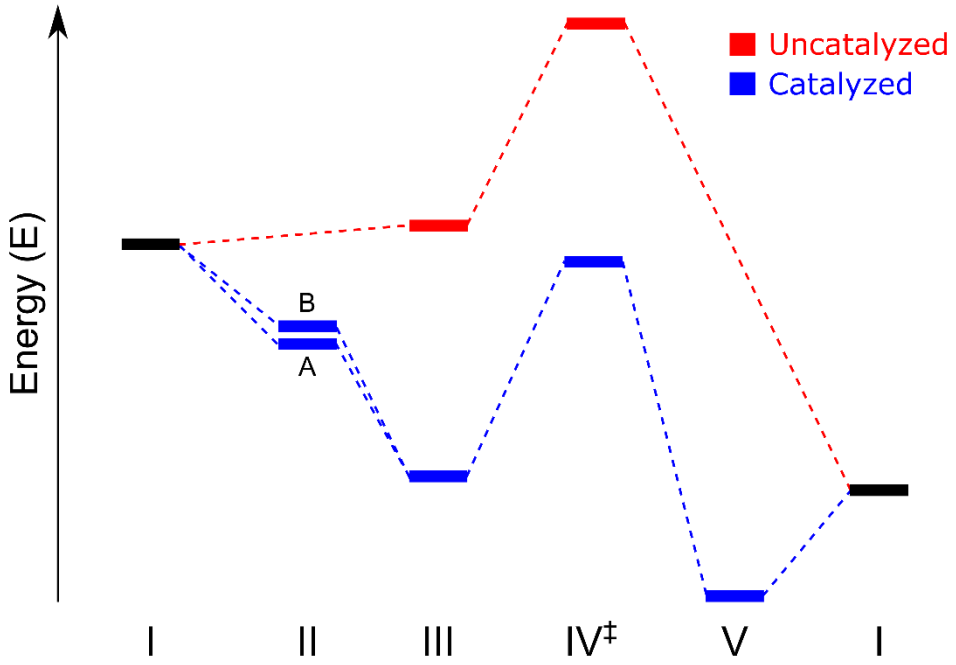

Figure 5.25: Hypothetical energy profile corresponding to the Gibbs free energy profile in Figure 5.24.

To better illustrate the consistency of these requirements, the corresponding electronic energy profile is given in Figure 5.25. **II$_A$** and **II$_B$** have approximately the same electronic energy – formation of **II$_B$** results in loss of rotational entropy, whereas formation of **II$_A$** does not. Stabilization of complex **III** by catalyst (energy difference between the two curves) is large and roughly the sum of catalyst interactions with fluoride and substrate individually. Fluoride-substrate interaction is therefore relatively small, consistent with the energy of the complex on the uncatalyzed pathway.

When considering the reactivity of the fluorinase enzyme, it is known that the fluorinase binds fluoride weakly, but substrate strongly, consistent with achieving catalysis on similar principles to the above profile.[32] A further important factor is that the fluorinase binds substrate in a reactive conformation, where the barrier to fluorination is reduced from 92 (112) kJ/mol to 53 (62) kJ/mol (BP86/TZVP+ and (B3LYP/TZVP+) with solvation effects in COSMO(H_2O) where applicable).[33] This effect is mainly down to the ground state conformation of substrate, and prevents the strongly bound

catalyst-fluoride-substrate complex from being too low in energy, where it could inhibit turnover. Potentially, binding of substrate only in a reactive conformation could be employed with a small molecule catalyst to enable strong substrate binding, without creating a low energy TDI.

5.3.8 Hydrogen Bonding Phase-Transfer Catalysis

The full mechanism of HB PTC is highly complex and challenging to investigate both experimentally and computationally due to the heterogeneous nature of the reaction and the presence of tight ion pairing in the low polarity solvent. The mechanism is, as yet, not fully understood, although the importance of the hydrogen bonding catalyst in phase-transfer and ion transport has been established (Chapter 3).

Clearly, the mechanism of HB PTC is far more complex than a simple homogeneous fluorination. Notably, stronger hydrogen bonding catalysts lead to higher TOF for the reaction, inconsistent with reactive complex as TDI and fluoride delivery TS as TDTS (Section 5.3.4). The heterogeneous nature of the setup plausibly suggests the TDI of the reaction being solid metal fluoride salt + free catalyst, with no catalyst-fluoride hydrogen bonding, due to the high lattice energy of the metal fluoride. In this case, the dependence of rate on donor strength can be reproduced when the TDTS involves the catalyst hydrogen bonding to fluoride in any capacity. Increasing the strength of the hydrogen bond donor lowers the TDTS but leaves the TDI unaffected. It is possible that the TOF limiting TS corresponds to fluoride delivery or is related to ion transport and phase-transfer. Identification of the TDTS in a reaction profile is sensitive to the phase-transfer process and ongoing mechanistic work suggests it is substrate dependent. Further, the degree of ion pairing is sensitive to concentration and the hydrogen bonding catalyst will be subject to competition between binding leaving group and fluoride.

5.3.9 Strengths and Weaknesses of the Fluoride Binding Approach

The strengths and weaknesses of the fluoride binding approach for nucleophilic substitution can be summarized as follows. Strengths: i) As the only engineered interaction is hydrogen bonding to fluoride, the principle is very general, and can be demonstrated by very simple hydrogen bonding catalysts such as *N,N'*-diphenylurea, ii) this interaction is strong enough to activate potassium fluoride in apolar solvents, and is shown directly to solubilize cesium fluoride, iii) as fluoride is neutralized over the reaction, product does not sequester catalyst, iv) small (catalytic) quantities of hydrogen bond donor are sufficient. Limitations: i) In a homogeneous system, hydrogen bonding to fluoride alone cannot catalyze fluorination from fluoride, ii) the effect of hydrogen bond donor strength on turnover frequency is complex, depending on the exact mechanism of the transformation, iii) solid-liquid phase-transfer hinders mechanistic study, iv) hydrogen bonding to fluoride strongly links tuning of reactivity and selectivity, potentially leading to compromises in catalyst design.

5.4 Conclusions

This chapter summarizes the insight and knowledge that has been gained through the investigation of the effects of hydrogen bond donors on the reactivity and selectivity of fluoride, through computational and theoretical methods.

Computational insight gained into the origins of enantioselectivity for HB PTC fluorination of episulfonium and aziridinium ions underlines the challenges in achieving high enantioselectivities with broad substrate scope. Computation defines the problem and is currently being used for the rational design of a second-generation of catalysts with an engineered substrate binding group, that reduces the accessible conformations of the substrate in the catalytic pocket. Designs that have been tested so far are hindered by low

activity, however the design principles are broad and, combined with experimental screening, provides a promising area of future research.

The complex and varying ways in which hydrogen bonding to fluoride affects the rate of a fluorination reaction are discussed in depth, and seemingly contradictory experimental observations are shown to be consistent with kinetic theory. Several scenarios are outlined with varying effects of hydrogen bond donor strength on catalytic turnover frequency. The kinetics of HB PTC fluorination reactions, where stronger hydrogen bonding leads to increased TOF, can be explained in terms of a catalyst resting state where the catalyst is not hydrogen bonding to fluoride – plausibly with fluoride strongly bound in the insoluble fluoride salt. Under homogeneous conditions, a donor hydrogen bonding to fluoride, alone, cannot catalyze fluorination from fluoride, however exploitation of catalyst-substrate interactions can potentially make this possible. Several model systems are computed with catalyst-substrate π-π stacking or catalyst-substrate hydrogen bonding. Ultimately, these principles may be applied to aqueous fluorination, without requiring an enzymatic environment, however, it remains to be seen whether these constraints are achievable in practice with a small molecule catalyst. Whilst optimization of catalyst-substrate interactions mandates development of multi-functional catalysts, which are more synthetically challenging, this chapter outlines the circumstances in which they are necessary to pursue.

The strengths and weaknesses of our fluoride binding approach for fluorination from fluoride are summarized, establishing the approach as complimentary to existing methods. Overall, this work highlights the importance, benefits and plausibility of real-time collaboration of computation and experiment to tackle challenging problems in organic chemistry.

5.5 References

(1) Lee, J.-W. W.; Oliveira, M. T.; Jang, H. Bin; Lee, S.; Chi, D. Y.; Kim, D. W.; Song, C. E. Hydrogen-Bond Promoted Nucleophilic Fluorination: Concept, Mechanism and Applications in Positron Emission Tomography. *Chem. Soc. Rev.* **2016**, *45*, 4638–4650.

(2) Liang, S.; Hammond, G. B.; Xu, B. Hydrogen Bonding: Regulator for Nucleophilic Fluorination. *Chem. Eur. J.* **2017**, *23*, 17850–17861.

(3) Vincent, M. A.; Hillier, I. H. The Solvated Fluoride Anion Can Be a Good Nucleophile. *Chem. Commun.* **2005**, 5902–5903.

(4) Kim, D. W.; Jeong, H.; Lim, S. T.; Sohn, M.; Katzenellenbogen, J. A.; Chi, D. Y. Facile Nucleophilic Fluorination Reactions Using *Tert*-Alcohols as a Reaction Medium: Significantly Enhanced Reactivity of Alkali Metal Fluorides and Improved Selectivity. *J. Org. Chem.* **2008**, *73*, 957–962.

(5) Yang, L.; Dong, T.; Revankar, H. M.; Zhang, C.-P. P. Recent Progress on Fluorination in Aqueous Media. *Green Chem.* **2017**, *19*, 3951–3992.

(6) Kim, D. W.; Ahn, D. S.; Oh, Y. H.; Lee, S.; Kil, H. S.; Oh, S. J.; Lee, S. J.; Kim, J. S.; Ryu, J. S.; Moon, D. H.; Chi, D. Y. A New Class of S_N2 Reactions Catalyzed by Protic Solvents: Facile Fluorination for Isotopic Labeling of Diagnostic Molecules. *J. Am. Chem. Soc.* **2006**, *128*, 16394–16397.

(7) Jadhav, V. H.; Choi, W.; Lee, S. S.; Lee, S.; Kim, D. W. Bis-*Tert*-Alcohol-Functionalized Crown-6-Calix[4]Arene: An Organic Promoter for Nucleophilic Fluorination. *Chem. Eur. J.* **2016**, *22*, 4515–4520.

(8) Kozuch, S.; Shaik, S. How to Conceptualize Catalytic Cycles? The Energetic Span Model. *Acc. Chem. Res.* **2011**, *44*, 101–110.

(9) Kozuch, S. A Refinement of Everyday Thinking : The Energetic Span Model for Kinetic Assessment of Catalytic Cycles. *WIREs Comput. Mol .Sci.* **2012**, *2*, 795–815.

(10) Uhe, A.; Hölscher, M.; Leitner, W. Carboxylation of Arene C-H Bonds with CO_2: A DFT-Based Approach to Catalyst Design. *Chem. Eur. J.* **2012**, *18*, 170–177.

(11) Kozuch, S.; Lee, S. E.; Shaik, S. Theoretical Analysis of the Catalytic Cycle of a Nickel Cross-Coupling Process: Application of the Energetic Span Model. *Organometallics* **2009**, *28*, 1303–1308.

(12) Lin, X.; Sun, J.; Xi, Y.; Lin, D. How Racemic Secondary Alkyl Electrophiles Proceed to Enantioselective Products in Negishi Cross-Coupling Reactions. *Organometallics* **2011**, *30*, 3284–3292.

(13) Kozuch, S.; Martin, J. M. L. What Makes for a Bad Catalytic Cycle? A Theoretical Study on the Suzuki-Miyaura Reaction within the Energetic Span Model. *ACS Catal.* **2011**, *1*, 246–253.

(14) Wodrich, M. D.; Sawatlon, B.; Solel, E.; Kozuch, S.; Corminboeuf, C. Activity-Based Screening of Homogeneous Catalysts through the Rapid Assessment of Theoretically Derived Turnover Frequencies. *ACS Catal.* **2019**, *9*, 5716–5725.

(15) Kozuch, S.; Martin, J. M. L. "Turning Over" Definitions in Catalytic Cycles. *ACS Catal.* **2012**, *2*, 2787–2794.

(16) Frisch, M. J.; Trucks, G. W.; Schlegel, H. B.; Scuseria, G. E.; Robb, M. A.; Cheeseman, J. R.; Scalmani, G.; Barone, V.; Petersson, G. A.; Nakatsuji, H.; Li, X.; Caricato, M.; Marenich, A.; Bloino, J.; Janesko, B. G.; Gomperts, R.; Mennucci, B.; Hratchian, H. P.; Ortiz, J. V.; Izmaylov, A. F.; Sonnenberg, J. L.; Williams-Young, D.; Ding, F.; Lipparini, F.; Egidi, F.; Goings, J.; Peng, B.; Petrone, A.; Henderson, T.; Ranasinghe, D.; Zakrzewski, V. G.; Gao, J.; Rega, N.; Zheng, G.; Liang, W.; Hada, M.; Ehara, M.; Toyota, K.; Fukuda, R.; Hasegawa, J.; Ishida, M.; Nakajima, T.; Honda, Y.; Kitao, O.; Nakai, H.; Vreven, T.; Throssell, K.; Montgomery Jr., J. A.; Peralta, J. E.; Ogliaro, F.; Bearpark, M.; Heyd, J. J.; Brothers, E.; Kudin, K. N.; Staroverov, V. N.; Keith, T.; Kobayashi, R.; Normand, J.; Raghavachari, K.; Rendell, A.; Burant, J. C.; Iyengar, S. S.; Tomasi, J.; Cossi, M.; Millam, J. M.; Klene, M.; Adamo, C.; Cammi, R.; Ochterski, J.

W.; Martin, R. L.; Morokuma, K.; Farkas, O.; Foresman, J. B.; Fox, D. J. Gaussian 16. Gaussian Inc: Wallingford, CT 2016.
(17) Zhao, Y.; Truhlar, D. G. The M06 Suite of Density Functionals for Main Group Thermochemistry, Thermochemical Kinetics, Noncovalent Interactions, Excited States, and Transition Elements: Two New Functionals and Systematic Testing of Four M06-Class Functionals and 12 Other Functionals. *Theor. Chem. Acc.* **2008**, *120*, 215–241.
(18) Rappoport, D.; Furche, F. Property-Optimized Gaussian Basis Sets for Molecular Response Calculations. *J. Chem. Phys.* **2010**, *133*, 134105.
(19) Weigend, F.; Ahlrichs, R. Balanced Basis Sets of Split Valence, Triple Zeta Valence and Quadruple Zeta Valence Quality for H to Rn: Design and Assessment of Accuracy. *Phys. Chem. Chem. Phys.* **2005**, *7*, 3297–3305.
(20) Leininger, T.; Nicklass, A.; Küchle, W.; Stoll, H.; Dolg, M.; Bergner, A. The Accuracy of the Pseudopotential Approximation: Non-Frozen-Core Effects for Spectroscopic Constants of Alkali Fluorides XF (X = K, Rb, Cs). *Chem. Phys. Lett.* **1996**, *255*, 274–280.
(21) Barone, V.; Cossi, M. Quantum Calculation of Molecular Energies and Energy Gradients in Solution by a Conductor Solvent Model. *J. Phys. Chem. A* **1998**, *102*, 1995–2001.
(22) Cossi, M.; Rega, N.; Scalmani, G.; Barone, V. Energies, Structures, and Electronic Properties of Molecules in Solution with the C-PCM Solvation Model. *J. Comput. Chem.* **2003**, *24*, 669–681.
(23) Takano, Y.; Houk, K. N. Benchmarking the Conductor-like Polarizable Continuum Model (CPCM) for Aqueous Solvation Free Energies of Neutral and Ionic Organic Molecules. *J. Chem. Theory Comput.* **2005**, *1*, 70–77.
(24) Funes-Ardoiz, I.; Paton, R. S. Goodvibes v2.0. **2018**, http://doi.org/10.5281/zenodo.3346166.
(25) Grimme, S. Supramolecular Binding Thermodynamics by Dispersion-Corrected Density Functional Theory. *Chem. Eur. J.* **2012**, *18*, 9955–9964.
(26) Neese, F. The ORCA Program System. *Wiley Interdiscip. Rev. Comput. Mol. Sci.* **2012**, *2*, 73–78.
(27) Neese, F. Software Update: The ORCA Program System, Version 4.0. *Wiley Interdiscip. Rev. Comput. Mol. Sci.* **2018**, *8*, e1237.
(28) Chai, J.-D.; Head-Gordon, M. Long-Range Corrected Hybrid Density Functionals with Damped Atom–Atom Dispersion Corrections. *Phys. Chem. Chem. Phys.* **2008**, *10*, 6615–6620.
(29) Lin, Y.-S.; Li, G.-D.; Mao, S.-P.; Chai, J.-D. Long-Range Corrected Hybrid Density Functionals with Improved Dispersion Corrections You-Sheng. *J. Chem. Theory Comput.* **2013**, *9*, 263–272.
(30) Grimme, S.; Antony, J.; Ehrlich, S.; Krieg, H. A Consistent and Accurate Ab Initio Parametrization of Density Functional Dispersion Correction (DFT-D) for the 94 Elements H-Pu. *J. Chem. Phys.* **2010**, *132*, 154104.
(31) Zheng, J.; Xu, X.; Truhlar, D. G. Minimally Augmented Karlsruhe Basis Sets. *Theor. Chem. Acc.* **2011**, *128*, 295–305.
(32) Zhu, X.; Robinson, D. A.; McEwan, A. R.; O'Hagan, D.; Naismith, J. H. Mechanism of Enzymatic Fluorination in Streptomyces Cattleya. *J. Am. Chem. Soc.* **2007**, *129*, 14597–14604.
(33) Senn, H. M.; O'Hagan, D.; Thiel, W. Insight into Enzymatic C-F Bond Formation from QM and QM/MM Calculations. *J. Am. Chem. Soc.* **2005**, *127*, 13643–13655.

6 Appendices

6.1 Supporting Information – Chapter 2

6.1.1 Selectivity for S_N2 vs E2 Reactivity

All ureas investigated are slightly non-planar and have two low energy conformers described approximately by the C_s and C_2 point groups. In all cases, the C_2 conformer is preferred by an insignificant energy difference – **Urea$_{CF3}$(C_s)** could not be located. The C_2 conformers are used in the rest of the work. All ureas become planar on binding fluoride.

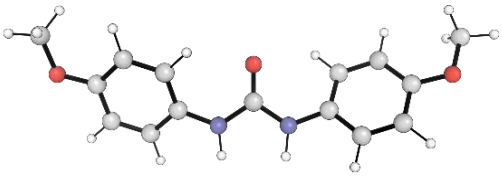

Urea$_{OMe}$(C_2)

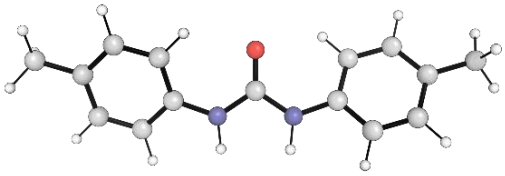

Urea$_{Me}$(C_2)

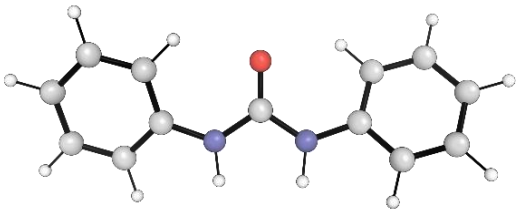

Urea$_{H}$(C_2)

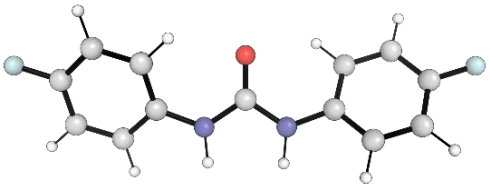

Urea$_{F}$(C_2)

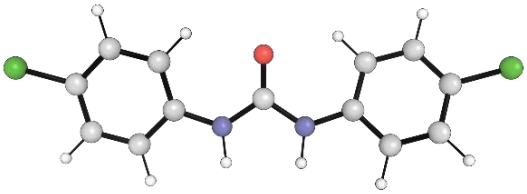

Urea$_{Cl}$(C_2)

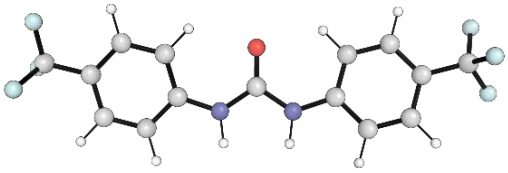

Urea$_{CF3}$(C_2)

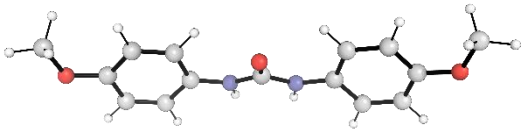

Urea$_{OMe}$(Cs) +1.5 kJ/mol

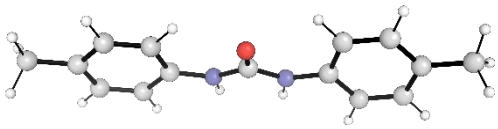

Urea$_{Me}$(Cs) +2.7 kJ/mol

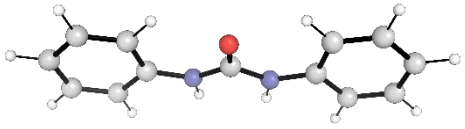

Urea$_{H}$(Cs) +1.8 kJ/mol

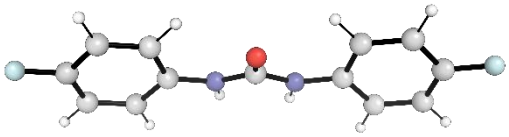

Urea$_{F}$(Cs) +2.4 kJ/mol

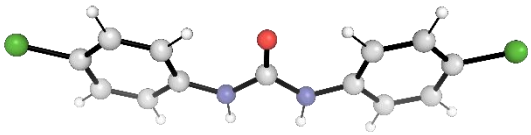

Urea$_{Cl}$(Cs) +1.0 kJ/mol

Figure S1: Urea geometries. Gibbs free energy differences at 343.15 K.

The ureas with more electron withdrawing substituents are generally closer to the planar structure than those with electron donating substituents. Dihedral angles are measured about the bond between urea nitrogen and aromatic group *ipso* carbon.

Table S1: Distortion of Ureas from Planar Structure.

Urea		**Urea Distortion from Planarity (Dihedral) / º**	
		1	**2**
OMe	**C_2**	31.9	31.9
Me	**C_2**	23.9	23.9
H	**C_2**	21.4	21.3
F	**C_2**	28.3	28.3
Cl	**C_2**	12.5	12.5
CF_3	**C_2**	8.5	7.1
OMe	**C_s**	30.8	-29.7
Me	**C_s**	15.5	-24.6
H	**C_s**	13.4	-13.3
F	**C_s**	26.5	-28.2
Cl	**C_s**	12.6	-14.3

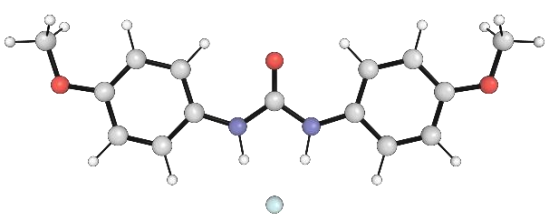

[$U_{OMe}F$]$^-$

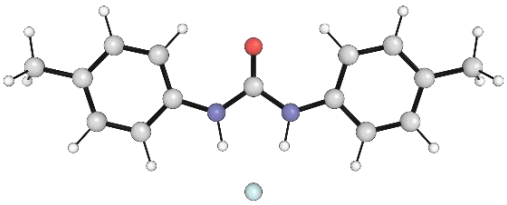

[$U_{Me}F$]$^-$

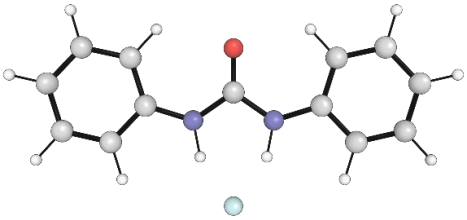

[$U_{H}F$]$^-$

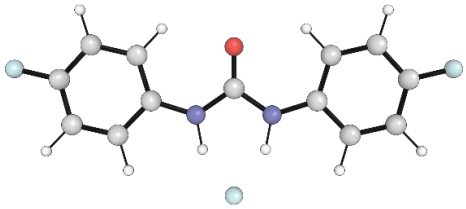

[$U_{F}F$]$^-$

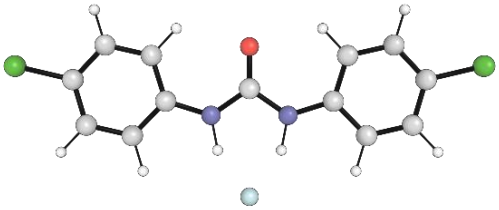

[$U_{Cl}F$]$^-$

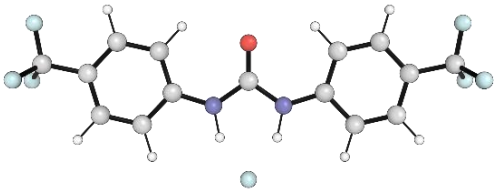

[$U_{CF3}F$]$^-$

Figure S2: Urea-fluoride complex geometries.

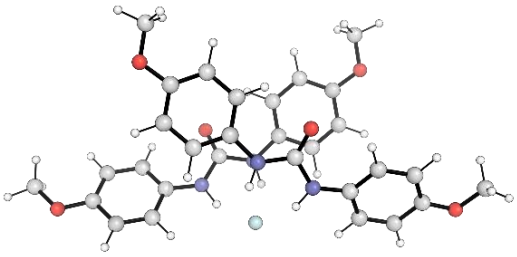

[$U_{OMe\ 2}F$]$^-$

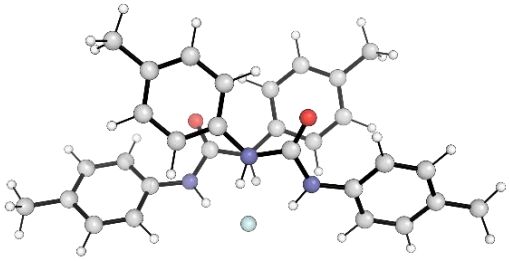

[$U_{Me\ 2}F$]$^-$

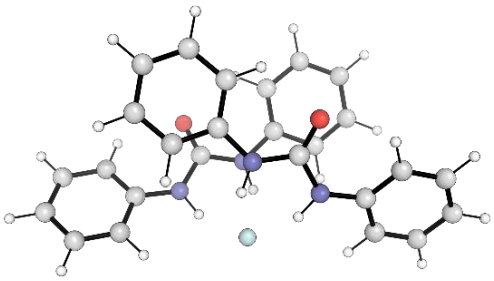

[$U_{H\ 2}F$]$^-$

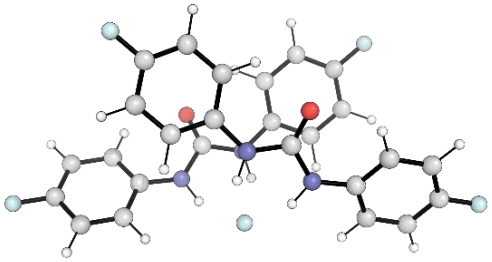

[$U_{F\ 2}F$]$^-$

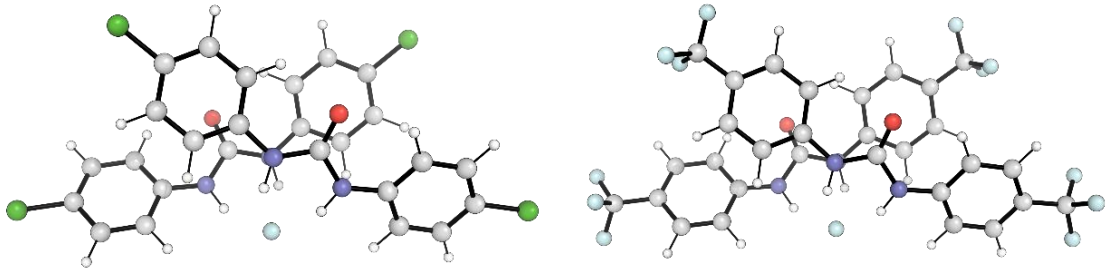

$[U_{Cl\ 2}F]^-$ **$[U_{CF3\ 2}F]^-$ ***

Figure S3: Bis urea-fluoride complex geometries. *Low imaginary frequency.

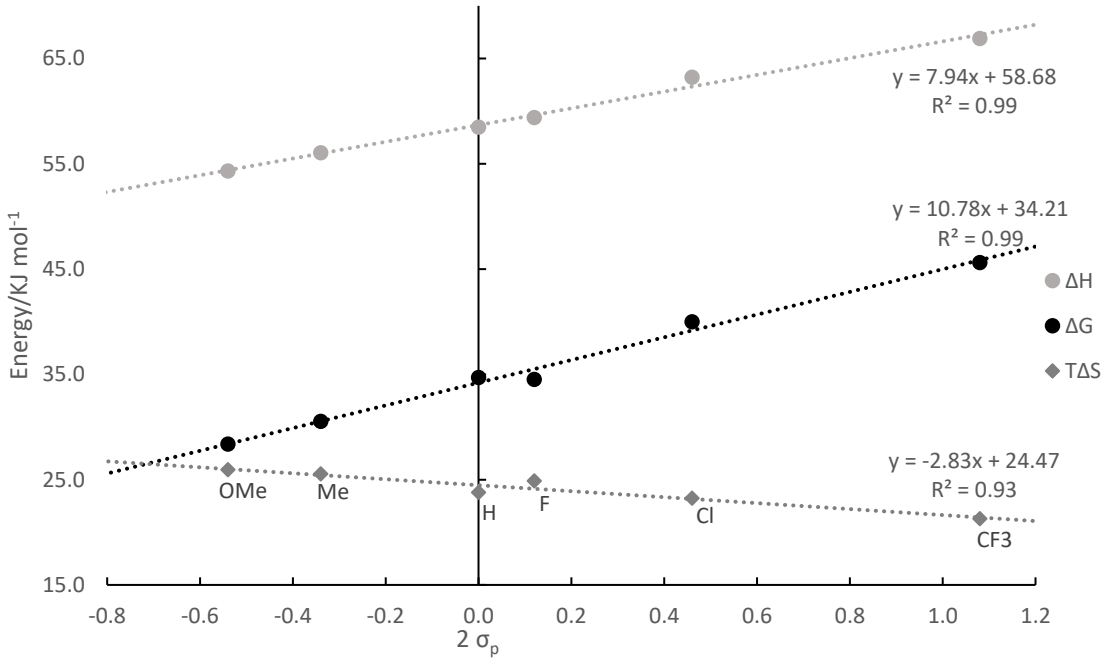

Figure S4: Computed Gibbs free energies, enthalpies and entropies of binding for $[UF]^-$ complexes, plotted against Hammett σ_p (298.15 K, 1 M). Points from left to right represent $\mathbf{U_X}$ where X = OMe, Me, H, F, Cl, CF_3.

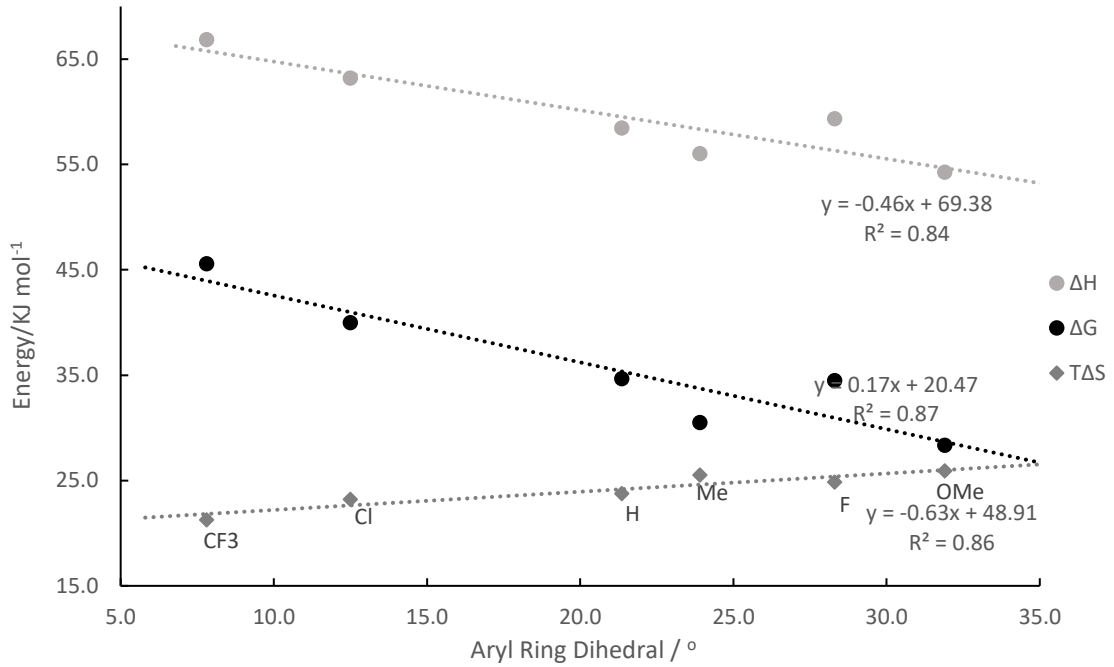

Figure S5: Computed Gibbs free energies, enthalpies and entropies of binding for $[UF]^-$ complexes, plotted against the planarity of the (C_2) urea when uncoordinated, represented by dihedral angle (Table S1). Points from left to right represent $\mathbf{U_X}$ where X = OMe, Me, H, F, Cl, CF_3.

The difference in entropy of coordination between different ureas originates from the change in vibrational entropy upon fluoride binding.

Table S2: Change in (Uncorrected) Entropic Terms of Ureas upon Fluoride Binding.

Urea	**TΔS of fluoride binding, 298.15 K, 1 atm / kJ/mol**				
	Total	**Elec**	**Trans**	**Rot**	**Vib**
CF_3	-23.7	0.0	-44.0	0.5	19.9
Cl	-29.2	0.0	-44.0	0.7	14.1
F	-32.2	0.0	-43.9	0.7	11.0
H	-31.2	0.0	-43.9	0.8	11.9
Me	-35.2	0.0	-43.9	0.7	7.9
OMe	-34.2	0.0	-43.9	0.6	9.2

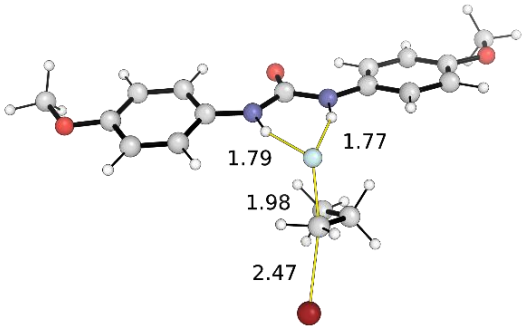

TS-S$_N$2-OMe

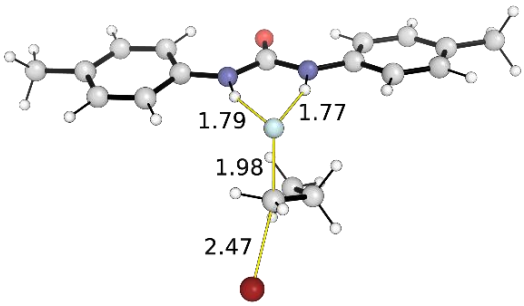

TS-S$_N$2-Me

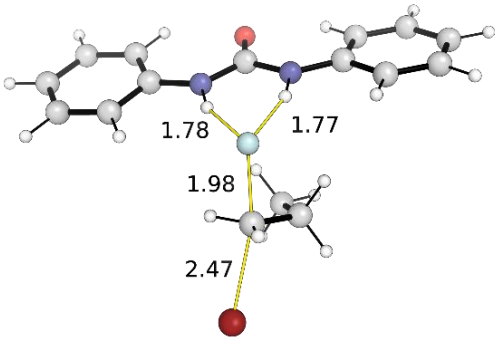

TS-S$_N$2-H

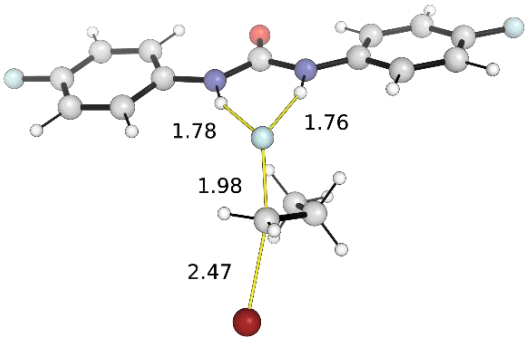

TS-S$_N$2-F

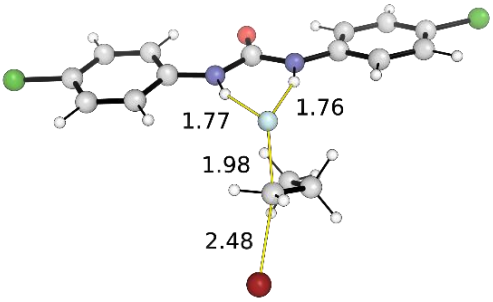

TS-S$_N$2-Cl

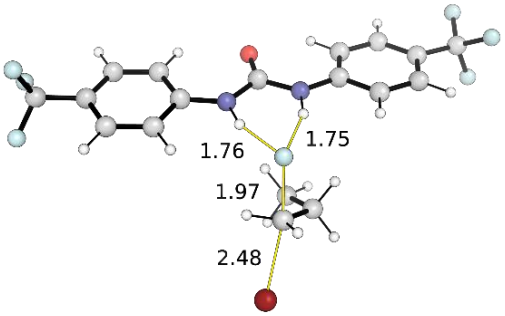

TS-S$_N$2-CF$_3$

Figure S6: S$_N$2 transition state structures.

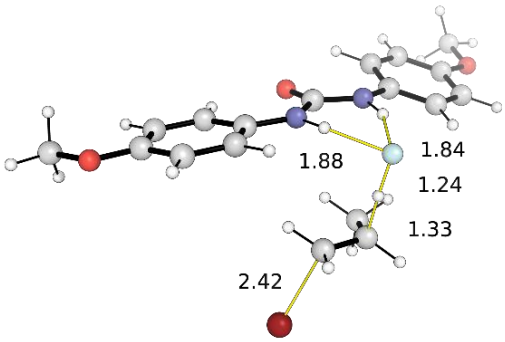

TS-E2-OMe

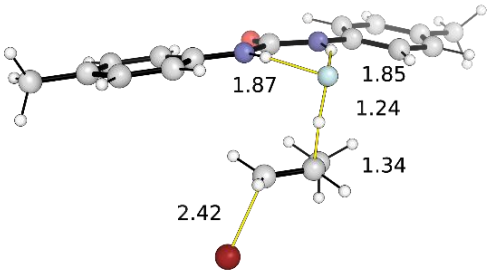

TS-E2-Me

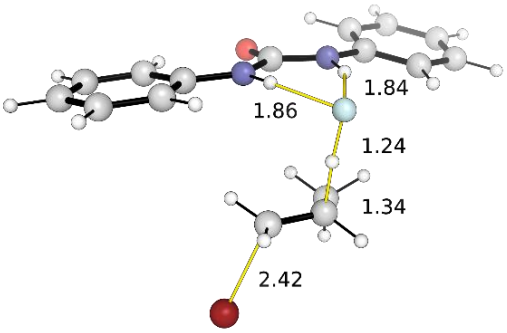

TS-E2-H

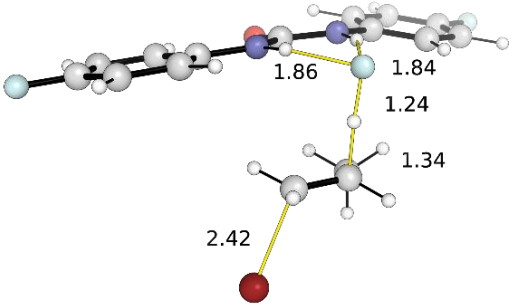

TS-E2-F

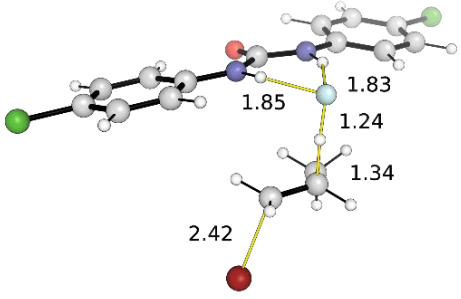

TS-E2-Cl

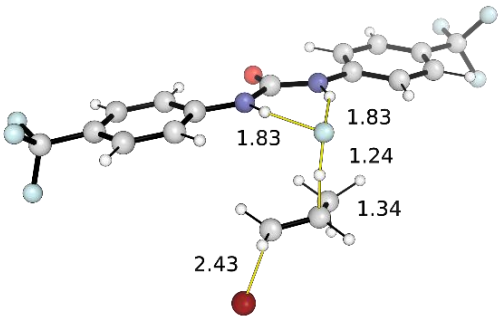

TS-E2-CF_3

Figure S7: E2 transition state structures.

Table S3: Key Bond Distances for S_N2 and E2 TSs with $[UF]^-$ Complexes.

Species	Sub^n	S_N2			E2				$[UF]^-$
		C-F	C-Br	N-F	H-F	C-H	C-Br	N-F	N-F
No urea	n/a	2.045	2.394	n/a	1.247	1.319	2.299	n/a	n/a
Urea	**OMe**	1.983	2.471	2.750	1.244	1.335	2.417	2.809	2.656
	Me	1.982	2.471	2.747	1.244	1.335	2.419	2.808	2.653
	H	1.979	2.473	2.743	1.241	1.337	2.421	2.804	2.647
	F	1.979	2.474	2.738	1.241	1.337	2.422	2.800	2.642
	Cl	1.977	2.477	2.733	1.241	1.338	2.425	2.794	2.634
	CF_3	1.973	2.481	2.725	1.238	1.339	2.431	2.786	2.621
R^2 vs σ_p		1.00	0.98	0.99	0.97	0.96	0.99	0.98	0.99
PrBr		n/a	1.968	n/a	n/a	1.094	1.968	n/a	n/a
PrF		1.400	n/a	n/a	n/a	n/a	n/a	n/a	n/a
HF		n/a	n/a	n/a	0.923	n/a	n/a	n/a	n/a

Bond lengths reported in Å. N-F distances are reported as an average.

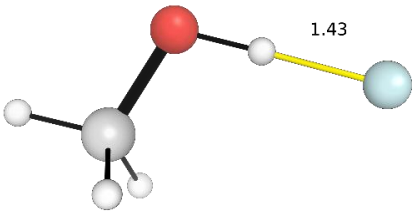

$[MeOH-F]^-$

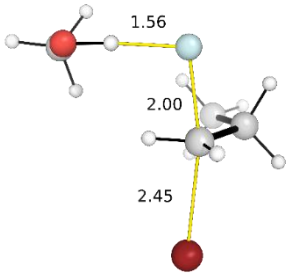

TS-S_N2-MeOH

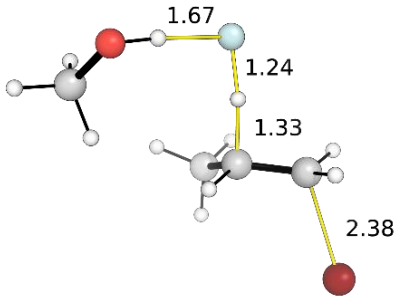

TS-E2-MeOH

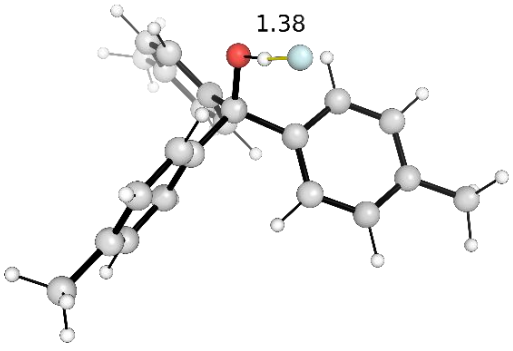

$[AF]^-$

Figure S8: Alcohol-fluoride species.

6.1.2 Fluoride Geometric Preference

Table S4: Geometric Data for Fluoride Hydrogen Fluoride Hydrogen Bonded Complexes.

Complex	F**H---F** distance / Å		F**H---F---H**F angle / ^{o}		**Point Group**‡
	1*	**2**	**1**	**2**	
$[F(HF)_1]^-$	1.135	-	180.0	-	$D_{\infty}h$
$[F(HF)_2]^-$	1.338	-	118.0	-	C_{2v}
$[F(HF)_3]^-$	1.429	-	120.0-120.1	-	C_{3v}
$[F(HF)_4]^-$	1.507	-	109.5	-	T_d
$[F(HF)_5]^-$	1.622	1.581	119.8-120.4	90.0-90.1	D_3h
$[F(HF)_6]^-$	1.675	-	90.0	-	O_h

*Axial distance where applicable. ‡Allowing for computational uncertainty where appropriate.

6.1.3 Thermodynamic Data

Thermochemistry evaluated at 343.15 K and 0.5 M concentration.

Table S5: Benchmarking.

	Energies / Ha		
	E (opt)	**G (opt)**	**G-qh (opt)**
E2_anti_M06L	-2792.692115	-2792.641616	-2792.641476
E2_syn_M06L	-2792.679597	-2792.629512	-2792.629236
S_N2_M06L	-2792.693589	-2792.637416	-2792.637300
E2_anti_TPSSTPSS	-2792.692115	-2792.641616	-2792.641476
E2_syn_TPSSTPSS	-2792.679597	-2792.629512	-2792.629236
S_N2_TPSSTPSS	-2792.693589	-2792.637416	-2792.637300
Urea_H_B3LYP_small	-787.436180	-787.258728	-787.256249
Urea_H_B3LYP_TZVPP(D)	-787.764895	-787.590051	-787.586919
Urea_H_M062X_small	-787.052187	-786.875011	-786.871587
Urea_H_M062X_TZVPP(D)	-787.377162	-787.202921	-787.198728
Urea_H_M06L_small	-787.052187	-786.875011	-786.871587
Urea_H_M06L_TZVPP(D)	-787.574547	-787.400005	-787.396654
Urea_H_OLYP_small	-787.106626	-786.936170	-786.932833
Urea_H_OLYP_TZVPP(D)	-787.408823	-787.240993	-787.237552
Urea_H_TPSSTPSS_small	-787.502654	-787.331699	-787.328504
Urea_H_TPSSTPSS_TZVPP(D)	-787.812000	-787.643091	-787.639639
Urea_H_ωB97XD_small	-787.124639	-786.948122	-786.943804
Urea_H_ ωB97XD _TZVPP(D)	-787.431087	-787.257450	-787.252532

Table S6: Complex Energies.

	Energies / Ha				
	E (opt)	**G (opt)**	**G-qh (opt)**	**E (sp)**	**G-qh (sp)**
$Urea_{OMe}(C_2)$	-916.412980	-916.177736	-916.173713	-916.528843	-916.289576
$Urea_{Me}(C_2)$	-765.980840	-765.756811	-765.750856	-766.089317	-765.859333
$Urea_{H}(C_2)$	-687.359330	-687.181514	-687.177960	-687.446520	-687.265150
$Urea_{F}(C_2)$	-885.864255	-885.706360	-885.702588	-885.964083	-885.802416
$Urea_{Cl}(C_2)$	-1606.566409	-1606.413417	-1606.408716	-1606.674100	-1606.516407
$Urea_{CF3}(C_2)$	-1361.548772	-1361.376099	-1361.368997	-1361.686814	-1361.507039
$Urea_{OMe}(C_s)$	-916.412949	-916.176798	-916.173133	-916.528809	-916.288993
$Urea_{Me}(C_s)$	-765.980784	-765.754779	-765.749961	-766.089129	-765.858306
$Urea_{H}(C_s)$	-687.359283	-687.180250	-687.177327	-687.446424	-687.264469
$Urea_{F}(C_s)$	-885.864204	-885.704776	-885.701650	-885.964072	-885.801518
$Urea_{Cl}(C_s)$	-1606.566397	-1606.412497	-1606.408412	-1606.674029	-1606.516044
$Urea_{CF3}(C_s)$	-1361.548772	-1361.376101	-1361.368997	-1361.686814	-1361.507040
$[U_{OMe}F]^-$	-1016.429497	-1016.195828	-1016.191877	-1016.555930	-1016.318310
$[U_{Me}F]^-$	-865.997885	-865.775149	-865.769938	-866.116884	-865.888937
$[U_{H}F]^-$	-787.377162	-787.202921	-787.198728	-787.474839	-787.296405
$[U_{F}F]^-$	-985.882609	-985.727404	-985.723267	-985.992877	-985.833535
$[U_{Cl}F]^-$	-1706.585862	-1706.437319	-1706.431655	-1706.703894	-1706.549687
$[U_{CF3}F]^-$	-1461.569784	-1461.404230	-1461.394568	-1461.717742	-1461.542526
$[U_{OMe\ 2}F]^-$	-1932.872324	-1932.377543	-1932.366349	-	-
$[U_{Me\ 2}F]^-$	-1632.008556	-1631.532127	-1631.521137	-	-
$[U_{H\ 2}F]^-$	-1474.766473	-1474.383842	-1474.376992	-	-
$[U_{F\ 2}F]^-$	-1871.777431	-1871.434823	-1871.426279	-	-
$[U_{Cl\ 2}F]^-$	-3313.183153	-3312.850627	-3312.840645	-	-
$[U_{CF3\ 2}F]^-$	-2823.150111	-2822.776628	-2822.761798	-	-

Table S7: Transition State Structures.

	Energies / Ha				
	E (opt)	**G (opt)**	**G-qh (opt)**	**E (sp)**	**G-qh (sp)**
TS-S_N2	-2792.686015	-2792.627199	-2792.627005	-2792.757647	-2792.698638
TS-S_N2-OMe	-3709.124474	-3708.810930	-3708.802419	-3709.307992	-3708.985936
TS-S_N2-Me	-3558.692777	-3558.387291	-3558.379341	-3558.869000	-3558.555564
TS-S_N2-H	-3480.071778	-3479.814404	-3479.807739	-3480.226748	-3479.962708
TS-S_N2-F	-3678.576928	-3678.338293	-3678.331765	-3678.744493	-3678.499331
TS-S_N2-Cl	-4399.279778	-4399.048068	-4399.039859	-4399.455131	-4399.215213
TS-S_N2-CF_3	-4154.263063	-4154.010230	-4154.000214	-4154.468790	-4154.205941
TS-E2-anti	-2792.684291	-2792.631746	-2792.631618	-2792.753093	-2792.700421

TS-E2-syn	-2792.670783	-2792.618412	-2792.618281	-2792.738135	-2792.685633
TS-E2-OMe	-3709.118592	-3708.809178	-3708.801868	-3709.299039	-3708.982315
TS-E2-Me	-3558.686754	-3558.389029	-3558.380083	-3558.859896	-3558.553225
TS-E2-H	-3480.065584	-3479.813328	-3479.807355	-3480.217451	-3479.959222
TS-E2-F	-3678.570665	-3678.339088	-3678.331972	-3678.735246	-3678.496554
TS-E2-Cl	-4399.273303	-4399.047010	-4399.039198	-4399.445772	-4399.211667
TS-E2-CF_3	-4154.256307	-4154.009956	-4153.999996	-4154.459171	-4154.202861

Table S8: Alcohol-Fluoride Species.

	Energies / Ha				
	E (opt)	**G (opt)**	**G-qh (opt)**	**E (sp)**	**G-qh (sp)**
Ar_3COH (A)	-926.783520	-926.466617	-926.461902	-926.918613	-926.596995
$[AF]^-$	-1026.793671	-1026.480522	-1026.475170	-1026.938426	-1026.619925
TS-S_N2-Ar_3COH	-3719.493766	-3719.095605	-3719.089008	-3719.697639	-3719.292880
TS-E2-Ar_3COH	-3719.486433	-3719.096745	-3719.088950	-3719.688915	-3719.291432
MeOH	-115.722861	-115.695129	-115.695129	-115.750187	-115.722456
$[MeOH-F]^-$	-215.730190	-215.707593	-215.707509	-215.770860	-215.748179
TS-S_N2-MeOH	-2908.425688	-2908.322658	-2908.320849	-2908.521176	-2908.416337
TS-E2-MeOH	-2908.419932	-2908.324627	-2908.322548	-2908.513592	-2908.416208

Table S9: Miscellaneous.

	Energies / Ha				
	E (opt)	**G (opt)**	**G-qh (opt)**	**E (sp)**	**G-qh (sp)**
PrBr	-2692.717436	-2692.654534	-2692.654527	-2692.776060	-2692.713151
Bromide	-2574.379818	-2574.395942	-2574.395942	-2574.403094	-2574.419219
PrF	-218.369337	-218.302011	-218.302007	-218.415836	-218.348506
Propene	-117.887659	-117.834329	-117.834329	-117.919106	-117.865776
HF	-100.460216	-100.467420	-100.467420	-100.476847	-100.484051
Fluoride	-99.987167	-100.000970	-100.000970	-100.006244	-100.020048

Table S10: Fluoride Geometric Preference.

	Energies / Ha		
	E (opt)	**G (opt)**	**G-qh (opt)**
$[F(HF)_1]^-$	-200.259262	-200.271526	-200.271526
$[F(HF)_2]^-$	-300.628862	-300.634919	-300.634449
$[F(HF)_3]^-$	-400.992907	-400.994700	-400.991948
$[F(HF)_4]^-$	-501.351881	-501.342685	-501.339702
$[F(HF)_5]^-$	-601.702165	-601.689218	-601.685617
$[F(HF)_6]^-$	-702.050472	-702.029285	-702.024388

6.2 Supporting Information – Chapter 3

Much of this supplementary material has been reproduced from own work in *Science* 2018, *360*, 638-642.[1]

6.2.1 Modelling Phase-Transfer

Table S11: Tabulated Standard Enthalpy and Entropy Changes at 298.15 K.

	Source	**ΔH / kJ/mol**	**ΔS / J/K/mol**
Δ_f ($CsF_{(s)}$)	Ref (2)	-553.5	-
Δ_f ($CsBr_{(s)}$)	Ref (2)	-405.8	-
Δ_f ($CsCl_{(s)}$)	Ref (2)	-443.0	-
Δ_{atm} (F_2)	Ref (2)	+79.38	-
Δ_{atm} (Br_2)	Ref (2)	+111.87	-
Δ_{atm} (Cl_2)	Ref (2)	+121.301	-
E_{EA}(F)	Ref (2)	+328.1649	-
E_{EA}(Br)	Ref (2)	+324.5369	-
E_{EA}(Cl)	Ref (2)	+348.5750	-
$\Delta_{solv}(F^-)$	Computed	-317.8	-26.7*
$\Delta_{solv}(Br^-)$	Computed	-240.6	-26.7*
$\Delta_{solv}(Cl^-)$	Computed	-257.8	-26.7*
K1 (F^-) **Cat 1**	Computed	+103.0	+88.7
K1 (Br^-) **Cat 1**	Computed	+51.51	+85.2
K1 (Cl^-) **Cat 1**	Computed	+58.65	+86.3
K1 (F^-) **Cat 7**	Computed	+83.30	+76.7
K1 (Br^-) **Cat 7**	Computed	+39.05	+83.3
K1 (F^-) **Cat 8**	Computed	+104.5	+75.9
K1 (Br^-) **Cat 8**	Computed	+49.2	+73.8

* Entropy change associated with a change in standard state from 1 bar to 1 M.

Table S12: Tabulated Standard Molar Entropies at 298.15 K.

	Source	**S / J/K/mol**
$CsF_{(s)}$	Ref (2)	92.8
$CsBr_{(s)}$	Ref (2)	113.1
$CsCl_{(s)}$	Ref (2)	101.2
$F^-_{(g)}$	Ref (3)	145.59
$Br^-_{(g)}$	Ref (3)	163.57
$Cl^-_{(g)}$	Ref (3)	154.40

Table S13: Thermodynamic Values of Phase-Transfer with Different Cations and Episulfonium Ion Precursor Leaving Groups.

Urea	Cation	Leaving Group	$\Delta_{PT}G$/ kJ/mol	$\Delta_{PT}H$/ kJ/mol	$\Delta_{PT}S$/ J/K/mol
Uncatalyzed	Cs	Br	+33.7	+34.4	+2.31
Uncatalyzed	K	Br	+57.5	+60.8	+11.3
Uncatalyzed	Na	Br	+93.6	+98.8	+17.7
Cat 1	Cs	Br	-16.7	-17.1	-1.16
Cat 1	K	Br	+7.00	+9.33	-7.84
Cat 1	Na	Br	+43.1	+47.3	-14.2
Cat 7	Cs	Br	-7.02	-8.30	-4.29
Cat 7	K	Br	+16.7	+18.1	+4.71
Cat 7	Na	Br	+52.8	+56.1	+11.1
Cat 8	Cs	Br	-21.0	-20.9	+0.29
Uncatalyzed	Cs	Cl	+29.2	+29.0	-0.52
Cat 1	Cs	Cl	-14.5	-15.4	-2.96

6.2.2 The Gibbs Free Energy Profile

6.2.2.1 Achiral Urea *syn-anti* Isomers

The possibility of *syn-anti* isomerism was checked for achiral urea **1** (Schreiner's urea), urea **7** and thiourea **8**. For both ureas, the *anti-anti* conformer, with urea hydrogen bond donors pointing parallel, are lowest in energy. For Schreiner's urea, the Gibbs free energy difference is substantial at 11.8 kJ/mol, whereas for unsubstituted urea **7**, it is marginal at 1.7 kJ/mol. Similarly, thiourea **8** has a small preference for *anti-anti*, now split into C2 and Cs symmetric conformers due to the size of the sulfur atom preventing planarity of the structure. For an in-depth look at urea and thiourea conformations, see reference 4.

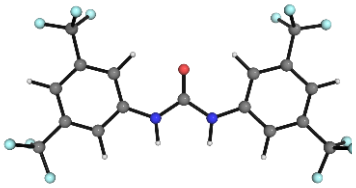

Cat 1$_{aa}$
(G_{rel} = 0 kJ/mol)

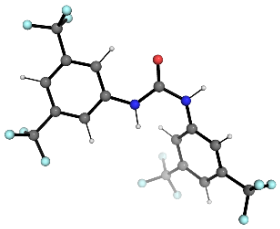

Cat 1$_{as}$
(G_{rel} = +11.8 kJ/mol)

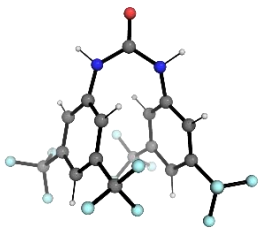

Cat 1$_{ss}$
(G_{rel} = +35.4 kJ/mol)

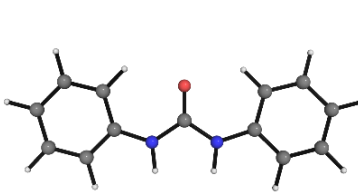

Cat 7_{aa}
(G_{rel} = 0 kJ/mol)

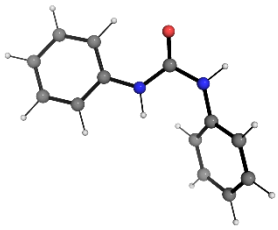

Cat 7_{as}
(G_{rel} = +1.7 kJ/mol)

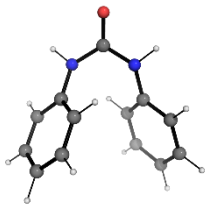

Cat 7_{ss}
(G_{rel} = +10.9 kJ/mol)

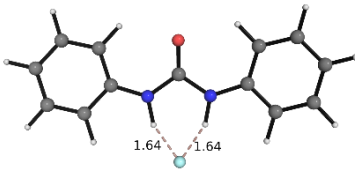

Cat 7-F

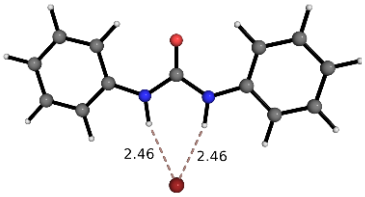

Cat 7-Br

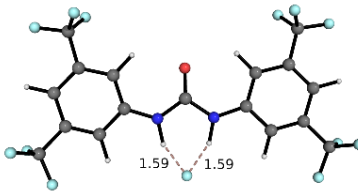

Cat 1-F

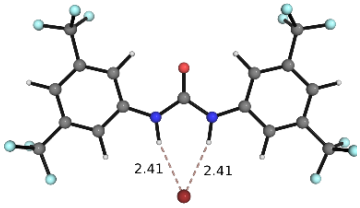

Cat 1-Br

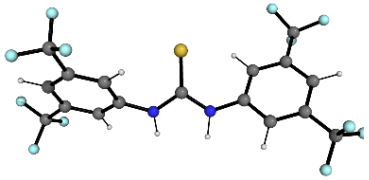

Cat 8_{aa} C2
(G_{rel} = 0 kJ/mol)

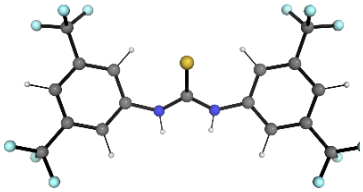

Cat 8_{aa} Cs
(G_{rel} = +1.1 kJ/mol)

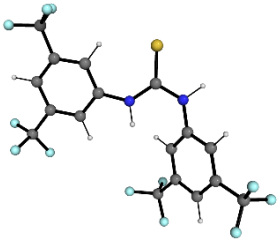

Cat 8_{as}
(G_{rel} = +2.3 kJ/mol)

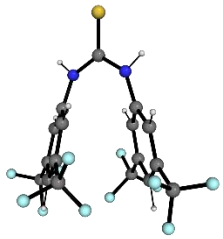

Cat 8_{ss}
(G_{rel} = +15.0 kJ/mol)

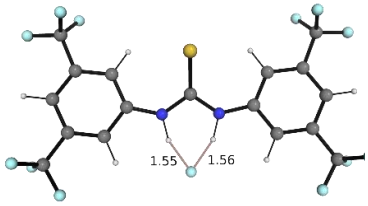

Cat 8-F

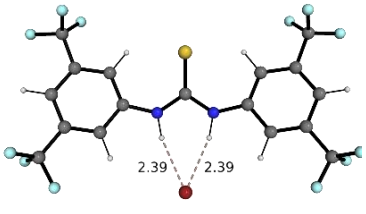

Cat 8-Br

Figure S9: Geometries and relative Gibbs free energies of (thio)urea conformers. Adapted from Ref 1.

6.2.2.2 Stationary Points and Additional Data

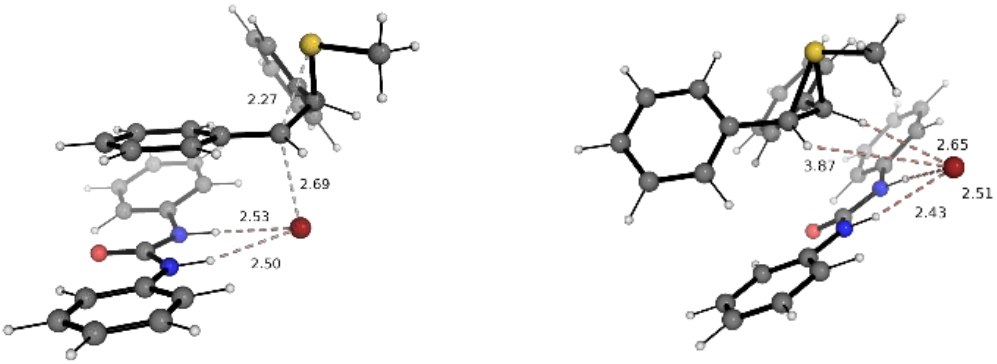

TS_{Br}(Cat 7) **IP_{Br}(Cat 7)**

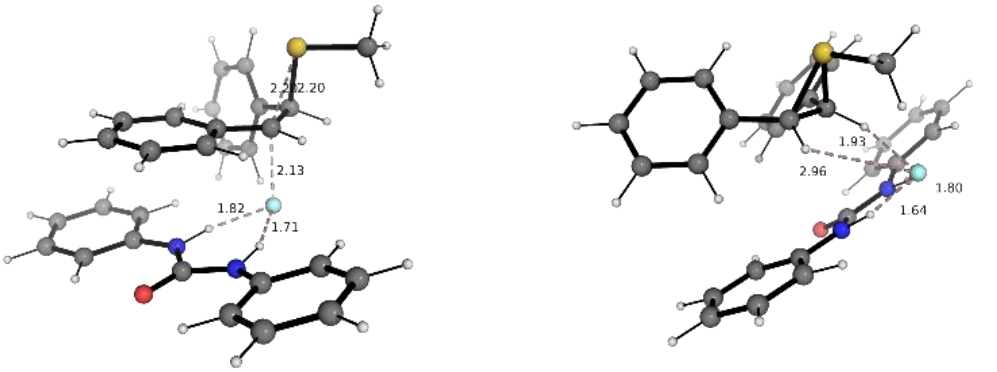

TS_{F}(Cat 7) **IP_{F}(Cat 7)**

Figure S10: Stationary points for reaction catalyzed by achiral urea, Cat **7**. Adapted from Ref 1.

Table S14: Additional Geometric Data for Stationary Points.

	Key Distances / Å				Key Angles / °	
	C-X	**C-S**	**H-bond 1**	**H-bond 2**	**α-Dihedral†**	**β-Dihedral†**
Cat 1-F	-	-	1.591	1.591	-	-
Cat 1-Br	-	-	2.408	2.408	-	-
Cat 7-F	-	-	1.641	1.641	-	-
Cat 7-Br	-	-	2.464	2.464	-	-
Cat 8-F	-	-	1.554	1.556	-	-
Cat 8-Br	-	-	2.387	2.387	-	-
TS_{Br}(Cat 7)	2.694	2.266	2.531	2.498	-33.7	82.7
6_{anti}	-	1.834*	-	-	-	-
IP_{Br}(Cat 7)	-	-	2.433	2.517	-	-
IP_{F}(Cat 7)	-	-	1.645	1.805	-	-
TS_{F}(Cat 7)	2.133	2.198	1.818	1.705	-12.2	-69.4

* Average value. †Phenyl ring dihedrals measured relative to C-C bond.

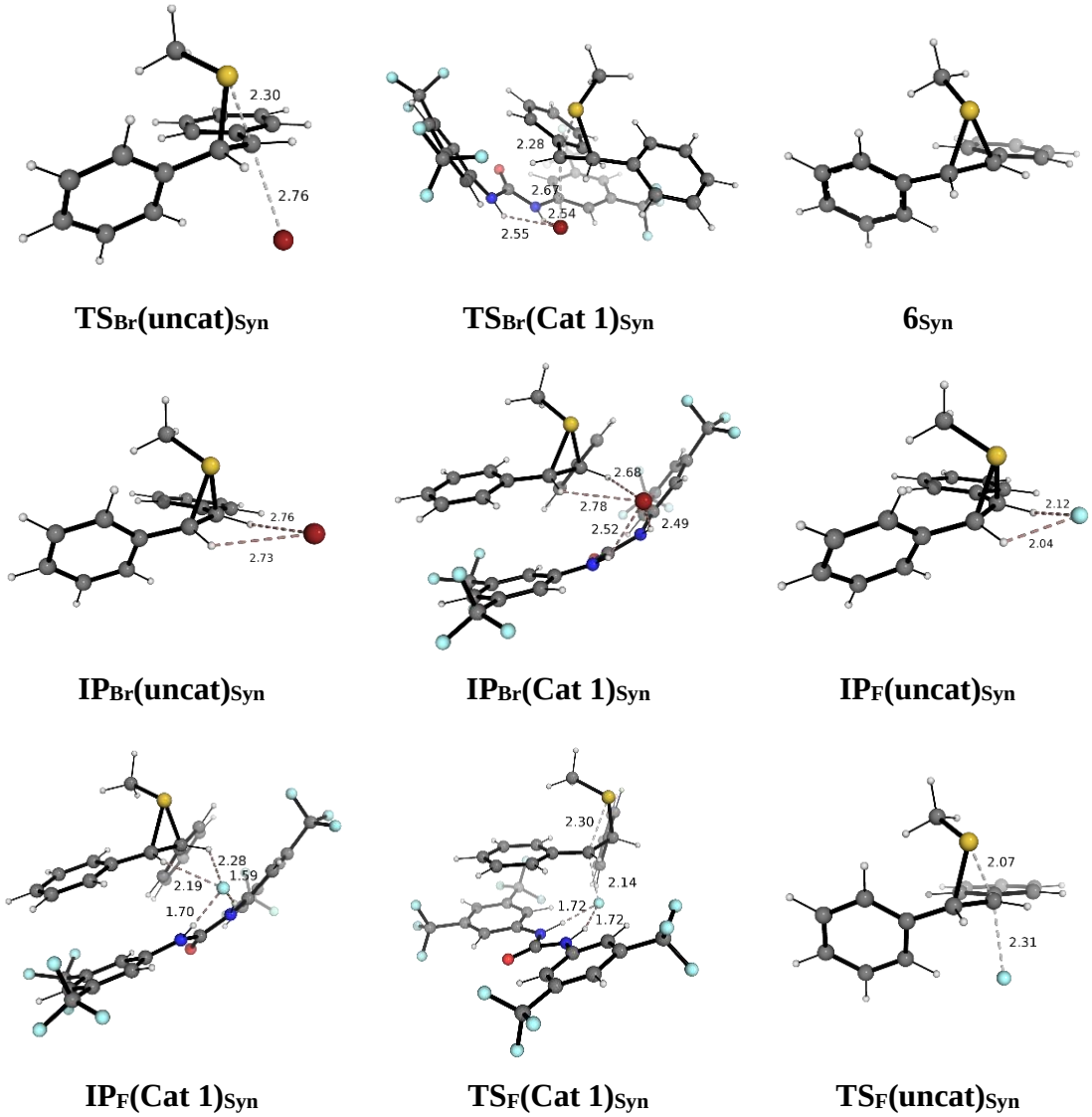

$TS_{Br}(uncat)_{Syn}$ **$TS_{Br}(Cat\ 1)_{Syn}$** **6_{Syn}**

$IP_{Br}(uncat)_{Syn}$ **$IP_{Br}(Cat\ 1)_{Syn}$** **$IP_{F}(uncat)_{Syn}$**

$IP_{F}(Cat\ 1)_{Syn}$ **$TS_{F}(Cat\ 1)_{Syn}$** **$TS_{F}(uncat)_{Syn}$**

Figure S11: Stationary points with episulfonium, **6**, methyl group *syn*. Adapted from Ref 1.

Table S15: Geometric Data for Stationary Points with Episulfonium $\mathbf{6_{syn}}$.

	Key Distances / Å				Key Angles / °	
	C-X	**C-S**	**H-bond 1**	**H-bond 2**	**α-Dihedral†**	**β-Dihedral†**
$TS_{Br}(uncat)_{Syn}$	2.758	2.295	-	-	-9.4	-9.4
$TS_{Br}(Cat\ 1)_{Syn}$	2.665	2.285	2.547	2.540	-49.7	-49.7
6_{Syn}	-	1.866*	-	-	-	-
$IP_{Br}(Cat\ 1)_{Syn}$	-	-	2.519	2.486	-	-
$IP_{F}(Cat\ 1)_{Syn}$	-	-	1.699	1.587	-	-
$TS_{F}(uncat)_{Syn}$	2.309	2.068	-	-	-0.1	-49.1
$TS_{F}(Cat\ 1)_{Syn}$	2.136	2.299	1.719	1.717	-12.9	-47.9

* Average value. †Phenyl ring dihedrals measured relative to C-C bond.

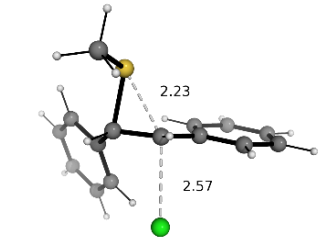

TS_{Cl}(uncat)

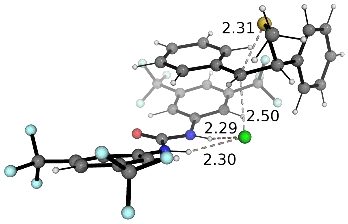

TS_{Cl}(Cat 1)

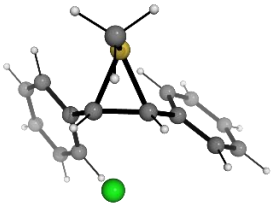

IP_{Cl}(uncat)

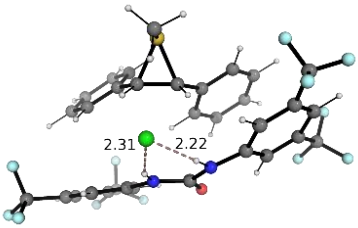

IP_{Cl}(Cat 1)

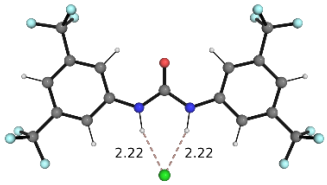

Cat 1-Cl

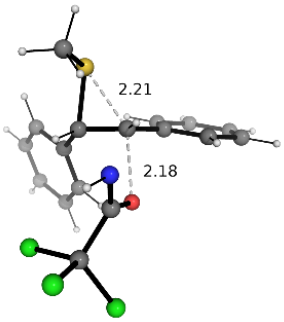

TS_{TCA}(uncat)

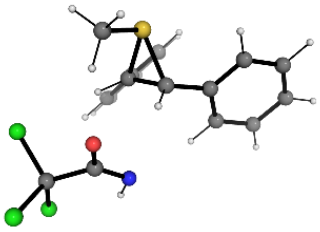

IP_{TCA}(uncat)

Figure S12: Stationary points with chloride and TCA leaving groups. Adapted from Ref 1.

Table S16: Geometric Data for Stationary Points with Different Leaving Groups.

	Key Distances / Å				Key Angles / °	
	C-X	**C-S**	**H-bond 1**	**H-bond 2**	**α-Dihedral†**	**β-Dihedral†**
TS_{Cl}(uncat)	2.571	2.233	-	-	5.6	-43.4
TS_{Cl}(Cat 1)	2.498	2.315	2.305	2.292	-12.5	-69.8
IP_{Cl}(Cat 1)	-	-	2.306	2.220	-	-
Cat 1-Cl	-	-	2.219	2.218	-	-
TS_{TCA}(uncat)	2.182	2.206	-	-	12.0	-47.9

†Phenyl ring dihedrals measured relative to C-C bond.

6.2.3 Catalyst Alkylation

Table S17: Distribution of Binding Modes in 6 x 20 ns Runs with Tetradentate Catalyst, Cat **9**.

Run #	**Starting point**	**Binding mode weightings**		
		Bis	**Cooperative**	***syn-anti***
1	Cooperative	3 %	0 %	96 %
2	Cooperative	73 %	0 %	27 %
3	Cooperative	100 %	0 %	0 %
4	Bis	77 %	0 %	22 %
5	Bis	30 %	0 %	69 %
6	Bis	65 %	0 %	34 %
Average	Cooperative	59 %	0 %	41 %
Average	Bis	57 %	0 %	42 %
	Overall	58 %	0 %	42 %

Table S18: Geometric Data for Trial Fluoride Delivery Transition State Structures with Cat **9**.

	G_{rel}/ kJ/mol	**H-bond Lengths (N-H --- F) /Å**				**H-bond Angles (N-H---F) /°**				**TS Distances /Å**	
		1	**2**	**3**	**4**	**1**	**2**	**3**	**4**	**C - F**	**C - S**
TS Cat 9-F epi tetra	21.3	1.882	1.699	3.218	1.917	150.5	158.1	125.5	134.4	2.069	2.242
TS Cat9 -F epi tri	0.0	1.867	1.741	2.186	-	152.5	152.8	151.4	-	2.108	2.259

6.2.4 Conformers of Methylated Catalyst 10

Conformers of Cat **10** were determined by MD simulation of the catalyst for 100 ns. Frames were clustered at 0.7 Å RMSD and the 20 most populous clusters optimized using DFT, generating 16 unique structures.

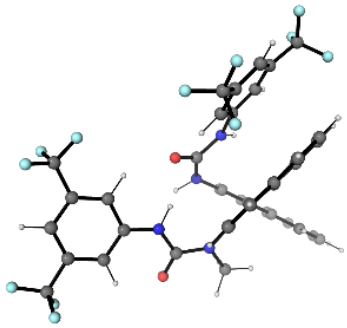

Cat 10-1
+ 0.0 kJ/mol

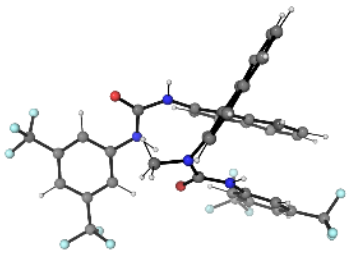

Cat 10-2
+ 1.4 kJ/mol

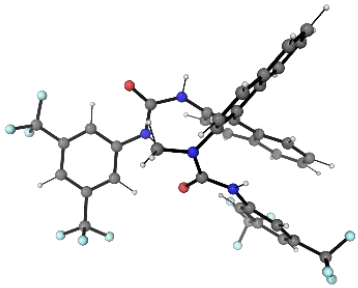

Cat 10-3
+ 1.6 kJ/mol

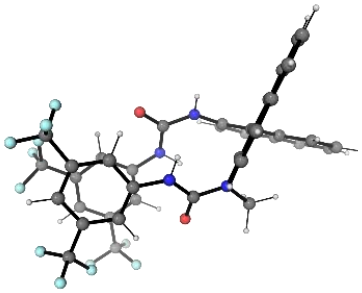

Cat 10-4
+ 12.9 kJ/mol

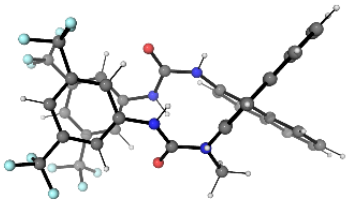

Cat 10-5
+ 14.2 kJ/mol

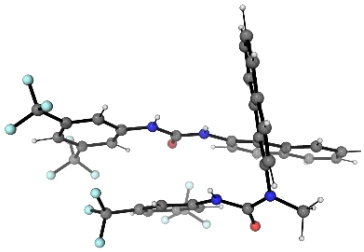

Cat 10-6
+ 14.6 kJ/mol

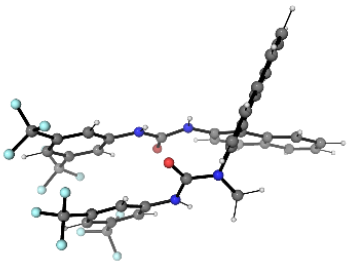

Cat 10-7
+ 14.9 kJ/mol

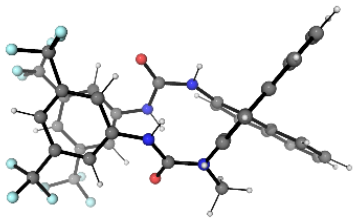

Cat 10-8
+ 15.2 kJ/mol

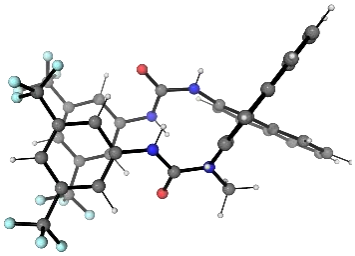

Cat 10-9
+ 16.6 kJ/mol

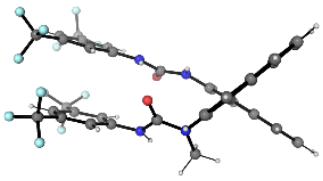

Cat 10-10
+ 16.7 kJ/mol

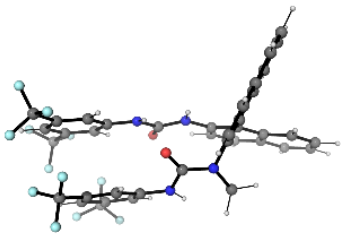

Cat 10-11
+ 16.8 kJ/mol

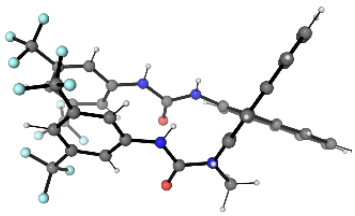

Cat 10-12
+ 17.1 kJ/mol

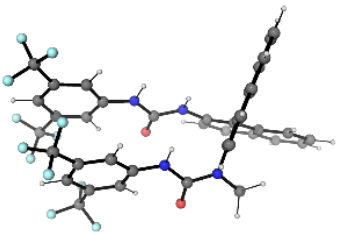

Cat 10-13
+ 18.5 kJ/mol

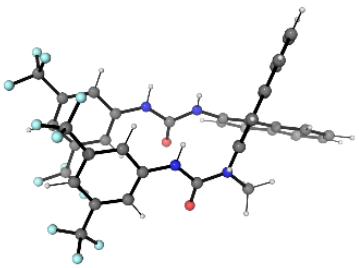

Cat 10-14
+ 19.6 kJ/mol

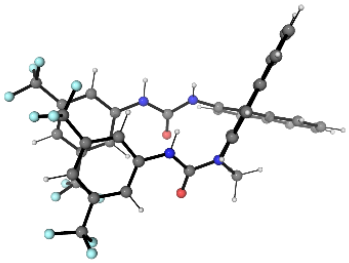

Cat 10-15
+ 20.3 kJ/mol

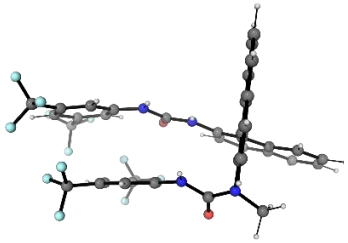

Cat 10-16
+ 22.5 kJ/mol

Figure S13: Conformations of catalyst **10** with relative Gibbs free energies. Adapted from Ref 1.

6.2.5 Complexes of Methylated Catalyst 10

Binding modes of Cat **10** with CsF were determined by MD simulation for 100 ns. 96 % of frames correspond to a tridentate fluoride binding mode, which is stable once formed. RMSD clustering was performed at 1.1 Å RMSD and the 2 high weighted clusters optimized with DFT. The lowest energy of these was reoptimized with isopropyl catalyst, Cat **13**. Complexes with bromide and chloride ions were located by replacing fluoride with the appropriate anion and reoptimizing with DFT. Water coordinating fluoride has a large effect on fluoride binding energy, however, the effect remains smaller than the difference calculated between the catalyzed and uncatalyzed pathways with achiral urea. Further, water has a similar effect on both pathways, so this does not alter mechanistic conclusions.

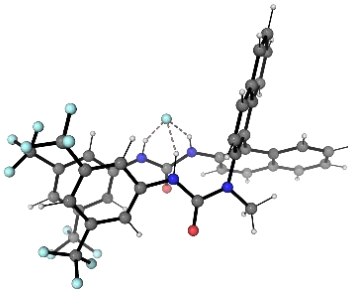

Cat 10-F 1
+ 0.0 kJ/mol

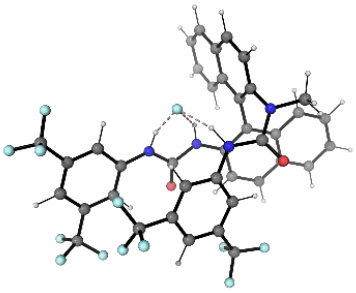

Cat 10-F 2
+ 1.7 kJ/mol

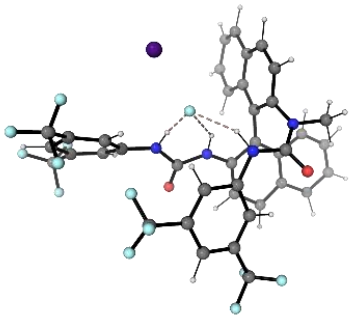

IP Cat 10-F Cs 1
–37.7 kJ/mol

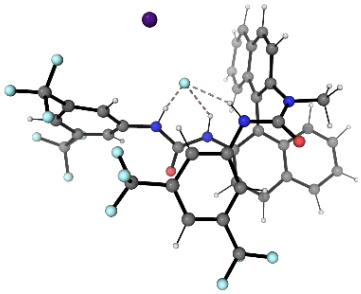

IP Cat 10-F Cs 2
–36.8 kJ/mol

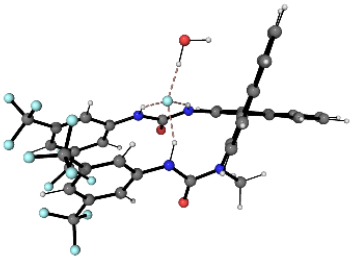

Cat 10-F•H_2O

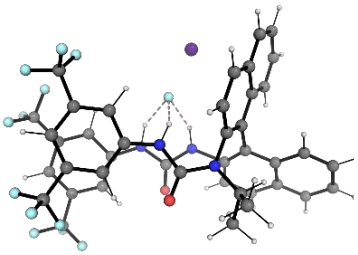

IP Cat 13-F Cs 1

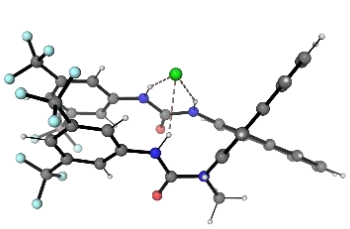

Cat 10-Cl 1
+ 0.0 kJ/mol

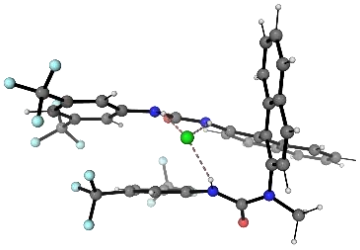

Cat 10-Cl 2
+ 0.0 kJ/mol

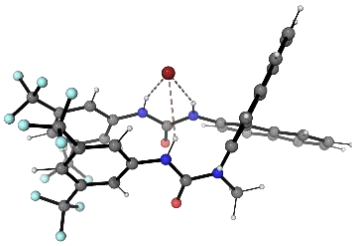

Cat 10-Br 1
+ 0.0 kJ/mol

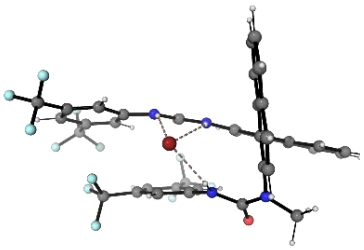

Cat 10-Br 2
+ 1.5 kJ/mol

Figure S14: Stationary points for Cat **10** binding anions. Adapted from Ref 1.

Table S19: Geometric Data for Tridentate Urea–Anion Complexes.

	Key Distances / Å				Key Angles / °	
	H-bond 1	**H-bond 2**	**H-bond 3**	**Cs - F**	**H-bond 3**	**Backbone**
Cat 10-F 1	1.779	1.649	1.670	-	154.1	68.8
Cat 10-F 2	1.894	1.566	1.664	-	159.9	108.8
Cat 10-F•H_2O	1.786	1.736	1.744	-	151.4	70.0
IP Cat 10-F Cs 1	1.781	1.753	1.740	2.720	152.0	69.8
IP Cat 10-F Cs 2	1.814	1.641	1.851	2.759	144.5	99.3
IP Cat 13-F Cs 1	1.738	1.795	1.756	2.716	152.7	72.2
Cat 10-Cl 1	2.354	2.208	2.354	-	145.1	69.7
Cat 10-Cl 2	2.494	2.154	2.362	-	154.8	109.2
Cat 10-Br 1	2.543	2.384	2.662	-	144.0	69.8
Cat 10-Br 2	2.712	2.344	2.562	-	154.6	109.4

Table S20: Binding Gibbs Free Energies and Equilibrium Constants with Catalyst **10**.

Bound Species	**ΔG**	**K**
Br^-	-21.9	5×10^3
Cl^-	-28.9	1×10^5
F^-	-76.1	2×10^{13}
$F^- \bullet (H_2O)^{\dagger}$	-49.4	2×10^8
CsF*	-31.6	-

Equilibrium constants computed from conformer ensemble. †K calculated from lowest energy conformers.
*Binding of CsF ion pair by catalyst 10.

6.2.6 Transition State Structures with Methylated Catalyst 10

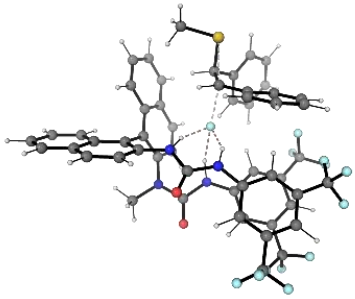

TS Cat 10-F major 1
298.15 K: + 0.0 kJ/mol
243.15 K: + 0.0 kJ/mol

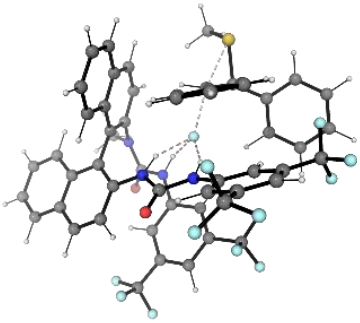

TS Cat 10-F major 2
298.15 K: + 2.8 kJ/mol
243.15 K: + 2.7 kJ/mol

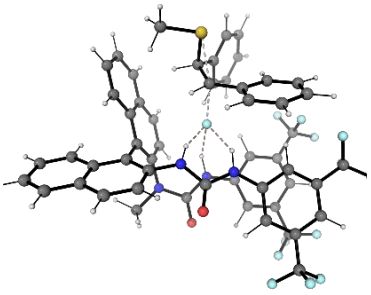

TS Cat 10-F major 3
298.15 K: + 9.9 kJ/mol
243.15 K: + 9.9 kJ/mol

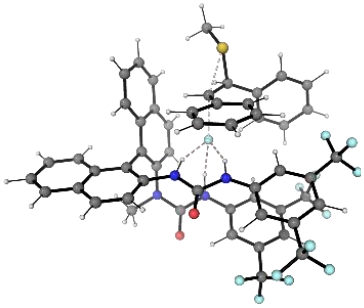

TS Cat 10-F major 4
298.15 K: + 18.4 kJ/mol
243.15 K: + 18.2 kJ/mol

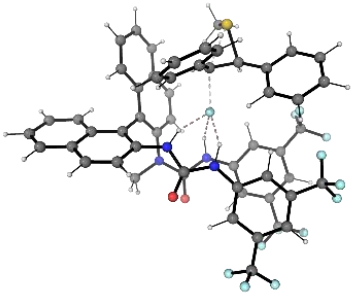

TS Cat 10-F major 5
298.15 K: + 21.1 kJ/mol
243.15 K: + 21.3 kJ/mol

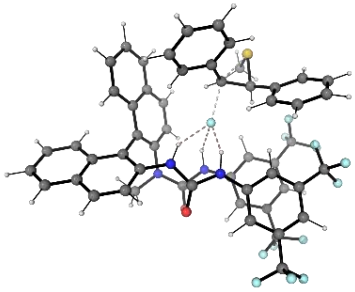

TS Cat 10-F major 6
298.15 K: + 25.7 kJ/mol
243.15 K: + 25.4 kJ/mol

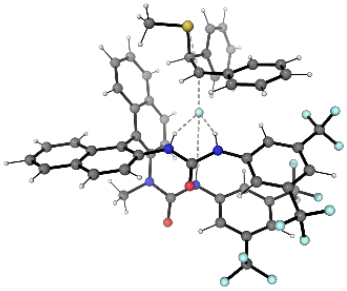

TS Cat 10-F major 7
298.15 K: + 32.6 kJ/mol
243.15 K: + 32.6 kJ/mol

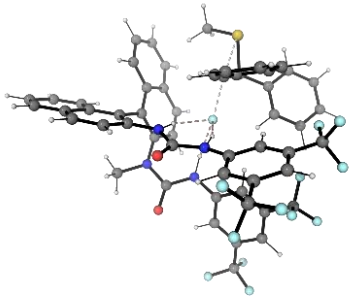

TS Cat 10-F major 8
298.15 K: + 32.9 kJ/mol
243.15 K: + 33.6 kJ/mol

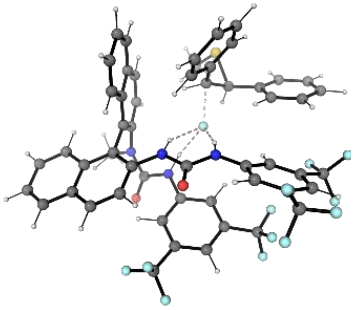

TS Cat 10-F major 9
298.15 K: + 42.2 kJ/mol
243.15 K: + 42.7 kJ/mol

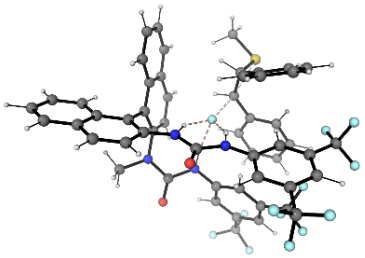

TS Cat 10-F minor 1
298.15 K: + 6.0 kJ/mol
243.15 K: + 6.8 kJ/mol

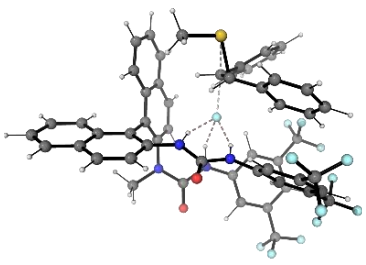

TS Cat 10-F minor 2
298.15 K: + 10.0 kJ/mol
243.15 K: + 10.0 kJ/mol

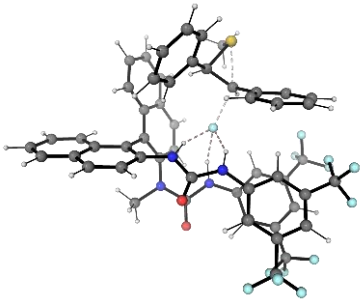

TS Cat 10-F minor 3
298.15 K: + 10.6 kJ/mol
243.15 K: + 10.5 kJ/mol

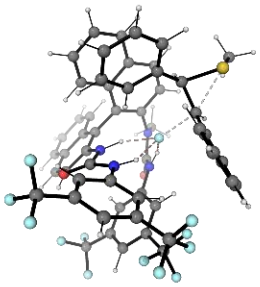

TS Cat 10-F minor 4
298.15 K: + 10.7 kJ/mol
243.15 K: + 11.1 kJ/mol

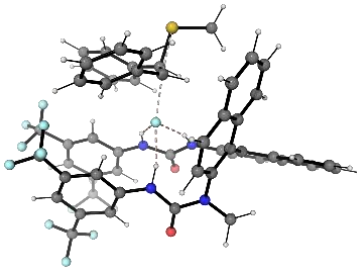

TS Cat 10-F minor 5
298.15 K: + 20.4 kJ/mol
243.15 K: + 20.2 kJ/mol

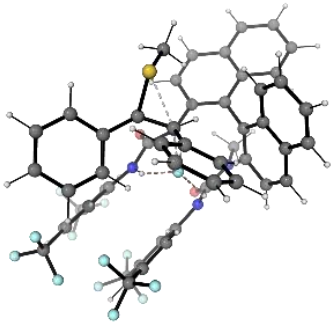

TS Cat 10-F minor 6
298.15 K: + 23.0 kJ/mol
243.15 K: + 22.9 kJ/mol

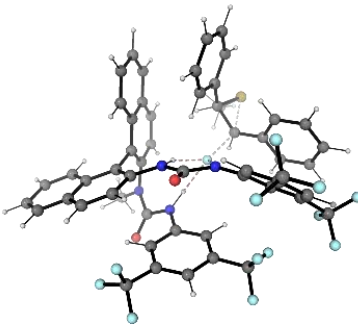

TS Cat 10-F minor 7
298.15 K: + 29.7 kJ/mol
243.15 K: + 30.0 kJ/mol

Figure S15: Fluoride delivery TS for catalyst **10** with episulfonium substrate **6**. Adapted from Ref 1.

The lowest energy transition state structure, **TS Cat 10-F major 1**, was reoptimized with bromide ion to assess whether the tridentate catalyst could lower the barrier to bromide removal. The barrier was reduced from 90.2 kJ/mol in the absence of catalyst, to 82.7 kJ/mol with catalyst. No additional conformational searching was performed.

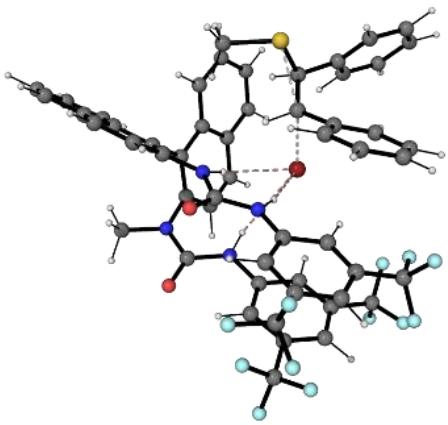

TS Br Cat 10

Figure S16: Transition state structure for episulfonium ion formation by removal of the bromide leaving group, catalyzed by Cat **10**. Adapted from Ref 1.

6.2.7 Complete Ensemble of Transition State Structures with Catalyst 13

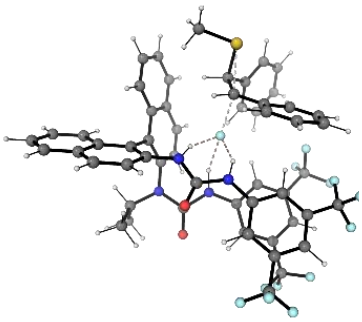

TS Cat 13-F epi major 1
298.15 K: + 0.0 kJ/mol
243.15 K: + 0.0 kJ/mol

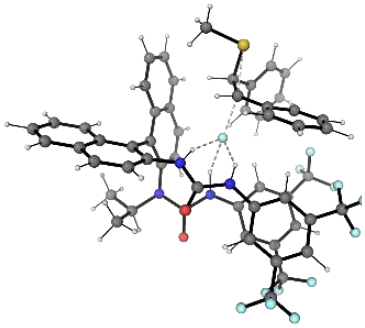

TS Cat 13-F epi major 2
298.15 K: + 10.4 kJ/mol
243.15 K: + 10.0 kJ/mol

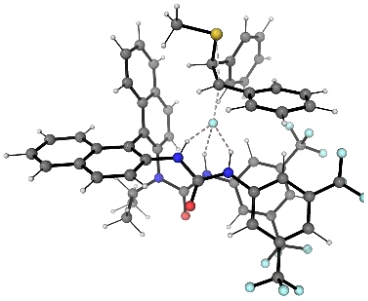

TS Cat 13-F epi major 3
298.15 K: + 10.6 kJ/mol
243.15 K: + 10.7 kJ/mol

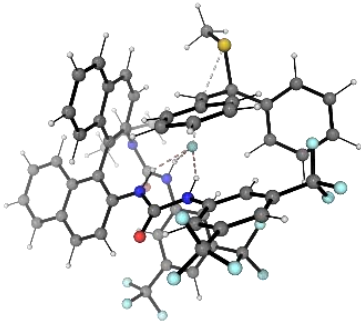

TS Cat 13-F epi major 4
298.15 K: + 15.9 kJ/mol
243.15 K: + 16.2 kJ/mol

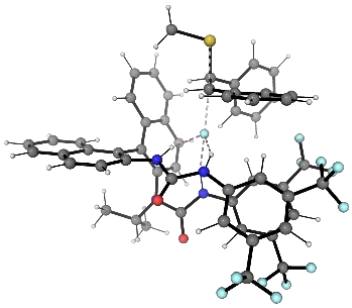

TS Cat 13-F epi major 5
298.15 K: + 19.8 kJ/mol
243.15 K: + 19.3 kJ/mol

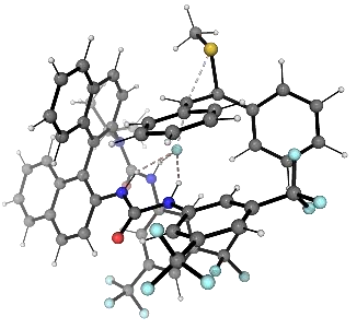

TS Cat 13-F epi major 6
298.15 K: + 19.7 kJ/mol
243.15 K: + 19.7 kJ/mol

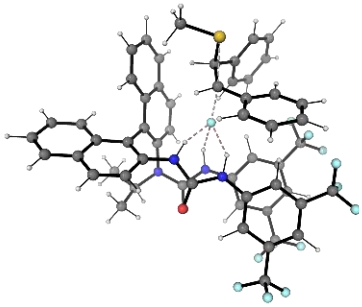

TS Cat 13-F epi major 7
298.15 K: + 20.9 kJ/mol
243.15 K: + 20.6 kJ/mol

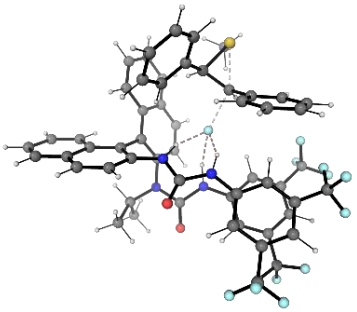

TS Cat 13-F epi Minor 1
298.15 K: + 7.8 kJ/mol
243.15 K: + 7.8 kJ/mol

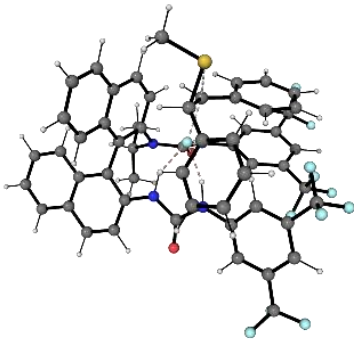

TS Cat 13-F epi Minor 2
298.15 K: +8.4 kJ/mol
243.15 K: + 9.1 kJ/mol

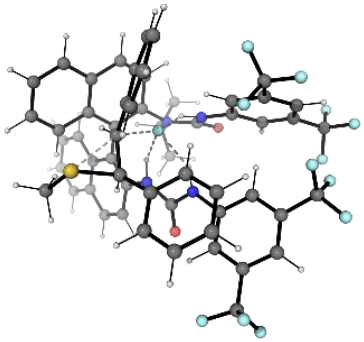

TS Cat 13-F epi Minor 3
298.15 K: + 10.4 kJ/mol
243.15 K: + 10.6 kJ/mol

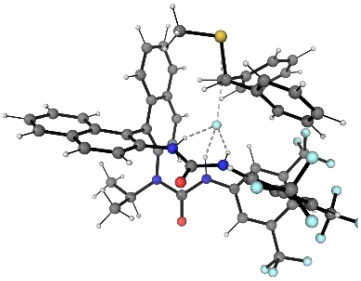

TS Cat 13-F epi Minor 4
298.15 K: + 20.0 kJ/mol
243.15 K: + 20.0 kJ/mol

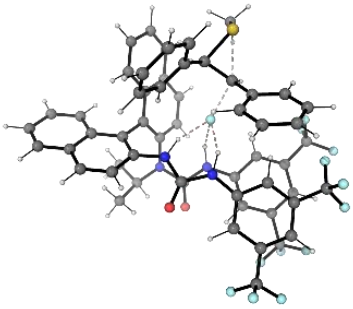

TS Cat 13-F epi Minor 5
298.15 K: + 21.8 kJ/mol
243.15 K: + 21.4 kJ/mol

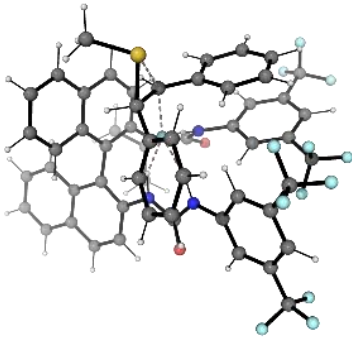

TS Cat 13-F epi Minor 6
298.15 K: + 21.1 kJ/mol
243.15 K: +21.4 kJ/mol

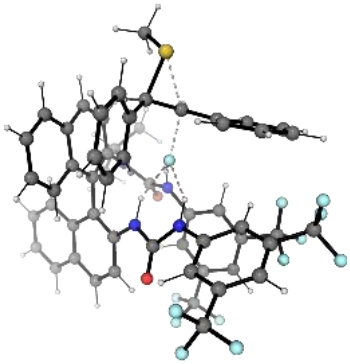

TS Cat 13-F epi Minor 7
298.15 K: + 22.9 kJ/mol
243.15 K: + 23.8 kJ/mol

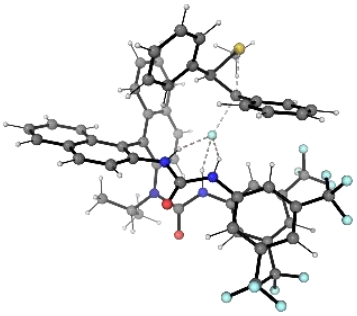

TS Cat 13-F epi Minor 8
298.15 K: +30.1 kJ/mol
243.15 K: + 29.6 kJ/mol

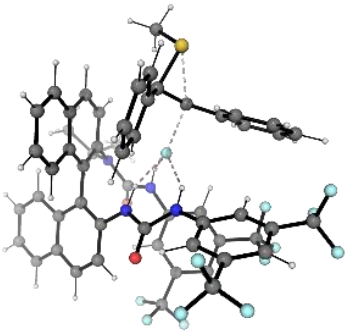

TS Cat 13-F epi Minor 9
298.15 K: 29.6 kJ/mol
243.15 K: + 30.2 kJ/mol

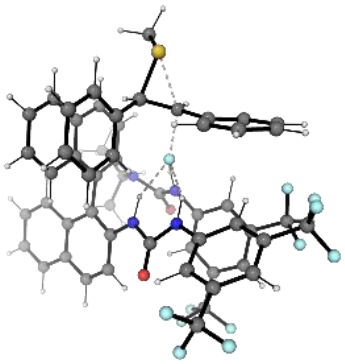

TS Cat 13-F epi Minor 10
298.15 K: + 40.6 kJ/mol
243.15 K: + 41.1 kJ/mol

Figure S17: Complete ensemble of TSs optimized with catalyst **13**. Adapted from Ref 1.

6.2.8 On the stability of β-Fluorosulfides

Structures of fluoroepisulfuranes.

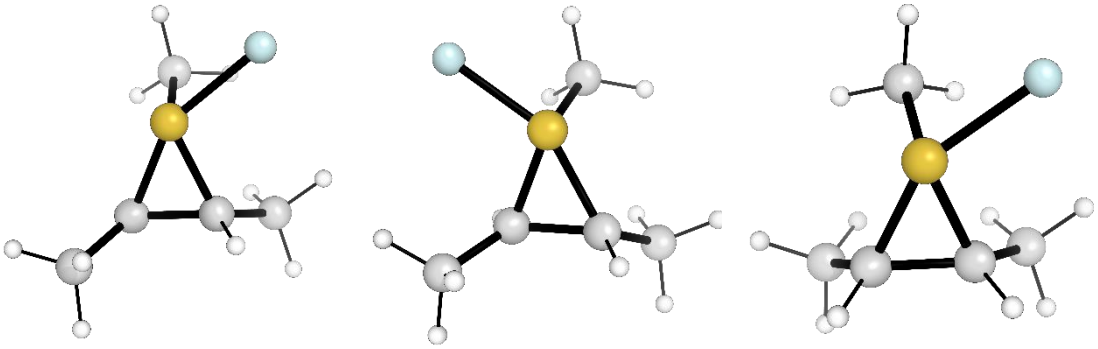

16a (r_{S-F} = 1.970 Å) **16b** (r_{S-F} = 1.968) **17a** (r_{S-F} = 1.980)

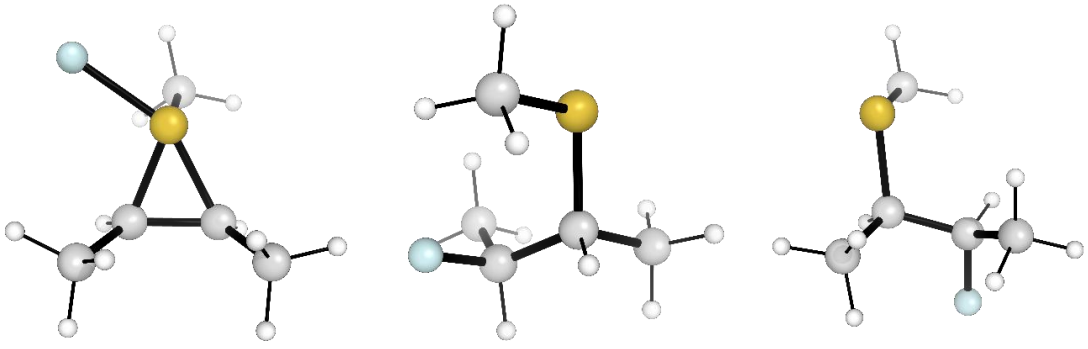

17b (r_{S-F} = 1.962) **14** (lowest conformer) **15** (lowest conformer)

Figure S18: Stationary points for fluoroepisulfuranes and precursors.

Table S21: NMR Isotropic Shielding Constants – ^{1}H and ^{19}F.

Structure	^{1}H Isotropic Shielding Constant / ppm					^{19}F / ppm
	1	2	3	4	5	
16a	30.2106	29.2454	30.5167	30.7610	29.2759	116.0953
16b	30.3856	29.3157	30.6305	30.5435	29.1879	114.1359
17a	30.3102	28.8425	30.1857	30.6591	29.4528	126.5725
17b	30.3922	28.8381	30.0657	30.7818	29.0714	117.1396
14-1	30.8418	28.4409	26.7584	30.4634	29.5475	364.2482
14-2	30.3666	29.2765	27.1137	30.3332	29.8404	376.6387
14-3	30.5562	29.4128	27.3996	30.3301	29.5954	362.5516
14-4	30.6201	29.1206	26.7185	30.5452	29.6635	396.7013
14-5	30.4380	28.8686	27.3923	30.4979	29.6845	370.5096
14-6	30.5413	29.1668	26.7302	30.5385	29.6340	390.9678
14-7	30.4034	29.2975	26.5418	30.5714	29.5668	388.1368
14-8	30.5945	28.6783	26.9174	30.6284	29.6671	370.6863
14-9	30.5531	28.6628	26.9688	30.4435	29.7637	368.4782
15-1	30.7133	28.7580	26.7289	30.5033	29.6495	377.8126
15-2	30.2818	29.3216	26.7973	30.3270	29.7070	382.7658
15-3	30.7766	29.0595	27.1209	30.5247	29.4466	364.9138
15-4	30.5292	28.6829	26.8006	30.6702	29.5991	368.6208
15-5	30.3778	29.1421	26.8715	30.3760	29.6663	389.9772
15-6	30.7041	28.9108	27.4324	30.4944	29.6771	369.7990
15-7	30.5837	29.2195	27.1434	30.5668	29.8425	367.1508
15-8	30.5074	29.2358	26.8812	30.3418	29.6140	391.1477
15-9	30.5190	28.7049	26.9384	30.4900	29.7719	363.0017

Table S22: NMR Isotropic Shielding Constants – ^{13}C.

Structure	^{13}C Isotropic Shielding Constant / ppm				
	1	2	3	4	5
16a	174.9487	144.7885	143.4460	171.4790	154.6122
16b	170.2104	138.0573	148.4206	172.9942	154.8353
17a	175.9968	138.6071	149.1692	176.7381	146.1956
17b	181.5151	150.7049	152.6804	178.4486	162.9704
14-1	171.0545	134.4945	88.1734	174.0355	165.4705
14-2	170.9664	139.3160	93.3405	167.3702	175.5346
14-3	168.7573	133.7409	88.9747	166.6772	165.3280
14-4	175.3506	133.9577	98.6959	168.8770	168.8806
14-5	170.1921	135.0451	92.0245	167.1954	170.0447
14-6	175.4291	132.8861	92.2128	168.4444	168.0817
14-7	175.7224	140.1223	85.4276	167.7026	172.4375
14-8	169.8636	132.3093	92.7174	172.4166	169.0921
14-9	171.5629	139.5606	91.5011	172.6244	171.8380
15-1	174.5644	136.9966	95.3041	174.3153	168.3899
15-2	169.8093	138.1066	89.1870	167.0661	172.8073
15-3	171.0374	133.2398	83.6080	167.0029	164.4584
15-4	174.7639	135.9114	94.0461	172.7664	168.4397
15-5	168.5938	132.0560	91.8118	167.7654	168.6679

15-6	171.5579	132.5279	92.5024	167.3553	169.7353
15-7	170.3955	137.8246	97.0729	167.4288	176.0161
15-8	167.5164	131.8045	91.9377	167.4854	164.4290
15-9	177.1459	143.3929	91.3117	173.1131	173.3973

6.2.9 Thermodynamic Data

Table S23: Pathway with Achiral Urea.

	Energies / Ha				
	E (opt)	**G (opt)**	**G-qh (opt)**	**E (sp)**	**G-qh (sp)**
Cat 1$_{aa}$	-2033.353700	-2033.169216	-2033.159297	-2035.910612	-2035.716209
Cat 1$_{as}$	-2033.349097	-2033.163487	-2033.154014	-2035.906815	-2035.711732
Cat 1$_{ss}$	-2033.353644	-2033.159334	-2033.154211	-2035.902173	-2035.702740
Cat 1-F	-2133.373665	-2133.191831	-2133.181208	-2135.938385	-2135.745928
Cat 1-Br	-4607.746838	-4607.568062	-4607.556044	-4610.320359	-4610.129565
Cat 7$_{aa}$	-686.592580	-686.403598	-686.400697	-687.441567	-687.249684
Cat 7$_{as}$	-686.590424	-686.401679	-686.398774	-687.440712	-687.249062
Cat 7$_{ss}$	-686.586950	-686.396627	-686.394565	-687.437932	-687.245547
Cat 7-F	-786.604866	-786.418795	-786.415088	-787.461699	-787.271921
Cat 7-Br	-3260.981282	-3260.798779	-3260.793709	-3261.846836	-3261.659263
TS$_{Br}$(uncat)	-3552.313308	-3552.099059	-3552.096054	-3553.071744	-3552.854490
TS$_{Br}$(Cat 1)	-5585.700428	-5585.277217	-5585.262671	-5589.004716	-5588.566959
TS$_{Br}$(Cat 7)	-4238.934182	-4238.510177	-4238.502137	-4240.536668	-4240.104623
6$_{anti}$	-977.934363	-977.715799	-977.713498	-978.672665	-978.451800
IP$_{Br}$(uncat)	-3552.327903	-3552.114714	-3552.110708	-3553.087609	-3552.870414
IP$_{Br}$(Cat 1)	-5585.720703	-5585.299111	-5585.283707	-5589.026043	-5588.589047
IP$_{Br}$(Cat 7)	-4238.951489	-4238.527116	-4238.519030	-4240.553001	-4240.120542
IP$_{F}$(uncat)	-1077.944669	-1077.728265	-1077.725249	-1078.696148	-1078.476728
IP$_{F}$(Cat 1)	-3111.351814	-3110.924654	-3110.911336	-3114.646474	-3114.205996
IP$_{F}$(Cat 7)	-1764.581152	-1764.152806	-1764.145923	-1766.172929	-1765.737700
TS$_{F}$(uncat)	-1077.931232	-1077.714931	-1077.712483	-1078.682835	-1078.464086
TS$_{F}$(Cat 1)	-3111.333561	-3110.907849	-3110.893899	-3114.632833	-3114.193171
TS$_{F}$(Cat 7)	-1764.563519	-1764.136424	-1764.128860	-1766.158998	-1765.724339
TS$_{Br}$(uncat)$_{Syn}$	-3552.314667	-3552.098689	-3552.096189	-3553.072956	-3552.854478
TS$_{Br}$(Cat 1)$_{Syn}$	-5585.695928	-5585.270984	-5585.256659	-5588.999015	-5588.559746
6$_{Syn}$	-977.932392	-977.711698	-977.709984	-978.670160	-978.447752
IP$_{Br}$(uncat)$_{Syn}$	-3552.325789	-3552.110440	-3552.107121	-3553.083582	-3552.864914
IP$_{Br}$(Cat 1)$_{Syn}$	-5585.721447	-5585.294962	-5585.281452	-5589.021329	-5588.581334
IP$_{F}$(uncat)$_{Syn}$	-1077.930972	-1077.713062	-1077.710892	-1078.681477	-1078.461397
IP$_{F}$(Cat 1)$_{Syn}$	-1077.940540	-1077.721570	-1077.719401	-1078.689932	-1078.468793
TS$_{F}$(uncat)$_{Syn}$	-3111.333036	-3110.906408	-3110.892635	-3114.632407	-3114.192006
TS$_{F}$(Cat 1)$_{Syn}$	-1077.930518	-1077.712361	-1077.710403	-1078.681423	-1078.461308
Cat 1-Cl	-2493.745562	-2493.564446	-2493.553453	-2496.312863	-2496.120754

IP_{Cl}(uncat)	-1438.325448	-1438.110886	-1438.107288	-1439.078804	-1438.860644
IP_{Cl}(Cat 1)	-3471.722329	-3471.295377	-3471.282386	-3475.017991	-3474.578048
TS_{Cl}(uncat)	-1438.310957	-1438.095721	-1438.092884	-1439.063141	-1438.845068
TS_{Cl}(Cat 1)	-3471.698687	-3471.275025	-3471.260681	-3474.998817	-3474.560811
IP_{TCA}(uncat)	-2565.401972	-2565.163174	-2565.156926	-2566.275419	-2566.030373
TS_{TCA}(uncat)	-2565.390450	-2565.150917	-2565.145234	-2566.264159	-2566.018943
Cat 8_{aa} C_s	-2356.242028	-2356.059599	-2356.050146	-2358.849266	-2358.657384
Cat 8_{aa} C_2	-2356.242176	-2356.059864	-2356.050464	-2358.849507	-2358.657795
Cat 8_{as}	-2356.241488	-2356.059100	-2356.049303	-2358.849116	-2358.656931
Cat 8_{ss}	-2356.250239	-2356.059190	-2356.053767	-2358.848538	-2358.652066
Cat 8-F	-2456.264202	-2456.087093	-2456.075591	-2458.877728	-2458.689117
Cat 8-Br	-4930.635637	-4930.461170	-4930.448352	-4933.258430	-4933.071145

Table S24: Starting Materials and Products.

	Energies / Ha				
	E (opt)	**G (opt)**	**G-qh (opt)**	**E (sp)**	**G-qh (sp)**
4-1	-3552.349602	-3552.134441	-3552.130859	-3553.107610	-3552.888867
4-2	-3552.340139	-3552.122829	-3552.120101	-3553.096913	-3552.876875
4-3	-3552.347694	-3552.132204	-3552.128731	-3553.105749	-3552.886786
4-4	-3552.345284	-3552.129334	-3552.126041	-3553.102214	-3552.882971
4-5	-3552.348631	-3552.131856	-3552.129023	-3553.105882	-3552.886274
4-6	-3552.342835	-3552.126177	-3552.123292	-3553.099249	-3552.879706
4-7	-3552.341024	-3552.123968	-3552.121118	-3553.098766	-3552.878860
4-8	-3552.345270	-3552.127062	-3552.124525	-3553.102599	-3552.881854
4-9	-3552.341424	-3552.123633	-3552.121115	-3553.097556	-3552.877247
4-10	-3552.338915	-3552.121719	-3552.118829	-3553.095400	-3552.875314
4-11	-3552.339750	-3552.121824	-3552.119351	-3553.096422	-3552.876023
4-12	-3552.340139	-3552.122829	-3552.120101	-3553.096910	-3552.876872
4-13	-3552.339750	-3552.121828	-3552.119355	-3553.096421	-3552.876026
5-1	-1078.003107	-1077.783673	-1077.780394	-1078.747642	-1078.52493
5-2	-1078.00365	-1077.784834	-1077.781383	-1078.748316	-1078.52605
5-3	-1078.004291	-1077.785309	-1077.781913	-1078.750116	-1078.52774
5-4	-1078.005161	-1077.786005	-1077.782736	-1078.750915	-1078.52849
5-5	-1078.003503	-1077.783251	-1077.780522	-1078.747937	-1078.52496
5-6	-1078.005080	-1077.785660	-1077.782468	-1078.749839	-1078.52723
5-7	-1078.002886	-1077.783190	-1077.780074	-1078.748758	-1078.52595
5-8	-1078.004062	-1077.784577	-1077.781462	-1078.748790	-1078.52619
5-9	-1078.000578	-1077.778922	-1077.776482	-1078.745884	-1078.52179
5-10	-1077.996285	-1077.776270	-1077.773407	-1078.740453	-1078.51758
5-11	-1077.997826	-1077.776618	-1077.773935	-1078.742626	-1078.51874
SM Cl-1	-1438.355099	-1438.138131	-1438.134843	-1439.104987	-1438.884731
SM Cl-2	-1438.352819	-1438.136176	-1438.132757	-1439.102935	-1438.882873

SM Cl-3	-1438.354862	-1438.136916	-1438.134003	-1439.103661	-1438.882802
SM Cl-4	-1438.354204	-1438.136447	-1438.133509	-1439.103351	-1438.882656
SM Cl-5	-1438.353043	-1438.135978	-1438.132596	-1439.102907	-1438.882460
SM Cl-6	-1438.352750	-1438.135472	-1438.132232	-1439.101679	-1438.881161
SM Cl-7	-1438.352484	-1438.133881	-1438.131336	-1439.101090	-1438.879942
SM Cl-8	-1438.350730	-1438.130977	-1438.128611	-1439.100052	-1438.877933
SM Cl-9	-1438.350529	-1438.132376	-1438.129609	-1439.098830	-1438.877910
SM Cl-10	-1438.346536	-1438.127877	-1438.125169	-1439.095915	-1438.874548
SM Cl-11	-1438.347454	-1438.128950	-1438.126160	-1439.095528	-1438.874234
SM Cl-12	-1438.346298	-1438.128144	-1438.125299	-1439.094311	-1438.873312
SM Cl-13	-1438.344664	-1438.125056	-1438.122806	-1439.093324	-1438.871466
SM TCA-1	-2565.452546	-2565.210573	-2565.204218	-2566.321590	-2566.073262
SM TCA-2	-2565.451583	-2565.209240	-2565.203206	-2566.321064	-2566.072687
SM TCA-3	-2565.452862	-2565.208848	-2565.203461	-2566.321230	-2566.071829
SM TCA-4	-2565.450169	-2565.208660	-2565.202090	-2566.319761	-2566.071682
SM TCA-5	-2565.451754	-2565.208442	-2565.202762	-2566.320487	-2566.071495
SM TCA-6	-2565.449840	-2565.209075	-2565.201866	-2566.319271	-2566.071297
SM TCA-7	-2565.451039	-2565.208409	-2565.202371	-2566.319940	-2566.071272
SM TCA-8	-2565.451922	-2565.207890	-2565.202498	-2566.320477	-2566.071053
SM TCA-9	-2565.451867	-2565.208237	-2565.202586	-2566.319886	-2566.070605
SM TCA-10	-2565.451575	-2565.207986	-2565.202434	-2566.319448	-2566.070307
SM TCA-11	-2565.449238	-2565.206793	-2565.200882	-2566.318648	-2566.070292
SM TCA-12	-2565.452287	-2565.207971	-2565.202570	-2566.319860	-2566.070143
SM TCA-13	-2565.450265	-2565.205579	-2565.200497	-2566.318061	-2566.068293
SM TCA-14	-2565.449122	-2565.205836	-2565.200102	-2566.317297	-2566.068277
SM TCA-15	-2565.449624	-2565.205375	-2565.200122	-2566.317239	-2566.067737
SM TCA-16	-2565.449020	-2565.204895	-2565.199666	-2566.316768	-2566.067414
SM TCA-17	-2565.450488	-2565.205095	-2565.200112	-2566.316998	-2566.066622
SM TCA-18	-2565.447862	-2565.203157	-2565.197780	-2566.316399	-2566.066317
SM TCA-19	-2565.446923	-2565.203405	-2565.197655	-2566.315160	-2566.065892
SM TCA-20	-2565.449467	-2565.202916	-2565.198553	-2566.316618	-2566.065704
SM TCA-21	-2565.446408	-2565.201964	-2565.196582	-2566.313927	-2566.064101
SM TCA-22	-2565.445298	-2565.200455	-2565.195433	-2566.313748	-2566.063883
SM TCA-23	-2565.444836	-2565.200389	-2565.194871	-2566.313149	-2566.063184
SM TCA-24	-2565.443789	-2565.201120	-2565.194997	-2566.311557	-2566.062765
SM TCA-25	-2565.441691	-2565.197287	-2565.192180	-2566.307937	-2566.058426

Table S25: Unalkylated Tetradentate Catalyst, Cat **9**.

Index	**Energies / Ha**				
	E (opt)	**G (opt)**	**G-qh (opt)**	**E (sp)**	**G-qh (sp)**
TS Cat 9-F epi tetra	-4103.703284	-4102.991767	-4102.974341	-4108.180127	-4107.451184
TS Cat 9-F epi tri	-4103.714953	-4102.998148	-4102.983416	-4108.190824	-4107.459287

Table S26: Methylated Tridentate Catalyst, Cat **10**.

Index	Energies / Ha				
	E (opt)	G (opt)	G-qh (opt)	E (sp)	G-qh (sp)
Cat 10-1	-3064.986424	-3064.490460	-3064.476912	-3068.773763	-3068.264251
Cat 10-2	-3064.987219	-3064.490110	-3064.476928	-3068.773999	-3068.263708
Cat 10-3	-3064.986698	-3064.489846	-3064.476566	-3068.773786	-3068.263654
Cat 10-4	-3064.994152	-3064.492587	-3064.481799	-3068.771678	-3068.259325
Cat 10-5	-3064.992995	-3064.491042	-3064.480778	-3068.771067	-3068.258850
Cat 10-6	-3064.986817	-3064.489007	-3064.476686	-3068.768822	-3068.258691
Cat 10-7	-3064.994705	-3064.493090	-3064.482298	-3068.770990	-3068.258583
Cat 10-8	-3064.994058	-3064.491212	-3064.481279	-3068.771259	-3068.258480
Cat 10-9	-3064.991288	-3064.488805	-3064.478575	-3068.770634	-3068.257921
Cat 10-10	-3064.995184	-3064.491055	-3064.481609	-3068.771466	-3068.257891
Cat 10-11	-3064.995991	-3064.491813	-3064.482275	-3068.771581	-3068.257865
Cat 10-12	-3064.991921	-3064.489612	-3064.479813	-3068.769863	-3068.257755
Cat 10-13	-3064.990429	-3064.489078	-3064.478726	-3068.768912	-3068.257209
Cat 10-14	-3064.990818	-3064.487932	-3064.478080	-3068.769520	-3068.256782
Cat 10-15	-3064.991178	-3064.489268	-3064.479018	-3068.768666	-3068.256506
Cat 10-16	-3064.988637	-3064.487813	-3064.476789	-3068.767538	-3068.255690

Table S27: Methylated Tridentate Catalyst, Cat **10**, Complexes.

	Energies / Ha				
	E (opt)	G (opt)	G-qh (opt)	E (sp)	G-qh (sp)
Cat 10-F 1	-3165.019236	-3164.518732	-3164.507896	-3168.805120	-3168.293780
Cat 10-F 2	-3165.014392	-3164.515957	-3164.503978	-3168.803552	-3168.293138
IP Cat 10-F Cs 1	-3185.082242	-3184.582209	-3184.571139	-3188.943324	-3188.432221
IP Cat 10-F Cs 2	-3185.079080	-3184.583659	-3184.570500	-3188.940455	-3188.431875
Cat 10-F•H_2O	-3241.469500	-3240.947941	-3240.936300	-3245.274813	-3244.741613
Cat 10-Cl 1	-3525.39086	-3524.89129	-3524.88019	-3529.177920	-3528.667249
Cat 10-Cl 2	-3525.385259	-3524.889117	-3524.876315	-3529.176182	-3528.667238
Cat 10-Br 1	-5639.39259	-5638.89422	-5638.88265	-5643.185958	-5642.676018
Cat 10-Br 2	-5639.38687	-5638.89211	-5638.87873	-5643.183590	-5642.675449

Table S28: Cat **10**-F-Episulfonium Reactive Ion Pairs.

	Energies / Ha				
	E (opt)	G (opt)	G-qh (opt)	E (sp)	G-qh (sp)
IP Cat 10-F epi 1	-4142.993600	-4142.255848	-4142.238021	-4147.517967	-4146.762388
IP Cat 10-F epi 2	-4142.993974	-4142.253725	-4142.237081	-4147.518838	-4146.761945
IP Cat 10-F epi 3	-4142.986996	-4142.249185	-4142.231444	-4147.517049	-4146.761497
IP Cat 10-F epi 4	-4142.996868	-4142.253311	-4142.238222	-4147.518733	-4146.760087
IP Cat 10-F epi 5	-4142.992901	-4142.253274	-4142.236590	-4147.515959	-4146.759648
IP Cat 10-F epi 6	-4142.988950	-4142.250082	-4142.232630	-4147.515032	-4146.758712

IP Cat 10-F epi 7	-4142.988601	-4142.248683	-4142.232097	-4147.514225	-4146.757721
IP Cat 10-F epi 8	-4142.983972	-4142.246189	-4142.228540	-4147.512619	-4146.757187
IP Cat 10-F epi 9	-4142.980129	-4142.241181	-4142.224249	-4147.510941	-4146.755061
IP Cat 10-F epi 10	-4142.988032	-4142.246282	-4142.230455	-4147.511781	-4146.754204
IP Cat 10-F epi 11	-4142.986052	-4142.242718	-4142.228058	-4147.510436	-4146.752442
IP Cat 10-F epi 12	-4142.983498	-4142.243063	-4142.226290	-4147.508809	-4146.751601

Table S29: Transition State Structures, Catalyst **10**.

Index	Energies / Ha					
	E (opt)	**G (opt)**	**G-qh (opt)**	**E (sp)**	**G-qh (sp)**	**G-qh 243.15 K (sp)**
TS Cat 10-F epi major 1	-4142.982972	-4142.240007	-4142.224875	-4147.507966	-4146.749869	-4146.726778
TS Cat 10-F epi major 2	-4142.976870	-4142.234393	-4142.218967	-4147.506718	-4146.748815	-4146.725767
TS Cat 10-F epi major 3	-4142.979913	-4142.238243	-4142.222399	-4147.503595	-4146.746081	-4146.723007
TS Cat 10-F epi major 4	-4142.974862	-4142.231326	-4142.216940	-4147.500783	-4146.742861	-4146.719857
TS Cat 10-F epi major 5	-4142.974597	-4142.233207	-4142.217164	-4147.499259	-4146.741826	-4146.718677
TS Cat 10-F epi major 6	-4142.973872	-4142.230443	-4142.215939	-4147.498024	-4146.740091	-4146.717086
TS Cat 10-F epi major 7	-4142.972144	-4142.229100	-4142.214755	-4147.494836	-4146.737447	-4146.714362
TS Cat 10-F epi major 8	-4142.964220	-4142.224090	-4142.207050	-4147.494490	-4146.737320	-4146.713977
TS Cat 10-F epi major 9	-4142.961376	-4142.221118	-4142.204790	-4147.490373	-4146.733787	-4146.710501
TS Cat 10-F epi minor 1	-4142.971969	-4142.233025	-4142.216508	-4147.503029	-4146.747568	-4146.724197
TS Cat 10-F epi minor 2	-4142.974176	-4142.231943	-4142.216583	-4147.503648	-4146.746055	-4146.722981
TS Cat 10-F epi minor 3	-4142.980133	-4142.236252	-4142.221542	-4147.504421	-4146.745830	-4146.722789
TS Cat 10-F epi minor 4	-4142.969500	-4142.229719	-4142.213057	-4147.502255	-4146.745812	-4146.722557
TS Cat 10-F epi minor 5	-4142.976723	-4142.233558	-4142.218614	-4147.500221	-4146.742112	-4146.719087
TS Cat 10-F epi minor 6	-4142.975739	-4142.233099	-4142.217823	-4147.499007	-4146.741091	-4146.718064
TS Cat 10-F epi minor 7	-4142.966408	-4142.225070	-4142.209160	-4147.495812	-4146.738564	-4146.715339
TS Br Cat 10	-6617.344967	-6616.606991	-6616.590423	-6621.876134	-6621.121590	-

Table S30: Transition State Structures, Catalyst **13**.

Index	Energies / Ha					
	E (opt)	**G (opt)**	**G-qh (opt)**	**E (sp)**	**G-qh (sp)**	**G-qh 243.15 K (sp)**
TS Cat 13-F epi major 1	-4221.515301	-4220.717951	-4220.702774	-4226.149514	-4225.336987	-4225.313215
TS Cat 13-F epi major 2	-4221.513746	-4220.714222	-4220.699884	-4226.146899	-4225.333037	-4225.309402
TS Cat 13-F epi major 3	-4221.512162	-4220.715512	-4220.699979	-4226.145124	-4225.332941	-4225.309148
TS Cat 13-F epi major 4	-4221.503969	-4220.709103	-4220.692304	-4226.142614	-4225.330949	-4225.307045
TS Cat 13-F epi major 5	-4221.509583	-4220.710273	-4220.695429	-4226.143581	-4225.329427	-4225.305846
TS Cat 13-F epi major 6	-4221.503864	-4220.707918	-4220.691489	-4226.141861	-4225.329486	-4225.305697
TS Cat 13-F epi major 7	-4221.510403	-4220.711598	-4220.696967	-4226.142467	-4225.329031	-4225.305383
TS Cat 13-F epi minor 1	-4221.512146	-4220.714976	-4220.699766	-4226.146414	-4225.334034	-4225.310226
TS Cat 13-F epi minor 2	-4221.504642	-4220.710922	-4220.694430	-4226.143989	-4225.333777	-4225.309732
TS Cat 13-F epi minor 3	-4221.506389	-4220.710996	-4220.694746	-4226.144666	-4225.333023	-4225.309159
TS Cat 13-F epi minor 4	-4221.504242	-4220.707763	-4220.691809	-4226.141803	-4225.329370	-4225.305593
TS Cat 13-F epi minor 5	-4221.510668	-4220.710656	-4220.696231	-4226.143123	-4225.328686	-4225.305067
TS Cat 13-F epi minor 6	-4221.500602	-4220.705226	-4220.689368	-4226.140188	-4225.328954	-4225.305058
TS Cat 13-F epi minor 7	-4221.496899	-4220.704826	-4220.686655	-4226.138524	-4225.328280	-4225.304133
TS Cat 13-F epi minor 8	-4221.506543	-4220.706992	-4220.692146	-4226.139923	-4225.325526	-4225.301953
TS Cat 13-F epi minor 9	-4221.496203	-4220.702901	-4220.685220	-4226.136704	-4225.325721	-4225.301711
TS Cat 13-F epi minor 10	-4221.492108	-4220.698086	-4220.681046	-4226.132594	-4225.321532	-4225.297565

Table S31: Miscellaneous.

Index	Energies / Ha				
	E (opt)	G (opt)	G-qh (opt)	E (sp)	G-qh (sp)
Br(g)*	-2574.27728	-2574.290436	-2574.290436	-2574.298613	-2574.311769
Br(DCM)				-2574.39026	-2574.403416
F(g)*	-99.854602	-99.865742	-99.865742	-99.868379	-99.879519
F(DCM)				-99.989411	-100.000551
F•H_2O	-176.428994	-176.426887	-176.426888	-176.4606374	-176.4585314
Cl(g)*	-460.266789	-460.278793	-460.278793	-460.281805	-460.293809
Cl(DCM)				-460.379998	-460.392002
Cs(g)*	-19.934066	-19.947960	-19.947960	-20.013829	-20.027723
Cs(DCM)				-20.110183	-20.124077
(*Z*)-TCA	-1587.435872	-1587.432886	-1587.432227	-1587.572235	-1587.568590
(*E*)-TCA	-1587.434039	-1587.431808	-1587.430707	-1587.571196	-1587.567864
CsBr(g)*	-2594.377610	-2594.400681	-2594.40066	-2594.475060	-2594.498110
CsBr(DCM)	-2594.422237	-2594.445944	-2594.445749	-2594.525198	-2594.548710
CsF(g)*	-120.001129	-120.021281	-120.021283	-120.088507	-120.108661
CsF(DCM)	-120.040461	-120.061202	-120.061202	-120.135181	-120.155922

*Evaluated at 1 mol/dm^3 concentration

Table S32: On the Stability of β-Fluorosulfides.

Index	Energies / Ha				
	E (opt)	G (opt)	G-qh (opt)	E (sp)	G-qh (sp)
16a	-695.065603	-694.943721	-694.943432	-695.087171	-694.965000
16b	-695.064986	-694.942918	-694.942805	-695.086648	-694.964466
17a	-695.062987	-694.940551	-694.940312	-695.084760	-694.962086
17b	-695.064948	-694.944482	-694.943620	-695.086180	-694.964853
14-1	-695.146954	-695.023927	-695.022980	-695.156974	-695.033000
14-2	-695.146495	-695.023118	-695.022372	-695.156767	-695.032644
14-3	-695.146546	-695.022838	-695.022340	-695.156737	-695.032531
14-4	-695.144148	-695.021911	-695.020759	-695.155747	-695.032359
14-5	-695.146092	-695.023163	-695.022188	-695.156226	-695.032321
14-6	-695.144449	-695.021424	-695.020627	-695.155848	-695.032026
14-7	-695.146053	-695.022202	-695.021584	-695.156440	-695.031970
14-8	-695.143976	-695.021658	-695.020447	-695.155353	-695.031824
14-9	-695.143892	-695.019294	-695.019028	-695.155443	-695.030578
15-1	-695.146989	-695.023919	-695.023060	-695.157265	-695.033337
15-2	-695.146657	-695.024602	-695.023130	-695.156641	-695.033114
15-3	-695.146379	-695.023100	-695.022369	-695.156851	-695.032840

15-4	-695.146105	-695.023450	-695.022389	-695.156243	-695.032527
15-5	-695.144526	-695.022088	-695.021089	-695.155412	-695.031976
15-6	-695.143705	-695.020869	-695.019888	-695.155550	-695.031733
15-7	-695.143984	-695.020077	-695.019543	-695.156037	-695.031596
15-8	-695.144494	-695.020766	-695.020284	-695.155647	-695.031437
15-9	-695.145689	-695.020980	-695.020656	-695.156141	-695.031109

6.3 Supporting Information – Chapter 4

Much of this supplementary material has been reproduced from own work in *J. Am. Chem. Soc.* **2019**, *141*, 2878-2883.[5]

6.3.1 Fluorination of Aziridinium Ions with an Achiral Urea Catalyst

6.3.1.1 Stationary Points and Additional Data

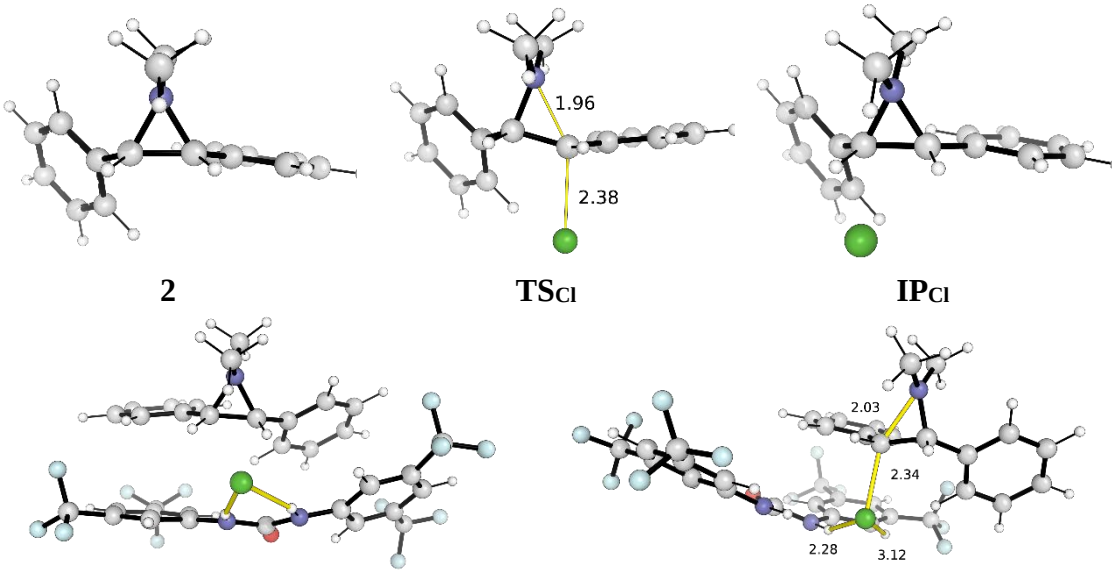

2 **TS_{Cl}** **IP_{Cl}**

IP_{Cl}(Cat) **TS_{Cl}(Cat 15)**

Figure S19: Stationary points for fluorination of aziridinium ions with achiral catalyst.

6.3.2 Metal Fluoride Solubilization

Tabulated thermodynamic data:

Table S33: Standard Enthalpy and Entropy Changes, 298.15 K.

	Source	ΔH (kJ/mol)	ΔS (J/K/mol)
Δ_f ($CsF_{(s)}$)	Ref 6	-554.7	-
Δ_f ($KF_{(s)}$)	Ref 6	-568.6	-
Δ_f ($CsF_{(g)}$)	Ref 6	-356.5	-
Δ_f ($KF_{(g)}$)	Ref 6	-326.8	-
Δ_{solv} (CsF)	Computed	-122.8	-22.3
Δ_{solv} (KF)	Computed	-130.8	-23.1

Gas phase entropies evaluated at 1 bar pressure. Solution phase at 1 M concentration

Table S34: Standard Molar Entropies, 298.15 K.

	Source	ΔS (J/K/mol)
$CsF_{(s)}$	Ref 6	88.3
$CsF_{(g)}$	Ref 6	243.2
$KF_{(s)}$	Ref 6	66.6
$KF_{(g)}$	Ref 6	226.6

6.3.3 Catalyst 12 Conformers

Conformers of catalyst **12** were generated by simulating the system in chloroform for 300 ns. All frames in the trajectory were clustered using 0.7 Å RMSD cut-off, with the 11 highest weighted clusters (>0.5 % weighting) optimized using DFT. The following RMSD framework was used for clustering frames.

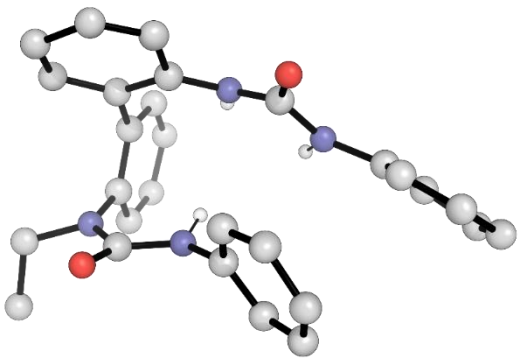

Figure S20: Framework used for RMSD clustering of MD trajectory of cat **12**. Adapted from Ref 5.

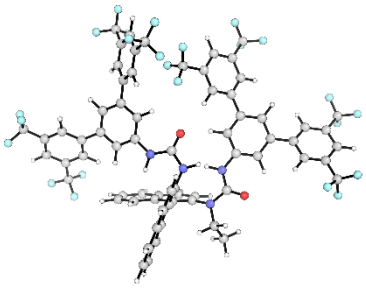

Cat 12-1
0.0 kJ/mol

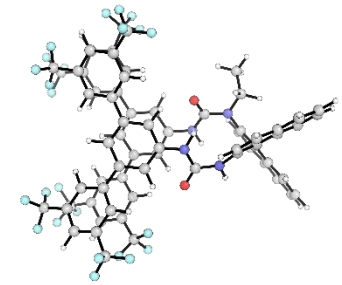

Cat 12-2
+13.7 kJ/mol

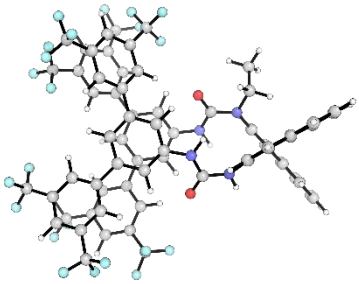

Cat 12-3
+15.0 kJ/mol

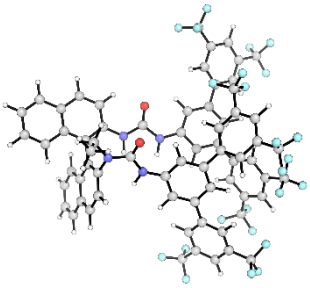

Cat 12-4
+15.3 kJ/mol

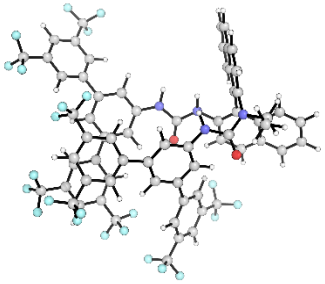

Cat 12-5
+15.8 kJ/mol

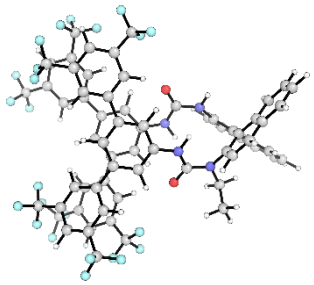

Cat 12-6
+17.5 kJ/mol

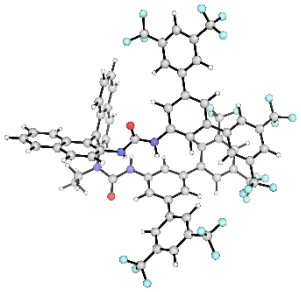

Cat 12-7
+20.4 kJ/mol

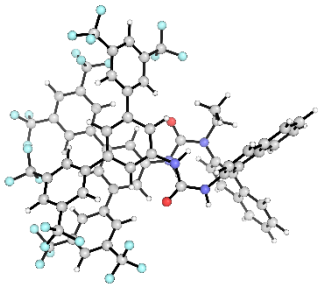

Cat 12-8
+26.2 kJ/mol

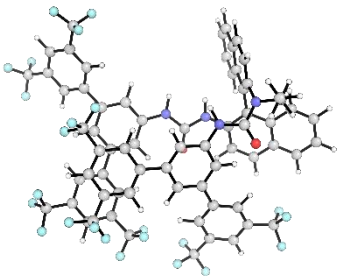

Cat 12-9
+26.2 kJ/mol

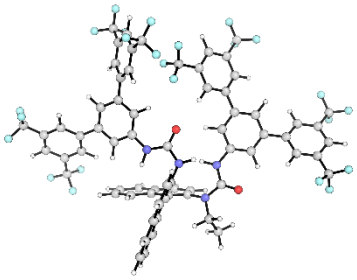

Cat 12-10
+32.9 kJ/mol

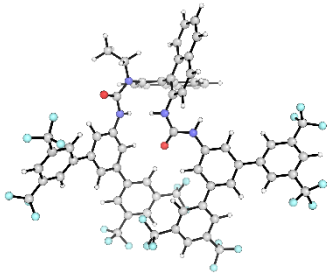

Cat 12-11
+36.3 kJ/mol

Figure S21: DFT optimized Cat **12** conformers with relative Gibbs free energies. Adapted from Ref 5.

6.3.4 Transition State Structure Analysis

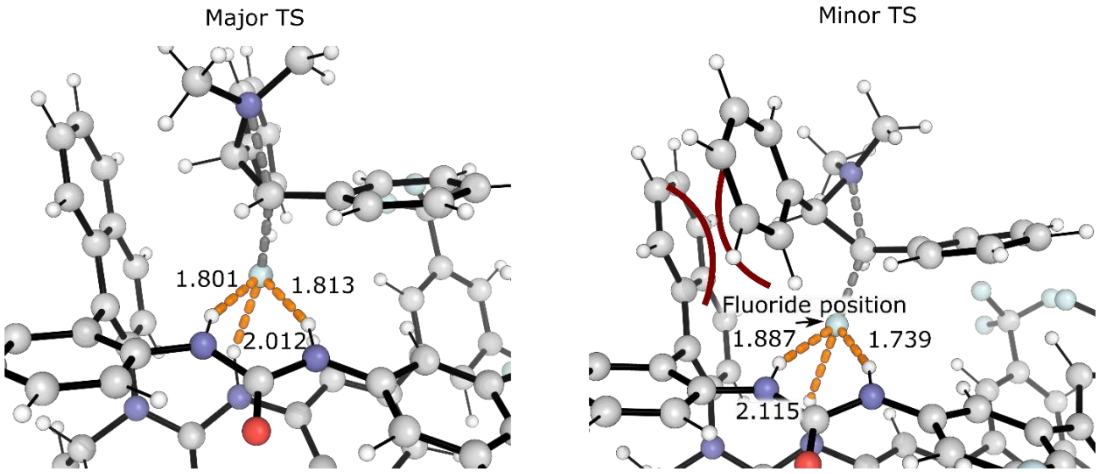

Figure S22: Close up of fluoride position in $\mathbf{TS_{Major}}$ and $\mathbf{TS_{Minor}}$ showing evidence of greater steric congestion in the latter. Figure reproduced from Ref 5.

6.3.5 Thermodynamic Data

Table S35: Pathway with Achiral Urea.

	Energies / Ha				
	E (opt)	**G (opt)**	**G-qh (opt)**	**E (sp)**	**G-qh (sp)**
TS_{Br}(uncat)	-3248.722254	-3248.463243	-3248.460558	-3249.530399	-3249.268703
TS_{Br}(Cat 1)	-5282.107423	-5281.641319	-5281.626615	-5285.463095	-5284.982287
2	-674.363354	-674.096895	-674.095042	-675.150261	-674.881948
IP_{Br}(uncat)	-3248.754495	-3248.493510	-3248.489947	-3249.562859	-3249.298311
IP_{Br}(Cat 1)	-5282.151151	-5281.679105	-5281.665524	-5285.502786	-5285.017160
IP_{F}(uncat)	-774.368372	-774.104944	-774.102055	-775.168840	-774.902523
IP_{F}(Cat 1)	-2807.780092	-2807.303415	-2807.291590	-2811.121557	-2810.633056
TS_{F}(uncat)	-774.344834	-774.082339	-774.080171	-775.146338	-774.881675
TS_{F}(Cat 1)	-2807.741411	-2807.270802	-2807.256955	-2811.090799	-2810.606342
IP_{Cl}(uncat)	-1134.751692	-1134.489495	-1134.486242	-1135.553527	-1135.288077
IP_{Cl}(Cat 1)	-3168.150378	-3167.676988	-3167.664077	-3171.495866	-3171.009565
TS_{Cl}(uncat)	-1134.720492	-1134.459646	-1134.457347	-1135.522397	-1135.259253
TS_{Cl}(Cat 1)	-3168.106811	-3167.639743	-3167.625264	-3171.456457	-3170.974910

Table S36: Starting Materials and Products

	Energies / Ha				
	E (opt)	**G (opt)**	**G-qh (opt)**	**E (sp)**	**G-qh (sp)**
1-1	-3248.756862	-3248.496740	-3248.493506	-3249.565120	-3249.301765
1-2	-3248.752008	-3248.492311	-3248.489189	-3249.559821	-3249.297002
1-3	-3248.753669	-3248.492201	-3248.489627	-3249.560423	-3249.296381
1-4	-3248.750972	-3248.490886	-3248.487682	-3249.558313	-3249.295022
1-5	-3248.750772	-3248.489236	-3248.486309	-3249.558375	-3249.293912

1-6	-3248.750880	-3248.489460	-3248.486826	-3249.557517	-3249.293463
1-7	-3248.749925	-3248.489381	-3248.486677	-3249.556523	-3249.293275
1-8	-3248.749932	-3248.487749	-3248.485533	-3249.555690	-3249.291291
1-9	-3248.748066	-3248.486123	-3248.483587	-3249.555581	-3249.291102
1-10	-3248.746654	-3248.485515	-3248.482767	-3249.554969	-3249.291082
1-11	-3248.745945	-3248.485272	-3248.482248	-3249.552963	-3249.289266
16-1	-1134.761855	-1134.500105	-1134.497004	-1135.561921	-1135.297070
16-2	-1134.757668	-1134.496438	-1134.493377	-1135.557458	-1135.293166
16-3	-1134.759799	-1134.496909	-1134.494400	-1135.558490	-1135.293091
16-4	-1134.757514	-1134.495290	-1134.492503	-1135.556051	-1135.291040
16-5	-1134.755829	-1134.493986	-1134.491291	-1135.554415	-1135.289877
16-6	-1134.756436	-1134.492954	-1134.490358	-1135.555923	-1135.289845
16-7	-1134.756881	-1134.493480	-1134.491168	-1135.555522	-1135.289808
16-8	-1134.756281	-1134.492716	-1134.490551	-1135.553657	-1135.287927
16-9	-1134.753611	-1134.490096	-1134.487747	-1135.552676	-1135.286812
16-10	-1134.752182	-1134.488977	-1134.486552	-1135.552228	-1135.286598
16-11	-1134.750959	-1134.489488	-1134.486268	-1135.550193	-1135.285502
16-12	-1134.761855	-1134.500105	-1134.497004	-1135.561921	-1135.297070
16-13	-1134.757668	-1134.496438	-1134.493377	-1135.557458	-1135.293166
16-14	-1134.759799	-1134.496909	-1134.494400	-1135.558490	-1135.293091
3-1	-774.410585	-774.146650	-774.143555	-775.206782	-774.939751
3-2	-774.411357	-774.146762	-774.144113	-775.205486	-774.938242
3-3	-774.408056	-774.144125	-774.141206	-775.204026	-774.937177
3-4	-774.410481	-774.145299	-774.142862	-775.204541	-774.936922
3-5	-774.408354	-774.144471	-774.141256	-775.203057	-774.935959
3-6	-774.406568	-774.142039	-774.139322	-775.201502	-774.934256
3-7	-774.407923	-774.142510	-774.140279	-775.201318	-774.933674
3-8	-774.406033	-774.140786	-774.138018	-775.201487	-774.933473
3-9	-774.403959	-774.138493	-774.136087	-775.198715	-774.930843
3-10	-774.401704	-774.136114	-774.133814	-775.197341	-774.929452

Table S37: Metal Fluoride Solubilization with Methylated Tridentate Catalyst **7**.

	Energies / Ha				
	E (opt)	**G (opt)**	**G-qh (opt)**	**E (sp)**	**G-qh (sp)**
Cat 7	-3064.986424	-3064.490460	-3064.476912	-3068.773763	-3068.264251
Cat 7 F•Cs	-3185.082340	-3184.585204	-3184.572779	-3188.943228	-3188.433667
Cat 7 F•K	-3764.904108	-3764.406820	-3764.394299	-3768.696028	-3768.186219

Table S38: Uncoordinated Ethylated Tridentate Catalyst **12**.

	Energies / Ha				
	E (opt)	**G (opt)**	**G-qh (opt)**	**E (sp)**	**G-qh (sp)**
Cat 12-1	-5374.209878	-5373.382114	-5373.356062	-5380.855333	-5380.001517
Cat 12-2	-5374.228039	-5373.389687	-5373.369400	-5380.854932	-5379.996293
Cat 12-3	-5374.230811	-5373.390093	-5373.370810	-5380.855792	-5379.995791
Cat 12-4	-5374.212056	-5373.381566	-5373.357044	-5380.850705	-5379.995693
Cat 12-5	-5374.214784	-5373.381662	-5373.358268	-5380.852000	-5379.995484
Cat 12-6	-5374.223051	-5373.386103	-5373.364819	-5380.853067	-5379.994835
Cat 12-7	-5374.201461	-5373.374535	-5373.348240	-5380.846975	-5379.993755
Cat 12-8	-5374.227783	-5373.389910	-5373.368635	-5380.850705	-5379.991556
Cat 12-9	-5374.213794	-5373.380408	-5373.357475	-5380.847852	-5379.991532
Cat 12-10	-5374.193262	-5373.366071	-5373.339738	-5380.842507	-5379.988984
Cat 12-11	-5374.190779	-5373.367488	-5373.339304	-5380.839176	-5379.987700

Table S39: Fluoride Complexes of Ethylated Tridentate Catalyst **12**.

	Energies / Ha				
	E (opt)	**G (opt)**	**G-qh (opt)**	**E (sp)**	**G-qh (sp)**
Cat 12 F-1	-5474.244879	-5473.410096	-5473.387919	-5480.881541	-5480.024581
Cat 12 F-2	-5474.246598	-5473.409569	-5473.389287	-5480.881334	-5480.024023
Cat 12 F-3	-5474.228022	-5473.400973	-5473.374906	-5480.877042	-5480.023925
Cat 12 F-4	-5474.219531	-5473.392783	-5473.366686	-5480.875802	-5480.022957
Cat 12 F-5	-5474.247213	-5473.408169	-5473.388308	-5480.881400	-5480.022495
Cat 12 F-6	-5474.224673	-5473.399835	-5473.372668	-5480.874245	-5480.022240
Cat 12 F-7	-5474.236455	-5473.403109	-5473.380553	-5480.877899	-5480.021998
Cat 12 F-8	-5474.248257	-5473.409339	-5473.389425	-5480.880066	-5480.021234
Cat 12 F-9	-5474.238684	-5473.403568	-5473.381433	-5480.878410	-5480.021160
Cat 12 F-10	-5474.243694	-5473.405371	-5473.384767	-5480.879874	-5480.020947
Cat 12 F-11	-5474.248476	-5473.408220	-5473.388610	-5480.877945	-5480.018079
Cat 12 F•K-1	-6074.138225	-6073.302407	-6073.280984	-6080.776963	-6079.919723
Cat 12 F•K-2	-6074.136304	-6073.300721	-6073.278988	-6080.776652	-6079.919336
Cat 12 F•K-3	-6074.132760	-6073.298404	-6073.275528	-6080.774851	-6079.917620
Cat 12-F•K-4	-6074.115471	-6073.289652	-6073.262649	-6080.770231	-6079.917409
Cat 12-F•K-5	-6074.139953	-6073.303028	-6073.281797	-6080.775534	-6079.917379
Cat 12-F•K-6	-6074.106044	-6073.284670	-6073.255697	-6080.767244	-6079.916896
Cat 12-F•K-7	-6074.134805	-6073.298567	-6073.277711	-6080.773858	-6079.916764
Cat 12-F•K-8	-6074.114247	-6073.290510	-6073.262567	-6080.767683	-6079.916002
Cat 12-F•K-9	-6074.138144	-6073.300149	-6073.279590	-6080.773103	-6079.914550
Cat 12-F•K-10	-6074.123575	-6073.287110	-6073.265514	-6080.769170	-6079.911108
Cat 12-F•K-11	-6074.125895	-6073.291268	-6073.268698	-6080.768092	-6079.910894

Table S40: Reactive Catalyst **12**-Fluoride-Aziridinium Ion Pairs.

	Energies / Ha				
	E (opt)	**G (opt)**	**G-qh (opt)**	**E (sp)**	**G-qh (sp)**
Cat 12-F-Azir 1	-6148.639173	-6147.519998	-6147.491095	-6156.073614	-6154.925536
Cat 12-F-Azir 2	-6148.636685	-6147.520388	-6147.489509	-6156.072391	-6154.925215
Cat 12-F-Azir 3	-6148.658183	-6147.527920	-6147.504483	-6156.076418	-6154.922719
Cat 12-F-Azir 4	-6148.653838	-6147.524558	-6147.500643	-6156.075710	-6154.922515
Cat 12-F-Azir 5	-6148.646573	-6147.521140	-6147.495077	-6156.073840	-6154.922343
Cat 12-F-Azir 6	-6148.649583	-6147.524317	-6147.498962	-6156.070828	-6154.920208
Cat 12-F-Azir 7	-6148.644443	-6147.519600	-6147.493603	-6156.066932	-6154.916092

Table S41: Transition State Structures with Catalyst **12**.

	Energies / Ha (278.15 K)				
TS_ 12-FAzir-	**E (opt)**	**G (opt)**	**G-qh (opt)**	**E (sp)**	**G-qh (sp)**
Major 1	-6148.620859	-6147.482565	-6147.459223	-6156.047669	-6154.886032
Major 2	-6148.621222	-6147.482462	-6147.459606	-6156.047206	-6154.885590
Major 3	-6148.620397	-6147.478730	-6147.457556	-6156.046317	-6154.883475
Major 4	-6148.621335	-6147.478758	-6147.458213	-6156.046283	-6154.883160
Major 5	-6148.615643	-6147.476561	-6147.454183	-6156.041464	-6154.880004
Major 6	-6148.608842	-6147.470890	-6147.447411	-6156.039741	-6154.878311
Major 7	-6148.614400	-6147.469990	-6147.449556	-6156.032544	-6154.867700
Minor 1	-6148.616610	-6147.478326	-6147.455128	-6156.044981	-6154.883498
Minor 2	-6148.617157	-6147.478132	-6147.455271	-6156.044371	-6154.882485
Minor 3	-6148.617085	-6147.477681	-6147.455286	-6156.043888	-6154.882090
Minor 4	-6148.620942	-6147.479131	-6147.458279	-6156.043213	-6154.880551
Minor 5	-6148.619145	-6147.478918	-6147.456607	-6156.041499	-6154.878961
Minor 6	-6148.618055	-6147.475814	-6147.454514	-6156.042275	-6154.878734
Minor 7	-6148.618091	-6147.475443	-6147.454226	-6156.042070	-6154.878205
Minor 8	-6148.592956	-6147.458077	-6147.432952	-6156.028361	-6154.868357

Table S42: Transition State Structures with Cyclopentene Derived Substrate, **18**.

	Energies / Ha				
	E (opt)	**G (opt)**	**G-qh (opt)**	**E (sp)**	**G-qh (sp)**
TS_{Major} derived	-5803.627644	-5802.594789	-5802.571170	-5810.655598	-5809.599124
TS_{Minor} derived	-5803.633596	-5802.598001	-5802.575598	-5810.657745	-5809.599747

Table S43: Miscellaneous Species.

	Energies / Ha				
	E (opt)	**G (opt)**	**G-qh (opt)**	**E (sp)**	**G-qh (sp)**
$CsF_{(g)}$	-120.001129	-120.021281	-120.021283	-120.088507	-120.108661
$CsF_{(DCM)}$	-120.040461	-120.061200	-120.061202	-120.135181	-120.155922
$KF_{(g)}$	-699.816535	-699.834673	-699.834674	-699.839431	-699.857570
$KF_{(DCM)}$	-699.866799	-699.885504	-699.885506	-699.889109	-699.907816

6.4 Supporting Information – Chapter 5

6.4.1 Second-Generation Catalysts

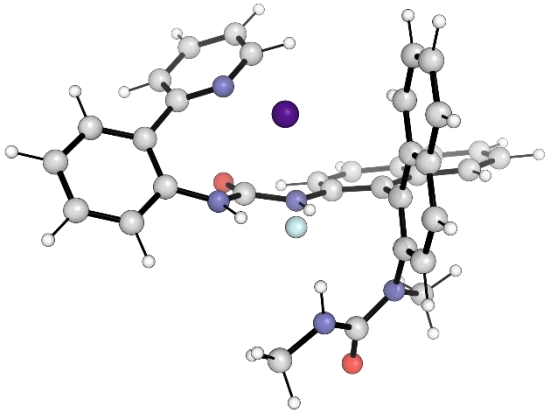

Figure S23: **Cat-py** binding cesium fluoride, showing interaction of cesium with the pyridine motif.

Additional transition state structures with **H_8-cat-py**

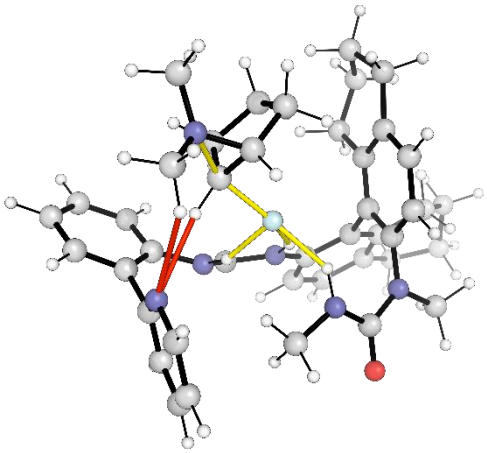

H8-cat-py-3 (Major, +10.7 kJ/mol)

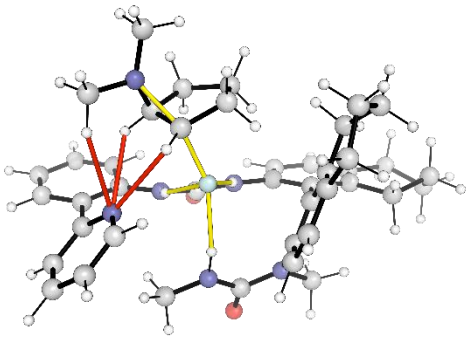

H8-cat-py-4 (Minor, +30.5 kJ/mol)

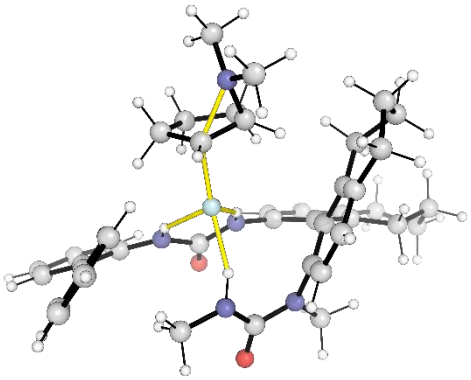

H8-cat-py-5 (Major, +33.1 kJ/mol)

Figure S24: Additional computed TSs for fluorination with **H_8-cat-py**.

6.4.2 Towards Homogeneous Catalytic Fluorination

Lowest energy conformers are illustrated.

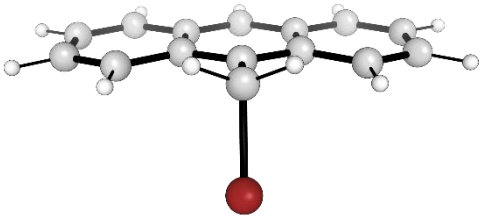

Ar_3Br

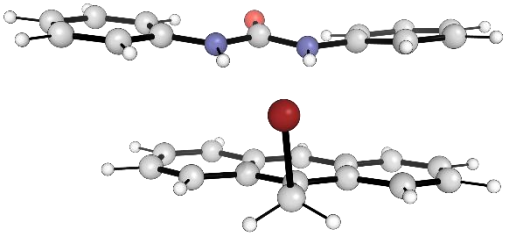

$Ar_3Br\text{-}Urea_H$

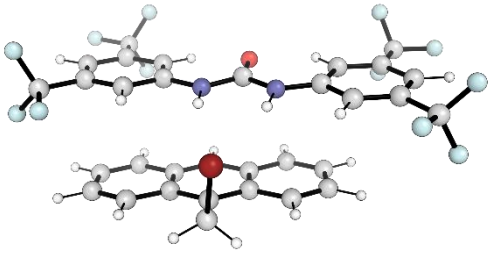

$Ar_3Br\text{-}Urea_{Schreiner}$

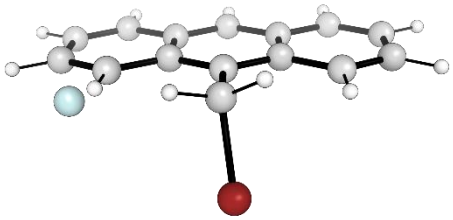

$Ar_3Br\text{-}F$

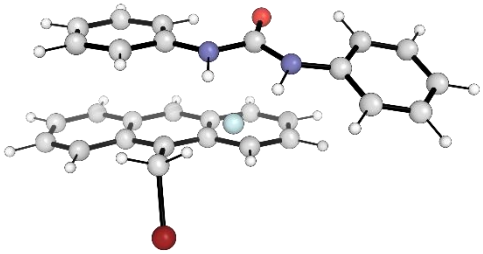

$Ar_3Br\text{-}F\text{-}Urea_H$

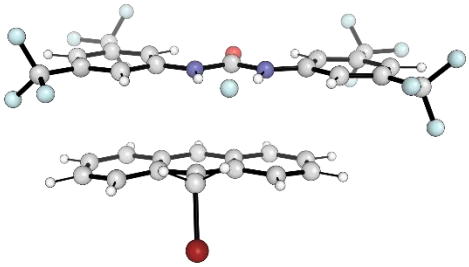

$Ar_3Br\text{-}F\text{-}Urea_{Schreiner}$

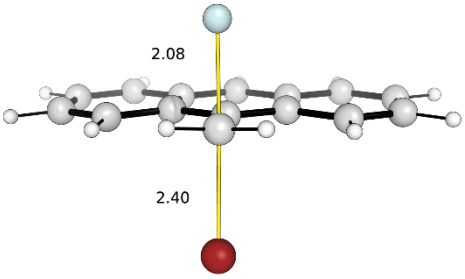

TS-F

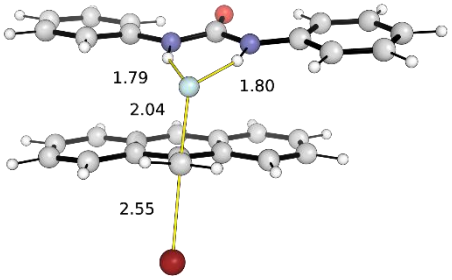

TS-F-Urea$_{H}$

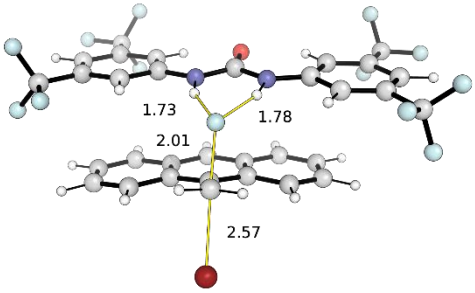

TS-F-Urea$_{Schreiner}$

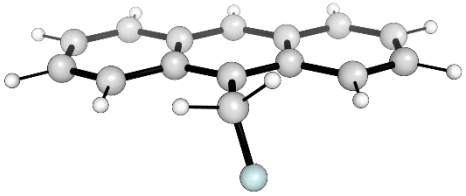

Ar$_3$F

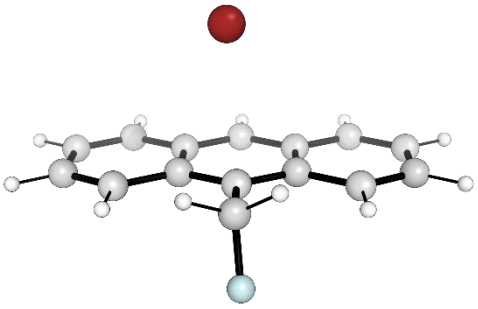

Ar$_3$F-Br

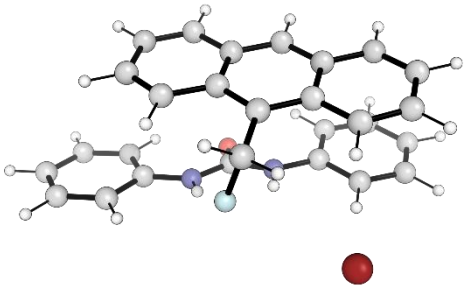

Ar$_3$F-Br-Urea$_{H}$

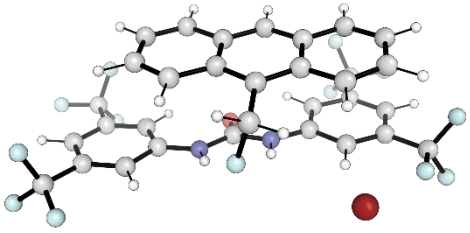

Ar$_3$F-Br-Urea$_{Schreiner}$

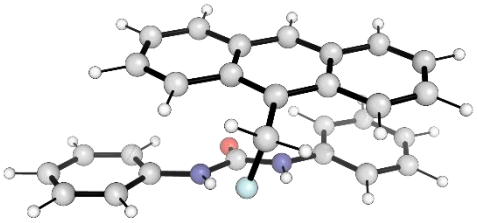

Ar$_3$F-Urea$_{H}$

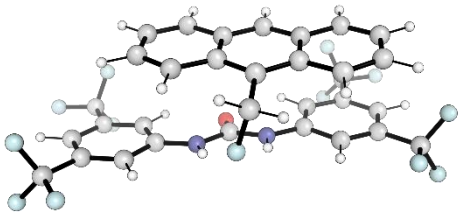

Ar$_3$F-Urea$_{Schreiner}$

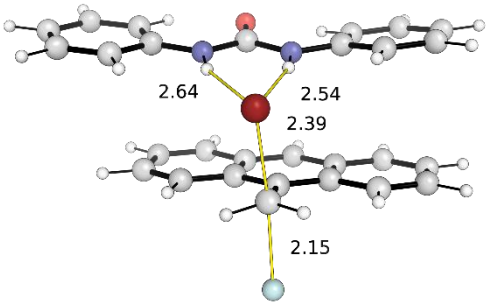

TS-Br-Urea$_H$ (+ 25 kJ/mol)

Figure S25: Geometries of key species for homogeneous fluorination of bromide substrate.

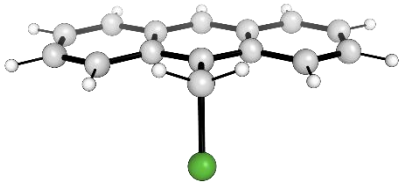

Ar$_3$Cl

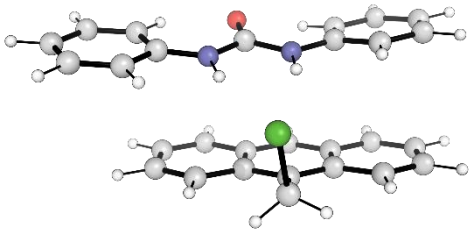

Ar$_3$Cl-Urea$_H$

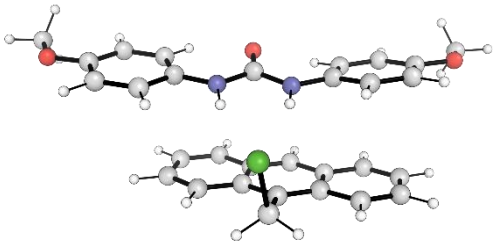

Ar$_3$Cl-Urea$_{OMe}$

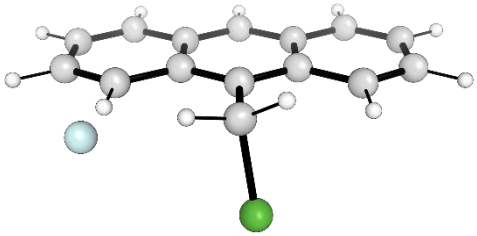

Ar$_3$Cl-F

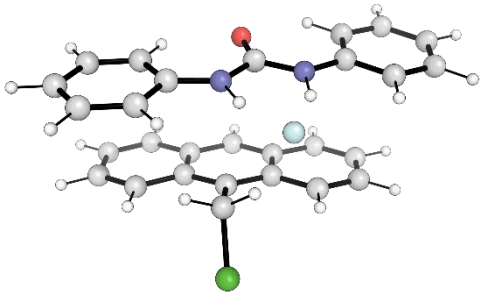

Ar$_3$Cl-F-Urea$_H$

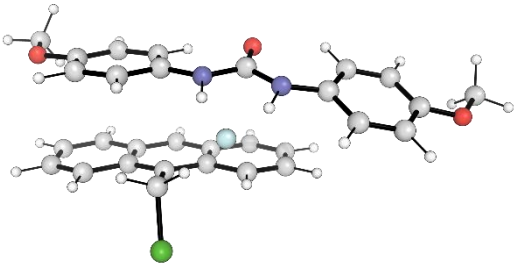

Ar$_3$Cl-F-Urea$_{OMe}$

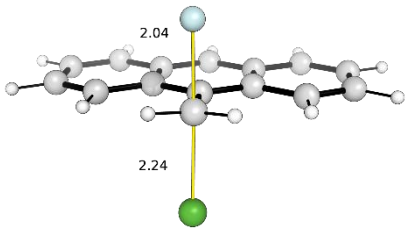

TS-F

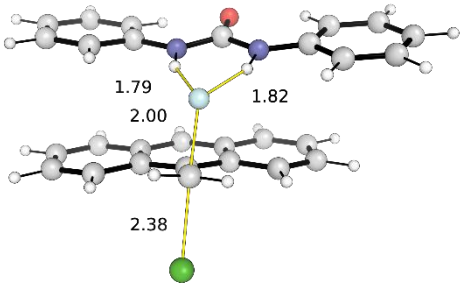

TS-F-Urea$_{H}$

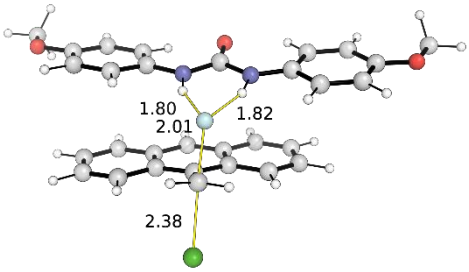

TS-F-Urea$_{OMe}$

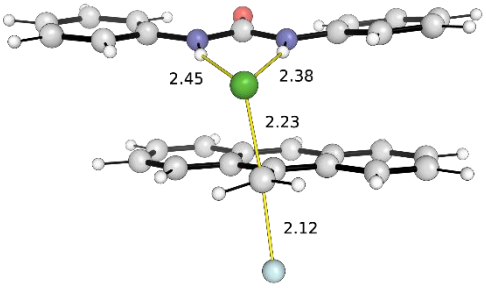

TS-Cl-Urea$_{H}$ (+ 24 kJ/mol)

Figure S26: Geometries of key species for homogeneous fluorination of chloride substrate.

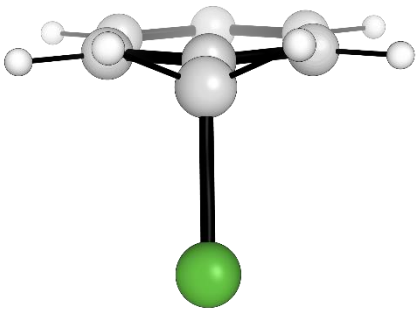

Ar$_1$Cl

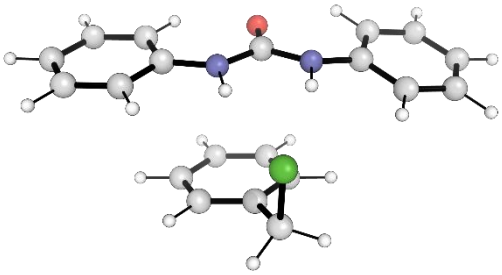

Ar$_1$Cl-Urea$_{H}$

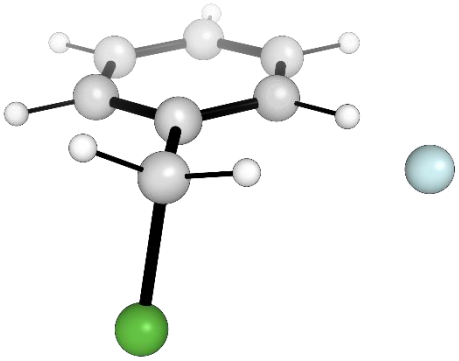

Ar$_1$Cl-F

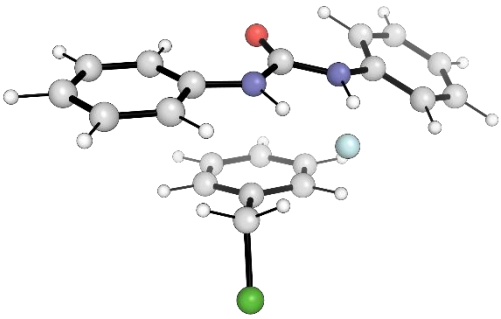

Ar$_1$Cl-F-Urea$_{H}$

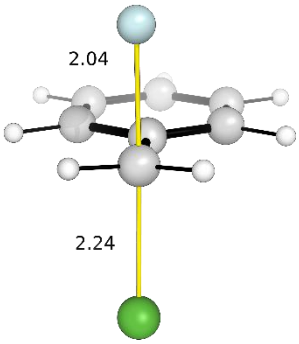

TS-Ar$_1$Cl-F

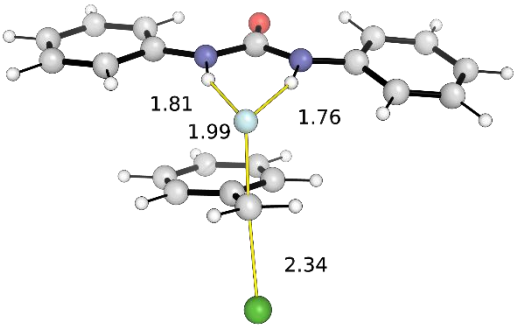

TS-Ar$_1$Cl-F-Urea$_H$

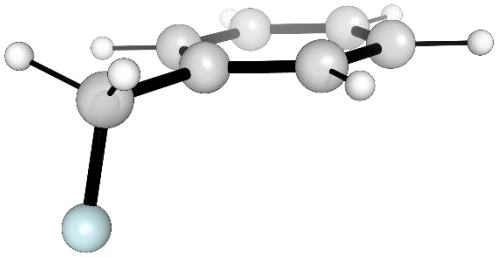

Ar$_1$F

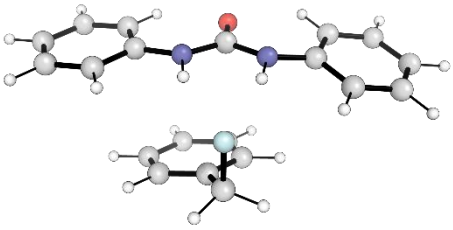

Ar$_1$F-Urea$_H$

Figure S27: Geometries of key species for homogeneous fluorination of **Ar$_1$Cl** substrate.

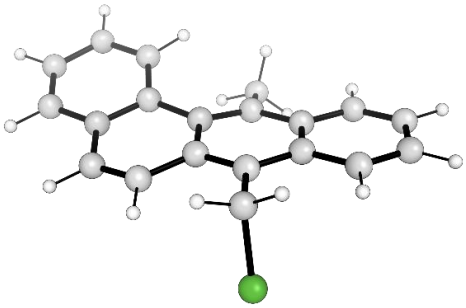

Ar$_4$Cl

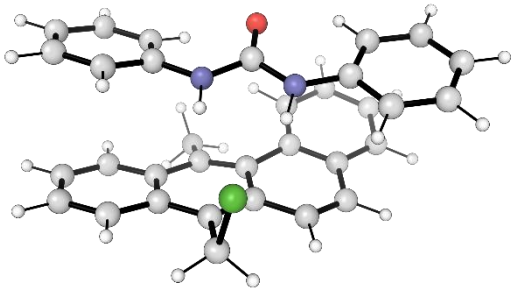

Ar$_4$Cl-Urea$_H$

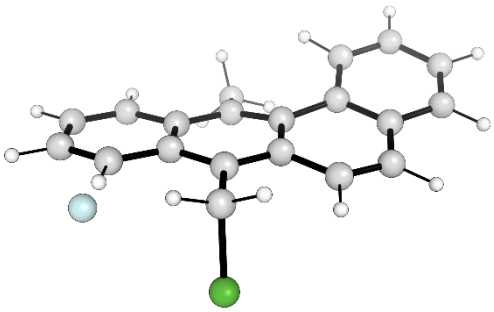

Ar$_4$Cl-F

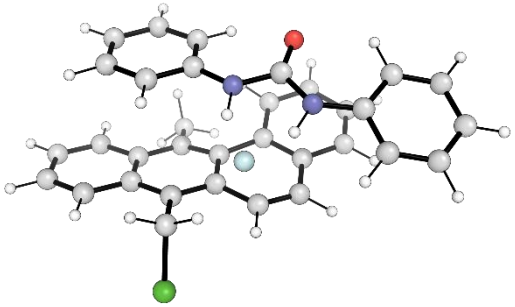

Ar$_4$Cl-F-Urea$_H$

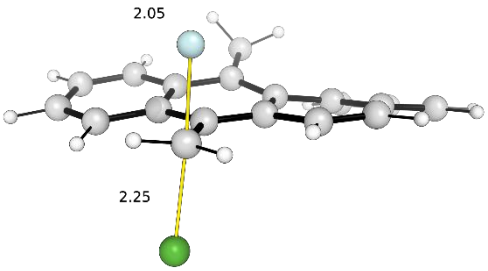

TS-Ar$_4$Cl-F

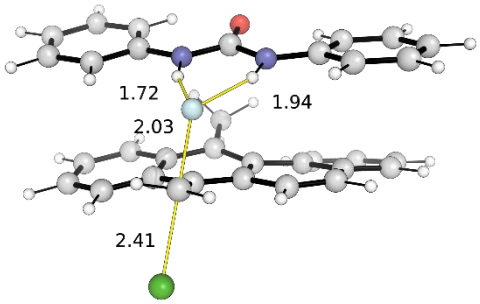

TS-Ar$_4$Cl-F-Urea$_H$

Figure S28: Geometries of key species for homogeneous fluorination of **Ar$_4$Cl** substrate.

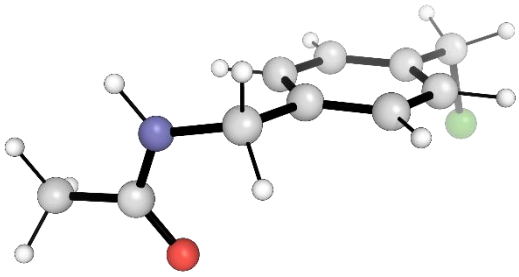

HB-Ar$_1$Cl

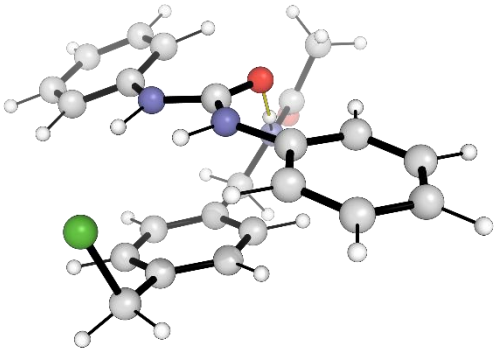

HB-Ar$_1$Cl-UreaH

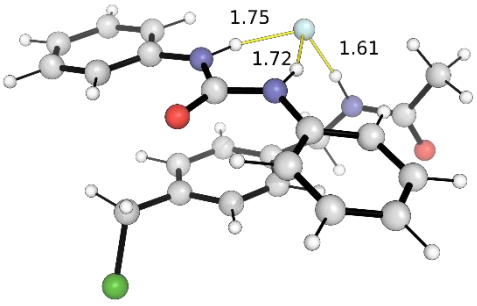

HB-Ar$_1$Cl-F-Urea$_H$ 1

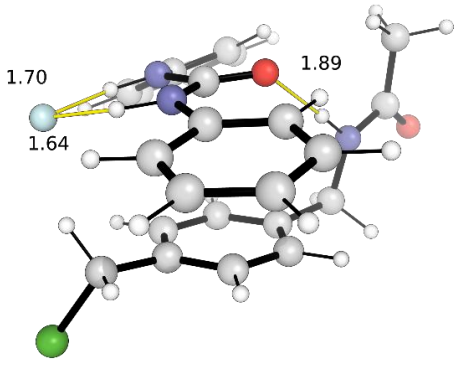

HB-Ar$_1$Cl-F-Urea$_H$ 2 (+ 13 kJ/mol)

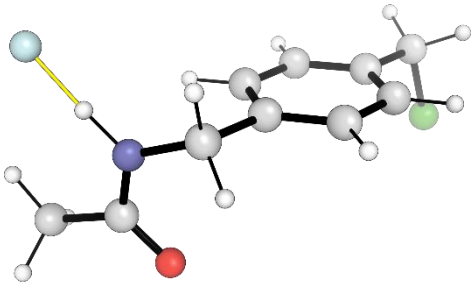

HB-Ar$_1$Cl-F 1

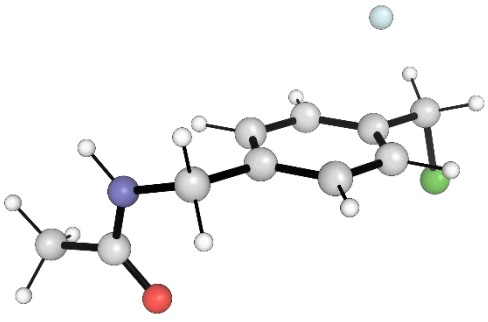

HB-Ar$_1$Cl-F 2 (+ 30 kJ/mol)

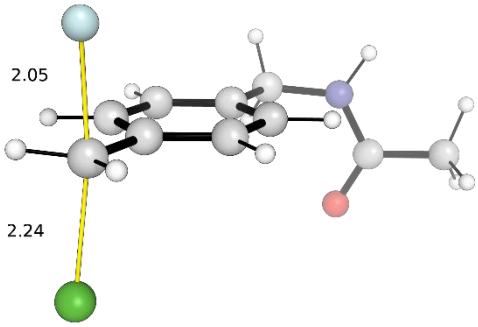

TS-HB-Ar$_1$Cl-F

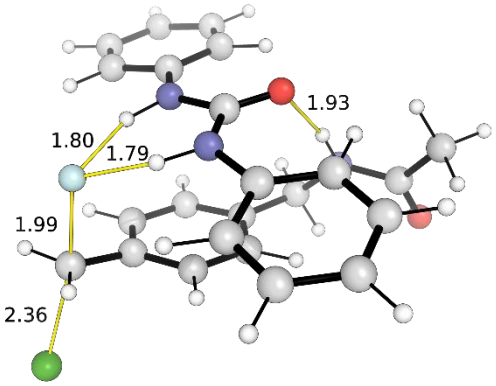

TS-HB-Ar$_1$Cl-F-Urea$_H$

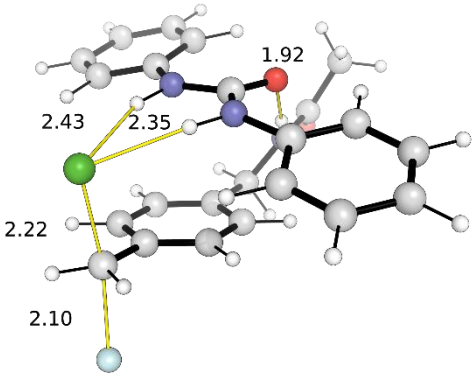

TS-HB-Ar$_1$Cl-Cl-Urea$_H$ (+26 kJ/mol)

Figure S29: Geometries of key species for homogeneous fluorination of **HB-Ar$_1$Cl** substrate.

6.4.3 Thermodynamic Data

Table S44: Second-Generation Catalysts.

	Energies / Ha				
	E (opt)	**G (opt)**	**G-qh (opt)**	**E (sp)**	**G-qh (sp)**
H8-cat-py-major	-2207.699509	-2206.902840	-2206.893622	-2210.309992	-2209.504105
H8-cat-py-minor	-2207.691504	-2206.898420	-2206.887380	-2210.304963	-2209.500839
H8-cat-py-3	-2207.692634	-2206.897216	-2206.887514	-2210.305155	-2209.500036
H8-cat-py-4	-2207.697114	-2206.896653	-2206.888505	-2210.301107	-2209.492498
H8-cat-py-5	-2207.693715	-2206.893646	-2206.885464	-2210.299734	-2209.491483
Cat-py-major	-2202.905692	-2202.198777	-2202.189763	-2205.461614	-2204.745685
Cat-py-minor	-2202.899913	-2202.194941	-2202.184871	-2205.458141	-2204.743100
Cat-py-CsF	-1893.590753	-1893.084282	-1893.075418	-	-

Table S45: Homogeneous Fluorination of 9-(bromomethyl)anthracene (298.15 K).

	Energies / Ha				
	E (opt)	**G (opt)**	**G-qh (opt)**	**E (sp)**	**G-qh (sp)**
$Urea_H$*	-686.606836	-686.419106	-686.415568	-687.448126	-687.256858
$Urea_{Schreiner}$	-2033.446586	-2033.263100	-2033.253486	-2035.918006	-2035.724906
$Urea_H$-F	-786.507967	-786.320933	-786.317634	-787.476991	-787.286657
$Urea_{Schreiner}$-F	-2133.354001	-2133.175552	-2133.164119	-2135.950596	-2135.760715
$Urea_H$-Br	-3260.698307	-3260.514561	-3260.510062	-3261.863384	-3261.675139
$Urea_{Schreiner}$-Br	-4607.541111	-4607.365015	-4607.352389	-4610.334699	-4610.145976
Ar_3Br	-3151.470482	-3151.292218	-3151.290721	-3152.499324	-3152.319563
Ar_3Br-$Urea_H$	-3838.102511	-3837.714503	-3837.708219	-3839.963551	-3839.569258
Ar_3Br-$Urea_{Schreiner}$	-5184.948335	-5184.563128	-5184.550209	-5188.438029	-5188.039903
Ar_3Br-F	-3251.347828	-3251.171899	-3251.169761	-3252.508452	-3252.330385
Ar_3Br-F-$Urea_H$	-3938.000886	-3937.615193	-3937.607926	-3939.990647	-3939.597687
Ar_3Br-F-$Urea_{Schreiner}$	-5284.852089	-5284.469740	-5284.456242	-5288.467979	-5288.072132
TS-F	-3251.328414	-3251.153145	-3251.151112	-3252.486380	-3252.309078
TS-F-$Urea_H$	-3937.978289	-3937.591778	-3937.585323	-3939.966889	-3939.573923
TS-F-$Urea_{Schreiner}$	-5284.828029	-5284.444625	-5284.431447	-5288.440663	-5288.044081
Ar_3F	-677.309700	-677.127366	-677.126247	-678.132935	-677.949482
Ar_3F-Br	-3251.389165	-3251.215238	-3251.210804	-3252.540375	-3252.362014
Ar_3F-Br-$Urea_H$	-3938.020117	-3937.635898	-3937.626852	-3940.004012	-3939.610747
Ar_3F-Br-$Urea_{Schreiner}$	-5284.866831	-5284.483966	-5284.469053	-5288.477447	-5288.079668
Ar_3F-$Urea_H$	-1363.939338	-1363.549079	-1363.542413	-1365.595654	-1365.198728
Ar_3F-$Urea_{Schreiner}$	-3251.389165	-3251.215238	-3251.210804	-3252.540375	-3252.362014
Fluoride	-99.869574	-99.880714	-99.880714	-100.007667	-100.018807
Bromide	-2574.076488	-2574.089645	-2574.089645	-2574.406666	-2574.419823
TS-Br-$Urea_H$	-3937.966001	-3937.581455	-3937.574392	-3939.955850	-3939.564240

* Low imaginary frequency.

Table S46: Homogeneous Fluorination of 9-(chloromethyl)anthracene (298.15 K).

	Energies / Ha				
	E (opt)	**G (opt)**	**G-qh (opt)**	**E (sp)**	**G-qh (sp)**
$Urea_{OMe}$	-915.403981	-915.156670	-915.152422	-916.531188	-916.279629
$Urea_{OMe}$-F	-1015.303910	-1015.058931	-1015.053897	-1016.558720	-1016.308707
Ar_3Cl	-1037.629667	-1037.449937	-1037.448580	-1038.492661	-1038.311575
Ar_3Cl-$Urea_H$	-1724.261447	-1723.872048	-1723.865970	-1725.956051	-1725.560574
Ar_3Cl-$Urea_{OMe}$	-1953.058875	-1952.610067	-1952.602555	-1955.039300	-1954.582980
Ar_3Cl-F	-1137.506735	-1137.328821	-1137.327201	-1138.501635	-1138.322101
Ar_3Cl-F-$Urea_H$	-1824.159688	-1823.770404	-1823.764588	-1825.984329	-1825.589230

Ar_3Cl-F-$Urea_{OMe}$	-2052.958504	-2052.510601	-2052.502786	-2055.067390	-2054.611671
TS-F	-1137.483768	-1137.306911	-1137.305123	-1138.475825	-1138.297180
TS-F-$Urea_H$	-1824.132931	-1823.744845	-1823.738859	-1825.955462	-1825.561390
TS-Ar_3Cl-F-$Urea_{OMe}$	-2052.929723	-2052.483225	-2052.475330	-2055.038100	-2054.583707
TS- Ar_3Cl-Cl-$Urea_H$	-1824.122576	-1823.734701	-1823.728811	-1825.945831	-1825.552066

Table S47: Homogeneous Fluorination of **Ar_xCl** Substrates.

	Energies / Ha				
	E (opt)	**G (opt)**	**G-qh (opt)**	**E (sp)**	**G-qh (sp)**
Ar_1Cl	-730.694907	-730.603687	-730.602947	-731.201618	-731.109658
Ar_1Cl-$Urea_H$	-1417.319795	-1417.021414	-1417.015352	-1418.660551	-1418.356108
Ar_1Cl-F	-830.569443	-830.481574	-830.480036	-831.209610	-831.120203
Ar_1Cl-F-$Urea_H$	-1517.218875	-1516.920704	-1516.914897	-1518.688424	-1518.384445
TS-Ar_1Cl-F	-830.547958	-830.459074	-830.458383	-831.184833	-831.095258
TS-Ar_1Cl-F-$Urea_H$	-1517.190406	-1516.892741	-1516.887005	-1518.658470	-1518.355068
Ar_1F	-370.376216	-370.283931	-370.282497	-370.843474	-370.749755
Ar_1F-$Urea_H$	-1057.000201	-1056.698890	-1056.693171	-1058.301120	-1057.994090
Ar_4Cl	-1230.362339	-1230.111347	-1230.109277	-1231.458320	-1231.205258
Ar_4Cl-$Urea_H$	-1916.997941	-1916.536312	-1916.529751	-1918.925159	-1918.456969
Ar_4Cl-F	-1330.239539	-1329.990701	-1329.988047	-1331.467480	-1331.215988
Ar_4Cl-F-$Urea_H$	-2016.894601	-2016.433744	-2016.427092	-2018.951273	-2018.483765
TS-Ar_4Cl-F	-1330.216064	-1329.968480	-1329.965790	-1331.441418	-1331.191145
TS-Ar_4Cl-F-$Urea_H$	-2016.868041	-2016.407817	-2016.401498	-2018.923209	-2018.456666

Table S48: Homogeneous Fluorination with **HB-Ar_1Cl**.

	Energies / Ha				
	E (opt)	**G (opt)**	**G-qh (opt)**	**E (sp)**	**G-qh (sp)**
HB-Ar_1Cl	-977.759110	-977.595229	-977.591505	-978.580952	-978.413347
HB-Ar_1Cl-$Urea_H$	-1664.391499	-1664.016661	-1664.008923	-1666.045226	-1665.662649
HB-Ar_1Cl-F 1	-1077.648393	-1077.487251	-1077.483379	-1078.600237	-1078.435223
HB-Ar_1Cl-F 2	-1077.633426	-1077.471911	-1077.467663	-1078.589410	-1078.423647
HB-Ar_1Cl-F-$Urea_H$ 1	-1764.295369	-1763.922164	-1763.913714	-1766.079087	-1765.697431
HB-Ar_1Cl-F-$Urea_H$-2	-1764.290674	-1763.917001	-1763.908957	-1766.074345	-1765.692628
TS-HB-Ar_1Cl-F	-1077.612116	-1077.450084	-1077.446469	-1078.564144	-1078.398497
TS-HB-Ar_1Cl-F-$Urea_H$	-1764.262443	-1763.889443	-1763.881185	-1766.043631	-1765.662374
TS-HB-Ar_1Cl-Cl-$Urea_H$	-1764.251513	-1763.877247	-1763.869961	-1766.034154	-1765.652602

6.5 References

(1) Pupo, G.; Ibba, F.; Ascough, D. M. H.; Vicini, A. C.; Ricci, P.; Christensen, K. E.; Pfeifer, L.; Morphy, J. R.; Brown, J. M.; Paton, R. S.; Gouverneur, V. Asymmetric Nucleophilic Fluorination under Hydrogen Bonding Phase-Transfer Catalysis. *Science* **2018**, *360*, 638–642.

(2) Haynes, W. M.; Lide, D. R.; Bruno, T. J. *CRC Handbook of Chemistry and Physics*, 97th editi.; Taylor & Francis Inc., 2017.

(3) Marcus, Y.; Loewenschuss, A. Standard Entropies of Hydration of Ions. *Annu. Rep. Prog. Chem., Sect. C Phys. Chem.* **1984**, *81*, 81–135.

(4) Luchini, G.; Ascough, D. M. H.; Alegre-Requena, J. V.; Gouverneur, V.; Paton, R. S. Data-Mining the Diaryl(Thio)Urea Conformational Landscape: Understanding the Contrasting Behavior of Ureas and Thioureas with Quantum Chemistry. *Tetrahedron* **2019**, *75*, 697–702.

(5) Pupo, G.; Vicini, A. C.; Ascough, D. M. H.; Ibba, F.; Christensen, K. E.; Thompson, A. L.; Brown, J. M.; Paton, R. S.; Gouverneur, V. Hydrogen Bonding Phase-Transfer Catalysis with Potassium Fluoride: Enantioselective Synthesis of β-Fluoroamines. *J. Am. Chem. Soc.* **2019**, *141*, 2878–2883.

(6) Chase Jr., M. W. NIST-JANAF Thermochemical Tables, Fourth Edition. *J. Phys. Chem. Ref. Monogr. 9* **1998**, 1–1951.